frontiers | Research Topics

Bioactive substances-mediated targeted therapy of cardio-cerebrovascular diseases

Edited by
Guixue Wang, Yi Tan, Xiaoyong Tong and Linxi Chen

Published in
Frontiers in Pharmacology

ISSN 1664-8714
ISBN 978-2-83251-699-7
DOI 10.3389/978-2-83251-699-7

About Frontiers

Frontiers is more than just an open access publisher of scholarly articles: it is a pioneering approach to the world of academia, radically improving the way scholarly research is managed. The grand vision of Frontiers is a world where all people have an equal opportunity to seek, share and generate knowledge. Frontiers provides immediate and permanent online open access to all its publications, but this alone is not enough to realize our grand goals.

Frontiers journal series

The Frontiers journal series is a multi-tier and interdisciplinary set of open-access, online journals, promising a paradigm shift from the current review, selection and dissemination processes in academic publishing. All Frontiers journals are driven by researchers for researchers; therefore, they constitute a service to the scholarly community. At the same time, the *Frontiers journal series* operates on a revolutionary invention, the tiered publishing system, initially addressing specific communities of scholars, and gradually climbing up to broader public understanding, thus serving the interests of the lay society, too.

Dedication to quality

Each Frontiers article is a landmark of the highest quality, thanks to genuinely collaborative interactions between authors and review editors, who include some of the world's best academicians. Research must be certified by peers before entering a stream of knowledge that may eventually reach the public - and shape society; therefore, Frontiers only applies the most rigorous and unbiased reviews. Frontiers revolutionizes research publishing by freely delivering the most outstanding research, evaluated with no bias from both the academic and social point of view. By applying the most advanced information technologies, Frontiers is catapulting scholarly publishing into a new generation.

What are Frontiers Research Topics?

Frontiers Research Topics are very popular trademarks of the *Frontiers journals series*: they are collections of at least ten articles, all centered on a particular subject. With their unique mix of varied contributions from Original Research to Review Articles, Frontiers Research Topics unify the most influential researchers, the latest key findings and historical advances in a hot research area.

Find out more on how to host your own Frontiers Research Topic or contribute to one as an author by contacting the Frontiers editorial office: frontiersin.org/about/contact

Bioactive substances-mediated targeted therapy of cardio-cerebrovascular diseases

Topic editors

Guixue Wang — Chongqing University, China
Yi Tan — University of Louisville, United States
Xiaoyong Tong — Chongqing University, China
Linxi Chen — University of South China, China

Citation

Wang, G., Tan, Y., Tong, X., Chen, L., eds. (2023). *Bioactive substances-mediated targeted therapy of cardio-cerebrovascular diseases*. Lausanne: Frontiers Media SA. doi: 10.3389/978-2-83251-699-7

Table of contents

frontiers | Frontiers in Pharmacology

TYPE Editorial
PUBLISHED 02 February 2023
DOI 10.3389/fphar.2023.1146426

OPEN ACCESS

EDITED AND REVIEWED BY
Ajeet Kaushik,
Florida Polytechnic University,
United States

*CORRESPONDENCE
Xiaoyong Tong,
xiaoyongtong@cqu.edu.cn
Guixue Wang,
wanggx@cqu.edu.cn

SPECIALTY SECTION
This article was submitted to Cardiovascular and Smooth Muscle Pharmacology, a section of the journal Frontiers in Pharmacology

RECEIVED 17 January 2023
ACCEPTED 27 January 2023
PUBLISHED 02 February 2023

CITATION
Tong X, Tan Y, Chen L and Wang G (2023), Editorial: Bioactive substances-mediated targeted therapy of cardio-cerebrovascular diseases.
Front. Pharmacol. 14:1146426.
doi: 10.3389/fphar.2023.1146426

Editorial: Bioactive substances-mediated targeted therapy of cardio-cerebrovascular diseases

Xiaoyong Tong[1]*, Yi Tan[2], Linxi Chen[3] and Guixue Wang[4]*

[1]School of Pharmaceutical Sciences, Chongqing University, Chongqing, China, [2]University of Louisville School of Medicine, Louisville, KY, United States, [3]Institute of Pharmacy and Pharmacology, University of South China, Hengyang, Hunan, China, [4]Key Laboratory of Biorheological and Technology of Ministry of Education, State and Local Joint Engineering Laboratory for Vascular Implants, Modern Life Science Experiment Teaching Center at Bioengineering College of Chongqing University, Chongqing, China

KEYWORDS

cardio-cerebrovascular diseases, bio-nanotechnology, bioactive substance, Traditional Chinese Medicine, targeted drug delivery

Editorial on the Research Topic
Bioactive substances-mediated targeted therapy of cardio-cerebrovascular diseases

Cardio-cerebrovascular diseases (CVDs), one of the leading causes of death worldwide, are a broad spectrum of serious health conditions including heart disease, hypertension, stroke, atherosclerosis, retinopathy, etc. The pathogenesis and clinical features of CVDs have been well-studied in the past decades. However, precision medicine which leaves out normal tissue and only targets pathogenic molecules or cells is limited. The currently available or FDA-approved drugs are insufficient to treat most of these diseases, so there is an urgent need for new candidate drugs and/or strategies for drug delivery.

The rapid advances in bio-nanotechnology and bioactive substances allow the feasibility of the design and implementation of strategies for targeted drug delivery to treat CVDs and the invention of cardio-cerebrovascular regenerative medicine. Compared with newly discovered drugs, the active ingredients and derivatives of Traditional Chinese Medicine (TCM) have attracted more attention in CVD treatment as they involve lower risk, possible reduction of expenditure and shorter development time for they have been sold and tested on the market for a long time.

The Research Topic "Bioactive substances-mediated targeted therapy of cardio-cerebrovascular diseases" aims to create a forum for current advances in preclinical and clinical studies utilizing bioactive substances materials and active components of TCM and related composites, to design and develop therapies that specifically target molecular and cellular pathogenesis of CVD to support, enhance, or replace damaged CVD tissues or biological functions while focusing on the topics within the scope of the journal. This topic is led by the above four Guest Editors, who are experts on this topic and supervise the whole editing process of submitting papers. A total of eleven articles were published, including eight original research and three review articles.

Ferroptosis is closely related to cardiomyocyte death. Clioquinol can inhibit ferroptosis. Li et al. used porous lipid-poly (lactic-co-glycolic acid) microbubbles as carriers to deliver clioquinol, which showed the advantages of high drug loading, good biocompatibility,

sustained release, improved effect of clioquinol and reduced its cytotoxicity as tested in cardiomyocytes.

Bhattacharjee et al. reported that the phenolic compounds in Garcinia pedunculata extract protected against isoproterenol-induced rat cardiac hypertrophy by reducing oxidative stress and inflammation, suggesting the cardioprotective potential of Garcinia pedunculata.

Lv et al. reported that Icariside II, a flavonol glycoside derived from the TCM Herba Epimedii, suppressed vascular smooth muscle cell phenotypic transition by modulating the focal adhesion signaling pathway, and improved vascular remodeling in a rat's balloon injury model. Their research emphasizes the therapeutic efficacy and underlying mechanisms of Icariside II on vascular remodeling.

Dan-Shen-Yin is a TCM used in the treatment of CVDs. Endothelial-to-mesenchymal transition plays an important role in the pathogenesis of atherosclerosis. Hong et al. employed a network pharmacology-based strategy and found that Dan-Shen-Yin could inhibit endothelial-to-mesenchymal transition by suppressing the integrin/PI3K/AKT signaling pathway, proposing a potential therapeutic intervention for atherosclerosis.

Rhizoma Corydalis is clinically used to treat myocardial infarction in China. By network pharmacology and experimental verification, Li et al. reported that Rhizoma Corydalis protected against myocardial infarction by activating the PI3K/AKT pathway, providing a scientific basis for Rhizoma Corydalis in treating myocardial infarction.

In a transverse aortic constriction mouse model, Zhang et al. found that a (Pro)renin receptor decoy inhibitor PRO20 retarded cardiac remodeling and heart failure by increasing cAMP levels and reducing endoplasmic reticulum stress in both cardiomyocytes and cardiac fibroblasts.

Safflower is an important TCM for promoting blood circulation and removing blood stasis. Wang et al. reported that its bioactive compound 6-hydroxykaempferol 3,6-di-O-glucoside-7-O-glucuronide protected against endothelial injury by regulating expressions of hypoxia-inducible factor-1 alpha and nuclear factor kappa B, and exhibited anti-thrombotic activity in phenylhydrazine-induced zebrafish thrombosis model.

Obesity is a potential risk factor for CVDs. Jiang et al. used transcriptomic analyses to identify genes associated with the regulation of myogenic differentiation and found that apolipoprotein L 9a regulated myogenic differentiation by activating the ERK1/2 pathway, which provides a promising therapeutic target for intervention in obesity-induced muscle atrophy.

In a review article, Yang et al. discussed the drug delivery system based on nanoparticles for CVD treatment. The drug delivery system based on nanoparticles changes the biological distribution of therapeutic agents through targeted delivery and controlled drug release of precise drugs. Nanoparticles based on metals, lipids and polymers are ideal materials for CVD treatment. In addition, this review also discusses the potential role of nanoparticles in metabolism and post-therapeutic toxicity.

Macrophage is a major contributor to atherosclerosis progression, and its associated pathological process is an important target for diagnosing and treating atherosclerosis. In a review article, Hu et al. specifically summarized the macrophage-targeted nanomedicine for the diagnosis and management of atherosclerosis, their potential applications and clinical benefits.

Stem cell-based therapies have emerged as promising treatment options for CVDs. In a mini review, Ma et al. summarized the current means of treatment of long non-coding RNAs from stem cell-derived exosomes for CVDs and discussed the current challenges and prospects of long non-coding RNAs treatment for CVDs.

Despite progress in the management of CVDs, drug treatment is still not ideal due to poor pharmacokinetics and high toxicity. This Research Topic has an in-depth understanding of the latest research findings and updates related to the ongoing strategy and drug discovery research in various treatment areas of current interest, including technological progress and challenges. The rapid development of biological nanotechnology, bioactive substances as well as the development of active ingredients and derivatives of TCM have received more attention, however, challenges lie ahead. Key assessments of preclinical, clinical and observational data/evidence are needed to investigate candidate drug efficacy and safety/toxicity.

Author contributions

All authors listed have made a substantial, direct, and intellectual contribution to the work and approved it for publication.

Acknowledgments

The authors would like to thank all the authors and reviewers for their invaluable contributions to this Research Topic.

Conflict of interest

The authors declare that the research was conducted in the absence of any commercial or financial relationships that could be construed as a potential conflict of interest.

Publisher's note

frontiers | Frontiers in Pharmacology

ORIGINAL RESEARCH
published: 13 June 2022
doi: 10.3389/fphar.2022.897615

Icariside II Restores Vascular Smooth Muscle Cell Contractile Phenotype by Enhancing the Focal Adhesion Signaling Pathway in the Rat Vascular Remodeling Model

*Junyuan Lv[1], Xintong Li[2], Hongyu Wu[3], Jiayang Li[4], Boyang Luan[5], Yiqi Li[3], Yeli Li[3], Danli Yang[3] and Hao Wen[5]**

[1]Breast and Thyroid Surgery, Department of General Surgery, The Affiliated Hospital of Zunyi Medical University, Zunyi, China, [2]Department of Vascular Surgery, The First Affiliated Hospital of China Medical University, Shenyang, China, [3]Key Laboratory of Basic Pharmacology of Ministry of Education and Joint International Research Laboratory of Ethnomedicine of Ministry of Education, Zunyi Medical University, Zunyi, China, [4]Drug Clinical Trial Institution, The Affiliated Hospital of Zunyi Medical University, Zunyi, China, [5]Department of Trauma Center, The First Affiliated Hospital of China Medical University, Shenyang, China

OPEN ACCESS

Edited by:
Yi Tan,
University of Louisville, United States

Reviewed by:
Jinwei Tian,
The Second Affiliated Hospital of Harbin Medical University, China
Jun Ren,
Fudan University, China

***Correspondence:**
Hao Wen
wenhao@cmu.edu.cn

Specialty section:
This article was submitted to Cardiovascular and Smooth Muscle Pharmacology, a section of the journal Frontiers in Pharmacology

Received: *16 March 2022*
Accepted: *03 May 2022*
Published: *13 June 2022*

Citation:
Lv J, Li X, Wu H, Li J, Luan B, Li Y, Li Y, Yang D and Wen H (2022) Icariside II Restores Vascular Smooth Muscle Cell Contractile Phenotype by Enhancing the Focal Adhesion Signaling Pathway in the Rat Vascular Remodeling Model. Front. Pharmacol. 13:897615. doi: 10.3389/fphar.2022.897615

Vascular smooth muscle cell (VSMC) phenotypic transition represents the fundamental pathophysiological alteration in the vascular remodeling process during the initiation and progression of cardiovascular diseases. Recent studies have revealed that Icariside II (ICS-II), a flavonol glycoside derived from the traditional Chinese medicine Herba Epimedii, exhibited therapeutic effects in various cardiovascular diseases. However, the therapeutic efficacy and underlying mechanisms of ICS-II regarding VSMC phenotypic transition were unknown. In this study, we investigated the therapeutic effects of ICS-II on vascular remodeling with a rat's balloon injury model *in vivo*. The label-free proteomic analysis was further implemented to identify the differentially expressed proteins (DEPs) after ICS-II intervention. Gene ontology and the pathway enrichment analysis were performed based on DEPs. Moreover, platelet-derived growth factor (PDGF-BB)-induced primary rat VSMC was implemented to verify the restoration effects of ICS-II on the VSMC contractile phenotype. Results showed that ICS-II could effectively attenuate the vascular remodeling process, promote SMA-α protein expression, and inhibit OPN expression *in vivo*. The proteomic analysis identified 145 differentially expressed proteins after ICS-II intervention. Further, the bioinformatics analysis indicated that the focal adhesion signaling pathway was enriched in the ICS-II group. *In vitro* studies showed that ICS-II suppressed VSMC proliferation and migration, and promoted VSMC contractile phenotype by modulating the focal adhesion signaling pathway. Taken together, our results suggest that ICS-II attenuates the vascular remodeling process and restores the VSMC contractile phenotype by promoting the focal adhesion pathway.

Keywords: icariside II, vascular smooth muscle cell, phenotypic transition, vascular remodeling, herbal medicine

INTRODUCTION

Cardiovascular diseases (CVD) and associated co-morbidities are the leading cause of death globally (Roth et al., 2020). Many of these pathologies such as hypertension (Renna et al., 2013), atherosclerosis (Kiechl and Willeit, 1999), stenosis (Pasterkamp et al., 2000), and aneurysms (Frösen et al., 2019; Cañes et al., 2021) are accompanied by sophisticated pathophysiological alterations of the vascular tone and structure, in response to external stimuli as well as genetic preconditioning, which is termed as vascular remodeling (Lyle and Taylor, 2019). The phenotypic transition of vascular smooth muscle cells (VSMCs) in the media, the most dominant cell type in vessel wall composition, plays an essential role in vascular remodeling (Jaminon et al., 2019; Shi et al., 2019). Thereby, medical treatments targeting the VSMC phenotypic transition are crucial for overcoming the tremendous burden caused by vascular remodeling of CVDs on human health (Chakraborty et al., 2021).

To date, several pharmaceuticals targeting VSMC phenotypic transition, including rapamycin and paclitaxel, have been applied in clinical practice to reverse the vascular remodeling process (Briguori et al., 2021). In addition, recently, herbal medicines, especially derivatives from anti-atherosclerotic plants, are raising attention for modulating the VSMC phenotypic transition (Saleh Al-Shehabi et al., 2016). Icariside II (ICS-II, C27H30O10, 514.57 g/mol), the bioactive metabolic ingredients of the traditional Chinese medicine Herba Epimedii, have been reported to exhibit a wide range of biological and pharmacological properties including anti-inflammatory, anti-apoptotic, and anti-cancer properties (Zheng et al., 2020). Furthermore, substantial investigations revealed the valid therapeutic efficacy of ICS-II in various cardiovascular diseases (Qi et al., 2017; Liu et al., 2018; Guan et al., 2020). However, evidence about ICS-II in the VSMC phenotypic modulation is still limited and needs to be further elucidated.

Thus, the present study aims to investigate the pharmacological effects of ICS-II on the VSMC phenotypic transition and reveal the underlying mechanisms through *in vivo* and *in vitro* experiments. Our results highlight the therapeutic benefits of ICS-II targeting VSMC phenotypic transition and support the potential of pharmacological strategies in CVD management.

MATERIALS AND METHODS

Ethics

The protocols and procedures in this present study were approved by the Experimental Ethics Committee of Zunyi Medical University. All protocols were consistent with the Guide for the Care and Use of Experimental Animals at the Animal Center of Zunyi Medical University.

Study Design and Animal Model Induction

A total of 30 SPF (specific pathogen-free) male Sprague–Dawley (SD) rats (body weight:300–400 g) were used in this study. The rats were randomly divided into three groups and subjected to the following treatments: the sham group (n = 10): received a sham operation with the same volume of saline by gavage daily; the control group (n = 10): model induction with the same volume of saline by gavage daily; the ICS-II group (n = 10): model induction with ICS-II 20 mg/kg by gavage daily. The protocols for the rat carotid artery balloon injury model were described previously (Lv et al., 2018). Briefly, the rats were anesthetized with 5% isoflurane in oxygen. A midline cervical incision was made to expose the bilateral carotid arteries. A 2F Fogarty balloon catheter (Edwards Lifesciences Corporation; United States) was inserted into the left common carotid artery (CCA) three times to disrupt the endothelium through the external carotid artery (ECA). After that, the ECA was sutured and the left CCA was re-perfused. All processes during the operation were performed by a single researcher. All rats were euthanized on day 14 for the following experiments.

Morphometric Analysis

For the morphometric analysis, artery samples were fixed in 4% paraformaldehyde, embedded in paraffin, and then sectioned into 4 mm thickness. After deparaffinization and rehydration, sections were stained with hematoxylin and eosin (H&E) to observe the morphological changes. For each section, five randomly selected non-continuous microscopic fields were pictured to determine the mean thickness value of the intima and media, respectively. Finally, the thickness ratio of intima to media of each section was determined.

Immunohistochemistry

IHC experiments were implemented for assessing the protein expression level of the VSMC synthetic marker OPN *in vitro*. Protocols for the IHC experiments were described previously (Wen et al., 2020). In brief, after de-paraffinization and rehydration, sections were incubated with 3% H_2O_2 to deactivate endogenous peroxidase followed by a heat-induced antigen retrieval process. Then, sections were incubated with primary and secondary antibodies before image acquisition.

Tissue Lysis and Protein Extraction

The arterial tissue samples were lysed with an SDT (4% SDS in 0.1 M Tris-HCl, pH = 7.6) solution, transferred into a Lysing Matrix A (MP, cat: 6910-100-99219) tube, and homogenized and broken with an MP homogenizer (MP Fastprep-24 5G, 24 × 2, 6.0 M/S, 60 s, twice). The supernatant was filtered through a 0.22 μm centrifuge tube and the filtrate was collected. Protein quantification was performed using the BCA (Beyotime Biotechnology, P0012) method. About 80 μg of the protein solution was taken for each sample, and DTT (dithiothreitol, Sigma, 43819-5G) was added to a final concentration of 100 mM, boiled for 5 min, and cooled to room temperature. Then, 200 μL of the UA (8 M urea in 0.15 M Tris-HCl, pH = 8.5) buffer was added, mixed, and transferred to a 30 kDa ultracentrifuge tube (Sartorius, VN01H22); the mixture was centrifuged at 12,500 g for 15 min, and the filtrate (repeat this step once) was discarded. Further, 100 μL of IAA (iodoacetamide, Sigma, I1149-5G) buffer (100 mM IAA in UA) was added and the mixture was shaken at

600 rpm for 1 min and centrifuged at room temperature for 30 min at 12,500 g for 15 min. Then, 100 μL of the UA buffer was added and centrifuged at 12,500 g for 15 min. Subsequently, 100 μL of 40 mM NH_4HCO_3 solution was added, centrifuged at 12,500 g for 15 min, and the procedure was repeated twice. After that, 40 μL of trypsin buffer (4 μg of trypsin in 40 μL of 40 mM NH_4HCO_3 solution) was added and the mixture was shaken at 600 rpm for 1 min, and allowed to stand at 37°C for 16–18 h. The collection tube was replaced with a new one and centrifuged at 12,500 g for 15 min; then 20 μL of 40 mM NH_4HCO_3 solution was added and centrifuged at 12,500 g for 15 min, and the filtrate was collected. The peptide was desalted by C18 Cartridge (Waters, WAT023590), and 40 μL of 0.1% formic acid (Thermo Fisher Scientific, A117) solution was added after the peptide was lyophilized; the peptide was quantified (OD 280).

Label-free Quantitative Proteomic Analysis

For LC–MS/MS analysis, each sample was analyzed using the Easy nLC system (Thermo Fisher Scientific). Buffer solution A was 0.1% formic acid in water and solution B was 0.1% formic acid with 80% acetonitrile in water. The chromatographic column was equilibrated with 100% solution A. Samples were separated by autosampler loading onto an analytical column (Thermo Fisher Scientific, Acclaim PepMap RSLC 50 μm × 15 cm, nano Viper, P/N164943) at a flow rate of 300 nL/min. The samples were separated by chromatography and analyzed by mass spectrometry using a Q Exactive (Thermo Fisher Scientific) mass spectrometer. Precursor mass spectra were recorded in a 350–1,800m/z (mass/charge ratio) mass range at 70,000 resolution and 17,500 resolution for fragment ions. Data obtained were analyzed using MaxQuant (version 1.5.5.1) against the UniProt database (Uniprot_RattusNorvegicus_36080_20180123) based on the LFQ (label-free quantitation) method (Cox et al., 2014) with the following parameters: enzyme, trypsin; max missed cleavages, two; main search, 4.5 ppm; first search, 20 pp; MS/MS tolerance, 20 ppm; fixed modification, carbamidomethyl (C); dynamic modification, oxidation (M), acetyl (protein N-term); peptide and protein FDR (false discovery rate), <0.01.

Analysis of Differentially Expressed Proteins (DEPs)

The DEP Package (Zhang et al., 2018) in R software (version: 4.0.2) was applied for differentially expressed protein analysis. Proteins were filtered to remove contaminants and missing values in more than one sample per group. Then, background correction and normalization by the variance-stabilizing transformations method (Huber et al., 2002) were performed. The remaining missing values were estimated and imputed by impute.MinProb function for left-censored missing data (Lazar, 2015). A differential expression analysis based on protein-wise linear models with empirical Bayes statistics was then performed on the imputed dataset. Proteins with the absolute value of fold change >1.5 and p-value < 0.05 were identified as significant DEPs.

Construction of Protein–Protein Interaction (PPI) Network

Construction of the PPI network was implemented with the Search Tool for Retrieval of Interacting Genes/Proteins (STRING: https://string-db.org/) database (Szklarczyk et al., 2019) with criteria of medium confidence (interaction score >0.4). Then, the derived PPI network was visualized and analyzed by the analysis network function via Cytoscape (version 3.8.0) (Shannon et al., 2003) software. Proteins in the aforementioned PPI network with a degree >5 were selected for visualization and subsequent enrichment analysis.

Functional and Pathway Enrichment Analysis

Enrichment analysis regarding Gene Ontology (GO) (Ashburner et al., 2000) terms describing the biological process (BP), molecular function (MF), and cellular component (CC), as well as the Kyoto Encyclopedia of Genes and Genomes (KEGG) (Ogata et al., 1999) pathway, were performed by using the clusterProfiler (Yu et al., 2012) package in R. Enriched terms with FDR <0.05 were selected and visualized.

Cell Culture and Experimental Design

Rat VSMCs were primarily isolated and cultured by the explant method as described previously (Li et al., 2020). In brief, thoracic aortas were gently dissected from 8-week-old male SD rats and the surrounding connective tissue was removed. Aortas were longitudinally dissected, and the epithelial monolayer was detached by scraping. Tissue fragments were delivered to culture plates with Dulbecco's modified Eagle's medium (DMEM) supplemented with 10% fetal bovine serum (FBS) and 1% penicillin/streptomycin. After 2 days, tissue fragments were removed and the sprouting VSMCs were maintained until 80% confluence. Cells were trypsinized and seeded on a culture flask for *in vitro* experiments. All cells were maintained in a humidified atmosphere containing 5% CO_2 at 37°C, and passages between three and six were used in the present study.

The primarily cultured VSMCs were randomly divided into three experimental groups: the control group, 0.5% DMSO; the PDGF group, 25 ng/ml PDGF; and the ICS-II group, 20 μM ICS-II + 25 ng/ml PDGF. All experimental cell groups were incubated with corresponding drugs for 24 h, respectively.

Immunofluorescence (IF)

Briefly, cells were seeded onto coverslips and incubated for 24 h in 6-well plates. After that, the cells were fixed with formaldehyde and permeabilized with 0.25% Triton X-100 in PBS and 1% bovine serum albumin (BSA) for 5 min. Cells were then blocked with 5% goat serum in PBS for 1 h. Then, the cells were incubated with primary antibodies overnight at 4°C and treated with secondary antibodies in 3% BSA in PBS for 2.5 h at room temperature. Then, the nuclei were stained with 4′,6-diamidino-2-phenylindole (DAPI) and observed under a fluorescence microscope. Negative isotypes were incubated with PBS under the same conditions.

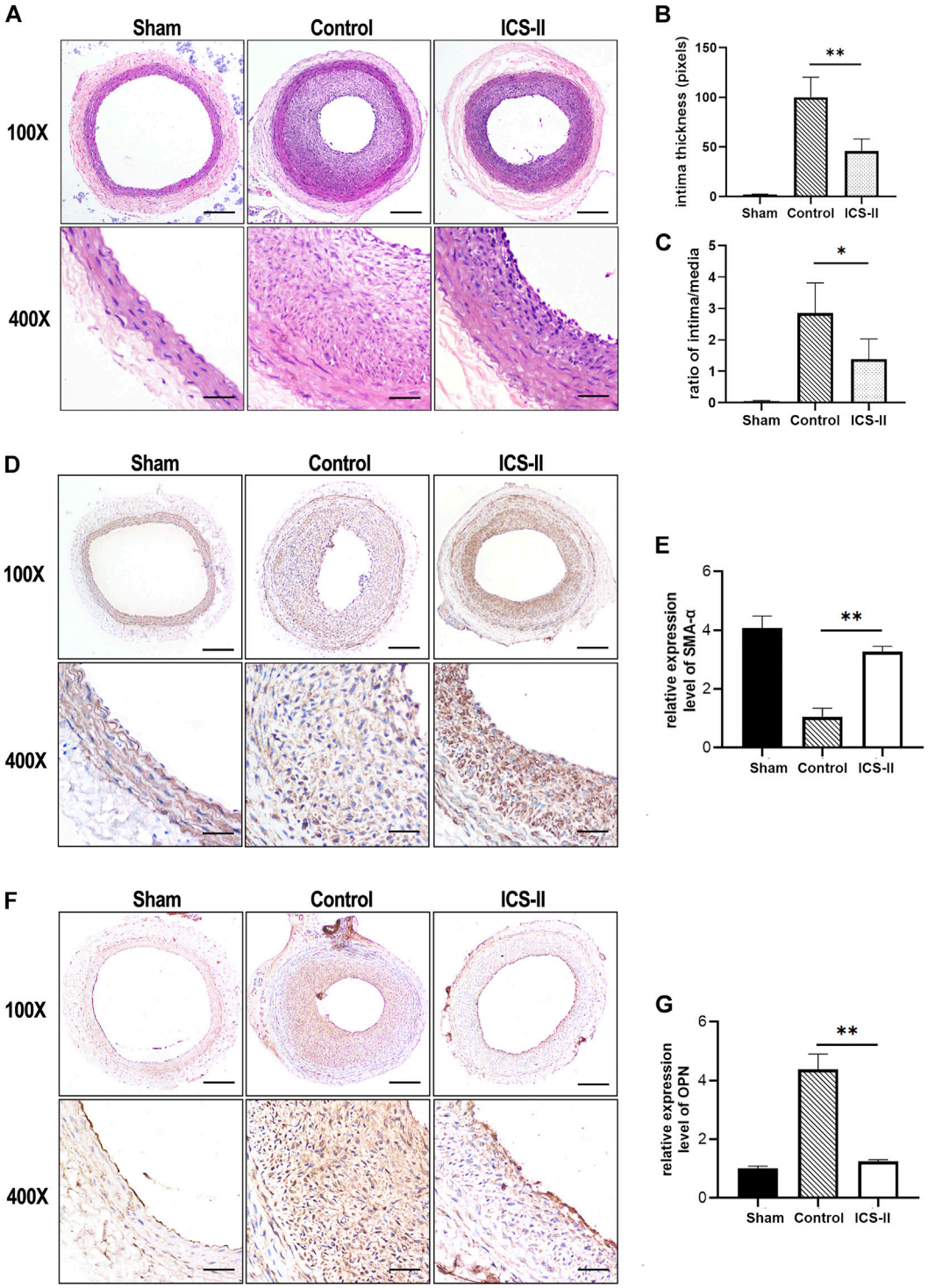

FIGURE 1 | ICS-II attenuated vascular remodeling and restored the VSMC contractile phenotype in vivo. **(A)** Representative H&E staining images of the injured left common carotid arteries from the sham group, control group, and ICS-II group, respectively. **(B)** Quantification of the intima thickness. **(C)** The lesion was calculated using the ratio of intima/media. **(D)** Representative IHC images of SMA-α in the sham group, control group, and ICS-II group, respectively. **(E)** Quantification of the SMA-α expression level in vivo. **(F)** Representative IHC images of OPN in the sham group, control group, and ICS-II group, respectively. **(G)** Quantification of the OPN expression level in vivo. X100, scale bar = 100 μm; X400, scale bar = 20 μm; Data are presented as mean ± S.E.M. N = 5 per group. $^{*}p < 0.05$, $^{**}p < 0.01$, $^{***}p < 0.001$, $^{****}p < 0.0001$.

Western Blot

Briefly, the total proteins from different groups were extracted by lysing VSMCs with RIPA buffer (Beyotime, Shanghai, China), and the protein concentration was determined by using a BCA Protein Assay Kit (Beyotime, Shanghai, China). Then, the protein samples were separated by SDS–PAGE and subsequently transferred to PVDF membranes (Millipore, United States). After being blocked in 5% BSA at room temperature for 2 h, membranes were incubated for 12 h at 4°C with primary antibodies. After being washed three times with PBS, HRP-conjugated secondary antibodies were used to incubate the membranes for 1 h at room temperature. Finally, protein bands were visualized using chemiluminescence equipment.

In vitro Scratch Assay

The primarily cultured VSMCs were seeded into 6-well plates at a cell density of 5×10^5 until 80% confluence. The cells were scratched with a 10 μL pipette tip, the residue was rinsed, and the corresponding drugs with the medium containing 1% serum were added. The cell scratch assay was observed under an inverted microscope (Olympus, Japan), and photographed at 0 and 24 h, respectively.

Transwell Migration Assay

The VSMC transwell migration assay was implemented using 24-well transwell chambers (8 μm pore size; BD Biosciences, United States). Briefly, a total of 10,000 cells per well were re-suspended in a serum-free medium with corresponding interventions, respectively. Cells were then added into the top chamber with the same medium containing 10% FBS at the bottom of the chambers. After 24 h, the migrated cells through the biofilms were fixed and stained with a crystal violet staining solution (C0121, Beyotime, China) for morphological observation with the microscope (Olympus, Japan).

Statistical Analysis

Results are expressed as mean ± SEM (standard error of the mean) and the statistical significance between the means of the two groups was determined by the two-tailed *t*-test or Mann–Whitney test. The p-value < 0.05 was considered statistically significant. GraphPad Prism (version 8.2.1, United States) was used for all statistical analyses.

RESULTS

ICS-II Attenuated Vascular Remodeling and Restored VSMC Contractile Phenotype *in vivo*

To investigate the role of ICS-II in vascular remodeling, a rat carotid artery balloon injury model was implemented, which is capable of mimicking vascular remodeling as well as VSMC phenotypic transition validly *in vivo* (Tulis, 2007; Zhang and Trebak, 2014). Results from the morphometric analysis showed that ICS-II significantly suppressed intima thickness and intima/media ratio (**Figure 1A–C**) at day 14 compared to the control group ($p < 0.05$). Immunohistochemistry experiments showed that SMA-α, a contractile phenotype marker of VSMC, was significantly enhanced in the arterial tissue compared with the control group ($p < 0.05$), as shown in **Figures 1D,E**. In contrast, the expression level of synthetic marker OPN was attenuated after ICS-II administration (**Figure 1F,G**). The data aforementioned indicated that ICS-II effectively attenuated the vascular remodeling process and restored VSMC contractile phenotype *in vivo*.

DEP Analysis After ICS-II Intervention

To further elucidate the proteomic changes after ICS-II intervention in vascular remodeling, the label-free quantitative proteomic analysis was implemented. With the steps of filtering, normalization, and imputing missing values embedded in the DEP algorithm (**Figure 2A–D**), a total of 145 differential proteins (including 70 up-regulated proteins and 75 down-regulated proteins) in the ICS-II group compared to the control group, were identified. The volcano plot of the differential analysis is presented in **Figure 2E**. In addition, the expression levels of PTK2, PXN, ZYX, and ELN are plotted in **Figure 2F**, respectively. Results indicated significantly higher protein expression levels of PTK2, PXN, ZYX, and ELN in the ICS-II group compared to the control group ($p < 0.05$).

Bioinformatic Analysis Indicated ICS-II Enhanced VSMC Contractile Phenotype Through the Focal Adhesion Pathway

To further elucidate the underlying protein–protein interactions and intricated networks, the PPI network, and enrichment analyses were conducted. Seventy up-regulated and 75 down-regulated proteins in the ICS-II group were imported into the STRING database to derive the PPI network, as shown in **Figure 3A,F**, respectively. Proteins with degrees >5 were further selected for the enrichment analysis. The biological process enrichment analysis showed that up-regulated DEPs were mainly enriched in the artery development, actomyosin structure organization, response to transforming growth factor β, actin filament bundle assembly, and organization. (**Figure 3B**). The cellular components enrichment analysis showed that up-regulated DEPs were mainly enriched in the stress fiber, contractile actin filament bundle, actin filament, focal adhesion, actin cytoskeleton, myofibril, etc. (**Figure 3C**). For molecular function, enriched terms mainly included actin binding, actinin binding, muscle alpha-actinin binding, etc. (**Figure 3D**). The KEGG pathway enrichment analysis revealed that up-regulated DEPs were mainly correlated with focal adhesion, regulation of actin cytoskeleton, VEGF pathway, etc. (**Figure 3E**). For down-regulated DEPs, enriched terms mainly included fatty acid metabolism, respiratory chain complex, regulation of reactive oxygen species biosynthetic and metabolic processes, amino acid metabolism, etc. (**Figure 3G–J**). The aforementioned bioinformatic results indicated that ICS-II attenuated vascular remodeling through the focal adhesion pathway by enhancing the VSMC contractile phenotype and suppressing signaling pathways related to cellular metabolism.

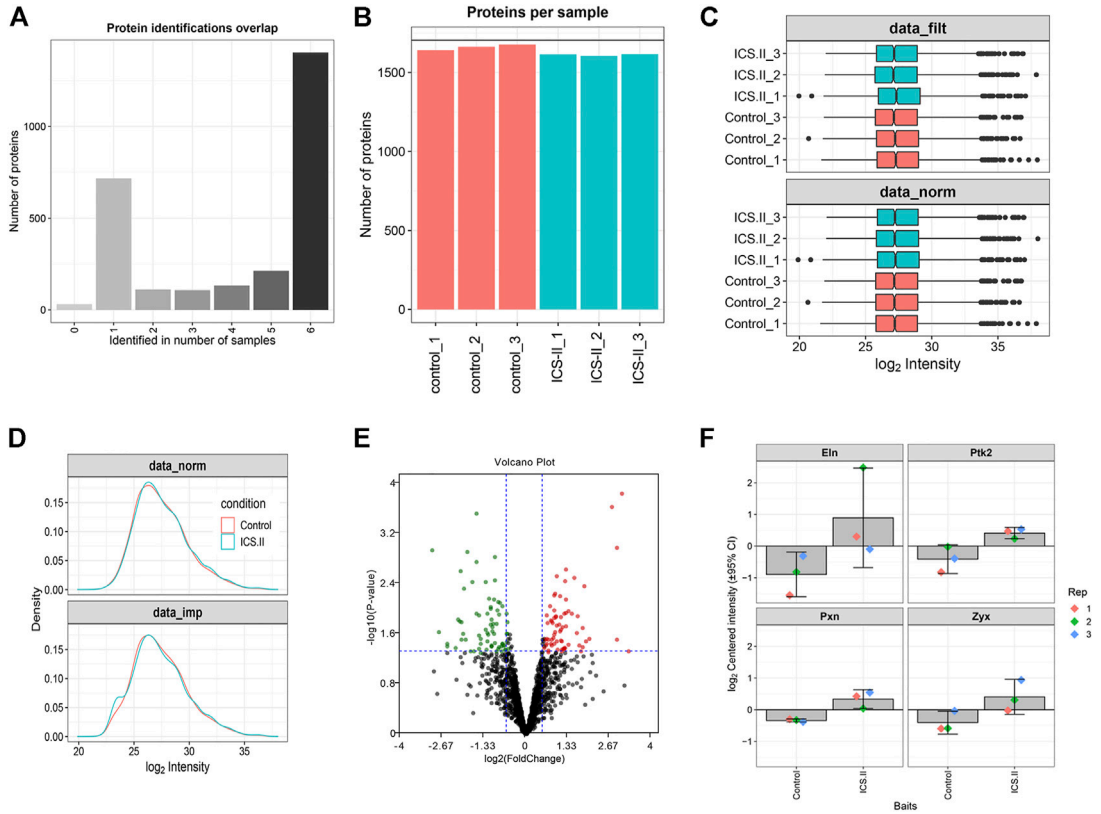

FIGURE 2 | Differentially expressed protein (DEP) analysis after ICS-II intervention. **(A)** Overlap of protein identifications between samples. **(B)** The number of identified proteins per sample. **(C)** Comparison of raw and normalized data. **(D)** Protein intensity distributions before and after missing value imputation. **(E)** Volcano plot for DEPs between the ICS-II group and control group. **(F)** Bar plots of ELN, PTK2, PXN, and ZYX expression levels. ELN: elastin; PTK2: protein tyrosine kinase 2; PXN: paxilline; ZYX: Zyxin.

ICS-II Inhibited VSMC Proliferation and Migration

To further verify that ICS-II restored the VSMC contractile phenotype during vascular remodeling, we used primarily cultured rat aortic VSMC to conduct *in vitro* experiments (**Figure 4A,B**). Excessive proliferation is the major feature during VSMC phenotypic modulation. Western blot results showed that ICS-II significantly attenuated the protein expression levels of PCNA and CCND1 (**Figure 4C–E**), which indicated that ICS-II inhibited VSMC proliferation. Cell migration represents another essential hallmark for the VSMC phenotypic transition. Therefore, *in vitro* scratch assay and transwell assay were implemented to assess the ability of VSMC migration after ICS-II intervention. Results of the scratch assay revealed the suppressed migration ability of VSMC after ICS-II intervention compared to the PDGF-BB group ($p < 0.05$, **Figure 4F,G**). The transwell assay showed similar results, as shown in **Figure 4H,I**.

ICS-II Restored VSMC Contractile Phenotype Through the Focal Adhesion Signaling Pathway

We next examined the protein expression level of SMA-α and OPN by cellular IF experiments. Results revealed that the ICS-II intervention significantly enhanced the SMA-α expression level while it inhibited the OPN protein expression compared to the PDGF-BB group ($p < 0.05$, **Figures 5A–D**). The aforementioned results showed that ICS-II restored the VSMC contractile phenotype *in vitro*.

To elucidate the role of the focal adhesion pathway in the ICS-II-induced VSMC contractile phenotype, we next examined the protein expression levels of PTK2, PXN, and ZYX after ICS-II intervention. Western blot showed significantly enhanced PTK2, PXN, and ZYX protein levels in the ICS-II group compared to PDGF-BB stimulation ($p < 0.05$, **Figures 5E–H**). Taken together, ICS-II restored VSMC contractile phenotype by enhancing focal adhesion signaling activity.

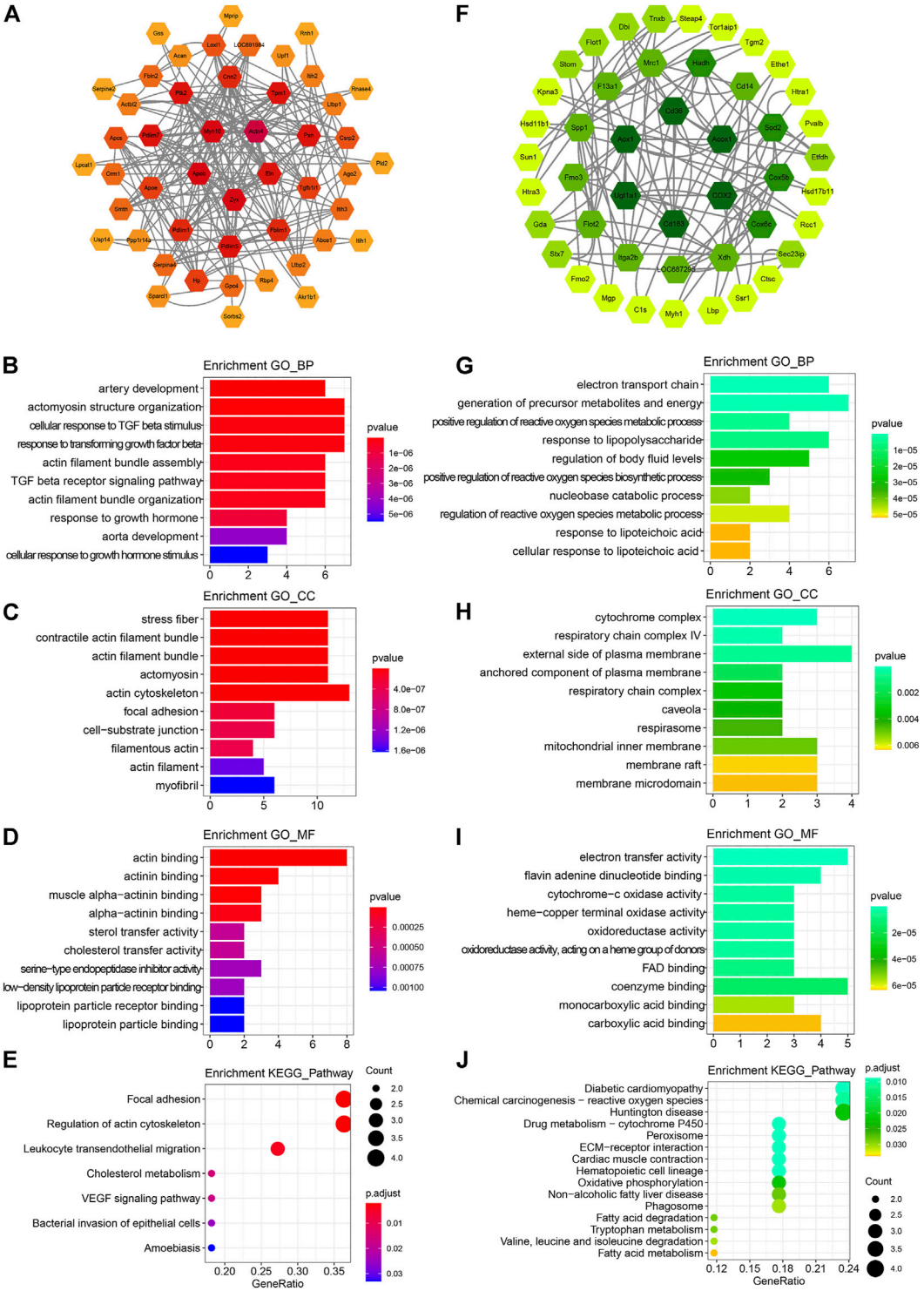

FIGURE 3 | PPI network construction and functional annotation. **(A)** PPI network construction, **(B)** biological process, **(C)** cellular component, **(D)** molecular function, and **(E)** KEGG pathway enrichment analysis based on 70 up-regulated DEPs, respectively. **(F)** PPI network construction, **(G)** biological process, **(H)** cellular component, **(I)** molecular function, and **(J)** KEGG pathway enrichment analysis based on 75 down-regulated DEPs. DEPs: differentially expressed proteins; PPI: protein–protein interaction; BP: biological process; CC: cellular component; MF: molecular function; KEGG: Kyoto Encyclopedia of Genes and Genomes.

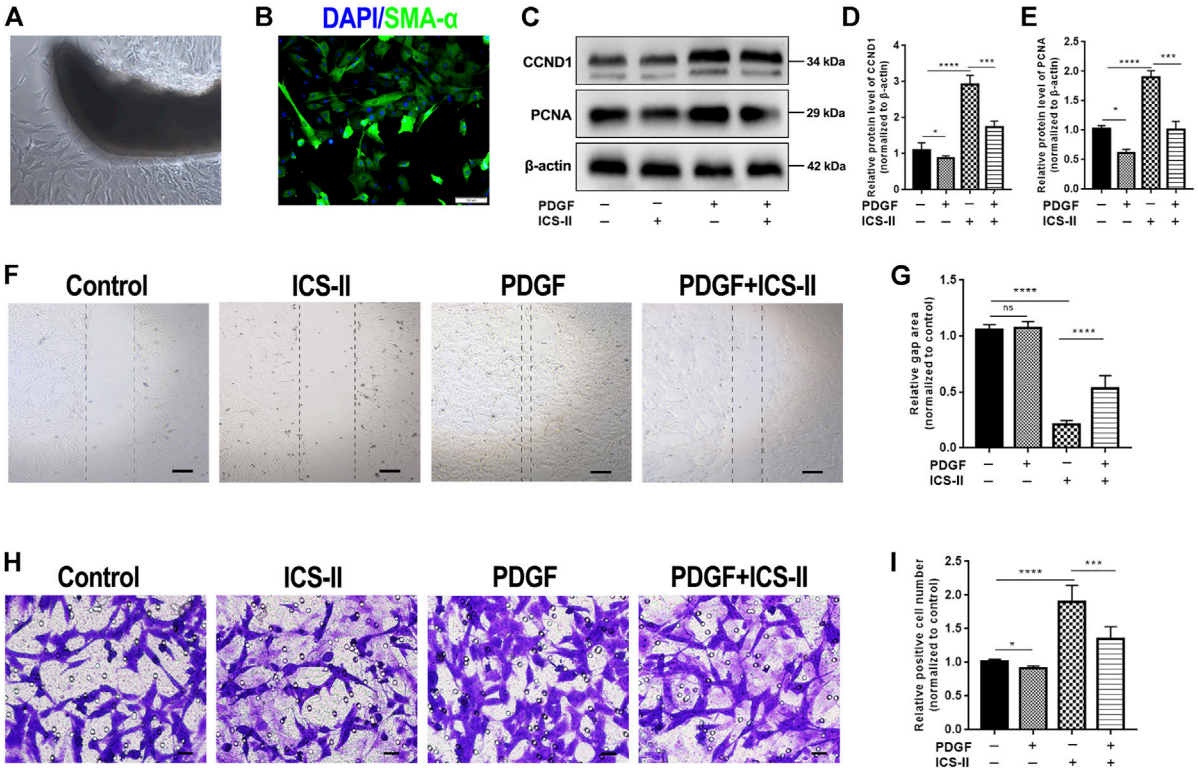

FIGURE 4 | ICS-II inhibited VSMC proliferation and migration. **(A)** VSMCs were primarily cultured by using the explant method. **(B)** Verification of VSMCs at passage 3 with SMA-α (green) and DAPI (blue) staining. **(C)** Western blot images for PCNA and CCND1. Quantification of **(D)** CCND1 and **(E)** PCNA protein levels, respectively. **(F)** *In vitro* scratch assay for control, ICS-II and PDGF-BB, and PDGF-BB + ICS-II groups, respectively. **(G)** Quantification of the gap area in the scratch assay. **(H)** Transwell migration assay for control, ICS-II, and PDGF-BB and PDGF-BB + ICS-II groups, respectively. **(I)** Quantification of migrated cell number in the transwell assay. Scale bar = 20 μm; Data are presented as mean ± S.E.M. $N = 5$ per group. $^{*}p < 0.05$, $^{**}p < 0.01$, $^{***}p < 0.001$, $^{****}p < 0.0001$.

DISCUSSION

The vascular remodeling process mediated by VSMC phenotypic transition is the major pathophysiological basis of numerous cardiovascular diseases (Lyle and Taylor, 2019). Pharmacological inhibition of the VSMC phenotypic transition will inevitably provide solid strategies for the prevention and treatment of cardiovascular diseases. Emerging basic pharmacological studies underscored the vital implication of traditional Chinese herbal medicine for cardiovascular diseases and vascular remodeling processes (Liu and Huang, 2016; Wang et al., 2020). Herein, ICS-II, a bioactive flavonol glycoside derived from the traditional Chinese medicine Herba Epimedii, was validated for its therapeutic value in the vascular remodeling process. Results indicated that ICS-II attenuated vascular remodeling by restoring the VSMC contractile phenotype through the focal adhesion pathway.

The rat carotid artery balloon injury model is one of the most well-characterized and frequently practiced rodent models for investigating vascular remodeling (Holt and Tulis, 2013). Pathophysiological responses to this model include VSMC dedifferentiation into synthetic phenotype featured by VSMC proliferation and migration, enhanced extracellular matrix synthesis and deposition, and proliferation of endothelium and luminal narrowing. Deciphering the mechanisms of VSMC phenotypic regulation and elucidating how these mechanisms can be targeted for treatment are fundamental for cardiovascular diseases (Chakraborty et al., 2021). In this study, a rat carotid artery balloon injury model was selected for the therapeutic efficacy of ICS-II in vascular remodeling. The morphometric analysis revealed that ICS-II significantly suppressed the vascular remodeling process *in vivo*. Moreover, *in vitro* studies using PDGF-BB-stimulated VSMC further indicated that ICS-II restored VSMC contractile phenotype.

Maintenance of three-dimensional cellular integrity is crucial for VSMC contraction and preservation of the contractile phenotype (Yamin and Morgan, 2012). The major intracellular cytoskeletal components for contractile units of VSMC include actin, myosin, microtubules, and filaments. Moreover, the physical interactions between VSMC contractile units and the extracellular matrix also contribute to VSMC contractile capability, which is termed focal adhesion (Zhang and Gunst, 2008). Focal adhesions are integrin-mediated multi-protein assemblies that provide mechanical bridges between the intracellular actin skeleton and the extracellular matrix in numerous cell types (Geiger et al., 2009). Emerging studies have highlighted the fundamental role of the focal adhesion signaling pathway, beyond the classical calcium-dependent

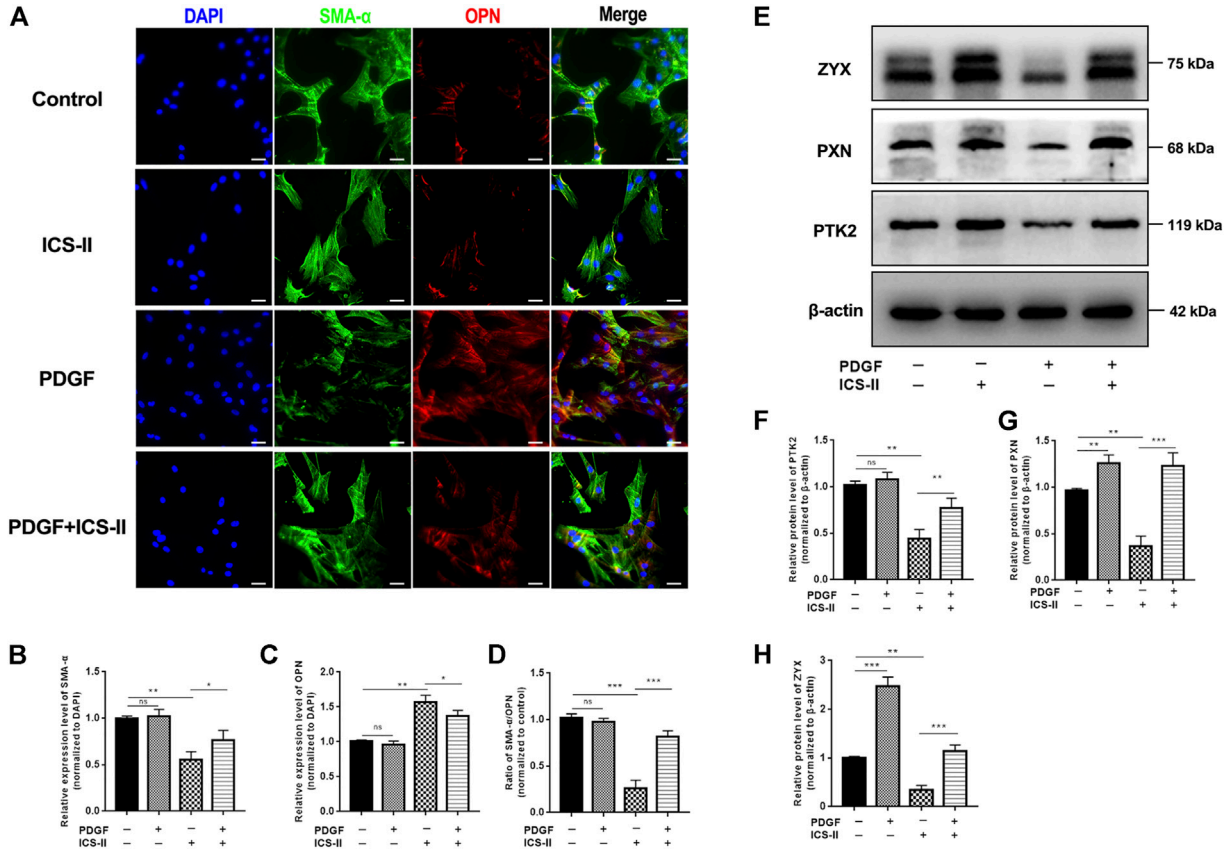

FIGURE 5 | ICS-II restored VSMC contractile phenotype through the focal adhesion signaling pathway. **(A)** Co-staining of SMA-α (green) and OPN (red) for control, ICS-II, and PDGF-BB and PDGF-BB + ICS-II groups, respectively. Quantification of the relative expression level of **(B)** SMA-α, **(C)** OPN, and **(D)** ratio of SMA-α/OPN, respectively. **(E)** Western blot images for PTK2, PXN, and ZYX. Quantification of **(F)** PTK2, **(G)** PXN, and **(H)** ZYX protein levels, respectively. Scale bar = 20 μm; Data are presented as mean ± S.E.M. $N = 5$ per group. $^{*}p < 0.05$, $^{**}p < 0.01$, $^{***}p < 0.001$, $^{****}p < 0.0001$.

pathways, in modulating VSMC contraction and phenotypic alteration (Ribeiro-Silva et al., 2021). PTK2 (also named FAK) and PXN are signaling transducers that translate mechanical signals from transmembrane integrin to biochemical signals in the focal adhesion pathway; meanwhile, zyxin (coded by ZYX gene) acts as downstream actin cross-linking mediator that is tightly associated with the actomyosin apparatus (Horton et al., 2015). In our study, proteomic and enrichment analyses indicated that the focal adhesion signaling pathway was activated in VSMC after ICS-II treatment. Moreover, *in vitro* studies showed the enhanced protein expression levels of PTK2, PXN, and ZYX in the ICS-II group. Taken together, the current research suggests that the focal adhesion signaling pathway participates in ICS-II-induced VSMC contractile phenotype modulation.

Elastin (encoded by ELN) is the main extracellular matrix protein deposited on the arterial wall. Recent studies have indicated that elastin is not only required for ensuring the elasticity of the arterial wall but also promotes VSMC phenotypic modulation. Karnik et al. (2003) highlighted the critical role of ELN in inducing actin stress fiber organization and maintaining VSMC contractile phenotype (. Similarly, using an ELN deficiency model, Lin et al. (2021)showed that ELN knockout contributes to neointima hyperplasia and alters the VSMC phenotype (. In another study, the same group illustrated that the loss of elastin gene expression in VSMC causes discontinuous internal elastic lamina, which facilitates VSMC migration into the lumen, thus leading to neointima hyperplasia (Lin et al., 2019). Taken together, ELN, as an extracellular matrix component, is not only involved in the structural integrity of the vessel wall but also regulates VSMC phenotypic transformation in neointima formation and vascular remodeling.

Sophisticated interactive signaling pathways determined the phenotypic transition of VSMC and facilitated the development of cardiovascular diseases (Frismantiene et al., 2018). Liao et al. (2017) reported that the VEGF signaling pathway promoted VSMC proliferation and thus negatively correlated with the VSMC contractile phenotype. It is controversial that the VEGF signaling pathway was enriched in the up-regulated protein set after ICS-II intervention in our study. This may be attributed to the fact that endothelium proliferation is another major feature of the present animal model in addition to the VSMC phenotypic transition, and the VEGF signaling pathway is the major mechanism that promotes endothelium proliferation, although we scraped the endothelium during the sampling process. It is

also noteworthy that the two genes enriched to the VEGF signaling pathway happened to be mainly involved in the focal adhesion pathway, which may lead to false-positive results of the enrichment analysis. The TGF-β signaling pathway was reported to be critical for VSMC phenotypic maintenance, and impairment of the TGF-β signaling pathway leads to the development of various cardiovascular diseases (Goumans et al., 2009). Consistent with this, we found that the TGF-β signaling pathway was enriched after ICS-II intervention. Conclusively, more in-depth studies are encouraged to decrypt the molecular basis and complicated signaling networks in the VSMC phenotypic transition process.

Increasing studies revealed that the VSMC phenotypic transition was driven by the metabolic switch, and VSMCs altered their metabolism to accommodate the bioenergetic demands during the phenotypic transition (Shi et al., 2020). Evidence showed that abnormal metabolic modulation of glucose, fatty acids, and amino acids, as well as metabolic crosstalk between VSMC and other cell types, played a role in the VSMC phenotypic transition during cardiovascular diseases (Shi et al., 2020). In our study, several metabolic signaling pathways were enriched after ICS-II intervention, such as oxidative phosphorylation, fatty acid metabolism, tryptophan, valine, leucine, and isoleucine metabolism, etc. Our results highlighted the underlying pivotal role of metabolism processes in the VSMC phenotypic transition during vascular remodeling; further studies are needed to emphasize the related metabolic signaling pathways during the VSMC phenotypic transition.

CONCLUSION

In conclusion, the present study demonstrates that ICS-II, a plant flavonol glycoside, attenuates vascular remodeling by restoring the VSMC contractile phenotype *in vivo* and *in vitro*. The focal adhesion pathway participated in the pharmaceutical effects of ICS-II in VSMC phenotypic modulation. Our results highlighted the potential therapeutic efficacy of ICS-II in vascular remodeling diseases such as neointima formation and restenosis. Further investigations are needed to elucidate the underlying molecular mechanisms and signaling pathways related to VSMC phenotypic modulation after ICS-II intervention in vascular remodeling.

DATA AVAILABILITY STATEMENT

The datasets presented in this study can be found in online repositories. The mass spectrometry proteomics data have been deposited to the ProteomeXchange Consortium (http://proteomecentral.proteomexchange.org) via the iProX partner repository with the dataset identifier PXD033724.

ETHICS STATEMENT

The animal study was reviewed and approved by the Experimental Ethics Committee of Zunyi Medical University (approval number: 2020.2-385).

AUTHOR CONTRIBUTIONS

HW and JL conceived and designed the whole study. HW, YL, YL and DY conducted the animal experiments and proteomic analysis. JL implemented bioinformatic analysis. XL and BL performed *in vitro* experiments. JL drafted the paper and HW revised it.

FUNDING

This study was supported by the National Natural Science Foundation of China (No. 81860715) and Doctor Foundation of Affiliated Hospital of Zunyi Medical University (No. 201712).

REFERENCES

Ashburner, M., Ball, C. A., Blake, J. A., Botstein, D., Butler, H., Cherry, J. M., et al. (2000). Gene Ontology: Tool for the Unification of Biology. The Gene Ontology Consortium. *Nat. Genet.* 25 (1), 25–29. doi:10.1038/75556

Briguori, C., Visconti, G., Golino, M., Focaccio, A., Scarpelli, M., Nuzzo, S., et al. (2021). Paclitexel versus Sirolimus-Coated Balloon in the Treatment of Coronary Instent Restenosis. *Panminerva. Med.* [Epub ahead of print]. doi:10.23736/s0031-0808.21.04573-0

Cañes, L., Alonso, J., Ballester-Servera, C., Varona, S., Escudero, J. R., Andrés, V., et al. (2021). Targeting Tyrosine Hydroxylase for Abdominal Aortic Aneurysm: Impact on Inflammation, Oxidative Stress, and Vascular Remodeling. *Hypertension* 78 (3), 681–692. doi:10.1161/HYPERTENSIONAHA.121.17517

Chakraborty, R., Chatterjee, P., Dave, J. M., Ostriker, A. C., Greif, D. M., Rzucidlo, E. M., et al. (2021). Targeting Smooth Muscle Cell Phenotypic Switching in Vascular Disease. *JVS Vasc. Sci.* 2, 79–94. doi:10.1016/j.jvssci.2021.04.001

Cox, J., Hein, M. Y., Luber, C. A., Paron, I., Nagaraj, N., and Mann, M. (2014). Accurate Proteome-wide Label-free Quantification by Delayed Normalization and Maximal Peptide Ratio Extraction, Termed MaxLFQ. *Mol. Cell. Proteomics* 13 (9), 2513–2526. doi:10.1074/mcp.M113.031591

Frismantiene, A., Philippova, M., Erne, P., and Resink, T. J. (2018). Smooth Muscle Cell-Driven Vascular Diseases and Molecular Mechanisms of VSMC Plasticity. *Cell. Signal* 52, 48–64. doi:10.1016/j.cellsig.2018.08.019

Frösen, J., Cebral, J., Robertson, A. M., and Aoki, T. (2019). Flow-induced, Inflammation-Mediated Arterial Wall Remodeling in the Formation and Progression of Intracranial Aneurysms. *Neurosurg. Focus* 47 (1), E21. doi:10.3171/2019.5.FOCUS19234

Geiger, B., Spatz, J. P., and Bershadsky, A. D. (2009). Environmental Sensing through Focal Adhesions. *Nat. Rev. Mol. Cell. Biol.* 10 (1), 21–33. doi:10.1038/nrm2593

Goumans, M. J., Liu, Z., and ten Dijke, P. (2009). TGF-beta Signaling in Vascular Biology and Dysfunction. *Cell. Res.* 19 (1), 116–127. doi:10.1038/cr.2008.326

Guan, B. F., Dai, X. F., Huang, Q. B., Zhao, D., Shi, J. L., Chen, C., et al. (2020). Icariside II Ameliorates Myocardial Ischemia and Reperfusion Injury by Attenuating Inflammation and Apoptosis through the Regulation of the PI3K/AKT Signaling Pathway. *Mol. Med. Rep.* 22 (4), 3151–3160. doi:10.3892/mmr.2020.11396

Holt, A. W., and Tulis, D. A. (2013). Experimental Rat and Mouse Carotid Artery Surgery: Injury & Remodeling Studies. *ISRN Minim. Invasive Surg.* 2013. doi:10.1155/2013/167407

Horton, E. R., Byron, A., Askari, J. A., Ng, D. H. J., Millon-Frémillon, A., Robertson, J., et al. (2015). Definition of a Consensus Integrin Adhesome

and its Dynamics during Adhesion Complex Assembly and Disassembly. *Nat. Cell. Biol.* 17 (12), 1577–1587. doi:10.1038/ncb3257

Huber, W., von Heydebreck, A., Sültmann, H., Poustka, A., and Vingron, M. (2002). Variance Stabilization Applied to Microarray Data Calibration and to the Quantification of Differential Expression. *Bioinformatics* 18 (Suppl. 1), S96–S104. doi:10.1093/bioinformatics/18.suppl_1.s96

Jaminon, A., Reesink, K., Kroon, A., and Schurgers, L. (2019). The Role of Vascular Smooth Muscle Cells in Arterial Remodeling: Focus on Calcification-Related Processes. *Int. J. Mol. Sci.* 20 (22). doi:10.3390/ijms20225694

Karnik, S. K., Brooke, B. S., Bayes-Genis, A., Sorensen, L., Wythe, J. D., Schwartz, R. S., et al. (2003). A Critical Role for Elastin Signaling in Vascular Morphogenesis and Disease. *Development* 130 (2), 411–423. doi:10.1242/dev.00223

Kiechl, S., and Willeit, J. (1999). The Natural Course of Atherosclerosis. Part II: Vascular Remodeling. Bruneck Study Group. *Arterioscler. Thromb. Vasc. Biol.* 19 (6), 1491–1498. doi:10.1161/01.atv.19.6.1491

Lazar, C. (2015). imputeLCMD: A Collection of Methods for Left-Censored Missing Data Imputation. R Package Version 20. Available at: https://CRAN.R-project.org/package=imputeLCMD.

Li, Y. Q., Li, Y. L., Li, X. T., Lv, J. Y., Gao, Y., Li, W. N., et al. (2020). Osthole Alleviates Neointimal Hyperplasia in Balloon-Induced Arterial Wall Injury by Suppressing Vascular Smooth Muscle Cell Proliferation and Downregulating Cyclin D1/CDK4 and Cyclin E1/CDK2 Expression. *Front. Physiol.* 11, 514494. doi:10.3389/fphys.2020.514494

Liao, X. H., Xiang, Y., Li, H., Zheng, L., Xu, Y., Xi Yu, C., et al. (2017). VEGF-A Stimulates STAT3 Activity via Nitrosylation of Myocardin to Regulate the Expression of Vascular Smooth Muscle Cell Differentiation Markers. *Sci. Rep.* 7 (1), 2660. doi:10.1038/s41598-017-02907-6

Lin, C-J., Staiculescu, M. C., Wagenseil, J., and Mecham, R. P. (2019). VASCULAR SMOOTH MUSCLE-SPECIFIC ELASTIN DELETION IS A NOVEL GENETIC MODEL FOR NEOINTIMAL HYPERPLASIA. *J. Am. Coll. Cardiol.* 73 (9_Supplement_1), 2035. doi:10.1016/s0735-1097(19)32641-5

Lin, C. J., Hunkins, B. M., Roth, R. A., Lin, C. Y., Wagenseil, J. E., and Mecham, R. P. (2021). Vascular Smooth Muscle Cell Subpopulations and Neointimal Formation in Mouse Models of Elastin Insufficiency. *Arterioscler. Thromb. Vasc. Biol.* 41 (12), 2890–2905. doi:10.1161/ATVBAHA.120.315681

Liu, C., and Huang, Y. (2016). Chinese Herbal Medicine on Cardiovascular Diseases and the Mechanisms of Action. *Front. Pharmacol.* 7, 469. doi:10.3389/fphar.2016.00469

Liu, X. Y., Liao, H. H., Feng, H., Zhang, N., Yang, J. J., Li, W. J., et al. (2018). Icariside II Attenuates Cardiac Remodeling via AMPKα2/mTORC1 In vivo and In vitro. *J. Pharmacol. Sci.* 138 (1), 38–45. doi:10.1016/j.jphs.2018.08.010

Lv, J., Wang, L., Zhang, J., Lin, R., Wang, L., Sun, W., et al. (2018). Long Noncoding RNA H19-Derived miR-675 Aggravates Restenosis by Targeting PTEN. *Biochem. Biophys. Res. Commun.* 497 (4), 1154–1161. doi:10.1016/j.bbrc.2017.01.011

Lyle, A. N., and Taylor, W. R. (2019). The Pathophysiological Basis of Vascular Disease. *Lab. Invest.* 99 (3), 284–289. doi:10.1038/s41374-019-0192-2

Ogata, H., Goto, S., Sato, K., Fujibuchi, W., Bono, H., and Kanehisa, M. (1999). KEGG: Kyoto Encyclopedia of Genes and Genomes. *Nucleic Acids Res.* 27 (1), 29–34. doi:10.1093/nar/27.1.29

Pasterkamp, G., de Kleijn, D. P., and Borst, C. (2000). Arterial Remodeling in Atherosclerosis, Restenosis and after Alteration of Blood Flow: Potential Mechanisms and Clinical Implications. *Cardiovasc Res.* 45 (4), 843–852. doi:10.1016/s0008-6363(99)00377-6

Qi, W., Li, Q., Liew, C. W., Rask-Madsen, C., Lockhart, S. M., Rasmussen, L. M., et al. (2017). SHP-1 Activation Inhibits Vascular Smooth Muscle Cell Proliferation and Intimal Hyperplasia in a Rodent Model of Insulin Resistance and Diabetes. *Diabetologia* 60 (3), 585–596. doi:10.1007/s00125-016-4159-1

Renna, N. F., de Las Heras, N., and Miatello, R. M. (2013). Pathophysiology of Vascular Remodeling in Hypertension. *Int. J. Hypertens.* 2013, 808353. doi:10.1155/2013/808353

Ribeiro-Silva, J. C., Miyakawa, A. A., and Krieger, J. E. (2021). Focal Adhesion Signaling: Vascular Smooth Muscle Cell Contractility beyond Calcium Mechanisms. *Clin. Sci. (Lond)* 135 (9), 1189–1207. doi:10.1042/CS20201528

Roth, G. A., Mensah, G. A., Johnson, C. O., Addolorato, G., Ammirati, E., Baddour, L. M., et al. (2020). Global Burden of Cardiovascular Diseases and Risk Factors, 1990-2019: Update from the GBD 2019 Study. *J. Am. Coll. Cardiol.* 76 (25), 2982–3021. doi:10.1016/j.jacc.2020.11.010

Saleh Al-Shehabi, T., Iratni, R., and Eid, A. H. (2016). Anti-atherosclerotic Plants Which Modulate the Phenotype of Vascular Smooth Muscle Cells. *Phytomedicine* 23 (11), 1068–1081. doi:10.1016/j.phymed.2015.10.016

Shannon, P., Markiel, A., Ozier, O., Baliga, N. S., Wang, J. T., Ramage, D., et al. (2003). Cytoscape: a Software Environment for Integrated Models of Biomolecular Interaction Networks. *Genome Res.* 13 (11), 2498–2504. doi:10.1101/gr.1239303

Shi, J., Yang, Y., Cheng, A., Xu, G., and He, F. (2020). Metabolism of Vascular Smooth Muscle Cells in Vascular Diseases. *Am. J. Physiol. Heart Circ. Physiol.* 319 (3), H613–H31. doi:10.1152/ajpheart.00220.2020

Shi, N., Mei, X., and Chen, S. Y. (2019). Smooth Muscle Cells in Vascular Remodeling. *Arterioscler. Thromb. Vasc. Biol.* 39 (12), e247–e52. doi:10.1161/ATVBAHA.119.312581

Szklarczyk, D., Gable, A. L., Lyon, D., Junge, A., Wyder, S., Huerta-Cepas, J., et al. (2019). STRING V11: Protein-Protein Association Networks with Increased Coverage, Supporting Functional Discovery in Genome-wide Experimental Datasets. *Nucleic Acids Res.* 47 (D1), D607–D13. doi:10.1093/nar/gky1131

Tulis, D. A. (2007). Rat Carotid Artery Balloon Injury Model. *Methods Mol. Med.* 139, 1–30. doi:10.1007/978-1-59745-571-8_1

Wang, Y., Zhang, Y., Li, T. J., Laher, I., and Wang, H. (2020). Editorial: The Potential Effect and Mechanism of Chinese Traditional Medicine on Vascular Homeostasis and Remodeling. *Front. Pharmacol.* 11, 599766. doi:10.3389/fphar.2020.599766

Wen, H., Wang, M., Gong, S., Li, X., Meng, J., Wen, J., et al. (2020). Human Umbilical Cord Mesenchymal Stem Cells Attenuate Abdominal Aortic Aneurysm Progression in Sprague-Dawley Rats: Implication of Vascular Smooth Muscle Cell Phenotypic Modulation. *Stem Cells Dev.* 29 (15), 981–993. doi:10.1089/scd.2020.0058

Yamin, R., and Morgan, K. G. (2012). Deciphering Actin Cytoskeletal Function in the Contractile Vascular Smooth Muscle Cell. *J. Physiol.* 590 (17), 4145–4154. doi:10.1113/jphysiol.2012.232306

Yu, G., Wang, L. G., Han, Y., and He, Q. Y. (2012). clusterProfiler: an R Package for Comparing Biological Themes Among Gene Clusters. *OMICS* 16 (5), 284–287. doi:10.1089/omi.2011.0118

Zhang, W., and Gunst, S. J. (2008). Interactions of Airway Smooth Muscle Cells with Their Tissue Matrix: Implications for Contraction. *Proc. Am. Thorac. Soc.* 5 (1), 32–39. doi:10.1513/pats.200704-048VS

Zhang, W., and Trebak, M. (2014). Vascular Balloon Injury and Intraluminal Administration in Rat Carotid Artery. *J. Vis. Exp.* 94. doi:10.3791/52045

Zhang, X., Smits, A. H., van Tilburg, G. B., Ovaa, H., Huber, W., and Vermeulen, M. (2018). Proteome-wide Identification of Ubiquitin Interactions Using UbIA-MS. *Nat. Protoc.* 13 (3), 530–550. doi:10.1038/nprot.2017.147

Zheng, Y., Deng, Y., Gao, J. M., Lv, C., Lang, L. H., Shi, J. S., et al. (2020). Icariside II Inhibits Lipopolysaccharide-Induced Inflammation and Amyloid Production in Rat Astrocytes by Regulating IKK/IκB/NF-κB/BACE1 Signaling Pathway. *Acta Pharmacol. Sin.* 41 (2), 154–162. doi:10.1038/s41401-019-0300-2

Conflict of Interest: The authors declare that the research was conducted in the absence of any commercial or financial relationships that could be construed as a potential conflict of interest.

Publisher's Note: All claims expressed in this article are solely those of the authors and do not necessarily represent those of their affiliated organizations, or those of the publisher, the editors, and the reviewers. Any product that may be evaluated in this article, or claim that may be made by its manufacturer, is not guaranteed or endorsed by the publisher.

frontiers | Frontiers in Pharmacology

ORIGINAL RESEARCH
published: 22 July 2022
doi: 10.3389/fphar.2022.927488

Uncovering the Effect and Mechanism of *Rhizoma Corydalis* on Myocardial Infarction Through an Integrated Network Pharmacology Approach and Experimental Verification

Jingyan Li[1†], *Junxuan Wu*[1,2,3†], *Junying Huang*[4], *Yuanyuan Cheng*[1], *Dawei Wang*[2*] and *Zhongqiu Liu*[1*]

[1]*Guangdong Key Laboratory for Translational Cancer Research of Chinese Medicine, Joint Laboratory for Translational Cancer Research of Chinese Medicine of the Ministry of Education of the People's Republic of China, Guangdong-Hong Kong-Macau Joint Lab on Chinese Medicine and Immune Disease Research International, International Institute for Translational Chinese Medicine, School of Pharmaceutical Science, Guangzhou University of Chinese Medicine, Guangzhou, China,* [2]*Shunde Hospital of Guangzhou University of Translational Chinese Medicine, Foshan, China,* [3]*The Second Affiliated Hospital of Guangzhou University of Chinese Medicine, Guangdong Provincial Hospital of Chinese Medicine, Guangzhou, China,* [4]*College of Life Sciences, Guangzhou University, Guangzhou, China*

OPEN ACCESS

Edited by:
Xiaoyong Tong,
Chongqing University, China

Reviewed by:
Nathan Andrew Holland,
Texas Tech University Health Sciences Center El Paso, United States
Umesh B. Mahajan,
R. C. Patel Institute of Pharmaceutical Education and Research, India

***Correspondence:**
Dawei Wang
david@gzucm.edu.cn
Zhongqiu Liu
liuzq@gzucm.edu.cn

[†]*These authors have contributed equally to this work*

Specialty section:
This article was submitted to Cardiovascular and Smooth Muscle Pharmacology, a section of the journal Frontiers in Pharmacology

Received: *24 April 2022*
Accepted: *21 June 2022*
Published: *22 July 2022*

Citation:
Li J, Wu J, Huang J, Cheng Y, Wang D and Liu Z (2022) Uncovering the Effect and Mechanism of Rhizoma Corydalis on Myocardial Infarction Through an Integrated Network Pharmacology Approach and Experimental Verification. Front. Pharmacol. 13:927488. doi: 10.3389/fphar.2022.927488

Background: Myocardial infarction (MI), characterized by reduced blood flow to the heart, is a coronary artery disorder with the highest morbidity and mortality among cardiovascular diseases. Consequently, there is an urgent need to identify effective drugs to treat MI. *Rhizoma Corydalis* (RC) is the dry tuber of *Corydalis yanhusuo* W.T. Wang, and is extensively applied in treating MI clinically in China. Its underlying pharmacological mechanism remains unknown. This study aims to clarify the molecular mechanism of RC on MI by utilizing network pharmacology and experimental verification.

Methods: Based on network pharmacology, the potential targets of the RC ingredients and MI-related targets were collected from the databases. Furthermore, core targets of RC on MI were identified by the protein-protein interaction (PPI) network and analyzed with Gene Ontology (GO) analysis and the Kyoto Encyclopedia of Genes and Genomes (KEGG) pathway enrichment analysis. Molecular docking was used to validate the binding affinity between the core targets and the bioactive components. Oxygen-glucose deprivation (OGD) was performed on H9c2 cells to mimic MI *in vitro*. A Cell Counting Kit-8 assay was used to assess the cardioprotective effect of the active ingredient against OGD. Western blot analysis and RT-qPCR were used to measure the cell apoptosis and inflammation level of H9c2 cells.

Results: The network pharmacology obtained 60 bioactive components of RC, 431 potential targets, and 1131 MI-related targets. In total, 126 core targets were screened according to topological analysis. KEGG results showed that RC was closely related to the phosphatidylinositol 3-kinase (PI3K)/Protein kinase B (PKB, also called Akt) signaling pathway. The experimental validation data showed that tetrahydropalmatine (THP) pretreatment preserved cell viability after OGD exposure. THP suppressed

cardiomyocyte apoptosis and inflammation induced by OGD, while LY294002 blocked the inhibition effect of THP on OGD-induced H9c2 cell injury. Moreover, the molecular docking results indicated that THP had the strongest binding affinity with Akt over berberine, coptisine, palmatine, and quercetin.

Conclusion: THP, the active ingredient of RC, can suppress OGD-induced H9c2 cell injury by activating the PI3K/Akt pathway, which in turn provides a scientific basis for a novel strategy for MI therapy and RC application.

Keywords: *Corydalis yanhusuo*, tetrahydropalmatine, myocardial infarction, network pharmacology, apoptosis, PI3k/Akt signaling pathway

INTRODUCTION

Myocardial infarction (MI), characterized by myocardial necrosis, is a major cause of morbidity and mortality worldwide, resulting in an estimated 7.4 million deaths per year (Xu et al., 2020). The acknowledged pathophysiology of MI is that thrombus formation in a coronary artery induces a reduction in myocardial perfusion (Frangogiannis, 2015). The general therapy includes coronary artery bypass grafting (CABG), percutaneous coronary intervention (PCI), and pharmacological management (Anderson and Morrow, 2017). However, reperfusion therapies, such as CABG and PCI, cause myocardial ischemia/reperfusion injury (MI/RI); antiplatelet therapy increases bleeding risk; and statin therapy may lead to drug-induced hepatic injury (Meurer and Cohen, 2020; Zheleva-Kyuchukova and Gelev, 2020; He et al., 2022). Consequently, identification of effective drugs to treat MI is urgently required.

R. Corydalis (RC) is the dried tuber of *C. yanhusuo* W.T. Wang, which belongs to the Papaveraceae family. RC was first recorded by Shennong Herbal Classic and believed to be able to activate blood, move "Qi" (vital energy) and alleviate painful conditions (Commission, 2015). Pharmacological studies display the multiple therapeutic effects of RC, including its anti-depression and anti-anxiety, anti-arrhythmia, anti-myocardial infarction, cerebral ischemia reperfusion (I/R) injury protection, anti-thrombosis, liver protection, anti-inflammation, and anticancer effects (Tian et al., 2020). Previous studies have revealed that separate or combined application of RC extracts can provide protection for the myocardium (Wu et al., 2007a; Xue et al., 2013; Li et al., 2020). However, the fact that the mechanism is unknown prevents extensive application of RC worldwide, hence the need for a precise evaluation.

Network pharmacology is an approach based on network construction and analysis technology and can systematically integrate and analyze information about bioactive components and the potential targets of components and diseases (Boezio et al., 2017). Recently, network pharmacology has been utilized to explore traditional Chinese medicine (TCM) in depth and has contributed to its modernization (Wang et al., 2021). In the present study, a network pharmacology approach, combined with specific experimental validation, was used to comprehensively elucidate the effect, and explore the molecular mechanism of RC on MI (a diagram of the study strategy is shown in **Figure 1**). This study provides a scientific basis for understanding the effect and mechanism of RC against MI and may suggest a novel therapeutic approach for MI.

MATERIALS AND METHODS

Screening for the Bioactive Components of RC

The bioactive components of RC were filtered from the following databases: the Traditional Chinese Medicine Systems Pharmacology (TCMSP) Database (Ru et al., 2014), the Encyclopedia of Traditional Chinese Medicine (ETCM) Database (Xu et al., 2019) and the Traditional Chinese Medicine Integrated Database (TCMID) (Huang et al., 2018). RC is mainly taken orally, thus oral bioavailability (OB) and drug-likeness (DL) were used as filter conditions. The filter conditions were OB equal to or greater than 30% and DL equal to or greater than 0.18 (Li et al., 2019a). Components in the ETCM database for which the drug-likeness grading was moderate and good were screened. Components that met the conditions in the three databases were defined as bioactive components. All chemical information about the components, including molecular formulas, molecular weight, and 3D structures, was obtained from the PubChem database (Kim et al., 2019).

Obtaining Potential Targets of RC and Identification of MI-Related Targets

Potential targets of bioactive components of RC were obtained from the PharmMapper database (Wang et al., 2017a) and human protein targets were selected. The MI-related targets were obtained from the following databases: DisGeNET (Pinero et al., 2020), GeneCards (Stelzer et al., 2016), DrugBank (Wishart et al., 2018), Therapeutic Target Database (TTD) (Yang et al., 2016), and Gene Expression Omnibus (GEO) datasets (Barrett et al., 2007). We used "myocardial infarction" as the search term, and the organism was restricted to *Homo sapiens*. The UniProtKB database was used to unify and standardize the targets (UniProt, 2015).

Network Construction

The Cytoscape plugin BisoGenet was utilized to construct a protein-protein interaction (PPI) network of RC potential

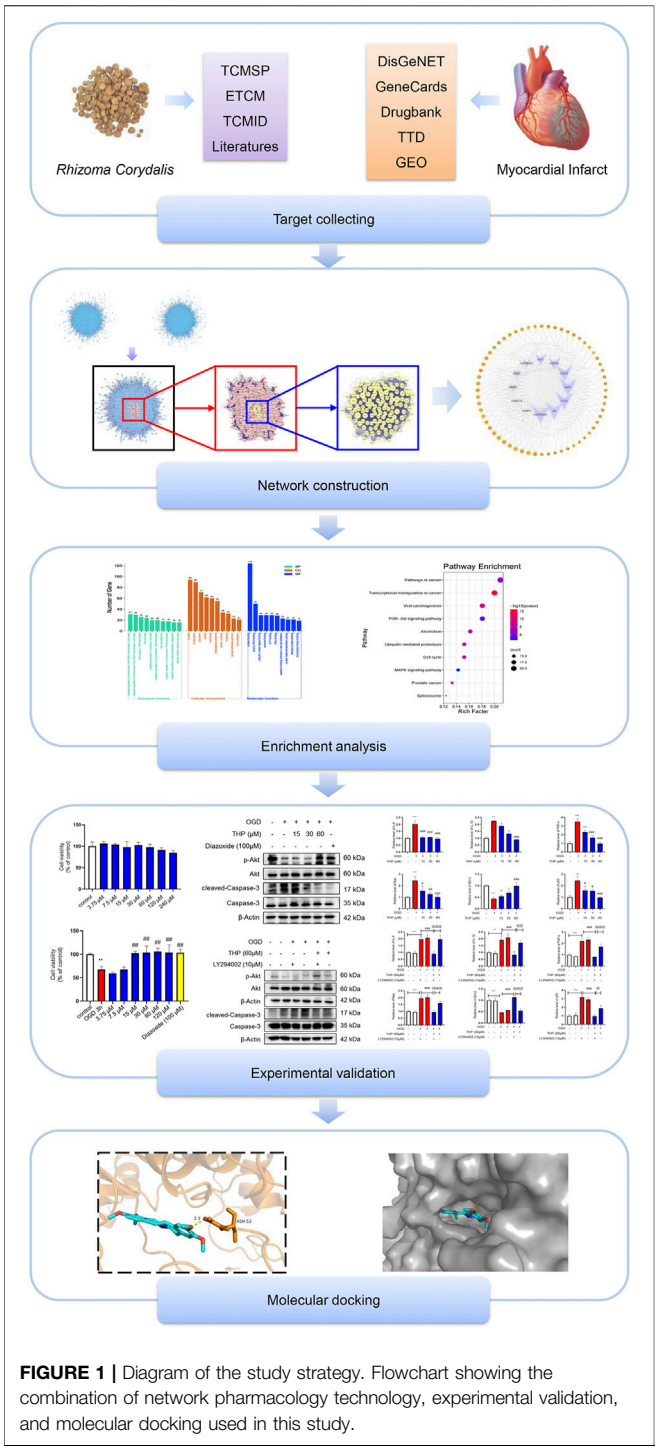

FIGURE 1 | Diagram of the study strategy. Flowchart showing the combination of network pharmacology technology, experimental validation, and molecular docking used in this study.

targets together with MI-related targets (Martin et al., 2010), and topological analysis was conducted by the Cytoscape plugin CytoNCA (Tang et al., 2015). The central PPI network was acquired after filtering twice by analyzing topological parameters degree centrality (DC), betweenness centrality (BC), closeness centrality (CC), eigenvector centrality (EC), local average connectivity-based method centrality (LAC), and network centrality (NC). The PPI network, component-target network, and Kyoto Encyclopedia of Genes and Genomes (KEGG) network were visualized using Cytoscape software.

Enrichment Analysis

To explore the biological processes of core targets, Gene Ontology (GO) biological function and KEGG pathway enrichment analyses were performed with the online tool DAVID Bioinformatics Resources 6.8 (Chen et al., 2017). The screening criteria were set as $p < 0.05$, and the species was limited to *H. sapiens*.

Molecular Docking

The crystal structure of core targets (macromolecules) was sought in the Protein Data Bank, and the structure (in SDF format) of the ligand (component) was retrieved from the PubChem database. We then changed the format of the molecules to pdb using OpenBabel software, and utilized AutoDockTools (version 1.5.6) for molecular docking. PyMOL software was then employed to display the docking model. All websites of the databases used in this study are listed in **Table 1**.

Chemicals and Reagents

Tetrahydropalmatine (THP, B74569) (purity ≥ 98%, HPLC) was purchased from Shanghai Yuanye Biotechnology Co., Ltd. (Shanghai, China). The THP powder was dissolved in dimethyl sulfoxide (DMSO, Sigma, St. Louis, MO, United States). Diazoxide (01131863) was provided by Adamas-beta (Basel, Switzerland), and LY294002 (S1105) was provided by Selleck (Shanghai, China).

Cell Culture and Treatment

H9c2 cells were plated into a dish (35 mm) at a density of 1×10^6 cells and then maintained in Dulbecco's modified Eagle's medium (DMEM) containing 10% fetal bovine serum (FBS). The cells were grown at 37°C in humidified 5% CO_2. Before the subsequent experiments, a serum-free conditioned medium was used for cell culture.

Cell Viability Assay

A Cell Counting Kit-8 (CCK-8) assay kit (GLPBIO, California, United States) was used to examine cell activity. Briefly, H9c2 cells were seeded into 96-well plates. After treatment, the cells were incubated with 10 μl CCK-8 solution per well for 2 h at 37°C, and after incubation, the absorbance value at 450 nm was measured using a microplate reader (Thermo Varioskan LUX, MA, United States).

Western Blot Analysis

Western blot assays were performed as we previously reported (Li et al., 2016b; Li et al., 2019b). Primary antibodies against phospho-Akt (Ser473) (Cat# 4060), Akt (Cat# 4691), and caspase-3 (Cat# 9692) were provided by Cell Signaling Technology (Danvers, Massachusetts, United States). A primary antibody against cleaved-caspase-3 (bsm-33199M) was provided by Bioss (Beijing). Anti-β-actin antibody (GB12001) was provided by Servicebio (Wuhan). Equivalent amounts of protein (20 μg protein extracts) were separated by 8%–12%

TABLE 1 | The websites of the databases used in this study.

Database	Website
TCMSP	http://tcmspw.com/
ETCM	http://www.tcmip.cn/ETCM/index.php/Home/Index/
TCMID	http://www.megabionet.org/tcmid/
PubChem	https://pubchem.ncbi.nlm.nih.gov/
PharmMapper	http://lilab.ecust.edu.cn/pharmmapper/
DisGeNET	https://www.disgenet.org/
GeneCards	https://www.genecards.org/
DrugBank	https://www.drugbank.ca/
TTD	http://db.idrblab.net/ttd/
GEO	https://www.ncbi.nlm.nih.gov/geo/
UniProtKB	https://www.uniprot.org/
DAVID	https://david.ncifcrf.gov/
Protein Data Bank	https://www.rcsb.org/

sodium dodecyl sulfate polyacrylamide gel electrophoresis (SDS-PAGE) and then transferred to polyvinylidene fluoride (PVDF) membranes (Millipore, United States). The PVDF membranes were incubated overnight with the primary antibodies at 4°C.

After overnight incubation, appropriate horseradish peroxidase (HRP)-conjugated secondary antibodies were added and incubated at room temperature for 1 h. The protein level signals were visualized using ECL-enhanced chemiluminescence (Tanon, Shanghai), and the band intensities were quantified by ImageJ software (Bio-Rad).

Quantitative Real-Time Polymerase Chain Reaction

The H9c2 cells were lysed with Accurate Biology RNAex Pro Reagent (AG21102, Accurate Biology, Hunan, China) to extract total RNA. Then 2 μg of RNA was reversely transcribed to cDNA with the Evo M-MLV RT Kit (Accurate Biotechnology, Human, China). The mRNA levels were determined with a SYBR Green qPCR kit (Accurate Biotechnology, Human, China) by QuantStudio 5 Real-Time PCR instrument (Thermo Fisher Scientific, MA, United States). Rat-specific primers for BCL2 Associated X (Bax), B cell lymphoma-2 (Bcl-2), p53, interleukin-6 (IL-6), interleukin-1 beta (IL-1β), tumor necrosis factor-α (TNF-α), and β-actin were synthesized by Sangon Biotech (Shanghai) (**Table 2**). All semiquantitative and quantitative real-time polymerase chain reaction (RT-qPCR) data were quantified with respect to β-actin. The results were calculated by the $2^{-\Delta\Delta Ct}$ method.

TdT-Mediated dUTP Nick-End Labeling Staining

A one Step TdT-Mediated dUTP Nick-End Labeling (TUNEL) Apoptosis Assay Kit (Beyotime, China) was used to measure cell apoptosis. H9c2 cells were washed with phosphate buffered saline (PBS) three times and fixed with 4% paraformaldehyde for 10 min. After washing with PBS three times, H9c2 cells were incubated with 50 μl of TUNEL detection solution at 37°C for 1 h in the dark and then incubated with 4′,6-diamidino-2-phenylindole (DAPI) for 10 min to visualize nuclei. The green spectrum and blue spectrum were used to detect TUNEL-positive cells and nuclei, respectively. Finally, the cells were photographed by confocal scanning microscopy (Leica TCS SP8, Leica, Germany). TUNEL-positive cells were quantified and analyzed from four different views. Data were expressed as the percentage of the number of TUNEL-positive nuclei in the total number of nuclei detected by DAPI staining. ImageJ software was used to calculate the number of TUNEL positive cells.

Statistical Analysis

The data in this study are presented as mean ± SD from three independent replicates. One-way analysis of variance (ANOVA) with the Bonferroni post-hoc test was performed among the multiple groups. In all cases, $p < 0.05$ was considered statistically significant.

RESULTS

Target Prediction and Analysis

To collect the components of RC, we searched three databases, and in all, 60 bioactive components were collected by filtering the TCMSP, ETCM, and TCMID databases by the limitations of OB ≥ 30% and DL ≥ 0.18. The active ingredients mainly included berberine, sitosterol, tetrahydropalmatine, corydaline, and quercetin. The information about the components is listed in **Supplementary Table S1**. The potential targets were predicted according to the PharmMapper database, which was based on a large-scale reverse pharmacophore mapping strategy. Finally, we obtained 431 potential targets after removing duplicates. The component-target network is shown in **Supplementary Figure S1**.

To facilitate statistics, we set screening conditions for MI targets derived from corresponding databases. After taking the third quartile value, a relevance score ≥ 3.66 was set as the threshold for targets from the GeneCards database, and a score ≥ 0.1 was set as the threshold for those from the DisGeNET database. While searching GEO datasets, we selected the reference series GSE48060 to obtain the differentially expressed genes between normal cardiac function

TABLE 2 | Nucleotide sequences of the gene-specific primers used for RT-qPCR.

Primer	Sequences
Bax	Forward: 5′-TGGGATGGCCTCCTTTCCTA-3′
	Reverse: 5′-TTCCCCGTTCCCCATTCATC-3′
Bcl-2	Forward: 5′-TGGAGAGCGTCAACAGGGAGATG-3′
	Reverse: 5′ -GTGCAGATGCCGGTTCAGGTAC-3′
p53	Forward: 5′-CCTTACCATCATCACGCTGGAAGAC-3′
	Reverse: 5′-AGGACAGGCACAAACACGAACC-3′
IL-6	Forward: 5′-ACTTCCAGCCAGTTGCCTTCTTG-3′
	Reverse: 5′-TGGTCTGTTGTGGGTGGTATCCTC-3′
IL-1β	Forward: 5′-TGCAGGCTTCGAGATGAAC-3′
	Reverse: 5′-GGGATTTTGTCGTTGCTTGTC-3′
TNF-α	Forward: 5′-CTTCTGTCTACTGAACTTCGGG-3′
	Reverse: 5′-CTACGGGCTTGTCACTCG-3′
β-Actin	Forward: 5′-TCGTGCGTGACATTAAAGAG-3′
	Reverse: 5′-ATTGCCGATAGTGATGACCT-3′

controls and first-time MI patients (Suresh et al., 2014). The filter conditions were adjusted as $p < 0.05$ and absolute fold change of 1.5 or greater. After deleting duplicates, 1,131 targets were obtained in total.

Protein-Protein Network Analysis

We used the Cytoscape plugin BisoGenet to construct a PPI network of RC potential targets (8,287 nodes and 296,987 edges) (**Figure 2A**) and MI-related targets (11,735 nodes and 391,369 edges) (**Figure 2B**). To identify a comprehensive RC-MI-target network, we merged the two PPI networks and there were 7,462 nodes and 279,264 edges in total in the new PPI network (**Figure 2C**). From topological analysis conducted by the plugin CytoNCA, we performed filtration twice. The first screening condition is that DC is greater than and equal to double median (DC ≥ 92) (**Figure 2D**), and the second screening condition is that DC, BC, EC, LAC, and NC are greater than and equal to double median (DC ≥ 158, BC ≥ 1955.51, EC ≥ 0.03, LAC ≥ 23.37, and NC ≥ 25.48), and CC is greater than and equal to median (CC ≥ 0.50). Ultimately, a central PPI network with 126 nodes and 3,245 edges was obtained (**Figure 2E**). The 126 nodes represented 126 core targets associated with both RC and MI, and the information about the 126 core targets is listed in **Supplementary Table S2**. We also performed a component-core target network and found that 12 of the 126 core targets, including androgen receptor (AR), estrogen receptor 1 (ESR1), cyclin-dependent kinase 2 (CDK2), heat shock protein 90 kDa alpha A1 (HSP90AA1), heat shock 70 kDa protein 8 (HSPA8), epidermal growth factor receptor (EGFR), AKT1, poly (ADP-ribose) polymerase 1 (PARP1), growth factor receptor-bound protein 2 (GRB2), mouse doubleminute 2 (MDM2), heat shock protein 90 kDa alpha (cytosolic), class B member 1 (HSP90AB1), and heat shock 70 kDa protein 1A (HSPA1A), could be regulated by the 60 bioactive components (**Figure 3**; **Supplementary Table S3**).

GO Analysis and KEGG Analysis of the Core Targets

To identify the biological function of the core targets, GO and KEGG enrichment analyses of the 126 core targets were performed using the DAVID online tool. Ultimately, a total of 126 targets were analyzed by GO, while 105 targets were enriched in KEGG pathways. The top 10 results of biological process analysis, cellular component analysis, and molecular function analysis of GO function and the top 10 major KEGG enriched pathways are shown in **Figure 4**. The results suggest that 126 core targets could regulate biological processes involving positive regulation of transcription from RNA polymerase II promoter (p = 0.000000000020993, 31 targets/981), negative regulation of transcription from RNA polymerase II promoter (p = 0.000000000000054, 30 targets/720), transcription, DNA-templated (p = 0.004630802658299, 26 targets/1955), viral process (p = 0.000000000000000, 24 targets/299), negative regulation of apoptotic process (p = 0.000000001107359, 20 targets/455), negative regulation of transcription, DNA-templated (p = 0.000000005053472, 20 targets/499), cell-cell adhesion (p = 0.000000000017396, 18 targets/271), positive regulation of transcription, DNA-templated (p = 0.000000270675033, 18 targets/515), negative regulation of gene expression, epigenetic (p = 0.000000000000000, 16 targets/50) and cellular protein metabolic process (p = 0.000000000000010, 16 targets/118).

The top 10 cellular components were nucleus (p = 0.000000000000000, 94 targets/5,415), nucleoplasm (p = 0.000000000000000, 90 targets/2,784), cytoplasm (p = 0.000000000132580, 71 targets/5,222), cytosol (p = 0.000000000000005, 62 targets/3,315), membrane (p = 0.000000000000000, 60 targets/2,200), extracellular exosome (p = 0.000000000000097, 55 targets/2,811), protein complex (p = 0.000000000000000, 34 targets/412), nucleolus (p = 0.000000000000013, 32 targets/857), cell-cell adherens junction (p = 0.000000000000000, 23 targets/323) and focal adhesion (p = 0.000000000002406, 21 targets/391).

The major molecular functions were protein binding (p = 0.000000000000000, 124 targets/8,785), poly(A) RNA binding (p = 0.000000000000000, 50 targets/1,129), ubiquitin protein ligase binding (p = 0.000000000000000, 29 targets/287), enzyme binding (p = 0.000000000000000, 29 targets/333), ATP binding (p = 0.000003513330142, 29 targets/1,495), DNA binding (p = 0.000078465083276, 28 targets/1,674), cadherin binding involved in cell-cell adhesion (p = 0.000000000000000, 23 targets/290), protein heterodimerization activity (p = 0.000000000209051, 21 targets/465), identical protein binding (p = 0.000000600209776, 21 targets/749) and transcription factor binding (p = 0.000000000003245, 19 targets/284).

As the KEGG analysis of the core target results showed, among the 10 pathways, we found that the 126 core targets were primarily involved in the phosphatidylinositol 3-kinase (PI3K)/protein kinase B (PKB, also called Akt) signaling pathway (p = 0.000003284827250, 19 targets/345). As **Figure 3** shows, most components had the potential to regulate Akt. The PI3K/Akt pathway was enriched with 15 core targets, as shown in **Figure 5**.

Results of Molecular Docking Analysis

Among these bioactive components (**Figure 3**), some were dedicated to pain relief or cancer treatment (Gao et al., 1994; Xu et al., 2012; Chen et al., 2016; Wang et al., 2016; Wang et al., 2019), while berberine, coptisine, THP, palmatine, and quercetin were reported to be cardioprotective (Kim et al., 2009; Guo et al., 2013; Zhu et al., 2020; Albadrani et al., 2021). In this study, we conducted molecular docking of the 5 components with AKT1, the core target related to the PI3K/Akt pathway. The results are displayed in **Figure 6** and **Supplementary Figure S2**. Among the 5 components, THP had the lowest binding energy with AKT1. A previous study suggested that THP plays a beneficial role in MI-induced heart failure and MI/RI (Wu et al., 2007a), while its effect on MI remains elusive. THP was recently reported to modulate the PI3K/Akt/mTOR pathway to protect against limb ischemia/reperfusion injury (Wen et al., 2020). Therefore, we speculated that THP may alleviate MI injury by regulating the PI3K/Akt pathway. To this end, we conducted molecular docking. A docking diagram of Akt (PDB 6HHG) and THP (CAS: 6024-85-7) is displayed in **Figures 6A,B**. Hydrogen bonds were formed between THP

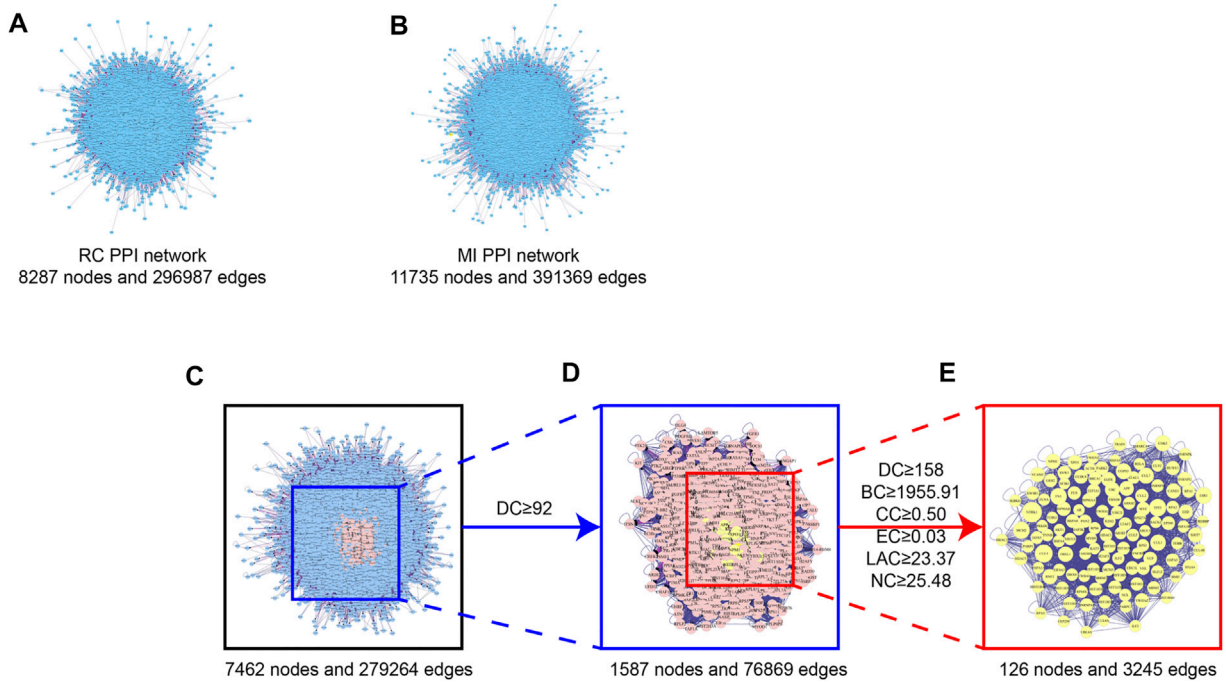

FIGURE 2 | Topological screening process of PPI network. **(A)** PPI network of the potential targets of the RC ingredients. 8,287 nodes represent the interactive proteins of RC, 2,96,987 edges represent the interactive relationship. **(B)** PPI network of the MI-related targets. 11,735 nodes represent the interactive proteins of MI, 3,91,369 edges represent the interactive relationship. **(C)** PPI network of merged RC and MI. 7,462 nodes represent the interactive proteins of the merged network, 2,79,264 edges represent the interactive relationship. **(D)** PPI network of merged RC and MI with DC ≥ 92. 1,587 nodes represent the interactive proteins of the merged network with DC ≥ 92, 76,869 edges represent the interactive relationship. **(E)** Central PPI network of merged RC and MI. 126 nodes represent the core proteins of the merged network, 3,245 edges represent the interactive relationship.

and amino acid residues Asn 53 in the crystal structure of Akt. The binding affinity of THP with the Akt crystal structure was −7.12 kcal/mol (**Figure 6C**). This result demonstrated that THP has a strong binding capacity with Akt. Thus, THP was used for the subsequent experimental validation.

THP Protected H9c2 Cells Against OGD-Induced Injury

To elucidate the efficacy of THP (Chemical structure of THP showed in **Figure 7A**) against MI, we first assessed the cytotoxicity of THP on the growth of H9c2 cells. The results showed that in resting cells, THP had no toxicity to H9c2 cells below 240 μM (**Figure 7B**). Under ischemic conditions, a reduction in glucose and oxygen causes damage to cardiomyocytes. Among the various methods for simulating the pathological process of ischemia *in vitro*, oxygen and glucose deprivation insult has been widely used as a classic approach. Therefore, to investigate the cardioprotective effect of THP, we constructed an OGD model in H9c2 cells. H9c2 cells were exposed to OGD insult for the indicated times, and cell viability was determined using a CCK8 assay kit. As **Figure 7C** shows, after OGD for 1, 3, or 6 h, the viability of H9c2 cells was significantly reduced. Because cell injury was the most obvious at 3 h, experimental measurements were taken after the cells were treated for 3 h. We then treated H9c2 cells with various doses of THP and the positive control drug diazoxide for 48 h before being exposed to OGD. As shown in **Figure 7D**, THP treatment (15 μM or more) protected H9c2 cells against OGD-induced injury. Thus, 15, 30, and 60 μM THP were chosen for the following experiments.

THP Decreased OGD-Induced Apoptosis in H9c2 Cells

As shown in **Figures 8A,C**, OGD notably elevated the cell apoptosis level, as indicated by the increased protein level of cleaved caspase-3/caspase-3, as well as the increased mRNA level of Bax, and the reduced mRNA level of Bcl2 (**Figures 8D,E**). Moreover, the mRNA level of p53 was increased after OGD for 3 h (**Figure 8F**), and THP treatment significantly reduced OGD-induced apoptosis (**Figures 8A–F**). The anti-apoptosis effect of 60 μM THP seemed equal to that of 100 μM diazoxide. Our results showed that THP greatly decreased apoptosis of H9c2 cells after OGD exposure, supporting the protective effect of THP in MI injury.

THP Decreased the OGD-Induced Expression of Inflammatory Factors

In the present study, OGD induced a series of inflammatory changes that mediated cardiomyocyte injury. The mRNA

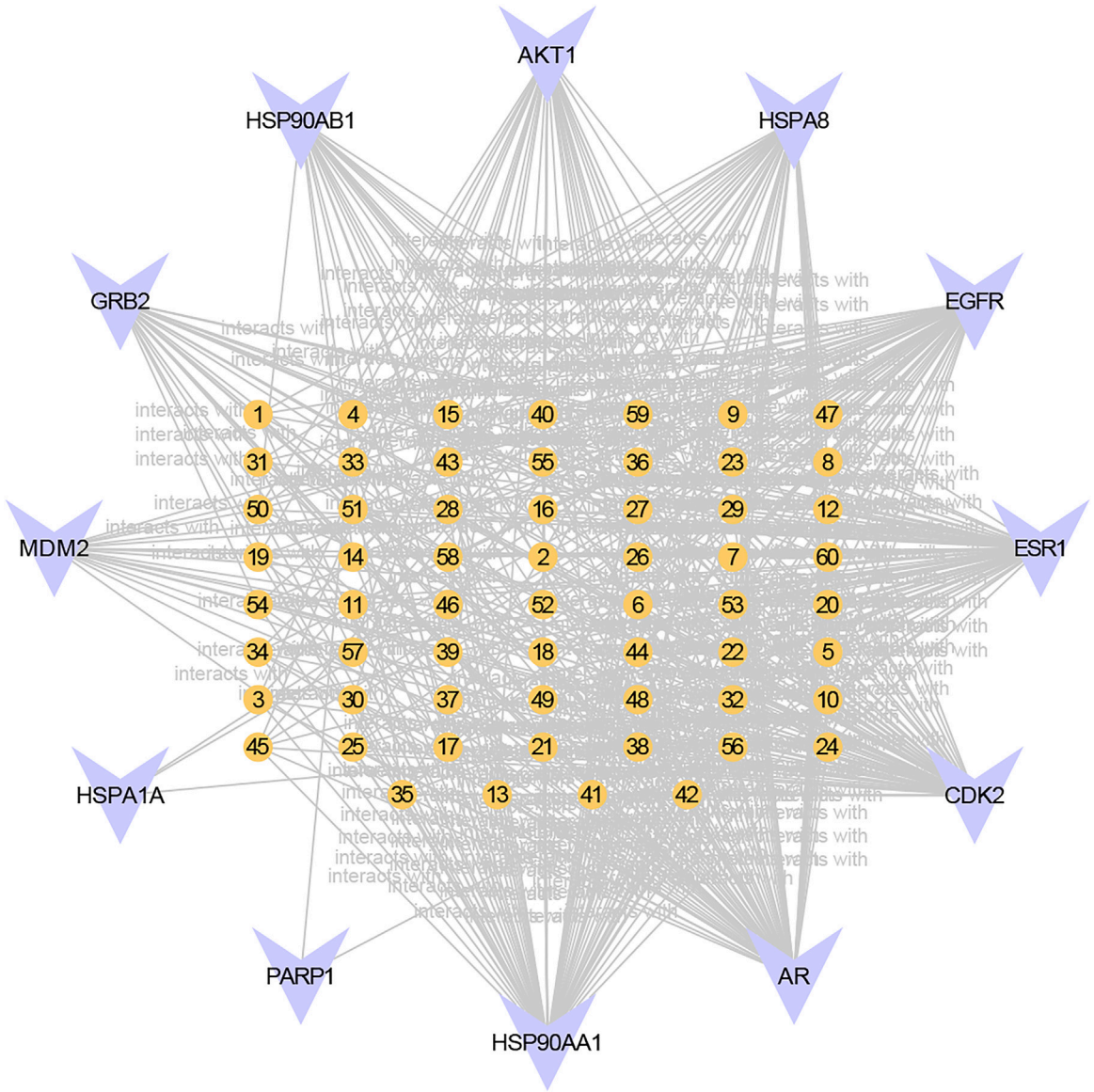

FIGURE 3 | Component-core target network of RC and 12 core targets. 12 of the 126 core targets were RC-targets that correlated with 60 total bioactive components. The orange nodes represent the potential active ingredients, and the violet nodes represent the core targets.

expression levels of inflammatory factors, including IL-6, IL-1β, and TNF-α, were significantly increased in the OGD group compared to the control group. However, THP treatment (15, 30, and 60 μM) significantly inhibited the overproduction of these inflammatory biomarkers compared to the OGD-induced group (**Figures 8G–I**). Collectively, THP was shown to significantly suppress the inflammatory process.

THP Elevated Akt Phosphorylation

The results from KEGG enrichment showed that RC and THP were closely related to the PI3K/Akt signaling pathway against MI and that most components could regulate Akt. Therefore, to confirm whether THP exhibits a protective effect via the regulation of Akt, the phosphorylation level and protein expression of Akt were detected. As shown in **Figure 8A**, OGD significantly decreased Akt phosphorylation (Ser473). Moreover, THP strongly elevated Akt phosphorylation in a dose-dependent manner, without affecting the expression of total Akt. These data suggest that THP might suppress MI injury by regulating the Akt signaling pathway.

THP Exhibited Anti-Apoptotic and Anti-Inflammatory Effects *via* the PI3K/Akt Signaling Pathway

The PI3K/Akt signaling pathway is significant in defending against myocardial infarction damage (Feng et al., 2020; Ruan et al., 2020). According to previous experiments, we ascertained

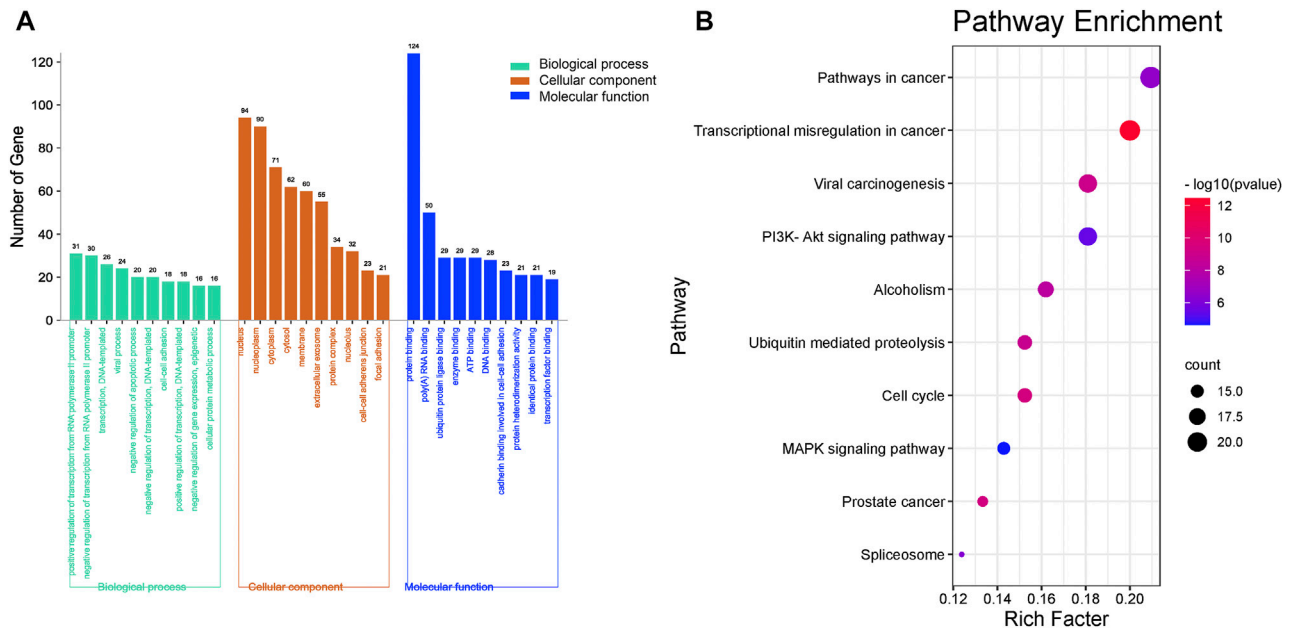

FIGURE 4 | Enrichment of GO and KEGG analysis of the 126 key genes targeted by RC against MI. **(A)** The GO enrichment results of biological processes, cellular components, and molecular function. **(B)** Enriched KEGG pathways of potential key targets. The top 10 major enriched pathways are shown.

that THP plays an important role in inhibiting apoptosis and inflammation. To further clarify the significance of the PI3K/Akt signaling pathway in this process, we used LY294002, an inhibitor of the PI3K/Akt pathway, to block the PI3K/Akt pathway. In our experiment we found that the upregulated cleaved caspase-3/caspase-3, Bax, and p53 that had been induced by OGD were downregulated by THP, and the downregulated Bcl2, induced by OGD, was upregulated by THP, but these effects were diminished by LY294002 (10 μM) treatment (**Figures 9A–F**). Moreover, LY294002 treatment also prevented the anti-inflammatory effect of THP, as indicated by the reduced mRNA levels of IL-6, IL-1β, and TNF-α (**Figures 9G–I**). In addition, the TUNEL assay results showed that OGD induced a marked elevation in the number of TUNEL-positive cells (green nuclear staining), whereas THP treatment reduced the number of TUNEL-positive cells. However, LY294002 treatment reversed the anti-apoptotic effect of THP in H9c2 cells stimulated with OGD (**Figure 10**). Accordingly, these findings demonstrate that THP protected H9c2 cells from OGD-induced apoptosis by activating the PI3K/Akt pathway.

DISCUSSION

MI is a severe disease with high motility that places a heavy burden on individuals and society. The current mechanisms of MI include cell death, mitochondrial dysfunction, inflammatory response, oxidative stress, and ATP depletion (Frangogiannis, 2014; Frangogiannis, 2015; Kurian et al., 2016). In addition, MI can lead to various complications, such as arrhythmia, heart failure, and cardiac rupture (Gong et al., 2021). TCM, including individual herbs or combination formulas that contain multiple compounds, may have positive pharmacological benefits in the treatment of MI. RC is usually applied alone or in a formula in treating MI in China. RC can ameliorate symptoms and reduce the incidence of severe complications, although the specific mechanism remains unknown. In this study, a network pharmacology approach, accompanied by experimental validation and molecular docking analysis, was applied to explore the underlying pharmacological mechanism of RC in treating MI (**Figure 1**).

The chemical components of RC can be classified as alkaloids (including berberine, aporphine, opiates, isoquinoline, steroids, organic acid, carbohydrates, and others) (Tian et al., 2020). In this study, after screening RC in the TCMSP, ETCM, and TCMID databases with the standards of OB ≥ 30%, as well as DL ≥ 0.18, we filtered 60 bioactive components, of which many have been shown to be cardioprotective (**Supplementary Figure S1**; **Supplementary Table S1**). Quercetin can protect cardiomyocytes against ischemia, hypoxia or isoproterenol (ISO) insults due to its anti-inflammatory, antioxidant, and anti-apoptotic effects, and by partly regulating silent information regulatory factor 1 (SIRT1) and adenosine monophosphate-activated protein kinase (AMPK) pathways (Li et al., 2016a; Kumar et al., 2017; Guo et al., 2019; Tang et al., 2019). Emodin inhibit apoptosis and the inflammatory response to protect the myocardium from ischemia or hypoxia-induced injury (Wu et al., 2007b; Ye et al., 2019; Zhang et al., 2019). Palmatine can produce antioxidant and anti-inflammatory actions to reduce myocardial I/R injury by decreasing serum levels of creatine phosphokinase (CK), lactate dehydrogenase (LDH), and malonaldehyde (MDA), and also hinders decline

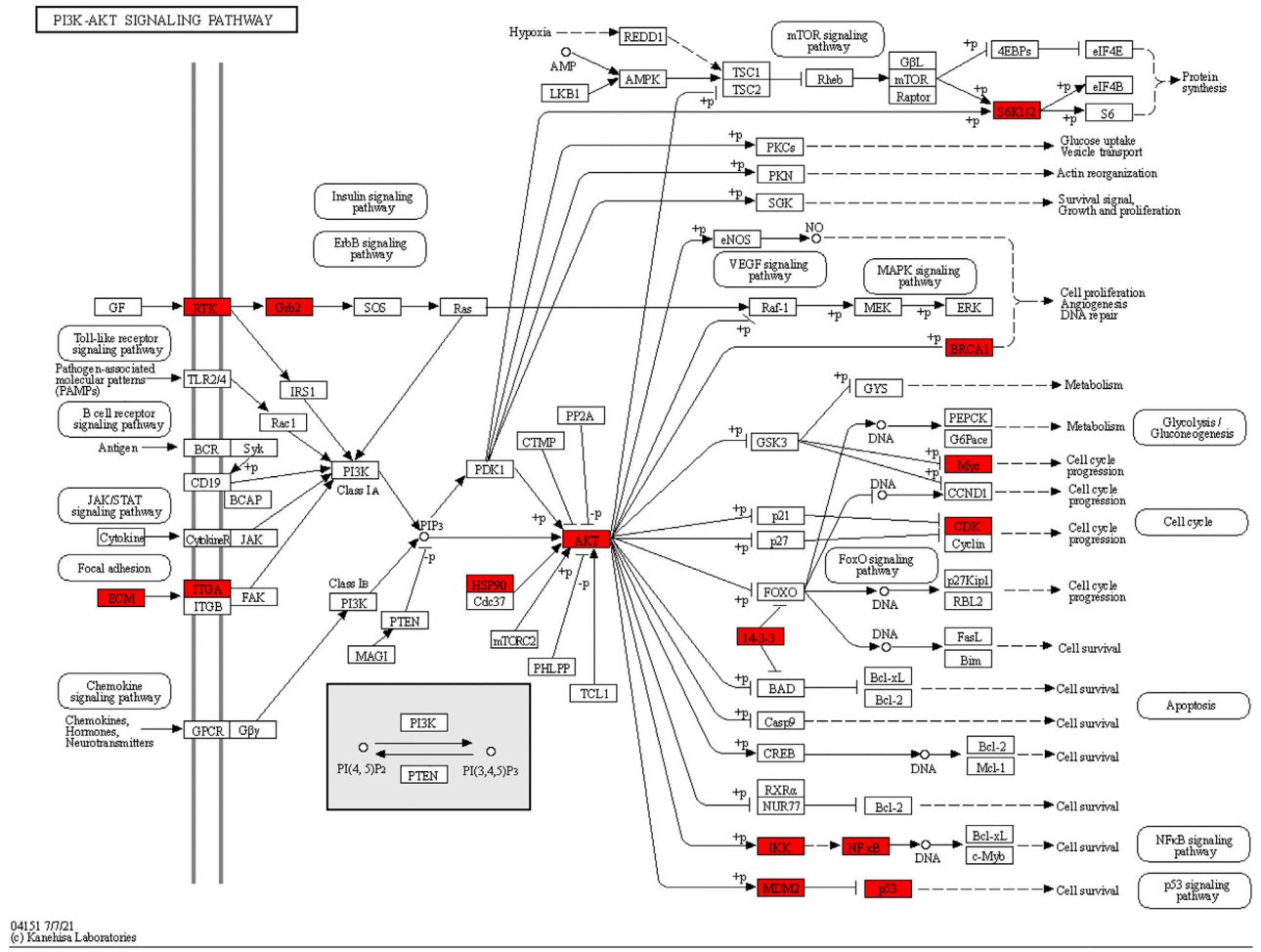

FIGURE 5 | Core targets enriched in the PI3K/Akt pathway. The red nodes represent 15 core targets enriched in the PI3K/Akt pathway.

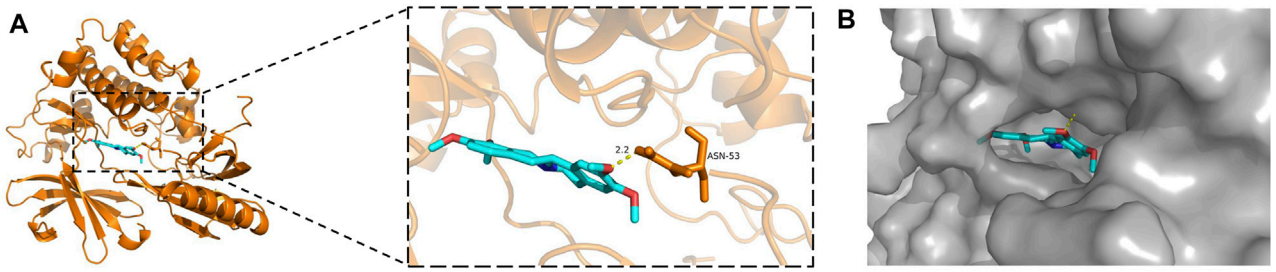

C

Macromolecule	Ligand	Binding Energy (kcal/mol)
AKT1	Tetrahydropalmatine	-7.27

FIGURE 6 | Molecular docking diagram of Akt with THP. **(A)** Structure diagram of Akt docked with THP. Yellow lines represent hydrogen bond. **(B)** Surface diagram of Akt docked with THP. **(C)** The binding energy for THP docked into the Akt crystal structure.

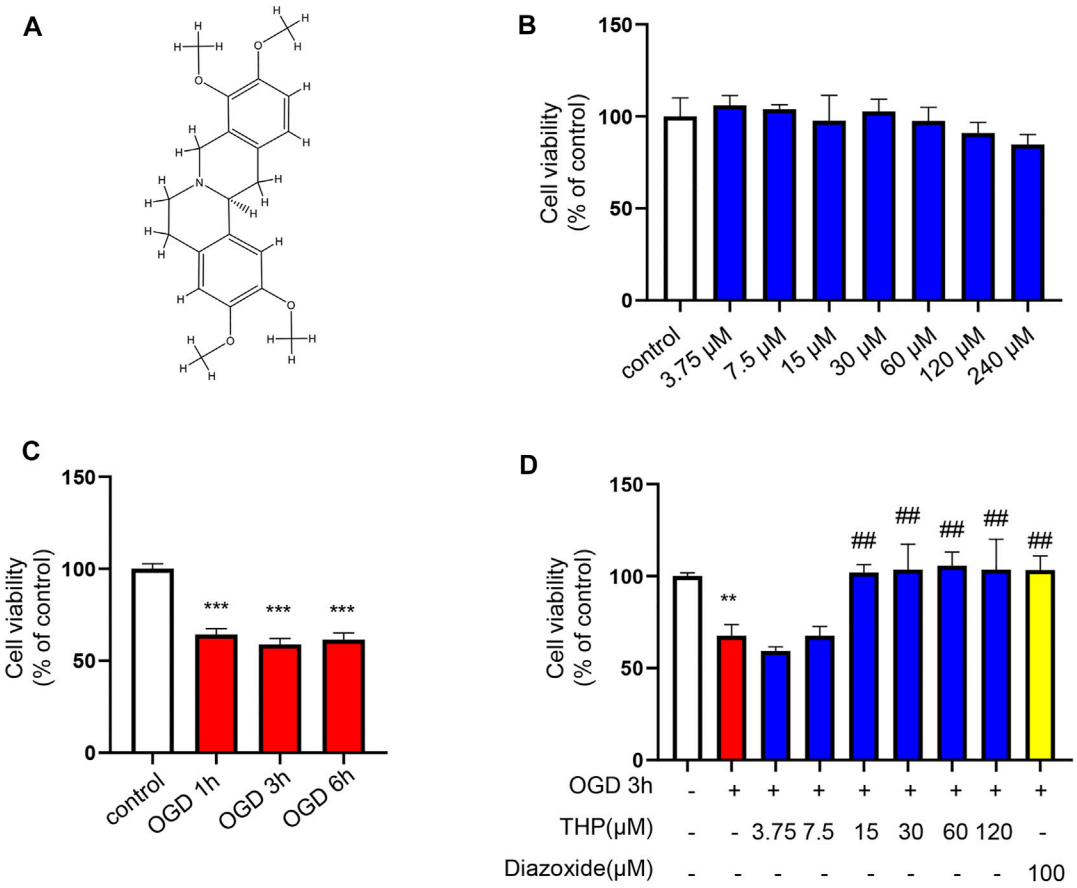

FIGURE 7 | THP had no cellular toxicity on H9c2 cells under 240 μM and protected H9c2 against OGD-induced injury. **(A)** Chemical structure of THP. **(B)** H9c2 cells were incubated with THP for the indicated concentrations ranging from 3.75 to 240 μM for 24 h. **(C,D)** The effect of THP on the OGD-induced H9c2 cells. H9c2 cells were treated with different concentrations of THP or diazoxide for 48 h following OGD exposure. Then the H9c2 cells were cultured under OGD condition for the indicated time. A CCK-8 assay was used to determine cell viability. Data are presented as the mean ± SD. $^{**}p < 0.01$, $^{***}p < 0.001$ vs. control, $^{\#\#}p < 0.01$ vs. OGD. $n = 3$ (three independent replicates).

in the activity of superoxide dismutase (SOD) and catalase (Kim et al., 2009). Berberine has anti-oxidant, anti-apoptosis, and anti-inflammation functions, promoting autophagy and attenuating endoplasmic reticulum (ER) stress to protect the myocardium from I/R injury by regulating the toll-like receptor 4 (TLR4) pathway, PI3K/Akt signaling pathway, SIRT1 pathway, Janus kinase 2 (JAK2)/signal transducer and activator of transcription 3 (STAT3) pathway, and hypoxia inducible factor-1α (HIF-1α) pathway (Liu et al., 2019; Zhu et al., 2020). Vanillic acid reduces infarct size and inhibits the apoptosis pathway by regulating caspase-9, caspase-3, and Bcl-2 (Prince et al., 2011; Stanely Mainzen Prince et al., 2015; Radmanesh et al., 2017). Coptisine reduces infarct size and protects cardiomyocytes from apoptosis and oxidative stress, partly through the Beclin-1/SIRT1 pathway and RhoA/Rho-associated kinase pathway (Gong et al., 2012; Guo et al., 2013; Wang et al., 2017b). Glaucine, dehydrocorydaline, canadine, tetrahydrocoptisine, and corydaline exhibit antiplatelet activity that strongly inhibits thrombin-induced platelet aggregation (Zhang et al., 2016). Allocryptopine exhibits an antiarrhythmic effect and can blunt the atrial late sodium current increase, reduce the current densities of the outward potassium current and slow the delayed rectifier potassium current (Fu et al., 2016; Dong et al., 2019). Protopine is reported to provide protection for rats with cerebral ischemic injury and suppress platelet aggregation and inflammatory response (Chia et al., 2006; Xiao et al., 2007; Bae et al., 2012; Alam et al., 2019). Additionally, protopine may be cardioprotective against MI according to the above effects. All of this evidence suggests that RC alleviates MI injury due to its multitarget and multicomponent activity. Therefore, in the present study, network pharmacology and experimental validation were performed to conduct systematic analysis of RC at the molecular level, to reveal the effect and underlying pharmacological mechanism of RC for treating MI.

Moreover, we obtained a PPI network by merging the active component target PPI of RC and the potential target PPI of MI (**Figure 2C**). Then, according to the following parameters, that is DC, BC, EC, LAC, NC, and CC, the topological characteristics of the PPI

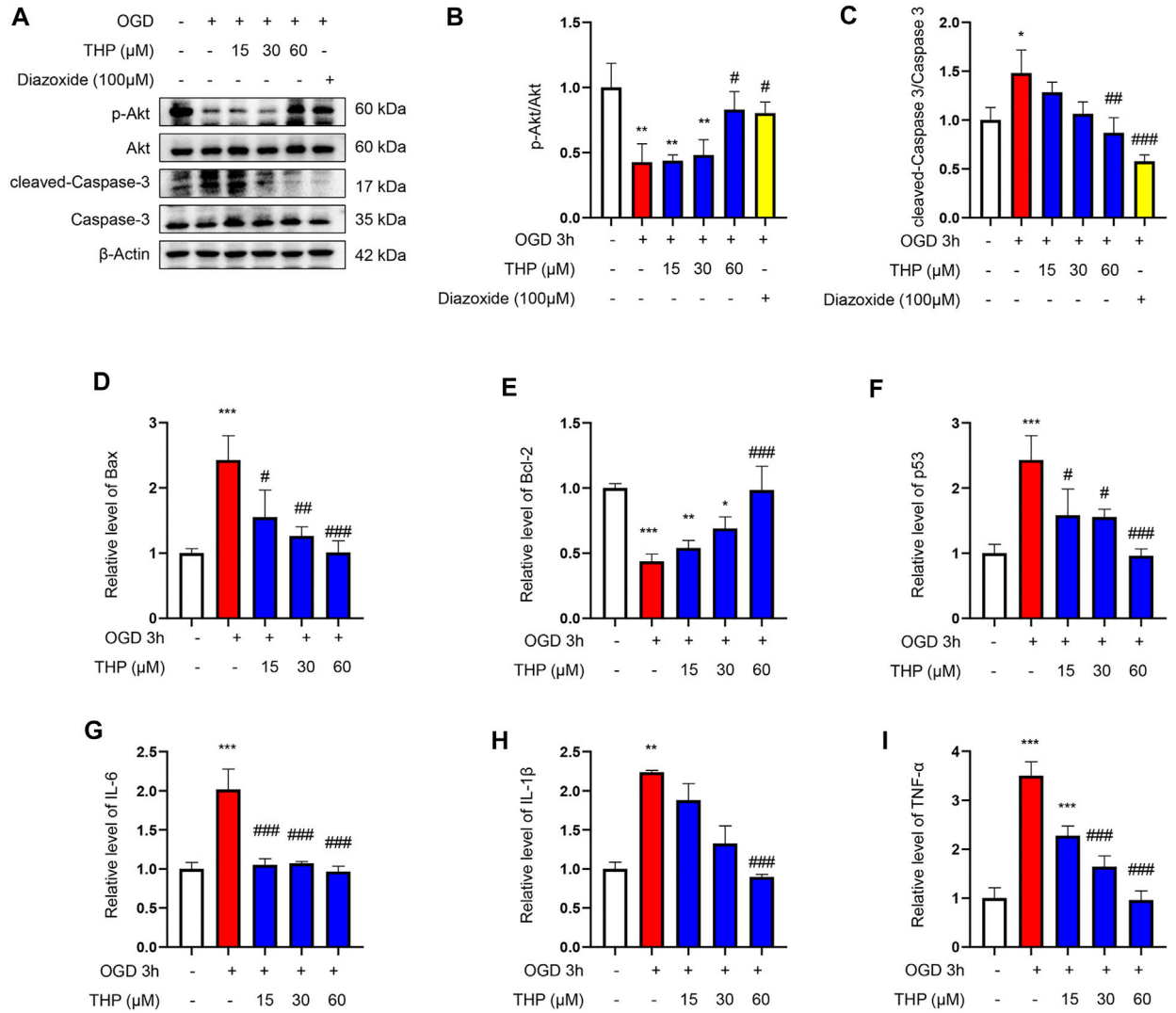

FIGURE 8 | THP was able to suppress apoptosis and the expressions of inflammatory factors induced by OGD in H9c2 cells. The cultured cells were treated with different concentrations of THP or diazoxide and stimulated with OGD for 3 h **(A–C)** The protein expressions of p-Akt, total Akt, cleaved caspase-3, and caspase-3. **(D–F)** The mRNA expressions of apoptosis factors (Bax, Bcl-2, and p53). **(G–I)** The mRNA expressions of inflammatory factors (IL-6, IL-1β, and TNF-α). Data are shown as the mean ± SD. $^{*}p < 0.05$, $^{**}p < 0.01$, $^{***}p < 0.001$ vs. control; $^{\#}p < 0.05$, $^{\#\#}p < 0.01$, $^{\#\#\#}p < 0.001$ vs. OGD. $n = 3$ (three independent replicates).

network were analyzed. A total of 126 core targets were found (**Figure 2E**; **Supplementary Table S2**). We also constructed a component-core target network and found that 60 bioactive components regulated 12 core targets, including AR, ESR1, CDK2, HSP90AA1, HSPA8, EGFR, AKT1, PARP1, GRB2, MDM2, HSP90AB1, and HSPA1A, which are closely involved in the apoptotic process (**Figure 3**; **Supplementary Table S3**). Apoptosis, which can be triggered by MI, is an energy-dependent programmed process responsible for cell removal (Zhang et al., 2022). Mitochondrial dysfunction is an important part of apoptosis caused by MI and is related to the impaired permeability of the mitochondrial outer membrane, causing the release of apoptosis-related proteins, such as apoptosis-inducing factor, Bcl-2 proteins, and cytochrome c (Ong and Gustafsson, 2012; Del Re et al., 2019). We then performed GO enrichment and KEGG enrichment analyses of the crucial targets. GO enrichment analysis can be performed to reveal the biological mechanisms of the core targets in disease. GO enrichment analysis was performed based on the following three terms: biological processes, cellular component, and molecular function terms (Ashburner et al., 2000). The results of GO enrichment analysis showed that the protective effects of RC on inhibiting MI are achieved through the simultaneous activation of multiple biological processes, cellular components, and molecular functions (**Figure 4A**). Next, we used the KEGG database to demonstrate the systematic functions and biological relevance of the potential targets (Chen et al., 2015). The KEGG pathway enrichment analysis of core targets indicated that RC may ameliorate MI-induced apoptosis by regulating multiple pathways, including pathways in cancer, transcriptional misregulation in cancer, viral carcinogenesis, the PI3K/Akt signaling pathway, alcoholism,

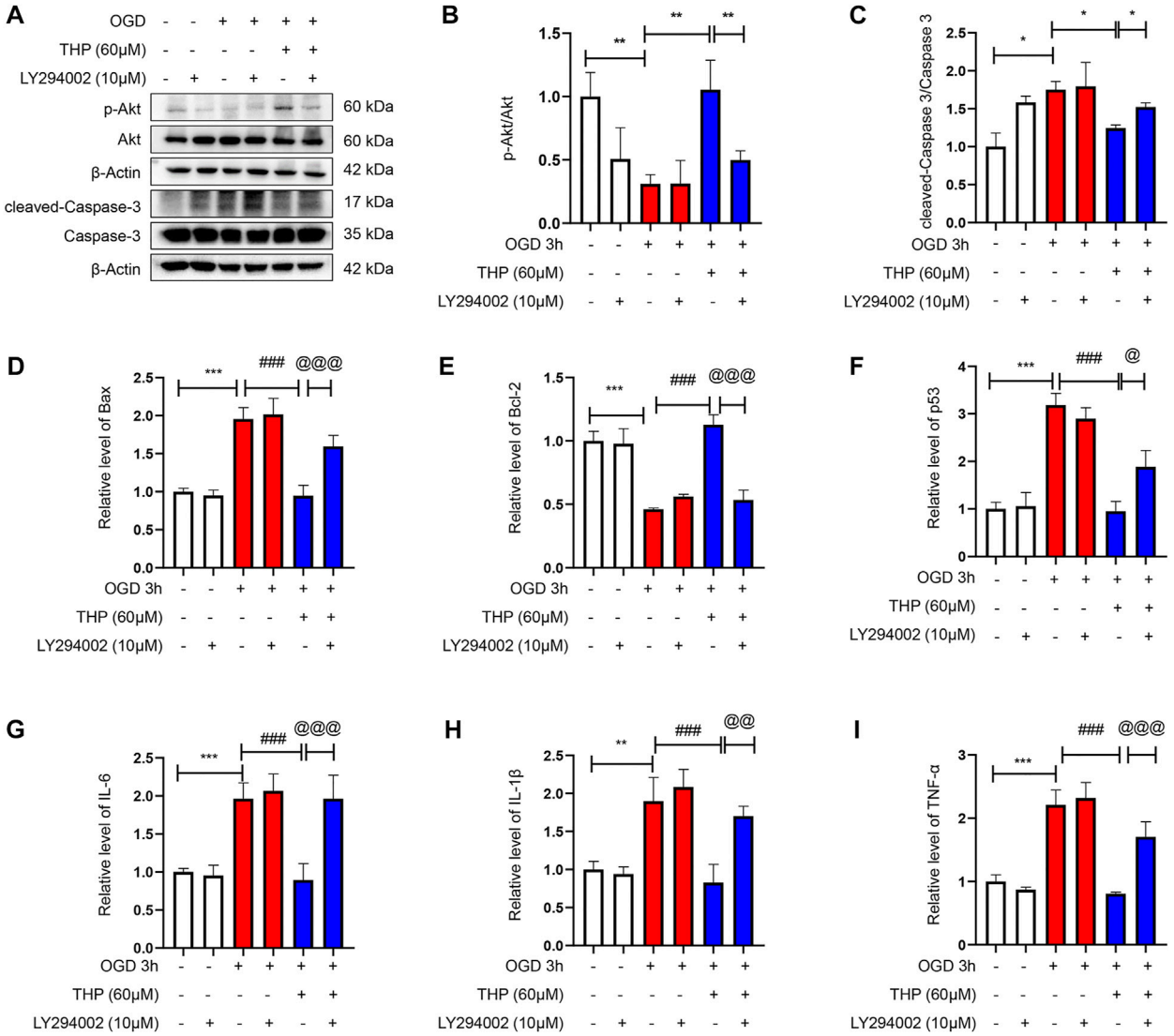

FIGURE 9 | THP exhibited anti-apoptotic effect and suppressed the expression of inflammatory factors via regulating the PI3K/Akt signaling pathway. H9c2 cells were incubated with LY294002 (10 μM, diluted in DMSO), an inhibitor of the PI3K/Akt pathway or treated with THP (60 μM) for 48 h, and then the cells were stimulated with OGD. **(A–C)** The protein expressions of p-Akt, total Akt, cleaved caspase-3, and caspase-3. **(D–F)** The mRNA expressions of apoptosis factors (Bax, Bcl-2, and p53). **(G–I)** The mRNA expressions of inflammatory factors (IL-6, IL-1β, and TNF-α). Data are shown as the mean ± SD. $^{*}p < 0.05$, $^{**}p < 0.01$, $^{***}p < 0.001$ vs. control; $^{\#}p < 0.05$, $^{\#\#}p < 0.01$, $^{\#\#\#}p < 0.001$ vs. OGD, $^{@}p < 0.05$, $^{@@}p < 0.01$, $^{@@@}p < 0.001$ vs. OGD + THP. $n = 3$ (three independent replicates).

ubiquitin-mediated proteolysis, etc. (**Figure 4B**). Among the pathways, the PI3K/Akt signaling pathway primarily regulates cellular survival and downstream targets, including endothelial nitric oxide synthase (eNOS), the mammalian target of rapamycin (mTOR), the Bcl-2 family, and glycogen synthase kinase 3 beta (GSK-3β) (Ghafouri-Fard et al., 2022). The activation of the PI3K/Akt pathway during MI leads to a smaller infarct and inhibition of apoptosis (Cheng et al., 2019; Meng et al., 2019). Therefore, the main pathway of RC against MI may be the classical PI3K/Akt signaling pathway. Moreover, the PI3K/Akt pathway was enriched with 15 core targets (**Figure 5**). To clarify the potential antiapoptotic mechanism of RC against MI, we then performed experimental validation in addition to network pharmacology analysis. Among the bioactive components of RC (**Figure 3**), berberine, coptisine, THP, palmatine, and quercetin were reported to be cardioprotective (Ruan et al., 2020; Wen et al., 2020; Zhu et al., 2020; Albadrani et al., 2021). In this study, we conducted molecular docking of the 5 components with AKT1, the core target that relates to the PI3K/AKT pathway. The results showed that THP had the lowest binding energy with AKT1 among the 5 components. Moreover, based on the evidence that THP improves cardiac function after MI/RI and modulates PI3K/Akt-mediated autophagy in an ischemia/reperfusion model (Han et al., 2012; Wen et al., 2020), we selected THP as the bioactive component for subsequent experimental study. The network pharmacology results indicate that RC might inhibit the pathogenesis of MI by activating the PI3K/Akt signaling pathway.

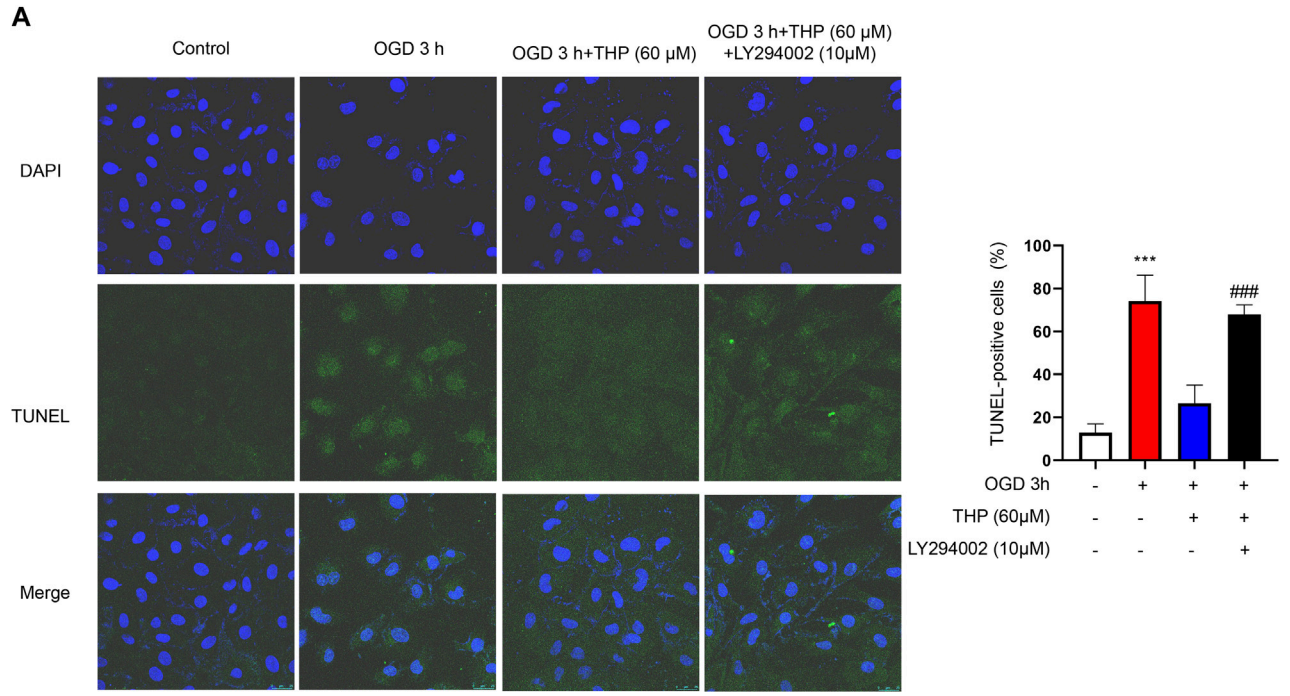

FIGURE 10 | THP decreased H9c2 cells apoptosis by activating the PI3K/Akt signaling pathway. H9c2 cells were incubated with LY294002 (10 μM, diluted in DMSO) or treated with THP (60 μM) for 48 h, and then the cells were stimulated with OGD. **(A)** H9c2 cells apoptosis was assessed through TUNEL assay (scale bar = 25 μm).

Thus, molecular docking analysis, an effective and rapid approach for forecasting the binding affinity between the components of TCM and their targets in view of the spatial structure of ligands and receptors, was performed to further validate the potential mechanism of THP against MI (Gan et al., 2019). As shown in **Figure 6**, the molecular docking results indicate that THP has high affinity with Akt, suggesting that activation of the PI3K/Akt pathway via effective activation of Akt may be closely related to the mechanism of THP against MI. These results further confirm that THP may be the representative component of RC, and exhibits potent inhibitory activity against MI by regulating Akt and its various downstream signaling pathways.

Next, to determine the effect of THP on OGD-induced injury, we first performed a CCK8 assay to assess whether THP had cellular toxicity on H9c2 cells. The results showed that the viability of H9c2 cells was higher than 80% when H9c2 cells were treated with 3.75–240 μM THP. This result indicated that THP had no remarkable toxicity for H9c2 cells and could be used for further experiments. Further experiments showed that THP significantly reduced cardiomyocyte apoptosis after OGD exposure, as indicated by the recovery of cell viability (**Figure 7**), the decreased ratio of cleaved caspase-3 protein expression to caspase-3 protein expression, and reduced mRNA levels of Bax, Bcl-2 and p53 (**Figure 8**). IL-6, IL-1β, and TNFα are crucial cytokines in the inflammatory response and immune reaction of MI patients (Di Stefano et al., 2009; Silvain et al., 2020). Therefore, we investigated the expression of IL-6, IL-1β, and TNFα using RT-qPCR analysis and found that their expression was significantly augmented by the OGD stimulus and observably diminished by THP treatment in a dose-dependent manner (**Figure 8**). THP may exhibit anti-inflammatory and cardioprotective effects by downregulating the expression of IL-6, IL-1β, and TNFα. The PI3K/Akt pathway is closely associated with the oxidation and reduction of intracellular mitochondria and is a key regulatory pathway for protein synthesis *in vivo* (Chi et al., 2019). This pathway is inhibited in the myocardial cells of rats with MI, causing an apparent increase in myocardial apoptosis (Fujio et al., 2000; Wu et al., 2000; Yamashita et al., 2001). The results from KEGG enrichment showed that the PI3K/Akt signaling pathway may be closely related to the treatment of RC against OGD exposure, and most components had the potential to regulate Akt. However, THP regulation via the PI3k/Akt pathway needs to be comprehensively investigated. In this study, we found that THP treatment could lead to a higher phosphorylation level of Akt (**Figure 8A**). Further experiments demonstrated that blocking the PI3K/Akt pathway with the specific inhibitor LY294002 could diminish the anti-inflammatory and antiapoptotic effects of THP (**Figures 8–10**). These results indicated that THP protected against OGD-induced cardiac injury by increasing the phosphorylation level of Akt and decreasing its various downstream inflammatory factors, such as IL-6, IL-1β, and TNF-α.

However, there were some shortcomings in the study: 1) The internal absorption and utilization of RC is a complicated process, meaning the function of RC may not simply accumulate the effects of multiple compounds. 2) The predicted targets are greatly affected by the quality of the databases and the algorithm. 3) The anti-apoptotic effect and the exact

mechanism of THP against MI should be further demonstrated with animal models and AKT knockout animals.

CONCLUSION

In conclusion, the present study aimed to investigate the effect and mechanism of RC against MI via network pharmacology analysis, experimental validation and molecular docking studies. We identified 60 bioactive components with 431 potential targets and 1,131 MI-related targets through network pharmacology analysis. Then, 126 core targets were screened by PPI network topology analysis. The KEGG enrichment results and the experimental validation results suggested that RC achieves the protective effect against MI via the PI3K/Akt signaling pathway. The molecular mechanisms by which RC inhibits MI were associated with a high binding affinity between THP and AKT. In light of these findings, understanding the function and mechanism of RC can provide novel insight for therapeutic strategies to treat MI.

DATA AVAILABILITY STATEMENT

The datasets presented in this study can be found in online repositories. The names of the repository/repositories and accession number(s) can be found in the article/ **Supplementary Material**.

ETHICS STATEMENT

The animal study was reviewed and approved by the Experimental Animal Ethics Committee, School of Pharmaceutical Sciences, Guangzhou University of Chinese Medicine.

AUTHOR CONTRIBUTIONS

JL, JW, DW, and ZL conceived and designed the experiments. JL, JW, JH, and YC performed the experiments and analyzed the data. JL and JW wrote the manuscript. DW and ZL supervised the manuscript.

FUNDING

This work was supported by grants from the National Natural Science Foundation of China (No. 82104163, 82003826, 81720108033, and 81930114), the State Commission of Science Technology of China (No. 2017YFE0119900), Guangdong Basic and Applied Basic Research Foundation (No. 2019A1515110607, 2021A1515011016, and 2020B1515130005), Guangdong Key Laboratory for translational Cancer research of Chinese Medicine (No. 2018B030322011), Key-Area Research and Development Program of Guangdong Province (No. 2020B1111100004), Guangdong Science and Technology Project "Overseas Master" Project (No. 2020A141401022), and Guangzhou Basic Research Program (No. 202102010376).

SUPPLEMENTARY MATERIAL

The Supplementary Material for this article can be found online at: https://www.frontiersin.org/articles/10.3389/fphar.2022.927488/full#supplementary-material

Supplementary Figure S1 | Component-target network. There were 60 bioactive components and 431 potential targets of RC. The orange nodes represent the potential active ingredients, and the violet nodes represent the core targets.

Supplementary Figure S2 | Molecular docking diagram of Akt with berberine, coptisine, palmatine, and quercetin. Structure diagram of Akt docked **(A)** berberine, **(B)** coptisine, **(C)** palmatine, and **(D)** quercetin. Yellow lines represent hydrogen bond. **(E)** The binding energy for berberine, coptisine, palmatine, and quercetin docked into the Akt crystal structure.

REFERENCES

Alam, M. B., Ju, M. K., Kwon, Y. G., and Lee, S. H. (2019). Protopine Attenuates Inflammation Stimulated by Carrageenan and LPS via the MAPK/NF-κB Pathway. *Food Chem. Toxicol.* 131, 110583. doi:10.1016/j.fct.2019.110583

Albadrani, G. M., Binmowyna, M. N., Bin-Jumah, M. N., El-Akabawy, G., Aldera, H., and Al-Farga, A. M. (2021). Quercetin Prevents Myocardial Infarction Adverse Remodeling in Rats by Attenuating TGF-β1/Smad3 Signaling: Different Mechanisms of Action. *Saudi J. Biol. Sci.* 28, 2772–2782. doi:10.1016/j.sjbs.2021.02.007

Anderson, J. L., and Morrow, D. A. (2017). Acute Myocardial Infarction. *N. Engl. J. Med.* 376, 2053–2064. doi:10.1056/NEJMra1606915

Ashburner, M., Ball, C. A., Blake, J. A., Botstein, D., Butler, H., Cherry, J. M., et al. (2000). Gene ontology: tool for the unification of biology. The Gene Ontology Consortium. *Nat. Genet.* 25, 25–29. doi:10.1038/75556

Bae, D. S., Kim, Y. H., Pan, C. H., Nho, C. W., Samdan, J., Yansan, J., et al. (2012). Protopine reduces the inflammatory activity of lipopolysaccharide-stimulated murine macrophages. *BMB Rep.* 45, 108–113. doi:10.5483/BMBRep.2012.45.2.108

Barrett, T., Troup, D. B., Wilhite, S. E., Ledoux, P., Rudnev, D., Evangelista, C., et al. (2007). NCBI GEO: mining tens of millions of expression profiles--database and tools update. *Nucleic Acids Res.* 35, D760–D765. doi:10.1093/nar/gkl887

Boezio, B., Audouze, K., Ducrot, P., and Taboureau, O. (2017). Network-based Approaches in Pharmacology. *Mol. Inf.* 36. doi:10.1002/minf.201700048

Chen, J., Li, C., Zhu, Y., Sun, L., Sun, H., Liu, Y., et al. (2015). Integrating GO and KEGG terms to characterize and predict acute myeloid leukemia-related genes. *Hematology* 20, 336–342. doi:10.1179/1607845414Y.0000000209

Chen, J., Lu, X., Lu, C., Wang, C., Xu, H., Xu, X., et al. (2016). 13-Methyl-palmatrubine induces apoptosis and cell cycle arrest in A549 cells *In Vitro* and *In Vivo*. *Oncol. Rep.* 36, 2526–2534. doi:10.3892/or.2016.5093

Chen, L., Zhang, Y. H., Wang, S., Zhang, Y., Huang, T., and Cai, Y. D. (2017). Prediction and analysis of essential genes using the enrichments of gene ontology and KEGG pathways. *PLoS One* 12, e0184129. doi:10.1371/journal.pone.0184129

Cheng, S., Zhang, X., Feng, Q., Chen, J., Shen, L., Yu, P., et al. (2019). Astragaloside IV exerts angiogenesis and cardioprotection after myocardial infarction via regulating PTEN/PI3K/Akt signaling pathway. *Life Sci.* 227, 82–93. doi:10.1016/j.lfs.2019.04.040

Chi, Y., Ma, Q., Ding, X. Q., Qin, X., Wang, C., and Zhang, J. (2019). Research on protective mechanism of ibuprofen in myocardial ischemia-reperfusion injury

in rats through the PI3K/Akt/mTOR signaling pathway. *Eur. Rev. Med. Pharmacol. Sci.* 23, 4465–4473. doi:10.26355/eurrev_201905_17958

Chia, Y. C., Chang, F. R., Wu, C. C., Teng, C. M., Chen, K. S., and Wu, Y. C. (2006). Effect of isoquinoline alkaloids of different structural types on antiplatelet aggregation *In Vitro*. *Planta Med.* 72, 1238–1241. doi:10.1055/s-2006-947196

Commission, C. P. (2015). *Pharmacopoeia of the People's Republic of China*. Beijing, China: Chinese Medical Science and Technology Press.

Del Re, D. P., Amgalan, D., Linkermann, A., Liu, Q., and Kitsis, R. N. (2019). Fundamental Mechanisms of Regulated Cell Death and Implications for Heart Disease. *Physiol. Rev.* 99, 1765–1817. doi:10.1152/physrev.00022.2018

Di Stefano, R., Di Bello, V., Barsotti, M. C., Grigoratos, C., Armani, C., Dell'omodarme, M., et al. (2009). Inflammatory markers and cardiac function in acute coronary syndrome: difference in ST-segment elevation myocardial infarction (STEMI) and in non-STEMI models. *Biomed. Pharmacother.* 63, 773–780. doi:10.1016/j.biopha.2009.06.004

Dong, Y., Huang, Y., Wu, H. L., Ke, J., Yin, Y. L., Zhu, C., et al. (2019). Change in late sodium current of atrial myocytes in spontaneously hypertensive rats with allocryptopine treatment. *Cardiovasc J. Afr.* 30, 79–86. doi:10.5830/CVJA-2018-072

Feng, Q., Li, X., Qin, X., Yu, C., Jin, Y., and Qian, X. (2020). PTEN inhibitor improves vascular remodeling and cardiac function after myocardial infarction through PI3k/Akt/VEGF signaling pathway. *Mol. Med.* 26, 111. doi:10.1186/s10020-020-00241-8

Frangogiannis, N. G. (2015). Pathophysiology of Myocardial Infarction. *Compr. Physiol.* 5, 1841–1875. doi:10.1002/cphy.c150006

Frangogiannis, N. G. (2014). The inflammatory response in myocardial injury, repair, and remodelling. *Nat. Rev. Cardiol.* 11, 255–265. doi:10.1038/nrcardio.2014.28

Fu, Y. C., Zhang, Y., Tian, L. Y., Li, N., Chen, X., Cai, Z. Q., et al. (2016). Effects of allocryptopine on outward potassium current and slow delayed rectifier potassium current in rabbit myocardium. *J. Geriatr. Cardiol.* 13, 316–325. doi:10.11909/j.issn.1671-5411.2016.04.008

Fujio, Y., Nguyen, T., Wencker, D., Kitsis, R. N., and Walsh, K. (2000). Akt promotes survival of cardiomyocytes *In Vitro* and protects against ischemia-reperfusion injury in mouse heart. *Circulation* 101, 660–667. doi:10.1161/01.cir.101.6.660

Gan, D., Xu, X., Chen, D., Feng, P., and Xu, Z. (2019). Network Pharmacology-Based Pharmacological Mechanism of the Chinese Medicine Rhizoma drynariae Against Osteoporosis. *Med. Sci. Monit.* 25, 5700–5716. doi:10.12659/MSM.915170

Gao, J., Shi, J., He, K., Zhang, Q., Li, S., Lee, S. M., et al. (1994). Yanhusuo Extract Inhibits Metastasis of Breast Cancer Cells by Modulating Mitogenactivated Protein Kinase Signaling Pathways. *Oncol. Rep.* 20 (4), 819–824.

Ghafouri-Fard, S., Khanbabapour Sasi, A., Hussen, B. M., Shoorei, H., Siddiq, A., Taheri, M., et al. (2022). Interplay between PI3K/AKT pathway and heart disorders. *Mol. Biol. Rep.* doi:10.1007/s11033-022-07468-0

Gong, F. F., Vaitenas, I., Malaisrie, S. C., and Maganti, K. (2021). Mechanical Complications of Acute Myocardial Infarction: A Review. *JAMA Cardiol.* 6, 341–349. doi:10.1001/jamacardio.2020.3690

Gong, L. L., Fang, L. H., Wang, S. B., Sun, J. L., Qin, H. L., Li, X. X., et al. (2012). Coptisine exert cardioprotective effect through anti-oxidative and inhibition of RhoA/Rho kinase pathway on isoproterenol-induced myocardial infarction in rats. *Atherosclerosis* 222, 50–58. doi:10.1016/j.atherosclerosis.2012.01.046

Guo, G., Gong, L., Sun, L., and Xu, H. (2019). Quercetin supports cell viability and inhibits apoptosis in cardiocytes by down-regulating miR-199a. *Artif. Cells Nanomed Biotechnol.* 47, 2909–2916. doi:10.1080/21691401.2019.1640711

Guo, J., Wang, S. B., Yuan, T. Y., Wu, Y. J., Yan, Y., Li, L., et al. (2013). Coptisine protects rat heart against myocardial ischemia/reperfusion injury by suppressing myocardial apoptosis and inflammation. *Atherosclerosis* 231, 384–391. doi:10.1016/j.atherosclerosis.2013.10.003

Han, Y., Zhang, W., Tang, Y., Bai, W., Yang, F., Xie, L., et al. (2012). l-Tetrahydropalmatine, an active component of Corydalis yanhusuo W.T. Wang, protects against myocardial ischaemia-reperfusion injury in rats. *PLoS One* 7, e38627. doi:10.1371/journal.pone.0038627

He, J., Liu, D., Zhao, L., Zhou, D., Rong, J., Zhang, L., et al. (2022). Myocardial ischemia/reperfusion injury: Mechanisms of injury and implications for management (Review). *Exp. Ther. Med.* 23, 430. doi:10.3892/etm.2022.11357

Huang, L., Xie, D., Yu, Y., Liu, H., Shi, Y., Shi, T., et al. (2018). TCMID 2.0: a comprehensive resource for TCM. *Nucleic Acids Res.* 46, D1117–D1120. doi:10.1093/nar/gkx1028

Kim, S., Chen, J., Cheng, T., Gindulyte, A., He, J., He, S., et al. (2019). PubChem 2019 update: improved access to chemical data. *Nucleic Acids Res.* 47, D1102–D1109. doi:10.1093/nar/gky1033

Kim, Y. M., Ha, Y. M., Jin, Y. C., Shi, L. Y., Lee, Y. S., Kim, H. J., et al. (2009). Palmatine from Coptidis rhizoma reduces ischemia-reperfusion-mediated acute myocardial injury in the rat. *Food Chem. Toxicol.* 47, 2097–2102. doi:10.1016/j.fct.2009.05.031

Kumar, M., Kasala, E. R., Bodduluru, L. N., Kumar, V., and Lahkar, M. (2017). Molecular and biochemical evidence on the protective effects of quercetin in isoproterenol-induced acute myocardial injury in rats. *J. Biochem. Mol. Toxicol.* 31, 1–8. doi:10.1002/jbt.21832

Kurian, G. A., Rajagopal, R., Vedantham, S., and Rajesh, M. (2016). The Role of Oxidative Stress in Myocardial Ischemia and Reperfusion Injury and Remodeling: Revisited. *Oxid. Med. Cell Longev.* 2016, 1656450. doi:10.1155/2016/1656450

Li, B., Yang, M., Liu, J. W., and Yin, G. T. (2016a). Protective mechanism of quercetin on acute myocardial infarction in rats. *Genet. Mol. Res.* 15, 15017117. doi:10.4238/gmr.15017117

Li, F., Duan, J., Zhao, M., Huang, S., Mu, F., Su, J., et al. (2019a). A network pharmacology approach to reveal the protective mechanism of Salvia miltiorrhiza-Dalbergia odorifera coupled-herbs on coronary heart disease. *Sci. Rep.* 9, 19343. doi:10.1038/s41598-019-56050-5

Li, J., Cao, G. Y., Zhang, X. F., Meng, Z. Q., Gan, L., Li, J. X., et al. (2020). Chinese Medicine She-Xiang-Xin-Tong-Ning, Containing Moschus, Corydalis and Ginseng, Protects from Myocardial Ischemia Injury via Angiogenesis. *Am. J. Chin. Med.* 48, 107–126. doi:10.1142/S0192415X20500068

Li, J., Gao, H., Huang, J., Wang, P., Huang, Y., Luo, W., et al. (2016b). PKCζ interacts with STAT3 and promotes its activation in cardiomyocyte hypertrophy. *J. Pharmacol. Sci.* 132, 15–23. doi:10.1016/j.jphs.2016.03.010

Li, J., Huang, J., Lu, J., Guo, Z., Li, Z., Gao, H., et al. (2019b). Sirtuin 1 represses PKC-ζ activity through regulating interplay of acetylation and phosphorylation in cardiac hypertrophy. *Br. J. Pharmacol.* 176, 416–435. doi:10.1111/bph.14538

Liu, D. Q., Chen, S. P., Sun, J., Wang, X. M., Chen, N., Zhou, Y. Q., et al. (2019). Berberine protects against ischemia-reperfusion injury: A review of evidence from animal models and clinical studies. *Pharmacol. Res.* 148, 104385. doi:10.1016/j.phrs.2019.104385

Martin, A., Ochagavia, M. E., Rabasa, L. C., Miranda, J., Fernandez-De-Cossio, J., and Bringas, R. (2010). BisoGenet: a new tool for gene network building, visualization and analysis. *BMC Bioinforma.* 11, 91. doi:10.1186/1471-2105-11-91

Meng, H., Zhang, Y., An, S. T., and Chen, Y. (2019). Annexin A3 gene silencing promotes myocardial cell repair through activation of the PI3K/Akt signaling pathway in rats with acute myocardial infarction. *J. Cell Physiol.* 234, 10535–10546. doi:10.1002/jcp.27717

Meurer, L., and Cohen, S. M. (2020). Drug-Induced Liver Injury from Statins. *Clin. Liver Dis.* 24, 107–119. doi:10.1016/j.cld.2019.09.007

Ong, S. B., and Gustafsson, A. B. (2012). New roles for mitochondria in cell death in the reperfused myocardium. *Cardiovasc Res.* 94, 190–196. doi:10.1093/cvr/cvr312

Piñero, J., Ramírez-Anguita, J. M., Saüch-Pitarch, J., Ronzano, F., Centeno, E., Sanz, F., et al. (2020). The DisGeNET knowledge platform for disease genomics: 2019 update. *Nucleic Acids Res.* 48, D845–D855. doi:10.1093/nar/gkz1021

Prince, P. S., Dhanasekar, K., and Rajakumar, S. (2011). Preventive effects of vanillic acid on lipids, bax, bcl-2 and myocardial infarct size on isoproterenol-induced myocardial infarcted rats: a biochemical and *In Vitro* study. *Cardiovasc Toxicol.* 11, 58–66. doi:10.1007/s12012-010-9098-3

Radmanesh, E., Dianat, M., Badavi, M., Goudarzi, G., and Mard, S. A. (2017). The cardioprotective effect of vanillic acid on hemodynamic parameters, malondialdehyde, and infarct size in ischemia-reperfusion isolated rat heart exposed to PM10. *Iran. J. Basic Med. Sci.* 20, 760–768. doi:10.22038/ijbms.2017.9007

Ru, J., Li, P., Wang, J., Zhou, W., Li, B., Huang, C., et al. (2014). TCMSP: a database of systems pharmacology for drug discovery from herbal medicines. *J. Cheminform* 6, 13. doi:10.1186/1758-2946-6-13

Ruan, Y., Jin, Q., Zeng, J., Ren, F., Xie, Z., Ji, K., et al. (2020). Grape Seed Proanthocyanidin Extract Ameliorates Cardiac Remodelling After Myocardial Infarction Through PI3K/AKT Pathway in Mice. *Front. Pharmacol.* 11, 585984. doi:10.3389/fphar.2020.585984

Silvain, J., Kerneis, M., Zeitouni, M., Lattuca, B., Galier, S., Brugier, D., et al. (2020). Interleukin-1β and Risk of Premature Death in Patients With Myocardial Infarction. *J. Am. Coll. Cardiol.* 76, 1763–1773. doi:10.1016/j.jacc.2020.08.026

Stanely Mainzen Prince, P., Dhanasekar, K., and Rajakumar, S. (2015). Vanillic acid prevents altered ion pumps, ions, inhibits Fas-receptor and caspase mediated apoptosis-signaling pathway and cardiomyocyte death in myocardial infarcted rats. *Chem. Biol. Interact.* 232, 68–76. doi:10.1016/j.cbi.2015.03.009

Stelzer, G., Rosen, N., Plaschkes, I., Zimmerman, S., Twik, M., Fishilevich, S., et al. (2016). The GeneCards Suite: From Gene Data Mining to Disease Genome Sequence Analyses. *Curr. Protoc. Bioinforma.* 54, 1 30 33–31 30 33. doi:10.1002/cpbi.5

Suresh, R., Li, X., Chiriac, A., Goel, K., Terzic, A., Perez-Terzic, C., et al. (2014). Transcriptome from circulating cells suggests dysregulated pathways associated with long-term recurrent events following first-time myocardial infarction. *J. Mol. Cell Cardiol.* 74, 13–21. doi:10.1016/j.yjmcc.2014.04.017

Tang, J., Lu, L., Liu, Y., Ma, J., Yang, L., Li, L., et al. (2019). Quercetin improve ischemia/reperfusion-induced cardiomyocyte apoptosis *In Vitro* and *In Vivo* study via SIRT1/PGC-1α signaling. *J. Cell Biochem.* 120, 9747–9757. doi:10.1002/jcb.28255

Tang, Y., Li, M., Wang, J., Pan, Y., and Wu, F. X. (2015). CytoNCA: a cytoscape plugin for centrality analysis and evaluation of protein interaction networks. *Biosystems* 127, 67–72. doi:10.1016/j.biosystems.2014.11.005

Tian, B., Tian, M., and Huang, S. M. (2020). Advances in phytochemical and modern pharmacological research of Rhizoma Corydalis. *Pharm. Biol.* 58, 265–275. doi:10.1080/13880209.2020.1741651

Uniprot, C. (2015). UniProt: a hub for protein information. *Nucleic Acids Res.* 43, D204–D212. doi:10.1093/nar/gku989

Wang, L., Zhang, Y., Wang, Z., Gong, N., Kweon, T. D., Vo, B., et al. (2016). The Antinociceptive Properties of the Corydalis yanhusuo Extract. *PLoS One* 11, e0162875. doi:10.1371/journal.pone.0162875

Wang, X., Shen, Y., Wang, S., Li, S., Zhang, W., Liu, X., et al. (2017a). PharmMapper 2017 update: a web server for potential drug target identification with a comprehensive target pharmacophore database. *Nucleic Acids Res.* 45, W356–W360. doi:10.1093/nar/gkx374

Wang, X., Wang, Z.-Y., Zheng, J.-H., and Li, S. (2021). TCM network pharmacology: A new trend towards combining computational, experimental and clinical approaches. *Chin. J. Nat. Med.* 19, 1–11. doi:10.1016/s1875-5364(21)60001-8

Wang, Y., Wang, Q., Zhang, L., Ke, Z., Zhao, Y., Wang, D., et al. (2017b). Coptisine protects cardiomyocyte against hypoxia/reoxygenation-induced damage via inhibition of autophagy. *Biochem. Biophys. Res. Commun.* 490, 231–238. doi:10.1016/j.bbrc.2017.06.027

Wang, Z., Mei, W., Wang, Q., Guo, R., Liu, P., Wang, Y., et al. (2019). Role of Dehydrocorybulbine in Neuropathic Pain After Spinal Cord Injury Mediated by P2X4 Receptor. *Mol. Cells* 42, 143–150. doi:10.14348/molcells.2018.0028

Wen, H., Zhang, H., Wang, W., and Li, Y. (2020). Tetrahydropalmatine protects against acute lung injury induced by limb ischemia/reperfusion through restoring PI3K/AKT/mTOR-mediated autophagy in rats. *Pulm. Pharmacol. Ther.* 64, 101947. doi:10.1016/j.pupt.2020.101947

Wishart, D. S., Feunang, Y. D., Guo, A. C., Lo, E. J., Marcu, A., Grant, J. R., et al. (2018). DrugBank 5.0: a major update to the DrugBank database for 2018. *Nucleic Acids Res.* 46, D1074–D1082. doi:10.1093/nar/gkx1037

Wu, L., Ling, H., Li, L., Jiang, L., and He, M. (2007a). Beneficial effects of the extract from Corydalis yanhusuo in rats with heart failure following myocardial infarction. *J. Pharm. Pharmacol.* 59, 695–701. doi:10.1211/jpp.59.5.0010

Wu, W., Lee, W. L., Wu, Y. Y., Chen, D., Liu, T. J., Jang, A., et al. (2000). Expression of constitutively active phosphatidylinositol 3-kinase inhibits activation of caspase 3 and apoptosis of cardiac muscle cells. *J. Biol. Chem.* 275, 40113–40119. doi:10.1074/jbc.M004108200

Wu, Y., Tu, X., Lin, G., Xia, H., Huang, H., Wan, J., et al. (2007b). Emodin-mediated protection from acute myocardial infarction via inhibition of inflammation and apoptosis in local ischemic myocardium. *Life Sci.* 81, 1332–1338. doi:10.1016/j.lfs.2007.08.040

Xiao, X., Liu, J., Hu, J., Li, T., and Zhang, Y. (2007). Protective effect of protopine on the focal cerebral ischaemic injury in rats. *Basic Clin. Pharmacol. Toxicol.* 101, 85–89. doi:10.1111/j.1742-7843.2007.00075.x

Xu, H. Y., Zhang, Y. Q., Liu, Z. M., Chen, T., Lv, C. Y., Tang, S. H., et al. (2019). ETCM: an encyclopaedia of traditional Chinese medicine. *Nucleic Acids Res.* 47, D976–D982. doi:10.1093/nar/gky987

Xu, W., Wang, L., Zhang, R., Sun, X., Huang, L., Su, H., et al. (2020). Diagnosis and prognosis of myocardial infarction on a plasmonic chip. *Nat. Commun.* 11, 1654. doi:10.1038/s41467-020-15487-3

Xu, Z., Chen, X., Fu, S., Bao, J., Dang, Y., Huang, M., et al. (2012). Dehydrocorydaline inhibits breast cancer cells proliferation by inducing apoptosis in MCF-7 cells. *Am. J. Chin. Med.* 40, 177–185. doi:10.1142/S0192415X12500140

Xue, M., Liu, M., Zhu, X., Yang, L., Miao, Y., Shi, D., et al. (2013). Effective Components of Panax quinquefolius and Corydalis tuber Protect Myocardium through Attenuating Oxidative Stress and Endoplasmic Reticulum Stress. *Evid. Based Complement. Altern. Med.* 2013, 482318. doi:10.1155/2013/482318

Yamashita, K., Kajstura, J., Discher, D. J., Wasserlauf, B. J., Bishopric, N. H., Anversa, P., et al. (2001). Reperfusion-activated Akt kinase prevents apoptosis in transgenic mouse hearts overexpressing insulin-like growth factor-1. *Circ. Res.* 88, 609–614. doi:10.1161/01.res.88.6.609

Yang, H., Qin, C., Li, Y. H., Tao, L., Zhou, J., Yu, C. Y., et al. (2016). Therapeutic target database update 2016: enriched resource for bench to clinical drug target and targeted pathway information. *Nucleic Acids Res.* 44, D1069–D1074. doi:10.1093/nar/gkv1230

Ye, B., Chen, X., Dai, S., Han, J., Liang, X., Lin, S., et al. (2019). Emodin alleviates myocardial ischemia/reperfusion injury by inhibiting gasdermin D-mediated pyroptosis in cardiomyocytes. *Drug Des. Devel Ther.* 13, 975–990. doi:10.2147/DDDT.S195412

Zhang, Q., Chen, C., Wang, F. Q., Li, C. H., Zhang, Q. H., Hu, Y. J., et al. (2016). Simultaneous screening and analysis of antiplatelet aggregation active alkaloids from Rhizoma Corydalis. *Pharm. Biol.* 54, 3113–3120. doi:10.1080/13880209.2016.1211714

Zhang, Q., Wang, L., Wang, S., Cheng, H., Xu, L., Pei, G., et al. (2022). Signaling pathways and targeted therapy for myocardial infarction. *Signal Transduct. Target Ther.* 7, 78. doi:10.1038/s41392-022-00925-z

Zhang, X., Qin, Q., Dai, H., Cai, S., Zhou, C., and Guan, J. (2019). Emodin protects H9c2 cells from hypoxia-induced injury by up-regulating miR-138 expression. *Braz J. Med. Biol. Res.* 52, e7994. doi:10.1590/1414-431X20187994

Zheleva-Kyuchukova, I., and Gelev, V. (2020). Antiplatelet therapy after PCI in patients with high risk of bleeding. *Phar* 67, 135–143. doi:10.3897/pharmacia.67.e52737

Zhu, N., Li, J., Li, Y., Zhang, Y., Du, Q., Hao, P., et al. (2020). Berberine Protects Against Simulated Ischemia/Reperfusion Injury-Induced H9C2 Cardiomyocytes Apoptosis *In Vitro* and Myocardial Ischemia/Reperfusion-Induced Apoptosis *In Vivo* by Regulating the Mitophagy-Mediated HIF-1α/BNIP3 Pathway. *Front. Pharmacol.* 11, 367. doi:10.3389/fphar.2020.00367

Conflict of Interest: The authors declare that the research was conducted in the absence of any commercial or financial relationships that could be construed as a potential conflict of interest.

Publisher's Note: All claims expressed in this article are solely those of the authors and do not necessarily represent those of their affiliated organizations, or those of the publisher, the editors, and the reviewers. Any product that may be evaluated in this article, or claim that may be made by its manufacturer, is not guaranteed or endorsed by the publisher.

GLOSSARY

Akt protein kinase B
Bcl2 B cell lymphoma-2
Bax BCL2 associated X
BC betweenness centrality
CCK8 cell counting Kit-8
CC closeness centrality
CABG coronary artery bypass grafting
DC degree centrality
DL drug-likeness
EC eigenvector centrality
ETCM encyclopedia of traditional Chinese medicine
GEO gene expression omnibus
GO gene ontology
IL-1β interleukin-1 beta
IL-6 interleukin-6
KEGG Kyoto encyclopedia of genes and genomes
LAC local average connectivity-based method centrality
MI myocardial infarction
MI/RI myocardial ischemia/reperfusion injury
NC network centrality
OB oral bioavailability
OGD oxygen and glucose deprivation
PCI percutaneous coronary intervention
PI3K phosphatidylinositol 3-kinase
PPI protein-protein interaction
RC *Rhizoma corydalis*
TUNEL TdT-mediated dUTP nick-end labeling
THP tetrahydropalmatine
TTD therapeutic target database
TCM traditional Chinese medicine
TCMID traditional Chinese medicine integrated database
TCMSP traditional Chinese medicine systems pharmacology
TNF-α tumor necrosis factor-α

frontiers | Frontiers in Pharmacology

ORIGINAL RESEARCH
published: 22 July 2022
doi: 10.3389/fphar.2022.918292

Therapeutic Effect of Ultrasound Combined With Porous Lipid Clioquinol/PLGA Microbubbles on Ferroptosis in HL-1 Cardiac Cell Induced by Isoproterenol Attack

Nana Li[1†], Lei Dong[1†], Yuanyuan Shen[2], Yongling Wang[3], Liansheng Chang[4], Hongwei Wu[5], Yuqiao Chang[1], Menghao Li[1], Dan Li[1], Zhaoyi Li[1], Mei He[1], Cheng Li[1], Yao Wei[1], Haiqin Xie[6*] and Feng Wang[1*]*

[1]Henan Key Laboratory of Medical Tissue Regeneration, School of Basic Medical Sciences, Xinxiang Medical University, Xinxiang, China, [2]National-Regional Key Technology Engineering Laboratory for Medical Ultrasound, School of Biomedical Engineering, Health Science Center, Shenzhen University, Shenzhen, China, [3]Department of Physiology and Pathophysiology, School of Basic Medical Sciences, Xinxiang Medical University, Xinxiang, China, [4]Department of Human Anatomy, Histology and Embryology, School of Basic Medical Sciences, Xinxiang Medical University, Xinxiang, China, [5]Department of Chemistry, Xinxiang Medical University, Xinxiang, China, [6]Department of Ultrasound, Peking University Shenzhen Hospital, Shenzhen, China

In recent years, studies have shown a close relationship between cardiomyocyte death and ferroptosis. Clioquinol (CQ) can inhibit ferroptosis. Porous lipid-poly (lactic-co-glycolic acid) (PLGA) microbubbles (MBs) were prepared by double emulsification ($W_1/O/W_2$) using 1,2-dioctadecanoyl-sn-glycero-3-phophocholine and PLGA as raw materials. Porous lipid-PLGA MBs were used as carriers to prepare CQ/PLGA MBs containing CQ. CQ/PLGA had the advantages of high drug loading, good biocompatibility, and sustained release. Our results showed that CQ/PLGA improved the effect of CQ and reduced its cytotoxicity. Under low-frequency ultrasound with certain parameters, CQ/PLGA showed steady-state cavitation, which increased the membrane permeability of mouse cardiomyocyte HL-1 to a certain extent and further prevented the process of ferroptosis in mouse cardiomyocyte HL-1.

Keywords: ferroptosis, clioquinol, microbubbles, low-frequency ultrasound, cardiovascular diseases

OPEN ACCESS

Edited by:
Guixue Wang,
Chongqing University, China

Reviewed by:
Wei Shao,
Westlake University, China
Saba Naqvi,
National Institute of Pharmaceutical Education and Research, India

***Correspondence:**
Haiqin Xie
xiehaiqin@126.com
Yuanyuan Shen
shenyy@szu.edu.cn
Feng Wang
wfeng100@126.com

[†]These authors have contributed equally to this work

Specialty section:
This article was submitted to Cardiovascular and Smooth Muscle Pharmacology, a section of the journal Frontiers in Pharmacology

Received: *12 April 2022*
Accepted: *01 June 2022*
Published: *22 July 2022*

Citation:
Li N, Dong L, Shen Y, Wang Y, Chang L, Wu H, Chang Y, Li M, Li D, Li Z, He M, Li C, Wei Y, Xie H and Wang F (2022) Therapeutic Effect of Ultrasound Combined With Porous Lipid Clioquinol/PLGA Microbubbles on Ferroptosis in HL-1 Cardiac Cell Induced by Isoproterenol Attack. Front. Pharmacol. 13:918292. doi: 10.3389/fphar.2022.918292

INTRODUCTION

According to public data from the World Health Organization, noncommunicable diseases (NCDs) account for 71% of all deaths (Lowe, 2020). Cardiovascular and cerebrovascular diseases are the leading causes of death, accounting for 44% of all deaths due to NCDs, twice as many as cancer deaths (Lowe, 2020). The total number of deaths from cardiovascular diseases is expected to exceed 23 million by 2030(Birn and Nervi, 2020). On the whole, the prevalence and mortality of cardiovascular diseases are still on the rise. Especially in recent years, the mortality rate of cardiovascular diseases in rural areas has become higher than that in urban areas (Zhou and Bei, 2020). A rapid increase in the total cost of hospitalization due to cardiovascular and cerebrovascular diseases has increased the burden of cardiovascular diseases, making them a major public health problem. Cardiovascular diseases should urgently be prevented and cured. Therefore, the pathogenesis of cardiovascular diseases, the mechanism of cardiomyocyte death, and intervention methods should immediately be studied (Zhou and Bei, 2020; Piccoli, 2021).

Recent studies have shown that ferroptosis is closely related to cardiomyocyte death (Li et al., 2020; Ma et al., 2020; Wu et al., 2021). Ferroptosis is a mode of regulatory cell death. The hypothesis of "siderogenic heart disease" was formally put forward by Sullivan in 1981 and was named by Dixon et al. for the first time in 2012 (Li et al., 2020). At present, the mechanism of ferroptosis is thought to be related to amino acid metabolism, iron metabolism, and lipid metabolism (Wu et al., 2021). The initiation and execution of ferroptosis are based on the intersection of amino acid metabolism, fat metabolism, and iron metabolism, which results from the disturbance of phospholipid oxidation metabolism in the cell membrane. When lipid peroxides accumulate to the limit of glutathione peroxidase reduction, iron ion-mediated Fenton reaction catalyzes the production of lipid-free radicals. A large number of lipid-free radicals accumulate in cells and lead to cell death (Chen et al., 2021).

Clioquinol (CQ), with the chemical formula $C_9H_5C_lIN_O$, was used to treat diseases, such as dysentery, in the 20th century and has been found to regulate the dynamic balance of Fe^{2+} ions in tissue through their effective chelation (Lv et al., 2021). The clinical application of CQ is seriously limited because of its poor water solubility, low bioavailability, and acute cytotoxicity (Khan et al., 2020).

Microbubbles (MBs) have a variety of therapeutic use. For example, they are used as contrast agents in ultrasound (US) to improve their diagnostic efficacy (Luo et al., 2017). However, conventional lipid-based MBs have some disadvantages such as poor drug encapsulation, weak drug loading efficiency, and weak drug release ability (Luo et al., 2017; Rix et al., 2020; Klibanov, 2021). Chen et al. developed a new type of porous lipid-poly (lactic-co-glycolic acid) (PLGA) MBs (lipid/PLGA MBs), which solved the dilemma of MBs as imaging agents and drug carriers (Chen et al., 2019; Wang et al., 2021). When irradiated with US with appropriate energy, lipid/PLGA MBs oscillated rapidly and changed the size of MBs periodically (Chen et al., 2019). The oscillation of lipid/PLGA MBs might produce stable cavitation and inertial cavitation to increase the permeability of the cell membrane, thus promoting the transmembrane drug delivery into the cell.

Based on these facts, we synthesized porous lipid/PLGA hybrid MBs (CQ/PLGA MBs) containing CQ while testing the characterization of CQ/PLGA, including drug loading, entrapment efficiency, and particle size potential distribution. Ferroptosis in HL-1 of mouse cardiomyocytes was induced using erastin, which verified the effect of CQ in blocking ferroptosis in HL-1. CQ had certain cytotoxicity. In addition, isoproterenol (ISO) could induce ferroptosis in HL-1 cells, which could be blocked by CQ. We further explored the inhibitory effect of CQ/PLGA on ferroptosis in HL-1 and the ultrasonic sensitivity of CQ/PLGA. Finally, our results showed that CQ could block the occurrence of ferroptosis in HL-1. Under the action of US, the "steady-state cavitation effect" of CQ/PLGA MBs caused an increase in the cell membrane permeability of HL-1 cells in a short period of time. At the same time, CQ/PLGA released CQ, and CQ entered the cell through the open space of the cell membrane and bound to Fe^{2+} ions, blocking the occurrence of ferroptosis in HL-1 cells (**Figure 1**). The better inhibition of the process of ferroptosis in HL-1 is expected to provide a new scheme for the treatment of cardiovascular diseases.

MATERIALS AND METHODS

Synthesis of Clioquinol/PLGA MBs

1,2-Dioctadecanoyl-sn-glycero-3-phophocholine (DSPC, 0.0025 g, Avanti polar lipids Inc, United States) and 0.05 g of PLGA (Guangzhou Cellcook Biotech, Guangzhou, China) were dissolved in 1 ml of dichloromethane to form a colorless transparent solution. NH_4HCO_3 (0.06 g) was dissolved in 1 ml of double-distilled water, and 200 μl of the mixture was extracted into the aforementioned solution. The obtained mixed solution was emulsified using an ultrasonic cell pulverizer (SCIENTZ-1200E, Ningbo Scientz Biotechnology, Ningbo, China) with a power of 650 W (the trigger interval was 3 s, the power ratio was 45%, and the horn was Φ 6). A 4% PVA solution (5 ml) was added to the mixed solution, and the solution was homogenized. Double-distilled water (10 ml) was added to the solution obtained previously, mixed well, stirred for 2.5–3 h, and centrifuged three times (4500 rpm, 5 min). The supernatant was poured into 1 ml of double-distilled water and frozen for 3–4 h in a refrigerator at −80°C. The freeze-dried powder of porous lipid-PLGA MBs was obtained after freeze-drying in a vacuum freeze-dryer for about 24 h. The obtained powder was stored in a refrigerator at 4°C and set aside. When preparing CQ/PLGA lipid MBs, a certain quality of CQ (Shanghai Aladdin Biochemical Technology, Shanghai, China) could be dissolved in a dichloromethane solution.

Characterization of Clioquinol/PLGA MBs

CQ/PLGA was dissolved in dimethyl sulfoxide. The CQ absorption at 322 nm wavelength was measured using an ultraviolet spectrophotometer (GENESYS 10S UV–vis spectrophotometer, Thermo Scientific, MA, United States). Under the above wavelength, the drug efficiency and drug entrapment efficiency of CQ/PLGA were detected using an enzyme labeling instrument (BioTek, Winooski, VT, United States). Then, the drug loading and entrapment efficiencies of CQ/PLGA dissolved in dimethyl sulfoxide were calculated. Drug loading was calculated as LE (%) = We/Wm × 100%, where LE is the drug loading efficiency, W_e is the amount of drug encapsulated in the lipid, and W_m is the total weight of CQ/PLGA MBs. Entrapment efficiency was calculated as EN (%) = $(1 - C_f/C_t) \times 100$, where EN is the drug entrapment efficiency as a percentage, C_f is the amount of free drug, and C_t is the total amount of drug (free and entrapped). The particle size of CQ/PLGA was measured using a particle size analyzer (Zetasizer Nano, Malvern Instruments, Malvern, United Kingdom). The shape of CQ/PLGA was observed using a scanning electron microscope (SEM, Akishima, Tokyo, Japan). We tested the stability of CQ/PLGA MBs. The particle size and concentration of CQ/PLGA MBs were measured at the initial, 1st, 2nd, 4th, 6th, and 8th days. The concentration of porous lipid CQ/PLGA MBs is expressed by OD_{500}.

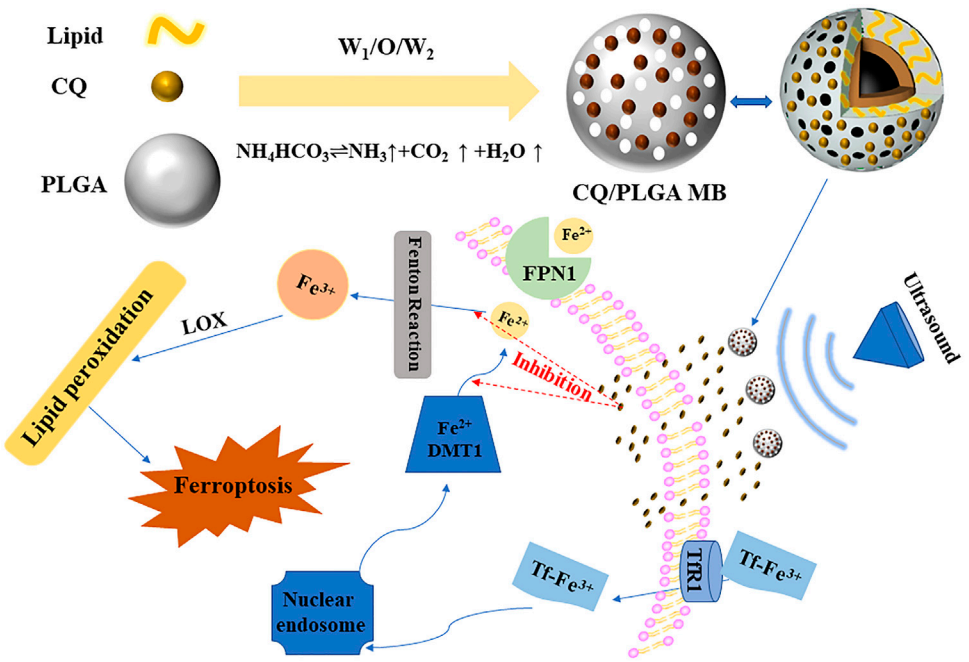

FIGURE 1 | Ultrasound combined with CQ/PLGA MBs inhibited the ferroptosis pattern of mouse cardiomyocytes. Under the action of ultrasound, the "steady-state cavitation effect" of CQ/PLGA MBs caused the increase in cell membrane permeability of HL-1 cells in a short period of time. At the same time, CQ/PLGA releases CQ, and CQ enters the cell through the open space of the cell membrane and binds to Fe^{2+} ions, blocking the occurrence of ferroptosis in HL-1 cells.

Cell Cultures

Cardiomyocyte HL-1 cells were purchased from Shanghai Cell Bank (Shanghai, China). Fetal bovine serum (FBS), penicillin–streptomycin (PS), and trypsin were purchased from Gibco (CA, United States). HL-1 cells were cultured in a conventional humidified CO_2 incubator at 37°C. These cells were routinely cultured in a high glucose medium (Dulbecco's Modified Eagle Medium) supplemented with 10% FBS and 1% PS. The culture medium was changed every 2 days, and the cell fusion degree reached 80%.

Cell Viability Assay (CCK-8)

Cell viability was determined using the CCK-8 assay (Dojindo Laboratories, Shanghai, China). The cell suspension was inoculated in a 96-well plate (100 μl per well), and the same sample could be repeated three times. After different treatments, the culture plate was put into an incubator for 24 h (37°C, 5% CO_2). CCK-8 solution (10 μl) was added to each hole, and the culture plate was put into an incubator for 1–4 h. The absorbance value (OD) at 450 nm was measured using an enzyme labeling instrument. Cell viability (%) = [A (1) − A (blank)]/[A (0) − A (blank)] × 100. A (1): OD values of pores with cells, CCK-8 solutions, and drug solutions. A (0): OD value of pores with cell and CCK-8 solution but no drug solution. A (blank): OD value of hole without cells.

Cytotoxicity Evaluation of Clioquinol

HL-1 Cells were seeded at a density of 5 × 104 cells/ml in a 96-well plate (100 μl per well). When the degree of cell fusion was 80%, the medium containing 0, 10, 20, 40, 60, 80, and 100 μg/ml CQ was replaced. After 24 h, the cell state was observed under a microscope, and the cell viability of HL-1 cells corresponding to each concentration of CQ was detected using CCK-8.

US-Guided Drug Release

The maximum ultraviolet absorption peak of CQ detected using an ultraviolet spectrophotometer was 322 nm. Under 322 nm, the OD value of CQ/PLGA suspension before and after ultrasonication was detected using an enzyme labeling instrument (96-hole plate, 100 μl per hole, and five compound holes). The release amount of CQ in the solution was calculated. The center frequency of US was 949 kHz; the pulse interval was 1 s; the pulse cycle was 10,000; the intensity of US was 60, 80, 100, 110, 120, and 130 mvpp; and the duration was 60 s. When the US intensity was 100 mvpp, the shape changes in CQ/PLGA before and after US were observed using an SEM after continuous action for 60 s.

Occurrence and Intervention of Ferroptosis in HL-1

As mentioned previously, HL-1 cells were inoculated in 96-well plates. When the degree of cell fusion was 80%, HL-1 cells were incubated with erastin, a ferroptosis inducer at the concentrations of 0, 2, and 4 μM, for 24 h. ISO was obtained from Cayman Chemical (Cayman Chemical, Ann Arbor, MI, United States). ISO, an inducer of cardiomyocyte apoptosis, was incubated with HL-1 cells for 24 h. The HL-1

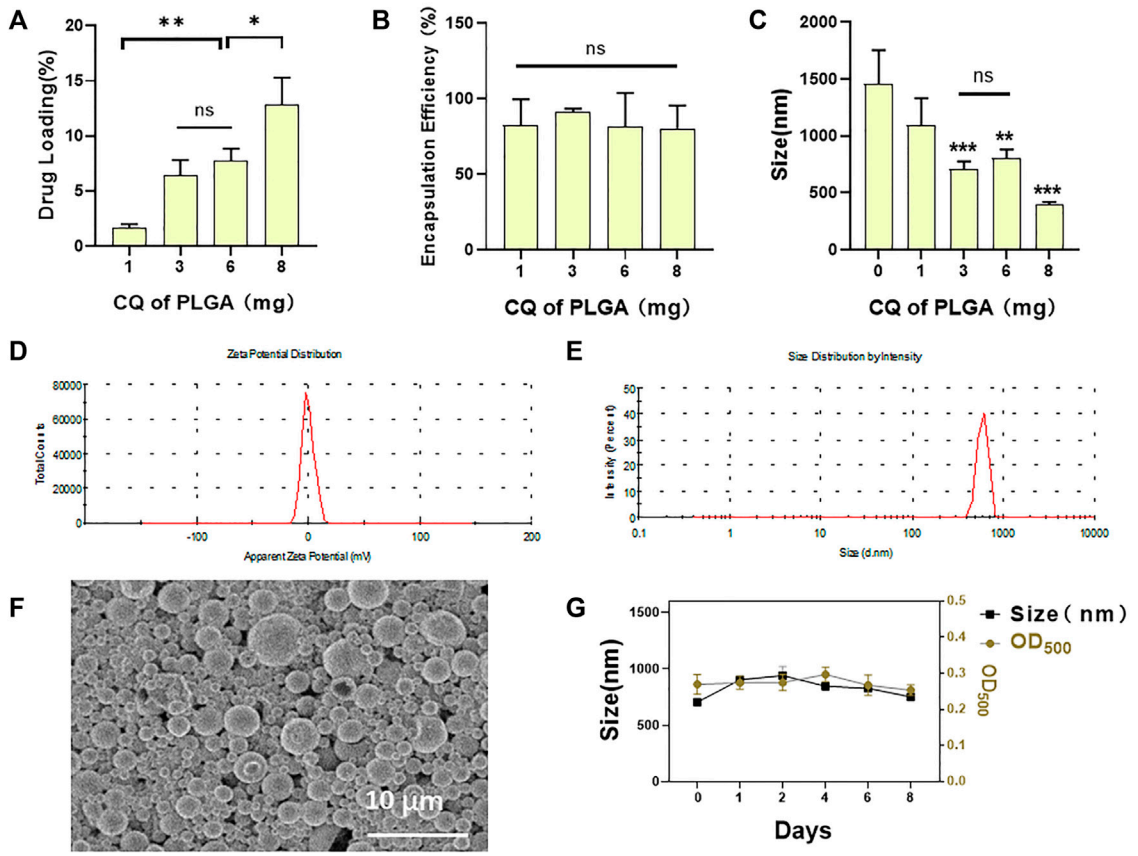

FIGURE 2 | Characterization of CQ/PLGA. **(A)** The drug loading of CQ/PLGA prepared by adding 1-, 3-, 6-, and 8-mg CQ per 50-mg PLGA (comparison between groups, $^{*}p < 0.05$, $^{**}p < 0.01$). **(B)** The entrapment efficiency of CQ/PLGA prepared by adding 1-, 3-, 6-, and 8-mg CQ per 50-mg PLGA. **(C)** Particle size distribution of CQ/PLGA prepared by adding 1-, 3-, 6-, and 8-mg CQ per 50-mg PLGA (vs. "0-mg group," $^{**}p < 0.01$, $^{***}p < 0.001$, $n = 5$). **(D)** The average particle size of CQ/PLGA MBs prepared by adding 6-mg CQ to 50-mg PLGA is 801.78 ± 69.10 nm. **(E)** The average potential of the particle size distribution of CQ/PLGA MBs prepared by adding 6-mg CQ to 50-mg PLGA is −6.57 ± 0.15 mV. **(F)** CQ/PLGA nanoparticles were prepared by adding 6 mg CQ to every 50 mg PLGA. SEM micrographs of nanoparticles showing the shape and the surface characteristics of CQ/PLGA. **(G)** The particle size and concentration of porous lipid CQ/PLGA MBs were measured at the initial, 1st, 2nd, 4th, 6th, and 8th days. The concentration of porous lipid CQ/PLGA MBs is expressed by OD_{500}.

cells were incubated with 4-μM erastin medium or 2-mM ISO medium and CQ at 0, 10, 20, 40, 60, 80, and 100 μg/ml (control group without erastin and CQ) for 24 h. The viability of cells was detected using the CCK-8 reagent, and the survival status of cells was observed under a microscope.

Propidium Iodide Fluorescence Apoptosis Detection

An Annexin V-FITC/PI double-stained apoptosis detection kit was purchased from Keygen Biotech Co. (Nanjing, China). Similar to that mentioned above, HL-1 cells were inoculated in 96-well plates. When the cell fusion was 80%, the cells underwent five different treatments: the control group did not undergo any treatment, the ISO group was treated with ISO, the CQ group was incubated with ISO and CQ, the CQ/PLGA group was incubated with ISO and CQ/PLGA, and the US + CQ/PLGA group was incubated with ISO and CQ/PLGA. The ultrasonic treatment was carried out at the same time. The concentration of ISO was 2 mM, and the final concentration of CQ was 80 μg/ml. The ultrasonic intensity was 100 mvpp, and other ultrasonic parameters were the same as above. 4′,6-Diamidino-2-phenylindole labeled nucleus. PI was used to label apoptotic cells. Phosphate-buffered saline was used to wash the dye. Fluorescence brightness was observed using a fluorescence microscope (Leica; Berlin, Germany). ImageJ (ImageJ, Marlyand, United States).

Data Analysis

All data were statistically analyzed using GraphPad Prism 6.0 (GraphPad Prism 6.0 GraphPad www.graphpad.com) and SPSS 25.0 (IBM SPSS Statistics for Windows, Version 25.0; Armonk, NY, United States) software. The measurement data were expressed as mean value ± standard deviation (x ± SD). Comparisons between multiple groups were performed using one-way analysis of variance. $p < 0.05$ was considered statistically significant ($^{*}p < 0.05$, $^{**}p < 0.01$, $^{***}p < 0.001$, $^{\#}p < 0.05$, $^{\#\#}p < 0.01$, $^{\#\#\#}p < 0.001$).

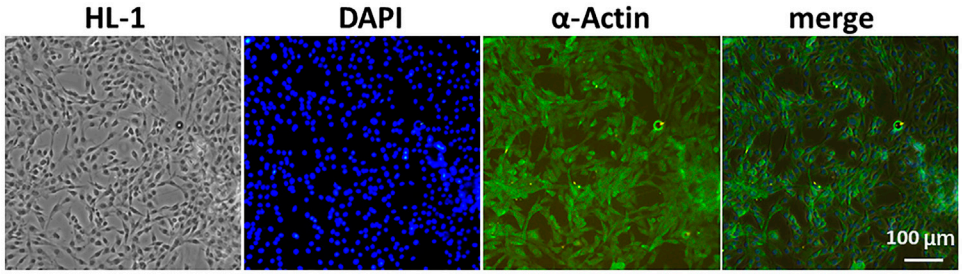

FIGURE 3 | Mouse cardiomyocytes (HL-1 cells) were identified using immunofluorescence. We selected α-actin protein highly expressed in HL-1 cells for green fluorescence labeling and then verified the accuracy of mouse cardiomyocytes. DAPI labeled the nucleus. Bar = 100 μm.

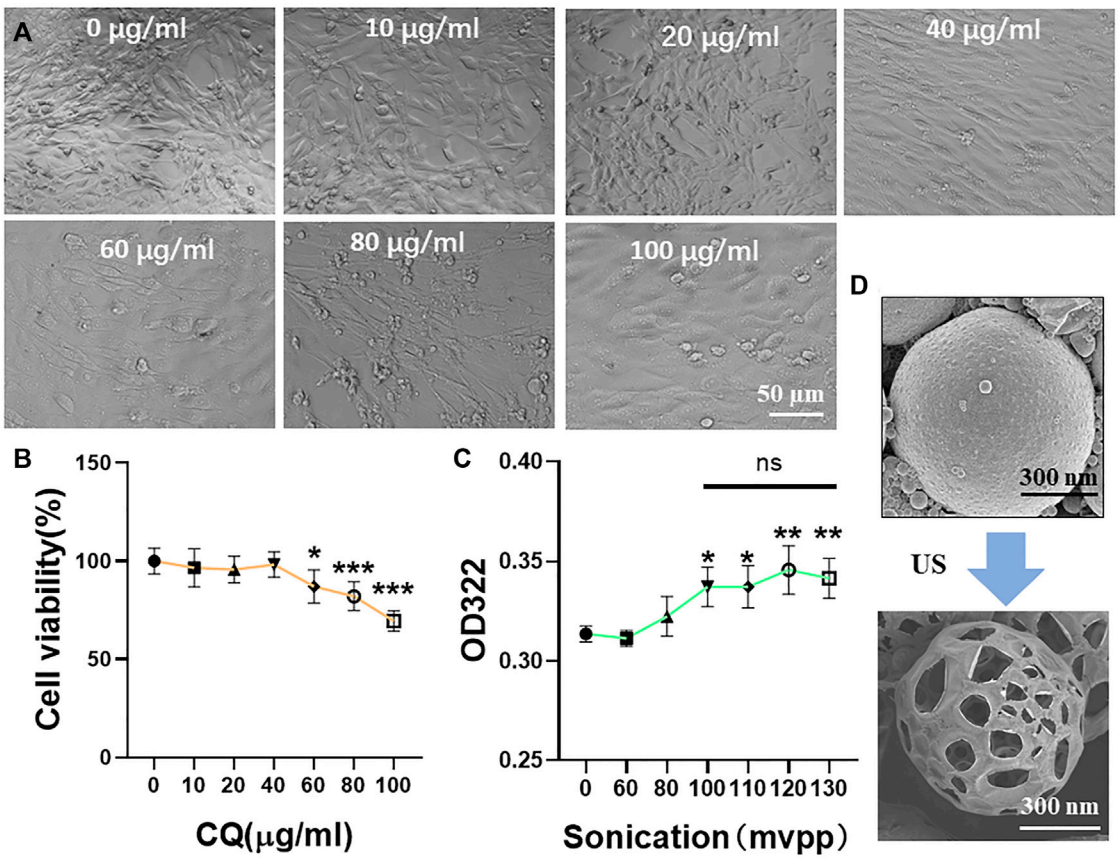

FIGURE 4 | Cytotoxicity test of CQ and ultrasound-assisted drug release. **(A,B)** HL-1 cells were incubated with a medium containing 0, 10, 20, 40, 60, 80, and 100 μg/ml CQ for 24 h to detect the cell viability and observe the cell survival state under a microscope. When the concentration of CQ was 60–100 μg/ml, HL-1 had obvious cytotoxicity (VS. "0-μg/ml group," $^{*}p < 0.05$, $^{***}p < 0.001$, $n = 5$, Bar = 50 μm). When the concentration of CQ was 60 μg/ml, the viability of HL-1 cells was 87.9% ± 7.73%. **(C)** The maximum UV absorption peak of CQ detected using a UV spectrophotometer was 322 nm. The release of CQ in 100 μl CQ/PLGA suspension was detected after continuous action of different ultrasonic intensities for 60 s. When the ultrasound intensity was 100–130 mvpp, CQ/PLGA was triggered to release CQ (vs. "0-mvpp group," $^{*}p < 0.05$, $^{**}p < 0.01$, $n = 5$). **(D)** When the ultrasound intensity was 100 mvpp, the shape changes in CQ/PLGA before and after ultrasound were observed using a SEM after continuous action for 60 s.

RESULTS

Characterization of Lipid Clioquinol/PLGA MBs

CQ/PLGA MBs were prepared by adding 6 mg of CQ to every 50 mg of PLGA. The characterization of CQ/PLGA has been tested (**Figure 2A**). The drug loading of CQ/PLGA was 9.01% ± 2.34% (**Figure 2A**) (vs. "8-mg group," $^{*}p < 0.05$, vs. "1-mg group," $^{**}p < 0.01$). The entrapment efficiency of CQ/PLGA was 75.03% ± 19.46% (**Figure 2B**). The results of the Malvern particle size analyzer showed that the particle size of CQ/PLGA was 801.78 ± 69.10 nm (vs. "0-mg group," $^{*}p < 0.05$),

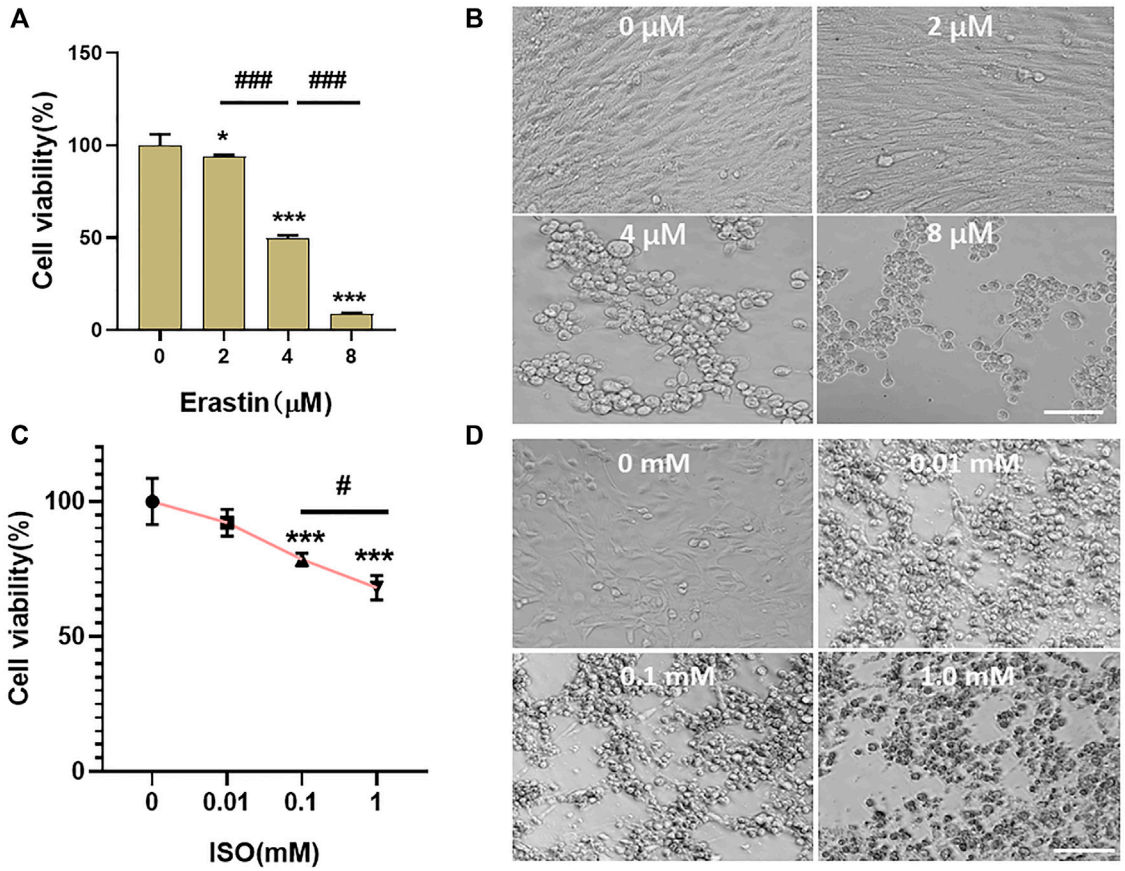

FIGURE 5 | Ferroptosis occurred in HL-1 of mouse cardiomyocytes. **(A,B)** Erastin was incubated with HL-1 cells at concentrations of 0, 2, 4, and 8 μM for 24 h. The viability of cells was detected using the CCK-8 reagent, and the survival status of cells was observed under a microscope. When the concentration of erastin was 4 μM, the cell viability of HL-1 cells was 49.53% ± 1.63% (vs. "0-μM group," ***$p < 0.001$, $n = 5$, Bar = 50 μm). **(C,D)** ISO was incubated with HL-1 cells at concentrations of 0, 0.01, 0.1, and 1.0 mM for 24 h. The viability of cells was detected using the CCK-8 reagent, and the survival status of cells was observed under a microscope. When the concentration of ISO was 0.1 mM, the cell viability of HL-1 cells was 78.52% ± 2.13% (vs. "0-μM group," ***$p < 0.001$, $n = 5$, Bar = 50 μm).

and the potential distribution was 6.57 ± 0.15 mV (**Figures 2D,E**). Scanning electron microscopy showed that CQ/PLGA was spherical and uniformly dispersed (**Figure 2F**). CQ/PLGA was found to have good stability by continuously monitoring the particle size and concentration of CQ/PLGA microbubbles for 8 days (**Figure 2G**). Therefore, we prepared CQ/PLGA MBs, explored the optimum ratio of CQ to PLGA, and tested their characterization.

Clioquinol Cytotoxicity Assay and Ultrasound-Assisted Drug Release

We selected a highly expressed α-actin protein in HL-1 cells for green fluorescence labeling. The results showed that the green fluorescence signal was strong, which verified the accuracy of mouse cardiomyocytes. Mouse cardiomyocytes (HL-1 cells) were identified using immunofluorescence (**Figure 3**). The cytotoxicity of CQ and US-assisted drug release was tested (**Figure 4B**). HL-1 cells were coincubated with 60 μg/ml CQ for 24 h. The cell viability detected using the CCK-8 reagent was 87.9% ± 7.73% (vs. "0-μg/ml group," *$p < 0.05$). The survival state of HL-1 cells was observed under a microscope. The results showed that when the concentration of CQ was 60–100 μg/ml, the volume of HL-1 cells was increased, the density was reduced, and the survival condition was gradually deteriorated (**Figure 4A**). At 322 nm, the drug release from CQ/PLGA was obvious after 60 s of treatment with a US of 100 mvpp intensity, and the OD value was 0.337 ± 0.01 (vs. "0-mvpp group," *$p < 0.05$; **Figure 4C**). When the US intensity was 100 mvpp, the shape changes in CQ/PLGA before and after US were observed using an SEM after continuous action for 60 s. The results show that CQ/PLGA evolves from spherical to a large number of voids on the surface, that is, the "cavitation effect" occurs and CQ is released (**Figure 4D**). Therefore, CQ had certain cytotoxicity and could trigger CQ/PLGA to release CQ under the action of US with certain parameters.

Occurrence of Ferroptosis in HL-1 Cells

A classic ferroptosis inducer, erastin, was coincubated with HL-1 cells for 24 h at the concentration of 4 μM (**Figure 5**). The results showed that the cell viability of HL-1 cells was 49.53% ± 1.63% (**Figure 5A**) (vs. "0-μM group," *$p < 0.001$). Microscopic

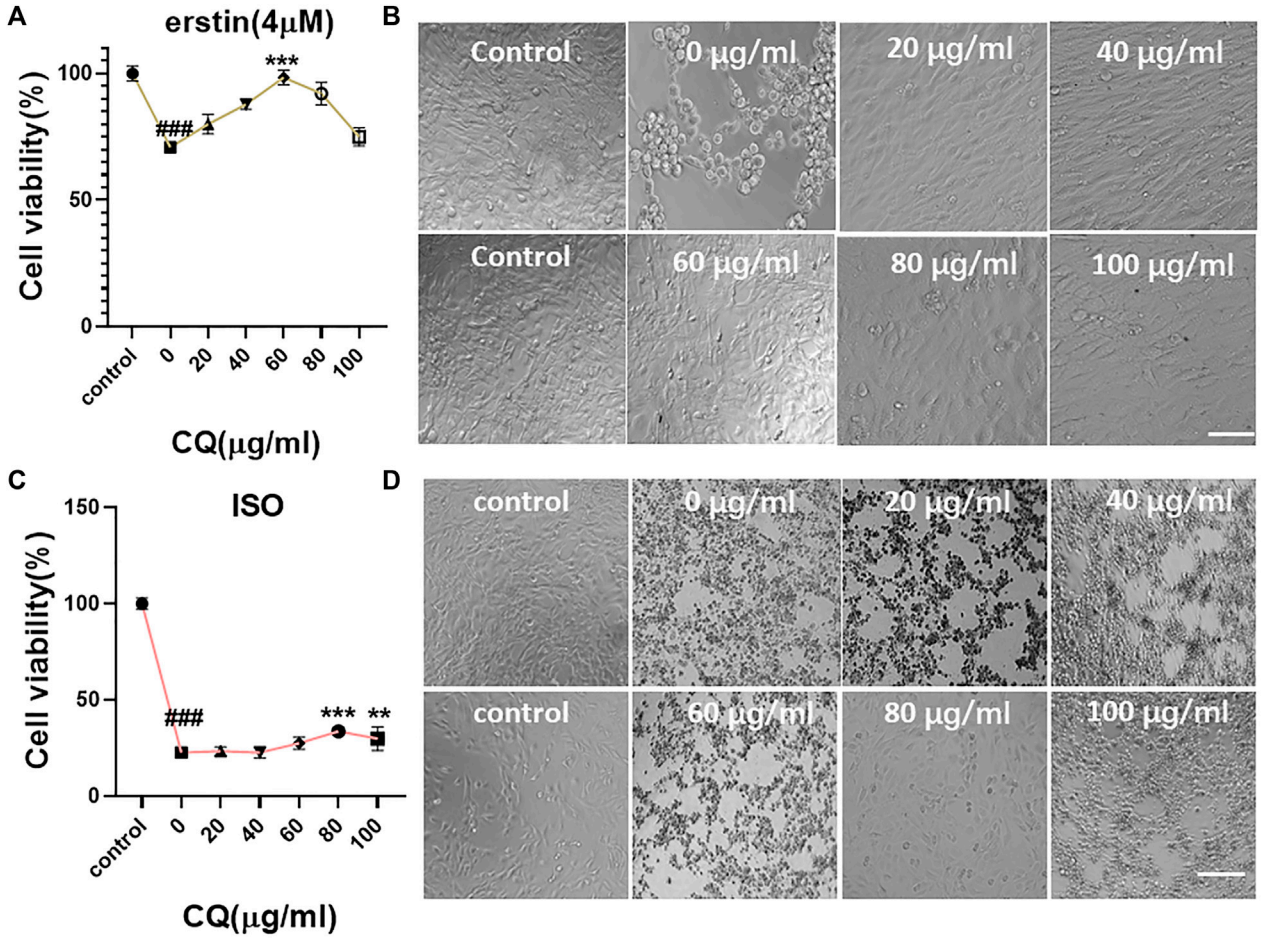

FIGURE 6 | Blocking effect of CQ on ferroptosis in mouse cardiomyocytes. **(A,B)** The medium containing 4 μM erastin and different concentrations of CQ (control group without erastin and CQ) were coincubated with HL-1 cells for 24 h. The viability of cells was detected using the CCK-8 reagent, and the survival status of cells was observed under a microscope. When the concentration of CQ was 0 μg/ml, the cell viability was 70.79% ± 1.91%. When the concentration of CQ was 60 μg/ml, the cell viability was 98.42% ± 2.65% (vs. control group, ###$p < 0.001$, vs. "0-μM group," ***$p < 0.001$, $n = 5$, Bar = 50 μm). **(C,D)** The medium containing 2-mM ISO and different concentrations of CQ (control group without ISO and CQ) were coincubated with HL-1 cells for 24 h. The viability of cells was detected using the CCK-8 reagent, and the survival status of cells was observed under a microscope. When the concentration of CQ was 0 μg/ml, the cell viability was 22.52% ± 1.18%. When the concentration of CQ was 80 μg/ml, the cell viability was 33.56% ± 1.84% (vs. control group, ###$p < 0.001$, vs. "0-μM group," ***$p < 0.001$, $n = 5$, Bar = 50 μm).

investigation showed that the cells condensed together and lost their original spindle shape (**Figure 5B**). ISO was coincubated with HL-1 cells for 24 h at the concentration of 0.1 mM. The viability of HL-1 cells was 78.52% ± 2.13% (vs. "0-μM group," ***$p < 0.001$, **Figure 5C**). Microscopic investigation showed that the state of HL-1 cells induced by erastin was consistent with that of ferroptosis (**Figure 5D**). Therefore, the mode of cardiomyocyte death was considered to be ferroptosis, and ISO could induce ferroptosis in HL-1 cells.

Clioquinol Inhibits Ferroptosis in HL-1 Cells

Ferroptosis in HL-1 cells was induced using a 4-μM erastin medium (**Figure 6**). The results showed that the occurrence of ferroptosis in HL-1 cells could be blocked to some extent when the concentration of CQ was 60 μg/ml. The cell viability was 98.42% ± 2.65% (**Figure 6A**) (vs. "0-μM group," ***$p < 0.001$; control group without erastin and CQ). Microscopic investigation showed that the cells were evenly distributed and spindle-shaped (**Figure 6B**). Ferroptosis in HL-1 cells was induced using the ISO medium at the concentration of 2 mM. When the concentration of CQ was 80 μg/ml, the cell viability was 33.56% ± 1.84% (vs. "0-μM group," ***$p < 0.001$, **Figure 6C**). Microscopic investigation showed that the cells were evenly distributed and close to the normal cell state (**Figure 6D**). Therefore, we verified that CQ could block the occurrence of ferroptosis in HL-1 cells and explored the optimal concentration.

Evaluation of the Effect of US Combined With Clioquinol/PLGA in Inhibiting Ferroptosis in HL-1

Ferroptosis in HL-1 cells was induced by the ISO medium at the concentration of 2 mM. The final concentration of CQ was 80 μg/ml (**Figure 7**). The viability of HL-1 cells in the CQ/PLGA group

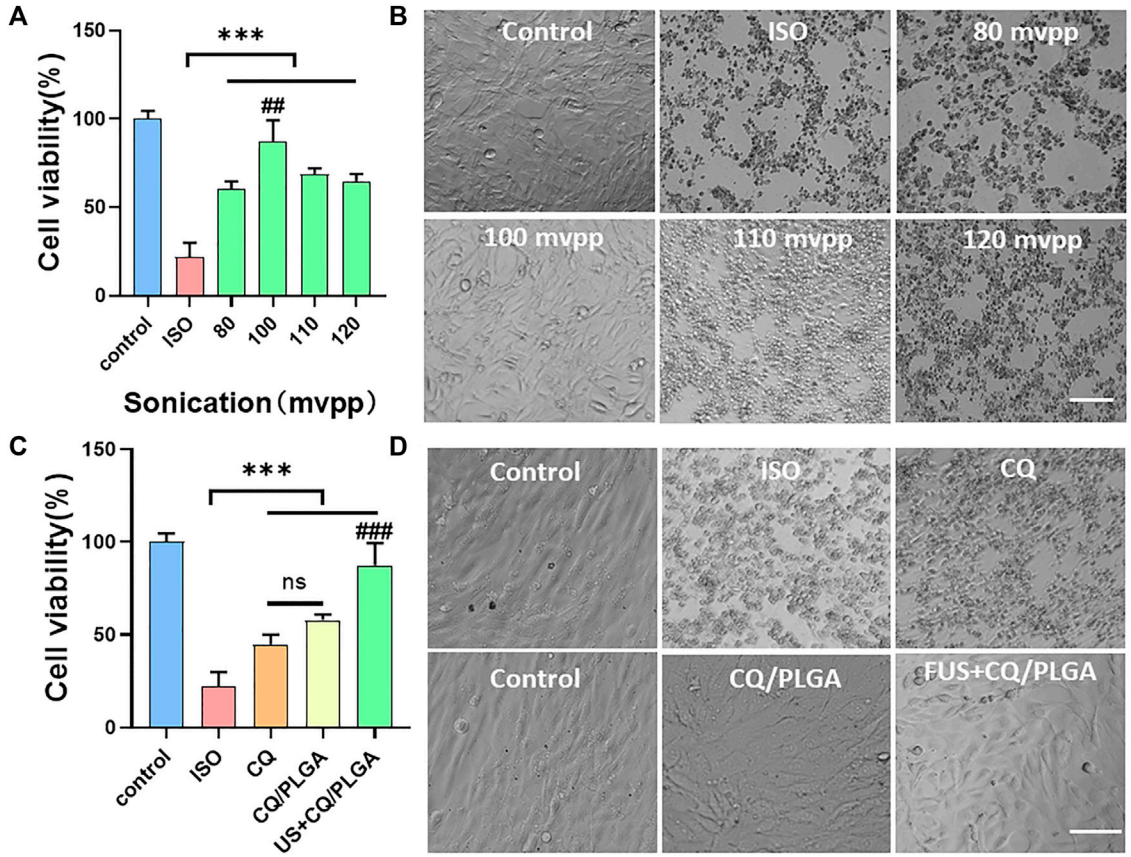

FIGURE 7 | Evaluation of the inhibitory effect of ultrasound combined with CQ/PLGA on ferroptosis in HL-1 via CCK-8 detection. **(A,B)** When the fusion degree of HL-1 cells reaches 80%, the culture medium containing ISO (concentration of 2 mM) and CQ/PLGA (concentration of final drug of CQ is 80 μg/ml) is added and treated with ultrasound for 30 s (ultrasound intensity is 0,80,100,110, and 120 mvpp), in which the control group does not do any treatment. After 24 h of incubation, the viability of cells was detected using the CCK-8 reagent, and the survival status of cells was observed under a microscope. When the intensity of ultrasound is 100 mvpp, ultrasound combined with CQ/PLGA has the best effect on inhibiting the occurrence of ferroptosis in HL-1. The cell viability was 87.39% ± 10.64% (vs. "ISO group," $^{***}p < 0.001$, vs. other groups, $^{\#\#}p < 0.01$, $n = 5$, Bar = 50 μm). **(C,D)** When the fusion degree of HL-1 cells reached 80%, the HL-1 cells were treated with different treatments and incubated for 24 h. The results showed that ultrasound combined with CQ/PLGA could better inhibit the ferroptosis process of HL-1 caused by ISO. The cell viability of the ISO group was 22.11% ± 7.02%, and the cell viability of ultrasound combined with the CQ/PLGA group was 83.16% ± 7.21% (vs. "ISO group," vs. other groups, $^{\#\#\#}p < 0.001$, $n = 5$, Bar = 50 μm).

was 57.92% ± 2.57% (vs. the ISO group, $^{***}p < 0.001$). When the ultrasonic intensity was 100 mvpp, the US combined with CQ/PLGA had the best inhibitory effect on ferroptosis in HL-1. The cell viability was 87.39% ± 10.64% (**Figure 7A**) (vs. the ISO group, $^{***}p < 0.001$, vs. other groups, $^{\#\#}p < 0.01$). Microscopic investigation showed that the cells were evenly distributed and close to the normal cell state (**Figure 7B**). Compared with CQ, CQ/PLGA group, US combined with CQ/PLGA could better inhibit the ferroptosis process of HL-1 caused by ISO. The corresponding cell viability of the US + CQ/PLGA group was 83.16% ± 7.21% (vs. the ISO group, $^{***}p < 0.001$, vs. other groups, $^{\#\#\#}p < 0.001$, **Figure 7C**). Microscopic investigation showed that the cells were evenly distributed in the US combined with CQ/PLGA treatment group, which was close to the normal cell state (**Figure 7D**).

The inhibitory effect of US combined with CQ/PLGA on ferroptosis in HL-1 using fluorescent apoptosis detection was evaluated (**Figure 8**). The results of the PI apoptosis fluorescence detection showed that the apoptosis rate of HL-1 cells in the ISO group was 58.08% ± 1.58% and that of HL-1 cells in the CQ/PLGA group was 21.52% ± 1.46% (vs. the ISO group, $^{***}p < 0.001$). The apoptosis rate of HL-1 cells in the US + CQ/PLGA group was 10.90% ± 0.68% (vs. control group, $^{**}p < 0.01$, vs. other groups, $^{\#\#}p < 0.01$; **Figures 8A,B**). Therefore, compared with CQ, CQ/PLGA had better biocompatibility and could improve the effect of CQ. When the sound pressure intensity was 100 mvpp and the action time was 30 s, the cavitation effect can occur in CQ/PLGA. The increased permeability of HL-1 cells further enhanced the inhibition of ferroptosis in HL-1 cells. Therefore, US combined with CQ/PLGA could effectively inhibit ferroptosis in HL-1 cells.

DISCUSSION

Ferroptosis is a recently discovered form of cell death caused by peroxidation induced by the accumulation of intracellular lipid

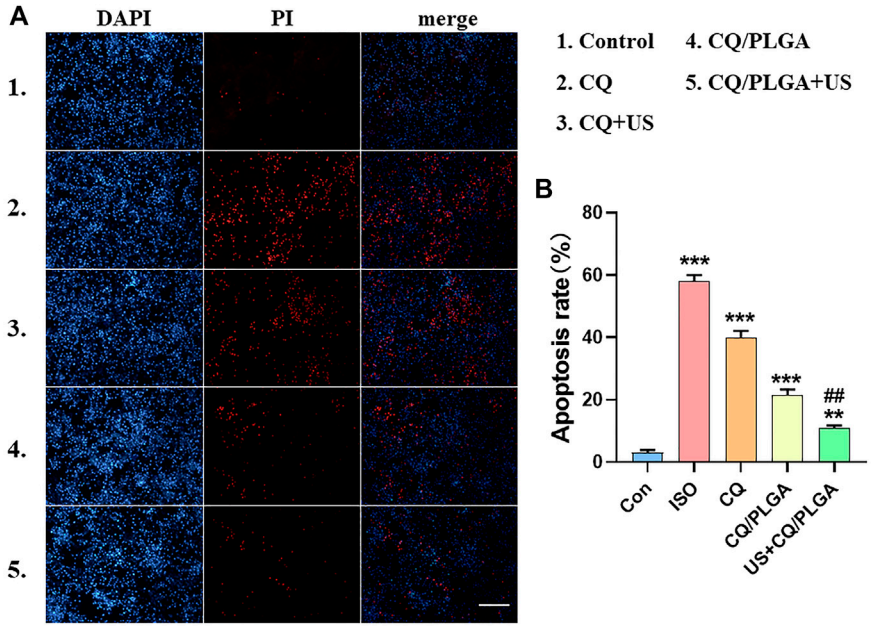

FIGURE 8 | Evaluation of the inhibitory effect of ultrasound combined with CQ/PLGA on ferroptosis in HL-1 using fluorescent apoptosis detection. **(A,B)** When the fusion degree of HL-1 cells reached 80%, HL-1 cells were treated with different treatments (the control group did not do any treatment). After incubation for 24 h, the nuclei were counterstained with PI. The results of ImageJ analysis showed that ultrasound combined with CQ/PLGA could inhibit the apoptosis of HL-1 induced by ISO. The apoptosis rate of the ISO group was 58.08% ± 1.58%, and the apoptosis rate of the US + CQ/PLGA group was 10.90% ± 0.68% (vs. control group, $^{**}p < 0.01$, $^{***}p < 0.001$, vs. other groups, $\#\#p < 0.01$, $n = 5$, Bar = 50 μm).

reactive oxygen species in an iron-dependent manner (Wu et al., 2021). Erastin could mediate ferroptosis through a variety of molecules including the cystine-glutamate transport receptor (system XC−), the voltage-dependent anion channel, and p53 (Yang et al., 2020; Li et al., 2021; Liu et al., 2021). ISO, a synthetic catecholamine and nonselective β-adrenergic receptor agonist, was widely used in a reproducible and well-standardized preclinical model of cardiac remodeling and dysfunction mainly due to excess production of reactive oxygen species by persistent β-adrenergic stimulation (Olmo et al., 2020; Zeng et al., 2020). Previously, Liu et al. demonstrated that ferroptosis-like cell death was observed in erastin- or ISO-treated H9c2 myocytes *in vitro* and in rats with aortic banding inducing HF, characterized by reduced cell viability with increased lipid peroxidation and labile iron pool (Liu et al., 2018). Here, interestingly, similar morphological changes were observed in HL-1 cells incubated with ISO or erastin. ISO, like erastin, induces ferroptosis in HL-1 cells. At the same time, the results showed that a certain concentration of clioquinol (CQ) could inhibit ferroptosis in HL-1 cells. CQ is a ferrous chelating agent and is also known as a metal protein attenuating compound (Lv et al., 2021; Xu et al., 2021). After entering the cells, CQ binds to Fe^{2+}, which blocks the occurrence of Fenton reaction and inhibits the occurrence of ferroptosis.

Ferroptosis is a way of cardiomyocyte death, and the metal ions closely related to ferroptosis are ferrous and ferric iron (Wu et al., 2021). CQ is an antibiotic that chelates both ferrous and ferric iron and is reported to alleviate neurodegenerative diseases and cancer (Lv et al., 2021; Maheshwaran et al., 2021; Xu et al., 2021). The lipophilic nature of CQ allows for its effective use at lower concentrations (Maheshwaran et al., 2021). However, CQ has the disadvantages of low bioavailability, poor water solubility, and cytotoxicity, which limit its application (Maheshwaran et al., 2021). In recent years, with the development of nanomedicine, studies have shown that PLGA nanoparticles have the advantages of high entrapment efficiency and drug loading. At the same time, PLGA nanoparticles also have high biocompatibility and sustained-release effect (Kapoor et al., 2015; Ding and Zhu, 2018). However, PLGA nanoparticles have some disadvantages, such as strong and rigid structure, low drug loading, poor imaging, and poor ultrasonic sensitivity (Su et al., 2021).

Chen et al. developed a new type of porous lipid drug-loaded PLGA MBs, which increased the drug loading of PLGA nanoparticles, while the addition of DSPC components improved the elasticity of the shell (Chen et al., 2019). This new type of porous lipid drug-loaded PLGA MBs could oscillate under the action of low-frequency US with certain parameters, that is, the "cavitation effect," which could increase the permeability of cell membrane and improve the efficiency of drug action (De Alwis et al., 2021; Guo et al., 2021). We chose this new type of porous lipid drug-loaded PLGA MBs as carriers to prepare lipid CQ/PLGA MBs containing CQ, which improved the shortcomings of low bioavailability, poor water solubility, and cytotoxicity of CQ (Khan et al., 2020; Lv et al., 2021).

Porous lipid CQ/PLGA MBs were prepared using a water/oil/water ($W_1/O/W_2$) double emulsification method (Chen et al., 2019). Under the action of US, porous lipid CQ/PLGA MBs produced a series of alternating changes, such as expansion,

contraction, oscillation, and implosion. The increase in cell membrane permeability, that is, the "sound pore effect," led to the better effect of CQ on HL-1 cells. Thus, we provided a new scheme to inhibit ferroptosis in cardiomyocytes and improve the cardiac function and remodeling caused by an ISO attack. However, this study has some limitations. Measuring the levels of any isoforms of arachidonate lipoxygenase (ALOX), GPX4 activity, or other antioxidants, iron content, and morphological findings would provide more relevance to ferroptosis. The clinical translation and patient compliance of the research must be investigated in the future.

CONCLUSION

In summary, our experimental results showed that a certain concentration of CQ could prevent the process of ferroptosis in HL-1 cells. Lipid CQ/PLGA MBs could improve the effect of CQ. At the same time, CQ/PLGA MBs had good ultrasonic sensitivity. When the frequency was 929 kHz, the sound pressure intensity was 100 mvpp, the action time was 30 s, and the pulse cycle was 10,000. Lipid CQ/PLGA MBs could further enhance the inhibitory effect of ferroptosis on HL-1 cells.

DATA AVAILABILITY STATEMENT

The raw data supporting the conclusions of this article will be made available by the authors, without undue reservation.

AUTHOR CONTRIBUTIONS

NL and LD conceived and performed the experiments, performed the data analysis, and wrote the manuscript. YW, LC, HW, and YC conducted the study. ML, DL, ZL, MH, CL, and YW collected the samples. HX and YS revised the manuscript, and FW approved the final version.

FUNDING

The study was supported by a grant from the National Key R&D Program of China (2020YFA0908800), the National Natural Science Fund of China (grant no. U1804187,12074269), the Medical Science and Technology Project of Henan Province (LHGJ20210527), and the Shenzhen Science and Technology Program (JCYJ20210324105415040, JCYJ20190809105207439, and JCYJ20210324110015040).

REFERENCES

Birn, A. E., and Nervi, L. (2020). (Re-)Making a People's WHO. *Am. J. Public Health* 110, 1352–1353. doi:10.2105/AJPH.2020.305806

Chen, X., Yu, C., Kang, R., Kroemer, G., and Tang, D. (2021). Cellular Degradation Systems in Ferroptosis. *Cell. Death Differ.* 28, 1135–1148. doi:10.1038/s41418-020-00728-1

Chen, Y., Liang, Y., Jiang, P., Li, F., Yu, B., and Yan, F. (2019). Lipid/PLGA Hybrid Microbubbles as a Versatile Platform for Noninvasive Image-Guided Targeted Drug Delivery. *ACS Appl. Mater Interfaces* 11, 41842–41852. doi:10.1021/acsami.9b10188

De Alwis, S., Abbasi Shirsavar, M., Singh, S., and Hashemi, N. N. (2021). Hydrodynamic Cavitation for Scalable Exfoliation of Few-Layered Graphene Nanosheets. *Nanotechnology* 32, 505701. doi:10.1088/1361-6528/ac2096

Ding, D., and Zhu, Q. (2018). Recent Advances of PLGA Micro/nanoparticles for the Delivery of Biomacromolecular Therapeutics. *Mater Sci. Eng. C Mater Biol. Appl.* 92, 1041–1060. doi:10.1016/j.msec.2017.12.036

Guo, C., Liu, J., Li, X., and Yang, S. (2021). Effect of Cavitation Bubble on the Dispersion of Magnetorheological Polishing Fluid under Ultrasonic Preparation. *Ultrason. Sonochem* 79, 105782. doi:10.1016/j.ultsonch.2021.105782

Kapoor, D. N., Bhatia, A., Kaur, R., Sharma, R., Kaur, G., and Dhawan, S. (2015). PLGA: a Unique Polymer for Drug Delivery. *Ther. Deliv.* 6, 41–58. doi:10.4155/tde.14.91

Khan, R., Khan, H., Abdullah, Y., and Dou, Q. P. (2020). Feasibility of Repurposing Clioquinol for Cancer Therapy. *Recent Pat. Anticancer Drug Discov.* 15, 14–31. doi:10.2174/1574892815666200227090259

Klibanov, A. L. (2021). Ultrasound Contrast: Gas Microbubbles in the Vasculature. *Invest. Radiol.* 56, 50–61. doi:10.1097/RLI.0000000000000733

Li, N., Wang, W., Zhou, H., Wu, Q., Duan, M., Liu, C., et al. (2020). Ferritinophagy-mediated Ferroptosis Is Involved in Sepsis-Induced Cardiac Injury. *Free Radic. Biol. Med.* 160, 303–318. doi:10.1016/j.freeradbiomed.2020.08.009

Li, Y., Zeng, X., Lu, D., Yin, M., Shan, M., and Gao, Y. (2021). Erastin Induces Ferroptosis via Ferroportin-Mediated Iron Accumulation in Endometriosis. *Hum. Reprod.* 36, 951–964. doi:10.1093/humrep/deaa363

Liu, B., Zhao, C., Li, H., Chen, X., Ding, Y., and Xu, S. (2018). Puerarin Protects against Heart Failure Induced by Pressure Overload through Mitigation of Ferroptosis. *Biochem. Biophys. Res. Commun.* 497, 233–240. doi:10.1016/j.bbrc.2018.02.061

Liu, M., Fan, Y., Li, D., Han, B., Meng, Y., Chen, F., et al. (2021). Ferroptosis Inducer Erastin Sensitizes NSCLC Cells to Celastrol through Activation of the ROS-Mitochondrial Fission-Mitophagy axis. *Mol. Oncol.* 15, 2084–2105. doi:10.1002/1878-0261.12936

Lowe, N. K. (2020). 2020 Is the World Health Organization's Year of the Nurse and the Midwife. *J. Obstet. Gynecol. Neonatal Nurs.* 49, 1–2. doi:10.1016/j.jogn.2019.11.008

Luo, M. H., Yeh, C. K., Situ, B., Yu, J. S., Li, B. C., and Chen, Z. Y. (2017). Microbubbles: A Novel Strategy for Chemotherapy. *Curr. Pharm. Des.* 23, 3383–3390. doi:10.2174/1381612823666170113092148

Lv, X., Zhang, W., Xia, S., Huang, Z., and Shi, P. (2021). Clioquinol Inhibits Cell Growth in a SERCA2-dependent Manner. *J. Biochem. Mol. Toxicol.* 35, e22727. doi:10.1002/jbt.22727

Ma, S., Sun, L., Wu, W., Wu, J., Sun, Z., and Ren, J. (2020). USP22 Protects against Myocardial Ischemia-Reperfusion Injury via the SIRT1-p53/SLC7A11-dependent Inhibition of Ferroptosis-Induced Cardiomyocyte Death. *Front. Physiol.* 11, 551318. doi:10.3389/fphys.2020.551318

Maheshwaran, S., Akilarasan, M., Chen, T. W., Chen, S. M., Tamilalagan, E., Jiang, T. Y., et al. (2021). Electrocatalytic Evaluation of Graphene Oxide Warped Tetragonal T-Lanthanum Vanadate (GO@LaVO4) Nanocomposites for the Voltammetric Detection of Antifungal and Antiprotozoal Drug (Clioquinol). *Mikrochim. Acta* 188, 102. doi:10.1007/s00604-021-04758-5

Olmo, F., Garoz-Ruiz, J., Carazo, J., Colina, A., and Heras, A. (2020). Spectroelectrochemical Determination of Isoprenaline in a Pharmaceutical Sample. *Sensors (Basel)* 20, 5179. doi:10.3390/s20185179

Piccoli, G. B. (2021). A Brand New World: from Cardiovascular Diseases to Aquaponics, Focusing on Challenges Can Bring New Hope. An Introduction to 2021 from Journal of Nephrology. *J. Nephrol.* 34, 1–2. doi:10.1007/s40620-021-00978-3

Rix, A., Curaj, A., Liehn, E., and Kiessling, F. (2020). Ultrasound Microbubbles for Diagnosis and Treatment of Cardiovascular Diseases. *Semin. Thromb. Hemost.* 46, 545–552. doi:10.1055/s-0039-1688492

Su, Y., Zhang, B., Sun, R., Liu, W., Zhu, Q., Zhang, X., et al. (2021). PLGA-based Biodegradable Microspheres in Drug Delivery: Recent Advances in Research and Application. *Drug Deliv.* 28, 1397–1418. doi:10.1080/10717544.2021.1938756

Wang, F., Dong, L., Wei, X., Wang, Y., Chang, L., Wu, H., et al. (2021). Effect of Gambogic Acid-Loaded Porous-Lipid/PLGA Microbubbles in Combination With Ultrasound-Triggered Microbubble Destruction on Human Glioma. *Front. Bioeng. Biotechnol.* 9, 711787. doi:10.3389/fbioe.2021.711787

Wu, X., Li, Y., Zhang, S., and Zhou, X. (2021). Ferroptosis as a Novel Therapeutic Target for Cardiovascular Disease. *Theranostics* 11, 3052–3059. doi:10.7150/thno.54113

Xu, L., Sai, J., Xue, D., Zhou, L., Pei, R., and Liu, A. (2021). Amplified Peroxidase-like Activity of Co2+ Using 8-Hydroxyquinoline and its Application for Ultrasensitive Colorimetric Detection of Clioquinol. *Chem. Asian J.* 16, 3957–3962. doi:10.1002/asia.202100997

Yang, Y., Luo, M., Zhang, K., Zhang, J., Gao, T., Connell, D. O., et al. (2020). Nedd4 Ubiquitylates VDAC2/3 to Suppress Erastin-Induced Ferroptosis in Melanoma. *Nat. Commun.* 11, 433. doi:10.1038/s41467-020-14324-x

Zeng, H., Li, H., Yue, M., Fan, Y., Cheng, J., Wu, X., et al. (2020). Isoprenaline Protects Intestinal Stem Cells from Chemotherapy-Induced Damage. *Br. J. Pharmacol.* 177, 687–700. doi:10.1111/bph.14883

Zhou, Q., and Bei, Y. (2020). Editorial: Gender Differences in Cardiovascular Diseases. *J. Cardiovasc Transl. Res.* 13, 1–2. doi:10.1007/s12265-020-09956-9

Conflict of Interest: The authors declare that the research was conducted in the absence of any commercial or financial relationships that could be construed as a potential conflict of interest.

Publisher's Note: All claims expressed in this article are solely those of the authors and do not necessarily represent those of their affiliated organizations or those of the publisher, the editors, and the reviewers. Any product that may be evaluated in this article, or claim that may be made by its manufacturer, is not guaranteed or endorsed by the publisher.

frontiers | Frontiers in Pharmacology

TYPE Original Research
PUBLISHED 12 August 2022
DOI 10.3389/fphar.2022.940365

OPEN ACCESS

EDITED BY
Guixue Wang,
Chongqing University, China

REVIEWED BY
Shengyu Mu,
University of Arkansas for Medical Sciences, United States
Venkatesh Katari,
University of Toledo, United States

*CORRESPONDENCE
Jia Yu,
yujia@gxmu.edu.cn

SPECIALTY SECTION
This article was submitted to Cardiovascular and Smooth Muscle Pharmacology, a section of the journal Frontiers in Pharmacology

RECEIVED 10 May 2022
ACCEPTED 15 July 2022
PUBLISHED 12 August 2022

CITATION
Zhang J, Cheng Y-J, Luo C-J and Yu J (2022), Inhibitory effect of (pro)renin receptor decoy inhibitor PRO20 on endoplasmic reticulum stress during cardiac remodeling.
Front. Pharmacol. 13:940365.
doi: 10.3389/fphar.2022.940365

Inhibitory effect of (pro)renin receptor decoy inhibitor PRO20 on endoplasmic reticulum stress during cardiac remodeling

Jing Zhang[1], Yun-Jiu Cheng[2], Chang-Jun Luo[1] and Jia Yu[3]*

[1]Department of Cardiology, Liuzhou Municipal Liutie Central Hospital, Liuzhou, China, [2]Department of Cardiology, The First Affiliated Hospital of Sun Yat-sen University, Guangzhou, China, [3]Department of General Practice School, Guangxi Medical University, Nanning, China

Background: Ectopic activation of renin-angiotensin-system contributes to cardiovascular and renal diseases. (Pro)renin receptor (PRR) binds to renin and prorenin, participating in the progression of nephrology. However, whether PRR could be considered as a therapeutic target for cardiac remodeling and heart failure remains unknown.

Materials and methods: Transverse aortic constriction (TAC) surgery was performed to establish a mouse model of chronic pressure overload-induced cardiac remodeling. Neonatal rat cardiomyocytes (CMs) and cardiac fibroblasts (CFs) were isolated and stimulated by Angiotensin II (Ang II). PRR decoy inhibitor PRO20 was synthesized and used to evaluate its effect on cardiac remodeling.

Results: Soluble PRR and PRR were significantly upregulated in TAC-induced cardiac remodeling and Ang II-treated CMs and CFs. Results of *In vivo* experiments showed that suppression of PRR by PRO20 significantly retarded cardiac remodeling and heart failure indicated by morphological and echocardiographic analyses. *In vitro* experiments, PRO20 inhibited CM hypertrophy, and also alleviated CF activation, proliferation and extracellular matrix synthesis. Mechanically, PRO20 enhanced intracellular cAMP levels, but not affected cGMP levels in CMs and CFs. Moreover, treatment of PRO20 in CFs markedly attenuated the production of reactive oxygen species and phosphorylation of IRE1 and PERK, two well-identified markers of endoplasmic reticulum (ER) stress. Accordingly, administration of PRO20 reversed ER stressor thapsigargin-induced CM hypertrophy and CF activation/migration.

Conclusion: Taken together, these findings suggest that inhibition of PRR by PRO20 attenuates cardiac remodeling through increasing cAMP levels and reducing ER stress in both CMs and CFs.

KEYWORDS

(Pro)renin receptor, PRO20, heart failure, cardiac remodeling, endoplasmic reticulum stress

Introduction

Cardiac remodeling is the common pathological change in the onset and development of multiple cardiovascular diseases, including hypertension, ischemic cardiomyopathy and non-ischemic cardiomyopathy (Abboud and Januzzi, 2021). During the pathological process, cardiac hypertrophy is characterized by increased cardiomyocyte (CM) size, enhanced protein synthesis and excessive organization of the sarcomere (Yang et al., 2020). Cardiac fibrosis, as a scarring event in the cardiac muscle, is characterized by net accumulation of extracellular matrix in the myocardium, mediated by cardiac fibroblast (CF) activation and differentiation into myofibroblasts (Yang et al., 2020; Frangogiannis, 2021). Thus, early inhibition and even reversal of cardiac remodeling is an effective therapeutic regime for retarding heart failure (HF).

Current knowledge proves that the renin-angiotensin system (RAS) plays a central role in the pathogenesis of cardiac remodeling and HF (Abboud and Januzzi, 2021). Inhibition of RAS by angiotensin-converting enzyme inhibitors (ACEIs) and angiotensin receptor blockers (ARBs) has been approved for the treatment of numerous cardiovascular diseases including hypertension, atherosclerosis and HF due to its beneficial effect on cardiovascular remodeling (Singh and Karnik, 2016). Prorenin receptor (PRR), a new component of the RAS, serves as a specific receptor for prorenin and renin to regulate their catalytic activity (Manerikar et al., 1976). Furthermore, the serum concentration of soluble PRR is a potential biomarker of tissue RAS activity (Fu et al., 2021). Previous studies provided full insights into the distribution and function of PRR in kidney diseases (Chen and Xu, 2020; Wang et al., 2020; Arthur et al., 2021). Accordingly, PRR decoy inhibitor PRO20 attenuated albumin overload-induced nephropathy in rats (Fang et al., 2018). However, the role of PRR decoy inhibitor in cardiac remodeling and HF remains unclear.

Endoplasmic reticulum (ER) is an organelle that functions in the folding, transport and secretion of lumen and membrane proteins and maintenance of intracellular calcium balance. Disruption of ER homeostasis provokes ER stress and causes the activation of downstream signaling such as inositol requiring enzyme 1 (IRE-1), PKR-like eukaryotic initiation factor 2a kinase (PERK), activating transcription factor-6 (ATF6) (Wang et al., 2018). Activation of unfolded protein response leads to ER stress via phosphorylation of IRE1 and PERK, or translocating ATF-6 to the Golgi apparatus and generating cleaved N-terminal cytoplasmic domain of ATF-6 (ATF-6 [N]) (Wang and Kaufman, 2016). Recent studies have indicated that ER stress is an essential signaling cascade for cardiovascular diseases (Wang et al., 2018; Zhang et al., 2020).

In the present study, we first assessed the plasma concentration of soluble PRR in mice with pressure overload and the expression of PRR in mouse failing hearts. Next, we investigated the effects of PRR blocker PRO20 on cardiac remodeling and cardiac dysfunction induced by transverse aortic contraction (TAC) in mice. In addition, we determined the underlying mechanism of PRO20 in CMs and CFs during cardiac remodeling. This study may extend our understanding of PRR and provide a new potential therapeutic target for HF.

Materials and methods

Mouse model

All experimental procedures involving animals were performed in accordance with the guidelines of the National Institutes of Health for the care and use of laboratory animals (NIH Publication, eighth Edition, 2011) and approved by the Animal Care and Use Committees of Liuzhou Municipal Liutie Central Hospital. TAC surgery was conducted to induce pathological cardiac hypertrophy *in vivo*. Briefly, 8-week-old C57BL/6J mice were anesthetized via intraperitoneal injections of a xylazine (5 mg/kg) and ketamine (80 mg/kg) mixture, and the aortic arch was visualized and ligated with 6–0 silk suture against a 27-gauge needle to form an approximately 70% aortic constriction. The needle was removed and the chest was closed with 5–0 silk suture (Xu et al., 2019). In order to improve the stability and reproducible of animal model, we arranged an experienced technician to perform TAC surgery. Three days prior to TAC surgery, PRO20 dissolved in saline was administered at 250 μg/kg/d or 500 μg/kg/d *via* subcutaneously implanted osmotic minipump according to previous reports (Wang et al., 2020). Equal volume of saline was administrated via subcutaneously implanted osmotic minipump in control group (Wang et al., 2019). At the end of the experiments, the mice were sacrificed by intraperitoneally injection of a lethal dose of pentobarbital sodium (100 mg/kg) to obtain the blood and heart for further analysis.

Echocardiographic analysis

Using B-mode imaging (Vevo770; VisualSonics, Canada), the transducer (30-MHz RMV707B) was positioned to image longitudinal or cross sections of the heart. All echocardiographic measurements were made 3 times and the average values were reported. We finally analyzed the fractional shortening (FS), left ventricular ejection fraction (LVEF), left ventricular internal diameter at end-systole (LVIDs) and left ventricular (LV) mass using the software Vevo 2100 (version 1.1.1, Visualsonics, Canada).

Histological analysis

Masson staining was performed to evaluate collagen volume according to the manufacturer's instructions

(Servicebio Technology, China). The cross-sectional areas of the heart tissues were assessed by wheat germ agglutinin (WGA) staining (Servicebio Technology, China). Cross sections were photographed using a microscope (Leica, Germany), and the data were analyzed with ImageJ software (NIH, United States).

Evaluation of oxidative stress

Dihydroethidium (DHE) staining solution (Sigma, United States) was added to the frozen sections of heart after dilution in PBS and incubated at 37°C in the dark for 30 min, then the cryosections were rinsed twice with cold PBS. Myocardial tissue homogenate of mice was used to measure malondialdehyde (MDA) and superoxide dismutase (SOD) activity by commercially available MDA and SOD assays (NanJing JianCheng Bioengineering Institute, China). Intracellular MDA activity was measured at 532 nm using a microtiter plate reader (Dragon Wellscan MK2, Finland) and was expressed as nmol/mg of protein. Intracellular SOD activity was measured at 550 nm and was expressed as units/mg of protein.

Isolation of cardiomyocytes and cardiac fibroblasts

Neonatal rat CMs and CFs were isolated from 0-3-day-old Sprague Dawley rats. In brief, the left ventricles were harvested, minced, and digested with collagenase type II (Worthington Biochemical Corporation, United States) and pancreatin (Sigma, United States) after anesthesia. To remove any contaminating fibroblasts, collected cells were seeded in uncoated 100 mm plastic dishes for 1 h at 37°C in 5% CO_2 humidified atmosphere. The supernatant, which consists mainly of CMs, was collected and cells were counted and plated on gelatinized 6 well plates 1×10^6 cells per well. The medium consisted of DMEM/M199 medium (ThermoFisher Scientific, United States) supplemented with 10% FBS, 1% penicillin/streptomycin and 100 μM bromodeoxyuridine. This procedure yields >90% pure CMs. For CFs culture, the supernatant was centrifuged for 5 min (400 x g), resuspended in DMEM medium (ThermoFisher Scientific, United States) supplemented with 10% FBS and plated in 6 well plates. The cells were starved in media containing 0.5% FBS for 12 h, and stimulated with Angiotensin (Ang) II (1 μM) for 24 h (Xu et al., 2019). In this regard, Lu et al, (2022) studied the pharmacokinetic and bioavailability of PRO20 and determined a preferred dosage of 10 nM *in vitro*. Then cells were incubated with PRO20 (10 nM), or thapsigargin (ER stressor, TG, 5 μM) for 24 h (Prola et al., 2017).

Cardiac fibroblast proliferation and migration analysis

Edu Cell Proliferation Kit (ThermoFisher Scientific, United States) was applied to measure CF proliferation according to the manufacturer's instructions. After 24-h treatment of DMSO or PRO20, CFs were incubated with Edu (20 μM) for 2 h at 37°C. Following fixation with 4% paraformaldehyde, permeabilized incubation with 0.5% Triton X-100 and staining with Click-iT EdU Alexa Fluor 594 and DAPI. Proliferative CFs were imaged using a fluorescent microscope (Leica, Germany).

The transwell chamber (8 μm pore size, Corning, United States) was applied for CF migration. After PRO20 treatments, CFs were digested with 0.25% trypsin (Hyclone, United States) and resuspended with DMEM without FBS. The 0.6 ml of DMEM with 0.5% FBS was added into lower chamber. Then 100 μl of cell suspension solution was added into the upper chambers and incubated at 37°C for 12 h. After removing the medium, 1 × PBS was used to wash the migrated cells on both side of the membranes and fix the cells with 4% glutaraldehyde for 20 min. CFs that had migrated through the membrane were stained with crystal violet for 30 min and counted with microscope (Leica, Germany).

RNA isolation and real-time quantitative reverse transcription

Total RNA was extracted from murine left ventricular tissue by TRIzol (Invitrogen, United States) according to the manufacturer's instructions. Total RNA were reverse transcribed to cDNA with iScriptTM cDNA synthesis Kit (Vazyme, China). Gene expression was analyzed by quantitative PCR using ABI-7900 Real-Time PCR Detection System. The relative expression level was calculated using the $2^{-\Delta\Delta Ct}$ method. GAPDH was used as an internal control. Primers sequences were listed in Supplementary Table S1.

Western blots

To determine the protein expression levels, cells were lysed with ice-cold RIPA buffer (Beyotime, United States) supplemented with protease and phosphatase inhibitor cocktail (ThermoFisher Scientific, United States), and the protein concentration was quantified via the bicinchoninic acid method. The protocol of western blots was described in previous study (Yuan et al., 2019). The primary antibodies against ANP (diluted 1:1000, Abcam, United States), BNP (diluted 1:1000, Abcam, United States), PRR (diluted 1:500, Abcam, United States), α-SMA (diluted 1:2000, Abcam,United States), Collagen Iα (diluted 1:1000, Abcam,

United States), t-IRE1 (diluted 1:1000, Cell Signaling Technology, United States), p-IRE1 (diluted 1:600, Cell Signaling Technology, United States), t-PERK (diluted 1:1000, Cell Signaling Technology, United States), p-PERK (diluted 1:6000, Cell Signaling Technology, United States), ATF-6 (diluted 1:1000, Abcam, United States) and GAPDH (1:5000, SantaCruz, United States) were used in the study. The images were analyzed using Image-Pro Plus software (Version 7.0).

Analysis of intracellular cAMP and cGMP content

Quantitative determination of intracellular cyclic adenosine-3′,5′-monophosphate (cAMP) and cyclic guanosine-3′,5′-monophosphate (cGMP) was performed according to the manufacture's introduction (Elabscience, China). The intracellular cAMP and cGMP contents were assessed by measuring absorbance at 450 nm using a microtiter plate reader (Dragon Wellscan MK2, Finland) and calculating from a standard curve.

Evaluation of soluble (Pro)renin receptor

The plasma content of soluble PRR in mice was determined by enzyme immunoassay kits according to the manufacturer's instructions (JP27782, IBL, Japan).

Quantification of angiotensin peptide in the plasma and heart tissues

Plasma was collected in tubes containing PMSF and EDTA. The isolated LV was dissected and homogenized on ice in 0.9% saline/0.1 M HCl containing 0.1 M aprotinin. Total protein content of the homogenate was determined. Then, angiotensin peptide quantification (including Ang I and Ang II) by liquid chromatography tandem-mass spectrometry analysis (LC-MS/MS) was performed in the plasma and heart tissues by Attoquant Diagnostics GmbH (Vienna, Austria) as previously described (Domenig et al., 2016).

Statistical analysis

Continuous variables were presented as the mean ± standard deviation (SD) for at least three independent experiments. Categorical variables were presented as numbers and percentages. Results were analyzed using GraphPad (SPSS, United States). The significant differences between categorical variables were determined using Chi-square test. The Student's t test was performed to investigate the difference in continuous variables of normal distribution between two groups. One-way ANOVA was used to compare multiple groups, if appropriate, with Bonferroni correction for post hoc analysis. A p-value < 0.05 was considered statistically significant.

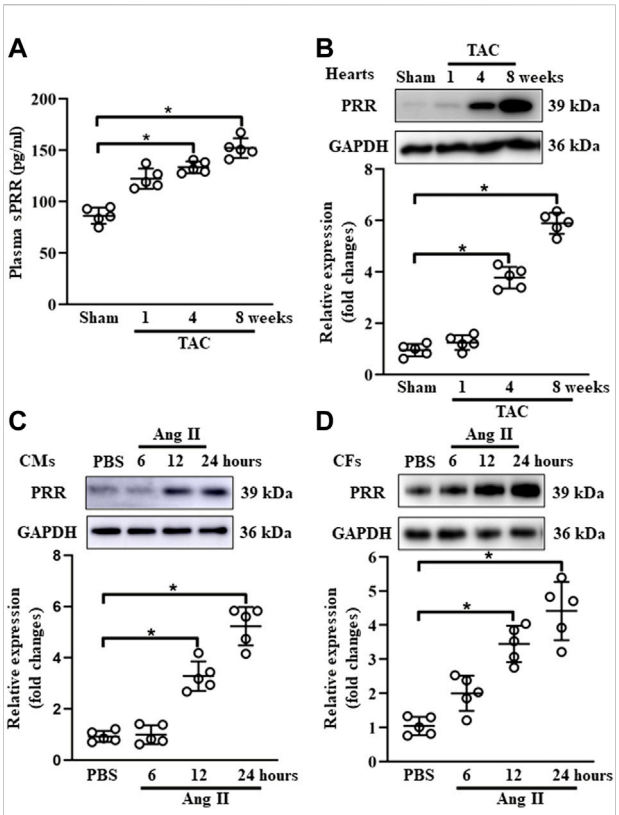

FIGURE 1
PRR expression is positively associated with cardiac remodeling. **(A)** The plasma concentration of soluble PRR in mice after 1, 4 and 8 weeks of transversus aortic constriction (TAC). **(B)** Immunoblot analysis of PRR in mouse failing hearts and quantitative analysis of the PRR protein level normalized to GAPDH. **(C)** Immunoblot analysis of PRR in Ang II-induced cardiomyocytes (CMs) and quantitative analysis of the PRR protein level normalized to GAPDH. **(D)** Immunoblot analysis of PRR in Ang II-induced cardiac fibroblasts (CFs) and quantitative analysis of the PRR protein level normalized to GAPDH. * p-value < 0.05. n = 5 per group. Data are expressed as mean ± SD.

Results

(Pro)renin receptor expression was upregulated in mouse failing hearts and ang II-induced cardiomyocytes and cardiac fibroblasts

To explore the potential involvement of PRR in cardiac remodeling, we set up a mouse model of chronic pressure

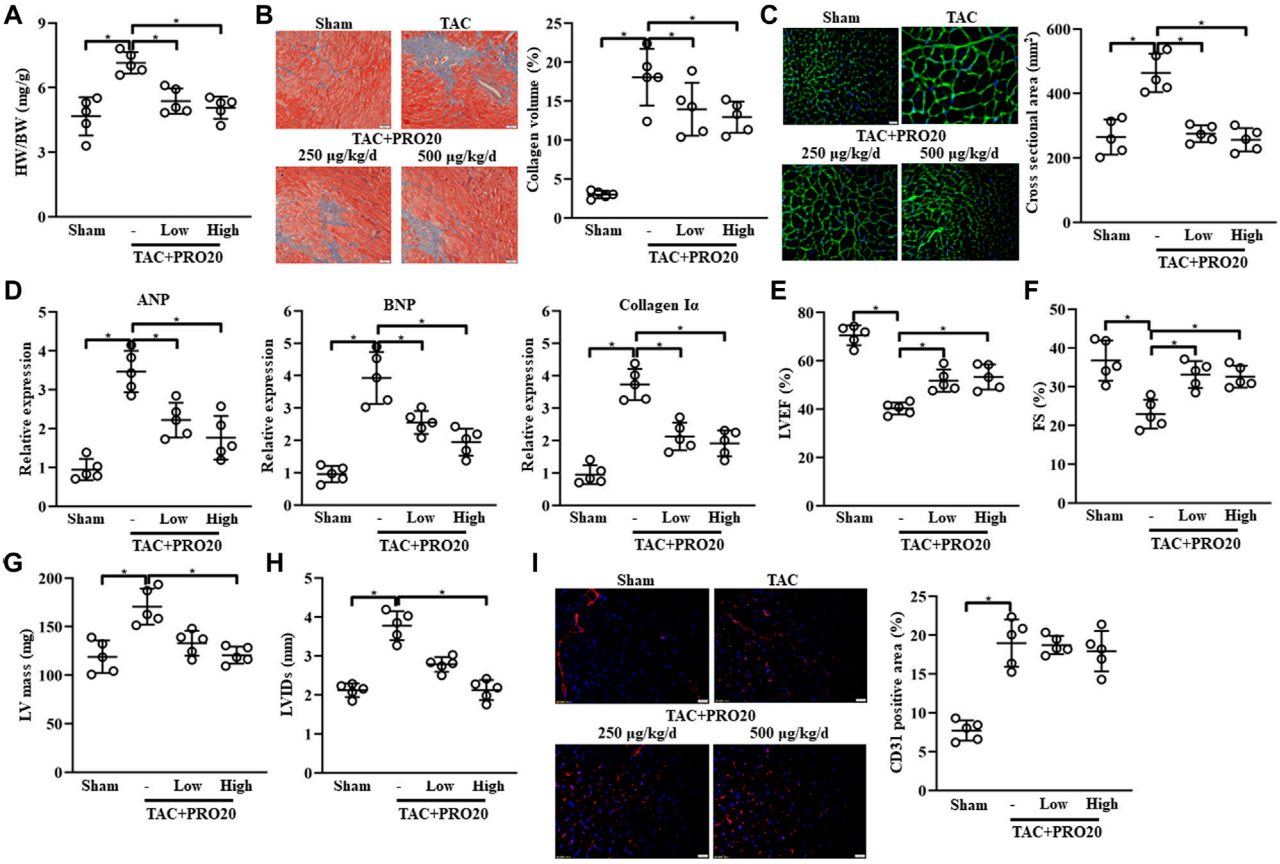

FIGURE 2
PRR decoy inhibitor PRO20 ameliorates HF in mice after 8 weeks of TAC surgery. **(A)** The ratios of heart weight and body weight (HW/BW) in TAC-induced mice with and without PRO20 treatment for 8 weeks (250 μg/kg/d and 500 μg/kg/d). **(B)** Representative images of Masson staining of heart sections from TAC-induced mice and quantitative analysis of cardiac fibrosis. **(C)** Representative images of wheat germ-agglutinin (WGA) staining of heart sections from TAC-induced mice and quantitative analysis of cardiac hypertrophy. **(D)** Relative mRNA expression of cardiac hypertrophy markers (ANP and BNP) and Collagen Iα in TAC-induced hearts with and without PRO20 treatment. **(E–H)** Echocardiographic analyses of left ventricular ejection fraction (LVEF), fractional shorting (FS), left ventricular mass (LV mass) and left ventricular internal diameter at end-systole (LVIDs) after 8 weeks of TAC operation. **(I)** Representative images of CD31 staining of heart sections from TAC-induced mice and quantitative analysis of angiogenesis. * p-value < 0.05. n = 5 per group. Data are expressed as mean ± SD.

overload-induced cardiac remodeling induced by TAC. As an initial step, we confirmed that heart weight/body weight (HW/BW) was gradually increased at 1-, 4- and 8-weeks post TAC surgery (Supplementary Figure S1A). The expression of hypertrophy-related markers (ANP and BNP) and collagen Iα was significantly upregulated at 4- and 8-weeks after TAC surgery (Supplementary Figure S1B-D). Echocardiography exhibited a reduction of LVEF and FS at 4- and 8-weeks after TAC surgery, while the parameters of cardiac hypertrophy documented as LV mass and LVIDs were increased at 8-weeks post TAC compared with sham group (Supplementary Figure S1E-H). The plasma concentration of soluble PRR was gradually increased in blood from TAC-induced mice (Figure 1A). In comparison with sham group, the protein expression of PRR in hearts was substantially upregulated at 4 and 8 weeks after TAC surgery in mice (Figure 1B). Given the key role of PRR in the formation of angiotensin peptide (Prieto et al., 2021), we also determined the Ang I and II expression in the plasma and heart tissues after TAC surgery. As expected, we found elevated Ang I and II in both plasma and heart tissue lysates in TAC models (Supplementary Figure S2), supporting *in vitro* Ang II induced experiments. Considering the important role of CMs and CFs in TAC-induced hypertrophic mouse hearts, neonatal rat CMs and CFs were isolated and stimulated with Ang II. As shown in Figures 1C,D, the protein expression of PRR in neonatal rat CMs and CFs were gradually increased after AngII treatment for 12 and 24 h. Together, these results indicated that PRR expression was upregulated in both CMs and CFs during TAC-induced cardiac remodeling.

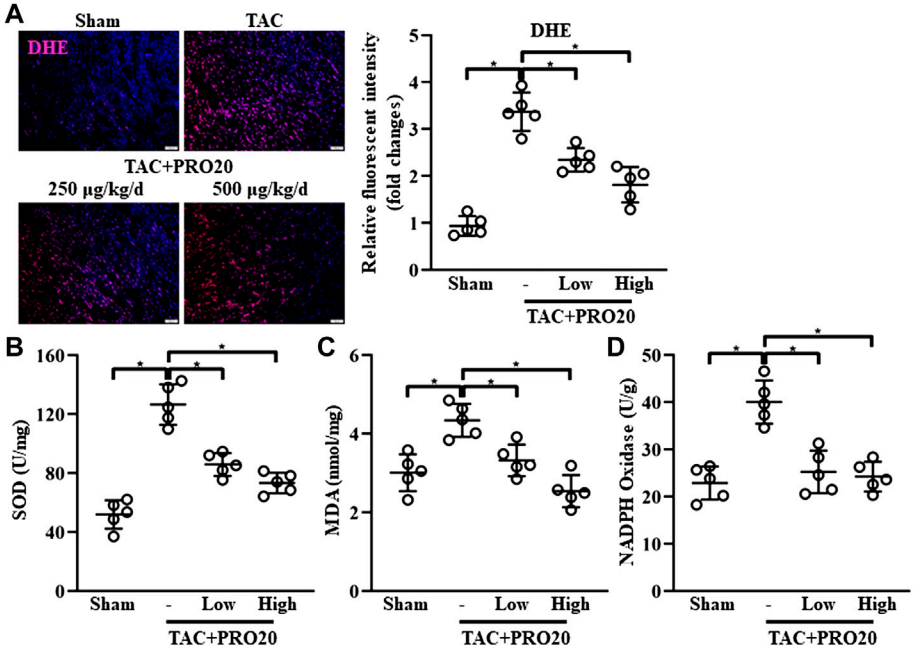

FIGURE 3
PRR decoy inhibitor PRO20 suppresses oxidative stress in TAC-induced mice. **(A)** Representative immunofluorescent images of the production of reactive oxygen species assessed by dihydroethidium (DHE, stained in red) in hearts from TAC-induced mice with and without PRO20 treatment for 8 weeks. Nuclei were counterstained with DAPI (blue). **(B–D)** The content of SOD, MDA and NADPH oxidase in hearts from TAC-induced mice with and without PRO20 treatment for 8 weeks * p-value < 0.05. n = 5 per group. Data are expressed as mean ± SD.

PRO20 retarded the transverse aortic constriction-induced cardiac remodeling

To investigate the role of PRR in TAC-induced cardiac remodeling, PRR decoy inhibitor PRO20 was synthesized and used to evaluate its inhibitory effect on cardiac remodeling. *In vivo* experiments, PRO20 treatment (250 μg/kg/d or 500 μg/kg/d) successfully attenuated the TAC-induced cardiac remodeling, as indicated by increased HW/BW (Figure 2A) and collagen deposition (Figure 2B). We also confirmed that administration of PRO20 (250 μg/kg/d or 500 μg/kg/d) 1 day after TAC surgery also alleviated cardiac hypertrophy and fibrosis (Supplementary Figure S3A, S3B). Furthermore, we measured the cross-sectional area (CSA) using WGA staining and found that PRO20 treatment retarded TAC-induced cardiac hypertrophy (Figure 2C). Moreover, increased mRNA expression of cardiac hypertrophic markers (ANP, BNP) and fibrotic marker (collagen Iα) induced by TAC were significantly reduced after PRO20 treatment (Figure 2D). In addition, PRO20 administration improved TAC-mediated LV dilation and dysfunction as evidenced by results of LVEF, FS, LV mass and LVIDs (Figures 2E–H). However, results of CD31 staining showed that PRO20 treatment did not affect angiogenesis in hearts of TAC mice (Figure 2I). Taken together, these results indicated that PRR decoy inhibitor PRO20 (250 μg/kg/d or 500 μg/kg/d) retarded the TAC-induced cardiac hypertrophy and fibrosis.

PRO20 suppressed oxidative stress in transverse aortic constriction-induced hypertrophic hearts

Considering the detrimental effect of PRR on oxidative stress response (Dong et al., 2019), we examined whether PRO20 could inhibit oxidative stress in TAC-induced hypertrophic hearts. DHE staining was used to assess ROS levels, indicating that the intracellular content of ROS production was substantially elevated from 1-week post TAC surgery (Supplementary Figure S4A). Results showed that PRO20 significantly suppressed the ROS generation in hypertrophic hearts induced by TAC (Figure 3A). Further, superoxide dismutase (SOD) activity, malondialdehyde (MDA) content and NADPH oxidase activity were measured after PRO20 treatment. As expected, PRO20 treatment significantly reduced the elevated SOD activity, MDA content and NADPH oxidase activity in hypertrophic hearts (Figures 3B–D). These findings indicated that PRO20 suppressed TAC-induced oxidative stress response.

10.3389/fphar.2022.940365

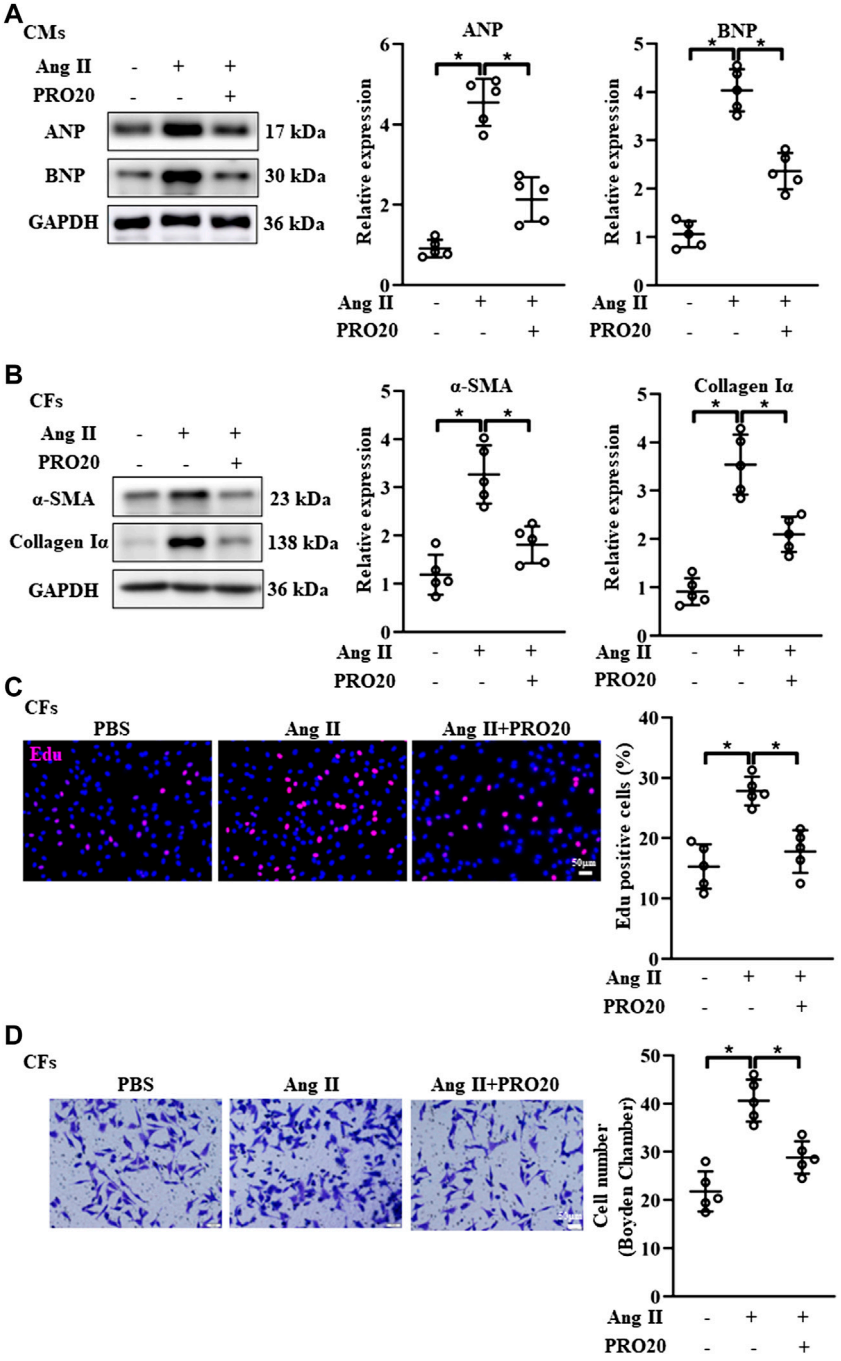

FIGURE 4
Inhibition of PRR by PRO20 alleviates CM hypertrophy and CF activation. **(A)** Immunoblot analysis of ANP and BNP in Ang II-induced CMs and quantitative analysis of the ANP and BNP protein level normalized to GAPDH. **(B)** Immunoblot analysis of α-SMA and Collagen Iα in Ang II-induced CFs and quantitative analysis of the α-SMA and Collagen Iα protein level normalized to GAPDH. **(C)** Effect of PRO20 on CF proliferation assessed by Edu assay. **(D)** Boyden chamber assay was performed to evaluate the migration of CFs with and without PRO20 treatment (10 nM) in the presence of Ang II. * p-value < 0.05. n = 5 per group. Data are expressed as mean ± SD.

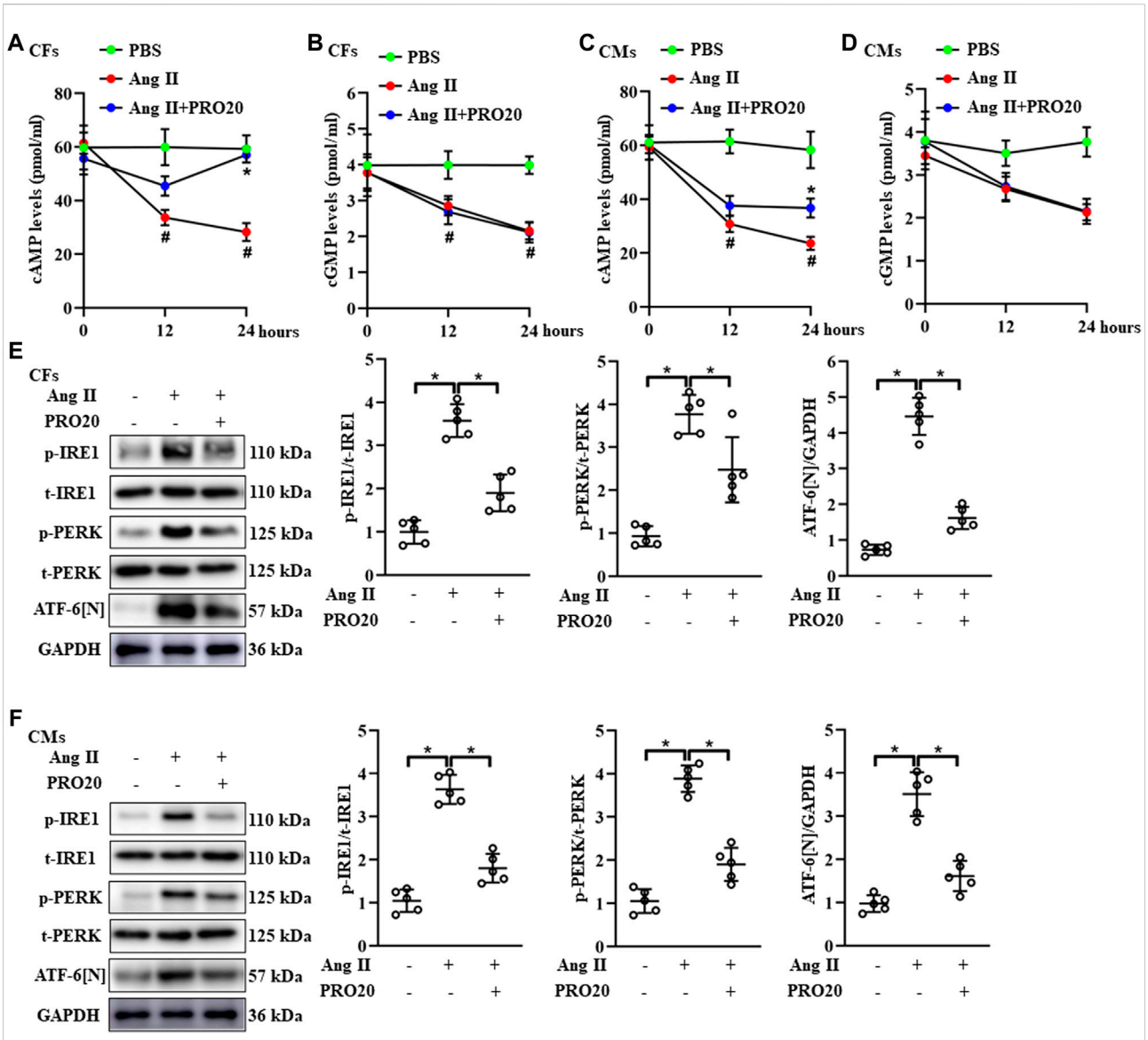

FIGURE 5
PRR decoy inhibitor PRO20 promotes intracellular cAMP content and suppresses endoplasmic reticulum stress. **(A–B)** The intracellular content of cAMP and cGMP in Ang II-induced CFs with and without PRO20 treatment (10 nM). #p < 0.05 vs. PBS group; * p-value < 0.05 vs. Ang II group at indicated time point. **(C–D)** The intracellular content of cAMP and cGMP in Ang II-induced CMs with and without PRO20 treatment (10 nM). #p < 0.05 vs. PBS group; * p-value < 0.05 vs. Ang II group at indicated time point. **(E)** Immunoblot analysis of IRE1, PERK and cleaved N-terminal cytoplasmic domain of ATF-6 (ATF-6 [N]) in Ang II-induced CFs and quantitative analysis of the IRE1 and PERK phosphorylation and the ATF-6 [N] activation. * p-value < 0.05. **(F)** Immunoblot analysis of IRE1, PERK and ATF-6 [N] in Ang II-induced CMs and quantitative analysis of the IRE1 and PERK phosphorylation and the ATF-6 [N] activation. * p-value < 0.05. n = 5 per group. Data are expressed as mean ± SD.

PRO20 inhibited cardiomyocyte hypertrophy and alleviated fibroblast activation

It is well established that cardiomyocyte hypertrophy and fibroblast activation play important roles in pathological cardiac remodeling (Chen et al., 2020; Vigil-Garcia et al., 2021). Then, we isolated the CMs and CFs *in vitro*, and evaluate the influence of PRO20 on these cells. In line with the findings *in vivo*, PRO20 treatment inhibited Ang II-induced cardiomyocyte hypertrophy, as indicated by the protein expression of ANP and BNP (Figure 4A). With regard to fibroblast activation, we first examined the expression of fibrotic markers, and results showed that Ang II increased the αSMA and collagen Iα, which

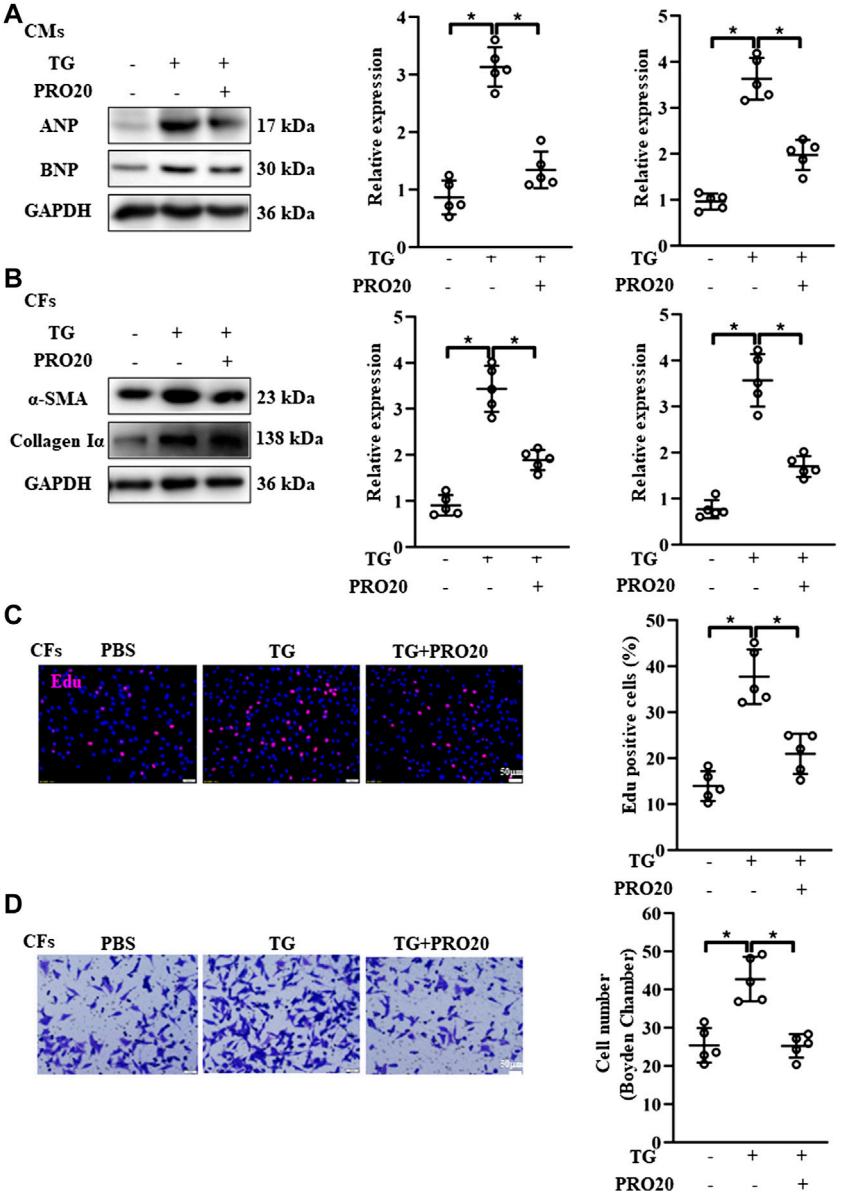

FIGURE 6
Effects of PRO20 on CM hypertrophy and CF activation induced by ER stressor TG. **(A)** Immunoblot analysis of ANP and BNP in TG-induced (5 μM) CMs with and without PRO20 treatment and quantitative analysis of the ANP and BNP protein level normalized to GAPDH. **(B)** Immunoblot analysis of α-SMA and Collagen Iα in CFs with and without TG treatment and quantitative analysis of the α-SMA and Collagen Iα protein level normalized to GAPDH. **(C)** Effect of PRO20 on TG-induced CF proliferation assessed by Edu assay in indicated groups. **(D)** Boyden chamber assay was performed to evaluate the migration of CFs in indicated groups. * p-value < 0.05. n = 5 per group. Data are expressed as mean ± SD.

was successfully attenuated by PRO20 administration (Figure 4B). Then, *in vitro* cell proliferation and migration of CFs were determined using Edu staining and Transwell assay. We found that PRO20 significantly suppressed Ang II-mediated cell proliferation and migration in CFs (Figures 4C,D). These findings indicated that PRO20 attenuated pathological cardiac remodeling through inhibition of cardiomyocyte hypertrophy and fibroblast activation.

PRO20 enhanced intracellular cAMP levels and attenuated endoplasmic reticulum stress

Since the cyclic nucleotides cAMP and cGMP were well-characterized second messenger molecules regulating many intracellular processes, such as cell proliferation, migration (Wolter et al., 2017), we further explored whether

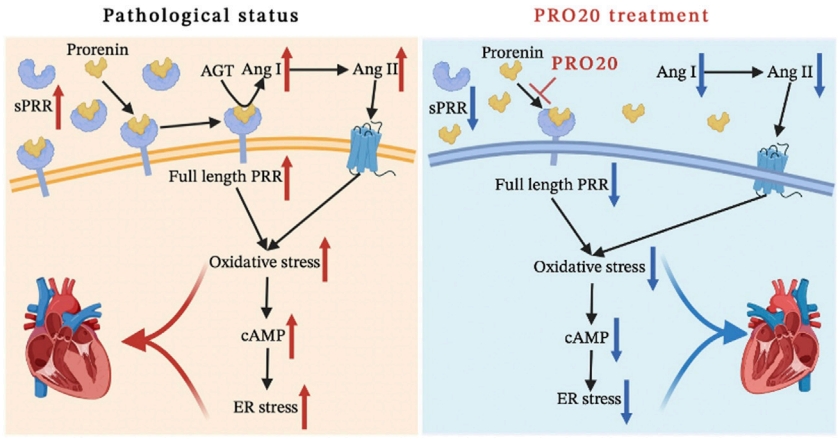

FIGURE 7
Schematic diagram of the mechanism. We systematically analyzed the mechanism of the PRO20 effect on cardiac remodeling, and found that PRO20 inhibited both oxidative stress and ER stress signaling pathways.

PRO20 inhibited pathological cardiac remodeling through modulating intracellular cAMP and cGMP levels. Upon Ang II stimulation in CFs and CMs, intracellular cAMP and cGMP levels were significantly decreased (Figures 5A–D). Of note, PRO20 treatment only reversed the upregulated cAMP levels induced by Ang II treatment in CFs and CMs, but did not affect intracellular cGMP levels (Figures 5A–D). These results suggested that PRO20 enhanced intracellular cAMP levels in CFs and CMs, but not cGMP levels.

Accumulating evidence showed that RAS activation promotes ER-stress related disease (Wu et al., 2017; Yang et al., 2017). Likewise, the phosphorylation of IRE1 and PERK, as well as ATF-6 [N] expression, were upregulated in hearts after TAC operation (Supplementary Figure S4B). Next, we investigated the effects of PRO20 on ER stress, including phosphorylation of IRE1 and PERK and ATF-6 cleavage. In CFs and CMs, Ang II administration significantly upregulated the activation of ATF-6 [N] and the phosphorylation of IRE1 and PERK as well, which was successfully abolished by PRO20 treatment (Figures 5E,F). To further verify whether PRO20 inhibits cardiac remodeling through ER stress, CMs and CFs were incubated with ER stressor TG in the presence of PRO20. Indeed, PRO20 was able to reverse TG-induced CM hypertrophy, CF activation and migration (Figures 6A,B). The findings indicated that PRO20 suppressed Ang II-induced ER stress in CFs and CMs.

Discussion

In the present study, we demonstrated for the first time that the importance of PRR during pathological cardiac remodeling in response to chronic pressure overload. We showed that PRR decoy inhibitor PRO20 ameliorated cardiomyocyte hypertrophy and fibroblast activation through suppression of oxidative stress, enhancement of intracellular cAMP levels and inhibition of ER stress *in vivo* and *in vitro* (Figure 7). These findings suggested that PRR decoy inhibitor PRO20 might serve as a potent pharmaceutical for pathological cardiac remodeling.

HF as a burgeoning problem affect more than 20 million individuals worldwide (Wu et al., 2017). However, mechanisms contributing to the development of pathological cardiac remodeling remains incompletely understood. Hence, HF remains challenging to treat, and there is an urgent need to identify new therapeutics. During the pathological cardiac remodeling process, cardiomyocytes integrate several signals from extracellular matrix, cell membrane, ion channels, cytoskeleton, sarcomere, mitochondria and ER to translate biomechanical forces to fetal gene expression, which contributes to alteration in cardiomyocyte shape and structure (Haque and Wang, 2017). ER as a multifunctional intracellular organelle, plays an important role in protein synthesis, protein folding and translocation. Pathological processes that disturb protein folding in ER lumens caused ER stress (Doyle et al., 2011). In response to ER stress, unfolded protein response is activated by three major ER membrane associated proteins, including IRE1, PERK, ATF6 (Zhang et al., 2017). Once activated, these sensors stimulate downstream signaling pathways to inhibit mRNA translation and protein load on the ER and facilitate retrotranslocation of proteins from the ER to the cytosol for proteasomal degradation. Notably, ATF-6 and IRE1 activation can directly upregulated the unfolded protein response gene mRNA transcription or processing (Lee et al., 2002; Yamamoto et al., 2007), while PERK inhibits the

initiation and decreases the protein load on the ER (Lee et al., 2002). ATF-6, IRE1 and PERK-induced deterioration of the Ca^{2+} ion balance leads to cardiac hypertrophy caused by hyperthyroidism (Bektur Aykanat et al., 2021), and PERK was also essential during the experiments for avoiding TAC-induced congestive HF (Liu et al., 2014). In line with these findings, we found that there was a remarkable change in the activation of IRE1, PERK and ATF-6 in Ang II-treated CMs and CFs, suggesting that the ER stress induced by Ang II participated in cardiomyocyte hypertrophy and fibroblast activation.

PRR as a member of RAS, activated prorenin and enhance the enzymatic activity of renin, and then promotes Ang II formation (Hennrikus et al., 2018). Numerous studies showed that PRR activation could stimulate intracellular pathways related to the cardiac damage (Mahmud et al., 2012; Hennrikus et al., 2018). In the heart, PRR not only promotes atrial structure and electrical remodeling (Lu et al., 2016), but also augments the cardiac damage in dilated cardiomyopathy (Mahmud et al., 2012) and diabetic cardiomyopathy (Dong et al., 2019). Further, a recent clinical study also showed that serum soluble PRR concentrations was associated with the severity of HF (Gong et al., 2019). Consistently, we observed significant increase of PRR protein levels and elevated plasma concentration of soluble PRR after TAC surgery. Feng et al. (Feng et al., 2021) revealed that Ang II activated PRR in inner medulla but did not affect their expression in renal cortex. In line with these findings, our results indicated that Ang II was also capable of stimulating PRR in hearts, implying a positive feedback between PRR and Ang II under pathological conditions such as hypertension and heart failure. Further studies are required to investigate their underlying mechanisms and distinguish whether the positive feedback was an autonomous or systematic manner. All these findings indicated that the PRR downregulation might be a therapeutic target for pathological cardiac remodeling.

Accumulating evidence indicates that inhibition of PRR ameliorates the cardiac fibrosis and impairment in cardiac function via reduction of ROS generation (Ellmers et al., 2016; Dong et al., 2019). PRR decoy inhibitor PRO20 (the first 20 amino acid residues of the prorenin prosegment) is a specific PRR ligand that blocks activation of prorenin by binding to the PRR (Li et al., 2015a). PRO20 not only attenuates prorenin, but also retards the development of DOCA-salt-induced hypertension and Ang II-dependent hypertension (Li et al., 2015a). However, the effects of PRO20 on pressure overload-induced pathological cardiac hypertrophy remain unknown. Therefore, in current study, TAC surgery was conducted to induce cardiac remodeling, followed by systematic administration of PRO20. As expected, PRO20 administration attenuated the pressure overload-induced oxidative stress during pathological cardiac remodeling. Further, PRO20 treatment in CMs and CFs produced similar RAS-suppressing effects, including suppression of cardiomyocyte hypertrophy and attenuation of fibroblast activation.

The second messengers cAMP and cGMP serve as the key regulators of cardiac remodeling, and mediate heart failure pathophysiology induced by different forms of injury and stress. As siblings, cardiac cAMP synthesis is catalyzed by adenylyl cyclases principally in response to adrenergic receptor stimulation, while production of cGMP is initiated by guanylyl cyclases, which are sensitive to either nitric oxide or natriuretic peptides (Preedy, 2020). Commonly, cAMP regulates the strength and frequency of cardiac contraction and relaxation, whereas cGMP modulates inotropy and metabolic responses (Chen and Yan, 2021). Further, the cyclic nucleotide phosphodiesterases (PDEs) facilitate cyclic nucleotide degradation of cAMP and cGMP, and are vital for mediating crosstalk between the two pathways. Several studies reported that Ang II mediates cAMP decrease (Li et al., 2006; Crajoinas et al., 2016), but some studies also observed that Ang II treatment has no effect on cAMP levels (Cano et al., 1994). These differences might be attributable to different cells in response to various stimuli. With regard to cGMP, augmentation of cGMP signaling is recommended as a potential therapeutic strategy in HF based on several preclinical and clinical studies that have investigated various mechanisms and effects of cGMP enhancement (Greene et al., 2013; Richards et al., 2021; Tripathi et al., 2021). In our present study, Ang II treatment significantly reduced intracellular cAMP and cGMP levels in both CMs and CFs. Ang II upregulates PRR expression both in cultured cells and in DOCA-salt hypertensive mice through activation of cAMP response element-binding protein (Li et al., 2015b). Besides, Huang et al. found that sodium depletion upregulates renal PRR expression via cGMP-protein kinase G signaling pathway (Huang and Siragy, 2012). Nevertheless, whether PRR inhibition by PRO20 could affect the intracellular cAMP and cGMP levels is still unknown. Through a series of *in vitro* experiments, we found that PRO20 only reversed Ang II-induced upregulation of cAMP levels in CMs and CFs, but did not affect the Ang II-mediated downregulation of cGMP levels. As to these discrepancies, the main reason responsible for them may be that PRO20 treatment affects cAMP-specific synthesis and/or degradation, but not cGMP. Further investigation is required to clarify whether PRO20 enhances cAMP through interplaying with specific PDEs or adenylyl cyclases.

In summary, PRR as an important component of RAS, is enrolled in pathological cardiac remodeling, and PRR decoy inhibitor PRO20 attenuated pressure overload induced cardiomyocyte hypertrophy and fibroblast activation through inhibition of the ROS generation and ER stress in CMs and CFs.

Data availability statement

The original contributions presented in the study are included in the article/Supplementary Materials, further inquiries can be directed to the corresponding author.

Ethics statement

The animal study was reviewed and approved by Liuzhou Municipal Liutie Central Hospital.

Author contributions

JZ and JY conceived the presented idea and prepared the manuscript. JZ and Y-JC performed the animal study. JZ and C-JL performed the cellular and molecular experiments. JZ conducted the statistical analysis. JY drafted the final version of the manuscript. All authors contributed to the article and approved the submitted version.

Funding

This study was supported by Guangxi Natural Science Foundation (Grant No. 2018GXNSFAA294137).

Conflict of interest

The authors declare that the research was conducted in the absence of any commercial or financial relationships that could be construed as a potential conflict of interest.

Publisher's note

Supplementary material

The Supplementary Material for this article can be found online at: https://www.frontiersin.org/articles/10.3389/fphar.2022.940365/full#supplementary-material

References

Abboud, A., and Januzzi, J. L. (2021). Reverse cardiac remodeling and ARNI therapy. *Curr. Heart Fail. Rep.* 18 (2), 71–83. doi:10.1007/s11897-021-00501-6

Arthur, G., Osborn, J. L., and Yiannikouris, F. B. (2021). (Pro)renin receptor in the kidney: function and significance. *Am. J. Physiol. Regul. Integr. Comp. Physiol.* 320 (4), R377–R383. doi:10.1152/ajpregu.00259.2020

Bektur Aykanat, N. E., Sahin, E., Kacar, S., Bagci, R., Karakaya, S., Burukoglu Donmez, D., et al. (2021). Cardiac hypertrophy caused by hyperthyroidism in rats: the role of ATF-6 and TRPC1 channels. *Can. J. Physiol. Pharmacol.* 99, 1226–1233. doi:10.1139/cjpp-2021-0260

Cano, A., Miller, R. T., Alpern, R. J., and Preisig, P. A. (1994). Angiotensin II stimulation of Na-H antiporter activity is cAMP independent in OKP cells. *Am. J. Physiol.* 266, C1603–C1608. doi:10.1152/ajpcell.1994.266.6.C1603

Chen, S., and Yan, C. (2021). An update of cyclic nucleotide phosphodiesterase as a target for cardiac diseases. *Expert Opin. Drug Discov.* 16 (2), 183–196. doi:10.1080/17460441.2020.1821643

Chen, S., Zhang, Y., Lighthouse, J. K., Mickelsen, D. M., Wu, J., Yao, P., et al. (2020). A novel role of cyclic nucleotide phosphodiesterase 10A in pathological cardiac remodeling and dysfunction. *Circulation* 141 (3), 217–233. doi:10.1161/CIRCULATIONAHA.119.042178

Chen, Y., and Xu, C. (2020). The interaction partners of (pro)renin receptor in the distal nephron. *FASEB J.* 34 (11), 14136–14149. doi:10.1096/fj.202001711R

Crajoinas, R. O., Polidoro, J. Z., Carneiro de Morais, C. P., Castelo-Branco, R. C., and Girardi, A. C. (2016). Angiotensin II counteracts the effects of cAMP/PKA on NHE3 activity and phosphorylation in proximal tubule cells. *Am. J. Physiol. Cell Physiol.* 311 (5), C768–C776. doi:10.1152/ajpcell.00191.2016

Domenig, O., Manzel, A., Grobe, N., Konigshausen, E., Kaltenecker, C. C., Kovarik, J. J., et al. (2016). Neprilysin is a mediator of alternative renin-angiotensin-system Activation in the murine and human kidney. *Sci. Rep.* 6, 33678. doi:10.1038/srep33678

Dong, X., Yu, S., Wang, Y., Yang, M., Xiong, J., Hei, N., et al. (2019). (Pro)renin receptor-mediated myocardial injury, apoptosis, and inflammatory response in rats with diabetic cardiomyopathy. *J. Biol. Chem.* 294 (20), 8218–8226. doi:10.1074/jbc.RA119.007648

Doyle, K. M., Kennedy, D., Gorman, A. M., Gupta, S., Healy, S. J., Samali, A., et al. (2011). Unfolded proteins and endoplasmic reticulum stress in neurodegenerative disorders. *J. Cell. Mol. Med.* 15 (10), 2025–2039. doi:10.1111/j.1582-4934.2011.01374.x

Ellmers, L. J., Rademaker, M. T., Charles, C. J., Yandle, T. G., and Richards, A. M. (2016). (Pro)renin receptor blockade ameliorates cardiac injury and remodeling and improves function after myocardial infarction. *J. Card. Fail.* 22 (1), 64–72. doi:10.1016/j.cardfail.2015.08.341

Fang, H., Deng, M., Zhang, L., Lu, A., Su, J., Xu, C., et al. (2018). Role of (pro)renin receptor in albumin overload-induced nephropathy in rats. *Am. J. Physiol. Ren. Physiol.* 315 (6), F1759–F1768. doi:10.1152/ajprenal.00071.2018

Feng, Y., Peng, K., Luo, R., Wang, F., and Yang, T. (2021). Site-1 protease-derived soluble (Pro)Renin receptor contributes to angiotensin II-induced hypertension in mice. *Hypertension* 77 (2), 405–416. doi:10.1161/HYPERTENSIONAHA.120.15100

Frangogiannis, N. G. (2021). Cardiac fibrosis. *Cardiovasc. Res.* 117 (6), 1450–1488. doi:10.1093/cvr/cvaa324

Fu, Z., Wang, F., Liu, X., Hu, J., Su, J., Lu, X., et al. (2021). Soluble (pro)renin receptor induces endothelial dysfunction and hypertension in mice with diet-induced obesity via activation of angiotensin II type 1 receptor. *Clin. Sci.* 135 (6), 793–810. doi:10.1042/CS20201047

Gong, L., Zhang, S., Li, L., Gao, X., Wang, D., Wu, D., et al. (2019). Elevated plasma soluble (pro)renin receptor levels are associated with left ventricular remodeling and renal function in chronic heart failure patients with reduced ejection fraction. *Peptides* 111, 152–157. doi:10.1016/j.peptides.2018.04.010

Greene, S. J., Gheorghiade, M., Borlaug, B. A., Pieske, B., Vaduganathan, M., Burnett, J. C., et al. (2013). The cGMP signaling pathway as a therapeutic target in heart failure with preserved ejection fraction. *J. Am. Heart Assoc.* 2 (6), e000536. doi:10.1161/JAHA.113.000536

Haque, Z. K., and Wang, D. Z. (2017). How cardiomyocytes sense pathophysiological stresses for cardiac remodeling. *Cell. Mol. Life Sci.* 74 (6), 983–1000. doi:10.1007/s00018-016-2373-0

Hennrikus, M., Gonzalez, A. A., and Prieto, M. C. (2018). The prorenin receptor in the cardiovascular system and beyond. *Am. J. Physiol. Heart Circ. Physiol.* 314 (2), H139–H145. doi:10.1152/ajpheart.00373.2017

Huang, J., and Siragy, H. M. (2012). Sodium depletion enhances renal expression of (pro)renin receptor via cyclic GMP-protein kinase G signaling pathway. *Hypertension* 59 (2), 317–323. doi:10.1161/HYPERTENSIONAHA.111.186056

Lee, K., Tirasophon, W., Shen, X., Michalak, M., Prywes, R., Okada, T., et al. (2002). IRE1-mediated unconventional mRNA splicing and S2P-mediated ATF6 cleavage merge to regulate XBP1 in signaling the unfolded protein response. *Genes Dev.* 16 (4), 452–466. doi:10.1101/gad.964702

Li, W., Liu, J., Hammond, S. L., Tjalkens, R. B., Saifudeen, Z., Feng, Y., et al. (2015). Angiotensin II regulates brain (pro)renin receptor expression through activation of cAMP response element-binding protein. *Am. J. Physiol. Regul. Integr. Comp. Physiol.* 309 (2), R138–R147. doi:10.1152/ajpregu.00319.2014

Li, W., Sullivan, M. N., Zhang, S., Worker, C. J., Xiong, Z., Speth, R. C., et al. (2015). Intracerebroventricular infusion of the (Pro)renin receptor antagonist PRO20 attenuates deoxycorticosterone acetate-salt-induced hypertension. *Hypertension* 65 (2), 352–361. doi:10.1161/HYPERTENSIONAHA.114.04458

Li, X. C., Carretero, O. A., Navar, L. G., and Zhuo, J. L. (2006). AT1 receptor-mediated accumulation of extracellular angiotensin II in proximal tubule cells: role of cytoskeleton microtubules and tyrosine phosphatases. *Am. J. Physiol. Ren. Physiol.* 291 (2), F375–F383. doi:10.1152/ajprenal.00405.2005

Liu, X., Kwak, D., Lu, Z., Xu, X., Fassett, J., Wang, H., et al. (2014). Endoplasmic reticulum stress sensor protein kinase R-like endoplasmic reticulum kinase (PERK) protects against pressure overload-induced heart failure and lung remodeling. *Hypertension* 64 (4), 738–744. doi:10.1161/HYPERTENSIONAHA.114.03811

Lu, A., Pu, M., Mo, S., Su, J., Hu, J., Li, C., et al. (2022). (Pro)renin receptor regulates phosphate homeostasis in rats via releasing fibroblast growth factor-23. *Front. Physiol.* 13, 784521. doi:10.3389/fphys.2022.784521

Lu, X., Wang, F., Xu, C., Soodvilai, S., Peng, K., Su, J., et al. (2016). Soluble (pro) renin receptor via beta-catenin enhances urine concentration capability as a target of liver X receptor. *Proc. Natl. Acad. Sci. U. S. A.* 113 (13), E1898–E1906. doi:10.1073/pnas.1602397113

Mahmud, H., Sillje, H. H., Cannon, M. V., van Gilst, W. H., and de Boer, R. A. (2012). Regulation of the (pro)renin-renin receptor in cardiac remodelling. *J. Cell. Mol. Med.* 16 (4), 722–729. doi:10.1111/j.1582-4934.2011.01377.x

Manerikar, S. S., Malaviya, A. N., Singh, M. B., Rajgopalan, P., and Kumar, R. (1976). Immune status and BCG vaccination in newborns with intra-uterine growth retardation. *Clin. Exp. Immunol.* 26 (1), 173–175.

Preedy, M. E. J. (2020). Cardiac cyclic nucleotide phosphodiesterases: roles and therapeutic potential in heart failure. *Cardiovasc. Drugs Ther.* 34 (3), 401–417. doi:10.1007/s10557-020-06959-1

Prieto, M. C., Gonzalez, A. A., Visniauskas, B., and Navar, L. G. (2021). The evolving complexity of the collecting duct renin-angiotensin system in hypertension. *Nat. Rev. Nephrol.* 17 (7), 481–492. doi:10.1038/s41581-021-00414-6

Prola, A., Pires Da Silva, J., Guilbert, A., Lecru, L., Piquereau, J., Ribeiro, M., et al. (2017). SIRT1 protects the heart from ER stress-induced cell death through eIF2α deacetylation. *Cell Death Differ.* 24 (2), 343–356. doi:10.1038/cdd.2016.138

Richards, D. A., Aronovitz, M. J., Liu, P., Martin, G. L., Tam, K., Pande, S., et al. (2021). CRD-733, a novel PDE9 (phosphodiesterase 9) inhibitor, reverses pressure overload-induced heart failure. *Circ. Heart Fail.* 14 (1), e007300. doi:10.1161/CIRCHEARTFAILURE.120.007300

Singh, K. D., and Karnik, S. S. (2016). Angiotensin receptors: structure, function, signaling and clinical applications. *J. Cell Signal.* 1 (2), 111. doi:10.4172/jcs.1000111

Tripathi, R., Sullivan, R. D., Fan, T. M., Mehta, R. M., Gladysheva, I. P., Reed, G. L., et al. (2021). A low-sodium diet boosts Ang (1-7) production and NO-cGMP bioavailability to reduce edema and enhance survival in experimental heart failure. *Int. J. Mol. Sci.* 22 (8), 4035. doi:10.3390/ijms22084035

Vigil-Garcia, M., Demkes, C. J., Eding, J. E. C., Versteeg, D., de Ruiter, H., Perini, I., et al. (2021). Gene expression profiling of hypertrophic cardiomyocytes identifies new players in pathological remodelling. *Cardiovasc. Res.* 117 (6), 1532–1545. doi:10.1093/cvr/cvaa233

Wang, F., Sun, Y., Luo, R., Lu, X., Yang, B., Yang, T., et al. (2020). COX-2-independent activation of renal (pro)renin receptor contributes to DOCA-salt hypertension in rats. *Am. J. Physiol. Ren. Physiol.* 319 (4), F647–F653. doi:10.1152/ajprenal.00112.2020

Wang, F., Xu, C., Luo, R., Peng, K., Ramkumar, N., Xie, S., et al. (2019). Site-1 protease-derived soluble (pro)renin receptor targets vasopressin receptor 2 to enhance urine concentrating capability. *JCI Insight* 4 (7), 124174. doi:10.1172/jci.insight.124174

Wang, M., and Kaufman, R. J. (2016). Protein misfolding in the endoplasmic reticulum as a conduit to human disease. *Nature* 529 (7586), 326–335. doi:10.1038/nature17041

Wang, S., Binder, P., Fang, Q., Wang, Z., Xiao, W., Liu, W., et al. (2018). Endoplasmic reticulum stress in the heart: insights into mechanisms and drug targets. *Br. J. Pharmacol.* 175 (8), 1293–1304. doi:10.1111/bph.13888

Wolter, S., Dittmar, F., and Seifert, R. (2017). cCMP and cUMP in apoptosis: concepts and methods. *Handb. Exp. Pharmacol.* 238, 25–47. doi:10.1007/164_2016_5007

Wu, Q. Q., Xiao, Y., Yuan, Y., Ma, Z. G., Liao, H. H., Liu, C., et al. (2017). Mechanisms contributing to cardiac remodelling. *Clin. Sci.* 131 (18), 2319–2345. doi:10.1042/CS20171167

Xu, D., Zhao, Y., Weng, X., Lu, Y., Li, W., Tang, K., et al. (2019). Novel role of mitochondrial GTPases 1 in pathological cardiac hypertrophy. *J. Mol. Cell. Cardiol.* 128, 105–116. doi:10.1016/j.yjmcc.2019.01.025

Yamamoto, K., Sato, T., Matsui, T., Sato, M., Okada, T., Yoshida, H., et al. (2007). Transcriptional induction of mammalian ER quality control proteins is mediated by single or combined action of ATF6alpha and XBP1. *Dev. Cell* 13 (3), 365–376. doi:10.1016/j.devcel.2007.07.018

Yang, D., Liu, H. Q., Liu, F. Y., Tang, N., Guo, Z., Ma, S. Q., et al. (2020). The roles of noncardiomyocytes in cardiac remodeling. *Int. J. Biol. Sci.* 16 (13), 2414–2429. doi:10.7150/ijbs.47180

Yang, J., Zhang, X., Yu, X., Tang, W., and Gan, H. (2017). Renin-angiotensin system activation accelerates atherosclerosis in experimental renal failure by promoting endoplasmic reticulum stress-related inflammation. *Int. J. Mol. Med.* 39 (3), 613–621. doi:10.3892/ijmm.2017.2856

Yuan, X., Pan, J., Wen, L., Gong, B., Li, J., Gao, H., et al. (2019). MiR-144-3p enhances cardiac fibrosis after myocardial infarction by targeting PTEN. *Front. Cell Dev. Biol.* 7, 249. doi:10.3389/fcell.2019.00249

Zhang, C., Syed, T. W., Liu, R., and Yu, J. (2017). Role of endoplasmic reticulum stress, autophagy, and inflammation in cardiovascular disease. *Front. Cardiovasc. Med.* 4, 29. doi:10.3389/fcvm.2017.00029

Zhang, Y., Chen, W., and Wang, Y. (2020). STING is an essential regulator of heart inflammation and fibrosis in mice with pathological cardiac hypertrophy via endoplasmic reticulum (ER) stress. *Biomed. Pharmacother.* 125, 110022. doi:10.1016/j.biopha.2020.110022

frontiers | Frontiers in Pharmacology

TYPE Original Research
PUBLISHED 24 August 2022
DOI 10.3389/fphar.2022.946193

OPEN ACCESS

EDITED BY
Xiaoyong Tong,
Chongqing University, China

REVIEWED BY
Shen Xiang-Chun,
Guizhou Medical University, China
Chaojun Tang,
Soochow University, China

*CORRESPONDENCE
Jiahui Cao,
caojiahui@gzucm.edu.cn

†These authors have contributed equally to this work and share first authorship

SPECIALTY SECTION
This article was submitted to Cardiovascular and Smooth Muscle Pharmacology, a section of the journal Frontiers in Pharmacology

RECEIVED 17 May 2022
ACCEPTED 22 July 2022
PUBLISHED 24 August 2022

CITATION
Hong M, Wu Y, Zhang H, Gu J, Chen J, Guan Y, Qin X, Li Y and Cao J (2022), Network pharmacology and experimental analysis to reveal the mechanism of Dan-Shen-Yin against endothelial to mesenchymal transition in atherosclerosis.
Front. Pharmacol. 13:946193.
doi: 10.3389/fphar.2022.946193

Network pharmacology and experimental analysis to reveal the mechanism of Dan-Shen-Yin against endothelial to mesenchymal transition in atherosclerosis

Mengyun Hong[1†], Yubiao Wu[1†], Haiyi Zhang[1], Jinchao Gu[1], Juanjuan Chen[2], Yancheng Guan[3], Xiude Qin[2], Yu Li[4] and Jiahui Cao[1*]

[1]The Research Center of Basic Integrative Medicine, Guangzhou University of Chinese Medicine, Guangzhou, China, [2]Encephalopathy Department, Shenzhen Traditional Chinese Medicine Hospital, The Fourth Clinical Medical College of Guangzhou University of Chinese Medicine, Shenzhen, China, [3]Obstetrics and Gynecology Department, Shenzhen Traditional Chinese Medicine Hospital, The Fourth Clinical Medical College of Guangzhou University of Chinese Medicine, Shenzhen, China, [4]Nursing Department, Guangzhou University of Chinese Medicine, Guangzhou, China

Atherosclerosis is a chronic inflammatory disease characterized by the formation of plaque and endothelial dysfunction. Under pro-inflammatory conditions, endothelial cells adopt a mesenchymal phenotype by a process called endothelial-to-mesenchymal transition (EndMT) which plays an important role in the pathogenesis of atherosclerosis. Dan-Shen-Yin (DSY) is a well-known traditional Chinese medicine used in the treatment of cardiovascular disease. However, the molecular mechanism whereby DSY mitigates atherosclerosis remains unknown. Therefore, we employed a network pharmacology-based strategy in this study to determine the therapeutic targets of DSY, and *in vitro* experiments to understand the molecular pharmacology mechanism. The targets of the active ingredients of DSY related to EndMT and atherosclerosis were obtained and used to construct a protein-protein interaction (PPI) network followed by network topology and functional enrichment analysis. Network pharmacology analysis revealed that the PI3K/AKT pathway was the principal signaling pathway of DSY against EndMT in atherosclerosis. Molecular docking simulations indicated strong binding capabilities of DSY's bioactive ingredients toward PI3K/AKT pathway molecules. Experimentally, DSY could efficiently modify expression of signature EndMT genes and decrease expression of PI3K/AKT pathway signals including integrin αV, integrin β1,

Abbreviations: AS, atherosclerosis; BC, betweenness centrality; CC, closeness centrality; CCK-8, cell counting kit-8; DSY, Dan-Shen-Yin; EndMT, endothelial to mesenchymal transition; GO, gene ontology; KEGG, Kyoto encyclopedia of genes and genomes; LASP1, LIM and SH3 protein 1; LAC, local average connectivity; PPI, protein-protein interaction; TCM, traditional Chinese medicine.

PI3K, and AKT1 in TGF-β2-treated HUVECs. LASP1, which is upstream of the PI3K/AKT pathway, had strong binding affinity to the majority of DSY's bioactive ingredients, was induced by EndMT-promoting stimuli involving IL-1β, TGF-β2, and hypoxia, and was downregulated by DSY. Knock-down of LASP1 attenuated the expression of integrin αV, integrin β1, PI3K, AKT1 and EndMT-related genes induced by TGF-β2, and minimized the effect of DSY. Thus, our study showed that DSY potentially exerted anti-EndMT activity through the LASP1/PI3K/AKT pathway, providing a possible new therapeutic intervention for atherosclerosis.

KEYWORDS

endothelial to mesenchymal transition, Dan-Shen-Yin, atherosclerosis, PI3K/AKT signaling, LASP1, network pharmacology

Introduction

Atherosclerosis (AS) is a progressive inflammatory disease triggered by numerous systemic risk factors, including smoking, diabetes, hyperlipidemia, hyperglycemia, hypertension and disturbed blood flow in local areas. These stimuli promote hardening and thickening of artery walls as well as the formation of plaques. Upon formation, plaques can result in intravascular thrombosis and interruption of blood flow, potentially leading to morbidity or death. Studies have shown that plaque formation is associated with the accumulation of mesenchymal cells in the arterial intima, which secrete pro-inflammatory molecules and synthesize extracellular matrix and metalloproteinases (Stoll and Bendszus 2006; Flores-Gomez et al., 2021). Although in past decades, the mesenchymal cells in the tunica intima have been widely studied, their origin is not well understood. Under pathological conditions, smooth muscle cells in the tunica media and fibroblasts in the tunica adventitia proliferate and migrate into the tunica intima leading to the thickening of the intima (Xu et al., 2007; Tillie et al., 2020; Miano et al., 2021). In addition, bone marrow-derived cells were also involved in tunica intimal thickening (Cochain and Zernecke 2017). More recently, studies of human, porcine, and mouse arterial plaques have shown that the mesenchymal cells in the tunica intima could be derived from endothelial cells (Chen et al., 2015; Mahmoud et al., 2017; Helmke et al., 2019).

Such cells are considered to arise from the transitional state of the endothelial to mesenchymal transition (EndMT), in which endothelial markers continue to be expressed and new mesenchymal markers are acquired. EndMT was first described during heart development and was characterized morphologically as representing a shift from a cobblestone-like shape to a spindle morphology accompanied by alterations in gene expression profiles (Markwald et al., 1977). EndMT has recently been suggested as a fundamental contributing factor to AS. In an *in vivo* lineage tracing experiment, the endothelial-specific Cre-lox system VE-cadherin-CreERT2 or SCL-CreERT2 in combination with ApoE$^{-/-}$ or LDLR$^{-/-}$ mouse AS models were used to study the deep relationship between EndMT and AS (Chen et al., 2015; Evrard et al., 2017). Approximately 30% of aortic endothelial cells underwent EndMT, as assessed by co-expression of lineage tracers and the mesenchymal markers, Notch3 (Chen et al., 2015) and FAP (Evrard et al., 2017) after 4 months of on a high-fat diet. Meanwhile, 50% of endothelial-derived mesenchymal cells completely lost the expression of VE-cadherin (Evrard et al., 2017), indicating that these cells had undergone a complete EndMT. Other researchers proved that EndMT was associated with the occurrence of AS (Chen et al., 2015; Anbara et al., 2020; Qin et al., 2020), and the degree of EndMT was closely related to the severity of atherosclerotic disease (Chen et al., 2015), suggesting that the EndMT process has important clinical significance. This evidence demonstrates that the EndMT process can serve as a potential target for the treatment of AS.

Dan-Shen-Yin (DSY) comes from the Shi Fang Ge Kuo and is comprised of red sage (*Salvia miltiorrhiza*), sandalwood and fructus amomi (amomi fruit). As a famous traditional Chinese formula, DSY has been considered to improve blood circulation in Chinese theory and has been prescribed for centuries to treat coronary artery disease. Studies have indicated that DSY exerted protective effects against inflammation and reduced oxidative stress in a rat model of diabetic AS (Yan et al., 2011) and acute ischemic myocardial injury (Yan et al., 2012). Furthermore, a modified DSY composed of red sage (*Salvia miltiorrhiza*), sandalwood, Chuanxiong rhizoma, carthami flos, Rehmanniae radix preparata, and *Angelica sinensis* radix showed beneficial therapeutic effects against AS in an ApoE$^{-/-}$ mouse model (Yang et al., 2020). The active ingredients in *Salvia miltiorrhiza*, including tanshinone IIA (Wang et al., 2017), dihydrotanshinone I (Zhao W. et al., 2016) and salvianolic acid A (Ma et al., 2020), could efficiently treat AS. It was reported that sandalwood extract exhibited anti-inflammatory activity and could attenuate hyperlipidemia in streptozotocin-induced diabetic rats (Kulkarni et al., 2012; Suganya et al., 2021). Fructus amomi has also been found to display anti-inflammatory properties (Zhang T. et al., 2017; Fan et al., 2022). Due to the fact that inflammation affects the EndMT process, we hypothesized that DSY could target EndMT to treat AS.

Traditional Chinese medicines have gained much therapeutic interest in treating AS because of their multiple components with multiple targets; but their underlying mechanisms have been difficult to decipher. Based on the rationale of 'disease-gene-target-medicine', network pharmacology has been extensively used to understand the complicated mechanisms of traditional Chinese medicine (TCM) in treating complex diseases. In this work, we used network pharmacology and experimental strategies to investigate and elucidate the mechanism of DSY's effects on EndMT to support the rationale of using DSY in treating AS. We obtained the ingredients of DSY with the help of several databases and screened them for their EndMT and AS targets, which were acquired with multi-source databases and literature. We then set up protein-protein interaction (PPI) networks to determine the interactions among these targets and in turn performed enrichment analysis using gene ontology (GO) and the Kyoto Encyclopedia of Genes and Genomes (KEGG). This analysis resulted in the identification of PI3K/AKT signaling as a potential target. We validated the involvement of PI3K/AKT signaling in DSY against EndMT in treating AS and found that PI3K/AKT was the downstream signaling pathway of LASP1.

Materials and methods

Screening bioactive ingredients of Dan-Shen-Yin

The compounds in DSY were acquired using several databases including SymMap (Wu et al., 2019) (www.symmap.org), TCMSP(Ru et al., 2014) (tcmsp-e.com), TCMID (Xue et al., 2013) (http://47.100.169.139/), HERB (Fang et al., 2021) (herb.ac.cn) and ETCM (Xu H. Y. et al., 2019) (http://www.tcmip.cn/ETCM/). The SMILES structures of the compounds were obtained from PubChem (https://pubchem.ncbi.nlm.nih.gov/). The parameters of oral bioavailability (OB) ≥20% in TCMSP, quantitative estimate scores ≥0.49 in ETCM (Xu H. Y. et al., 2019), the accepted result of drug-like soft filter in FAFDrugs4 (Lagorce et al., 2017) (https://fafdrugs4.rpbs.univ-paris-diderot.fr/), and ADME with 'high' GI in SwissADME (Daina et al., 2017) (http://www.swissadme.ch/) were designated as thresholds to screen for potential bioactive compounds. In addition, we included the ingredients not screened by the databases, but mentioned in the literature.

Identification of potential Dan-Shen-Yin targets in endothelial-to-mesenchymal transition and atherosclerosis

The potential targets of DSY compounds were collected by manually searching the HERB database, TCMSP database, TCMID database, SymMap database, as well as from CNKI (https://www.cnki.net/) and PubMed. Because we were unable to obtain the targets of some of the compounds from the databases or the literature, we then used SwissTargetPrediction (http://swisstargetprediction.ch/) to predict targets based on structurally similar molecules. Targets with probability ≥0.7 were retained. EndMT and AS target genes were searched from DisGeNET database (Pinero et al., 2020) (https://www.disgenet.org/), GeneCards database (Rebhan et al., 1998) (https://www.genecards.org/) and DrugBank database (Wishart et al., 2018) (https://go.drugbank.com/). The overlapping genes among targets of DSY, EndMT and AS were visualized by Jvenn (Bardou, Mariette et al., 2014) (http://jvenn.toulouse.inra.fr/app/example.html).

Network construction and correlation analysis

The component-target network was constructed by Cytoscape (v3.9.1) and the degree value of each node, which reflects the importance of components or targets, was calculated by Network Analyzer. PPI data were acquired from Cytoscape plug-in BisoGenet (Martin et al., 2010) which includes the data from several major repositories of PPI databases such as the database of interacting proteins, biomolecular interaction network database, human protein reference database, BioGRID, and molecular interaction database.

In order to study PPIs at the system level, we then merged the PPI networks of DSY, EndMT, and AS by Cytoscape, and the Cytoscape plugin, cytoNCA (Tang et al., 2015), was used to calculate the topological properties of each node, including degree, betweenness centrality (BC), closeness centrality (CC), local average connectivity (LAC), eigenvector, and network. The nodes with topological importance in the network were screened by the topological properties mentioned above.

Gene ontology and Kyoto encyclopedia of genes and genomes pathway enrichment analysis

GO term enrichment analysis was performed using the R package clusterProfiler. Pathway enrichment gene symbols were converted to entrez ID with the R package org.Hs.eg.db (Version3.10.0). All of the targets in the networks were also subjected to KEGG pathway enrichment analysis. The significant terms and pathways were selected according to adjusted p value < 0.05, and the associated GO terms and KEGG pathways were ranked by adjusted p value.

Docking simulation

Autodock vina (v1.1.2) in Autodock tools (v1.5.7) (Trott and Olson 2010) was used to perform molecular docking simulations

to predict the binding abilities between the bioactive ingredients in DSY and the target genes. The 3D crystal structures of target proteins were screened using the PDB database (http://www.rcsb.org/pdb/). The 3D structures of the bioactive ingredients in DSY were downloaded from PubChem database and ZINC database (https://zinc12.docking.org/) (Irwin et al., 2020). The proteins were dismissed water and added hydrogens followed by the charge were calculated before docking. For those proteins had no known active site cavity docking, a grid box was used to wrap the entire protein. Otherwise, the grid box was centered in a middle of the identified cavity. Twenty models were generated and the maximum affinity values were calculated. The higher the absolute affinity value, the stronger the binding affinity of DSY components with proteins.

Preparation and quality control of ethyl acetate extract of Dan-Shen-Yin

Salvia miltiorrhiza was bought from Kangmei Pharmaceutical Co.,Ltd., (#210800301), Fructus amomi was purchased from Sinopharm Holding Shenzhen Medicinal Materials Co., Ltd.(#210502), sandalwood was obtained from Lingnan Traditional Chinese Herbal Medicine Co., Ltd. (# 2006001). In total, 200 g of *Salvia miltiorrhiza*, 30 g fructus amomi and 30 g of sandalwood (following the ratio of usage 30 g of *Salvia miltiorrhiza*, 4.5 g of fructus amomi, and 4.5 g of sandalwood in a single formula) were extracted in 500 ml of ethyl acetate for 1 h with heating and refluxing. The extract was collected into a clean beaker and filtered. Afterwards, the extract was placed in an ultra-clean tube and evaporated to dryness. The dried powder was dissolved in DMSO and stored at -20°C for later usage. The stability of the product was verified by high performance liquid chromatography (HPLC) (Figure 4).

Cell culture

Human umbilical vein endothelial cells (HUVECs) were purchased from Cyagen (#HUVEC-2001). The HUVECs were cultured in a 1% gelatin coated plate in complete endothelial cell medium (ECM, #1001, ScienCell) containing 5% FBS, and endothelial growth factor and were maintained in a humidified chamber with 5% CO_2 at 37°C. Human umbilical vein smooth muscle cells (HVSMCs) were obtained from Otwo Biotech (#HTX2305) and maintained in DMEM supplemented with 10% FBS and 1% P/S. To establish the EndMT model, HUVECs were stimulated with 10 ng/ml TGF-β2 (#100-35B, Proteintech) in conditioned medium supplemented with 2.5% FBS for four consecutive days. For DSY application, HUVECs pretreated with TGF-β2 for 2 days were incubated with different doses of DSY for a further 2 days.

siRNA-mediated down-regulation of LASP1 in HUVEC

LASP1 siRNAs (#258:GAACUACAAGGGCUACGAGAA; #193: CUGGAUAAGUUCUGGCAUAAA; #446:CCGAGC UCCAGAGAAUCAAGA) and non-targeting siRNA (siNT: UUCUCCGAACGUGUCACGU) were obtained from Sangon Biotech. A total of 25–100 nM of specific or siNT was introduced into the cells using RNATransMate (#E607402, Sangon Biotech) according to the manufacturer's recommendations.

Viable cell counting by CCK-8 assay

HUVECs were plated in 96-well plates in complete ECM medium and cultured overnight. The following day, cells were changed to ECM medium containing 2.5% FBS and were supplemented with 10 ng/ml TGF-β2 for 1 day. Then different doses of DSY as well as *Salvia miltiorrhiza*, sandalwood and fructus amomi were added for an additional 2 days. For IC50 analysis, cells were treated with different doses of DSY for 1 day, then 10 μl of CCK-8 assay reagent (#GK10001, GLPBIO, United States) was added to each well. The absorbance at 450 nm was measured using a spectrophotometer. Linear-regression analysis in Graphpad Prism 7 was performed to calculate IC50 value.

Real-time quantitative PCR

HUVECs were homogenized in Trizol reagent (Thermo-Fisher Scientific) and total RNA was prepared using the EZ-press RNA purification Kit (#B0004DP, EZBioscience) according to the manufacturer's procedure. Reverse transcription was performed using the Color Reverse transcription kit (#A0010CGQ, EZBioscience) following the manufacture's instructions. RT-qPCR was conducted using 2xColor SYBR green qPCR mix (#A0012-R2, EZBioscience) on a C1000 thermocycler (Bio Rad), and measurements were normalized to the expression of the housekeeping gene GAPDH. The relevant primers are shown in Supplementary Table S1. The expression data are expressed as $2^{-\Delta\Delta CT}$.

Western blot analysis

Cells were rinsed with cold PBS and lysed in SDS buffer (#P0013G, Beyotime) containing 1x proteinase inhibitor cocktail and 1x phosphatase inhibitor cocktail. The determination of protein concentration was performed by Bradford protein assay. Equal amounts of protein were loaded and separated by 10% polyacrylamide gel electrophoresis, and proteins were transferred to a PVDF membrane by wet electroblotting. The

membrane was incubated with anti-SM22α (1:1000, #10493-1-AP, Proteintech), anti-LASP1 (1:1000, #10515-1-AP, Proteintech), anti-AKT1 (1:1000, #60203-2-lg, Proteintech), anti-phospho-AKT (Ser473) (1:1000, #AF0016, Affinity Bioscience), and anti-β-actin (1:1000, #66009-1-Ig, Proteintech) at 4°C overnight, followed by washing and incubation with secondary anti-mouse, -goat, and -rabbit antibodies (1:1000, Abcam). Immunoreactive bands were detected.

Immunofluorescence

HUVECs were fixed in 4% PFA for 15 min at RT and washed 3x with PBS containing 1% BSA followed by mild permeabilization with 0.1% Triton X-100 (#ST795, Beyotime, Biotechnology) for 10 min at 4°C. After three washes, cells were incubated with rabbit anti-SM22α (1:50), rabbit anti LASP1 (1:50) and goat anti-VE-cadherin (1:200, #AF1002, R&D Systems) overnight at 4°C. After four washes, samples were further incubated with appropriate AlexaFluor-coupled secondary antibodies (1:1000, #ab150129, Abcam) for 1 h at RT. Cells were then washed and mounted in mounting medium (FD8396, Hangzhou Ford Biological Technology Co., LTD).

Statistics

Statistical analyses were carried out using GraphPad Prism 7 software (GraphPad Software, La Jolla, CA, United States). The differences among more than two groups were compared using one-way ANOVA followed by Tukey's post-hoc test. A p value less than 0.05 was considered to be significant. Data are shown as the mean ± SEM from at least three independent experiments.

Results

Bioactive ingredients in Dan-Shen-Yin

A total of 113 compounds from *Salvia miltiorrhiza*, 97 compounds from fructus amomi and 38 compounds from sandalwood were extracted from SymMap, TCMSP, HERB, TCMID and ETCM databases. In addition, another four components from *Salvia miltiorrhiza* including caryophyllene oxide, rosmarinic acid, ailanthoidol, salvianolic acid L as well as three ingredients in fructus amomi including α-copaene, 4-methoxycinnamic acid, and 4-hydroxycinnamic acid were retrieved from the literature and included for subsequent analysis. A total of 227 ingredients were identified after merging and removing the duplicates. A detailed list of DSY ingredients is given in Supplementary Table S2.

Targets of compounds in Dan-Shen-Yin, endothelial to mesenchymal transition, and atherosclerosis

From the bioactive ingredients in *Salvia miltiorrhiza*, fructus amomi, and sandalwood, 3478, 3968, and 353 targets were identified, respectively (Supplementary Table S3). Because some ingredients shared the same targets, a total of 4,147 targets in DSY were identified after removing duplicates. The targets of EndMT (475) were obtained from GeneCards, DrugBank database and literature by manual screening (Supplementary Table S4). The targets of AS (4,772) were identified from DisGeNET, DrugBank and GeneCards database (Supplementary Table S5). The shared targets of DSY, EndMT and AS were eventually refined to 154 (Supplementary Figure S1A and Supplementary Table S6). Thereafter, the bioactive ingredients and their predicted shared targets were used to generate the compounds—target network with Cytoscape 3.9.1 (Supplementary Figure S1). The network contained 4,379 nodes and 9,725 interaction edges. The degree value of a node corresponded to its importance in the network. The average degree value of the compounds was 6.5, and the degree value of 25 compounds was >9 (Supplementary Table S7), indicating that those compounds were the potential bioactive ingredients in DSY that targeted EndMT in the treatment of AS.

Protein-protein interaction network construction and functional enrichment analysis

The shared targets of DSY, EndMT and AS were input into the BisoGenet plugin in Cytoscape to create a PPI network containing 8,879 nodes and 186,717 edges (Figure 1A). Next, we selected nodes that met the following conditions including degree, value, BC, CC, LAC, eigenvector, and network, and lastly we constructed a network comprising 125 nodes and 2,898 edges (Figure 1B, Supplementary Table S8). The candidate targets of the PPI network were then explored by GO and KEGG enrichment analysis. The GO category results suggested that the predicated targets were highly involved in multiple biological processes involving covalent chromatin modification, the mitotic cell cycle, catabolic processes (proteasome-mediated, ubiquitin-dependent protein catabolic, proteasomal protein catabolic process), rhythmic process, metabolic process, etc. The relevant molecular functions included chromosome binding (ubiquitin protein ligase binding, histone deacetylase binding, promoter specific chromatin binding), cell adhesion molecule binding, DNA binding (damaged DNA binding, single-stranded DNA binding, telomeric DNA binding), steroid hormone

FIGURE 1
Functional enrichment analysis of the PPI network. **(A)** The shared targets of PPI with regard to DSY, EndMT and AS. **(B)** The PPI network of DSY regulating EndMT in treating AS. **(C)** GO ontology analysis of biological process, molecular functions, and cellular components. **(D)** KEGG enrichment analysis. The *X*-axis indicated the counts of the target symbols in each pathway; the *Y*-axis represented the main pathways ($p < 0.05$).

receptor binding, and protein N-terminus binding. In addition, the cellular components were markedly linked to focal adhesion, chromosome-related complex (nuclear chromatin, chromosome, telomeric region, histone methytransferase complex, ubiquitin ligase complex), protein complexes with DNA (protein-DNA complex, COP9 signalosome, ATPase complex), and lumen organization (ficolin-1-rich granule lumen, vesicle lumen) (Figure 1C). KEGG enrichment analysis suggested that the involved signaling pathways were mainly classified into cancer (viral carcinogenesis, miRNAs in cancer, prostate cancer, transcriptional misregulation in cancer, chronic myeloid leukemia), cell cycle including DNA replication, PI3K/AKT pathway, inflammation (hepatitis B, hepatitis C, legionellosis), ubiquitin mediated proteolysis, and DNA repair (Figure 1D).

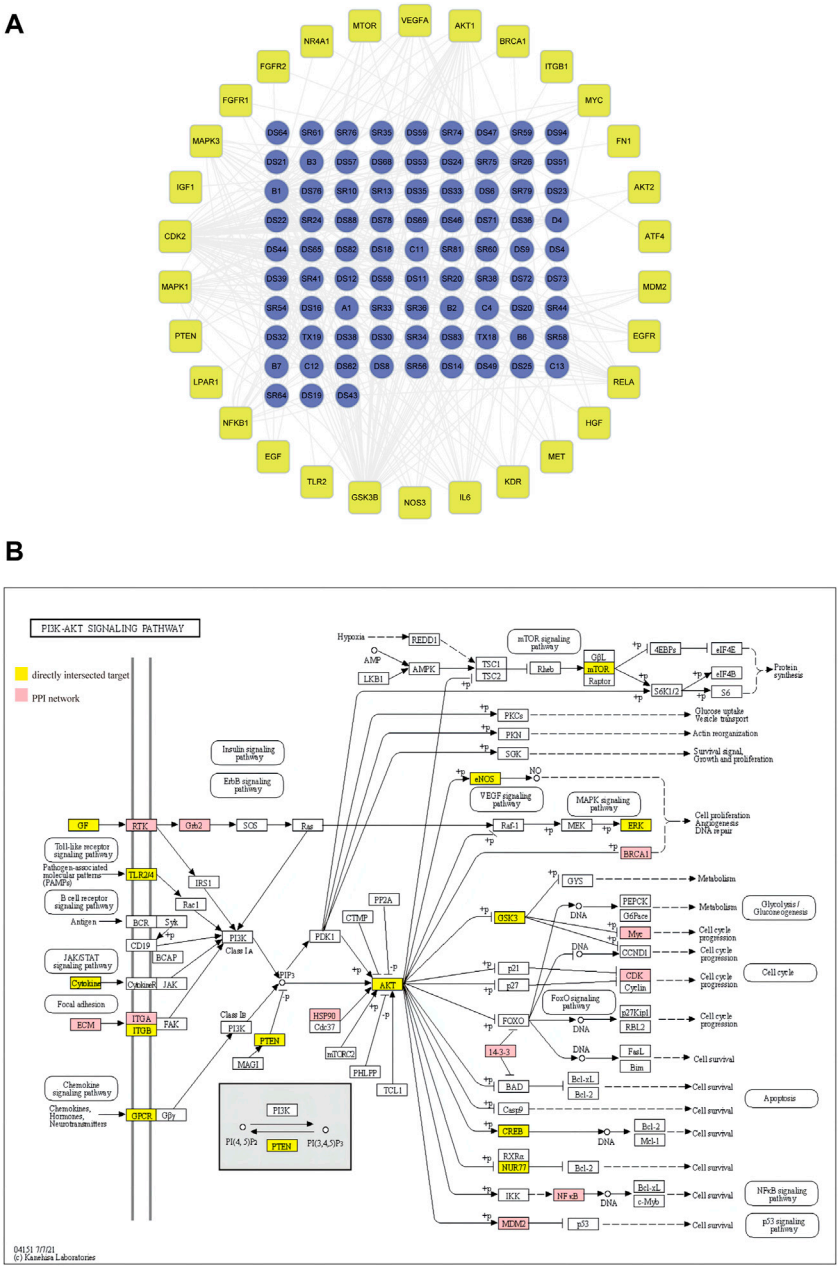

FIGURE 2
Screening of PI3K/AKT signaling pathway for regulation of EndMT in AS. **(A)** network of bioactive ingredients with PI3K/AKT targets extracted from directly intersected and PPI core targets. **(B)** The specific position and function of PI3K/AKT targets in signaling pathways. The red nodes and the yellow nodes represent the specific position of targets screened from PPI and from directly intersected targets respectively in the pathways.

Network of Dan-Shen-Yin ingredients with PI3K pathway signals

As shown in Figure 1D, the PI3K/AKT pathway was enriched in the PPI network as analyzed by the KEGG. We then established a network of target genes in the PI3K/AKT pathway with the bioactive ingredients in DSY based on the obtained direct targets and PPI hub genes (Figure 2A). From this analysis, we found that GSK3β, CDK2, MAPK1, AKT1, MAPK3, IL-6, and NF-κB were the targets of over 15 bioactive ingredients, suggesting that these genes may be the primary targets. For a clearer presentation, the targets from the PPI network were colored red while the targets from the directly intersected network were colored yellow in the signaling pathway

diagram in Figure 2B. It can be seen that PI3K/AKT-related targets were involved in multiple pathways, such as the toll-like receptor signaling pathway, B cell receptor signaling pathway, JAK/STAT signaling pathway, focal adhesion, and chemokine signaling pathways (Figure 2B). Since focal adhesion was one of the main cellular components by GO categorical analysis as shown in Figure 1B, we hypothesized that integrin-mediated PI3K/AKT activation was the main target of DSY for regulating EndMT in AS.

Effect of Dan-Shen-Yin on endothelial to mesenchymal transition

Next, we investigated the involvement of DSY in regulating the EndMT process. A total of 200 g of *Salvia miltiorrhiza*, 30 g of sandalwood, and 30 g of fructus amomi were extracted with ethyl acetate, yielding 1.4043 g of extract. The stability of the DSY extract was determined by HPLC (Figure 3A). To measure the toxicity of DSY, we conducted CCK-8 analysis and found that DSY dose-dependently reduced cell viability. The IC50 value of DSY for blocking cell proliferation in HUVECs was 10.86 μg/ml (Figure 3B). In this work, cells were incubated with TGF-β2 to induce the EndMT process and DSY had no effect on cell viability in the presence of TGF-β2 (Figure 3C). After TGF-β2 treatment, the cell phenotype underwent a significant change to a typical mesenchymal shape (Figure 4A). After DSY application, the cells adopted a cobblestone-like shape compared with TGF-β2 alone treatment (Figure 4A). Gene expression analysis by RT-PCR showed that TGF-β2 up-regulated the expression of mesenchymal markers like SM22α, calponin, collagen-type I alpha 1 chain (COL1A1), vimentin and the transcription factor, Snail, suggesting that EndMT was successfully induced. The ethyl acetate extract of DSY markedly decreased the expression of SM22α, calponin, vimentin, COL1A1, and Snail (Figure 4B). The decrease in SM22α protein expression by DSY was further confirmed by Western blot analysis (Figure 4C). From the results shown in Figures 4B,C, DSY at 2.5 μg/ml significantly decreased SM22α expression compared with DSY at 1.25 μg/ml. There was no obvious difference of SM22α expression between DSY at 2.5, 5, and 10 μg/ml; therefore, DSY at 2.5 μg/ml was used for subsequent experiments. The endothelial marker gene, VE-cadherin, was down-regulated by TGF-β2 treatment but this was reversed by DSY treatment (Figure 4C). The impact of DSY on SM22α and VE-cadherin was further confirmed by immunofluorescence staining (Figure 4D). To determine the time dependence of DSY on EndMT, HUVECs were pretreated with TGF-β2 for 3, 2, or 1 day followed by application of DSY for 1, 2, or 3 days, individually. Results indicated that DSY could inhibit EndMT in a time-dependent manner (Figure 4E). In the next experiment, the ethyl acetate extract of *Salvia miltiorrhiza*, fructus amomi and sandalwood were individually applied to HUVECs pretreated with TGF-β2. The RT-qPCR results showed that *Salvia miltiorrhiza* and sandalwood decreased SM22α, COL1A1 and calponin expression, but the effect of the single component was smaller compared to that with DSY. Fructus amomi did not affect gene expression (Figure 4F). These results suggested, on the one hand, that *Salvia miltiorrhiza* was the main component in DSY responsible for inhibiting EndMT process, while on the other hand, *Salvia miltiorrhiza,* and sandalwood showed synergistic effects against EndMT.

Dan-Shen-Yin down-regulated PI3K/AKT pathway expression

As shown above, we found enrichment of the PI3K/AKT signaling pathway in the PPI network and GO enrichment analysis. We then wanted to know if DSY could directly target PI3K-AKT signaling to regulate EndMT. We chose the compounds whose degree value was greater than 9 for docking simulation to estimate their binding affinity with PI3K/AKT pathway molecules. The specific degree values of compounds are shown in Supplementary Table S8. Fructus amomi had no effect on the expression of EndMT signature genes; therefore, the compounds identified in fructus amomi were excluded (Figure 4F). As a result, kaempferol (degree = 17), tanshinone I (degree value = 17), rosmarinic acid (degree value = 16), salvianolic acid b (degree value = 15), nsc 122421 (degree value = 14), tanshinone ii a (degree value = 12), vanillin (degree value = 10), cryptotanshinone (degree value = 9), and salvianolic acid a (degree value = 9) were screened. The results indicated that the majority of bioactive ingredients had strong binding affinities with the predicted PI3K/AKT pathway genes including Integrin αV, Integrin β1, PI3K, AKT1, GSK3β, CDK2, MAPK1, and NF-κB (Figure 5A, Supplementary Figures S2, S3). In turn, we detected the expression of PI3K/AKT signals, and found that TGF-β2 could significantly up-regulate the expression of AKT1, PI3K, integrin αV, and integrin β1, while DSY was able to reverse this expression. AKT2 expression was apparently not changed by TGF-β2 treatment (Figure 5B). This result suggested that DSY could target integrin-PI3K-AKT1 signaling expression.

Dan-Shen-Yin attenuated LIM and SH3 protein 1 expression in TGF-β2 treated cells

LIM and SH3 protein 1 (LASP1) is a specific focal adhesion protein that is induced under inflammatory conditions and in a variety of tumors (Zhang X. et al., 2017; Gao et al., 2018; Liu et al., 2018; Beckmann et al., 2021). It has been recently discovered that LASP1 can trigger the epithelial mesenchymal transition process and promote tumor progression by the PI3K/AKT pathway

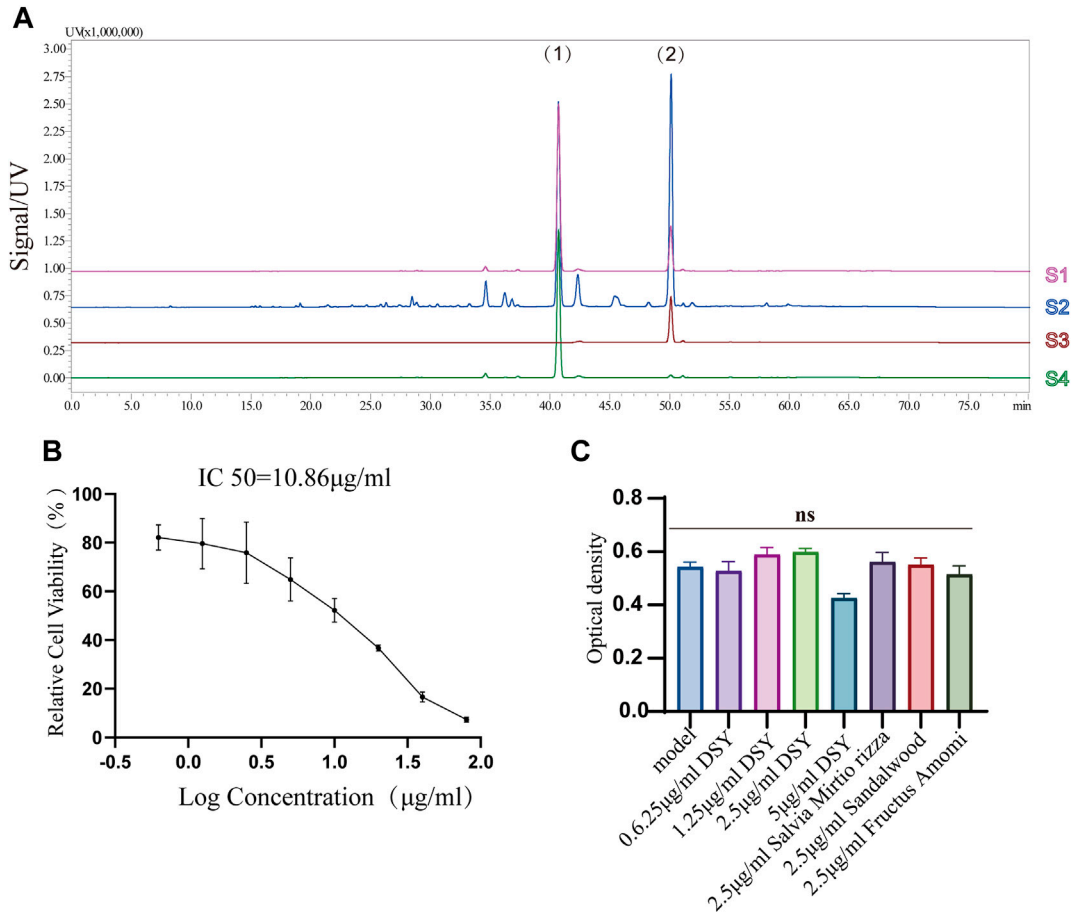

FIGURE 3
(A) HPLC chromatographic fingerprints of DSY. (1) and (2) represent cryptotanshinone and tanshinone IIA individually. S1: mixture of tanshinone IIA and cryptotanshinone; S2: DSY; S3: tanshinone IIA; S4: cryptotanshinone. **(B)** HUVECs were treated with different doses of DSY for 24 h followed by CCK-8 analysis. IC50 was calculated by linear-regression. **(C)** Cell viability influenced by DSY in the presence of TGF-β2 was determined by CCK-8 analysis.

(Wang et al., 2014; Shao et al., 2016; Gao et al., 2018; Gao et al., 2018; Zhong et al., 2018; Zhou et al., 2018; Xue et al., 2021). Integrins serve as adhesion receptors and their functions depend on focal adhesion signaling (Quach et al., 2009). As shown above, the expression of integrin αV and integrin β1 were significantly changed by DSY in TGF-β2-treated cells; we then wanted to know if LASP1 affected integrin expression to regulate EndMT. Because *Salvia miltiorrhiza* was the component in DSY with the greatest effect on inhibiting EndMT, we first performed docking simulations to estimate the binding abilities between the bioactive ingredients of *Salvia miltiorrhiza* and LASP1. The results suggested that the majority of bioactive ingredients including kaempfero, nsc 122421, rosmarinic acid, tanshinone, tanshinone IIA, cryptotanshinone, salvianolic acid A, and salvianolic acid B exhibited strong binding abilities towards LASP1 (Figure 6). Further, we discovered that LASP1 expression was higher in HVSMCs compared to HUVECs, and its expression in HUVECs could be induced by EndMT promoting stimuli like TGF-β2, IL-1β and hypoxia (Figures 7A,B). DSY decreased LASP1 expression induced by TGF-β2, as measured by RT-PCR and immunofluorescence assay (Figures 7C,D). As expected, knock-down of LASP1 decreased the expression of integrin αV, integrin β1, PI3K and AKT1 (Figure 7F) and down-regulated the phosphorylation level of AKT (Figure 7H). But there was no obvious difference in the expression of AKT1, PI3K, and p-AKT in cells containing siNT + DSY or siLASP1+DSY, suggesting that DSY was targeting the PI3K/AKT signaling pathway through LASP1. The same effect was observed regarding the mesenchymal-specific genes, *SM22α* and *calponin*. Expression of the endothelial functional gene, *VEGFR2*, was up-regulated by LASP1 deprivation (Figures 7G,H). Taken together, these results suggested that DSY could inhibit EndMT through the LASP1/integrin/PI3K/AKT signaling pathway.

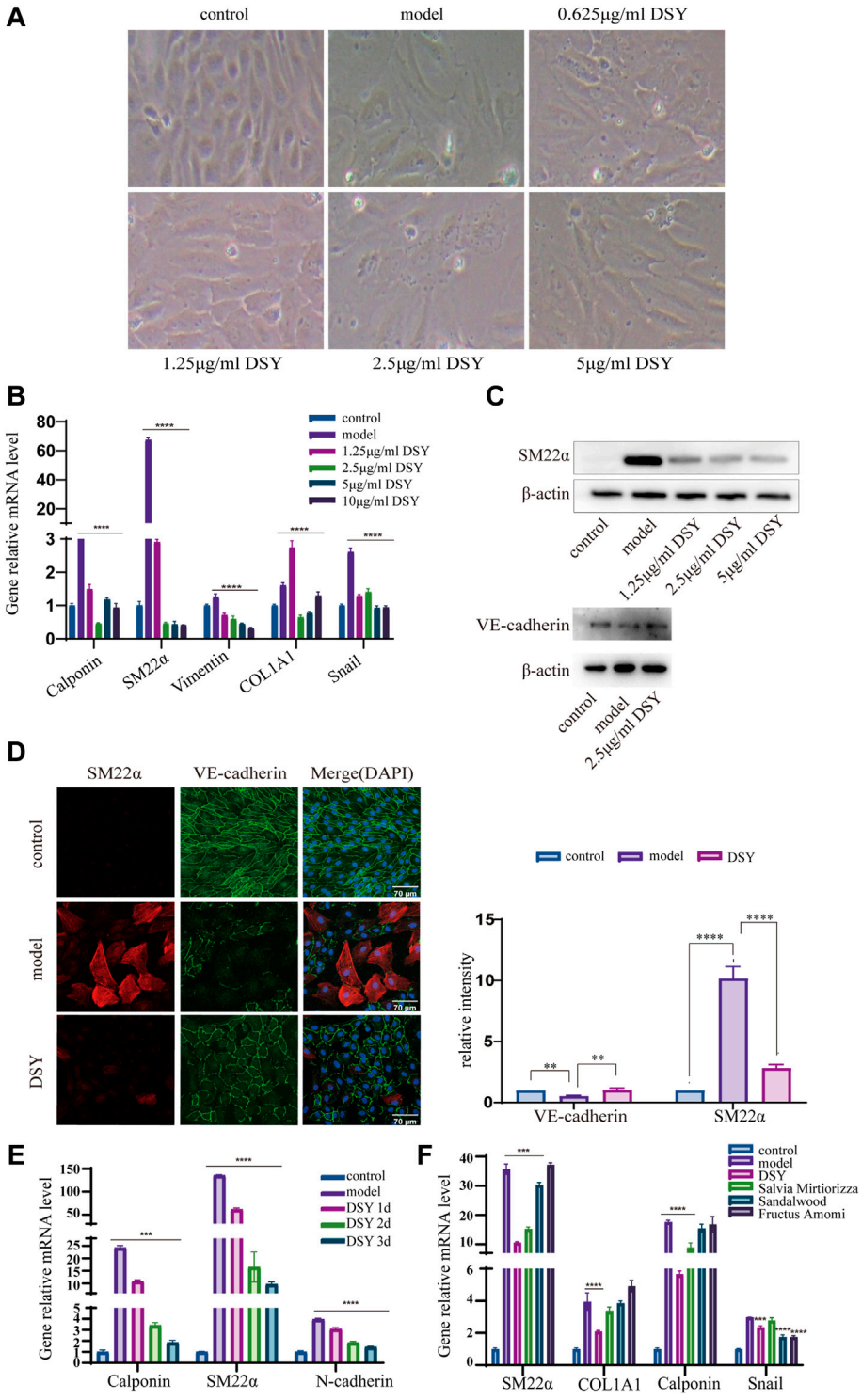

FIGURE 4
The effect of DSY on EndMT. **(A–E)** HUVECs pretreated with 10 ng/ml TGF-β2 for 2 days were incubated with different doses of DSY for another 2 d. **(A)** Representative phase contrast microscopy images. **(B)** RT-qPCR analysis of SM22α, calponin, vimentin, COL1A1, and Snail. **(C)** Western blot analysis was conducted to detect SM22α and VE-cadherin expression in DSY-treated cells. (**D, right panel**) Representative confocal images of HUVECs immune labeled with SM22α and VE-cadherin. (**D, left panel**) Relative intensities of SM22α and VE-cadherin were quantified by Fiji software. **(E)** HUVECs were pretreated with TGF-β2 for 3, 2, and 1 day followed by stimulation with 2.5 μg/ml DSY for another 1, 2, and 3 days. RT-qPCR analysis of SM22α, calponin and N-cadherin was demonstrated. **(F)** HUVECs pretreated with 10 ng/ml TGF-β2 for 2 days were treated with 2.5 μg/ml DSY, *Salvia miltiorrhiza*, fructus amomi and sandalwood for another 2 days. RT-PCR analysis of SM22α, calponin, COL1A1, and Snail was shown.

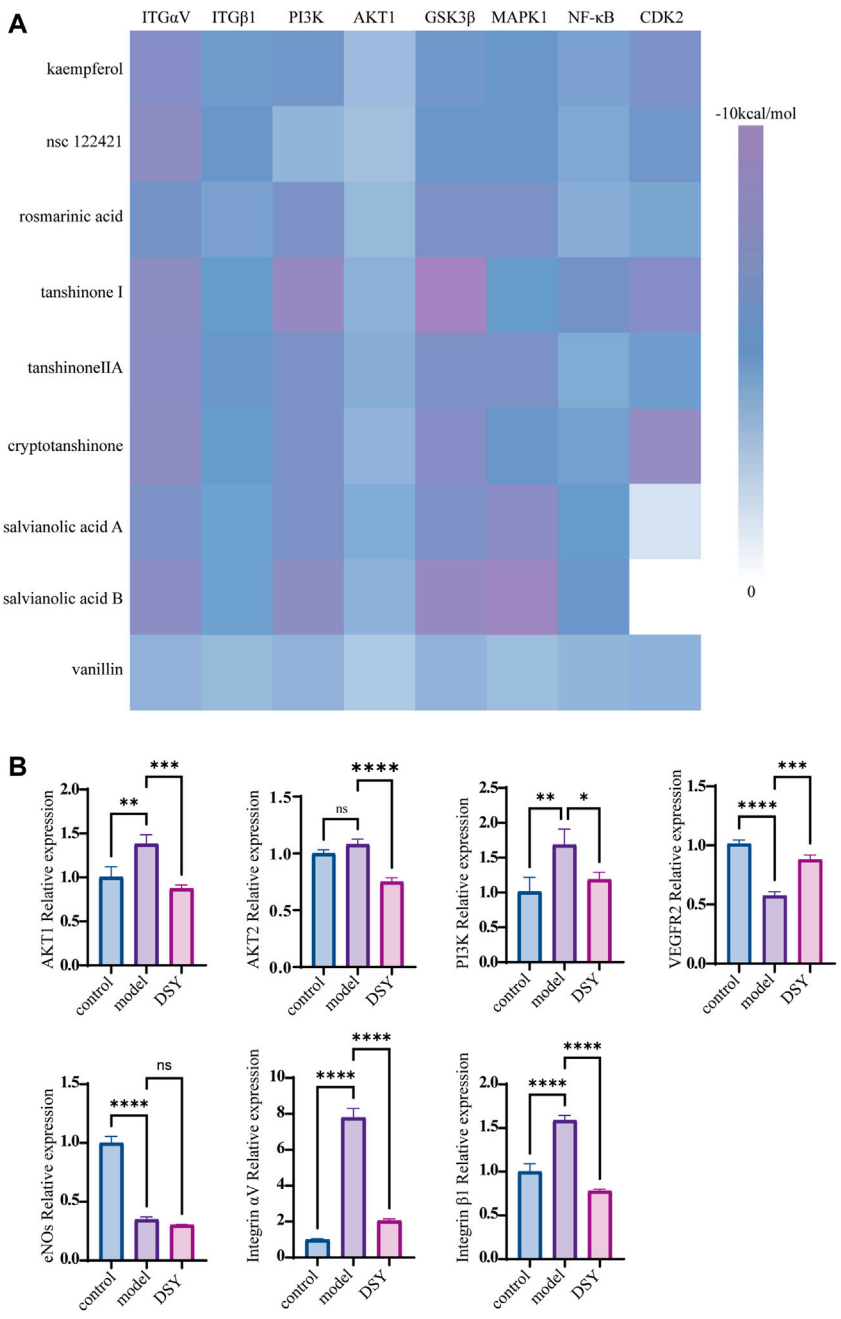

FIGURE 5
Impact of DSY on PI3K/AKT signaling. **(A)** Docking simulations of bioactive ingredients with PI3K/AKT molecules. Heat map of docking scores of binding affinity is shown. **(B)** HUVECs pretreated with 10 ng/ml TGF-β2 were subsequently stimulated with 2.5 μg/ml DSY. RT-qPCR analysis of PI3K, AKT1, AKT2, eNOS, integrin αV, and integrin β1.

Discussion

As the most common cardiovascular disease, AS gives rise to high morbidity and mortality worldwide. The endothelial lining on the inner surface of blood vessels has recently been determined to be transformed into mesenchymal cells through EndMT in response to various stimuli including growth factors, cytokines, hypoxia, and oscillatory flow, which contributes to the hardening and thickening of the arterial wall and plaque formation (Evrard et al., 2017; Mahmoud et al., 2017; Souilhol et al., 2018; Zhang et al., 2018). A substantial body of evidence has suggested that EndMT was the main inducer of AS development

A

Compound	Lowest affinity(kcal/mol)	Hydrogen bonding residues
kaempferol	-6.1kcal/mol	TYR-211
nsc 122421	-6.0kcal/mol	VAL-256
rosmarinic acid	-5.6kcal/mol	TYR-207
tanshinoneI	-6.6kcal/mol	ALA-206,TYR-207
tanshinoneIIA	-6.6kcal/mol	ALA-206
cryptotanshinone	-5.6kcal/mol	ASN-256,ALA-260
salvianolic acid A	-5.6kcal/mol	ASN-256
salvianolic acid B	-10.7kcal/mol	TYR-211

B

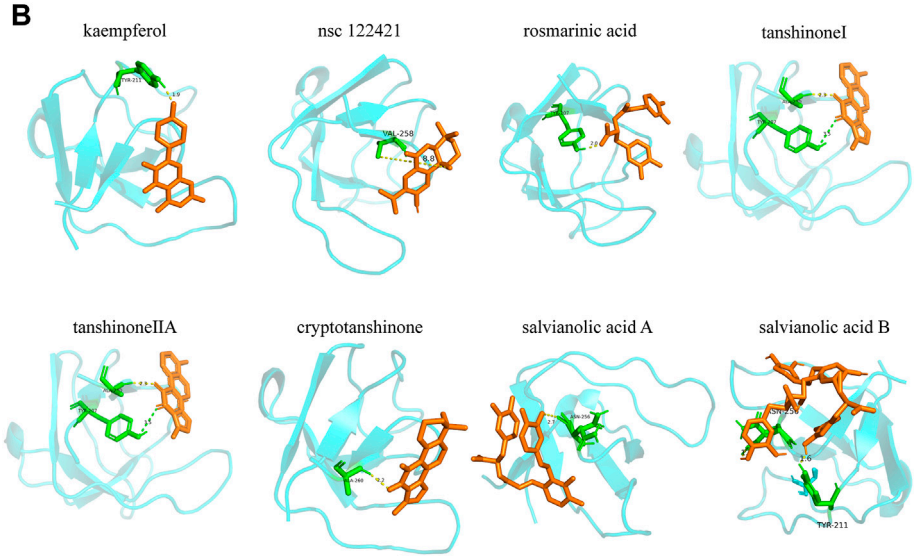

FIGURE 6
Docking simulations of bioactive ingredients with LASP1 molecule. **(A)** The binding affinities and the hydrogen bonding residues are shown. **(B)** The docking graph is shown.

(Chen et al., 2015; Souilhol et al., 2018; Liu H. T. et al., 2021; Testai et al., 2021), and that modifying EndMT may provide a promising new therapeutic strategy. TCM has shown significant therapeutic effects against AS by the synergistic effects of multiple ingredients with multiple targets.

DSY, which is composed of *Salvia miltiorrhiza*, fructus amomi, and sandalwood, is a famous traditional Chinese formula for treating cardiovascular disease. Pharmacological studies revealed that DSY possessed protective effects against acute ischemic myocardial injury, and diabetic AS by its anti-inflammatory and antioxidant activities (Yan et al., 2011; Yan et al., 2012); but, whether DSY could treat AS by targeting EndMT was unknown. In the present study, the parameters of OB and DL in the TCMSP database were utilized to build a compound—target network comprised of 227 bioactive ingredients and 154 corresponding targets against EndMT and AS, suggesting a potential role of DSY in regulating EndMT. Experimental analysis demonstrated that DSY could decrease mesenchymal signature genes as shown by RT-qPCR, western blot and immunofluorescence assay. By creating a PPI network, GO and KEGG pathway were then used to analyze the possible signaling pathway of DSY intervention in treating AS via EndMT. The KEGG results indicated that PI3K/AKT signaling was ranked first in pathway enrichment. PI3Ks are a family of lipid kinases that phosphorylate lipids at the cell membrane followed by recruitment and activation of AKT serine/threonine kinase, resulting in activation of downstream genes (Oyagbemi et al., 2017). The PI3K/AKT pathway has been implicated in several fundamental cellular processes such as proliferation and differentiation (Nagai et al., 2013; Yu and Cui 2016), and the abnormal functioning of the PI3K/AKT pathway has been seen in the onset and progression of many diseases like AS. Many AS risk factors result in activation of the PI3K/AKT pathway such as triggering of foam cell formation, intracellular lipid accumulation, and smooth muscle cell proliferation, which all contribute to plaque formation (Brito et al., 2009; Hongo et al., 2009; Huang et al., 2013). Blocking the PI3K/AKT pathway could attenuate the inflammation process

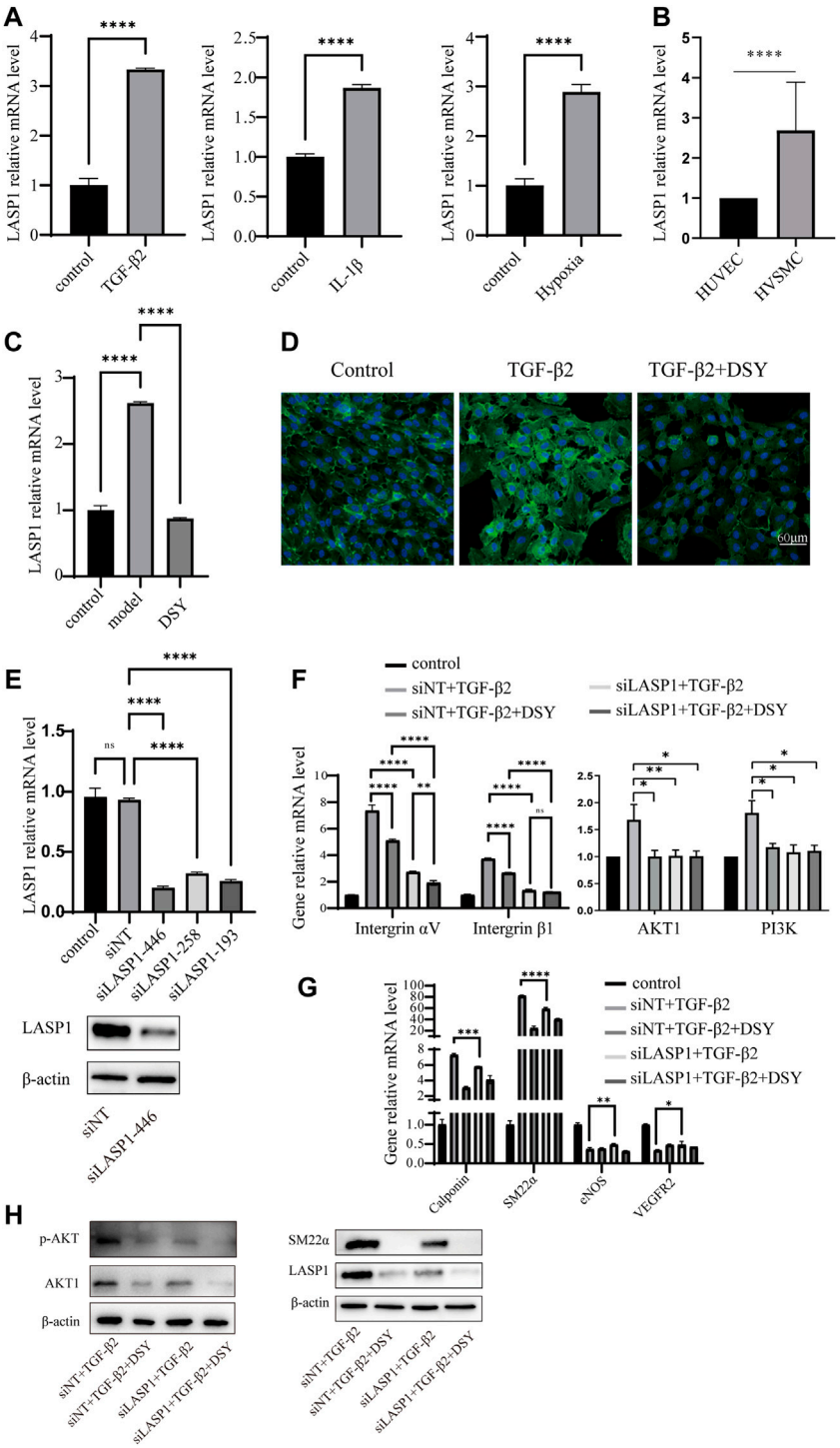

FIGURE 7
LASP1 mediated DSY down-regulation of integrin expression in TGF-β2-treated cells. **(A)** HUVECs were treated with 10 ng/ml IL-1β, TGF-β2 for 3 days or stimulated with hypoxia for 12 h. RT-qPCR analysis was then performed to detect LASP1 expression. **(B)** RT-qPCR comparison of LASP1 expression in HUVECs and HVSMCs. **(C,D)** LASP1 expression in TGF-β2-pretreated cells supplemented with different doses of DSY measured by **(C)** RT-qPCR and **(D)** immunofluorescence assay. (**E, upper panel**) RT-qPCR analysis of LASP1 expression after transfection with different siRNAs. (**E, lower panel**) LASP1 expression after transfection with siLASP-446 was checked by western blot. **(F)** HUVECs were transfected with siLASP1-446 followed by treatment with TGF-β2. One day later, 2.5 μg/ml DSY was added for another 2 d. **(F)** Analysis of integrin αV, integrin β1, PI3K, and AKT1 and **(G)** SM22α, calponin, and VEGFR2 expression by RT-qPCR analysis. **(H)** Western blot analysis of p-AKT, AKT1, SM22α and LASP1.

and could, in turn, decrease the AS lesion and plaque area in the ApoE$^{-/-}$ mouse model (Liu Z. Z. et al., 2021). Therefore, modulating PI3K/AKT signaling may provide a novel strategy for treating AS. In the current study, molecular docking results indicated that the majority of the bioactive ingredients had strong binding abilities with the predicted genes involved in the PI3K/AKT pathway. The hardening and thickening of the arterial wall in AS involves local remodeling of the vessel intima, which could be induced by multiple stimuli including pro-inflammatory cytokines, LPS, oxidized LDL and mechanical stress (Chen P. Y. et al., 2019; Gorabi et al., 2021; Guijarro and Cosin-Sales 2021; Wang et al., 2021). During this process, the integrin family of adhesion receptors has been shown to regulate the endothelial phenotype and could promote inflammation and fibrotic plaque formation (Finney et al., 2017; Chen X. et al., 2019; Al-Yafeai et al., 2021). In the current work, the expression of integrin αV and integrin β1, as well as their downstream signaling proteins, PI3K and AKT1, in TGF-β2-treated cells was significantly down-regulated by DSY, suggesting that DSY could target the integrin/PI3K/AKT signaling pathway to modify EndMT.

The remaining question was how the PI3K/AKT pathway was being regulated. Many papers had reported that the PI3K/AKT pathway was activated by LASP1 in many types of cancer cells (Shao et al., 2016; Zhong et al., 2018; Zhou et al., 2018). LASP1 is a specific focal adhesion protein that is up-regulated in destructive arthritis and a variety of tumors (Zhang T. et al., 2017; Gao, Tang et al., 2018; Liu et al., 2018; Beckmann et al., 2021). In addition, LASP1 could regulate adherens junction dynamics (Beckmann et al., 2021) and has been found to manipulate the epithelial mesenchymal transition (Xue et al., 2021). The expression of integrin can be mediated by many signals such as the adherens junction cadherins (Casal and Bartolome 2018) and focal adhesion kinase (Zhao X. K. et al., 2016). These observations led us to speculate that LASP1 may regulate EndMT via the integrin/PI3K/AKT pathway. In the current study, we found that LASP1 could be highly induced by TGF-β2, IL-1β, and hypoxia, the same factors that have been reported to promote EndMT (Kumarswamy et al., 2012; Lee et al., 2012; Maleszewska et al., 2013; Zhang et al., 2018; Glaser et al., 2020). Knock-down of LASP1 decreased integrin αV, and integrin β1 expression and reduced the expression level of mesenchymal signature genes. Above all, these results suggested that LASP1 was the key target of DSY in the regulation of EndMT.

Conclusions

TCM is a promising method for the treatment of cardiovascular disease due to its use of multiple compounds with multiple targets. We provide network pharmacology and molecular biology evidence that DSY regulates EndMT in AS mainly through the LASP1/PI3K/AKT pathway. In this work, experimental analysis uncovered that *Salvia miltiorrhiza* was the main active herb in DSY that exhibited inhibitory activity against EndMT, in agreement with the results from network pharmacology analysis that the majority of bioactive ingredients were from *Salvia miltiorrhiza*. Our work highlights the importance of *Salvia miltiorrhiza*in in treating AS, which has been suggested in other works (Li, Xu et al., 2018; Xu J. et al., 2019), but more importantly, we provided a new scenario for DSY's targeting of EndMT for the treatment of AS. However, further extensive in vitro and in vivo experiments have to be carried out to clarify the mechanism of DSY action and, more specifically, how *Salvia miltiorrhiza* regulated EndMT. Also, the effects and mechanisms of the bioactive ingredients in *Salvia miltiorrhiza* have to be characterized. Furthermore, we found that DSY could strongly decrease mesenchymal specific genes while moderately upregulating endothelial genes, suggesting their strong ability to inhibit the transition to the mesenchymal state, while preserving a relatively refined role in recovering the endothelial function. In future, more work has to be conducted to study the anti-AS effect of DSY in combination with other compounds with pro-endothelial activity.

Data availability statement

The original contributions presented in the study are included in the article/Supplementary Material, and further inquiries can be directed to the corresponding author.

Ethics statement

Ethical review and approval was not required for the study.

Author contributions

MH did most of the experiments, analyzed the data, and prepared the figures. YW contributed the network pharmacology analysis and prepared figures. JG conducted most of the docking simulations. JC and HZ were of great help in performing the PCR analysis. YG, XQ, and YL contributed critical discussions. JC supervised the entire work and wrote the manuscript.

Funding

This work was supported by the National Natural Science Foundation of China (grant NO: 32000551, 82174368), and the Science and Technology Program of Guangzhou, China (grant NO: JCYJ20180302173504891, JCYJ20190812161807600).

Conflict of interest

The authors declare that the research was conducted in the absence of any commercial or financial relationships that could be construed as a potential conflict of interest.

Publisher's note

All claims expressed in this article are solely those of the authors and do not necessarily represent those of their affiliated organizations, or those of the publisher, the editors or the reviewers. Any product that may be evaluated in this article, or claim that may be made by its manufacturer, is not guaranteed or endorsed by the publisher.

Supplementary material

The supplementary material for this article can be found online at: https://www.frontiersin.org/articles/10.3389/fphar.2022.946193/full#supplementary-material

References

Al-Yafeai, Z., Pearson, B. H., Peretik, J. M., Cockerham, E. D., Reeves, K. A., Bhattarai, U., et al. (2021). Integrin affinity modulation critically regulates atherogenic endothelial activation *in vitro* and *in vivo*. *Matrix Biol.* 96, 87–103. doi:10.1016/j.matbio.2020.10.006

Anbara, T., Sharifi, M., and Aboutaleb, N. (2020). Endothelial to mesenchymal transition in the cardiogenesis and cardiovascular diseases. *Curr. Cardiol. Rev.* 16 (4), 306–314. doi:10.2174/1573403X15666190808100336

Bardou, P., Mariette, J., Escudie, F., Djemiel, C., and Klopp, C. (2014). jvenn: an interactive Venn diagram viewer. *BMC Bioinforma.* 15, 293. doi:10.1186/1471-2105-15-293

Beckmann, D., Romer-Hillmann, A., Krause, A., Hansen, U., Wehmeyer, C., Intemann, J., et al. (2021). Lasp1 regulates adherens junction dynamics and fibroblast transformation in destructive arthritis. *Nat. Commun.* 12 (1), 3624. doi:10.1038/s41467-021-23706-8

Brito, P. M., Devillard, R., Negre-Salvayre, A., Almeida, L. M., Dinis, T. C., Salvayre, R., et al. (2009). Resveratrol inhibits the mTOR mitogenic signaling evoked by oxidized LDL in smooth muscle cells. *Atherosclerosis* 205 (1), 126–134. doi:10.1016/j.atherosclerosis.2008.11.011

Casal, J. I., and Bartolome, R. A. (2018). RGD cadherins and α2β1 integrin in cancer metastasis: A dangerous liaison. *Biochim. Biophys. Acta. Rev. Cancer* 1869 (2), 321–332. doi:10.1016/j.bbcan.2018.04.005

Chen, P. Y., Qin, L., Baeyens, N., Li, G., Afolabi, T., Budatha, M., et al. (2015). Endothelial-to-mesenchymal transition drives atherosclerosis progression. *J. Clin. Invest.* 125 (12), 4514–4528. doi:10.1172/JCI82719

Chen, P. Y., Qin, L., Li, G., Wang, Z., Dahlman, J. E., Malagon-Lopez, J., et al. (2019a). Endothelial TGF-beta signalling drives vascular inflammation and atherosclerosis. *Nat. Metab.* 1 (9), 912–926. doi:10.1038/s42255-019-0102-3

Chen, X., Lin, J., Hu, T., Ren, Z., Li, L., Hameed, I., et al. (2019b). Galectin-3 exacerbates ox-LDL-mediated endothelial injury by inducing inflammation via integrin β1-RhoA-JNK signaling activation. *J. Cell. Physiol.* 234 (7), 10990–11000. doi:10.1002/jcp.27910

Cochain, C., and Zernecke, A. (2017). Macrophages in vascular inflammation and atherosclerosis. *Pflugers Arch.* 469 (3-4), 485–499. doi:10.1007/s00424-017-1941-y

Daina, A., Michielin, O., and Zoete, V. (2017). SwissADME: A free web tool to evaluate pharmacokinetics, drug-likeness and medicinal chemistry friendliness of small molecules. *Sci. Rep.* 7, 42717. doi:10.1038/srep42717

Evrard, S. M., Lecce, L., Michelis, K. C., Nomura-Kitabayashi, A., Pandey, G., Purushothaman, K. R., et al. (2017). *Nature Communications*, 8.Endothelial to mesenchymal transition is common in atherosclerotic lesions and is associated with plaque instability (vol 7, 11853, 2016)

Fan, Y., Nguyen, T. V., Piao, C. H., Shin, H. S., Song, C. H., and Chai, O. H. (2022). Fructus Amomi extract attenuates nasal inflammation by restoring Th1/Th2 balance and down-regulation of NF-κB phosphorylation in OVA-induced allergic rhinitis. *Biosci. Rep.* 42 (3), BSR20212681. doi:10.1042/BSR20212681

Fang, S., Dong, L., Liu, L., Guo, J., Zhao, L., Zhang, J., et al. (2021). Herb: A high-throughput experiment- and reference-guided database of traditional Chinese medicine. *Nucleic Acids Res.* 49 (D1), D1197–D1206. doi:10.1093/nar/gkaa1063

Finney, A. C., Stokes, K. Y., Pattillo, C. B., and Orr, A. W. (2017). Integrin signaling in atherosclerosis. *Cell. Mol. Life Sci.* 74 (12), 2263–2282. doi:10.1007/s00018-017-2490-4

Flores-Gomez, D., Bekkering, S., Netea, M. G., and Riksen, N. P. (2021). Trained immunity in atherosclerotic cardiovascular disease. *Arterioscler. Thromb. Vasc. Biol.* 41 (1), 62–69. doi:10.1161/ATVBAHA.120.314216

Gao, Q., Tang, L., Wu, L., Li, K., Wang, H., Li, W., et al. (2018). LASP1 promotes nasopharyngeal carcinoma progression through negatively regulation of the tumor suppressor PTEN. *Cell Death Dis.* 9 (3), 393. doi:10.1038/s41419-018-0443-y

Glaser, S. F., Heumuller, A. W., Tombor, L., Hofmann, P., Muhly-Reinholz, M., Fischer, A., et al. (2020). The histone demethylase JMJD2B regulates endothelial-to-mesenchymal transition. *Proc. Natl. Acad. Sci. U. S. A.* 117 (8), 4180–4187. doi:10.1073/pnas.1913481117

Gorabi, A. M., Kiaie, N., Khosrojerdi, A., Jamialahmadi, T., Al-Rasadi, K., Johnston, T. P., et al. (2021). Implications for the role of lipopolysaccharide in the development of atherosclerosis. *Trends cardiovasc. Med.* doi:10.1016/j.tcm.2021.08.015

Guijarro, C., and Cosin-Sales, J. (2021). LDL cholesterol and atherosclerosis: The evidence. *Clin. Investig. Arterioscler.* 33 (1), 25–32. doi:10.1016/j.arteri.2020.12.004

Helmke, A., Casper, J., Nordlohne, J., David, S., Haller, H., Zeisberg, E. M., et al. (2019). Endothelial-to-mesenchymal transition shapes the atherosclerotic plaque and modulates macrophage function. *FASEB J.* 33 (2), 2278–2289. doi:10.1096/fj.201801238R

Hongo, S., Watanabe, T., Arita, S., Kanome, T., Kageyama, H., Shioda, S., et al. (2009). Leptin modulates ACAT1 expression and cholesterol efflux from human macrophages. *Am. J. Physiol. Endocrinol. Metab.* 297 (2), E474–E482. doi:10.1152/ajpendo.90369.2008

Huang, C. X., Zhang, Y. L., Wang, J. F., Jiang, J. Y., and Bao, J. L. (2013). MCP-1 impacts RCT by repressing ABCA1, ABCG1, and SR-BI through PI3K/Akt posttranslational regulation in HepG2 cells. *J. Lipid Res.* 54 (5), 1231–1240. doi:10.1194/jlr.M032482

Irwin, J. J., Tang, K. G., Young, J., Dandarchuluun, C., Wong, B. R., Khurelbaatar, M., et al. (2020). ZINC20-A free ultralarge-scale chemical database for ligand discovery. *J. Chem. Inf. Model.* 60 (12), 6065–6073. doi:10.1021/acs.jcim.0c00675

Kulkarni, C. R., Joglekar, M. M., Patil, S. B., and Arvindekar, A. U. (2012). Antihyperglycemic and antihyperlipidemic effect of Santalum album in streptozotocin induced diabetic rats. *Pharm. Biol.* 50 (3), 360–365. doi:10.3109/13880209.2011.604677

Kumarswamy, R., Volkmann, I., Jazbutyte, V., Dangwal, S., Park, D. H., and Thum, T. (2012). Transforming growth factor-beta-induced endothelial-to-mesenchymal transition is partly mediated by microRNA-21. *Arterioscler. Thromb. Vasc. Biol.* 32 (2), 361–369. doi:10.1161/ATVBAHA.111.234286

Lagorce, D., Bouslama, L., Becot, J., Miteva, M. A., and Villoutreix, B. O. (2017). FAF-Drugs4: Free ADME-tox filtering computations for chemical biology and early stages drug discovery. *Bioinformatics* 33 (22), 3658–3660. doi:10.1093/bioinformatics/btx491

Lee, J. G., Ko, M. K., and Kay, E. P. (2012). Endothelial mesenchymal transformation mediated by IL-1β-induced FGF-2 in corneal endothelial cells. *Exp. Eye Res.* 95 (1), 35–39. doi:10.1016/j.exer.2011.08.003

Li, Z. M., Xu, S. W., and Liu, P. Q. (2018). Salvia miltiorrhizaBurge (danshen): A golden herbal medicine in cardiovascular therapeutics. *Acta Pharmacol. Sin.* 39 (5), 802–824. doi:10.1038/aps.2017.193

Liu, H. T., Zhou, Z. X., Ren, Z., Yang, S., Liu, L. S., Wang, Z., et al. (2021a). EndMT: Potential target of H2S against atherosclerosis. *Curr. Med. Chem.* 28 (18), 3666–3680. doi:10.2174/0929867327999201116194634

Liu, Y., Gao, Y., Li, D., He, L., Iw, L., Hao, B., et al. (2018). LASP1 promotes glioma cell proliferation and migration and is negatively regulated by miR-377-3p. *Biomed. Pharmacother.* 108, 845–851. doi:10.1016/j.biopha.2018.09.068

Liu, Z. Z., Li, J., Lin, S., Wu, Y. H., He, D., and Qu, P. (2021b). PI3K regulates the activation of NLRP3 inflammasome in atherosclerosis through part-dependent AKT signaling pathway. *Exp. Anim.* 70 (4), 488–497. doi:10.1538/expanim.21-0002

Ma, Q., Yang, Q., Chen, J., Yu, C., Zhang, L., Zhou, W., et al. (2020). Salvianolic acid A ameliorates early-stage atherosclerosis development by inhibiting NLRP3 inflammasome activation in zucker diabetic fatty rats. *Molecules* 25 (5), E1089. doi:10.3390/molecules25051089

Mahmoud, M. M., Serbanovic-Canic, J., Feng, S., Souilhol, C., Xing, R., Hsiao, S., et al. (2017). Shear stress induces endothelial-to-mesenchymal transition via the transcription factor Snail. *Sci. Rep.* 7 (1), 3375. doi:10.1038/s41598-017-03532-z

Maleszewska, M., Moonen, J. R., Huijkman, N., van de Sluis, B., Krenning, G., and Harmsen, M. C. (2013). IL-1β and TGFβ2 synergistically induce endothelial to mesenchymal transition in an NFκB-dependent manner. *Immunobiology* 218 (4), 443–454. doi:10.1016/j.imbio.2012.05.026

Markwald, R. R., Fitzharris, T. P., and Manasek, F. J. (1977). Structural development of endocardial cushions. *Am. J. Anat.* 148 (1), 85–119. doi:10.1002/aja.1001480108

Martin, A., Ochagavia, M. E., Rabasa, L. C., Miranda, J., Fernandez-de-Cossio, J., and Bringas, R. (2010). BisoGenet: A new tool for gene network building, visualization and analysis. *BMC Bioinforma.* 11, 91. doi:10.1186/1471-2105-11-91

Miano, J. M., Fisher, E. A., and Majesky, M. W. (2021). Fate and state of vascular smooth muscle cells in atherosclerosis. *Circulation* 143 (21), 2110–2116. doi:10.1161/CIRCULATIONAHA.120.049922

Nagai, S., Kurebayashi, Y., and Koyasu, S. (2013). Role of PI3K/Akt and mTOR complexes in Th17 cell differentiation. *Ann. N. Y. Acad. Sci.* 1280, 30–34. doi:10.1111/nyas.12059

Oyagbemi, A. A., Omobowale, T. O., Asenuga, E. R., Ochigbo, G. O., Adejumobi, A. O., Adedapo, A. A., et al. (2017). Sodium arsenite-induced cardiovascular and renal dysfunction in rat via oxidative stress and protein kinase B (Akt/PKB) signaling pathway. *Redox Rep.* 22 (6), 467–477. doi:10.1080/13510002.2017.1308910

Pinero, J., Ramirez-Anguita, J. M., Sauch-Pitarch, J., Ronzano, F., Centeno, E., Sanz, F., et al. (2020). The DisGeNET knowledge platform for disease genomics: 2019 update. *Nucleic Acids Res.* 48 (D1), D845–D855. doi:10.1093/nar/gkz1021

Qin, W., Zhang, L., Li, Z., Xiao, D., Zhang, Y., Zhang, H., et al. (2020). Endothelial to mesenchymal transition contributes to nicotine-induced atherosclerosis. *Theranostics* 10 (12), 5276–5289. doi:10.7150/thno.42470

Quach, N. L., Biressi, S., Reichardt, L. F., Keller, C., and Rando, T. A. (2009). Focal adhesion kinase signaling regulates the expression of caveolin 3 and beta1 integrin, genes essential for normal myoblast fusion. *Mol. Biol. Cell* 20 (14), 3422–3435. doi:10.1091/mbc.e09-02-0175

Rebhan, M., Chalifa-Caspi, V., Prilusky, J., and Lancet, D. (1998). GeneCards: A novel functional genomics compendium with automated data mining and query reformulation support. *Bioinformatics* 14 (8), 656–664. doi:10.1093/bioinformatics/14.8.656

Ru, J., Li, P., Wang, J., Zhou, W., Li, B., Huang, C., et al. (2014). Tcmsp: A database of systems pharmacology for drug discovery from herbal medicines. *J. Cheminform.* 6, 13. doi:10.1186/1758-2946-6-13

Shao, Z. Y., Cai, Y. J., Xu, L. J., Yao, X. Q., Shi, J. L., Zhang, F. F., et al. (2016). Loss of the 14-3-3σ is essential for LASP1-mediated colorectal cancer progression via activating PI3K/AKT signaling pathway. *Sci. Rep.* 6, 25631. doi:10.1038/srep25631

Souilhol, C., Harmsen, M. C., Evans, P. C., and Krenning, G. (2018). Endothelial-mesenchymal transition in atherosclerosis. *Cardiovasc. Res.* 114 (4), 565–577. doi:10.1093/cvr/cvx253

Stoll, G., and Bendszus, M. (2006). Inflammation and atherosclerosis - novel insights into plaque formation and destabilization. *Stroke* 37 (7), 1923–1932. doi:10.1161/01.STR.0000226901.34927.10

Suganya, K., Liu, Q. F., and Koo, B. S. (2021). Santalum album extract exhibits neuroprotective effect against the TLR3-mediated neuroinflammatory response in human SH-SY5Y neuroblastoma cells. *Phytother. Res.* 35 (4), 1991–2004. doi:10.1002/ptr.6942

Tang, Y., Li, M., Wang, J., Pan, Y., and Wu, F. X. (2015). CytoNCA: A cytoscape plugin for centrality analysis and evaluation of protein interaction networks. *Biosystems.* 127, 67–72. doi:10.1016/j.biosystems.2014.11.005

Testai, L., Brancaleone, V., Flori, L., Montanaro, R., and Calderone, V. (2021). Modulation of EndMT by hydrogen sulfide in the prevention of cardiovascular fibrosis. *Antioxidants* 10 (6), 910. doi:10.3390/antiox10060910

Tillie, R., van Kuijk, K., and Sluimer, J. C. (2020). Fibroblasts in atherosclerosis: Heterogeneous and plastic participants. *Curr. Opin. Lipidol.* 31 (5), 273–278. doi:10.1097/MOL.0000000000000700

Trott, O., and Olson, A. J. (2010). AutoDock vina: Improving the speed and accuracy of docking with a new scoring function, efficient optimization, and multithreading. *J. Comput. Chem.* 31 (2), 455–461. doi:10.1002/jcc.21334

Wang, B., Ge, Z., Cheng, Z., and Zhao, Z. (2017). Tanshinone IIA suppresses the progression of atherosclerosis by inhibiting the apoptosis of vascular smooth muscle cells and the proliferation and migration of macrophages induced by ox-LDL. *Biol. Open* 6 (4), 489–495. doi:10.1242/bio.024133

Wang, H., Shi, J., Luo, Y., Liao, Q., Niu, Y., Zhang, F., et al. (2014). LIM and SH3 protein 1 induces TGFβ-mediated epithelial-mesenchymal transition in human colorectal cancer by regulating S100A4 expression. *Clin. Cancer Res.* 20 (22), 5835–5847. doi:10.1158/1078-0432.CCR-14-0485

Wang, J., Wang, Y., Sheng, L., He, T., Nin, X., Xue, A., et al. (2021). High fluid shear stress prevents atherosclerotic plaque formation by promoting endothelium denudation and synthetic phenotype of vascular smooth muscle cells. *Mol. Med. Rep.* 24 (2), 577. doi:10.3892/mmr.2021.12216

Wishart, D. S., Feunang, Y. D., Guo, A. C., Lo, E. J., Marcu, A., Grant, J. R., et al. (2018). DrugBank 5.0: A major update to the DrugBank database for 2018. *Nucleic Acids Res.* 46 (D1), D1074–D1082. doi:10.1093/nar/gkx1037

Wu, Y., Zhang, F., Yang, K., Fang, S., Bu, D., Li, H., et al. (2019). SymMap: An integrative database of traditional Chinese medicine enhanced by symptom mapping. *Nucleic Acids Res.* 47 (D1), D1110–D1117. doi:10.1093/nar/gky1021

Xu, F., Ji, J., Li, L., Chen, R., and Hu, W. C. (2007). Adventitial fibroblasts are activated in the early stages of atherosclerosis in the apolipoprotein E knockout mouse. *Biochem. Biophys. Res. Commun.* 352 (3), 681–688. doi:10.1016/j.bbrc.2006.11.073

Xu, H. Y., Zhang, Y. Q., Liu, Z. M., Chen, T., Lv, C. Y., Tang, S. H., et al. (2019a). Etcm: An encyclopaedia of traditional Chinese medicine. *Nucleic Acids Res.* 47 (D1), D976–D982. doi:10.1093/nar/gky987

Xu, J., Liu, Y. T., Zhao, Z., Zhao, L. Y., Wang, D. W., and Liu, Q. (2019b). The role of traditional Chinese medicine in the treatment of atherosclerosis through the regulation of macrophage activity. *Biomed. Pharmacother.* 118, 109375. doi:10.1016/j.biopha.2019.109375

Xue, Q., Jiang, H., Wang, J., and Wei, D. (2021). LASP1 induces epithelial-mesenchymal transition in lung cancer through the TGF-β1/smad/snail pathway. *Can. Respir. J.* 2021, 5277409. doi:10.1155/2021/5277409

Xue, R., Fang, Z., Zhang, M., Yi, Z., Wen, C., and Shi, T. (2013). Tcmid: Traditional Chinese Medicine integrative database for herb molecular mechanism analysis. *Nucleic Acids Res.* 41, D1089–D1095. doi:10.1093/nar/gks1100

Yan, K. P., Guo, Y., Xing, Z., Huang, X., Dai, S., Duan, M., et al. (2012). Dan-Shen-Yin protects the heart against inflammation and oxidative stress induced by acute ischemic myocardial injury in rats. *Exp. Ther. Med.* 3 (2), 314–318. doi:10.3892/etm.2011.404

Yan, K. P., Guo, Y., Xing, Z. H., Wei, X., Dai, S. P., Sun, X. H., et al. (2011). Dan-Shen-Yin has integrated protective effects in diabetic atherosclerosis rat models. *J. Med. Plants Res.* 5 (27), 6336–6343.

Yang, K., Zeng, L., Ge, A., Pan, X., Bao, T., Long, Z., et al. (2020). Integrating systematic biological and proteomics strategies to explore the pharmacological mechanism of danshen yin modified on atherosclerosis. *J. Cell. Mol. Med.* 24 (23), 13876–13898. doi:10.1111/jcmm.15979

Yu, J. S., and Cui, W. (2016). Proliferation, survival and metabolism: The role of PI3K/AKT/mTOR signalling in pluripotency and cell fate determination. *Development* 143 (17), 3050–3060. doi:10.1242/dev.137075

Zhang, B., Niu, W., Dong, H. Y., Liu, M. L., Luo, Y., and Li, Z. C. (2018). Hypoxia induces endothelialmesenchymal transition in pulmonary vascular remodeling. *Int. J. Mol. Med.* 42 (1), 270–278. doi:10.3892/ijmm.2018.3584

Zhang, T., Lu, S. H., Bi, Q., Liang, L., Wang, Y. F., Yang, X. X., et al. (2017a). Volatile oil from Amomi Fructus attenuates 5-fluorouracil-induced intestinal mucositis. *Front. Pharmacol.* 8, 786. doi:10.3389/fphar.2017.00786

Zhang, X., Liu, Y., Fan, C., Wang, L., Li, A., Zhou, H., et al. (2017b). Lasp1 promotes malignant phenotype of non-small-cell lung cancer via inducing phosphorylation of FAK-AKT pathway. *Oncotarget* 8 (43), 75102–75113. doi:10.18632/oncotarget.20527

Zhao, W., Li, C., Gao, H., Wu, Q., Shi, J., and Chen, X. (2016a). Dihydrotanshinone I attenuates atherosclerosis in ApoE-deficient mice: Role of NOX4/NF-κB mediated lectin-like oxidized LDL receptor-1 (LOX-1) of the endothelium. *Front. Pharmacol.* 7, 418. doi:10.3389/fphar.2016.00418

Zhao, X. K., Cheng, Y., Liang Cheng, M., Yu, L., Mu, M., Li, H., et al. (2016b). Focal adhesion kinase regulates fibroblast migration via integrin beta-1 and plays a central role in fibrosis. *Sci. Rep.* 6, 19276. doi:10.1038/srep19276

Zhong, C. H., Chen, Y. T., Tao, B., Peng, L. L., Peng, T. M., Yang, X. B., et al. (2018). LIM and SH3 protein 1 regulates cell growth and chemosensitivity of human glioblastoma via the PI3K/AKT pathway. *Bmc Cancer* 18, 722. doi:10.1186/s12885-018-4649-2

Zhou, R., Shao, Z., Liu, J., Zhan, W., Gao, Q., Pan, Z., et al. (2018). COPS5 and LASP1 synergistically interact to downregulate 14-3-3σ expression and promote colorectal cancer progression via activating PI3K/AKT pathway. *Int. J. Cancer* 142 (9), 1853–1864. doi:10.1002/ijc.31206

frontiers | Frontiers in Pharmacology

TYPE Mini Review
PUBLISHED 06 September 2022
DOI 10.3389/fphar.2022.986683

OPEN ACCESS

EDITED BY
Xiaoyong Tong,
Chongqing University, China

REVIEWED BY
Xiangqi Li,
Naval Medical University, China
Ying Xin,
Jilin University, China

*CORRESPONDENCE
Da Sun,
sunday@wzu.edu.cn
Libo Jin,
20160121@wzu.edu.cn

†These authors have contributed equally to this work

SPECIALTY SECTION
This article was submitted to Cardiovascular and Smooth Muscle Pharmacology, a section of the journal Frontiers in Pharmacology

RECEIVED 05 July 2022
ACCEPTED 12 August 2022
PUBLISHED 06 September 2022

CITATION
Ma J, Lei P, Chen H, Wang L, Fang Y, Yan X, Yang Q, Peng B, Jin L and Sun D (2022), Advances in lncRNAs from stem cell-derived exosome for the treatment of cardiovascular diseases. *Front. Pharmacol.* 13:986683. doi: 10.3389/fphar.2022.986683

Advances in lncRNAs from stem cell-derived exosome for the treatment of cardiovascular diseases

Jiahui Ma[1†], Pengyu Lei[1†], Haojie Chen[1], Lei Wang[1], Yimeng Fang[1], Xiaoqing Yan[2], Qinsi Yang[3], Bo Peng[3], Libo Jin[1*] and Da Sun[1*]

[1]Institute of Life Sciences & Biomedical Collaborative Innovation Center of Zhejiang Province, Wenzhou University, Wenzhou, China, [2]Department of Pharmacy, Chinese-American Research Institute for Diabetic Complications, Wenzhou Medical University, Wenzhou, China, [3]Wenzhou Institute, University of Chinese Academy of Sciences, Wenzhou, China

Cardiovascular diseases (CVDs) are the leading cause of mortality globally. Benefiting from the advantages of early diagnosis and precision medicine, stem cell-based therapies have emerged as promising treatment options for CVDs. However, autologous or allogeneic stem cell transplantation imposes a potential risk of immunological rejection, infusion toxicity, and oncogenesis. Fortunately, exosome can override these limitations. Increasing evidence has demonstrated that long non-coding RNAs (lncRNAs) in exosome from stem cell paracrine factors play critical roles in stem cell therapy and participate in numerous regulatory processes, including transcriptional silencing, transcriptional activation, chromosome modification, and intranuclear transport. Accordingly, lncRNAs can treat CVDs by directly acting on specific signaling pathways. This mini review systematically summarizes the key regulatory actions of lncRNAs from different stem cells on myocardial aging and apoptosis, ischemia-reperfusion injury, retinopathy, atherosclerosis, and hypertension. In addition, the current challenges and future prospects of lncRNAs treatment for CVDs are discussed.

KEYWORDS

lncRNA, exosome, stem cells, cardiovascular diseases, acellular therapy

Introduction

Cardiovascular diseases (CVDs), which mainly involve the heart and blood vessels (Schmidt, 2019), are the leading cause of morbidity and mortality worldwide (Luo et al., 2018; South et al., 2019). Cases of CVDs increased from 271 million in 1990 to 523 million in 2019, whereas related deaths increased from 12.1 million to 18.6 million (Liu et al., 2021). Currently, surgery and drug are the standard methods for treating CVDs. However, these choices do not enhance the regeneration of damaged myocardial tissue, increasing the chances of recurrence (Stefanini and Holmes, 2013; Rentrop and Feit, 2015). Given

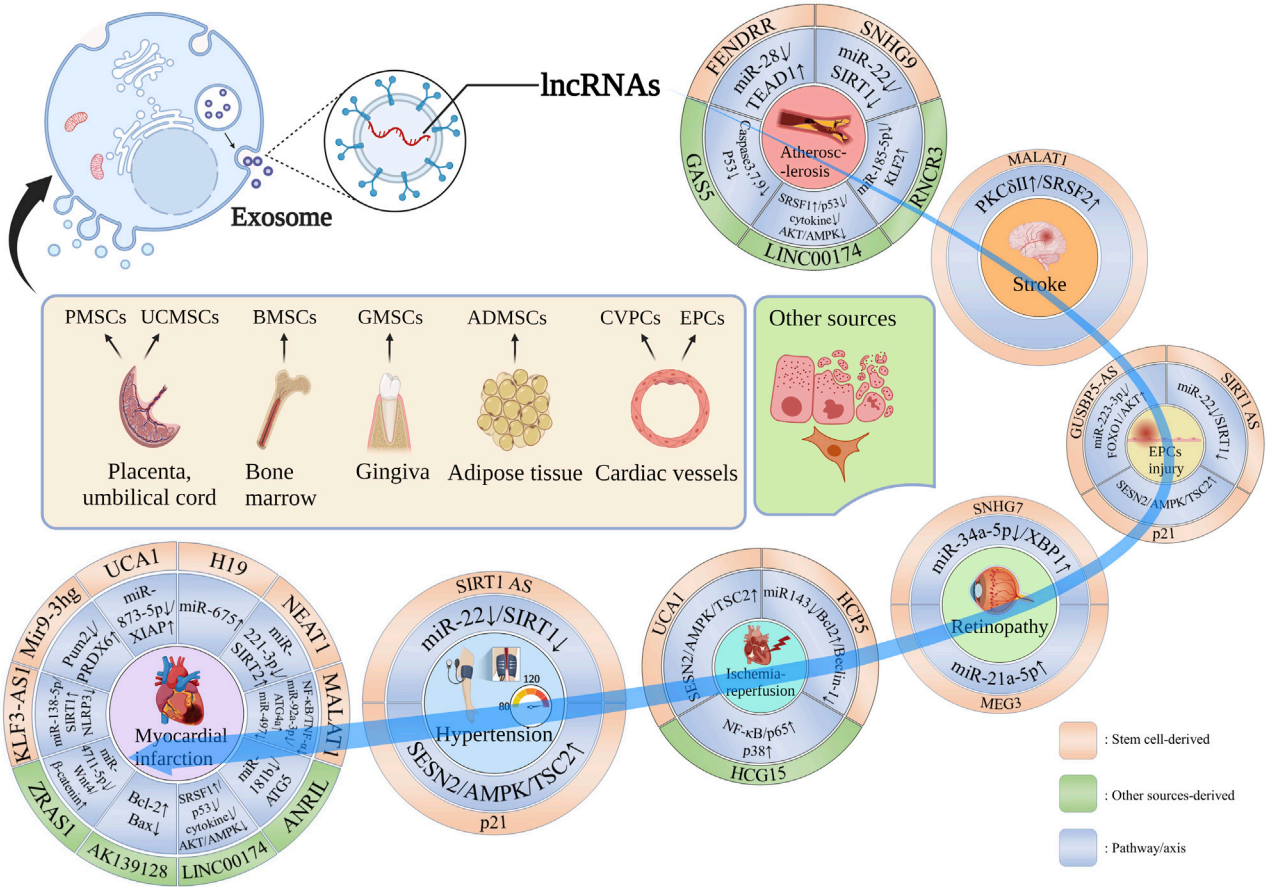

FIGURE 1
Stem cell-derived Exo-lncRNA with diverse organ sources and other sources in the CVDs occurrence and progression. lncRNA-FENDRR, lncRNA-SNHG9, lncRNA-RNCR3, LINC00174 and lncRNA-GAS5 contribute to AS occurrence and progression; lncRNA-MALAT1 promotes nerve repair after stroke; SIRT1 AS lncRNA, lncRNA-p21 and lncRNA GUSBP5-AS are involved in EPC repair, the former two are also promote vascular damage repair caused by hypertension; lncRNA-SNHG7 and lncRNA-MEG3 are involved in retinopathy; lncRNA-UCA1, lncRNA-HCP5 and lncRNA-HCG15 reduce I/R injury; lncRNA-KLF3-AS1, lncRNA Mir9-3hg, lncRNA-UCA1, lncRNA-H19, lncRNA-NEAT1, lncRNA-MALAT1, lncRNA-ANRIL, LINC00174, lncRNA-AK139128 and lncRNA-ZRAS1 participate in MI process.

that stem cells can differentiate into different mature cell types and possess self-renewal characteristics, stem cell therapy is a potential treatment for CVDs because they induce the regeneration of myocardial cells (Shen et al., 2015; Yamanaka, 2020).

However, the survival rate of transplanted stem cells is very low, decreasing the efficiency of transplantation and the therapeutic efficacy and increases the risk of immune rejection, infusion toxicity, and tumor formation (Liu W. et al., 2020; Zhuang et al., 2020). Recently, numerous studies have confirmed that stem cells mainly exert their effect on CVDs by inducing the secretion of paracrine factors mainly in exosome (Exo) (Elshaer et al., 2018; Terashvili and Bosnjak, 2019; Wu et al., 2020). Although the proportion of long non-coding RNAs (lncRNAs) in Exo is very low (Huang, 2020; Hui et al., 2020; Pham and Boon, 2020), research shows that lncRNAs, especially in stem cell-derived Exo, contribute significantly to treat CVDs by regulating gene expression at the transcriptional level, acting as a molecular sponge that targets miRNA, interfering with chromatin complexes to repress or activate gene expression in an epigenetic fashion and participating the processes of apoptosis, pyrosis, autophagy, myocardial fibrosis, and angiogenesis (Li et al., 2018; Deng et al., 2019; Pan et al., 2019; Yan et al., 2020; Chen et al., 2021a, 2021a; Yuan and Huang, 2021). For example, mesenchymal stem cells (MSCs)-Exo-lncRNA-FENDRR can be taken up by human vascular endothelial cells (HUV-EC-C), where they activate the TEA domain transcription factor 1 (TEAD1) by targeting microRNA (miR)-28 and, thus, inhibits apoptosis, oxidative stress, and inflammatory response of HUV-EC-C, reducing

the accumulation of oxidized low-density lipoprotein (ox-LDL), and reduces the formation of atherosclerotic plaques (Zhang N. et al., 2022). In addition, lncRNA-UCA1-rich Exo obtained by hypoxia-stimulated human MSCs secretion inhibit apoptosis *in vivo* and *in vitro via* the lncRNA-UCA1/miR-873-5p↓/X-Linked Inhibitor of Apoptosis Protein (XIAP)↑ axis (Hu et al., 2016; Sun L. et al., 2020). Meanwhile, compared with miRs, lncRNAs have more tissue-specific and developmental stage-specific (Thum and Condorelli, 2015; Zhu et al., 2016).

Adult stem cell (ASC) is more abundant, easier to obtain and does not present ethical dilemmas compared with embryonic stem cells (Barnabé et al., 2009; Shafei et al., 2018; Li et al., 2019; Jain et al., 2020). Therefore, the development of therapeutic approaches to treat CVDs applying ASC-Exo-lncRNA is of utmost importance. This review systematically reviews the research progress and mechanism underlying the function of different ASC-Exo-lncRNAs for CVDs therapy. The challenges and potential clinical application of stem cell-derived Exo-lncRNAs are also discussed.

ASCs-exo-lncRNAs with diverse organ sources

As summarized in Figure 1, Exo-lncRNAs derived from bone Marrow (Bone Marrow mesenchymal stem cells, BMSCs), placenta (placental mesenchymal stem cells, PMSCs), adipocyte (adipocyte mesenchymal stem cells, ADMSCs), umbilical cord (umbilical cord mesenchymal stem cells, UCMSCs), gingiva (gingival mesenchymal stem cell, GMSCs) and cardiac vessels (cardiovascular progenitor cells, CVPCs and endothelial progenitor cells, EPCs) have the potential to contribute to CVDs occurrence and progression (Shafei et al., 2018; Gao and Jin, 2020; Jain et al., 2020).

Cardiovascular protective effect of BMSCs-exo-lncRNAs

The beneficial effect of BMSCs in CVDs has been reported (Afzal et al., 2015). Preventing or reducing cardiomyocyte apoptosis or pyroptosis is necessary to ensure normal cardiac contractile function. Mao et al. (Mao et al., 2019) found that BMSCs- Exo overexpressing lncRNA-KLF3-AS1 in hypoxic cardiomyocytes and rats could improve the morphology of cardiomyocytes and inhibit the inflammatory response induced by pyroptosis. Meanwhile as a competitive endogenous RNA of sponge miR-138-5p, lncRNA-KLF3-AS1 mediates the expression of sirtuin 1 (SIRT1) and inhibits the activation of NOD-like receptor family pyrin domain containing 3 (NLRP3) inflammatory bodies and, thus, regulates the pyroptosis of cardiomyocytes and the progression of miocardial infarction (MI).

An increase of miR-497 during ischemia-reperfusion (I/R) injury may cause cardiomyocyte apoptosis. Li et al. (Li K.-S. et al., 2021) confirmed that Introducing Exo-lncRNA-HCP5 in hBMSCs into cardiomyocytes can protect cardiomyocytes from injury *via* the miR-497↓/insulin like growth factor-1 (IGF-1)/phosphatidylinositide 3-kinases (PI3K)/protein kinase B (AKT)↓ signal pathway. Meanwhile, Zhang et al. (Zhang J.-K. et al., 2022) treated HL-1 mouse cardiomyocytes and myocardial tissue of hypoxia reperfusion (H/R) myocardial cells ferroptosis mouse model with BMSCs-Exo-lncRNA-Mir9-3hg. The results showed that BMSCs-Exo-lncRNA-Mir9-3hg inhibits the upregulation of pumilio RNA binding family member 2 (Pum2), promotes glutathione content, peroxiredoxin 6 (PRDX6), the proliferation of HL-1 mouse cardiomyocytes, and inhibits the iron concentration, production of reactive oxygen species, and acyl CoA synthetase long chain family member 4 expression in HL-1 cells treated with H/R injury. In addition, high glucos initiated proliferation and migration of retinal endothelial cells, which is a critical step of diabetic retinopathy (DR) development. Cao et al. (Cao et al., 2021) found that human BMSCs-Exo transduces lncRNA-SNHG7 into human retinal microvascular endothelial cells (HRMECs) and inhibits the endothelial mesenchymal transformation and tubule formation of HRMECs *via* the miR-34a-5p↓/X-box binding protein 1 (XBP1)↑ (a transcription factor associated with endoplasmic reticulum stress regulation) axis. Accordingly, this axis is a feasible target for treating pathological fibrosis in DR.

Apart from the above, MSCs can enhance its protective effect on myocardial function after MI following appropriate drug treatment, such as atorvastatin (ATV) and migration inhibitory factor (MIF) (Li et al., 2015, 4; Liu X. et al., 2020). Huang et al. (Huang P. et al., 2020) treated BMSCs with ATV to obtain Exo overexpress lncRNA-H19 (MSC^{ATV}-Exo). The lncRNA regulated the activation of vascular endothelial growth factor and intercellular adhesion molecule-1 in endothelial cells and cardiomyocytes by targeting miR-675↑. lncRNA-H19 suppresses inflammation, promotes healing of infarct damage, reduces cardiomyocyte apoptosis, promotes angiogenesis, and elongates the endothelial cell survival in rat acute MI model and, thus, improves cardiac function. Concurrently, BMSCs-Exo overexpressed the lncRNA-NEAT1 by MIF treatment which had anti-aging effects on Dox-induced cardiomyopathy (DIC). On the contrary, silencing lncRNA-NEAT1 inhibited the effect of Exo on DIC^{MIF}, and this is because Exo^{MIF} attenuates cardiomyocyte senescence induced by Dox *via* the Exo/lncRNA-NEAT1↑/miR-221-3p↓/sirtuin 2 (SIRT2)↑ pathway (Zhuang et al., 2020). These findings provide an important reference on how to improve the role of lncRNAs.

ADMSCs-exo-lncRNAs reverse cardiomyocyte senescence and apoptosis and promote nerve repair after stroke

ADMSCs are easily obtained from adipose tissue (Shafei et al., 2018), and the Exo in supernatant enhances

angiogenesis (Almeria et al., 2019). Xia et al. (Xia et al., 2020) observed that hypoxia-induced ADMSCs-Exo-lncRNA-MALAT1 improves mitochondrial metabolism by regulating the miR-92a-3p↓/autophagy related genes 4a (ATG4a)↑ axis. Also, miR-92A-3p plays a cardioprotective role in DIC. ADMSCs-Exo-lncRNA-SNHG9 modulates inflammation by inhibiting endothelial cell apoptosis *via* the nuclear factor kappa-B (NF-κB)↓/TNF receptor type 1-associated death domain protein (TRADD)↓ pathway (Song et al., 2020). ADMSCs-Exo-lncRNA-SNHG9 is a potential therapeutic target for CVDs related to lipid metabolism and, thus, for AS treatment. In addition, MIF treatment induces the overexpression of lncRNA-NEAT1 in ADMSC-Exo which could prevent cardiomyocyte apoptosis induced by H_2O_2 *via* the lncRNA-NEAT1↑/miR-142-3p↓/Forkhead box O1 (FOXO1)↑ pathway. Also, lncRNA-NEAT1 can regulate oxidative stress and protect against neural injury (Chen H. et al., 2020), providing a new signaling pathway target for improving MI therapy.

On the other hand, given their unique self-renewal and differentiation abilities, stem cells have been designed to treat stroke (Chen H.-X. et al., 2020; Singh et al., 2020). Improving neural repair and recovery in the postacute phase of stroke may reduce the overall long-term burden of stroke (Murie-Fernández and Marzo, 2020). El Bassit et al. (El Bassit et al., 2016) revealed that human ADMSCs-Exo increases the expression of protein kinase CδII (PKCδII) on immortalized mouse hippocampal cell line (HT22) after injury and promotes the survival and proliferation of neurons. lncRNA-MALAT1 promotes alternative splicing of PKCδII, which increases the survival of neurons by inducing the recruitment of serine-arginine-rich splicing factor 2 (SRSF2). Meanwhile, insulin could further enhance the effect with lncRNA-MALAT1 application. Stroke treatment may be improved as a result of this research.

UCMSCs-exo-lncRNAs ameliorate the H/R and myocardial aging injury

UCMSCs have been exploited for treating CVDs and depend on paracrine effect (Chen et al., 2021b; Chang et al., 2021). For instance, human UCMSCs (hUCMSCs)-Exo prevents the apoptosis of cardiomyocytes and promotes tubular formation and migration of umbilical vein endothelial cells (Zhao et al., 2015). At the same time, hUCMSCs-Exo-lncRNA-UCA1 enhances the proliferation, invasion, migration of cardiac microvascular endothelial cells (CMECs) and inhibits the apoptosis and autophagy of CMECs caused by H/R *via* the miR143↓/B-cell lymphoma-2 (Bcl-2)↑/Beclin-1↓ axis (Diao and Zhang, 2021). Furthermore, Zhu et al. (Zhu et al., 2019) reported that among the lncRNAs that may possess anti-aging properties, only lncRNA-MALAT1 is highly expressed in Exo. HUCMSCs-Exo-lncRNA-MALAT1 can prevent cardiac dysfunction arising from aging through the NF-κB/tumor necrosis factor (TNF-α)↓ pathway. Meanwhile, lncRNA-MALAT1 silencing significantly reduces the anti-aging effect of Exo.

Exo-lncRNAs from PMSCs affect acute MI

Death of many cardiomyocytes causes strong inflammation after MI, and studies have shown that intestinal microflora participates in the occurrence of this kind of inflammation (Wang et al., 2018; Zununi Vahed et al., 2018). (Yang et al., 2022) pointed out that PMSCs-Exo shows angiogenesis and anti-inflammatory potential in the cell therapy of MI and regulates the intestinal microflora. Gene ontology enrichment analysis of the PMSCs-Exo-lncRNA target gene revealed that lncRNA performs numerous functions at the transcriptional level, suggesting that PMSCs-Exo-lncRNA is a potential target for MI therapy.

Exo-lncRNAs from GMSCs protect nerves in retina I/R

GMSCs which not only show the potential for self-renewal and multi-differentiation but also have immunomodulatory, anti-inflammatory, and effective tissue regeneration properties can easily be obtained from gum tissues (Liu et al., 2015; Al-Qadhi et al., 2021). MiR-21-5p overexpressed in TNF-α-stimulated GMSCs-Exo which reduces inflammation and death of mouse primary retinal ganglion cells and microglia simultaneously. Vitreous injection of GMSCs-Exo alleviated retinal I/R injury in mice induced by high intraocular pressure *via* the Exo-lncRNA-MEG3↑/miR-21-5p↑ axis (Yu et al., 2022). This is a potential target for glaucoma treatment and other retinal neuroinflammatory diseases.

CVPCs-exo-lncRNAs and EPCs as theranostic strategies for CVDs

CVPCs-Exo injected into the myocardium significantly improved the cardiac function of mice with acute MI. Moreover, overexpression of lncRNA-MALAT1 in hypoxic preconditioning Exo increases the viability of neonatal rat cardiomyocytes (NRCMs) damaged by oxygen and glycogen deprivation, and lncRNA-MALAT1 gene knockout inhibits tubular formation of human umbilical endothelial cells (HUVECs) promoted by CVPCs-Exo. In addition, lncRNA-MALAT1 improved the survival of NRCMs and HUVECs' formation by targeting miR-497 (Wu et al., 2020). Therefore, hypoxic preconditioning CVPCs-Exo could be used for treating MI with high lncRNA expression and promise option for cardiac repair. However, more basic research is required to understand their mechanism of action (Zhang et al., 2016).

On the other hand, hypertension induces autophagy due to the pressure on the vascular wall to maintain intracellular stability, and the reduction in autophagy causes angiotensin II (AngII)-induced senescence and damage to EPCs (Bianconi et al., 2018). EPCs-Exo-lncRNA-p21 can activate the sestrin 2 (SESN2)/AMP-activated protein kinase (AMPK)/tuberous sclerosis 2 (TSC2) pathway and enhance autophagy to prevent AngII-induced EPCs injury by promoting the transcriptional activity of p53 (Li C. et al., 2021). Meanwhile, stimulation of EPCs using niacinamide phosphoribosyltransferase upregulates the expression of SIRT1 and SIRT1 antisense long non-coding RNA (SIRT1 AS lncRNA). This overexpression of SIRT1 AS lncRNA in EPCs upregulates that of SIRT1, and inhibiting miR-22 abrogated the aging of EPCs and promoted the proliferation and migration of EPCs (Ming et al., 2016). In addition, regarding the clinically upregulated expression of lncRNA GUSBP5-AS (Enst00000511042) in EPCs of deep venous thrombosis patients, Sun et al. (Sun L.-L. et al., 2020, 1) revealed that lncRNA GUSBP5-AS regulates the expression of fibroblast growth factor 2 and matrix metalloproteinase 2/9 through the miR-223-3p↓/FOXO1/AKT↑ pathway and subsequently regulates angiogenesis, as well as proliferation and homing capacity of EPCs. Therefore, EPCs-Exo-lncRNA is a potential therapeutic target for vascular endothelial repair.

Exo-lncRNA from other sources as potential target lncRNAs for CVDs

Stem cell-derived Exo-lncRNA has shown excellent potential in treating CVDs. In fact, several Exo-lncRNAs which are contained in something else can also treat CVDs. For instance, Exo-lncRNA-RNCR3 in HUVECs which could regulates the dysfunction of endothelial cells and vascular smooth muscle cells (VSMCs) by targeting the miR-185-5p↓/kruppel-like factor (KLF)2↑ axis (Shan et al., 2016), highly expressed Exo-LINC01005 of ox-LDL-treated HUVECs which could regulate the miR-128-3p↓/KLF4↑ axis to promote the proliferation and migration of VSMCs (Zhang Z. et al., 2020), and the lncRNA-GAS5 derived from human acute monocytic leukemic cell line (THP-1) which could reduce the apoptosis of HUVECs *via* up-regulated the expressions of P53, Caspase 3, Caspase 7 and Caspase 9 (Chen et al., 2017) all participate in the occurrence and development of AS. Otherwise, Exo-lncRNA-ZRAS1 from human cardiomyocytes which could promote cardiac fibrosis *via* the miR-4711-5p↓/Wnt4/β-catenin↑ signaling pathway (Wang et al., 2021), hypoxia-induced cardiac myocytes (CMs) overexpressing Exo-lncRNA-AK139128 which could inhibit cardiac fibroblasts (CFs) proliferation and migration, elevates CFs apoptosis *via* increased level of Bcl-2 while decreased expression of Bax (Wang and Zhang, 2020), Exo-LINC00174 with high expression in endothelial cells which could inhibit apoptosis, vacuole, and autophagy of CMs *via* the SRSF1↑/p53↓/myocardin↓/AKT/AMPK↓ signaling pathway (Su et al., 2021) and Exo-lncRNA-ANRIL expression increased in CMECs treated with indoxyl sulfate which could be absorbed by CMs to increase autophagy, whereas recombinant autophagy-related gene 5 (ATG5) expression can be reduced in CMs by silencing ANRIL or upregulating miR-181b, thereby reversing the autophagy of CMs in uremic mice (Xu et al., 2021, 5) provide reference for the intervention of MI in order to obtain good therapeutic effect. Moreover, under hypoxia conditions, AC16 CMs express a high level of lncRNA-HCG15, which stimulates apoptosis, releases inflammatory factors, inhibits cell proliferation, and aggravates I/R injury in C57BL/6 J mice *via* the NF-κB/p65↑ and p38↑ pathways (Lin et al., 2021). Together, studies such as these could provide a new direction for early diagnosis and targeted treatment of CVDs.

Challenges in the applications of stem cell-derived Exo-lncRNA

Notably, there are several challenges in the applications of stem cell-derived Exo-lncRNA (Figure 2). The serum levels of lncRNA-LUNAR1 in patients with chronic total coronary occlusion are closely related to the development of coronary blood supply and collateral (Lu et al., 2020). Nevertheless, the causal relationship and whether it can be used as a treatment remains unclear. In addition, Further studies are needed to evaluate the clinical efficacy and safety of lncRNAs in CVDs, as well as their potential downstream targets (including different cell types and pathways), mechanisms of action and potential risks (such as off-target effects) (Dong et al., 2019; Braga et al., 2020; Chen et al., 2021a). At present, the standard procedure for purification of Exo or lncRNAs needs to be optimized if these molecules are to be applied in clinical treatment (Ma et al., 2019; Zhang W. et al., 2020). Meanwhile, the cell factory approaches for Exo simulations with specific miRs and lncRNAs in the self environment may be an alternative strategy to overcome the limitations of stability and potential immunogenicity (Rotini et al., 2018). In recent years of membrane-based delivery systems (such as erythrocyte, the advantage membranes) over nanoparticle drugs have been extensively demonstrated (Sun et al., 2019; Zhu et al., 2022). Consequently, the foundation is laid for developing lncRNA drug delivery systems for CVDs that are more stable and targeted. In addition, The separation rate of UCMSCs-Exo using tangential flow filtration (TFF) is 92.5 times more efficient than using the ultracentrifuge (UC)-based conventional method (Kim et al., 2021). TFF can therefore be used for mass purification of Exo-lncRNAs. Remarkably, lncRNA sequences in the published

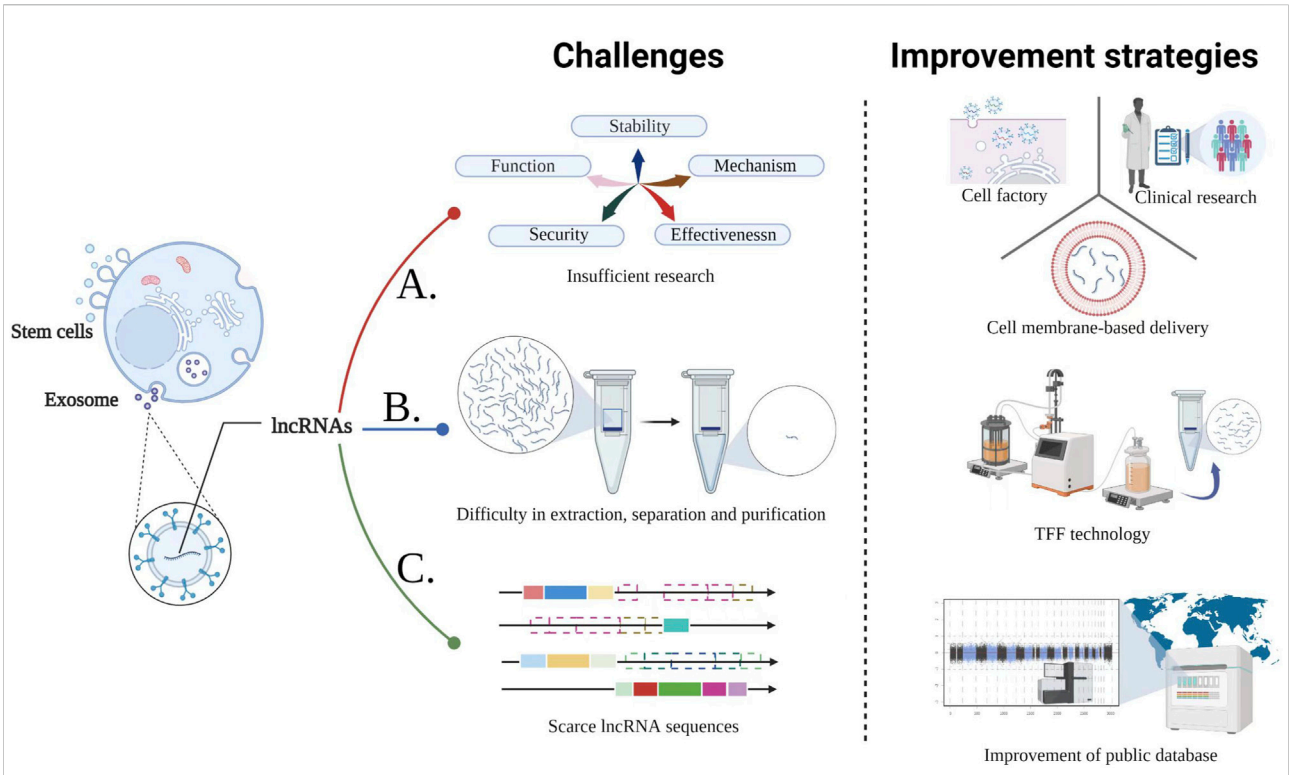

FIGURE 2
Challenges in the CVDs treatment with stem cell-derived Exo-lncRNA and the corresponding improvement strategies. A. The following three methods provide guidance for overcoming the deficiencies in studies related to the function, mechanism, stability, safety, and effectiveness of stem cell-derived Exo-lncRNA; B. TFF technology is efficient for large-scale production of lncRNA; C. Eatablishing and improving public databases will assist in solving the limitations of scarce lncRNA sequences, reducing confusion and improving convenience.

studies are scarce, and not all studies provide chromosome mapping. To minimize confusion and to facilitate the use and replication of data, more details should be provided (i.e. publicly public databases for lncRNA sequence data is needed) (Uchida and Dimmeler, 2015). Significantly, research has revealed dysregulated expression of 768 lncRNAs in the plasma of patients with MI (Lu and Thum, 2019). RNA sequencing data of epicardial adipose tissue collected from 6 atrial fibrillation, and 6 sinus rhythm showed that eight lncRNAs including LINC00694 are closely related to TNF-α signaling pathways demonstrating their broad application potential. Aside from biomedical functions, Exo-lncRNA delivery systems have a greater proliferation of targets than antibodies or small molecules, due to their proximity and tissue specificity, resulting in fewer off-targets of lncRNAs/miRs (Huang Y. et al., 2020, Huang et al., 2020 C.-K.; Zhao et al., 2020). Even though lncRNA is infant in clinical applications, it appears that it has substantial potential in this aspect, considering the clinical cases of miRs which utilize inhibitors and are delivered by endothelial microparticles delivery (Barwari et al., 2016; Nakaoka et al., 2018; Täubel et al., 2021). At present, although the specific differences of Exo-lncRNAs in stem cells from different sources are not clear, however, given ADMSC has extremely abundant yield, inhibits the growth of cancer *in vivo* and is less affected by aging, doubling quantity, and other negative factors, and ADMSC-Exo with exogenous factors has great therapeutic effects (Maguire, 2019; Shin et al., 2021). So going forward, ADMSCs-Exo-lncRNA will stand out in the clinical translation of CVDs treatment. In conclusion, these results are sufficient evidence that lncRNA can be applieed for a broad range of clinical diagnoses and applications.

Conclusion

Exo-lncRNA-based therapeutic strategies is novel but still in infancy. Nevertheless, the recent developments of Exo-lncRNA in CVDs have demonstrated their superior properties for early diagnosis and targeted therapy, thereby promoting the potential transition from bench to bedside. Presently, stem cell-derived

Exo-lncRNAs are gradually reducing their application limitations as technology advances, bioinformatics improves, and drug delivery strategies are continuously improved. Hence, these advantages ushered in a new dawn for the clinical application of stem cell-derived Exo-lncRNA. Determining the therapeutic efficacy and safety of Exo-lncRNA can accelerate their use for treating CVDs.

Author contributions

DS and LJ contributed to the conception of this review. JM, PL, and XY analyzed the literature and wrote the manuscript. QY, BP, YF, and JM completed the figure drawings. DS, JM, and PL revised the manuscript. All authors have read and agreed to the published version of the manuscript.

Funding

This work was supported by the National Natural Science Foundation of China (Nos. 51901160 and 81873466), Natural Science Foundation of Zhejiang Province (No. LY22H020005), Start-up funding from WIUCAS (No. wiucasqd2021017), Basic Scientific Research Foundation of Wenzhou Medical University (No. KYYW201907) and the Wenzhou Science and Technology Bureau (No. Y2020201) fund.

Conflict of interest

The authors declare that the research was conducted in the absence of any commercial or financial relationships that could be construed as a potential conflict of interest.

Publisher's note

All claims expressed in this article are solely those of the authors and do not necessarily represent those of their affiliated organizations, or those of the publisher, the editors and the reviewers. Any product that may be evaluated in this article, or claim that may be made by its manufacturer, is not guaranteed or endorsed by the publisher.

References

Afzal, M. R., Samanta, A., Shah, Z. I., Jeevanantham, V., Abdel-Latif, A., Zuba-Surma, E. K., et al. (2015). Adult bone marrow cell therapy for ischemic heart disease: Evidence and insights from randomized controlled trials. *Circ. Res.* 117, 558–575. doi:10.1161/CIRCRESAHA.114.304792

Al-Qadhi, G., Aboushady, I., and Al-Sharabi, N. (2021). The gingiva from the tissue surrounding the bone to the tissue regenerating the bone: A systematic review of the osteogenic capacity of gingival mesenchymal stem cells in preclinical studies. *Stem Cells Int.* 2021, 6698100. doi:10.1155/2021/6698100

Almeria, C., Weiss, R., Roy, M., Tripisciano, C., Kasper, C., Weber, V., et al. (2019). Hypoxia conditioned mesenchymal stem cell-derived extracellular vesicles induce increased vascular tube formation *in vitro*. *Front. Bioeng. Biotechnol.* 7, 292. doi:10.3389/fbioe.2019.00292

Barnabé, G. F., Schwindt, T. T., Calcagnotto, M. E., Motta, F. L., Martinez, G., de Oliveira, A. C., et al. (2009). Chemically-induced rat mesenchymal stem cells adopt molecular properties of neuronal-like cells but do not have basic neuronal functional properties. *PLoS ONE* 4, e5222. doi:10.1371/journal.pone.0005222

Barwari, T., Joshi, A., and Mayr, M. (2016). MicroRNAs in cardiovascular disease. *J. Am. Coll. Cardiol.* 68, 2577–2584. doi:10.1016/j.jacc.2016.09.945

Bianconi, V., Sahebkar, A., Kovanen, P., Bagaglia, F., Ricciuti, B., Calabrò, P., et al. (2018). Endothelial and cardiac progenitor cells for cardiovascular repair: A controversial paradigm in cell therapy. *Pharmacol. Ther.* 181, 156–168. doi:10.1016/j.pharmthera.2017.08.004

Braga, L., Ali, H., Secco, I., and Giacca, M. (2020). Non-coding RNA therapeutics for cardiac regeneration. *Cardiovasc. Res.* 117, 674–693. doi:10.1093/cvr/cvaa071

Cao, X., Xue, L.-D., Di, Y., Li, T., Tian, Y.-J., and Song, Y. (2021). MSC-derived exosomal lncRNA SNHG7 suppresses endothelial-mesenchymal transition and tube formation in diabetic retinopathy via miR-34a-5p/XBP1 axis. *Life Sci.* 272, 119232. doi:10.1016/j.lfs.2021.119232

Chang, D., Fan, T., Gao, S., Jin, Y., Zhang, M., and Ono, M. (2021). Application of mesenchymal stem cell sheet to treatment of ischemic heart disease. *Stem Cell Res. Ther.* 12, 384. doi:10.1186/s13287-021-02451-1

Chen, H.-X., Liang, F.-C., Gu, P., Xu, B.-L., Xu, H.-J., Wang, W.-T., et al. (2020b). Exosomes derived from mesenchymal stem cells repair a Parkinson's disease model by inducing autophagy. *Cell Death Dis.* 11, 288. doi:10.1038/s41419-020-2473-5

Chen, H., Xia, W., and Hou, M. (2020a). LncRNA-NEAT1 from the competing endogenous RNA network promotes cardioprotective efficacy of mesenchymal stem cell-derived exosomes induced by macrophage migration inhibitory factor via the miR-142-3p/FOXO1 signaling pathway. *Stem Cell Res. Ther.* 11, 31. doi:10.1186/s13287-020-1556-7

Chen, L., Yang, W., Guo, Y., Chen, W., Zheng, P., Zeng, J., et al. (2017). Exosomal lncRNA GAS5 regulates the apoptosis of macrophages and vascular endothelial cells in atherosclerosis. *PloS One* 12, e0185406. doi:10.1371/journal.pone.0185406

Chen, Y., Li, Z., Chen, X., and Zhang, S. (2021a). Long non-coding RNAs: From disease code to drug role. *Acta Pharm. Sin. B* 11, 340–354. doi:10.1016/j.apsb.2020.10.001

Chen, Y., Shen, H., Ding, Y., Yu, Y., Shao, L., and Shen, Z. (2021b). The application of umbilical cord-derived MSCs in cardiovascular diseases. *J. Cell. Mol. Med.* 25, 8103–8114. doi:10.1111/jcmm.16830

Deng, M., Yuan, H., Liu, S., Hu, Z., and Xiao, H. (2019). Exosome-transmitted LINC00461 promotes multiple myeloma cell proliferation and suppresses apoptosis by modulating microRNA/BCL-2 expression. *Cytotherapy* 21, 96–106. doi:10.1016/j.jcyt.2018.10.006

Diao, L., and Zhang, Q. (2021). Transfer of lncRNA UCA1 by hUCMSCs-derived exosomes protects against hypoxia/reoxygenation injury through impairing miR-143-targeted degradation of Bcl-2. *Aging* 13, 5967–5985. doi:10.18632/aging.202520

Dong, R., Liu, Y., Yang, Y., Wang, H., Xu, Y., and Zhang, Z. (2019). MSC-derived exosomes-based therapy for peripheral nerve injury: A novel therapeutic strategy. *Biomed. Res. Int.* 2019, 6458237. doi:10.1155/2019/6458237

El Bassit, G., Patel, R. S., Carter, G., Shibu, V., Patel, A. A., Song, S., et al. (2016). MALAT1 in human adipose stem cells modulates survival and alternative splicing of PKCδII in HT22 cells. *Endocrinology* 158, 183–195. doi:10.1210/en.2016-1819

Elshaer, S. L., Evans, W., Pentecost, M., Lenin, R., Periasamy, R., Jha, K. A., et al. (2018). Adipose stem cells and their paracrine factors are therapeutic for early retinal complications of diabetes in the Ins2Akita mouse. *Stem Cell Res. Ther.* 9, 322. doi:10.1186/s13287-018-1059-y

Gao, Y., and Jin, S.-Z. (2020). Strategies for treating oesophageal diseases with stem cells. *World J. Stem Cells* 12, 488–499. doi:10.4252/wjsc.v12.i6.488

Hu, X., Xu, Y., Zhong, Z., Wu, Y., Zhao, J., Wang, Y., et al. (2016). A large-scale investigation of hypoxia-preconditioned allogeneic mesenchymal stem cells for myocardial repair in nonhuman primates: Paracrine activity without remuscularization. *Circ. Res.* 118, 970–983. doi:10.1161/CIRCRESAHA.115.307516

Huang, C.-K., Kafert-Kasting, S., and Thum, T. (2020a). Preclinical and clinical development of noncoding RNA therapeutics for cardiovascular disease. *Circ. Res.* 126, 663–678. doi:10.1161/CIRCRESAHA.119.315856

Huang, P., Wang, L., Li, Q., Tian, X., Xu, J., Xu, J., et al. (2020b). Atorvastatin enhances the therapeutic efficacy of mesenchymal stem cells-derived exosomes in acute myocardial infarction via up-regulating long non-coding RNA H19. *Cardiovasc. Res.* 116, 353–367. doi:10.1093/cvr/cvz139

Huang, Y. (2020). Exosomal lncRNAs from mesenchymal stem cells as the novel modulators to cardiovascular disease. *Stem Cell Res. Ther.* 11, 315. doi:10.1186/s13287-020-01812-6

Huang, Y., Li, R., Ye, S., Lin, S., Yin, G., and Xie, Q. (2020c). Recent advances in the use of exosomes in Sjögren's syndrome. *Front. Immunol.* 11, 1509. doi:10.3389/fimmu.2020.01509

Hui, Z., Zhanwei, W., Xi, Y., Jin, L., Jing, Z., and Shuwen, H. (2020). Construction of ceRNA coexpression network and screening of molecular targets in colorectal cancer. *Dis. Markers* 2020, 2860582. doi:10.1155/2020/2860582

Jain, R., Awal, H., and Sen, S. (2020). Using adult stem cells to monitor endothelial dysfunction in diabetes mellitus. *J. Diabetes Complicat.* 34, 107588. doi:10.1016/j.jdiacomp.2020.107588

Kim, J. Y., Rhim, W.-K., Yoo, Y.-I., Kim, D.-S., Ko, K.-W., Heo, Y., et al. (2021). Defined MSC exosome with high yield and purity to improve regenerative activity. *J. Tissue Eng.* 12, 1–15. doi:10.1177/20417314211008626

Li, B., Xu, H., Han, H., Song, S., Zhang, X., Ouyang, L., et al. (2018). Exosome-mediated transfer of lncRUNX2-AS1 from multiple myeloma cells to MSCs contributes to osteogenesis. *Oncogene* 37, 5508–5519. doi:10.1038/s41388-018-0359-0

Li, C., Lin, L., Zhang, L., Xu, R., Chen, X., Ji, J., et al. (2021a). Long noncoding RNA p21 enhances autophagy to alleviate endothelial progenitor cells damage and promote endothelial repair in hypertension through SESN2/AMPK/TSC2 pathway. *Pharmacol. Res.* 173, 105920. doi:10.1016/j.phrs.2021.105920

Li, J., Yang, Y., Fan, J., Xu, H., Fan, L., Li, H., et al. (2019). Long noncoding RNA ANCR inhibits the differentiation of mesenchymal stem cells toward definitive endoderm by facilitating the association of PTBP1 with ID2. *Cell Death Dis.* 10, 492. doi:10.1038/s41419-019-1738-3

Li, K.-S., Bai, Y., Li, J., Li, S.-L., Pan, J., Cheng, Y.-Q., et al. (2021b). LncRNA HCP5 in hBMSC-derived exosomes alleviates myocardial ischemia reperfusion injury by sponging miR-497 to activate IGF1/PI3K/AKT pathway. *Int. J. Cardiol.* 342, 72–81. doi:10.1016/j.ijcard.2021.07.042

Li, N., Yang, Y.-J., Qian, H.-Y., Li, Q., Zhang, Q., Li, X.-D., et al. (2015). Intravenous administration of atorvastatin-pretreated mesenchymal stem cells improves cardiac performance after acute myocardial infarction: Role of CXCR4. *Am. J. Transl. Res.* 7, 1058–1070.

Lin, B., Chen, X., Lu, C., Xu, J., Qiu, Y., Liu, X., et al. (2021). Loss of exosomal LncRNA HCG15 prevents acute myocardial ischemic injury through the NF-κB/p65 and p38 pathways. *Cell Death Dis.* 12, 1007. doi:10.1038/s41419-021-04281-8

Liu, C., Du, L., Wang, S., Kong, L., Zhang, S., Li, S., et al. (2021). Differences in the prevention and control of cardiovascular and cerebrovascular diseases. *Pharmacol. Res.* 170, 105737. doi:10.1016/j.phrs.2021.105737

Liu, J., Yu, F., Sun, Y., Jiang, B., Zhang, W., Yang, J., et al. (2015). Concise reviews: Characteristics and potential applications of human dental tissue-derived mesenchymal stem cells. *Stem Cells* 33, 627–638. doi:10.1002/stem.1909

Liu, W., Rong, Y., Wang, J., Zhou, Z., Ge, X., Ji, C., et al. (2020a). Exosome-shuttled miR-216a-5p from hypoxic preconditioned mesenchymal stem cells repair traumatic spinal cord injury by shifting microglial M1/M2 polarization. *J. Neuroinflammation* 17, 47. doi:10.1186/s12974-020-1726-7

Liu, X., Li, X., Zhu, W., Zhang, Y., Hong, Y., Liang, X., et al. (2020b). Exosomes from mesenchymal stem cells overexpressing MIF enhance myocardial repair. *J. Cell. Physiol.* 235, 8010–8022. doi:10.1002/jcp.29456

Lu, D., and Thum, T. (2019). RNA-based diagnostic and therapeutic strategies for cardiovascular disease. *Nat. Rev. Cardiol.* 16, 661–674. doi:10.1038/s41569-019-0218-x

Lu, W., Sheng, Z., Zhang, Z., Ma, G., Chen, L., Huang, J., et al. (2020). LncRNA-LUNAR1 levels are closely related to coronary collaterals in patients with chronic total coronary occlusion. *J. Cardiovasc. Transl. Res.* 13, 171–180. doi:10.1007/s12265-019-09917-x

Luo, F., Wang, T., Zeng, L., Zhu, S., Cao, W., Wu, W., et al. (2018). Diagnostic potential of circulating LncRNAs in human cardiovascular disease: A meta-analysis. *Biosci. Rep.* 38, BSR20181610. doi:10.1042/BSR20181610

Ma, R., Zhao, Y., He, M., Zhao, H., Zhang, Y., Zhou, S., et al. (2019). Identifying a ten-microRNA signature as a superior prognosis biomarker in colon adenocarcinoma. *Cancer Cell Int.* 19, 360. doi:10.1186/s12935-019-1074-9

Maguire, G. (2019). The safe and efficacious use of secretome from fibroblasts and adipose-derived (but not bone marrow-derived) mesenchymal stem cells for skin therapeutics. *J. Clin. Aesthet. Dermatol.* 12, E57–E69.

Mao, Q., Liang, X.-L., Zhang, C.-L., Pang, Y.-H., and Lu, Y.-X. (2019). LncRNA KLF3-AS1 in human mesenchymal stem cell-derived exosomes ameliorates pyroptosis of cardiomyocytes and myocardial infarction through miR-138-5p/Sirt1 axis. *Stem Cell Res. Ther.* 10, 393. doi:10.1186/s13287-019-1522-4

Ming, G.-F., Wu, K., Hu, K., Chen, Y., and Xiao, J. (2016). NAMPT regulates senescence, proliferation, and migration of endothelial progenitor cells through the SIRT1 AS lncRNA/miR-22/SIRT1 pathway. *Biochem. Biophys. Res. Commun.* 478, 1382–1388. doi:10.1016/j.bbrc.2016.08.133

Murie-Fernández, M., and Marzo, M. M. (2020). Predictors of neurological and functional recovery in patients with moderate to severe ischemic stroke: The EPICA study. *Stroke Res. Treat.* 2020, 1419720. doi:10.1155/2020/1419720

Nakaoka, H., Hirono, K., Yamamoto, S., Takasaki, I., Takahashi, K., Kinoshita, K., et al. (2018). MicroRNA-145-5p and microRNA-320a encapsulated in endothelial microparticles contribute to the progression of vasculitis in acute Kawasaki Disease. *Sci. Rep.* 8, 1016. doi:10.1038/s41598-018-19310-4

Pan, Y., Zhang, Y., Liu, W., Huang, Y., Shen, X., Jing, R., et al. (2019). LncRNA H19 overexpression induces bortezomib resistance in multiple myeloma by targeting MCL-1 via miR-29b-3p. *Cell Death Dis.* 10, 106. doi:10.1038/s41419-018-1219-0

Pham, T. P., and Boon, R. A. (2020). Exosomes and non-coding RNA, the healers of the heart? *Cardiovasc. Res.* 116, 258–259. doi:10.1093/cvr/cvz190

Rentrop, K. P., and Feit, F. (2015). Reperfusion therapy for acute myocardial infarction: Concepts and controversies from inception to acceptance. *Am. Heart J.* 170, 971–980. doi:10.1016/j.ahj.2015.08.005

Rotini, A., Martínez-Sarrà, E., Pozzo, E., and Sampaolesi, M. (2018). Interactions between microRNAs and long non-coding RNAs in cardiac development and repair. *Pharmacol. Res.* 127, 58–66. doi:10.1016/j.phrs.2017.05.029

Schmidt, A. M. (2019). Diabetes mellitus and cardiovascular disease. *Arterioscler. Thromb. Vasc. Biol.* 39, 558–568. doi:10.1161/ATVBAHA.119.310961

Shafei, A. E.-S., Ali, M. A., Ghanem, H. G., Shehata, A. I., Abdelgawad, A. A., Handal, H. R., et al. (2018). Mechanistic effects of mesenchymal and hematopoietic stem cells: New therapeutic targets in myocardial infarction. *J. Cell. Biochem.* 119, 5274–5286. doi:10.1002/jcb.26637

Shan, K., Jiang, Q., Wang, X.-Q., Wang, Y.-N.-Z., Yang, H., Yao, M.-D., et al. (2016). Role of long non-coding RNA-RNCR3 in atherosclerosis-related vascular dysfunction. *Cell Death Dis.* 7, e2248. doi:10.1038/cddis.2016.145

Shen, H., Zhou, E., Wei, X., Fu, Z., Niu, C., Li, Y., et al. (2015). High density lipoprotein promotes proliferation of adipose-derived stem cells via S1P1 receptor and Akt, ERK1/2 signal pathways. *Stem Cell Res. Ther.* 6, 95. doi:10.1186/s13287-015-0090-5

Shin, S., Lee, J., Kwon, Y., Park, K.-S., Jeong, J.-H., Choi, S.-J., et al. (2021). Comparative Proteomic analysis of the mesenchymal stem cells secretome from adipose, bone marrow, placenta and Wharton's jelly. *Int. J. Mol. Sci.* 22, E845. doi:10.3390/ijms22020845

Singh, M., Pandey, P. K., Bhasin, A., Padma, M. V., and Mohanty, S. (2020). Application of stem cells in stroke: A multifactorial approach. *Front. Neurosci.* 14, 473. doi:10.3389/fnins.2020.00473

Song, Y., Li, H., Ren, X., Li, H., and Feng, C. (2020). SNHG9, delivered by adipocyte-derived exosomes, alleviates inflammation and apoptosis of endothelial cells through suppressing TRADD expression. *Eur. J. Pharmacol.* 872, 172977. doi:10.1016/j.ejphar.2020.172977

South, A. M., Shaltout, H. A., Washburn, L. K., Hendricks, A. S., Diz, D. I., and Chappell, M. C. (2019). Fetal programming and the angiotensin-(1–7) axis: A review of the experimental and clinical data. *Clin. Sci.* 133, 55–74. doi:10.1042/CS20171550

Stefanini, G. G., and Holmes, D. R. (2013). Drug-eluting coronary-artery stents. *N. Engl. J. Med.* 368, 254–265. doi:10.1056/NEJMra1210816

Su, Q., Lv, X.-W., Xu, Y.-L., Cai, R.-P., Dai, R.-X., Yang, X.-H., et al. (2021). Exosomal LINC00174 derived from vascular endothelial cells attenuates myocardial I/R injury via p53-mediated autophagy and apoptosis. *Mol. Ther. Nucleic Acids* 23, 1304–1322. doi:10.1016/j.omtn.2021.02.005

Sun, D., Chen, J., Wang, Y., Ji, H., Peng, R., Jin, L., et al. (2019). Advances in refunctionalization of erythrocyte-based nanomedicine for enhancing cancer-targeted drug delivery. *Theranostics* 9, 6885–6900. doi:10.7150/thno.36510

Sun, L.-L., Lei, F.-R., Jiang, X.-D., Du, X.-L., Xiao, L., Li, W.-D., et al. (2020b). LncRNA GUSBP5-AS promotes EPC migration and angiogenesis and deep vein thrombosis resolution by regulating FGF2 and MMP2/9 through the miR-223-3p/FOXO1/Akt pathway. *Aging* 12, 4506–4526. doi:10.18632/aging.102904

Sun, L., Zhu, W., Zhao, P., Wang, Q., Fan, B., Zhu, Y., et al. (2020a). Long noncoding RNA UCA1 from hypoxia-conditioned hMSC-derived exosomes: A

novel molecular target for cardioprotection through miR-873-5p/XIAP axis. *Cell Death Dis.* 11, 696. doi:10.1038/s41419-020-02783-5

Täubel, J., Hauke, W., Rump, S., Viereck, J., Batkai, S., Poetzsch, J., et al. (2021). Novel antisense therapy targeting microRNA-132 in patients with heart failure: Results of a first-in-human phase 1b randomized, double-blind, placebo-controlled study. *Eur. Heart J.* 42, 178–188. doi:10.1093/eurheartj/ehaa898

Terashvili, M., and Bosnjak, Z. J. (2019). Stem cell therapies in cardiovascular disease. *J. Cardiothorac. Vasc. Anesth.* 33, 209–222. doi:10.1053/j.jvca.2018.04.048

Thum, T., and Condorelli, G. (2015). Long noncoding RNAs and microRNAs in cardiovascular pathophysiology. *Circ. Res.* 116, 751–762. doi:10.1161/CIRCRESAHA.116.303549

Uchida, S., and Dimmeler, S. (2015). Long noncoding RNAs in cardiovascular diseases. *Circ. Res.* 116, 737–750. doi:10.1161/CIRCRESAHA.116.302521

Wang, L., and Zhang, J. (2020). Exosomal lncRNA AK139128 derived from hypoxic cardiomyocytes promotes apoptosis and inhibits cell proliferation in cardiac fibroblasts. *Int. J. Nanomedicine* 15, 3363–3376. doi:10.2147/IJN.S240660

Wang, X., Guo, Z., Ding, Z., and Mehta, J. L. (2018). Inflammation, autophagy, and apoptosis after myocardial infarction. *J. Am. Heart Assoc.* 7, e008024. doi:10.1161/JAHA.117.008024

Wang, Y., Cao, X., Yan, L., Zheng, Y., Yu, J., Sun, F., et al. (2021). Exosome-derived long non-coding RNA ZFAS1 controls cardiac fibrosis in chronic kidney disease. *Aging* 13. doi:10.18632/aging.202599

Wu, Q., Wang, J., Tan, W. L. W., Jiang, Y., Wang, S., Li, Q., et al. (2020). Extracellular vesicles from human embryonic stem cell-derived cardiovascular progenitor cells promote cardiac infarct healing through reducing cardiomyocyte death and promoting angiogenesis. *Cell Death Dis.* 11, 354. doi:10.1038/s41419-020-2508-y

Xia, W., Chen, H., Xie, C., and Hou, M. (2020). Long-noncoding RNA MALAT1 sponges microRNA-92a-3p to inhibit doxorubicin-induced cardiac senescence by targeting ATG4a. *Aging* 12, 8241–8260. doi:10.18632/aging.103136

Xu, Y., Chen, J., Wang, M., Yu, R., Zou, W., and Shen, W. (2021). Mechanism of lncRNA-ANRIL/miR-181b in autophagy of cardiomyocytes in mice with uremia by targeting ATG5. *PloS One* 16, e0256734. doi:10.1371/journal.pone.0256734

Yamanaka, S. (2020). Pluripotent stem cell-based cell therapy-promise and challenges. *Cell Stem Cell* 27, 523–531. doi:10.1016/j.stem.2020.09.014

Yan, Y., Song, D., Song, X., and Song, C. (2020). The role of lncRNA MALAT1 in cardiovascular disease. *IUBMB Life* 72, 334–342. doi:10.1002/iub.2210

Yang, L., Wang, T., Zhang, X., Zhang, H., Yan, N., Zhang, G., et al. (2022). Exosomes derived from human placental mesenchymal stem cells ameliorate myocardial infarction via anti-inflammation and restoring gut dysbiosis. *BMC Cardiovasc. Disord.* 22, 61. doi:10.1186/s12872-022-02508-w

Yu, Z., Wen, Y., Jiang, N., Li, Z., Guan, J., Zhang, Y., et al. (2022). TNF-α stimulation enhances the neuroprotective effects of gingival MSCs derived exosomes in retinal ischemia-reperfusion injury via the MEG3/miR-21a-5p axis. *Biomaterials* 284, 121484. doi:10.1016/j.biomaterials.2022.121484

Yuan, Z., and Huang, W. (2021). New developments in exosomal lncRNAs in cardiovascular diseases. *Front. Cardiovasc. Med.* 8, 709169. doi:10.3389/fcvm.2021.709169

Zhang, J.-K., Zhang, Z., Guo, Z.-A., Fu, Y., Chen, X.-J., Chen, W.-J., et al. (2022a). The BMSC-derived exosomal lncRNA Mir9-3hg suppresses cardiomyocyte ferroptosis in ischemia-reperfusion mice via the Pum2/PRDX6 axis. *Nutr. Metab. Cardiovasc. Dis.* 32, 515–527. doi:10.1016/j.numecd.2021.10.017

Zhang, N., Luo, Y., Zhang, H., Zhang, F., Gao, X., and Shao, J. (2022b). Exosomes derived from mesenchymal stem cells ameliorate the progression of atherosclerosis in ApoE-/- mice via FENDRR. *Cardiovasc. Toxicol.* 22, 528–544. doi:10.1007/s12012-022-09736-8

Zhang, W., Liu, Y., Jiang, J., Tang, Y., Tang, Y., and Liang, X. (2020a). Extracellular vesicle long non–coding RNA-mediated crosstalk in the tumor microenvironment: Tiny molecules, huge roles. *Cancer Sci.* 111, 2726–2735. doi:10.1111/cas.14494

Zhang, Y., Cao, N., Huang, Y., Spencer, C. I., Fu, J.-D., Yu, C., et al. (2016). Expandable cardiovascular progenitor cells reprogrammed from fibroblasts. *Cell Stem Cell* 18, 368–381. doi:10.1016/j.stem.2016.02.001

Zhang, Z., Yi, D., Zhou, J., Zheng, Y., Gao, Z., Hu, X., et al. (2020b). Exosomal LINC01005 derived from oxidized low-density lipoprotein-treated endothelial cells regulates vascular smooth muscle cell phenotypic switch. *Biofactors* 46, 743–753. doi:10.1002/biof.1665

Zhao, Y., Sun, X., Cao, W., Ma, J., Sun, L., Qian, H., et al. (2015). Exosomes derived from human umbilical cord mesenchymal stem cells relieve acute myocardial ischemic injury. *Stem Cells Int.* 2015, 761643. doi:10.1155/2015/761643

Zhao, Z., Sun, W., Guo, Z., Zhang, J., Yu, H., and Liu, B. (2020). Mechanisms of lncRNA/microRNA interactions in angiogenesis. *Life Sci.* 254, 116900. doi:10.1016/j.lfs.2019.116900

Zhu, B., Zhang, L., Liang, C., Liu, B., Pan, X., Wang, Y., et al. (2019). Stem Cell-derived exosomes prevent aging-induced cardiac dysfunction through a novel exosome/lncRNA MALAT1/NF-κB/TNF-α signaling pathway. *Oxid. Med. Cell. Longev.* 2019, 9739258. doi:10.1155/2019/9739258

Zhu, L., Zhong, Y., Wu, S., Yan, M., Cao, Y., Mou, N., et al. (2022). Cell membrane camouflaged biomimetic nanoparticles: Focusing on tumor theranostics. *Mat. Today. Bio* 14, 100228. doi:10.1016/j.mtbio.2022.100228

Zhu, P., Wang, Y., Huang, G., Ye, B., Liu, B., Wu, J., et al. (2016). lnc-β-Catm elicits EZH2-dependent β-catenin stabilization and sustains liver CSC self-renewal. *Nat. Struct. Mol. Biol.* 23, 631–639. doi:10.1038/nsmb.3235

Zhuang, L., Xia, W., Chen, D., Ye, Y., Hu, T., Li, S., et al. (2020). Exosomal LncRNA-NEAT1 derived from MIF-treated mesenchymal stem cells protected against doxorubicin-induced cardiac senescence through sponging miR-221-3p. *J. Nanobiotechnology* 18, 157. doi:10.1186/s12951-020-00716-0

Zununi Vahed, S., Barzegari, A., Zuluaga, M., Letourneur, D., and Pavon-Djavid, G. (2018). Myocardial infarction and gut microbiota: An incidental connection. *Pharmacol. Res.* 129, 308–317. doi:10.1016/j.phrs.2017.11.008

Glossary

ADMSCs Adipocyte mesenchymal stem cells
AKT Protein kinase B
AngII Angiotensin II
AMPK AMP-activated protein kinase
ATG5 autophagy-related gene 5
ASCs Adult stem cells
ATG4a Autophagy related genes 4a
ATV Atorvastatin
Bcl-2 B-cell lymphoma-2
BMSCs Bone marrow mesenchymal stem cells
CMs Cardiac myocytes
CFs Cardiac fibroblasts
CMECs Cardiac microvascular endothelial cells
CVDs Cardiovascular diseases
CVPCs Cardiovascular progenitor cells
DR Diabetic retinopathy
DIC Dox-induced cardiomyopathy
EPCs Endothelial progenitor cells
Exo Exosome
EAT Epicardial adipose tissue
FOXO1 Forkhead box O1
GMSCs Gingival mesenchymal stem cells
HUV-EC-C Human vascular endothelial cells
H/R Hypoxia reperfusion
HRMECs Human retinal microvascular endothelial cells
hUCMSCs Human UCMSCs
KLF Kruppel-like factor
NRCMs Neonatal rat cardiomyocytes
HUVECs Human umbilical endothelial cells
I/R Ischemia-reperfusion
IGF-1 Insulin like growth factor-1
lncRNAs Long non-coding RNAs
MSCs Mesenchymal stem cells
MI Myocardial infarction
MIF Migration inhibitory factor
miR MicroRNA
NF-κB Nuclear factor kappa-B
PMSCs Placental mesenchymal stem cells
Pum2 Pumilio RNA binding family member 2
PI3K phosphatidylinositide 3-kinases
PRDX6 Peroxiredoxin 6
PKCδII Protein kinase CδII
ox-LDL Oxidized low-density lipoprotein
SESN2 Sestrin 2
SIRT1 Sirtuin 1
SIRT2 Sirtuin 2
SRSF2 Serine-arginine-rich splicing factor 2
SIRT1 AS lncRNA SIRT1 antisense long non-coding RNA
TEAD1 TEA domain transcription factor 1
TFF Tangential flow filtration
TNF-α Tumor necrosis factor-α
TSC2 Tuberous sclerosis 2
UC Ultracentrifuge
UCMSCs Umbilical cord mesenchymal stem cells
VSMCs Vascular smooth muscle cells
XIAP X-Linked Inhibitor of Apoptosis Protein
XBP1 X-box binding protein 1

frontiers | Frontiers in Pharmacology

TYPE Review
PUBLISHED 09 September 2022
DOI 10.3389/fphar.2022.1000316

OPEN ACCESS

EDITED BY
Wenjing Qi,
Chongqing Normal University, China

REVIEWED BY
Li Zhang,
Nanchang University, China
Sai Jin Xiao,
East China University of Technology, China

*CORRESPONDENCE
Ping Ping Hu,
huping07@163.com
Xiao Yong Tong,
xiaoyongtong@cqu.edu.cn

SPECIALTY SECTION
This article was submitted to Cardiovascular and Smooth Muscle Pharmacology, a section of the journal Frontiers in Pharmacology

RECEIVED 22 July 2022
ACCEPTED 23 August 2022
PUBLISHED 09 September 2022

CITATION
Hu PP, Luo SX, Fan XQ, Li D and Tong XY (2022), Macrophage-targeted nanomedicine for the diagnosis and management of atherosclerosis. *Front. Pharmacol.* 13:1000316. doi: 10.3389/fphar.2022.1000316

Macrophage-targeted nanomedicine for the diagnosis and management of atherosclerosis

Ping Ping Hu[1]*, Shuang Xue Luo[2], Xiao Qing Fan[3], Di Li[4] and Xiao Yong Tong[2]*

[1]Chongqing Engineering Research Center for Pharmacodynamics Evaluation, College of Pharmacy, Chongqing Medical University, Chongqing, China, [2]School of Pharmaceutical Sciences, Chongqing University, Chongqing, China, [3]Department of Thoracic Surgery, Daping Hospital, Army Medical University, Chongqing, China, [4]Department of Pharmacy, The Second Affiliated Hospital of Chongqing Medical University, Chongqing, China

Atherosclerosis is the primary cause of cardiovascular diseases, such as myocardial infarction and stroke, which account for the highest death toll worldwide. Macrophage is the major contributor to atherosclerosis progression, and therefore, macrophage-associated pathological process is considered an extremely important target for the diagnosis and treatment of atherosclerosis. However, the existing clinical strategies still have many bottlenecks and challenges in atherosclerosis's early detection and management. Nanomedicine, using various nanoparticles/nanocarriers for medical purposes, can effectively load therapeutic agents, significantly improve their stability and accurately deliver them to the atherosclerotic plaques. In this review, we summarized the latest progress of the macrophage-targeted nanomedicine in the diagnosis and treatment of atherosclerosis, and their potential applications and clinical benefits are also discussed.

KEYWORDS

atherosclerosis, macrophage, nanomedicine, diagnostic imaging, therapeutic

Introduction

Atherosclerosis is the principal pathological basis of cardiovascular diseases (CVDs), which is responsible for the dominant cause of morbidity and mortality in the world (Virani et al., 2021). Atherosclerosis is a multifactorial, chronic inflammatory disease (Ross, 1999; Tabas et al., 2007), characterized by dysregulated lipid metabolism and plaque build-up inside the arterial wall (Negre-Salvayre et al., 2020). The genesis of atherosclerotic plaques is triggered by focal areas inflammation of the arterial tree, which is induced by the subendothelial retention of lipoproteins and immune cells. Endothelial cells (ECs) are damaged, the permeability of which increases, and a large amount of cytokines and chemokines are released, facilitating monocyte attachment and infiltration. Monocytes differentiate and mature into macrophages, and secrete inflammatory factors.

Smooth muscle cells (SMCs) in vascular tunica media differentiate to synthetic phenotype and migrate to intima (Que et al., 2020). With the high level of lipidic contents, macrophages and transformed SMCs ingest and accumulate large amounts of modified low-density lipoprotein (LDL), leading to the formation of foam cells and early atherosclerotic plaques (Katakami, 2018). The disintegration of lipid overloaded foam cells leads to the formation of necrosis. When plaques progress, the vessel wall continues to remodel, resulting in arteries thickening and lumen narrowing. Additionally, migrated SMCs proliferate and actively produce extracellular matrix, contributing to the formation of fibrous cap. Once the fibrous cap is broken, causing rupture of vulnerable plaques and acute thrombotic events (Wilson, 2010). There is no specific drug for the treatment of atherosclerosis in clinics. Conventional treatment is mainly based on lifestyle changes in diet and exercise, several drugs are also routinely used, including inhibiting endothelial dysfunction, lowering lipid retention, reducing inflammation and stabilizing plaques. Statins and notable inhibitors of proprotein convertase subtilisin/kexin type 9 (PCSK9) demonstrate great potential in the clearance of cholesterol-containing LDL particles, reducing the incidence of CVD (Forster et al., 2002; Lieb et al., 2018; Dhindsa et al., 2020). However, these medications can only prevent rapid deterioration, and always have potential adverse side effects. For example, statins, the first-line therapy for atherosclerosis, are reported to have liver and muscle toxicity (Maron et al., 2000), and induce depression, headaches, and some other issues with the gastrointestinal system, skin as well as eyes (Kiortsis et al., 2007; Bełtowski et al., 2009). There are also some safety concerns with the employment of cholesterol-lowering drugs in childhood (Chen et al., 2022). Moreover, inflammation is the primary cause of atherogenesis and plaque destabilization, and much effort has been devoted to the development of novel anti-inflammatory drugs, however, the low bioavailability, poor targeting, and high toxicity of which limited their usage clinically.

During the past few decades, the application of nanotechnology for atherosclerosis management has grown exponentially. Nanoparticles/nanocarriers, with dimensions ranging from 1 nm to 100 nm have become an important tool, which demonstrates particular advantages in the improvement of atherosclerosis diagnosis and treatment (Qiao H. et al., 2017; Xiao et al., 2017). By attaching the antibodies, peptides, or aptamers to the surface, nanomaterials are capable of specifically targeting the receptors or structures characterized in atherosclerosis (Shi et al., 2011). The extremely small size allows the nanoparticle products efficiently enter into living systems, including animals and the human body. Extensive studies reveal that nanomaterials possess strong encapsulation performance, which can protect the loaded therapeutic agents, such as small-molecule drugs, antibodies, peptides, and even small interfering RNA (siRNA) as well as microRNA (miRNA), from metabolic deactivation until they are delivered to target sites (Wang et al., 2016; Chen et al., 2022), reduce systemic adverse effects (Rosenblum et al., 2018) and improve pharmacokinetic and stability of the loaded diagnostic agents or therapeutic compounds (Lobatto et al., 2011), compared to systemic administration of the drugs alone. Notably, targeted nanoparticles are unusually designed to constitute imaging agents and improve the delivery of therapeutics to the local inflammatory macrophages of plaques, which is the critical cell type involved in atheroprogression.

In this review, the recent advances of various nanomedicine for molecular imaging, clinical diagnosis and intervention of atherosclerosis were summarized, and the application of macrophages in atherosclerotic plaques targeted nanoparticles were specially highlighted. Additional insights regarding the opportunities and challenges of macrophage-targeted nanotherapy in clinical translation are also discussed herein.

Macrophage biology in atherosclerosis progression

Atherogenesis involves the synergistic interaction between lipid metabolic factors and vascular cell components. Macrophages are one of the most important cells for atherogenesis, and they are critical during every stage of atherosclerosis progression. In the early step of atherosclerosis, activated ECs release chemokines (eg. monocyte chemotactic protein 1, MCP-1) and adhesion molecules (eg., intercellular adhesion molecule 1, ICAM1 and vascular cell adhesion molecule 1, VCAM1), inducing the attachment of monocytes to the arterial vessel wall (Potteaux et al., 2011; Moore et al., 2015). The recruited monocytes then differentiate into macrophages in the local damaged intima and acquire distinct phenotypes under different physiological and pathological stimuli (Hoeksema et al., 2012). M1 is the classical inflammatory macrophage, with the high expression of pro-inflammatory cytokines, and reactive oxygen/nitrogen species (ROS/RNS), while M2 is identified as the alternatively activated macrophage, characterized by the capacity of inhibiting inflammatory responses and promoting tissue remodeling and repairing (Hoeksema et al., 2012; Jinnouchi et al., 2020). Lesional macrophages in human atherosclerotic plaques are constituted of various macrophages with different phenotypes and functions, and the phenotype represents dynamic changes in the plaque tissue (Depuydt et al., 2020). A deep understanding of the mechanism that drives the pro-inflammatory and pro-resolving transformation of lesional macrophages may likely provide new therapeutic opportunities for atherosclerosis.

Extensive studies indicated that M1 macrophages are enriched in progressing atherosclerotic plaques, and avidly ingest modified lipoproteins *via* activated cholesterol-trafficking pathways, such as scavenger receptor A (SRA), LOX1 and CD36, resulting in the generation of "foamy"

macrophages in the plaques (Moore et al., 2015). Alternatively, excessive lipids are removed by macrophage transporters such as ATP-binding cassette transporter A family member 1 (ABCA1), ABCG1 and liver X receptor-α (LXRα) (Moore et al., 2015; Tall and Yvan-Charvet, 2015). LXRs have been identified as the main targets for intervention in atherosclerotic cardiovascular disease. By promoting cholesterol efflux in macrophages, atherosclerosis is significantly ameliorated in animal models (Tangirala et al., 2002; Naik et al., 2006; Park, 2014; Westerterp et al., 2016). However, the systemic pharmacological intervention of the traditional drugs does not only affect the target cells and organs but also may induce various adverse reactions. For example, synthetic LXR-targeted therapy is complicated, due to its dual effect of alleviating atherosclerosis and promoting hepatic steatosis and hypertriglyceridemia, which restricts the clinical translation of LXR agonists to human disease (Fessler, 2018). To solve this problem, macrophages targeted therapy arouses great attention, in which cholesterol is transferred directly to adjacent cells *in vitro*, instead of cholesterol efflux depending on ABC transporters (He et al., 2020).

Due to the critical role of macrophages in the progression and regression of atherosclerotic plaques, these cells are one of the most utilized therapeutic targets in managing atherosclerosis. In addition, the non-immune cell-targeted nanomaterials may be primarily taken up within the plaques (Beldman et al., 2019), and various nanoparticles/nanocarriers *via* macrophage-mediated uptake have emerged as promising candidates for diagnostic imaging and therapeutic applications in atherosclerosis.

Nanoparticles for diagnosis of atherosclerosis

An angiogram is the clinical "gold standard" for defining the presence and extent of coronary artery disease, which fails in reliable predicting the sudden rupture of vulnerable plaques. Growing studies reveal that the composition of plaques is the primary determinant of their stability, and unstable plaques are always characterized by an abundance of macrophages and necrotic lipid cores, surrounded by quite thin or disrupted fibrous caps (Finn et al., 2010). "Molecular imaging technology", a novel image-based technique, achieves to visualize atherosclerotic plaques with high spatiotemporal resolution in real-time in a non-invasive way. With the assistance of robust imaging agents and therapeutic drugs for anti-atherosclerosis, various nanoparticle-based imaging agents, that can specifically target lesional macrophages are designed, and pivotal insight into plaques is obtained. For example, many macrophages-targeted imaging nanomaterials have been commonly applied for the identification of atherosclerosis through magnetic resonance imaging (MRI) (Huang et al., 2012), computed tomography (CT) (Shilo et al., 2012), positron emission tomography (PET) (Phelps, 2000), fluorescence imaging (FI) (Qiao R. et al., 2017), photoacoustic imaging (PAI) (Ge et al., 2020) and combined imaging techniques. Each imaging system displays advantages and disadvantages, and two or more imaging platforms are recently combined to provide more comprehensive information about the pathophysiological process of atherosclerosis. Advances of nanotechnologies have then generated various types of nanomaterials that are robust and reliable for molecular imaging, which are summarized in Figure 1.

MRI, using magnetic iron oxide nanoparticles (MNPs) or Gd-containing nanoparticles as imaging agents, is a common technique for the early diagnosis of atherosclerosis. MRI can provide anatomical images with high resolution and satisfactory tissue contrast, but poor tissue penetration and low sensitivity, since atherosclerosis may occur anywhere (Huang et al., 2012). Macrophages can uptake nanoparticles or other foreign substances *via* pinocytosis, endocytosis and phagocytosis. The latter is the main process for engulfing large particles, while the uptake procedure is distinct depending on the size and nature of the surface coating of nanostructures. For example, dextran-coated superparamagnetic iron oxide nanoparticles (SPIONs) and ultra-small super-paramagnetic iron oxide nanoparticles (USPIONs) are known to be phagocytosed spontaneously by plaque macrophages. However, high doses are always required and the process is time-consuming to achieve a suitable contrast of plaques in the surrounding tissues. Macrophages in atherosclerotic plaque express a high level of SRA, which is involved in atherogenesis and associated with inflammatory responses (Moore et al., 2015), but it is impossible to be found in normal vessels. The substitution of dextran with dextran sulfate leads to magnetic nanoparticles recognized by the SRA receptor, which is reported to be specifically identified by polyanionic macromolecules, inducing an increment of 4-fold in the contrast ratio, in comparison with dextran (Tu et al., 2011). Moreover, some other targeting moieties, such as osteopontin (OPN) (Qiao H. et al., 2017), human ferritin protein cages (Terashima et al., 2011) or annexin V (Cheng et al., 2015) have been widely used to be coated in the surface of SPIONs, that can specifically bound with the epitopes on macrophage surface, facilitating the accumulation of nanoparticles in vulnerable plaques. In clinical studies, MNPs enhanced MRI has been successfully utilized to identify pro-inflammatory macrophages associated with atherosclerotic burdens, especially rupture-prone lesions (Kooi et al., 2003). Of note, magnetic high-density lipoprotein (HDL)-like nanostructures developed by Lüscher et al. demonstrated an atheroprotective effect by promoting reverse cholesterol transport (Lüscher et al., 2014).

CT imaging is one of the most convenient diagnostic imaging modalities in clinical settings. CT as a radiology biomedical imaging tool provides images with superior spatial resolution and short acquisition time to identify macrophages in plaques of

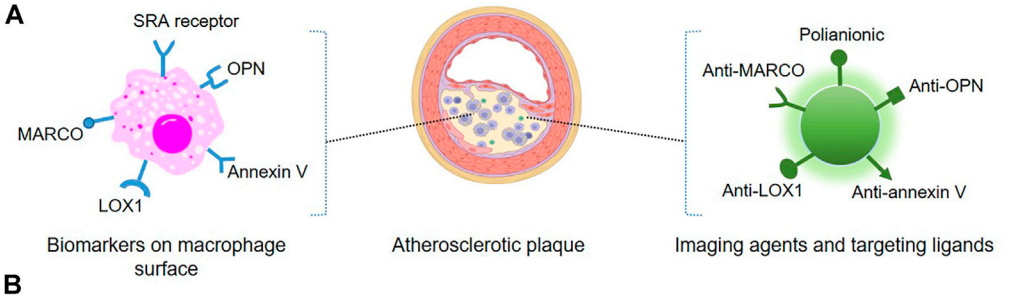

B

	MRI	CT	PET	FI	PAI
Advantages	• High resolution • Satisfactory tissue contrast	• High spatial resolution • Short acquisition time	• Elevated tissue penetration • High sensitivity	• Fast acquisition • Low cost • Lacking radiation-associated risk	• High sensitvity • Good spatial resolution and tissue contrast
Disadvantages	• Poor tissue penetration • Low sensitivity • Time-consuming	• Low sensitivity • Weak soft tissue contrast	• Lacking anatomical information • Exposure to irradiation	• Poor tissue penetration	• Limited tissue penetration • Insufficient intrinsic contrast
Imaging agents	• MNPs • Gd-containing nanoparticles	• Iodine-based nanoparticles • AuNPs	• ^{18}F, ^{89}Zr labelled nanoparticles	• Upconversion nanoparticles • Cyanine dyes • Quatum dots	• ICG-containing nanoparticles

FIGURE 1
Schematic representation of macrophage-targeted nanoplatforms for non-invasive atherosclerosis diagnostic imaging. **(A)** The commonly used epitopes overexpressed on the surface of lesional macrophages can be specifically recognized by targeted nanoparticle-based imaging agents. **(B)** Advantages, disadvantages and the associated imaging agents of the non-invasive imaging modalities.

coronary arteries, but it is difficult to distinguish different soft tissues (Yu and Watson, 1999; Shilo et al., 2012). The high atomic number iodine (Z = 53) can absorb X-rays effectively and is a present used CT contrast agent clinically. Considering that iodine molecules are easily eliminated by kidney, iodine-based liposomes, polymers and micelles are designed, and the iodine-containing nanomaterials are advantageous to assess pro-inflammatory macrophages of vulnerable plaques in the vascular system (Torchilin et al., 1999; Aviv et al., 2009; Hallouard et al., 2010). However, due to the poor sensitivity of CT, high doses of nanomaterials are required to obtain satisfactory images, which may be toxic and limit their future clinical translation. With recent advances in the development of nanotechnology, gold nanoparticles (AuNPs), with unique chemical stability, biodistribution and biosafety, can be synthesized commercially, and the flexibility in size, shape and surficial functional groups for targeting, makes AuNPs become the next promising generation of contrast agent for CT imaging (Kojima et al., 2010).

PET is an analytical imaging technology, which is particularly advantageous in non-invasive and quantitatively characterizing inflammatory macrophage-mediated atherosclerosis. PET displays excellent tissue penetration and high sensitivity, but anatomical information is not available, which is always coupled with MRI or CT imaging modalities as a consequence. To eliminate the false positive caused by traditional radioactive tracers (eg., ^{18}F-fluoro-2-deoxyglucose), which can be avidly taken up by both macrophages and cardiomyocytes (Lobatto et al., 2011), various nanomaterials labeled with PET radioactive tracers were designed. For instance, ^{18}F-labeled polyglucose nanoparticles, which can be identified by lesional macrophages with high efficiency, were developed to monitor plaques in animal models (Keliher et al., 2017). Additionally, nanoparticles labeled with ^{89}Zr have a long half-life, which facilitates the prolonged monitoring of macrophages (Pérez-Medina et al., 2016).

Fluorescence imaging technique provides a higher spatial resolution compared with other clinical imaging platforms. By detecting fluorophore emission spectra using fluorescence microscopy and derivatives, fluorescence imaging is fast, cheap and some functionalized fluorescent nanomaterials with good physicochemical properties have been tested to assess the status of macrophage-rich plaques in animal models. Emission spectra of currently used nanoparticle-based fluorescent probes are mainly in the near-infrared region to generate deep tissue penetration. Qiao et al. constructed $NaGdF_4$:Yb, Er@$NaGdF_4$

upconversion nanoparticles, and OPN antibodies were coated on the surface of the nanoparticles, which can specifically target the foamy macrophages in vulnerable plaques (Qiao R. et al., 2017). The resulting probes were then injected intravenously, fluorescence as well as MRI images are acquired to confirm the diagnostic application of the probes in distinguishing rupture-prone plaques from stable plaques *in vivo*. In a recent study, Flores and others pointed out that single-walled carbon nanotubes (SWNTs) can be robustly and preferentially taken up by macrophages, compared with non-phagocytic cells (Flores et al., 2020). SWNTs were then conjugated with a cyanine dye (Cy5.5), and a small-molecule inhibitor of SHP-1 was loaded, which achieved the diagnostic imaging of macrophages in atherosclerotic plaques and accurate delivery of therapeutic agents. In addition, a novel near-infrared (NIR) fluorescence nanoparticle, which can be specifically taken up by macrophages and fluorescence turns on in presence of a macrophage-associated enzyme, was engineered and show great potential in visualization the vulnerability of atherosclerotic plaques (Narita et al., 2019).

PAI Upon combining optical imaging with high sensitivity and ultrasonic imaging that has relatively deep tissue penetration, PAI, as a new non-invasive biomedical diagnostic platform, is applied to assess the plaque composition of arteries with atherosclerosis. Besides providing morphological information with good spatial resolution and tissue contrast, some endogenous contrast such as lipid and exogenous contrast (nanomaterials or organic dyes) are always involved in PAI, helping to distinguish disease tissues from normal ones (Sun et al., 2016; Sun et al., 2017; Zhou et al., 2019). With the emergence and rapid development of NIR nanoprobes, Ti_3C_2 nanosheets/indocyanine green (Ti_3C_2/ICG) nanocomposites were designed as PA nanoprobes, and similar to other targeted nanoprobes, the anti-OPN antibody was conjugated on the surface, and the resulting Ti_3C_2/ICG nanoprobes specifically accumulate in foam cells and vulnerable plaque tissues in mice, endowing the dual-modality imaging strategy for the precise diagnosis of atherosclerotic plaques (Ge et al., 2020). In another study, bovine serum albumin (BSA) based self-assemblies (BSA-Cy-Mito) displayed strong photoacoustic responses to GSH/H_2O_2 simultaneously (Gao et al., 2019). Systemic administration of the redox-responsive nanoprobe was further achieved to early identify the rupture-prone plaques in mice.

Nanoparticles for therapeutics of atherosclerosis

As mentioned above, intimal proinflammatory macrophages are the primary contributors in all stages of the atherogenic process, which are participated in atherogenic inflammations and aberrant lipid metabolism and subsequent generation of foam cells. As a result, many exogenous small molecule drugs and biomolecules (eg., siRNA, miRNA, circRNA, peptides and proteins) have great potential to improve the functions of plaque macrophages through activating or silencing the key signaling pathways in macrophages. Traditional drugs always have defects of short half-lives, side effects and inefficiency of oral administration, which greatly limited their applications. Interestingly, the permeability of vascular endothelium is found to increase in evolving atherosclerotic plaques, facilitating more lipoproteins or some other small particles such as nanoparticles/nanocarriers to enter into the intimal layer and atherosclerotic lesions (Atukorale et al., 2017). Since the first therapeutic application of nanoparticles in a clinical study (Cho and Han, 2018), nanotherapeutics in atherosclerosis have fueled interest to improve drug stability, precise targeting, and efficacy (Flores et al., 2019). In this section, we outline and discuss the latest developments of macrophage-targeted nanomaterials for atherosclerosis treatment, and the potential clinical prospect of these treatments is also evaluated. The primary macrophage-associated pathological processes of atherosclerosis such as macrophage accumulation and proliferation, obligatory atherogenic inflammations and excessive lipid accumulation are considered the compelling targets of anti-atherogenic nanotherapeutic agents.

Suppression of accumulation and proliferation of macrophages Experimental data indicates that impaired vascular endothelial function drives monocyte adhesion and infiltration to the arterial wall, resulting in macrophage accumulation in plaques (Jan et al., 2020). Besides, survival/proliferation of lesional macrophages may affect their overall content, and macrophage apoptosis amplifies inflammations and triggers further monocyte adhesion and recruitment (Gautier et al., 2009; Cheng et al., 2015). As a result, inhibition of accumulation and proliferation of macrophages becomes a promising therapeutic target, which can not only decrease the overall content of plaque macrophages but also prevent the rupture of plaque and acute atherothrombotic events (Lutgens et al., 2010; Potteaux et al., 2011). In a preclinical study, Lameijer et al. incorporated a small molecule inhibitor with reconstituted HDL, which blocks the interaction of CD40 and tumor necrosis factor receptor-associated factor 6 (TRAF6) (Lameijer et al., 2018). A 1-week treatment with the proposed nanocomposites (TRAF6i-HDL) demonstrated significant anti-plaque inflammatory effects, by decreasing monocyte recruitment as well as the number of lesional macrophages in atheroprone *ApoE*$^{-/-}$ mice. Of note, the safety of HDL-based nanoimmunotherapy has been established in both mouse models and non-human primates, suggesting their promising therapeutic applications for clinical transformation. Considering the important recruitment effect of vascular ECs to monocytes, Dr. Nahrendorf's group (Sager et al., 2016) developed siRNA encapsulated polymeric endothelial-avid nanoparticles to simultaneously silence five major endothelial adhesion

molecules, and the five-gene combination RNAi reduced the migration of macrophages into plaques in *ApoE*$^{-/-}$ mice after myocardial infarction. In another study, lipid polymer nanoparticles encapsulated with siRNA oligonucleotides were systemically injected into a mouse model of myocardial infarction by the same group (Krohn-Grimberghe et al., 2020). The nanoparticles mediated the silencing of MCP-1 in bone-marrow-derived ECs thereby inhibiting leukocyte release from the hematopoietic niche, reducing monocyte supply to plaques and attenuating heart failure in mice.

Besides inhibiting monocyte recruitment to reduce the lesional macrophage content, suppression of macrophage proliferation and apoptosis in atherosclerotic plaques using nanomaterials also serves as promising therapeutic avenues to stabilize vulnerable plaques. For example, localized delivery of anti-atherosclerotic drug rapamycin using biomimetic nanocomplexes, cloaked with leukosomes (Boada et al., 2020) or red blood cell membrane (Wang Y. et al., 2019), attenuated the progression of atherosclerosis significantly by suppressing macrophages proliferation within plaques and reducing key proinflammatory cytokines. Moreover, encouraged by the superior therapeutic effect of photosensitizers by producing cytotoxic ROS and inducing extensive macrophages apoptosis in artery atheroma in mice under 650 nm light, various photothermal agents such as SWNTs (Kosuge et al., 2012), silica-AuNPs (Kharlamov and Gabinsky, 2012), Au nanorods (Qin et al., 2015) and MoO_2 nanoclusters (Wang X. et al., 2019) were designed to reduce atherosclerotic plaque burden in preclinical studies. These nanoparticles with extremely high photothermal conversion efficiency and biocompatibility can be preferentially engulfed by pro-inflammatory macrophages. However, their treatment outcome varies in distinct stages of atherosclerosis, which still need tremendous effort (Tabas, 2005).

Anti-inflammatory therapies Atherosclerosis is widely considered a chronic inflammation-related disease, highlighting inflammation dampening as an essential therapeutic strategy. However, systemic administration with traditional anti-atherosclerotic drugs or anti-inflammatory cytokines always fail to reduce the serum level of pro-inflammatory cytokines, and great efforts have been made toward targeted delivery of the therapeutic agents to atherosclerotic plaques to effectively reduce inflammation and their adverse side effect during the past two decades. For example, precisely targeted delivery of interleukin 10 (IL-10), an anti-inflammatory cytokine, utilizing biodegradable controlled-release polyesters (PLGA) (Kamaly et al., 2016) or cRGD peptide conjugated pluronic based nanocarriers (Kim et al., 2020), is more potent in solving inflammation than free IL-10, which leads to increased fibrous cap thickness and decreased necrosis in an atheroprone mouse model. Wu and collogues molecularly engineered 5-aminolevulinate hydrochloride (HDL) electroporated M2 macrophage-derived exosomes (HAL@M2 Exo) with inherent inflammation tropism for the effective administration of atherosclerosis (Wu et al., 2020). In this study, the superior anti-inflammatory effect of M2 macrophages endows HAL@M2 Exo promoting the secretion and release of anti-inflammatory cytokines to alleviate the deterioration of the disease. Simultaneously, extra anti-inflammatory CO and bilirubin were generated with the employment of HAL for heme biosynthesis, therefore boosting the therapeutic effect in a mouse model. Moreover, some other targeted delivery platforms that can reduce the secretion of inflammatory cytokines of macrophages in plaques are also developed for atherosclerotic intervention. For example, MCC950, an NLRP3-inflammasome inhibitor, was delivered using platelet-derived extracellular vesicles, intravenous administration of which can selectively target inflammatory cells and reduce local inflammation and plaque size (Ma et al., 2021). A similar anti-inflammatory effect is reported by nanoparticles-based macrophage targeted delivery of methotrexate in mice (Stigliano et al., 2017; Francesco et al., 2020). Lastly, given the crucial role of ROS for lipids oxidative modification, activation of vascular cells especially ECs and macrophages during atherosclerosis progression, a series of superoxide dismutase mimics such as Cerium (Ce) (Wang et al., 2022) and cyclodextrin (Guo et al., 2019) based nanoparticles are synthesized, which show desirable efficacies to weaken the plaques *via* synergistic ROS scavenging and foam cell inhibition.

Lipid lowing therapies Lipid metabolism disorders induced lipid excessive deposition in macrophages and foam cell formation is a central pathological feature of atherosclerosis, and promoting reverse cholesterol transport (RCT) from foamy macrophages shows great potential to prevent foam cell formation in atherosclerotic plaques (Tangirala et al., 2002; Naik et al., 2006; Rosenson et al., 2012; Park, 2014). HDL, known as good cholesterol, is a type of endogenous lipidic nano-sized particle, constructed by cholesterol, phospholipids and apoA-I. HDL content is widely considered a biomarker of RCT-based cholesterol efflux from foamy macrophages to the liver. Given the antiatherogenic function of HDL, HDL-like nanoparticles are also of considerable interest in atherosclerosis treatment (Lüscher et al., 2014; Banik et al., 2016; Lameijer et al., 2018; Wu et al., 2020). For instance, a biodegradable HDL nanoparticle-based platform was constructed by Marrache and Dhar (Marrache and Dhar, 2013), which displays excellent biocompatibility, stability and nonimmunogenic properties, and is promising for future clinical translation to detect early plaques and prevent the progression of vulnerable plaques. The same group further optimized the HDL-mimicking polymer-lipid hybrid nanoparticles for cholesterol binding and efflux (Banik et al., 2017). The proposed HDL-mimetic NPs with superior M2 macrophage specificity as well as mitochondria targeted effect, can significantly accumulate in the heart and aorta of mice and deliver excess cholesterol to mitochondria to promote its metabolism.

Besides HDL-mimics-based nanoparticles, the upregulation of ABCA1 or ABCG1 expression is another important potential pathway to prevent excess lipid deposition in atherosclerotic

foam cells (Rothblat and Phillips, 2010; Westerterp et al., 2016). Accumulating studies demonstrate the therapeutic effect of miRNA-based oligonucleotides in atherosclerosis regression by targeting ABCA1 and ABCG1, such as miR-33, miR-26, miR-206, et al. (Feinberg and Moore, 2016; Nguyen et al., 2019). Chitosan (Nguyen et al., 2019) and cyclodextrin-based nanoparticles (Li et al., 2020) can efficiently deliver efflux-promoting miRNA mimics to macrophages, regulate cholesterol metabolism and substantially reduce lesional burden in an atheroprone mouse model. Additionally, activation of LXRs is also reported to be capable of promoting the removal of cholesterol by upregulating ABCA1 and ABCG1 (Naik et al., 2006). However, systemic LXR activation, which can promote the transportation of cholesterol to the liver and reduce the inflammatory response, is also known to be liver toxic (Fessler, 2018). Biodegradable collagen IV-targeted polymeric nanoparticles encapsulating LXR agonists GW3965 (Col IV-GW-NPs) are reported to specifically target atherosclerotic plaques in *Ldlr*$^{-/-}$ mice (Yu et al., 2017). Compared to non-targeting encapsulated GW, 5 weeks of administration of the nanoparticles (Col IV-GW-NPs) to pre-existing plaques, lesional macrophage content was significantly reduced, without altering hepatic lipid metabolism during the treatment period, which makes the novel targeted nanoparticle-based system promising for efficient delivery of therapeutic agents to combat lipid accumulation and atherosclerotic inflammation.

Conclusion

Over the past decades, much effort has been devoted to provide a comprehensive understanding of atherosclerosis pathophysiological processes, and the rapid development of innovative nanoparticles and nanotechnologies fueled the research of nanomedicine-mediated strategies for preclinical diagnosis and administration of atherosclerosis. In this review, we extensively summarized various nanoscopic therapies to diagnose and combat atherosclerosis, as well as the related ischemic CVDs. Especially, lesional macrophage targeted nanomaterial-based atherosclerotic imaging, diagnosis and therapeutics were highlighted. However, since there is a high degree of overlap between host defense and macrophage-involved mechanisms during atherosclerosis progression, the design of nanomedicines without interfering immunity is quite difficult. On the other hand, current imaging techniques remain to fail to precisely identify the composition of lesions or rupture-prone plaques. Furthermore, most atherosclerosis associated biomarkers mentioned above always overexpress only under particular biological conditions, which is a huge setback to the application of the active targeting approaches. Although obvious challenges remain existing, nanomedicine-based approaches show tremendous potential in preclinical settings of atherosclerosis. We believe they will be eventually employed diagnosing and managing patients with cardiovascular disease in the future.

Author contributions

PH wrote the original draft of the manuscript. SL, XF, and DL reviewed the manuscript. XT provided intelligent input and reviewed the manuscript. All authors read and approved the final manuscript.

Funding

This study was supported by the National Natural Science Foundation of China (81700237 to PH, 31571172 and 81870343 to XT); Chongqing Natural Science Foundation (cstc2021jcyj-msxmX0043 to XT); Chongqing Research Program of Basic Research and Frontier Technology (cstc2016jcyjA0407 to XT); Fundamental Research Funds for the Central Universities (2018CDYXYX0027 to PH and 2018CDQYYX0042 to XT).

Conflict of interest

The authors declare that the research was conducted in the absence of any commercial or financial relationships that could be construed as a potential conflict of interest.

Publisher's note

All claims expressed in this article are solely those of the authors and do not necessarily represent those of their affiliated organizations, or those of the publisher, the editors and the reviewers. Any product that may be evaluated in this article, or claim that may be made by its manufacturer, is not guaranteed or endorsed by the publisher.

References

Atukorale, P. U., Covarrubias, G., Bauer, L., and Karathanasis, E. (2017). Vascular targeting of nanoparticles for molecular imaging of diseased endothelium. *Adv. Drug Deliv. Rev.* 113, 141–156. doi:10.1016/j.addr.2016.09.006

Aviv, H., Bartling, S., Kieslling, F., and Margel, S. (2009). Radiopaque iodinated copolymeric nanoparticles for X-ray imaging applications. *Biomaterials* 30 (29), 5610–5616. doi:10.1016/j.biomaterials.2009.06.038

Banik, B., Askins, B. W., and Dhar, S. (2016). Mito-magneto: A tool for nanoparticle mediated mitochondria isolation. *Nanoscale* 8 (47), 19581–19591. doi:10.1039/c6nr05882e

Banik, B., Wen, R., Marrache, S., Kumar, A., Kolishetti, N., Howerth, E. W., et al. (2017). Core hydrophobicity tuning of a self-assembled particle results in efficient lipid reduction and favorable organ distribution. *Nanoscale* 10 (1), 366–377. doi:10.1039/c7nr06295h

Beldman, T. J., Malinova, T. S., Desclos, E., Grootemaat, A. E., Misiak, A. L. S., Velden, S. v. d., et al. (2019). Nanoparticle-aided characterization of arterial endothelial architecture during atherosclerosis progression and metabolic therapy. *ACS Nano* 13 (12), 13759–13774. doi:10.1021/acsnano.8b08875

Bełtowski, J., Wójcicka, G., and Jamroz-Wiśniewska, A. (2009). Adverse effects of statins - mechanisms and consequences. *Curr. Drug Saf.* 4 (3), 209–228. doi:10.2174/157488609789006949

Boada, C., Zinger, A., Tsao, C., Zhao, P., Martinez, J. O., Hartman, K., et al. (2020). Rapamycin-loaded biomimetic nanoparticles reverse vascular inflammation. *Circ. Res.* 126 (1), 25–37. doi:10.1161/CIRCRESAHA.119.315185

Chen, W., Schilperoort, M., Cao, Y., Shi, J., Tabas, I., and Tao, W. (2022). Macrophage-targeted nanomedicine for the diagnosis and treatment of atherosclerosis. *Nat. Rev. Cardiol.* 19 (4), 228–249. doi:10.1038/s41569-021-00629-x

Cheng, D., Li, X., Zhang, C., Tan, H., Wang, C., Pang, L., et al. (2015). Detection of vulnerable atherosclerosis plaques with a dual-modal single-photon-emission computed tomography/magnetic resonance imaging probe targeting apoptotic macrophages. *ACS Appl. Mat. Interfaces* 7 (4), 2847–2855. doi:10.1021/am508118x

Cho, Y. H., and Han, H.-K. (2018). Nanomedicines: Current status and future perspectives in aspect of drug delivery and pharmacokinetics. *J. Pharm. Investig.* 48 (1), 43–60. doi:10.1007/s40005-017-0370-4

Depuydt, M. A. C., Prange, K. H. M., Slenders, L., Örd, T., Elbersen, D., Boltjes, A., et al. (2020). Microanatomy of the human atherosclerotic plaque by single-cell transcriptomics. *Circ. Res.* 127 (11), 1437–1455. doi:10.1161/CIRCRESAHA.120.316770

Dhindsa, D. S., Sandesara, P. B., Shapiro, M. D., and Wong, N. D. (2020). The evolving understanding and approach to residual cardiovascular risk management. *Front. Cardiovasc. Med.* 7, 88. doi:10.3389/fcvm.2020.00088

Feinberg, M. W., and Moore, K. J. (2016). MicroRNA regulation of atherosclerosis. *Circ. Res.* 118 (4), 703–720. doi:10.1161/CIRCRESAHA.115.306300

Fessler, M. B. (2018). The challenges and promise of targeting the liver X receptors for treatment of inflammatory disease. *Pharmacol. Ther.* 181, 1–12. doi:10.1016/j.pharmthera.2017.07.010

Finn, A. V., Nakano, M., Narula, J., Kolodgie, F. D., and Virmani, R. (2010). Concept of vulnerable/unstable plaque. *Arterioscler. Thromb. Vasc. Biol.* 30 (7), 1282–1292. doi:10.1161/ATVBAHA.108.179739

Flores, A. M., Hosseini-Nassab, N., Jarr, K.-U., Ye, J., Zhu, X., Wirka, R., et al. (2020). Pro-efferocytic nanoparticles are specifically taken up by lesional macrophages and prevent atherosclerosis. *Nat. Nanotechnol.* 15 (2), 154–161. doi:10.1038/s41565-019-0619-3

Flores, A. M., Ye, J., Jarr, K.-U., Hosseini-Nassab, N., Smith, B. R., and Leeper, N. J. (2019). Nanoparticle therapy for vascular diseases. *Arterioscler. Thromb. Vasc. Biol.* 39 (4), 635–646. doi:10.1161/ATVBAHA.118.311569

Forster, L. F., Stewart, G., Bedford, D., Stewart, J. P., Rogers, E., Shepherd, J., et al. (2002). Influence of atorvastatin and simvastatin on apolipoprotein B metabolism in moderate combined hyperlipidemic subjects with low VLDL and LDL fractional clearance rates. *Atherosclerosis* 164 (1), 129–145. doi:10.1016/s0021-9150(02)00052-7

Francesco, V. D., Gurgone, D., Palomba, R., Ferreira, M. F. M. M., Catelani, T., Cervadoro, A., et al. (2020). Modulating lipoprotein transcellular transport and atherosclerotic plaque formation in ApoE $^{-/-}$ mice via nanoformulated lipid-methotrexate conjugates. *ACS Appl. Mat. Interfaces* 12 (34), 37943–37956. doi:10.1021/acsami.0c12202

Gao, W., Li, X., Liu, Z., Fu, W., Sun, Y., Cao, W., et al. (2019). A redox-responsive self-assembled nanoprobe for photoacoustic inflammation imaging to assess atherosclerotic plaque vulnerability. *Anal. Chem.* 91 (1), 1150–1156. doi:10.1021/acs.analchem.8b04912

Gautier, E. L., Huby, T., Witztum, J. L., Ouzilleau, B., Miller, E. R., Saint-Charles, F., et al. (2009). Macrophage apoptosis exerts divergent effects on atherogenesis as a function of lesion stage. *Circulation* 119 (13), 1795–1804. doi:10.1161/CIRCULATIONAHA.108.806158

Ge, X., Cui, H., Kong, J., Lu, S.-Y., Zhan, R., Gao, J., et al. (2020). A non-invasive nanoprobe for *in vivo* photoacoustic imaging of vulnerable atherosclerotic plaque. *Adv. Mat.* 32 (38), e2000037. doi:10.1002/adma.202000037

Guo, J., Li, D., Tao, H., Li, G., Liu, R., Dou, Y., et al. (2019). Cyclodextrin-derived intrinsically bioactive nanoparticles for treatment of acute and chronic inflammatory diseases. *Adv. Mat.* 31 (46), e1904607. doi:10.1002/adma.201904607

Hallouard, F., Anton, N., Choquet, P., Constantinesco, A., and Vandamme, T. (2010). Iodinated blood pool contrast media for preclinical X-ray imaging applications--a review. *Biomaterials* 31 (24), 6249–6268. doi:10.1016/j.biomaterials.2010.04.066

He, C., Jiang, H., Song, W., Riezman, H., Tontonoz, P., Weston, T. A., et al. (2020). Cultured macrophages transfer surplus cholesterol into adjacent cells in the absence of serum or high-density lipoproteins. *Proc. Natl. Acad. Sci. U. S. A.* 117 (19), 10476–10483. doi:10.1073/pnas.1922879117

Hoeksema, M. A., Stöger, J. L., and Winther, M. P. J. d. (2012). Molecular pathways regulating macrophage polarization: Implications for atherosclerosis. *Curr. Atheroscler. Rep.* 14 (3), 254–263. doi:10.1007/s11883-012-0240-5

Huang, J., Zhong, X., Wang, L., Yang, L., and Mao, H. (2012). Improving the magnetic resonance imaging contrast and detection methods with engineered magnetic nanoparticles. *Theranostics* 2 (1), 86–102. doi:10.7150/thno.4006

Jan, S., Melanie, H. R., Lubna, A., Hm, P. K., Jeffrey, K., van Weeghel, M., et al. (2020). Atherogenic lipoprotein(a) increases vascular glycolysis, thereby facilitating inflammation and leukocyte extravasation. *Circ. Res.* 126 (10), 1346–1359. doi:10.1161/CIRCRESAHA.119.316206

Jinnouchi, H., Guo, L., Sakamoto, A., Torii, S., Sato, Y., Cornelissen, A., et al. (2020). Diversity of macrophage phenotypes and responses in atherosclerosis. *Cell. Mol. Life Sci.* 77 (10), 1919–1932. doi:10.1007/s00018-019-03371-3

Kamaly, N., Fredman, G., Fojas, J. J. R., Subramanian, M., Choi, W. I., Zepeda, K., et al. (2016). Targeted interleukin-10 nanotherapeutics developed with a microfluidic chip enhance resolution of inflammation in advanced atherosclerosis. *ACS Nano* 10 (5), 5280–5292. doi:10.1021/acsnano.6b01114

Katakami, N. (2018). Mechanism of development of atherosclerosis and cardiovascular disease in diabetes mellitus. *J. Atheroscler. Thromb.* 25 (1), 27–39. doi:10.5551/jat.RV17014

Keliher, E. J., Ye, Y.-X., Wojtkiewicz, G. R., Aguirre, A. D., Tricot, B., Senders, M. L., et al. (2017). Polyglucose nanoparticles with renal elimination and macrophage avidity facilitate PET imaging in ischaemic heart disease. *Nat. Commun.* 8, 14064. doi:10.1038/ncomms14064

Kharlamov, A. N., and Gabinsky, J. L. (2012). Plasmonic photothermic and stem cell therapy of atherosclerotic plaque as a novel nanotool for angioplasty and artery remodeling. *Rejuvenation Res.* 15 (2), 222–230. doi:10.1089/rej.2011.1305

Kim, M., Sahu, A., Hwang, Y., Kim, G. B., Nam, G. H., Kim, I.-S., et al. (2020). Targeted delivery of anti-inflammatory cytokine by nanocarrier reduces atherosclerosis in Apo E $^{-/-}$ mice. *Biomaterials* 226, 119550. doi:10.1016/j.biomaterials.2019.119550

Kiortsis, D. N., Filippatos, T. D., Mikhailidis, D. P., Elisaf, M. S., and Liberopoulos, E. N. (2007). Statin-associated adverse effects beyond muscle and liver toxicity. *Atherosclerosis* 195 (1), 7–16. doi:10.1016/j.atherosclerosis.2006.10.001

Kojima, C., Umeda, Y., Ogawa, M., Harada, A., Magata, Y., and Kono, K. (2010). X-ray computed tomography contrast agents prepared by seeded growth of gold nanoparticles in PEGylated dendrimer. *Nanotechnology* 21 (24), 245104. doi:10.1088/0957-4484/21/24/245104

Kooi, M. E., Cappendijk, V. C., Cleutjens, K. B. J. M., Kessels, A. G. H., Kitslaar, P. J. E. H. M., Borgers, M., et al. (2003). Accumulation of ultrasmall superparamagnetic particles of iron oxide in human atherosclerotic plaques can be detected by *in vivo* magnetic resonance imaging. *Circulation* 107 (19), 2453–2458. doi:10.1161/01.CIR.0000068315.98705.CC

Kosuge, H., Sherlock, S. P., Kitagawa, T., Dash, R., Robinson, J. T., Dai, H., et al. (2012). Near infrared imaging and photothermal ablation of vascular inflammation using single-walled carbon nanotubes. *J. Am. Heart Assoc.* 16, e002568. doi:10.1161/JAHA.112.002568

Krohn-Grimberghe, M., Mitchell, M. J., Schloss, M. J., Khan, O. F., Courties, G., Guimaraes, P. P. G., et al. (2020). Nanoparticle-encapsulated siRNAs for gene silencing in the haematopoietic stem-cell niche. *Nat. Biomed. Eng.* 4 (11), 1076–1089. doi:10.1038/s41551-020-00623-7

Lameijer, M., Binderup, T., Leent, M. M. T. v., Senders, M. L., Fay, F., Malkus, J., et al. (2018). Efficacy and safety assessment of a TRAF6-targeted nanoimmunotherapy in atherosclerotic mice and non-human primates. *Nat. Biomed. Eng.* 2 (5), 279–292. doi:10.1038/s41551-018-0221-2

Li, C., Dou, Y., Chen, Y., Qi, Y., Li, L., Han, S., et al. (2020). Site-specific microRNA-33 antagonism by pH-responsive nanotherapies for treatment of atherosclerosis via regulating cholesterol efflux and adaptive immunity. *Adv. Funct. Mat.* 30, 2002131. doi:10.1002/adfm.202002131

Lieb, W., Enserro, D. M., Larson, M. G., and Vasan, R. S. (2018). Residual cardiovascular risk in individuals on lipid-lowering treatment: Quantifying absolute

and relative risk in the community. *Open Heart* 5 (1), e000722. doi:10.1136/openhrt-2017-000722

Lobatto, M. E., Fuster, V., Fayad, Z. A., and Mulder, W. J. M. (2011). Perspectives and opportunities for nanomedicine in the management of atherosclerosis. *Nat. Rev. Drug Discov.* 10 (11), 835–852. doi:10.1038/nrd3578

Lüscher, T. F., Landmesser, U., Eckardstein, A. v., and Fogelman, A. M. (2014). High-density lipoprotein: Vascular protective effects, dysfunction, and potential as therapeutic target. *Circ. Res.* 114 (1), 171–182. doi:10.1161/CIRCRESAHA.114.300935

Lutgens, E., Lievens, D., Beckers, L., Wijnands, E., Soehnlein, O., Zernecke, A., et al. (2010). Deficient CD40-TRAF6 signaling in leukocytes prevents atherosclerosis by skewing the immune response toward an antiinflammatory profile. *J. Exp. Med.* 207 (2), 391–404. doi:10.1084/jem.20091293

Ma, Q., Fan, Q., Han, X., Dong, Z., Xu, J., Bai, J., et al. (2021). Platelet-derived extracellular vesicles to target plaque inflammation for effective anti-atherosclerotic therapy. *J. Control. Release* 329, 445–453. doi:10.1016/j.jconrel.2020.11.064

Maron, D. J., Fazio, S., and Linton, M. F. (2000). Current perspectives on statins. *Circulation* 101 (2), 207–213. doi:10.1161/01.cir.101.2.207

Marrache, S., and Dhar, S. (2013). Biodegradable synthetic high-density lipoprotein nanoparticles for atherosclerosis. *Proc. Natl. Acad. Sci. U. S. A.* 110 (23), 9445–9450. doi:10.1073/pnas.1301929110

Moore, K., Sheedy, F., and Fisher, E. (2015). Macrophages in atherosclerosis: A dynamic balance. *Nat. Rev. Immunol.* 13 (10), 709–721. doi:10.1038/nri3520

Naik, S. U., Wang, X., Silva, J. S. D., Jaye, M., Macphee, C. H., Reilly, M. P., et al. (2006). Pharmacological activation of liver X receptors promotes reverse cholesterol transport *in vivo*. *Circulation* 113 (1), 90–97. doi:10.1161/CIRCULATIONAHA.105.560177

Narita, Y., Shimizu, K., Ikemoto, K., Uchino, R., Kosugi, M., Maess, M. B., et al. (2019). Macrophage-targeted, enzyme-triggered fluorescence switch-on system for detection of embolism-vulnerable atherosclerotic plaques. *J. Control. Release* 302, 105–115. doi:10.1016/j.jconrel.2019.03.025

Negre-Salvayre, A., Guerby, P., Gayral, S., Laffargue, M., and Salvayre, R. (2020). Role of reactive oxygen species in atherosclerosis: Lessons from murine genetic models. *Free Radic. Biol. Med.* 149, 88–22. doi:10.1016/j.freeradbiomed.2019.10.011

Nguyen, M.-A., Wyatt, H., Susser, L., Geoffrion, M., Rasheed, A., Duchez, A.-C., et al. (2019). Delivery of microRNAs by chitosan nanoparticles to functionally alter macrophage cholesterol efflux *in vitro* and *in vivo*. *ACS Nano* 13 (6), 6491–6505. doi:10.1021/acsnano.8b09679

Park, Y. M. (2014). CD36, a scavenger receptor implicated in atherosclerosis. *Exp. Mol. Med.* 46 (6), e99. doi:10.1038/emm.2014.38

Pérez-Medina, C., Binderup, T., Lobatto, M. E., Tang, J., Calcagno, C., Giesen, L., et al. (2016). *In vivo* PET imaging of HDL in multiple atherosclerosis models. *JACC. Cardiovasc. Imaging* 9 (8), 950–961. doi:10.1016/j.jcmg.2016.01.020

Phelps, M. E. (2000). Positron emission tomography provides molecular imaging of biological processes. *Proc. Natl. Acad. Sci. U. S. A.* 97 (16), 9226–9233. doi:10.1073/pnas.97.16.9226

Potteaux, S., Gautier, E. L., Hutchison, S. B., Rooijen, N. v., Rader, D. J., Thomas, M. J., et al. (2011). Suppressed monocyte recruitment drives macrophage removal from atherosclerotic plaques of Apoe-/- mice during disease regression. *J. Clin. Invest.* 121 (5), 2025–2036. doi:10.1172/JCI43802

Qiao, H., Wang, Y., Zhang, R., Gao, Q., Liang, X., Gao, L., et al. (2017a). MRI/optical dual-modality imaging of vulnerable atherosclerotic plaque with an osteopontin-targeted probe based on Fe_3O_4 nanoparticles. *Biomaterials* 112, 336–345. doi:10.1016/j.biomaterials.2016.10.011

Qiao, R., Qiao, H., Zhang, Y., Wang, Y., Chi, C., Tian, J., et al. (2017b). Molecular imaging of vulnerable atherosclerotic plaques *in vivo* with osteopontin-specific upconversion nanoprobes. *ACS Nano* 11 (2), 1816–1825. doi:10.1021/acsnano.6b07842

Qin, J., Peng, Z., Li, B., Ye, K., Zhang, Y., Yuan, F., et al. (2015). Gold nanorods as a theranostic platform for *in vitro* and *in vivo* imaging and photothermal therapy of inflammatory macrophages. *Nanoscale* 7 (33), 13991–14001. doi:10.1039/c5nr02521d

Que, Y., Shu, X., Wang, L., Hu, P., Wang, S., Xiong, R., et al. (2020). Inactivation of cysteine 674 in the SERCA2 accelerates experimental aortic aneurysm. *J. Mol. Cell. Cardiol.* 139, 213–224. doi:10.1016/j.yjmcc.2020.02.003

Rosenblum, D., Joshi, N., Tao, W., Karp, J. M., and Peerc, D. (2018). Progress and challenges towards targeted delivery of cancer therapeutics. *Nat. Commun.* 9, 1410. doi:10.1038/s41467-018-03705-y

Rosenson, R. S., Brewer, H. B., Davidson, W. S., Fayad, Z. A., Fuster, V., Goldstein, J., et al. (2012). Cholesterol efflux and atheroprotection: Advancing the concept of reverse cholesterol transport. *Circulation* 125 (15), 1905–1919. doi:10.1161/CIRCULATIONAHA.111.066589

Ross, R. (1999). Atherosclerosis--an inflammatory disease. *N. Engl. J. Med.* 340 (2), 115–126. doi:10.1056/NEJM199901143400207

Rothblat, G. H., and Phillips, M. C. (2010). High-density lipoprotein heterogeneity and function in reverse cholesterol transport. *Curr. Opin. Lipidol.* 21 (3), 229–238. doi:10.1097/mol.0b013e328338472d

Sager, H. B., Dutta, P., Dahlman, J. E., Hulsmans, M., Courties, G., Sun, Y., et al. (2016). RNAi targeting multiple cell adhesion molecules reduces immune cell recruitment and vascular inflammation after myocardial infarction. *Sci. Transl. Med.* 8 (342), 342ra80. doi:10.1126/scitranslmed.aaf1435

Shi, J., Xiao, Z., Kamaly, N., and Farokhzad, O. C. (2011). Self-assembled targeted nanoparticles: Evolution of technologies and bench to bedside translation. *Acc. Chem. Res.* 44 (10), 1123–1134. doi:10.1021/ar200054n

Shilo, M., Reuveni, T., Motiei, M., and Popovtzer, R. (2012). Nanoparticles as computed tomography contrast agents: Current status and future perspectives. *Nanomedicine (Lond)* 7 (2), 257–269. doi:10.2217/nnm.11.190

Stigliano, C., Ramirez, M. R., Singh, J. V., Aryal, S., Key, J., Blanco, E., et al. (2017). Methotraxate-loaded hybrid nanoconstructs target vascular lesions and inhibit atherosclerosis progression in $ApoE^{-/-}$ mice. *Adv. Healthc. Mat.* 6, 1601286. doi:10.1002/adhm.201601286

Sun, C., Wen, L., Zeng, J., Wang, Y., Sun, Q., Deng, L., et al. (2016). One-pot solventless preparation of PEGylated black phosphorus nanoparticles for photoacoustic imaging and photothermal therapy of cancer. *Biomaterials* 91, 81–89. doi:10.1016/j.biomaterials.2016.03.022

Sun, Z., Zhao, Y., Li, Z., Cui, H., Zhou, Y., Li, W., et al. (2017). TiL4-coordinated black phosphorus quantum dots as an efficient contrast agent for *in vivo* photoacoustic imaging of cancer. *Small* 13, 1602896. doi:10.1002/smll.201602896

Tabas, I. (2005). Consequences and therapeutic implications of macrophage apoptosis in atherosclerosis: The importance of lesion stage and phagocytic efficiency. *Arterioscler. Thromb. Vasc. Biol.* 25 (11), 2255–2264. doi:10.1161/01.ATV.0000184783.04864.9f

Tabas, I., Williams, K. J., and Borén, J. (2007). Subendothelial lipoprotein retention as the initiating process in atherosclerosis: Update and therapeutic implications. *Circulation* 116 (16), 1832–1844. doi:10.1161/CIRCULATIONAHA.106.676890

Tall, A. R., and Yvan-Charvet, L. (2015). Cholesterol, inflammation and innate immunity. *Nat. Rev. Immunol.* 15 (2), 104–116. doi:10.1038/nri3793

Tangirala, R. K., Bischoff, E. D., Joseph, S. B., Wagner, B. L., Walczak, R., Laffitte, B. A., et al. (2002). Identification of macrophage liver X receptors as inhibitors of atherosclerosis. *Proc. Natl. Acad. Sci. U. S. A.* 99 (18), 11896–11901. doi:10.1073/pnas.182199799

Terashima, M., Uchida, M., Kosuge, H., Tsao, P. S., Young, M. J., Conolly, S. M., et al. (2011). Human ferritin cages for imaging vascular macrophages. *Biomaterials* 32 (5), 1430–1437. doi:10.1016/j.biomaterials.2010.09.029

Torchilin, V. P., Frank-Kamenetsky, M. D., and Wolf, G. L. (1999). CT visualization of blood pool in rats by using long-circulating, iodine-containing micelles. *Acad. Radiol.* 6 (1), 61–65. doi:10.1016/s1076-6332(99)80063-4

Tu, C., Ng, T. S. C., Sohi, H. K., Palko, H. A., House, A., Jacobs, R. E., et al. (2011). Receptor-targeted iron oxide nanoparticles for molecular MR imaging of inflamed atherosclerotic plaques. *Biomaterials* 32 (29), 7209–7216. doi:10.1016/j.biomaterials.2011.06.026

Virani, S. S., Alonso, A., Aparicio, H. J., Benjamin, E. J., Bittencourt, M. S., Callaway, C. W., et al. (2021). Heart disease and stroke statistics-2021 update: A report from the American heart association. *Circulation* 143 (8), e254–e743. doi:10.1161/CIR.0000000000000950

Wang, S., Yang, W., Du, H., Guo, F., Wang, H., Chang, J., et al. (2016). Multifunctional reduction-responsive SPIO&DOX-loaded PEGylated polymeric lipid vesicles for magnetic resonance imaging-guided drug delivery. *Nanotechnology* 27 (16), 165101. doi:10.1088/0957-4484/27/16/165101

Wang, S., Zhou, Y., Liang, X., Xu, M., Li, N., and Zhao, K. (2022). Platinum-cerium bimetallic nano-raspberry for atherosclerosis treatment via synergistic foam cell inhibition and P2Y12 targeted antiplatelet aggregation. *Chem. Eng. J.* 430, 132859. doi:10.1016/j.cej.2021.132859

Wang, X., Wu, X., Qin, J., Ye, K., Lai, F., Li, B., et al. (2019a). Differential phagocytosis-based photothermal ablation of inflammatory macrophages in atherosclerotic disease. *ACS Appl. Mater Interfaces* 11 (44), 41009–41018. doi:10.1021/acsami.9b12258

Wang, Y., Zhang, K., Qin, X., Li, T., Qiu, J., Yin, T., et al. (2019b). Biomimetic nanotherapies: Red blood cell based core-shell structured nanocomplexes for atherosclerosis management. *Adv. Sci.* 6 (12), 1900172. doi:10.1002/advs.201900172

Westerterp, M., Tsuchiya, K., Tattersall, I. W., Fotakis, P., Bochem, A. E., Molusky, M. M., et al. (2016). Deficiency of ATP-binding cassette transporters

A1 and G1 in endothelial cells accelerates atherosclerosis in mice. *Arterioscler. Thromb. Vasc. Biol.* 36 (7), 1328–1337. doi:10.1161/ATVBAHA.115.306670

Wilson, H. M. (2010). Macrophages heterogeneity in atherosclerosis - implications for therapy. *J. Cell. Mol. Med.* 14 (8), 2055–2065. doi:10.1111/j.1582-4934.2010.01121.x

Wu, G., Zhang, J., Zhao, Q., Zhuang, W., Ding, J., Zhang, C., et al. (2020). Molecularly engineered macrophage-derived exosomes with Inflammation tropism and intrinsic heme biosynthesis for atherosclerosis treatment. *Angew. Chem. Int. Ed. Engl.* 59 (10), 4068–4074. doi:10.1002/anie.201913700

Xiao, S. J., Chu, Z. J., Zhao, X. J., Zhang, Z. B., and Liu, Y. H. (2017). Off-on-off detection of the activity of acetylcholine esterase and its inhibitors using MoOx quantum dots as a photoluminescent probe. *Microchim. Acta* 184, 4853–4860. doi:10.1007/s00604-017-2519-2

Yu, M., Amengual, J., Menon, A., Kamaly, N., Zhou, F., Xu, X., et al. (2017). Targeted nanotherapeutics encapsulating liver X receptor agonist GW3965 enhance antiatherogenic effects without adverse effects on hepatic lipid metabolism in Ldlr $^{-/-}$ mice. *Adv. Healthc. Mat.* 6 (20), 1700313. doi:10.1002/adhm.201700313

Yu, S.-B., and Watson, A. D. (1999). Metal-based X-ray contrast media. *Chem. Rev.* 99 (9), 2353–2378. doi:10.1021/cr980441p

Zhou, H.-C., Chen, N., Zhao, H., Yin, T., Zhang, J., Zheng, W., et al. (2019). Optical-resolution photoacoustic microscopy for monitoring vascular normalization during anti-angiogenic therapy. *Photoacoustics* 15, 100143. doi:10.1016/j.pacs.2019.100143

frontiers | Frontiers in Pharmacology

TYPE Review
PUBLISHED 12 September 2022
DOI 10.3389/fphar.2022.999404

OPEN ACCESS

EDITED BY
Fiorentina Roviezzo,
University of Naples Federico II, Italy

REVIEWED BY
Hermis Iatrou,
National and Kapodistrian University of Athens, Greece
Claudia Penna,
University of Turin, Italy

*CORRESPONDENCE
Qizhi Diao,
diaoqizhi@163.com

SPECIALTY SECTION
This article was submitted to Cardiovascular and Smooth Muscle Pharmacology, a section of the journal Frontiers in Pharmacology

RECEIVED 21 July 2022
ACCEPTED 25 August 2022
PUBLISHED 12 September 2022

CITATION
Yang F, Xue J, Wang G and Diao Q (2022), Nanoparticle-based drug delivery systems for the treatment of cardiovascular diseases.
Front. Pharmacol. 13:999404.
doi: 10.3389/fphar.2022.999404

Nanoparticle-based drug delivery systems for the treatment of cardiovascular diseases

Fangyu Yang[1], Jianjiang Xue[1], Guixue Wang[2] and Qizhi Diao[3]*

[1]Department of Clinical Laboratory Medicine, University-Town Hospital of Chongqing Medical University, Chongqing, China, [2]Key Laboratory for Bio-Rheological Science and Technology of Ministry of Education, State and Local Joint Engineering Laboratory for Vascular Implants, Bioengineering College of Chongqing University, Chongqing, China, [3]Department of Clinical Laboratory Medicine, Sanya Women and Children's Hospital Managed by Shanghai Children's Medical Center, Hainan, China

Cardiovascular disease is the most common health problem worldwide and remains the leading cause of morbidity and mortality. Despite recent advances in the management of cardiovascular diseases, pharmaceutical treatment remains suboptimal because of poor pharmacokinetics and high toxicity. However, since being harnessed in the cancer field for the delivery of safer and more effective chemotherapeutics, nanoparticle-based drug delivery systems have offered multiple significant therapeutic effects in treating cardiovascular diseases. Nanoparticle-based drug delivery systems alter the biodistribution of therapeutic agents through site-specific, target-oriented delivery and controlled drug release of precise medicines. Metal-, lipid-, and polymer-based nanoparticles represent ideal materials for use in cardiovascular therapeutics. New developments in the therapeutic potential of drug delivery using nanoparticles and the application of nanomedicine to cardiovascular diseases are described in this review. Furthermore, this review discusses our current understanding of the potential role of nanoparticles in metabolism and toxicity after therapeutic action, with a view to providing a safer and more effective strategy for the treatment of cardiovascular disease.

KEYWORDS

cardiovascular diseases, nanoparticles, drug delivery, nanomedicine, nanotoxicity

Introduction

Heart failure, arrhythmia, atherosclerosis, coronary heart disease, myocardial infarction (MI), peripheral arterial disease, deep vein thrombosis, and inflammatory heart disease, along with other cardiovascular diseases (CVDs) are a primary cause of death worldwide. The World Heart Federation has reported that CVDs account for 17.3 million deaths per year (Smith et al., 2012). The number of deaths is expected to increase over the next 10 years because of an increased prevalence in risk factors for CVDs, such as obesity, high non-high-density lipoprotein (HDL) cholesterol levels,

diabetes, hypertension, tobacco use, lack of physical activity, unhealthy diet, and expansion of the geriatric population (Iafisco et al., 2019). Deaths from CVDs are expected to reach 23.6 million each year by 2030 (Yusuf et al., 2020). Different treatments of CVDs are selected based on patient risks stratification and severity. The main purpose of all treatment protocols for CVDs is to better promote blood supply and diminish tissue damage to minimize cardiomyocyte loss and increase contractile area. Severe CVD cases are usually treated with surgery to remove blood clots, place artificial cardiac pacemakers in cases of arrhythmia, and repair the pathological organic cardiac changes. Not surprisingly, maintaining regular drug therapy is relatively difficult; in most circumstances, the treatment will have to be taken for life.

Statin therapy is recommended as first-line therapy for most patients with hypercholesterolemia. In addition to the lipid-regulating effects, statin therapy is efficacious in dissolving blood clots, fighting inflammation, and improving endothelial function (Fisher and Moonis, 2012). Aspirin is the most used drug for the secondary prevention of CVDs (Baigent et al., 2009). β-blockers are adrenergic receptor antagonists that can effectively antagonize sympathetic excitability and cardiotoxicity. Therefore, β-blockers are also prescribed as the first-line treatment of atrial fibrillation and CVDs; however, they are not suitable for patients with hypertension (Martinez-Milla et al., 2019). Angiotensin converting enzyme inhibitors and angiotensin II receptor blockers have become the drugs of choice for the treatment of heart failure, coronary artery disease, MI, and hypertension (Regoli et al., 2012). Angiotensin II receptor blocker-neprilysin inhibitor drugs both block the activation of the renin-angiotensin-aldosterone system in patients with heart failure and inhibit the activity of enkephalinase to increase the levels of various endogenous vasoactive peptides (Owens et al., 2017). The PARADIGM-HF and PARAGON-HF trials have confirmed that sacubitril-valsartan has an established role in the treatment of patients with heart failure with reduced or preserved ejection fraction (McMurray et al., 2014; Solomon et al., 2019). Although significant progress in existing treatments has been made in the past decade, the therapeutic effects of pharmacotherapy are suboptimal because of the non-specific cytotoxicity, poor solubility and absorption, first pass metabolism, poor biocompatibility, and low bioavailability of existing cardiovascular drugs (Karunakar et al., 2016).

Nanotechnology is a multidisciplinary research field involving electronics, biology, and medicine. At the end of the 19th century, the famous German bacteriologist Paul Ehrlich put forward the concept of the "magic bullet" (Valent et al., 2016). Nanomedicine or nano-biotechnology was considered one of the most active and rapid research areas of nanotechnology and had drawn worldwide attention in previous decades. Nanoparticle-based drug delivery systems (nano-DDSs) with various shapes, sizes, structures, and transport functions depend on the properties and synthesis methods of different nanomaterials, whereby ideal nanocarriers are constructed and designed (Lee et al., 2017). Nanoparticles (NPs) utilize the enhanced permeability and retention effect to precisely deliver drugs to atherosclerotic plaques, resulting in superior therapeutic effects and decreased tissue damage (Nakamura et al., 2016). In addition, nano-DDSs show considerable potential in improving drug efficacy, prolonging drug action, improving bioavailability, targeting passively or actively, reducing drug resistance, and reducing adverse drug reactions (Patra et al., 2018). In this paper, we summarize and discuss the progress of NPs as drug carriers in the treatment of CVDs and the deficiencies of nano-DDSs in clinical application. Greater emphasis is placed on NP-directed therapy for atherosclerosis and its associated complications, including arrhythmia, ventricular remodeling, MI, and myocardial ischemia-reperfusion injury (IRI), given their crucial status as CVDs (Figure 1).

Nanoparticles

NPs are organic or inorganic structures that are generally <100 nm in at least one dimension (Wang et al., 2008). Organic NPs consist of different biodegradable materials, such as lipids, liposomes or micelles, proteins, dendrimers, polymeric vesicles, or hyaluronic acid, and inorganic NPs are compounded from a variety of minute-sized structures including quantum dots, mesoporous silicon, graphene, carbon nanotubes, metals, or metal oxides (Khafaji et al., 2019). Metal-organic frameworks (also known as porous coordination polymers) comprising organic ligands and metal ions/metal clusters *via* coordinate bonds are highly porous and crystalline polymers (He et al., 2021). Metal-organic framework nanomaterial surfaces are enveloped with polyethylene glycol entirely, which reduces the clearance by the immune system (Cutrone et al., 2019). The characteristics of NPs in size and shape, interconnected macropores, tunable porosity, chemical composition, and easy surface functionalization have drawn global attention for the past few years in drug delivery research. The combination of cell carrier and nano-drug delivery technology is also becoming a hotspot because it uses the natural character of circulating cells to overcome the immunogenicity of nanomaterials (Kroll et al., 2017). For instance, NPs clothing themselves in a skin of platelet or red blood cell membranes were used to load rapamycin. It is well established that biomimetic NPs can avoid macrophage phagocytosis *in vitro*, and the therapeutic effect is superior to the traditional nano-drug delivery method *in vivo* (Wang et al., 2019; Han et al., 2022). At present, the most applicable and comprehensive nanomaterials in the diagnosis and treatment of CVDs mainly include liposomes,

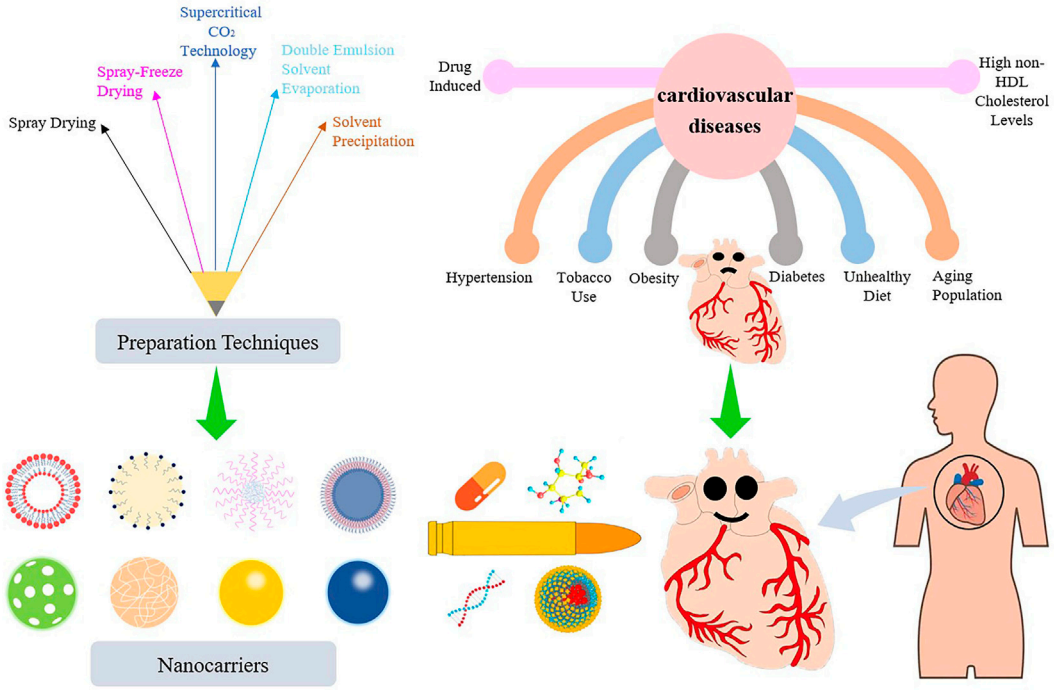

FIGURE 1
Nanoparticle-based drug delivery systems for the treatment of cardiovascular diseases.

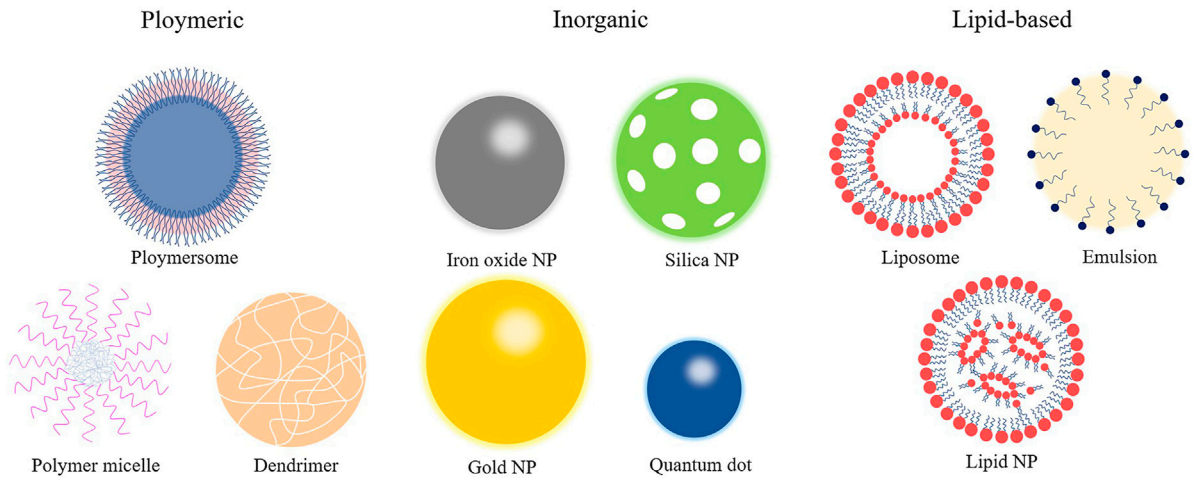

FIGURE 2
Types of nanoparticles.

micelles, dendrimers, polymer NPs, and metal NPs (Figure 2). As shown in Table 1, different types of some typical nanocarriers applications for the targeted delivery of cardioprotective agents have described.

Lipid-based nanoparticles

Liposomes are among the most typical subsets of lipid-based NPs, which are the monolayer and multilayer vesicles

TABLE 1 Nanoparticles studied for the efficient treatment of cardiovascular diseases.

Types of nanoparticles	Disease targeted	Drugs used in the treatment of CVDs	Model organisms used	Biological functions	References
Lipid-based NPs					
liposomes	Atherosclerosis	Glucocorticoids	Rabbit model	Diminished the number of macrophages in the plaque and anti-angiogenic effects	Lobatto et al. (2010)
liposomes	Arrhythmia	Amiodarone	Rat model	Reduced the mortality due to lethal arrhythmia and the negative hemodynamic changes caused by amiodarone	Takahama et al. (2013)
PEGylated liposome	Myocardial infarction	Growth factors and cytokines	Cardiac cell of rats and mouse model	Delivered therapeutic agents specifically to the infarcted heart	Dvir et al. (2011)
Recombinant HDL	Atherosclerosis	Pitavastatin	Mouse model and *in vitro*	Promoted the rapid regression of plaques	Jiang et al. (2019)
Micelle-based NPs					
Modular multifunctional micelles	Atherosclerosis	Antithrombin	Mouse model	Targeted atherosclerotic plaques initially and bound to clotted plasma proteins	Peters et al. (2009)
peptide amphiphilic micelles	Atherosclerosis	microRNA-145	Mouse model	Modulated the phenotype of VSMCs to slow plaque progression	Chin et al. (2021)
Polymeric-based NPs					
PLGA	Atherosclerosis	Pitavastatin	Mouse model	Inhibited plaque destabilization and rupture by regulating MCP-1/CCR2–dependent monocyte recruitment	Katsuki et al. (2014)
Methyl-β-cyclodextrin	Atherosclerosis	Simvastatin	Mouse model	Targeted atherosclerotic plaques and reduced plaque content of cholesterol and macrophages	Kim et al. (2020)
PLGA	Pulmonary arterial hypertension	Beraprost	Rat model	Decreased pulmonary vascular resistance and inhibited pulmonary vascular remodeling	Akagi et al. (2016)
PLGA	Ischemia-reperfusion injury	Irbesartan	Mouse model	Inhibited the recruitment of inflammatory monocytes, reduced the infarct size and ameliorated left ventricular remodeling	Nakano et al. (2016)
Chitosan-alginate NPs	Myocardial infarction	Placental growth factor	Rat model	Provide sustained slow-release placental growth factor therapy	Binsalamah et al. (2011)
Dendrimer-based NPs					
Poly (amidoamine)-histidine nanocarriers	Myocardial infarction	miRNAs	H9c2	Prevented the hypoxia/reperfusion-induced apoptosis critical in myocardial infarctions	Sayed et al. (2020)
Metal-based NPs					
CuS NPs	Atherosclerosis	Antibodies	Mouse model	Reduced lipid accumulation	Gao et al. (2018)
AuNPs	Hypertension	Antibodies	*In vitro*	The detection of cortisol ranged from 0.1 to 1000 ng/ml with a detection limit of 0.05 ng/ml at 3σ	Sun et al. (2017)
Fe_3O_4 NPs	Thrombosis	t-PA	Swine model	Delivered t-PA to the thrombosis area and the drug accumulation at the lesion site was significantly increased	Cicha. (2015)

synthesized from phospholipids through complex processes (Chiani et al., 2017). This special amphiphilic structure enables liposomes to easily carry and deliver drugs with different properties, such as hydrophilicity, hydrophobicity, and lipophilicity, and even adsorb hydrophilic and lipophilic compounds at the same time (Teymouri et al., 2019). Currently, numerous liposome formulations have been developed for the prevention and treatment of atherosclerosis and its complications. Lobatto et al. (2010) devised a nano-medicinal liposomal formulation of glucocorticoids. This liposome formulation utilized the high permeability of blood vessels to transport glucocorticoids to the vulnerable plaque, which significantly diminished the number of macrophages in the plaque. There was no obvious toxicity observed, indicating that this liposome formulation could be used as a high-quality anti-atherosclerosis drug formulation.

Micelle-based nanoparticles

Micelle-based NPs can be fashioned into various structure subpopulations; the spherical structure is most typical among

them. Micelles are self-assembled from lipids or amphiphilic molecules dissolved in water. They generally consist of a hydrophilic inner core and a hydrophobic shell. The inner core is the loading space for insoluble drugs, and the shell is the protective interface between the core and the external environment (Gothwal et al., 2016). Compared with liposomes, micelles are smaller in size, more compact in spatial structure, and have a relatively lower loading capacity. Hence, the ischemic myocardium is more permeable to micelles, which are more targeted to the lesions. In addition to providing conventional drug delivery, micelles can also target specific components of plaques. Peters et al. (2009) developed a modular multifunctional micelle loaded with antithrombin that targets atherosclerotic plaques initially and binds to clotted plasma proteins. The targeted micelles delivery system observably increased the antithrombin activity in diseased vessels and reduced the risk of plaque rupture.

Polymeric-based nanoparticles

Polymer NPs can be synthesized using a variety of natural or synthetic macromolecular materials with different structures, and the particle size and surface charge of NPs change along with the polymer type. Drugs are usually integrated into polymer NPs with various strategies, such as dissolution, encapsulation, embedding, or covalent attachment. Variation in positions and patterns of combining drugs with NPs results in differential drug delivery capabilities for polymer NPs. The biodegradable poly (lactic-co-glycolic acid) (PLGA) is the commonest among the polymer NPs. It has been reported that using the emulsified solvent diffusion method to package drugs in PLGA NPs can control drug release through mediating inflammatory cell recruitment and inhibiting atherosclerotic plaque instability (Katsuki et al., 2014).

Dendrimer-based nanoparticles

Dendrimers are highly dendritic polymers with complex three-dimensional structures. The complex structures include host structures and microenvironments, while possessing highly controllable physicochemical parameters. Targeted antibodies, genes, and other bioactive substances are modified on the peripheral groups of the host structures of the dendrimers. Dendrimer-based NPs are regarded as important drug delivery systems relying on several advantages: moderately-sized relative surface areas, high relative molecular masses, low intrinsic viscosities, and good biocompatibilities. Polyamide amine dendrimer is the most frequent selection among the numerous dendrimers used for drug delivery. The slow hydrolysis process of the polyamide amine dendrimer at physiological temperature helps to improve the sustained release of drugs. Dobrovolskaia et al. (2012) showed that platelet aggregation can be inhibited through reducing the positive charge of polyamide amine dendrimer, suggesting that it is very likely to be a potential formulation for anti-thrombosis effects or repairing endothelial injury.

Metal-based nanoparticles

Metal nanomaterials, including gold, silver, iron, are designed into various sizes, structures, and geometries. Metal NPs are generally smaller in size and exhibit more specific physical, chemical, and biological characteristics. Gold NPs with different shapes like nanospheres, nanorods, and nanoshells are among the most frequently been explored (Yang et al., 2021). Huge possibilities of these metal nanomaterials structures concern their potential use as drug delivery systems, in improving the quality of radiation-based anticancer therapy, in providing photothermal transforming effects for thermal-therapy, and in supporting molecular imaging, as well as being compounds with bactericidal, fungicidal, and anti-viral properties (Sharma et al., 2015; Klębowski et al., 2018).

Targeting strategies for nanomedicines

Because of the tight connection between microvascular endothelial cells in normal tissues and the large relative molecular weights of drug-loaded nanocarriers, their passing through vascular walls is difficult. The increased vascular permeability associated with the development of atherosclerosis provides a pathway for nano-drug delivery from the luminal side to the plaque interior (Figure 3).

The realization of passive targeting mainly depends on the high permeability and high retention of diseased blood vessels. Nanomedicines in the blood circulation are taken up by inflammatory cells (monocytes or macrophages), which then migrate to the inflammatory plaque to exert their functions. When coronary atherosclerosis, thrombosis, or MI occur, the blood vessel lumen is narrowed as the intima of the blood vessels grows laterally and plaque blood flow increases, resulting in an increase in fluid shear force. Nanomaterial-based shear-sensitive drug delivery systems came into existence because of these characteristics. The convex lens-shaped lipid-based NPs prepared by Holme et al. (2012) could not only maintain the structural stability of normal blood vessels, but also release drugs into plaques with structural changes under the action of high blood shear force.

With the in-depth study of specific cells and molecules in the development of atherosclerosis, researchers proposed active targeting strategies based on the pathologic features of atherosclerosis to improve the efficiency of drug targeted

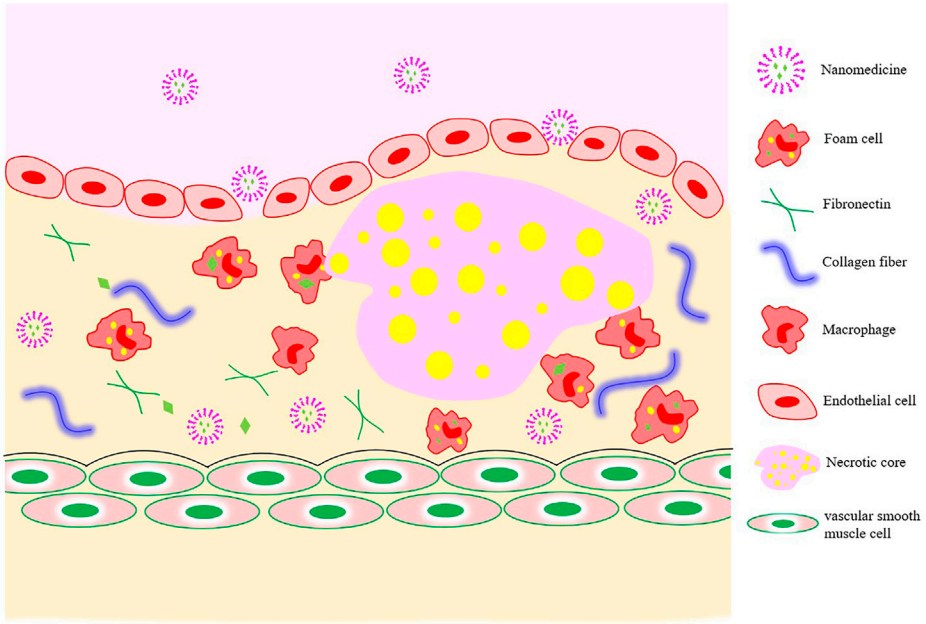

FIGURE 3
Nanomedicine-based strategies for targeting atherosclerotic plaques.

delivery to CVDs. Active targeting refers to artificially modifying the function of one or more nanocarrier targets so the drug can precisely reach a specific site to exert its effects. For example, expression of the angiotensin II type 1 receptor (AT1) in peripheral blood is elevated in the early period of myocardial IRI. Dvir et al. (2011) targeted liposomes to infarcted myocardium by modifying ligands that could specifically bind to AT1 on liposomes. With the continuous development of nanomedicines, natural nanomaterials that exhibit excellent inherent targeting properties have aroused strong interest among researchers. One of the most popular endogenous lipid-based NPs is HDL. In addition to removing cholesterol from plaques *via* reverse cholesterol transport, it also works by transporting lipids, proteins, or endogenous miRNA to recipient cells (Kornmueller et al., 2019). In 2019, Jiang et al. (2019) proposed and prepared dual-targeting NPs with recombinant HDL that effectively promoted the rapid regression of plaques. These studies provide new ideas and directions for the prevention and treatment of CVDs.

No matter what targeting strategy is used, including passive targeting, active targeting, intrinsic targeting, or novel strategies for targeting the diseased microenvironment with responsive nanomaterials, the final targeting efficiencies are closely correlated with the biological, physical, and chemical properties of the NPs themselves (Wang et al., 2018). In addition, the targeting efficiencies of nano-formulations are also deeply affected by many different types of objective factors, such as the developmental stage of CVDs, type, location, blood composition, and the wall shear stress.

Mechanisms of cardiovascular disease

Atherosclerosis is the root cause of most CVDs, and it has three main stages in its evolution. In the first stage, the formation of foam cells is a marker of the onset of atherosclerosis. Under the stimulation of harmful internal and external environmental conditions, the dysregulation of endothelial cells that comprise the capillary walls leads to an increase in permeability to macromolecules. Low-density lipoprotein (LDL) is more likely to cross the vascular wall and accumulate nearby, becoming oxidized LDL (ox-LDL) under the modification of enzymes and reactive oxygen species (Tousoulis et al., 2008; Lobatto et al., 2011). In addition, the expression of chemokines, including monocyte chemotactic protein-1, and inflammatory factors is up-regulated in the damaged vascular endothelial cells. Under the action of the above-mentioned factors, monocytes migrate to the endothelial cells. Monocytes cross the endothelium to differentiate into macrophages driven by adhesion molecules, such as vascular endothelial adhesion molecule (VCAM-1) and intercellular adhesion molecule-1 (ICAM-1). After recognizing and absorbing ox-LDL, macrophages are transformed into foam cells (Bobryshev et al., 2016). In the second stage, vascular smooth muscle cells (VSMCs) under the influence of immune cells and inflammatory factors undergo phenotypic

transformation (that is, from contractile phenotype to synthetic phenotype), migrate from the middle membrane to the intima, and begin to proliferate. Some VSMCs absorb ox-LDL and change into VSMC-derived foam cells, and other VSMCs secrete extracellular matrix molecules (such as collagen) to form fibrous caps, inducing neointima formation and vascular remodeling. Eventually, the accumulated foam cells gradually undergo apoptosis or necrosis and turn into the necrotic cores. The final stage is thrombosis or plaque rupture. During this phase, synthetic VSMCs secrete matrix metalloproteinases to degrade the extracellular collagen and thin the fibrous cap. In addition, prolonged oxidative stress promotes further expansion of the necrotic core (Dai et al., 2020; Ge et al., 2020; Park et al., 2020). The enlargement of necrotic core and the formation of new blood vessels may lead to unstable plaque rupture and intravascular thrombosis. Later, persistent arterial spasms ensue and eventually the dreaded lumen occlusions occur (Dai et al., 2016). MI is accompanied by the death of many cardiomyocytes. Even if blood reperfusion is achieved in a very short time, disordered energy metabolism may still occur in the myocardial tissue. In addition, some adverse reactions include the massive accumulation of oxygen free radicals caused by ischemia and hypoxia, Ca^{2+} overload, and inflammatory cascade reactions in myocardial cells, which further aggravate mitochondrial dysfunction, myocardial injury, and even complications from malignant arrhythmia, myocardial fibrosis, or heart failure (Ruytinx et al., 2018).

Application of nanoparticles in the treatment of atherosclerosis

At present, the non-stimuli-responsive NPs used in the treatment of atherosclerosis are mostly polymeric materials, such as PLGA, cyclodextrin, and chitosan (Psarros et al., 2012). Katsuki et al. reported that pitavastatin delivered by PLGA NPs significantly inhibited plaque rupture when compared with that of pitavastatin alone Kim et al. (2020) invented core-shell NPs based on the self-assembly of 2-hydroxypropyl-β-cyclodextrin and statins. 2-hydroxypropyl-β-cyclodextrin accelerated the removal of cholesterol in the plaque site, and the exchange of the statins in cyclodextrin and cholesterol in the plaque site was driven by host-object affinity. The results indicated that the concentrations of cholesterol and macrophages in plaque were remarkably decreased after the injection of the nanomedicines, which could effectively slow the occurrence of plaques. To further enhance the targeting of NPs, the researchers developed smart, responsive NPs utilizing endogenous stimulation (the specific microenvironment of the plaque site) or exogenous stimulation (e.g., light, ultrasound, and magnetism) (Maruf et al., 2019). In 2017, Dou et al. (2017) chemically modified β-cyclodextrin and encapsulated rapamycin to self-assemble acid-sensitive and reactive oxygen species-sensitive non-pro-inflammatory NPs Compared drug released from non-responsive NPs, drugs released from dual-responsive NPs are more available and achieve better therapeutic effects.

Active targeting NPs are modified with ligand, and the most used ligands are antibodies, peptides, and polymers. Antibodies can be used as target ligands for NPs because of their strong specificity, high affinity, and good stability. Gao et al. (2018) assembled specific antibodies targeting transient receptor potential vanilloid-1 (TRPV1) with CuS NPs to form a photothermal switch (CuS-TRPV1) and activated the TRPV1 channel of VSMCs with the help of a near-infrared laser, resulting in Ca^{2+} influx into VSMCs and the activation of the autophagy pathway. In addition, CuS-TRPV1 can be used in photoacoustic imaging of plaque sites and to accurately control TRPV1 channels, thereby prominently reducing lipid accumulation. Peptide ligands typically consist of 250 amino acids, which are sufficiently small compared with antibodies. They can be loaded into a shallow or hydrophobic binding pocket without compromising specificity or affinity. In addition, they have the advantages of low immunogenicity, simple manufacturing, and easy processing (Kim et al., 2018). Chin et al. (2021) prepared peptide amphiphilic micelles and delivered miR-145 to the plaque site by targeting the chemokine receptor 2 (CCR2) of synthetic VSMCs, thereby modulating the phenotype of VSMCs to slow plaque progression. Li et al. (2020) synthesized cyclodextrin-derived pH-responsive nanoparticles and further modified them with the integrin peptide ligand cRGDfK, which effectively delivered anti-miR33 to macrophages and significantly enhanced the therapeutic effect of the desirable anti-miR33 nanotherapy. Polymers can also serve as ligands, of which hyaluronic acid is the most widely used in atherosclerosis. Hyaluronic acid is an anti-inflammatory and biocompatible polysaccharide that specifically interacts with the CD44 and stabilin-2 receptors expressed by inflammatory and endothelial cells (Liu et al., 2014; Lee et al., 2015; Beldman et al., 2017; Nasr et al., 2020). Ye et al. (2019) successfully fabricated a multimodal and multifunctional NP targeting the class A scavenger receptors, which can be used to arrive at a specific diagnosis and to provide targeted treatment of vulnerable plaques. The designers embedded Fe_3O_4 in the shell membranes of NPs and encapsulated perfluorohexane in the core using a double-emulsified solvent evaporation method. Finally, dextran sulfate was adsorbed onto the NPs by electrostatic action. The NPs underwent phase transformation under the influence of low intensity focused ultrasound irradiation, consequently achieving ultrasound imaging, inducing macrophage apoptosis, and relieving plaque burden. Moreover, loaded Fe_3O_4 compensated for the deficiency of ultrasound imaging, conducting magnetic resonance imaging of plaques and evaluating vulnerable plaques accurately.

However, traditional NPs still face many challenges in effectively accumulating in atherosclerotic plaques, such as

accumulating off-target because of biomarker expression in normal tissues and reduced binding efficiency with limited ligand modification (Xue et al., 2019). At present, researchers have constructed a variety of biomimetic NPs, including recombinant HDL NPs, cell membrane biomimetic NPs, and extracellular vesicle-coated nanoparticles. The interaction between lecithin cholesterol acyltransferase and HDL in the peripheral blood circulation causes drug leakage before reaching the plaque. Furthermore, HDL receptors expressed on the surface of liver cells tend to accelerate HDL accumulation in the liver. Therefore, the most popular biomimetic strategies in recent years are cell membrane and extracellular vesicles. These biomimetic strategies take advantage of the biological function and homing ability of cells or cell components to evade the immune system, extend the circulation time, and implement personalized treatment (Gao et al., 2017).

Application of nanoparticles in the treatment of hypertension

Most of the main antihypertensive drugs currently used in the clinic have some deficiencies, such as poor water solubility, low bioavailability, and short half-lives. One study showed that compared with conventional dosage forms, the nanoemulsion system had a 2.8-fold increase in the plasma concentration of olmesartan, better antihypertensive efficacy, longer drug maintenance, and a nearly 3-fold reduction in the dose of olmesartan (Alam et al., 2017). Cabrales et al. (2010) used a new platform to prepare a nitric oxide (NO) controlled release systems based on hydrogel/glass hybrid nanoparticles. In addition, NPs served as a system for delivering siRNA and preventing its degradation by endonuclease and exonuclease in blood, serum, and cells. Cationic liposomes made from N-[1-(2,3-dioleoyloxy)]-N-N-N trimethyl ammonium propane (DOTAP) were administered intravenously for 12 days to reduce β1-adrenergic receptor expression and control blood pressure. Moreover, NPs have excellent performance in the early diagnosis of hypertension. An electrochemical immunosensor was sequentially surface-modified using magnetic functionalized diminished graphene oxide conjugated Fe_3O_4 NPs; subsequently, the surface of glassy carbon electrode was covered with AuNPs and cortisol antibody. The total amount of cortisol in plasma was detected through competitively combining with antibody sites; the results showed that the amount of cortisol in human plasma samples ranged from 1 to 1,000 ng/ml (Sun et al., 2017). Similarly, other physiological indicators, such as NO, galectin-3, leptin, sodium ions, growth hormone, and inflammatory factors, can be rapidly detected by nanosensors to achieve early diagnosis of hypertension (Madhurantakam et al., 2018).

Application of nanoparticles in the treatment of pulmonary arterial hypertension

Pulmonary arterial hypertension (PAH) is a highly dangerous and progressive disease characterized by increased pulmonary vascular resistance and elevated pulmonary arterial pressure. The ever-increasing pulmonary vascular resistance leads to pulmonary vasoconstriction and structural remodeling, which, in turn, affects right heart function and ultimately leads to right heart failure or death. The common targeted drugs for the treatment of PAH include prostacyclin (prostaglandin I2), endothelin receptor antagonists, phosphodiesterase type 5 inhibitors, and soluble guanylate cyclase agonists (Nakamura et al., 2017). Bosentan is a selective and competitive endothelin receptor antagonist and the solubility of bosentan NPs is seven times higher than unprocessed bosentan (Ghasemian et al., 2016). Akagi et al. (2016) revealed that PLGA NPs incorporating beraprost observably decreased pulmonary vascular resistance, inhibited pulmonary vascular remodeling, and minimized the occurrence of side effects in a rat model of PAH. Some studies indicated a greater inhibition of pulmonary artery smooth muscle cell proliferation with intratracheal administration of imatinib-incorporated NPs than that with imatinib alone (Akagi et al., 2015). Various nanomedicines including pitavastatin, fasudil, and oligonucleotides have excellent therapeutic effects in inhibiting pulmonary vascular remodeling, reducing pulmonary artery pressure, and improving survival rates (Nakamura et al., 2017).

Application of nanoparticles in the treatment of myocardial infarction

Because of the low proliferation and limited self-repair ability of cardiomyocytes, cardiac function will decline after acute MI and cannot be restored to the original state. Conventional myocardial reperfusion is not sufficient to repair apoptotic cardiomyocytes and stem cell therapy has become a new treatment method (Madigan and Atoui, 2018). Superparamagnetic iron oxide NPs with unique magnetic properties and good biocompatibility can be used to guide and monitor the therapeutic effect of stem cells on the MI (Zhu et al., 2016). Binsalamah et al. (2011) applied chitosan-alginate NPs to target delivery and sustained release of placental growth factor for the improvement of cardiac function at the site of MI. Leuschner et al. (2011) loaded CCR2-silencing siRNA onto liposomes and injected them intravenously into mice with MI, effectively reducing the aggregation of macrophages and the area of MI. Galagudza et al. (2012) designed silica NPs loaded with adenosine (a prototype cardioprotective agent) to reduce

infarct size; in addition, it reduced the hypotension and slow heart rate typically caused by systemic use of adenosine.

It is emphasized that the ischemic myocardium should be reperfused with blood as soon as possible after the occurrence of MI. However, coronary artery reperfusion can sometimes lead to the death of myocardial cells and progressively aggravate tissue damage, which is called myocardial IRI. Ichimura et al. (2016) administered intravenous PLGA NPs loaded with pitavastatin in a porcine myocardial IRI model, and they clearly found that the area of MI was significantly reduced and the left ventricular ejection fraction was distinctly improved 4 weeks later. Furthermore, there was no remarkable impact on blood pressure, heart rate, and biochemical indicators. Yajima et al. (2019) concluded that intravenously injected prostacyclin analog Ono-1301 NPs improved myocardial blood flow in a reperfusion injury model, and the NPs showed selective accumulation and long-term retention in ischemic myocardial tissue. Sayed et al. (2020) reported that a miRNA-loaded dendritic polymeric NPs precisely delivered miRNA into primary rat cardiomyocytes and effectually prevented cardiomyocyte apoptosis resulting from reperfusion. The α-cyclodextrin-based formulations as oxygen nanocarriers can limit IRI by injecting directly into the myocardial wall before starting full blood reperfusion (Femminò et al., 2018). Similarly, Penna et al. (2021) proposed cyclic nigerosyl-nigerose as oxygen nanocarriers, which showed a marked efficacy in controlled oxygenation and effectually protected cellular models from IRI.

Cardiac myocyte death and matrix degradation result in the activation of the innate immune system, and numerous inflammatory factors play a chemotactic role to aggregate neutrophils, monocytes, and macrophages in the damaged myocardium. The continuous stimulation of inflammation further worsens MI and ventricular remodeling. Nakano et al. (2016) have proposed that PLGA NPs doped with irbesartan can antagonize inflammatory monocyte recruitment. They have multiple benefits for alleviating myocardial IRI, diminishing infarct size, and improving left ventricular remodeling. Nicotinamide adenine dinucleotide phosphate oxidase 2 (Nox2), a major source for cardiac reactive oxygen species production, is up-regulated in infarcted myocardium and is closely related to ventricular remodeling. Somasuntharam et al. (2013) demonstrated acid-degradable polyketal particles as delivery vehicles for Nox2-siRNA. After intramyocardial injection into mice with MI, Nox2-siRNA particles not only successfully inhibited the upregulation of Nox2, but also prominently recovered cardiac function. Studies have confirmed that after macrophages phagocytose apoptotic cells, the expression of miRNA-21 is up-regulated and the inflammatory response is alleviated. Bejerano et al. (2018) employed self-assembled NPs *via* Ca^{2+} bridge-mediated hyaluronan-sulfate complexation with nucleic acid to deliver a miRNA-21 mimic to cardiac macrophages after MI. The miRNA-21 NPs induced a phenotype shift from pro-inflammatory to reparative, promoted angiogenesis, and reduced hypertrophy, fibrosis, and cell apoptosis in distal myocardium. Ultimately, left ventricular remodeling was decreased.

Ventricular fibrillation is the leading cause of death in the early stage of MI, especially before admission to the hospital. Amiodarone is currently considered one of the most effective drugs for the treatment of fatal arrhythmia, but there are still limitations in the use of amiodarone in patients with MI. For example, amiodarone may lead to hypotension and non-cardiac death Takahama et al. (2013) utilized liposome-based NPs for targeted delivery of amiodarone. Through *in vivo* intravenous injection in experimental rat models of MI reperfusion, liposome-based NPs not only reduced the mortality associated with malignant arrhythmias, but also attenuated hemodynamic changes induced by amiodarone alone.

Application of nanoparticles in the treatment of other cardiovascular diseases

As an innovative drug delivery platform, NPs also perform well in the treatment of many other CVDs. NPs targeted delivery of tissue plasminogen activator (t-PA) and other thrombolytic drugs, which played a role in rapid recanalization of occlusive blood vessels, improved the inefficiency of systemic medication, and decreased bleeding and other complications significantly (Torchilin, 2014). Intimal hyperplasia remains a major cause of poor patient outcomes after open vascular reconstructions to treat atherosclerosis. The application of the NPs platform for periadventitial drug delivery may benefit patients undergoing surgical revascularization (Chaudhary et al., 2016). One research team used magnetic NPs to deliver t-PA to the thrombosis area and the drug accumulation at the lesion site was significantly increased through the external magnetic field, requiring less than 1% of the dose of free drug to achieve an effective concentration (Cicha, 2015). Vani et al. (2016) indicated that fullerene NPs considerably decreased the brain IRI; in addition, the enhanced glutathione and superoxide dismutase availably scavenged free radicals and protected brain cells from oxidative damage. Some nano-drug carriers had the ability to cross the blood-brain barrier, which delivered the neuroprotective drug cytidine 5′-diphosphocholine directly into the brain to diminish brain damage caused by ischemia/reperfusion (Panagiotou and Saha, 2015). Evans et al., (2015) developed the polyplex nanocarrier platform to encapsulate vasoactive peptides for alleviation of pathological vasoconstriction. The α-cyclodextrin and α-cyclodextrin nanosponges used as oxygenated nanocarriers release oxygen for a long time and can also be perfused in sufficient solution during organ transportation. The adequate oxygenation may extend the usability time of the explanted organ and promote the postoperative recovery of the transplanted heart (Penna et al., 2022).

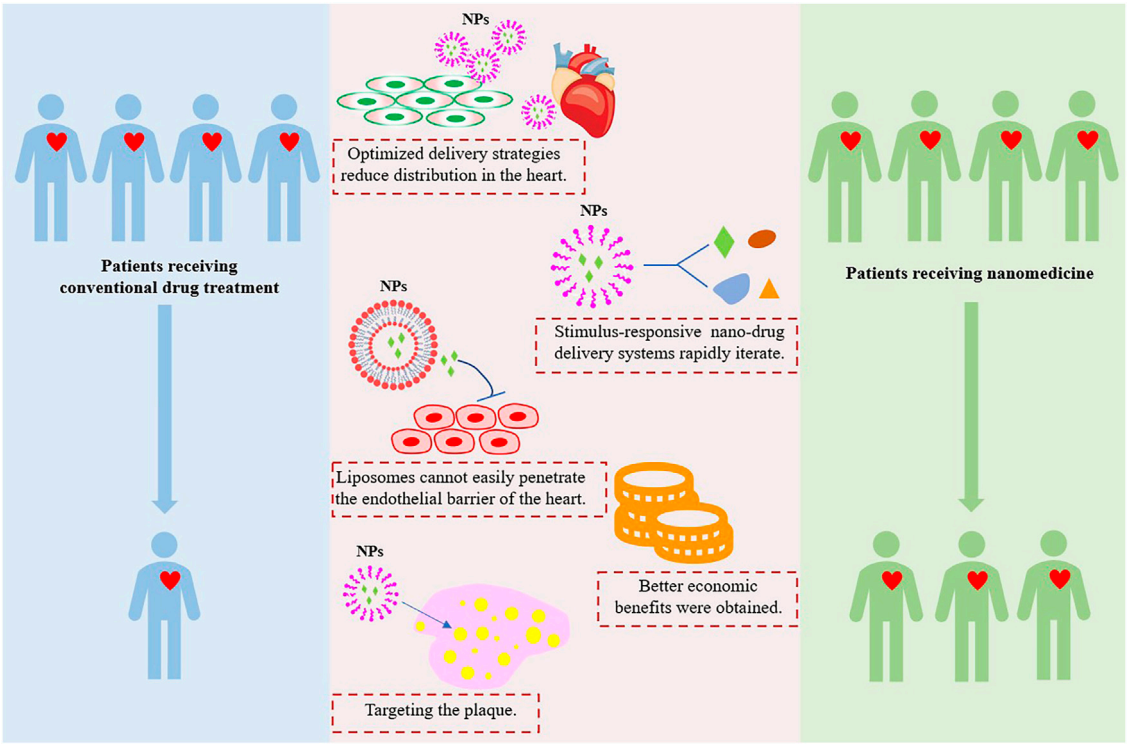

FIGURE 4
Nanotechnology applications in the advantages of reducing cardiotoxicity. Image adapted from Su et al. (2021).

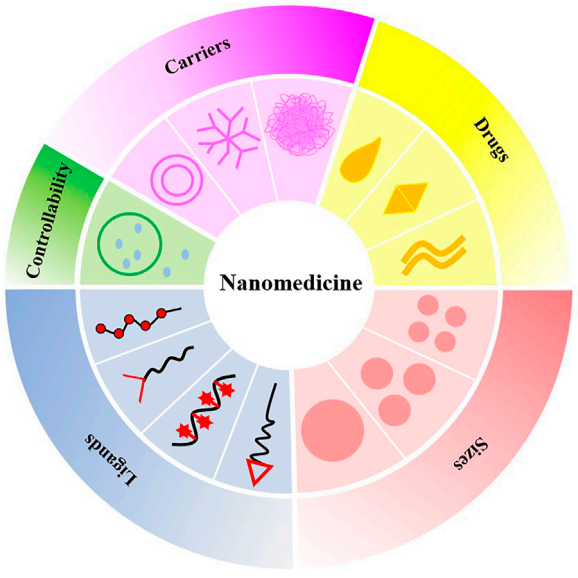

FIGURE 5
Properties required for ideal nanoparticle.

The nanotoxicity on patients with cardiovascular diseases

NPs can be distributed throughout the body by availably translocating in the blood circulation through membrane barriers and affect organs and tissues at both cellular and molecular levels. The interaction between NPs and cells may give rise to nanotoxicity. The narrow size distribution, large surface area to mass ratio, surface properties, charge, dose, and host immunity of NPs were considerably correlated with nanotoxicity. NPs can enter tissues and cells by invading membranes and cause cell damage and toxicity. Contents of oxidative stress (Harrison et al., 2003), inflammation (Libby et al., 2002), mitochondrial DNA damage to the aorta (Ballinger et al., 2000; Ballinger et al., 2002), and damage to vascular endothelial cells (Choksi et al., 2004) have been proposed to cause atherosclerosis. Studies have shown that exposure to NPs exacerbates all these potential triggers (Radomski et al., 2005; Guo et al., 2011; Su et al., 2012), accelerating the progression of atherosclerosis through platelet aggregation and vascular thrombosis (Massberg et al., 2002; Libby et al., 2011).

On the other hand, nanomedicine has attracted great attention, and its applications in CVDs treatment and cardiotoxicity reduction are relatively new and growing. The ideal nanomedicine should be able to target the plaque tissues, penetrate the core of the plaque, and completely remove the plaque without causing systemic damage, especially cardiotoxicity. There are five advantages of nanotechnology in reducing cardiotoxicity (Figure 4). However, the harmful effects of nanocarriers on patients are not fully understood, it is important to further explore the role of NPs in reducing cardiotoxicity in the treatment of CVDs, and long-term detailed toxicity assessments are needed to accurately evaluate the nanotoxicity.

Conclusion, challenges, and perspectives

To summarize, nanomedicine technology in the form of nanocarriers have unique advantages and potential and provide new ideas, approaches, and methods in the diagnosis and treatment of CVDs and a bright prospect for clinicians. Compared with traditional drug delivery methods, nano-drug delivery introduces different ligands into corresponding nanocarriers according to different pathological mechanisms and therapeutic strategies to directly target the lesion site. This strategy more efficaciously targets the atherosclerotic plaque region, increasing drug concentration to improve myocardial blood flow. However, because of the rapid blood flow and the frequent interaction between nanomedicine and numerous blood cells and immune cells and a variety of biomolecules such as chemokines and cytokines, it is difficult to achieve ideal diagnostic and therapeutic expectations. The biomimetic principle is becoming more and more popular in nano-DDSs. Compared with traditional NPs, biomimetic NPs have natural advantages in escaping immune system attack, extending circulation time *in vivo*, and enhancing targeting. Therefore, the combination of traditional NPs and novel biomimetic strategies is an effective treatment. Moreover, cells as nanocarriers are promising by virtue of their strong targeting ability, with some having therapeutic effects of their own. Because of the above NPs design strategy, combination with molecular imaging technology, the construction of integrated diagnosis and treatment NPs will further provide more abundant information for CVDs treatment. Certainly, to maximize the therapeutic efficacy of nanomedicine, more attention should be paid to the structural design, targeting, stability, and safety of NPs in the future (Perioli et al., 2019). Ideal NPs consist of the following parts: ligands that selectively combine with specific molecules, high-capacity drug-loading nanocarriers, the appropriate drug, and controllable drug release (Figure 5). It is also necessary to explore effective drugs for new targets, including how to promote the regeneration of myocardial cells after MI with nano-DDSs.

Nevertheless, the clinical transformation of NPs remains a huge challenge, because the construction of nanotherapeutic systems is complex, the quality control process is cumbersome, and the biosafety needs to be further substantiated. In addition, the interaction between nanoparticles and pathological tissues needs to be fully elucidated and the number of relevant studies in large-scale animal models needs to increase. To accelerate clinical transformation, future research should focus on how to reduce construction complexity and improve therapeutic effectiveness, and efforts should be made to elucidate relevant mechanisms, such as pharmacokinetics, and possible long-term side effects of NPs. Especially in the simplification of NPs, it is necessary to fully exploit the therapeutic effects of nanomaterials themselves, reducing modifications without sacrificing their targeting properties and achieving the integration of diagnosis and treatment as much as possible. It is believed that with the development of different disciplines, the treatment systems based on NPs will bring a new revolution in the treatment of CVDs.

Author contributions

FY and JX wrote the manuscript, while GW and QD made final revisions. All authors approved the submission and publication of the manuscript.

Funding

This work was supported by grants from the National Natural Science Foundation of China (31971242), the Chongqing Research Program of Basic research and Frontier Technology (cstc2019jcyjzdxmX0028) and the Chongqing Natural Science Foundation (cstc2020jcyj-msxmX0237).

Conflict of interest

The authors declare that the research was conducted in the absence of any commercial or financial relationships that could be construed as a potential conflict of interest.

Publisher's note

References

Akagi, S., Nakamura, K., Matsubara, H., Kondo, M., Miura, D., Matoba, T., et al. (2016). Intratracheal administration of prostacyclin analogue-incorporated nanoparticles ameliorates the development of monocrotaline and sugen-hypoxia-induced pulmonary arterial hypertension. *J. Cardiovasc. Pharmacol.* 67 (4), 290–298. doi:10.1097/FJC.0000000000000352

Akagi, S., Nakamura, K., Miura, D., Saito, Y., Matsubara, H., Ogawa, A., et al. (2015). Delivery of imatinib-incorporated nanoparticles into lungs suppresses the development of monocrotaline-induced pulmonary arterial hypertension. *Int. Heart. J.* 56, 354–359. doi:10.1536/ihj.14-338

Alam, T., Khan, S., Gaba, B., Haider, M. F., Baboota, S., and Ali, J. (2017). Nanocarriers as treatment modalities for hypertension. *Drug. Deliv.* 24 (1), 358–369. doi:10.1080/10717544.2016.1255999

Baigent, C., Baigent, L., Blackwell, R., Collins, J., Emberson, J., Godwin, R., et al. (2009). Aspirin in the primary and secondary prevention of vascular disease: Collaborative meta-analysis of individual participant data from randomised trials. *Lancet* 373 (9678), 1849–1860. doi:10.1016/S0140-6736(09)60503-1

Ballinger, S. W., Patterson, C., Knight-Lozano, C. A., Burow, D. L., Conklin, C. A., Hu, Z., et al. (2002). Mitochondrial integrity and function in atherogenesis. *Circulation* 106 (5), 544–549. doi:10.1161/01.cir.0000023921.93743.89

Ballinger, S. W., Patterson, C., Yan, C. N., Doan, R., Burow, D. L., Young, C. G., et al. (2000). Hydrogen peroxide- and peroxynitrite-induced mitochondrial DNA damage and dysfunction in vascular endothelial and smooth muscle cells. *Circ. Res.* 86 (9), 960–966. doi:10.1161/01.res.86.9.960

Bejerano, T., Etzion, S., Elyagon, S., Etzion, Y., and Cohen, S. (2018). Nanoparticle delivery of miRNA-21 mimic to cardiac macrophages improves myocardial remodeling after myocardial infarction. *Nano. Lett.* 18 (9), 5885–5891. doi:10.1021/acs.nanolett.8b02578

Beldman, T. J., Senders, M. L., Alaarg, A., Pérez-Medina, C., Tang, J., Zhao, Y., et al. (2017). Hyaluronan nanoparticles selectively target plaque-associated macrophages and improve plaque stability in atherosclerosis. *Acs. Nano.* 11 (6), 5785–5799. doi:10.1021/acsnano.7b01385

Binsalamah, Z. M., Paul, A., Khan, A. A., Prakash, S., and Shum-Tim, D. (2011). Intramyocardial sustained delivery of placental growth factor using nanoparticles as a vehicle for delivery in the rat infarct model. *Int. J. Nanomedicine.* 6, 2667–2678. doi:10.2147/IJN.S25175

Bobryshev, Y. V., Ivanova, E. A., Chistiakov, D. A., Nikiforov, N. G., and Orekhov, A. N. (2016). Macrophages and their role in atherosclerosis: Pathophysiology and transcriptome analysis. *Biomed. Res. Int.* 2016, 9582430. doi:10.1155/2016/9582430

Cabrales, P., Han, G., Roche, C., Nacharaju, P., Friedman, A. J., and Friedman, J. M. (2010). Sustained release nitric oxide from long-lived circulating nanoparticles. *Free. Radic. Biol. Med.* 49 (4), 530–538. doi:10.1016/j.freeradbiomed.2010.04.034

Chaudhary, M. A., Guo, L. W., Shi, X., Chen, G., Gong, S., Liu, B., et al. (2016). Periadventitial drug delivery for the prevention of intimal hyperplasia following open surgery. *J. Control. Release.* 233, 174–180. doi:10.1016/j.jconrel.2016.05.002

Chiani, M., Shokrgozar, M. A., Azadmanesh, K., Norouzian, D., Mehrabi, M. R., Najmafshar, A., et al. (2017). Preparation, characterization, and *in vitro* evaluation of bleomycin-containing nanoliposomes. *Chem. Biol. Drug. Des.* 89 (4), 492–497. doi:10.1111/cbdd.12869

Chin, D. D., Poon, C., Wang, J., Joo, J., Ong, V., Jiang, Z., et al. (2021). miR-145 micelles mitigate atherosclerosis by modulating vascular smooth muscle cell phenotype. *Biomaterials* 273, 120810. doi:10.1016/j.biomaterials.2021.120810

Choksi, K. B., Boylston, W. H., Rabek, J. P., Widger, W. R., and Papaconstantinou, J. (2004). Oxidatively damaged proteins of heart mitochondrial electron transport complexes. *Biochim. Biophys. Acta.* 1688 (2), 95–101. doi:10.1016/j.bbadis.2003.11.007

Cicha, I. (2015). Thrombosis: Novel nanomedical concepts of diagnosis and treatment. *World. J. Cardiol.* 7 (8), 434–441. doi:10.4330/wjc.v7.i8.434

Cutrone, G., Qiu, J., Menendez-Miranda, M., Casas-Solvas, J. M., Aykaç, A., Li, X., et al. (2019). Comb-like dextran copolymers: A versatile strategy to coat highly porous mof nanoparticles with a peg shell. *Carbohydr. Polym.* 223, 115085. doi:10.1016/j.carbpol.2019.115085

Dai, J., Tian, J., Hou, J., Xing, L., Liu, S., Ma, L., et al. (2016). Association between cholesterol crystals and culprit lesion vulnerability in patients with acute coronary syndrome: An optical coherence tomography study. *Atherosclerosis* 247, 111–117. doi:10.1016/j.atherosclerosis.2016.02.010

Dai, T., He, W., Yao, C., Ma, X., Ren, W., Mai, Y., et al. (2020). Applications of inorganic nanoparticles in the diagnosis and therapy of atherosclerosis. *Biomater. Sci.* 8 (14), 3784–3799. doi:10.1039/d0bm00196a

Dobrovolskaia, M. A., Patri, A. K., Simak, J., Hall, J. B., Semberova, J., De Paoli Lacerda, S. H., et al. (2012). Nanoparticle size and surface charge determine effects of PAMAM dendrimers on human platelets *in vitro*. *Mol. Pharm.* 9 (3), 382–393. doi:10.1021/mp200463e

Dou, Y., Chen, Y., Zhang, X., Xu, X., Chen, Y., Guo, J., et al. (2017). Non-proinflammatory and responsive nanoplatforms for targeted treatment of atherosclerosis. *Biomaterials* 143, 93–108. doi:10.1016/j.biomaterials.2017.07.035

Dvir, T., Bauer, M., Schroeder, A., Tsui, J. H., Anderson, D. G., Langer, R., et al. (2011). Nanoparticles targeting the infarcted heart. *Nano. Lett.* 11 (10), 4411–4414. doi:10.1021/nl2025882

Evans, B. C., Hocking, K. M., Kilchrist, K. V., Wise, E. S., Brophy, C. M., and Duvall, C. L. (2015). Endosomolytic nano-polyplex platform technology for cytosolic peptide delivery to inhibit pathological vasoconstriction. *Acs. Nano.* 9 (6), 5893–5907. doi:10.1021/acsnano.5b00491

Femminò, S., Penna, C., Bessone, F., Caldera, F., Dhakar, N., Cau, D., et al. (2018). α-Cyclodextrin and α-cyclodextrin polymers as oxygen nanocarriers to limit hypoxia/reoxygenation injury: Implications from an *in vitro* model. *Polym. (Basel)* 10 (2), 211. doi:10.3390/polym10020211

Fisher, M., and Moonis, M. (2012). Neuroprotective effects of statins: Evidence from preclinical and clinical studies. *Curr. Treat. Options. Cardiovasc. Med.* 14 (3), 252–259. doi:10.1007/s11936-012-0174-9

Galagudza, M., Korolev, D., Postnov, V., Naumisheva, E., Grigorova, Y., Uskov, I., et al. (2012). Passive targeting of ischemic-reperfused myocardium with adenosine-loaded silica nanoparticles. *Int. J. Nanomedicine.* 7, 1671–1678. doi:10.2147/IJN.S29511

Gao, J., Wang, S., and Wang, Z. (2017). High yield, scalable and remotely drug-loaded neutrophil-derived extracellular vesicles (EVs) for anti-inflammation therapy. *Biomaterials* 135, 62–73. doi:10.1016/j.biomaterials.2017.05.003

Gao, W., Sun, Y., Cai, M., Zhao, Y., Cao, W., Liu, Z., et al. (2018). Copper sulfide nanoparticles as a photothermal switch for TRPV1 signaling to attenuate atherosclerosis. *Nat. Commun.* 9 (1), 231–310. doi:10.1038/s41467-017-02657-z

Ge, X., Cui, H., Kong, J., Lu, S. Y., Zhan, R., Gao, J., et al. (2020). A non-invasive nanoprobe for *in vivo* photoacoustic imaging of vulnerable atherosclerotic plaque. *Adv. Mater* 32 (38), e2000037. doi:10.1002/adma.202000037

Ghasemian, E., Motaghian, P., and Vatanara, A. (2016). D-optimal design for preparation and optimization of fast dissolving bosentan nanosuspension. *Adv. Pharm. Bull.* 6 (2), 211–218. doi:10.15171/apb.2016.029

Gothwal, A., Khan, I., and Gupta, U. (2016). Polymeric micelles: Recent advancements in the delivery of anticancer drugs. *Pharm. Res.* 33 (1), 18–39. doi:10.1007/s11095-015-1784-1

Guo, Y. Y., Zhang, J., Zheng, Y. F., Yang, J., and Zhu, X. Q. (2011). Cytotoxic and genotoxic effects of multi-wall carbon nanotubes on human umbilical vein endothelial cells *in vitro*. *Mutat. Res.* 721 (2), 184–191. doi:10.1016/j.mrgentox.2011.01.014

Han, H., Bártolo, R., Li, J., Shahbazi, M. A., and Santos, H. A. (2022). Biomimetic platelet membrane-coated nanoparticles for targeted therapy. *Eur. J. Pharm. Biopharm.* 172, 1–15. doi:10.1016/j.ejpb.2022.01.004

Harrison, D., Griendling, K. K., Landmesser, U., Hornig, B., and Drexler, H. (2003). Role of oxidative stress in atherosclerosis. *Am. J. Cardiol.* 91 (3), 7A–11A. doi:10.1016/s0002-9149(02)03144-2

He, S., Wu, L., Li, X., Sun, H., Xiong, T., Liu, J., et al. (2021). Metal-organic frameworks for advanced drug delivery. *Acta. Pharm. Sin. B* 11 (8), 2362–2395. doi:10.1016/j.apsb.2021.03.019

Holme, M. N., Fedotenko, I. A., Abegg, D., Althaus, J., Babel, L., Favarger, F., et al. (2012). Shear-stress sensitive lenticular vesicles for targeted drug delivery. *Nat. Nanotechnol.* 7 (8), 536–543. doi:10.1038/nnano.2012.84

Hossaini Nasr, S. H., Rashidijahanabad, Z., Ramadan, S., Kauffman, N., Parameswaran, N., Zinn, K. R., et al. (2020). Effective atherosclerotic plaque inflammation inhibition with targeted drug delivery by hyaluronan conjugated atorvastatin nanoparticles. *Nanoscale* 12 (17), 9541–9556. doi:10.1039/d0nr00308e

Iafisco, M., Alogna, A., Miragoli, M., and Catalucci, D. (2019). Cardiovascular nanomedicine: The route ahead. *Nanomedicine (Lond)* 14 (18), 2391–2394. doi:10.2217/nnm-2019-0228

Ichimura, K., Matoba, T., Nakano, K., Tokutome, M., Honda, K., Koga, J. I., et al. (2016). A translational study of a new therapeutic approach for acute myocardial infarction: Nanoparticle-mediated delivery of pitavastatin into reperfused myocardium reduces ischemia-reperfusion injury in a preclinical porcine model. *PLoS. One.* 11 (9), e0162425. doi:10.1371/journal.pone.0162425

Jiang, C., Qi, Z., He, W., Li, Z., Tang, Y., Wang, Y., et al. (2019). Dynamically enhancing plaque targeting via a positive feedback loop using multifunctional biomimetic nanoparticles for plaque regression. *J. Control. Release.* 308, 71–85. doi:10.1016/j.jconrel.2019.07.007

Karunakar, G., Patel, N. P., and Kamal, S. S. (2016). Nano structured lipid carrier based drug delivery system. *J. Chem. Pharm. Res.* 8 (2), 627–643.

Katsuki, S., Matoba, T., Nakashiro, S., Sato, K., Koga, J. I., Nakano, K., et al. (2014). Nanoparticle-mediated delivery of pitavastatin inhibits atherosclerotic plaque destabilization/rupture in mice by regulating the recruitment of inflammatory monocytes. *Circulation* 129 (8), 896–906. doi:10.1161/CIRCULATIONAHA.113.002870

Khafaji, M., Zamani, M., Golizadeh, M., and Bavi, O. (2019). Inorganic nanomaterials for chemo/photothermal therapy: A promising horizon on effective cancer treatment. *Biophys. Rev.* 11 (3), 335–352. doi:10.1007/s12551-019-00532-3

Kim, H., Kumar, S., Kang, D. W., Jo, H., and Park, J. H. (2020). Affinity-driven design of cargo-switching nanoparticles to leverage a cholesterol-rich microenvironment for atherosclerosis therapy. *Acs. Nano.* 14 (6), 6519–6531. doi:10.1021/acsnano.9b08216

Kim, M., Sahu, A., Kim, G. B., Nam, G. H., Um, W., Shin, S. J., et al. (2018). Comparison of *in vivo* targeting ability between cRGD and collagen-targeting peptide conjugated nano-carriers for atherosclerosis. *J. Control. Release.* 269, 337–346. doi:10.1016/j.jconrel.2017.11.033

Klębowski, B., Depciuch, J., Parlińska-Wojtan, M., and Baran, J. (2018). Applications of noble metal-based nanoparticles in medicine. *Ijms* 19 (12), 4031. doi:10.3390/ijms19124031

Kornmueller, K., Vidakovic, I., and Prassl, R. (2019). Artificial high density lipoprotein nanoparticles in cardiovascular research. *Molecules* 24 (15), 2829. doi:10.3390/molecules24152829

Kroll, A. V., Fang, R. H., and Zhang, L. (2017). Biointerfacing and applications of cell membrane-coated nanoparticles. *Bioconjug. Chem.* 28 (1), 23–32. doi:10.1021/acs.bioconjchem.6b00569

Lee, G. Y., Kim, J. H., Choi, K. Y., Yoon, H. Y., Kim, K., Kwon, I. C., et al. (2015). Hyaluronic acid nanoparticles for active targeting atherosclerosis. *Biomaterials* 53, 341–348. doi:10.1016/j.biomaterials.2015.02.089

Lee, J. J., Saiful Yazan, L. S., and Che Abdullah, C. A. C. (2017). A review on current nanomaterials and their drug conjugate for targeted breast cancer treatment. *Int. J. Nanomedicine.* 12, 2373–2384. doi:10.2147/IJN.S127329

Leuschner, F., Dutta, P., Gorbatov, R., Novobrantseva, T. I., Donahoe, J. S., Courties, G., et al. (2011). Therapeutic siRNA silencing in inflammatory monocytes in mice. *Nat. Biotechnol.* 29 (11), 1005–1010. doi:10.1038/nbt.1989

Li, C., Dou, Y., Chen, Y., Qi, Y., Li, L., Han, S., et al. (2020). Site-specific MicroRNA-33 antagonism by pH-responsive nanotherapies for treatment of atherosclerosis via regulating cholesterol efflux and adaptive immunity. *Adv. Funct. Mat.* 30 (42), 2002131. doi:10.1002/adfm.202002131

Libby, P., Ridker, P. M., and Hansson, G. K. (2011). Progress and challenges in translating the biology of atherosclerosis. *Nature* 473 (7347), 317–325. doi:10.1038/nature10146

Libby, P., Ridker, P. M., and Maseri, A. (2002). Inflammation and atherosclerosis. *Circulation* 105 (9), 1135–1143. doi:10.1161/hc0902.104353

Liu, L., He, H., Zhang, M., Zhang, S., Zhang, W., and Liu, J. (2014). Hyaluronic acid-decorated reconstituted high density lipoprotein targeting atherosclerotic lesions. *Biomaterials* 35 (27), 8002–8014. doi:10.1016/j.biomaterials.2014.05.081

Lobatto, M. E., Fayad, Z. A., Silvera, S., Vucic, E., Calcagno, C., Mani, V., et al. (2010). Multimodal clinical imaging to longitudinally assess a nanomedical anti-inflammatory treatment in experimental atherosclerosis. *Mol. Pharm.* 7 (6), 2020–2029. doi:10.1021/mp100309y

Lobatto, M. E., Fuster, V., Fayad, Z. A., and Mulder, W. J. (2011). Perspectives and opportunities for nanomedicine in the management of atherosclerosis. *Nat. Rev. Drug. Discov.* 10 (11), 835–852. doi:10.1038/nrd3578

Madhurantakam, S., Babu, K. J., Rayappan, J. B. B., and Krishnan, U. M. (2018). Nanotechnology-based electrochemical detection strategies for hypertension markers. *Biosens. Bioelectron.* 116, 67–80. doi:10.1016/j.bios.2018.05.034

Madigan, M., and Atoui, R. (2018). Therapeutic use of stem cells for myocardial infarction. *Bioeng. (Basel)* 5 (2), 28. doi:10.3390/bioengineering5020028

Martínez-Milla, J., Raposeiras-Roubín, S., Pascual-Figal, D. A., and Ibáñez, B. (2019). Role of beta-blockers in cardiovascular disease in 2019. *Rev. Esp. Cardiol. Engl. Ed.* 72 (10), 844–852. doi:10.1016/j.rec.2019.04.014

Maruf, A., Wang, Y., Yin, T., Huang, J., Wang, N., Durkan, C., et al. (2019). Atherosclerosis treatment with stimuli-responsive nanoagents: Recent advances and future perspectives. *Adv. Healthc. Mat.* 8 (11), e1900036. doi:10.1002/adhm.201900036

Massberg, S., Brand, K., Grüner, S., Page, S., Müller, E., Müller, I., et al. (2002). A critical role of platelet adhesion in the initiation of atherosclerotic lesion formation. *J. Exp. Med.* 196 (7), 887–896. doi:10.1084/jem.20012044

McMurray, J. J., Packer, M., Desai, A. S., Gong, J., Lefkowitz, M. P., Rizkala, A. R., et al. (2014). Angiotensin-neprilysin inhibition versus enalapril in heart failure. *N. Engl. J. Med.* 371, 993–1004. doi:10.1056/NEJMoa1409077

Nakamura, K., Matsubara, H., Akagi, S., Sarashina, T., Ejiri, K., Kawakita, N., et al. (2017). Nanoparticle-mediated drug delivery system for pulmonary arterial hypertension. *J. Clin. Med.* 6 (5), 48. doi:10.3390/jcm6050048

Nakamura, Y., Mochida, A., Choyke, P. L., and Kobayashi, H. (2016). Nanodrug delivery: Is the enhanced permeability and retention effect sufficient for curing cancer? *Bioconjug. Chem.* 27 (10), 2225–2238. doi:10.1021/acs.bioconjchem.6b00437

Nakano, Y., Matoba, T., Tokutome, M., Funamoto, D., Katsuki, S., Ikeda, G., et al. (2016). Nanoparticle-mediated delivery of irbesartan induces cardioprotection from myocardial ischemia-reperfusion injury by antagonizing monocyte-mediated inflammation. *Sci. Rep.* 6 (1), 29601–29614. doi:10.1038/srep29601

Owens, A. T., Brozena, S., and Jessup, M. (2017). Neprilysin inhibitors: Emerging therapy for heart failure. *Annu. Rev. Med.* 68, 41–49. doi:10.1146/annurev-med-052915-015509

Panagiotou, S., and Saha, S. (2015). Therapeutic benefits of nanoparticles in stroke. *Front. Neurosci.* 9, 182. doi:10.3389/fnins.2015.00182

Park, J. H., Dehaini, D., Zhou, J., Holay, M., Fang, R. H., and Zhang, L. (2020). Biomimetic nanoparticle technology for cardiovascular disease detection and treatment. *Nanoscale. Horiz.* 5 (1), 25–42. doi:10.1039/c9nh00291j

Patra, J. K., Das, G., Fraceto, L. F., Campos, E. V. R., Rodriguez-Torres, M. D. P., Acosta-Torres, L. S., et al. (2018). Nano based drug delivery systems: Recent developments and future prospects. *J. Nanobiotechnology.* 16 (1), 71–33. doi:10.1186/s12951-018-0392-8

Penna, C., Femminò, S., Caldera, F., Rubin PedrazzoPedrazzo, A., Cecone, C., Alfì, E., et al. (2021). Cyclic nigerosyl-nigerose as oxygen nanocarrier to protect cellular models from hypoxia/reoxygenation injury: Implications from an *in vitro* model. *Int. J. Mol. Sci.* 22 (8), 4208. doi:10.3390/ijms22084208

Penna, C., Trotta, F., Cavalli, R., and Pagliaro, P. (2022). Nanocarriers loaded with oxygen to improve the protection of the heart to be transplanted. *Curr. Pharm. Des.* 28 (6), 468–470. doi:10.2174/1381612827666211109112723

Perioli, L., Pagano, C., and Ceccarini, M. R. (2019). Current highlights about the safety of inorganic nanomaterials in healthcare. *Curr. Med. Chem.* 26 (12), 2147–2165. doi:10.2174/0929867325666180723121804

Peters, D., Kastantin, M., Kotamraju, V. R., Karmali, P. P., Gujraty, K., Tirrell, M., et al. (2009). Targeting atherosclerosis by using modular, multifunctional micelles. *Proc. Natl. Acad. Sci. U. S. A.* 106 (24), 9815–9819. doi:10.1073/pnas.0903369106

Psarros, C., Lee, R., Margaritis, M., and Antoniades, C. (2012). Nanomedicine for the prevention, treatment and imaging of atherosclerosis. *Nanomedicine* 8 (1), S59–S68. doi:10.1016/j.maturitas.2011.12.01410.1016/j.nano.2012.05.006

Radomski, A., Jurasz, P., Alonso-Escolano, D., Drews, M., Morandi, M., Malinski, T., et al. (2005). Nanoparticle-induced platelet aggregation and vascular thrombosis. *Br. J. Pharmacol.* 146 (6), 882–893. doi:10.1038/sj.bjp.0706386

Regoli, D., Plante, G. E., and Gobeil, F., Jr (2012). Impact of kinins in the treatment of cardiovascular diseases. *Pharmacol. Ther.* 135 (1), 94–111. doi:10.1016/j.pharmthera.2012.04.002

Ruytinx, P., Proost, P., Van Damme, J., and Struyf, S. (2018). Chemokine-induced macrophage polarization in inflammatory conditions. *Front. Immunol.* 9, 1930. doi:10.3389/fimmu.2018.01930

Sayed, N., Tambe, P., Kumar, P., Jadhav, S., Paknikar, K. M., and Gajbhiye, V. (2020). miRNA transfection via poly(amidoamine)-based delivery vector prevents hypoxia/reperfusion-induced cardiomyocyte apoptosis. *Nanomedicine (Lond)* 15 (2), 163–181. doi:10.2217/nnm-2019-0363

Sharma, H., Mishra, P. K., Talegaonkar, S., and Vaidya, B. (2015). Metal nanoparticles: A theranostic nanotool against cancer. *Drug. Discov. Today.* 20 (9), 1143–1151. doi:10.1016/j.drudis.2015.05.009

Smith, S. C., Jr, Smith, A., Collins, R., Ferrari, D. R., Jr, Holmes, S., Logstrup, D. V., et al. (2012). Our time: A call to save preventable death from cardiovascular disease (heart disease and stroke). *Glob. Heart* 7 (23), 297–305. doi:10.1161/CIR.0b013e318267e99f10.1016/j.gheart.2012.08.002

Solomon, S. D., McMurray, J. J., Anand, I. S., Ge, J., Lam, C. S., Maggioni, A. P., et al. (2019). Angiotensin-neprilysin inhibition in heart failure with preserved ejection fraction. *N. Engl. J. Med.* 381 (17), 1609–1620. doi:10.1056/NEJMoa1908655

Somasuntharam, I., Boopathy, A. V., Khan, R. S., Martinez, M. D., Brown, M. E., Murthy, N., et al. (2013). Delivery of Nox2-NADPH oxidase siRNA with polyketal

nanoparticles for improving cardiac function following myocardial infarction. *Biomaterials* 34 (31), 7790–7798. doi:10.1016/j.biomaterials.2013.06.051

Su, L., Han, L., Ge, F., Zhang, S. L., Zhang, Y., Zhao, B. X., et al. (2012). The effect of novel magnetic nanoparticles on vascular endothelial cell function *in vitro* and *in vivo*. *J. Hazard. Mat.* 235-236, 316–325. doi:10.1016/j.jhazmat.2012.08.003

Su, X., Zhang, X., Liu, W., Yang, X., An, N., Yang, F., et al. (2021). Advances in the application of nanotechnology in reducing cardiotoxicity induced by cancer chemotherapy. *Seminars Cancer Biol.* S1044-579X (21), 00215–00217. doi:10.1016/j.semcancer.2021.08.003

Sun, B., Gou, Y., Ma, Y., Zheng, X., Bai, R., Ahmed Abdelmoaty, A. A. A., et al. (2017). Investigate electrochemical immunosensor of cortisol based on gold nanoparticles/magnetic functionalized reduced graphene oxide. *Biosens. Bioelectron.* 88, 55–62. doi:10.1016/j.bios.2016.07.047

Takahama, H., Shigematsu, H., Asai, T., Matsuzaki, T., Sanada, S., Fu, H. Y., et al. (2013). Liposomal amiodarone augments anti-arrhythmic effects and reduces hemodynamic adverse effects in an ischemia/reperfusion rat model. *Cardiovasc. Drugs. Ther.* 27 (2), 125–132. doi:10.1007/s10557-012-6437-6

Teymouri, M., Mashreghi, M., Saburi, E., Hejazi, A., and Nikpoor, A. R. (2019). The trip of a drug inside the body: From a lipid-based nanocarrier to a target cell. *J. Control. Release.* 309, 59–71. doi:10.1016/j.jconrel.2019.07.027

Torchilin, V. P. (2014). Multifunctional, stimuli-sensitive nanoparticulate systems for drug delivery. *Nat. Rev. Drug. Discov.* 13 (11), 813–827. doi:10.1038/nrd4333

Tousoulis, D., Charakida, M., and Stefanadis, C. (2008). Endothelial function and inflammation in coronary artery disease. *Postgrad. Med. J.* 84 (993), 368–371. doi:10.1136/hrt.2005.066936

Valent, P., Groner, B., Schumacher, U., Superti-Furga, G., Busslinger, M., Kralovics, R., et al. (2016). Paul Ehrlich (1854-1915) and his contributions to the foundation and birth of translational medicine. *J. Innate. Immun.* 8 (2), 111–120. doi:10.1159/000443526

Vani, J. R., Mohammadi, M. T., Foroshani, M. S., and Jafari, M. (2016). Polyhydroxylated fullerene nanoparticles attenuate brain infarction and oxidative stress in rat model of ischemic stroke. *EXCLI. J.* 15, 378–390. doi:10.17179/excli2016-309

Wang, L., Zhao, W., and Tan, W. (2008). Bioconjugated silica nanoparticles: Development and applications. *Nano Res.* 1 (2), 99–115. doi:10.1007/s12274-008-8018-3

Wang, Y., Li, L., Zhao, W., Dou, Y., An, H., Tao, H., et al. (2018). Targeted therapy of atherosclerosis by a broad-spectrum reactive oxygen species scavenging nanoparticle with intrinsic anti-inflammatory activity. *Acs. Nano.* 12 (9), 8943–8960. doi:10.1021/acsnano.8b02037

Wang, Y., Zhang, K., Qin, X., Li, T., Qiu, J., Yin, T., et al. (2019). Biomimetic nanotherapies: Red blood cell based core-shell structured nanocomplexes for atherosclerosis management. *Adv. Sci. (Weinh)* 6 (12), 1900172. doi:10.1002/advs.201900172

Xue, Y., Wu, Y., Wang, Q., Xue, L., Su, Z., and Zhang, C. (2019). Cellular vehicles based on neutrophils enable targeting of atherosclerosis. *Mol. Pharm.* 16 (7), 3109–3120. doi:10.1021/acs.molpharmaceut.9b00342

Yajima, S., Miyagawa, S., Fukushima, S., Sakai, Y., Iseoka, H., Harada, A., et al. (2019). Prostacyclin analogue-loaded nanoparticles attenuate myocardial ischemia/reperfusion injury in rats. *JACC. Basic. Transl. Sci.* 4 (3), 318–331. doi:10.1016/j.jacbts.2018.12.006

Yang, J., Jia, C., and Yang, J. (2021). Designing nanoparticle-based drug delivery systems for precision medicine. *Int. J. Med. Sci.* 18 (13), 2943–2949. doi:10.7150/ijms.60874

Ye, M., Zhou, J., Zhong, Y., Xu, J., Hou, J., Wang, X., et al. (2019). SR-A-targeted phase-transition nanoparticles for the detection and treatment of atherosclerotic vulnerable plaques. *Acs. Appl. Mat. Interfaces.* 11 (10), 9702–9715. doi:10.1021/acsami.8b18190

Yusuf, S., Joseph, P., Rangarajan, S., Islam, S., Mente, A., Hystad, P., et al. (2020). Modifiable risk factors, cardiovascular disease, and mortality in 155 722 individuals from 21 high-income, middle-income, and low-income countries (PURE): A prospective cohort study. *Lancet* 395 (10226), 795–808. doi:10.1016/S0140-6736(19)32008-2

Zhu, K., Li, J., Wang, Y., Lai, H., and Wang, C. (2016). Nanoparticles-assisted stem cell therapy for ischemic heart disease. *Stem Cells Int.* 2016, 1–9. doi:10.1155/2016/1384658

frontiers | Frontiers in Pharmacology

TYPE Original Research
PUBLISHED 13 September 2022
DOI 10.3389/fphar.2022.974216

OPEN ACCESS

EDITED BY
Guixue Wang,
Chongqing University, China

REVIEWED BY
Ren Jun Guo,
Xiyuan Hospital, China
Xiang Ma,
First Affiliated Hospital of Xinjiang Medical University, China

*CORRESPONDENCE
Yong-Bin Liu,
ybliu117@126.com
Chao-Mei Ma,
cmma@imu.edu.com

†These authors have contributed equally to this work and share first authorship

SPECIALTY SECTION
This article was submitted to Cardiovascular and Smooth Muscle Pharmacology, a section of the journal Frontiers in Pharmacology

RECEIVED 21 June 2022
ACCEPTED 15 August 2022
PUBLISHED 13 September 2022

CITATION
Wang L-W, He J-F, Xu H-Y, Zhao P-F, Zhao J, Zhuang C-C, Ma J-N, Ma C-M and Liu Y-B (2022), Effects and mechanisms of 6-hydroxykaempferol 3,6-di-O-glucoside-7-O-glucuronide from Safflower on endothelial injury in vitro and on thrombosis in vivo. *Front. Pharmacol.* 13:974216. doi: 10.3389/fphar.2022.974216

Effects and mechanisms of 6-hydroxykaempferol 3,6-*di*-*O*-glucoside-7-*O*-glucuronide from Safflower on endothelial injury *in vitro* and on thrombosis *in vivo*

Li-Wei Wang[1,2,3†], Jiang-Feng He[3†], Hai-Yan Xu[1,2], Peng-Fei Zhao[1,2], Jie Zhao[4], Cong-Cong Zhuang[1,2], Jian-Nan Ma[5], Chao-Mei Ma[1,2]* and Yong-Bin Liu[1]*

[1]State Key Laboratory of Reproductive Regulation and Breeding of Grassland Livestock, School of Life Sciences, Inner Mongolia University, Hohhot, China, [2]Key Laboratory of Herbage and Endemic Crop Biology of Ministry of Education, School of Life Sciences, Inner Mongolia University, Hohhot, China, [3]Biotechnology Research Institute, Inner Mongolia Academy of Agricultural and Animal Husbandry Sciences, Hohhot, China, [4]Center of Reproductive Medicine, The Affiliated Hospital of Inner Mongolia Medical University, Hohhot, China, [5]Department of Traditional Chinese Medicine Resources and Development, College of Pharmacy, Inner Mongolia Medical University, Hohhot, China

Background: The florets of *Carthamus tinctorius* L. (Safflower) is an important traditional medicine for promoting blood circulation and removing blood stasis. However, its bioactive compounds and mechanism of action need further clarification.

Objective: This study aims to investigate the effect and possible mechanism of 6-hydroxykaempferol 3,6-*di*-*O*-glucoside-7-*O*-glucuronide (HGG) from Safflower on endothelial injury *in vitro*, and to verify its anti-thrombotic activity *in vivo*.

Methods: The endothelial injury on human umbilical vein endothelial cells (HUVECs) was induced by oxygen-glucose deprivation followed by reoxygenation (OGD/R). The effect of HGG on the proliferation of HUVECs under OGD/R was evaluated by MTT, LDH release, Hoechst-33342 staining, and Annexin V-FITC apoptosis assay. RNA-seq, RT-qPCR, Enzyme-linked immunosorbent assay and Western blot experiments were performed to uncover the molecular mechanism. The anti-thrombotic effect of HGG *in vivo* was evaluated using phenylhydrazine (PHZ)-induced zebrafish thrombosis model.

Results: HGG significantly protected OGD/R induced endothelial injury, and decreased HUVECs apoptosis by regulating expressions of hypoxia inducible factor-1 alpha (HIF-1α) and nuclear factor kappa B (NF-κB) at both transcriptome and protein levels. Moreover, HGG reversed the mRNA expression of pro-inflammatory cytokines including *IL-1β*, *IL-6*, and *TNF-α*, and reduced the release of IL-6 after OGD/R. In addition, HGG exhibited

protective effects against PHZ-induced zebrafish thrombosis and improved blood circulation.

Conclusion: HGG regulates the expression of HIF-1α and NF-κB, protects OGD/R induced endothelial dysfunction *in vitro* and has anti-thrombotic activity in PHZ-induced thrombosis *in vivo*.

KEYWORDS

***Carthamus tinctorius*, 6-hydroxykaempferol 3,6-*di*-*O*-glucoside-7-*O*-glucuronide (HGG), human umbilical vein endothelial cells (HUVECs), oxygen glucose deprivation/reoxygenation (OGD/R), phenylhydrazine (PHZ), anti-thrombosis**

Introduction

Globally, coronary artery disease, particularly acute myocardial infarction (AMI) is one of the dominant causes of death and disability (Wang et al., 2020). AMI occurs when coronary artery becomes partially or totally occluded, leading to an acute loss of vital oxygen and glucose to heart tissue, thereby causing endothelial cells and tissue damage (Sattler et al., 2019). AMI is the major complication of atherosclerosis, thrombosis, etc., (Gulati et al., 2020). In AMI, due to the blockage of blood supply to heart, oxygen and nutrient supply restricts and cell apoptosis occurs, which triggers the intercellular signaling cascade. AMI occurs with the intense-inflammatory response to repair myocardial tissues, but exaggerated inflammatory response results in left-ventricular-remodeling and heart failure (Montrief et al., 2019). Vascular endothelial cells, uniquely positioned at the interface between the blood and tissue, plays a critical role in maintaining cardiovascular homeostasis (Wei et al., 2020). The injury or death of endothelial cells is believed to be the initial event in endothelial pathophysiological state, such as inflammation, vascular injury, and thrombosis (Qi et al., 2017; Mathiesen et al., 2021). In order to prevent acute myocardial infarction, it is necessary to relieve endothelial injury and eliminate thrombosis caused by ischemia and hypoxia.

Safflower is a traditional medicine renowned for its efficacy on promoting blood circulation and removing blood stasis (Chinese Pharmacopoeia Committee, 2020). Xuebijing (blood-cleaning) injection with Safflower extract as a major component could block Covid-19 proliferation, and inhibit the expression of pro-inflammatory cytokines (He et al., 2021). In addition, Xuebijing injection effectively improves cardiac function after hypoxia/reoxygenation injury (He et al., 2016). Safflower contains large amounts of chalcone and flavanols represented by hydroxysafflor yellow A (HSYA) and 6-hydroxykaempferol glycosides, respectively. Among them, HSYA has been the interest of Safflower bioactivity investigation in most documents, and its effects to protect endothelial cells against hypoxia-induced injury was also reported (Ji et al., 2009). However, little is known about the related effects and the underlying mechanism of the 6-hydroxykaempferol glycosides in Safflower.

The zebrafish offers unique characteristics for studying the pathology and screening therapeutic drugs for cardiovascular diseases. The transparent zebrafish embryo and larvae allows noninvasive observing and imaging the cardiac contraction, and blood flow *in vivo* (Bournele and Beis, 2016). Currently, Safflower, Safflower yellow (SY), and HSYA injections are widely used in treating cerebrovascular and cardiovascular diseases (Zhang et al., 2016). However, little is known about effects of 6-hydroxykaempferol glycosides in cerebrovascular and cardiovascular diseases. The 6-hydroxykaempferol 3,6-*di*-*O*-glucoside-7-*O*-glucuronide (HGG) is a representative 6-hydroxykaempferol glycoside in Safflower. Hence, we examined the effect of HGG on recovering ischemia-reperfusion injury (I/R) and preventing thrombosis. We utilized HUVECs in OGD/R to evaluate the protective effect of HGG on hypoxia/reoxygenation-induced endothelial injury, and revealed its potential molecular mechanisms through RNA-seq analysis. In addition, we used PHZ-induced zebrafish thrombosis model to evaluate the anti-thrombotic effect of HGG *in vivo*.

Materials and methods

Experimental materials

The plant material was obtained from Hebei All Thai Pharmaceutical Co., Ltd., (Lot:1711001, Hebei, China), which was identified and authenticated by the authors as the florets of *Carthamus tinctorius* L. Its voucher specimen (NPFFC-2018) was deposited in the Laboratory of Natural Products and Functional Foods, School of Life Sciences, Inner Mongolia University, China. Dulbecco's modified Eagle medium (DMEM), penicillin-streptomycin (P/S), trypsin-EDTA, and phosphate buffered saline (PBS) were purchased from Gibco (Thermo Fisher Scientific, Suzhou, China). Fetal bovine serum (FBS) was provided by Biological Industries (Kibbutz Beit Haemek, Israel). The 3-(4,5-dimethylthiazol-2-

yl)-2,5-diphenyltetrazolium bromide (MTT) was purchased from Sigma-Aldrich (St Louis, Mo, United States). Lactate dehydrogenase (LDH) assay kits were obtained from Nanjing Jiancheng Bioengineering Institute (Nanjing, China). Annexin V-FITC apoptosis kit was purchased from Sungene Biotech (Sungene, China). Hoechest-33342, BCA kit, and antibodies of NF-κB, p-NF-κB, HIF-1α, and β-actin were obtained from Wanleibio (Wanlei, China). NF-κB inhibitor BAY11-7082, and HIF-1α inhibitor Lw6 were purchased from selleck Chemicals (Selleck, Shanghai, China). The IL-6 ELISA Kit was purchased from NEOBIOSCIENCE. The RNAiso Plus, PrimeScriptTM RT reagent kit with gDNA Eraser, and TB Green™ Premix Ex Taq™ II were provided by Takara (Takara, Japan). The chemical constituents of Safflower used in this research were isolated, purified and identified in our laboratory as described previously (Wang et al., 2021).

Cell culture

HUVECs in DMEM containing 10% FBS, 100 U/ml penicillin, and 100 mg/ml streptomycin were cultured at 37°C in an atmosphere of 5% CO_2. Culture medium was changed to fresh once a day. At 80% confluence, the cells were passaged with 0.125% trypsin-EDTA solution.

Oxygen-glucose deprivation followed by reoxygenation model and drug treatment

The experiment was carried out referring to reported method (Lv et al., 2020). Briefly, HUVECs were cultured in a pre-warmed glucose-free DMEM for 12 h. Then, the cells were maintained in hypoxia condition (1% O_2, 94% N_2, and 5% CO_2) for 4 h, and then returned to normoxic condition (95% air, 5% CO_2) with normal medium for 10 h as reoxygenation. Cao et al. (2022) reported that protocatechualdehyde at 0.72, 1.45, and 3.62 μM significantly improved cell viability after OGD/R injury ($p < 0.01$), and thus HGG was tested at similar concentrations, 0.1, 1, and 10 μM, in this study. To determine the effect of HGG, cells were pre-incubated with HGG for 10 h, followed 4 h of OGD and 10 h of reoxygenation (R) (Lv et al., 2020). The HUVECs with neither HGG nor OGD/R treatment were served as control. At the end of cell treatments, different tests were carried out as described below.

Cytotoxicity measurements

Cell toxicity and protection effect were measured by three independent assays: MTT, LDH, and Hoechst 33342 staining assays, and apoptosis was assessed by Annexin V-FITC/PI. Briefly, HUVECs were seeded into 96-well plates at a density of 4×10^3 cells per well, and pre-treated with HGG for 10 h, followed 4 h of OGD and 10 h of reoxygenation.

For MTT assay, MTT (0.5 mg/ml, 20 μl) was added to each well, and co-cultured for another 4 h. At the end of incubation, the supernatant was carefully discarded and the formazan product was dissolved in 150 μl dimethyl sulfoxide (DMSO). The optical density was measured with a microplate reader at 570 nm.

LDH release was regarded as an indicator of cell viability and membrane integrity, and measured with LDH assay kit. To visualize the morphological of HUVECs during OGD/R, Hoechst-33342 was carried out. Following the treatment, cells were stained with Hoechest-33342 for 10 min in darkness at room temperature. Afterward, the cells were rinsed twice with PBS and analyzed under fluorescence microscopy.

The percentage of HUVECs apoptosis was analyzed by Annexin V-FITC and propidium iodide (PI). Briefly, the cells were harvested and washed twice with cold PBS. Cell suspension was stained with Annexin V-FITC and PI for 5 min at room temperature in darkness. The apoptotic cell population was analyzed by flow cytometer.

Library construction for transcriptome sequencing

Following the treatment, total RNA was extracted from HUVECs with RNAiso Plus, and the RNA quantity and purity were assessed using NanoPhotometer® spectrophotometer. Sequencing libraries were constructed as follows: mRNA was enriched with the magnetic-oligo (dT) beads and broken into short pieces by fragmentation buffer, and these fragments were used as templates to synthesize first-strand cDNA with random primers. Second-strand cDNA were synthesized with buffer, dNTPs, DNA polymerase I and RNase. Following end reparation and adenylation of 3′ end tailing, the cDNAs were purified with AMPure XP system. Finally, sequencing adaptors were connected to select different fragments and enrich the final cDNA library. The cDNA quality was assessed on the Agilent Bioanalyzer 2100system.

Transcription data analysis

Raw data were firstly processed through in-house Perl scripts. During this step, clean data was acquired by removing reads which contain adapter, poly-N, and poor-quality reads from raw data. Simultaneously, Q20, Q30, and GC-content of clean data were calculated. All downstream analyses were performed based on clean data with high-quality. Reference genome files and annotations were directly downloaded from NCBI (https://www.ncbi.nlm.nih.gov/genome/?term = *Homo* + *sapiens*), and then

paired-end clean reads were aligned to reference genome with HISAT2. The differentially expressed genes (DEGs) were picked out using the DESeq2 *R* package (1.16.1). For a more in-depth understanding of the screened DEGs, Gene Ontology (GO) function and Kyoto Encyclopedia of Gene and Genome (KEGG) pathway enrichment were performed using clusterProfiler *R* package. $p < 0.05$ was considered as the threshold to determine the DEGs between each treatment of compared samples.

RT-qPCR

For transcriptome analysis, nine DEGs from RNA-seq were validated by RT-qPCR. cDNA was synthesized from RNA using primeScriptTM RT reagent kit with gDNA Eraser, and RT-qPCR was obtained with TB Green™ Premix Ex Taq™ II. Table 1 shows the primer of randomly selected DEGs and inflammatory markers including interleukin *(IL)-1β*, *IL-6*, and tumor necrosis factor *(TNF)-α*. RT-qPCR amplification was performed on a LightCycler® 480II, and calculated by the $2^{-\Delta\Delta CT}$ formula.

Enzyme-linked immunosorbent assay

The level of interleukin-6 (IL-6) in cell supernatants was detected by the corresponding ELISA kits (Enzyme-linked Biotechnology Co., Ltd., Shanghai, China). The optical density was measured using the TECAN microplate reader (tecan Group Ltd., Seestrasse, Switzerland) at 450 nm.

Western blotting analysis

The protein expression of HUVECs with OGD/R was analyzed by Western blot experiment. HUVECs was collected and lysed in ice-cold RIPA buffer containing protease and phosphatase inhibitors. After BCA assay, equal amounts (40 μg) of protein samples were loaded, separated by 10% SDS-polyacrylamide gel (SDS-PAGE), and transferred to polyvinylidene fluoride membrane. The membrane was blocked with 5% non-fat milk, then incubated with targeted primary antibodies against NF-κB, p-NF-κB, HIF-1α, and anti-β-actin overnight at 4°C. The membrane was washed and then incubated with secondary antibodies IgG-HRP for 1 h at room temperature. Proteins were visualized with ECL reagents and analyzed by Image J.

Zebrafish thrombosis model and treatment

Adult wild-type AB strain zebrafish were obtained from China Zebrafish Resource Center, Wuhan, China, and the husbandry, breeding and feeding were described previously (Chen et al., 2019; Wang et al., 2021). Thrombosis in zebrafish was induced by PHZ stimulation as described in detail in previous report (Wang et al., 2021), in which, two chemical constituents from Safflower at 10, 50, and 100 μM protected zebrafish against PHZ-induced thrombosis, and 1, 10, 100 μM HGG were tested in this study. Briefly, zebrafish embryos ($n = 30$) were pretreated with HGG (1, 10, and 100 μM) or aspirin (100 μM) (positive control). The zebrafish in control and model groups were treated with DMSO (up to 0.05%). At 72 hpf (hour post-fertilization), the larvae were treated with 3 μM PHZ containing the corresponding concentration of HGG or aspirin, except for controls, and then incubated for 24 h at 28.5 ± 0.5°C. After PHZ treatment, the zebrafish thrombus was qualitatively and quantitatively analyzed by the caudal vein and heart red blood cells (RBC) intensity with O-dianisidine staining. The photo and video data were taken using an Olympus microscope. The anti-thrombotic effect was calculated as following: anti-thrombotic effect (%) = $[S(HGG)-S(Model)]/[S(Control)-S(Model)] \times 100\%$, where S represents the heart RBC intensity of different treat groups.

Results

Cytotoxicity of the chemical constituents of Safflower on human umbilical vein endothelial cells

The cytotoxicity on HUVECs of all the chemical constituents (Figure 1) isolated from Safflower (Wang et al., 2021) were examined by MTT method. As shown in Figure 2A, the chalcones (1, 2), the 6-hydroxykaempferol glycosides (3–7), the quercetin glycosides (11, 12), and the kaempferol diglycoside (10) were non-toxic to HUVECs up to 10 μM, while the kaempferol monoglycosides (8, 9) and the polyacetylenes (13, 14) were toxic to the cells.

Protective effects of the chemical constituents of Safflower on human umbilical vein endothelial cells under oxygen-glucose deprivation followed by reoxygenation

As shown in Figure 2B, on OGD for 2, 4, and 8 h followed by 10 h reoxygenation, the viability of HUVECs decreased to 77.2%, 62.5%, and 44.8% of control, respectively. On this base, the OGD4/R10 was used to screen the protective effects. Figure 2C shows the protective effects of compounds 1–7, and 10–12 at 0.1 μM on HUVECs under OGD4/R10. Hydroxysafflor yellow C (2) and HGG (3) protected the OGD/R-injured HUVECs significantly ($p < 0.05$).

TABLE 1 The primers of RT-qPCR.

Gene	Sequence 5′–3′ fwd. and rev.	Gene	Sequence 5′–3′ fwd. and rev.
SQSTM1	TGACCCCCGTCTCTCCA	*CITED2*	AGTGGTTGTGGGGGTAGGGG
	TTCTCATCTGCTCCGCC		GGGGACTGTGAACGGAGGGC
CTIF	GCCTGCCTCCCCCTTGTC	*GMPR2*	GATGTCTCGGATGGTATG
	TCAGCACCCCACCCCTCA		ACAGTGAGTCAGGTGGTG
INTS3	TGGTAGGCTTCGGTTTCGT	*MBD1*	CCCAGGAGCAGGGAATGAA
	GATCTCTTCTCCCTGGCGG		GCCAGCCAAGACTCGGAAA
NFKBIZ	GCACTGGCTGTTCGTTCTC	*JUN*	TGCCTCCAAGTGCCGAAA
	TCATTCGCCTCTTTTTGGA		GCTGTGCCACCTGTTCCC
NFKBIA	GCACCCAAGGACACCAAAAG	*TNF-α*	CCTCTCTCTAATCAGCCCTCTG
	AGGAAATACCCCCCTACACC		GAGGACCTGGGAGTAGATGAG
IL-1β	AGCTACGAATCTCCGACCAC	*IL-6*	ACTCACCTCTTCAGAACGAATTG
	CGTTATCCCATGTGTCGAAGAA		CCATCTTTGGAAGGTTCAGGTTG
β-actin	ACCCACACTGTGCCCATCTA		
	GCCACAGGATTCCATACCCA		

Hydroxysafflor yellow C is a chalcone compound having a similar structure to that of hydroxysafflor yellow A which has been reported to protect hypoxia-induced HUVEC injuries (Lv et al., 2020). HGG represents another characteristic structural type, the 6-hydroxykaempferol glycosides, in Safflower, and its related pharmacologic action has not been reported. Thus, further experiments were carried out on HGG to confirm its effect, and to investigate its underlying mechanisms.

The protective effects on HUVECs under OGD/R of HGG at different concentrations (0.1, 1, and 10 μM) were tested. HGG significantly decreased the OGD/R-induced endothelial cell apoptosis in a concentration-dependent manner (Figures 3A,B). As shown in Figure 3C, similar results were obtained by Hoechest-33342 assay, in which apoptotic HUVECs showed strong fluorescence, normal cells displayed weak fluorescence, and necrotic cells have no fluorescence. The results showed that HGG dose-dependently decreased HUVEC apoptosis. LDH is widely used as an indicator of cell apoptosis. The LDH release in ODG/R was 10.7-fold higher than that in the control. Treatment with HGG at 0.1, 1, and 10 μM reduced the LDH release to 8.7-, 6.2-, and 3.8-fold of that in the control, respectively (Figure 3D). Similar results were observed in Annexin V-FITC/PI assay (Figure 4). The apoptotic cells were 3.07% in the control, 7.72% in the OGD/R group, and 5.07%, 4.2%, and 3.74% ($p < 0.01$) in the HGG groups at 0.1, 1, and 10 μM, respectively.

These results strongly indicated that HGG concentration-dependently protected against OGD/R-induced endothelial injury *in vitro*. Consequently, the underlying mechanisms were investigated by RNA-seq and confirmed by Western blot and RT-qPCR.

Analysis of differentially expressed genes

The high-quality RNA-seq data (Table 2) were used for in depth analysis. For uncovering the potential mechanisms underlying the attenuation of HGG on OGD/R-induced injuries, the 227 DEGs ($p < 0.05$) (Figure 5A; Supplementary Table S1) were subjected to 81 GO ($p < 0.05$) (Figure 5D; Supplementary Table S2) and 212 KEGG pathways (Figure 5E; Supplementary Table S3) analyses. As shown in Figure 5D, the DEGs were classified into 3 functional groups (BP, CC, and MF). DEGs that were mainly enriched in BP group involved in response to decreased oxygen levels, nutrient levels, vascular smooth muscle cell proliferation, inflammatory response, and aging; DEGs in CC group were significantly enriched in nuclear speck; These DEGs in MF group were enriched in the structural constituent of cytoskeleton and protein ligase binding (Supplementary Table S2). According to KEGG enrichment results, we screened out 10 pathways based on the threshold of $p < 0.01$ (Figure 5E), and the results indicated that HGG attenuated OGD/R injury mainly through the TNF, apoptosis, IL-17, and HIF-1 signaling pathways. Venn diagram of DEGs analysis demonstrated that *JUN*, and *NFKBIA* were the hub genes among the apoptosis, TNF, and IL-17 signaling pathways (Figure 5C; Table 3).

RT-qPCR validation and Western blot analysis

To validate reliability of the expression data identified by RNA-seq, nine DEGs were randomly selected for RT-qPCR to determine their relative expression in OGD/R and OGD/R +

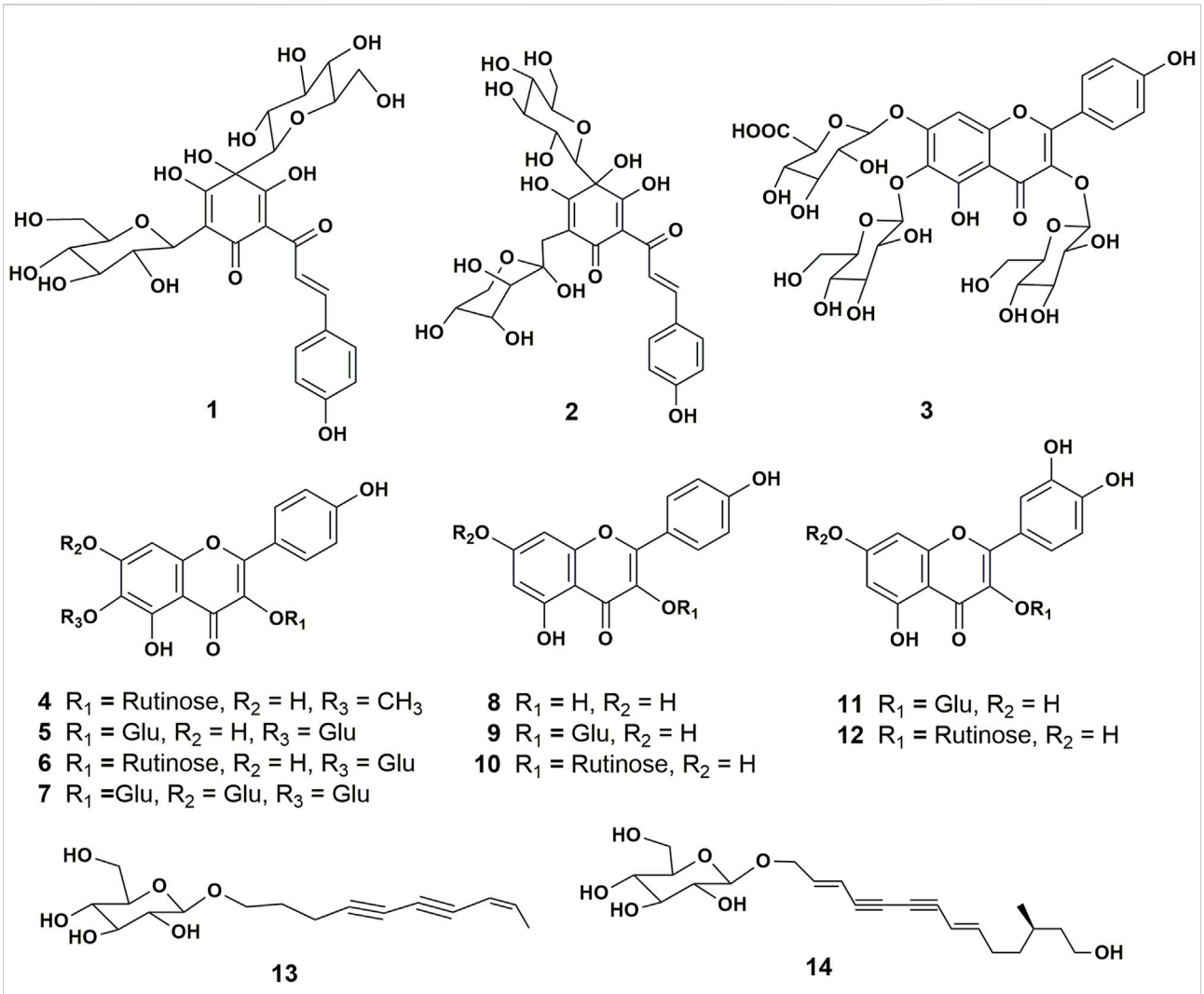

FIGURE 1
Structures of the chemical constituents isolated and identified from the florets of *C. tinctorius*. **1**, hydroxysafflor yellow A; **2,** hydroxysafflor yellow C; **3,** 6-hydroxykaempferol 3,6-di-*O*-glucoside-7-*O*-glucuronide (HGG); **4**, 5,7,4′-trihydroxy-6-methoxyflavone-3-*O*-rutinoside; **5**, 6-hydroxykaempferol 3,6-*di*-*β*-glucoside; **6**, 6-hydroxykaempferol 3-*O*-*β*-rutinoside-6-*O*-*β*-glucoside; **7**, 6-hydroxykaempferol 3,6,7-tri-*O*-*β*-glucoside; **8**, kaempferol; **9**, kaempferol 3-*O*-*β*-glucoside; **10**, kaempferol 3-rutinoside; **11**, quercetin 3-*O*-*β*-glucopyranoside; **12**, Rutin; **13**, bidenoside C; **14**, (2E,8E)-tetradecadiene-4,6-diyne-1,12,14-triol-1-*O*-*β*-glucopyranoside.

HGG groups. The results showed similar expression trends between RT-qPCR and RNA-seq (Figure 6A; Table 4), thereby, suggesting that the RNA-seq data were reliable.

As shown in Figure 6B, upon OGD/R treatment, the protein expression of HIF-1α was upregulated to a level of 2.06-fold higher than that of control ($p < 0.001$). After incubation with 0.1, 1, and 10 μM HGG, the protein expression decreased to 105.0%, 99.7%, and 88.9% ($p < 0.05$) of control. OGD/R treatment also significantly increased the protein expression levels of NF-κB and p-NF-κB as compared to normoxia group, whereas HGG treatment downregulated the expression levels compared to OGD/R group (Figures 6B,D,E). Given that HIF-1α plays a central role in many hypoxic events, we further investigated the protective effects of HGG on the inflammatory response in HUVECs subjected to OGD/R, and the role of the HIF-1α/NFκB signaling pathway in this process. Furthermore, we have used the specific inhibitors Lw6 (10 μM, a HIF-1α inhibitor) and BAY11-7082 (5 μM, a NFκB inhibitor) to verify the mechanism of HGG against OGD/R-mediated inflammatory response. As expected, the protein expression levels of p-NF-κB and NF-κB significantly reduced in OGD/R-stimulated HUVECs after treatment with BAY (Figures 7C,D), confirmed the central role of NFκB signaling pathway in OGD/R-induced endothelial dysfunction. Compared with OGD/R group, inhibitors Lw6 and BAY significantly alleviated endothelial injuries (Figures 7A,B), mitigated OGD/R-induced increases in inflammatory markers

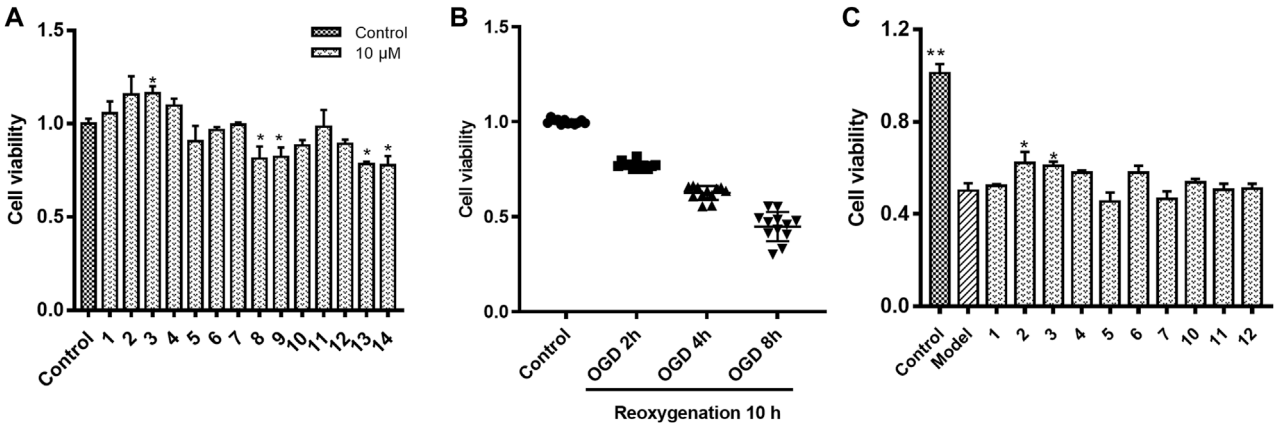

FIGURE 2
HUVECs viability in different culture compositions. **(A)** HUVECs viability in normoxic condition co-cultured with individual chemical constituent of Safflower; **(B)** HUVECs viability in oxygen-glucose deprivation (OGD) for 2, 4, or 8 h followed by reoxygenation for 10 h; **(C)** Protective effects of compounds 1–7 and 10–12 on HUVECs under OGD/R. $*p < 0.05$, $**p < 0.01$ vs. OGD/R.

including *IL-6*, *TNF-α* and *IL-1β* mRNA expression (Figures 7F–H), and inhibited the secretion of pro-inflammatory cytokine IL-6 (Figure 7E). OGD/R promoted the mRNA expression of pro-inflammatory cytokines, such as *IL-1β*, *IL-6*, and *TNF-α*, and resulted in production of pro-inflammatory cytokine IL-6 in the culture supernatant, while pretreatment with HGG inhibited *IL-1β*, *IL-6*, and *TNF-α* mRNA expression and the release of IL-6 (Figures 7E–H). These results confirmed that HGG prevented HUVECs from OGD/R-induced injury partly through the regulation of HIF-1α/NF-κB pathway, and that HGG may have therapeutic value for protecting endothelial cells from IR injury.

6-hydroxykaempferol 3,6-di-O-glucoside-7-*O*-glucuronide mitigated phenylhydrazine-induced thrombosis

To evaluate the protective effect of HGG on PHZ-induced zebrafish thrombosis model, the O-dianisidine stained zebrafish images were captured by microscope. After PHZ treatment, the red blood cells (RBCs) initiated to aggregate and accumulate in the caudal veins, suggesting thrombus formation (Figures 8D,E; Supplementary Video S1). Notably, compared with OGD/R group, pre-treatment with HGG at 1, 10, 100 μM significantly enhanced zebrafish heart RBCs intensity to a level similar to that treated with 100 μM aspirin (positive control) (Figure 8D), indicating that thrombosis formation was reduced by HGG. The anti-thrombotic effect was 33.0% for 100 μM aspirin, and 11.9%, 43.3%, and 64.0% for 1, 10, and 100 μM HGG, respectively (Figure 8A,C; Supplementary Video S2). The results also showed for the first time that HGG significantly inhibited the tail vein thrombus and restored the quantity of heart RBCs in zebrafish thrombosis model. We subsequently examined the effects of HGG on the blood flow rate of zebrafish tail vein at selected regions. Compared with OGD/R group, 10, 100 μM and HGG treatment significantly increased the blood flow rate to the level similar to that treated with 100 μM aspirin (Figure 8F). These results indicate that HGG could significantly inhibit PHZ-induced thrombosis *in vivo*.

Discussion and conclusion

The objective of this study was to investigate the protective effects and possible mechanism of HGG from Safflower on human umbilical vein endothelial cells (HUVECs) subjected to oxygen-glucose deprivation/reoxygenation (OGD/R) *in vitro*, and evaluate its anti-thrombotic effects in PHZ-induced zebrafish thrombosis *in vivo*. Excitingly, treatment with HGG successfully alleviated OGD/R-induced endothelial dysfunction. To gain further insight into the potential mechanisms, an integrative analysis of transcriptome data under OGD/R and HGG + OGD/R treatment in HUVECs was performed. According to GO and KEGG analysis, these DEGs were mainly involved and enriched in apoptosis and inflammatory pathways. HGG reduced OGD/R-induced cytotoxicity and apoptosis. HGG protected OGD/R injury by suppressing inflammatory response *via* HIF-1α/NFκB signaling pathway in HUVECs. Furthermore, HGG exhibited anti-thrombotic effects in PHZ-induced zebrafish thrombosis model, enhanced the

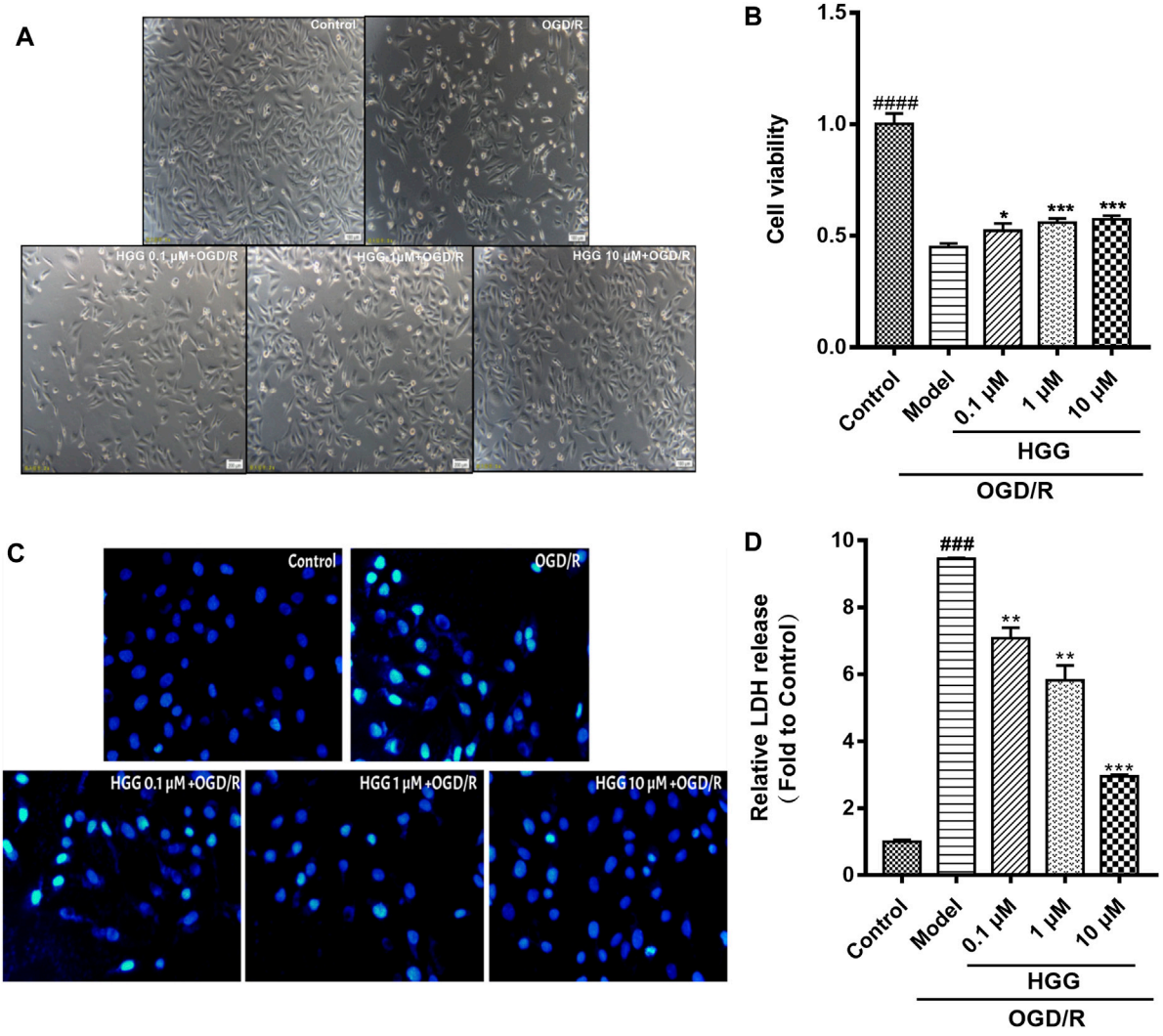

FIGURE 3
HGG significantly prevents OGD/R-induced damage on HUVECs in a dose-dependent manner. **(A)** Morphology of HUVECs cultured in normoxic, and in HGG-treated HUVECs after OGD/R; **(B)** Cell viability of HUVECs under OGD/R and treated with or without HGG; **(C)** The morphological features of cell apoptosis of OGD/R by Hoechest-33342 staining; **(D)** LDH release in HGG-treated HUVECs after OGD/R; All data are presented as means ± SD from independent experiments performed in triplicate. $^{###}p < 0.001$, $^{####}p < 0.0001$ vs. Control; $^{*}p < 0.05$, $^{**}p < 0.01$, $^{***}p < 0.001$ vs. OGD/R.

blood flow rates, restored the heart RBCs intensity and alleviated caudal vein thrombus *in vivo*. Therefore, HGG exerted protective effects on endothelial dysfunction by HIF-1α/NF-κB pathway and prevented from PHZ-stimulated zebrafish thrombosis by ameliorating vascular obstruction and enhancing the blood flow.

AMI is the leading cause of hospitalizations and deaths worldwide (Collaborators et al., 2016). AMI is usually caused by thrombotic occlusion of coronary artery and atherosclerotic plaque rupture or erosion of endothelium, leading to inadequate of oxygen and nutrients, which is characterized by endothelial injury and thrombus formation (Reed et al., 2017; Lv et al., 2020). Timely reperfusion therapy after AMI has been considered the most effective treatment for reducing acute myocardial injury, protecting heart function, and improving clinical outcomes. However, to some extent, reperfusion itself has been regarded as a "double-edged sword", as reperfusion may induce cell apoptosis and aggravation of myocardial damage, a phenomenon termed ischemia-reperfusion (I/R) injury (Yellon and Hausenloy, 2007; Neri et al., 2017). I/R injury is a complicated pathophysiological process involving cardiomyocyte apoptosis, endothelial dysfunction, and inflammatory reaction (Cao et al., 2020; Wu et al., 2020).

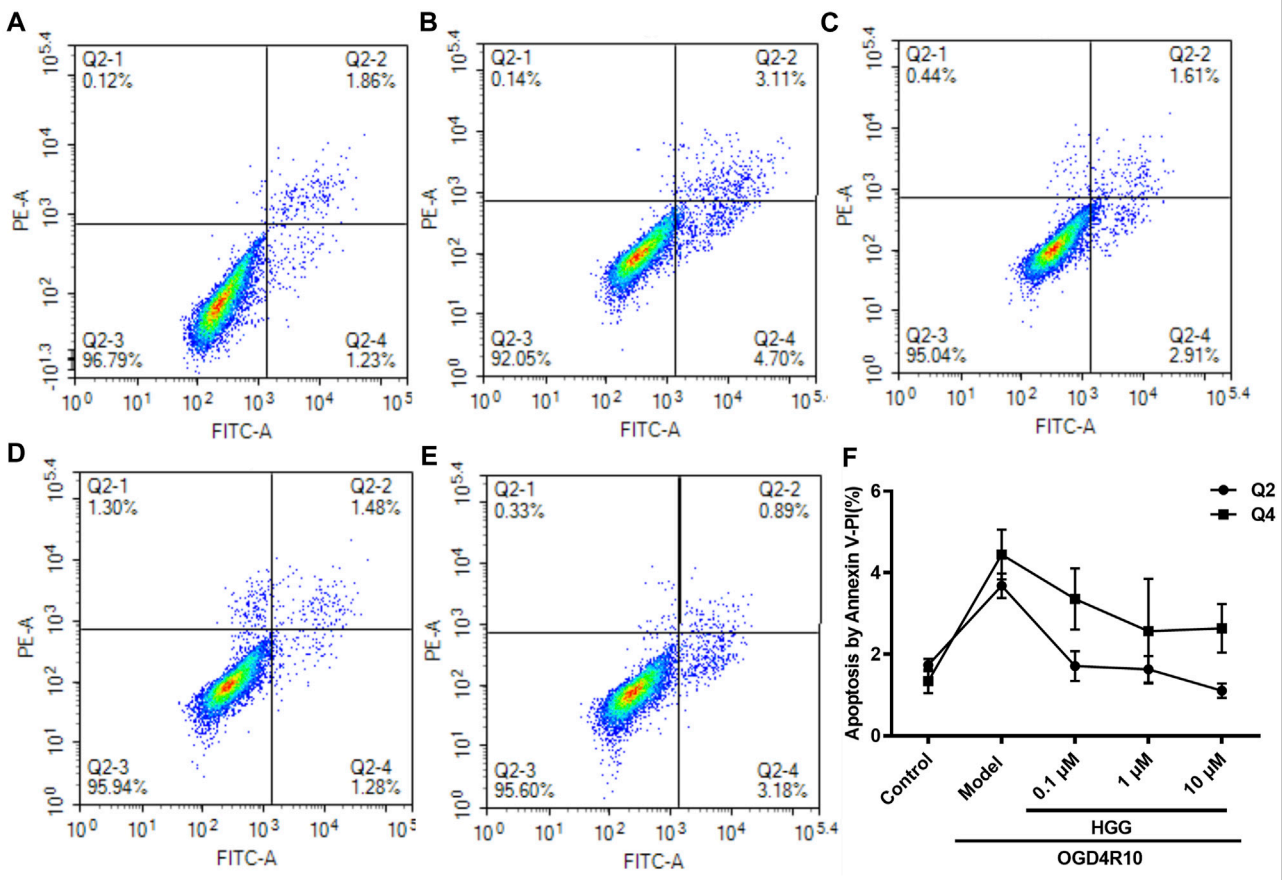

FIGURE 4
OGD/R-induced apoptosis in HUVECs using Annexin V-FITC/PI staining. **(A)** Control; **(B)** OGD/R; **(C)** 0.1 μM HGG + OGD/R; **(D)** 1 μM HGG + OGD/R; **(E)** 10 μM HGG + OGD/R. Quadrant distinction: upper left corner quadrant for dead cells, lower left corner quadrant for living cells, upper right corner quadrant for advanced apoptotic cells, and lower right corner quadrant for the early apoptotic cells. **(F)** The apoptosis rate of HUVECs after exposure to OGD/R.

TABLE 2 Statistical summary analysis of transcriptional sequencing data of HUVECs.

Sample	Means for reads				Means for mapping	
	Raw read	Clean reads	Q20 (%)	GC-pct (%)	Map reads	Unique reads
Control	4,35,09,653	4,29,48,056	97.78	49.39	4,11,89,883 (95.90%)	3,91,33,040 (91.12%)
OGD/R	4,53,41,180	4,46,68,277	97.92	49.18	4,28,27,944 (95.88%)	4,06,98,524 (91.11%)
HGG + OGD/R	5,41,63,926	5,33,47,148	98	49.47	5,11,27,553.5 (95.84%)	4,85,33,437 (90.98%)

Among them, endothelial dysfunction, an important characteristic of I/R, plays an important role in the development of atherosclerosis and thrombus formation (Heusch, 2019). Thus, alleviation of endothelial injury has become a strategy to prevent and treat acute myocardial infarction.

Endothelial cells form the first barrier between the circulating blood and the surrounding tissues, and the integrity of vascular endothelium has a crucial role for the maintenance of vascular homeostasis. In turn, endothelial injury has been considered an early marker of vascular complications, such as atherosclerosis and thrombosis (Wu

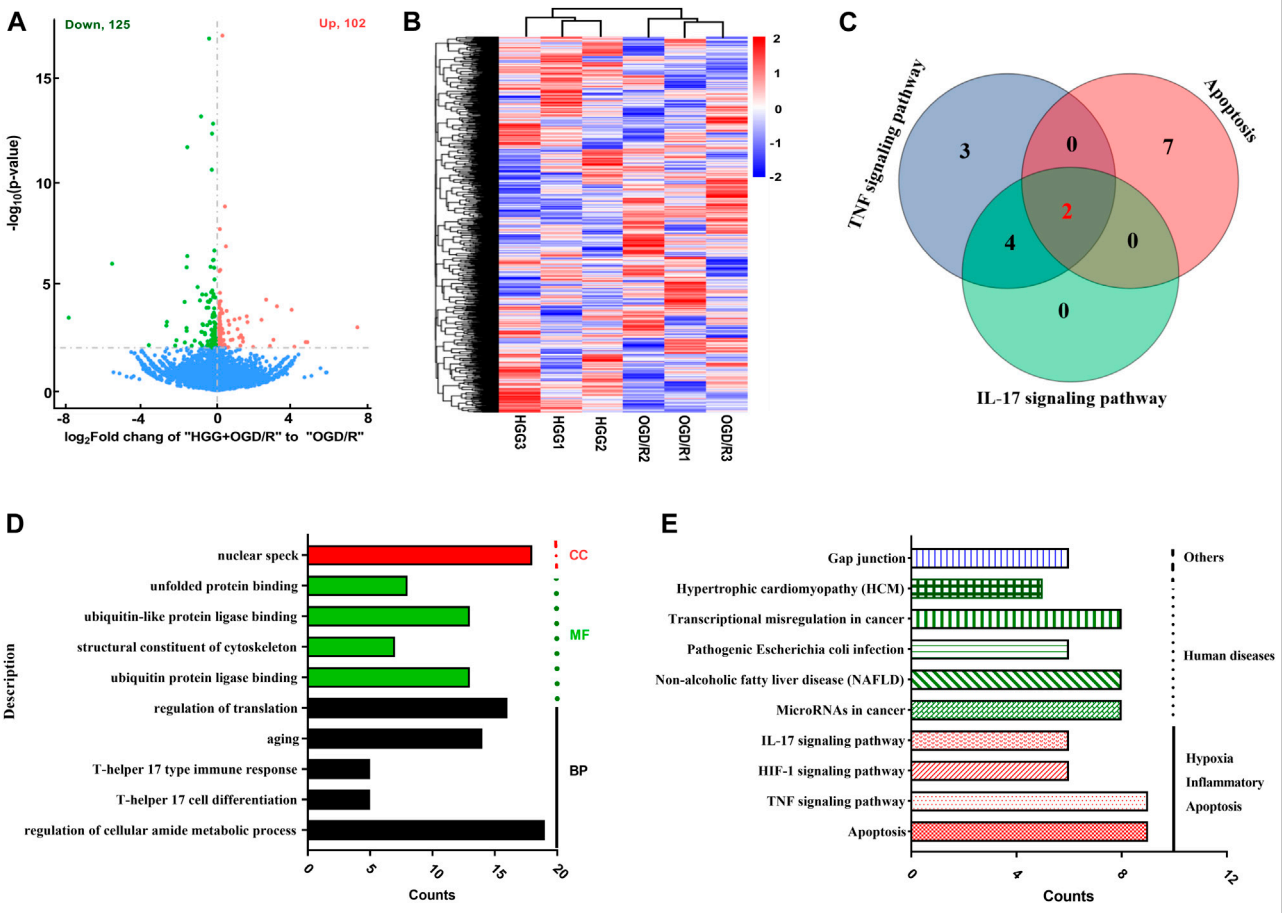

FIGURE 5
Analysis results from transcription study in OGD/R-exposed HUVECs treated with HGG. **(A)** The volcano graph of 227 DEGs between incubated HGG + OGD/R group and OGD/R group. Red, upregulated DEGs; green, downregulated DEGs; **(B)** Heat map representation; **(C)** The venn diagram of DEGs in KEGG signaling pathway; **(D)** GO enrichment and **(E)** KEGG pathway analysis of 227 DEGs in HGG treated HUVECs after OGD/R.

TABLE 3 DEGs in KEGG signaling pathways.

Signaling pathways	Total	DEGs
Apoptosis, IL-17 and TNF signaling pathway	2	*NFKBIA, JUN*
IL-7 and TNF signaling pathway	4	*CSF2, MMP3, IL6, TNFAIP3*
TNF signaling pathway	3	*SOCS3, LIF, EDN1*
Apoptosis	7	*DDIT3, LMNA, HRAS, TUBA1A, TUBA4A, TUBA1B, LMNB2*

et al., 2019). A considerable body of evidence has demonstrated that the endothelium is sensitive to ischemia-reperfusion (I/R) or hypoxia-reoxygenation injury, and the maintenance and repair of vascular endothelial cells determines recovery from injury (Somani et al., 2019). To assess the effect of HGG on I/R injury *in vitro*, we used an OGD/R model in HUVECs by treating them with OGD/R-induced endothelial injury *in vitro* to mimic I/R injury. Apoptosis, a form of programmed cell death that is activated under hypoxic stress is a major cause of I/R injury. Therefore, inhibiting HUVECs apoptosis during OGD/R-injured may effectively ameliorate the myocardial infarction during I/R

10.3389/fphar.2022.974216

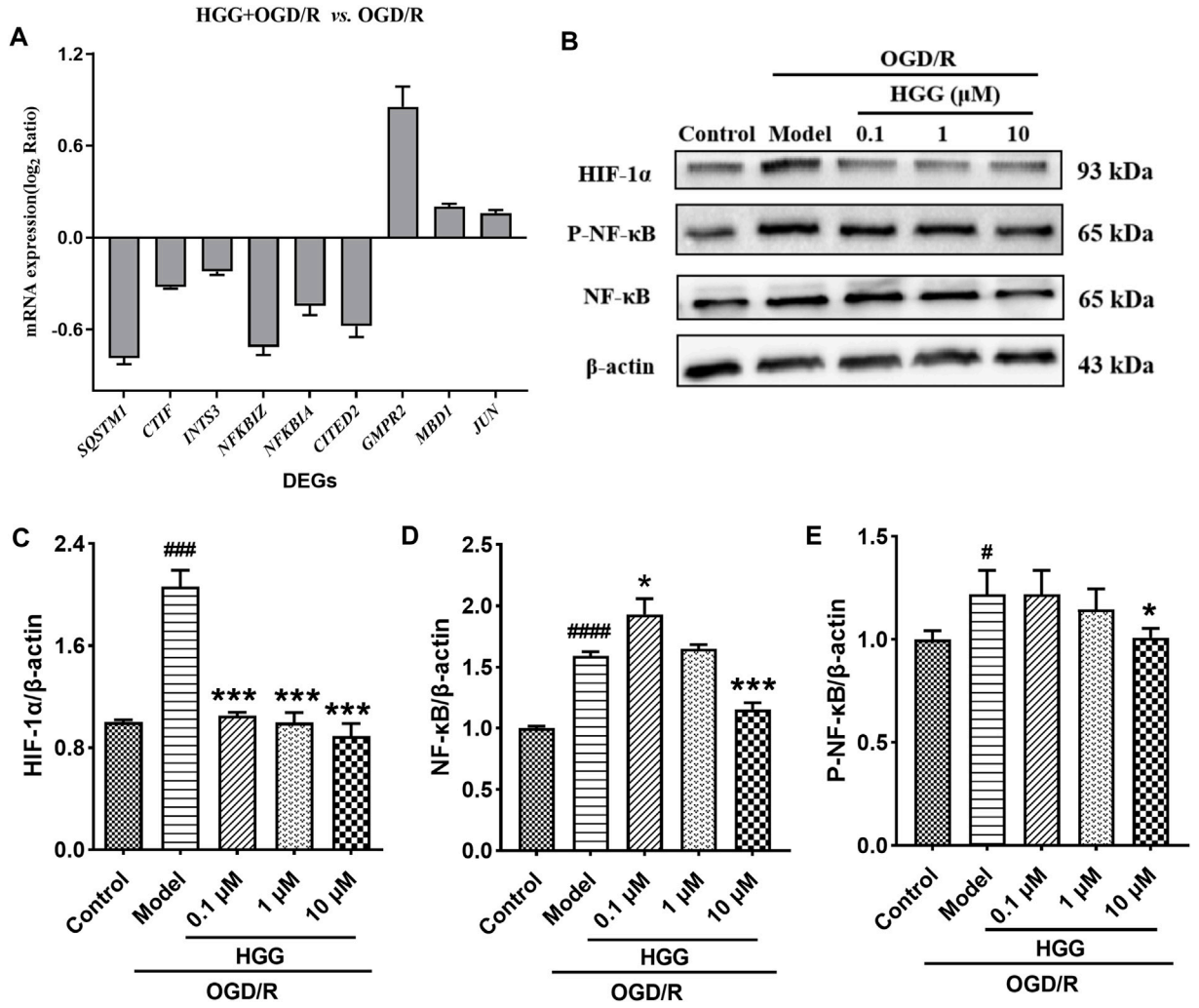

FIGURE 6
HGG protects HUVECs against OGD/R-induced apoptosis *via* HIF-1α/NF-κB pathway. **(A)** The mRNA expression levels of nine DEGs after OGD/R incubation; **(B)** The protein expression levels of HIF-1α, NF-κB, and p-NF-κB in Western blot experiment for HUVECs under OGD/R and treated with HGG at 0.1, 1, and 10 μM; **(C–E)** Semi-quantification of protein expression by Image J analysis. All data were presented as means ± SD (n = 3). $^{\#}p < 0.05$, $^{\#\#\#}p < 0.001$ vs. Control; $^{*}p < 0.05$, $^{**}p < 0.01$, $^{***}p < 0.001$ vs. OGD/R.

TABLE 4 Significantly upregulated or downregulated genes in HGG + OGD/R vs. OGD/R.

Gene name	Gene description	log2 FoldChange	*p*-Value	Regulation
SQSTM1	Sequestosome 1	−1.69	0.005638	Down
CTIF	Cap binding complex dependent translation initiation factor	−1.60	1.64E-06	Down
INTS3	Integrator complex subunit 3	−0.85	1.30E-13	Down
NFKBIZ	NFKB inhibitor zeta	−0.27	8.40E-13	Down
NFKBIA	NFKB inhibitor alpha	−0.19	2.99E-05	Down
CITED2	Cbp/p300 interacting transactivator with Glu/Asp rich carboxy-terminal domain 2	−0.43	2.87E-17	Down
GMPR2	Guanosine monophosphate reductase 2	2.56	5.43E-05	Up
MBD1	Methyl-CpG binding domain protein 1	0.18	6.40E-05	Up
JUN	Jun proto-oncogene, AP-1 transcription factor subunit	0.27	2.10E-17	Up

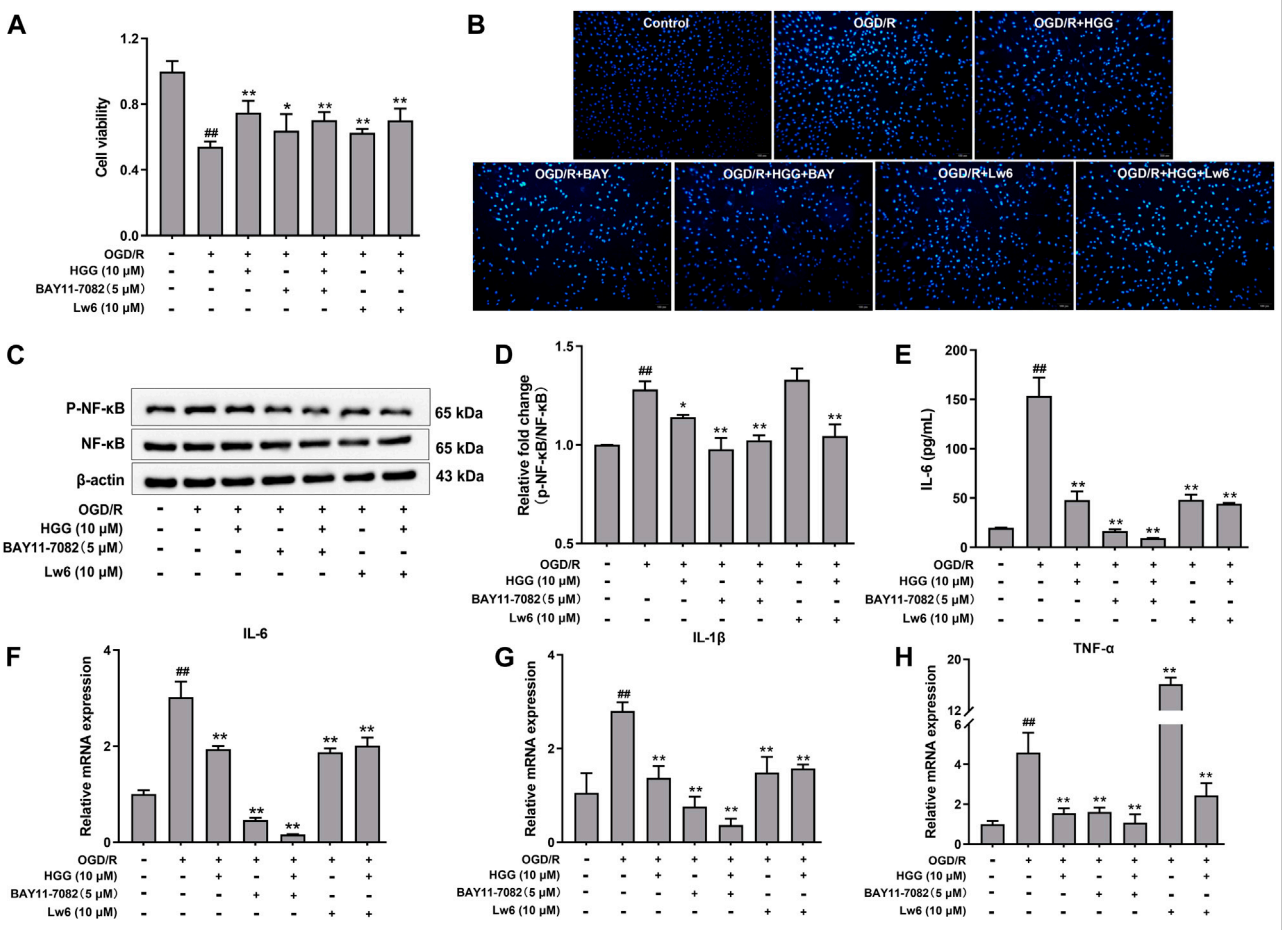

FIGURE 7
Effects of Lw6 (a HIF-1α inhibitor) and BAY11-7082 (a NFκB inhibitor) on OGD/R induced inflammation in HUVECs. The cell viability, expression of pro-inflammatory cytokines, and Western blot analysis of OGD/R-treated HUVECs in the presence or absence of HGG. **(A)** Cell viability of HUVECs determined by MTT assay. **(B)** Apoptosis assay with hochest-33342 staining, Scale bar = 100 μm. **(C)** The protein expression levels of p-NF-κB and NF-κB were determined using Western blot analysis. **(D)** The relative expression of p-NF-κB/NF-κB in HUVECs after OGD/R. **(E)** Concentration of IL-6 in the cell supernatants was measured by Elisa kits. RT-qPCR was performed to assess the expression of pro-inflammatory cytokines including **(F)** *IL-6*, **(G)** *IL-1β*, and **(H)** *TNF-α*. Data are presented as means ± SD (n = 3), $^{\#\#}p < 0.01$ vs. Control; $^{*}p < 0.05$, $^{**}p < 0.01$ vs. OGD/R.

injury (Yu et al., 2016). In this study, we demonstrated that HGG alleviate endothelial injury and significantly attenuate OGD/R-injured apoptosis of HUVECs *in vitro*. Moreover, we identified several DEGs with enriched apoptosis and inflammatory pathways underlying OGD/R injury by RNA-seq coupled with bioinformatic analysis. Inflammatory response to I/R injury plays a pivotal role in acute myocardial infarction, making it a potential therapeutic target (Ong et al., 2018). Following I/R injury, the initial pro-inflammatory response is activated, and a large number of pro-inflammatory cytokines, such as TNF-α, IL-6, IL-1β, promote the inflammatory response's progression (Zhao et al., 2000; van Hout et al., 2016). Our results showed that HGG could inhibit the mRNA expression of pro-inflammatory factors *TNF-α*, *IL-6*, and *IL-1β* and regulate the levels of IL-6 in culture supernatant of HUVECs with OGD/R injury. NF-κB as an important transcription factor plays an important role in I/R injury involved in inflammation, apoptosis, and oxidative stress (Liu et al., 2017). In I/R injury, activated NF-κB transfers to the nucleus, and thereby participating in I/R injury. Matsui et al. (2005) found that inhibition of NF-κB activation reduced I/R injury in rats. Similarly, we also found that HGG significantly attenuated OGD/R-induced HUVECs injury and decreased the protein expression of NF-κB.

I/R injury may initially provoke hypoxia response. Insufficient oxygen supplement may lead to aggravation of I/R injury and AMI (Wu et al., 2018). Hypoxia inducible factor 1α (HIF-1α) is a master transcription factor that responses to hypoxia or reduction of available oxygen. In normoxia, the

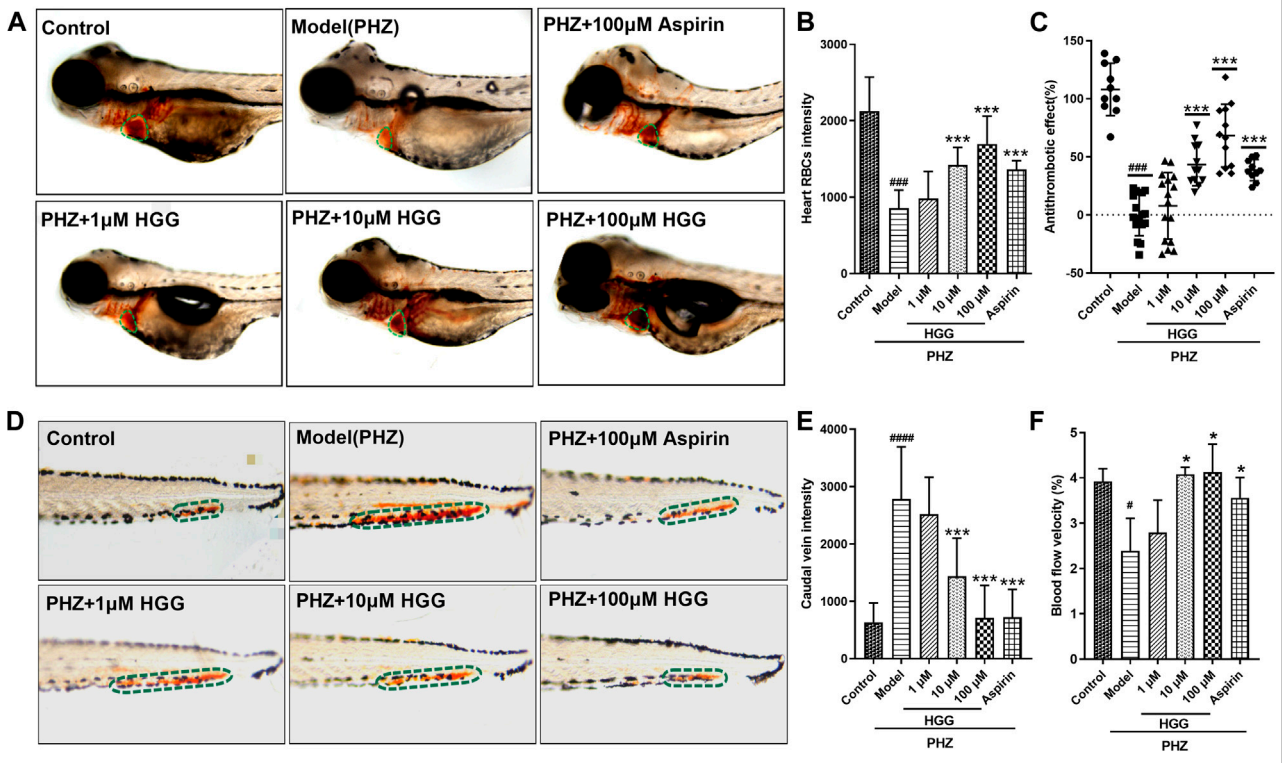

FIGURE 8
Thrombus formation and hemodynamic changes in PHZ-stimulated zebrafish with different concentrations of HGG, and anti-thrombotic drug aspirin. **(A)** Representative images of the heart RBC (green dotted line) stained with O-dianisidine after HGG, or aspirin treatment; **(B)** Quantitative analysis of heart RBCs intensity; **(C)** The anti-thrombotic effect based on heart RBC intensity; **(D)** Erythrocytes aggregation in the caudal vein (circled with green dotted line); **(E)** Quantitative analysis of the caudal vein intensity for thrombotic zebrafish; **(F)** Determination of blood flow in the caudal vein after treated with PHZ, and co-treated with HGG. $^{###}p < 0.001$ vs. Control, $^{***}p < 0.001$ vs. Model.

HIF-1α is unstable and easily degraded by prolyl hydroxylases. However, under hypoxia, the degradation and accumulation of HIF-1α is inhibited (Semenza, 2007). Yu et al. (2020) found that inhibition of serum HIF-1 and VEGF concentrations can improve the left-ventricular function in rats with AMI. In this study, we found that the HIF-1α protein in HUVECs suffered with OGD/R injury significantly increased, whereas HGG treatment ameliorated such phenomenon.

AMI usually occurs when ruptured plaques of atherosclerotic cause artery occlusion and thrombosis and unruptured plaques lead to severe coronary stenosis, reducing blood supply to heart region, and leading to irreversible myocardial ischemic injury (Libby, 2013). Therefore, anti-thrombotic therapy is required to stabilize vulnerable plaques and eliminate occlusion to restore vessel patency, reduce I/R injury, and improve cardiac function in patients with AMI (Kumar and Cannon, 2009). Safflower is frequently used in Chinese medicinal formulae for cerebrovascular and cardiovascular diseases (Chinese Pharmacopoeia Committee, 2020). To assess the anti-thrombotic effect of HGG *in vivo*, we tested the compound in a zebrafish thrombosis model. Aspirin, as a clinically anti-platelet drug, is extensively used to treat cardiovascular diseases. Aspirin could decrease the blood viscosity and ameliorate artery vascular stenosis or obstruction, exerting its protective effect in cardiovascular and cerebrovascular diseases (Cortellini et al., 2017). In this study, we demonstrated that the 6-hydroxykaempferol glycoside of Safflower, HGG, had potent anti-thrombosis activity similar to aspirin. Both HGG and aspirin significantly enhanced blood flow velocity and alleviated zebrafish tail vascular stenosis or occlusion.

In conclusion, 6-hydroxykaempferol-3,6-*di*-*O*-*β*-glucoside-7-*O*-*β*-glucuronide (HGG), as a major 6-hydroxykaempferol glycoside in Safflower protects OGD/R-induced ischemia-reperfusion injury *in vitro*. The

mechanism of action involves the mitigation of inflammatory response through HIF-1α/NF-κB signaling pathway. In addition, HGG has anti-thrombotic activity on PHZ-induced thrombosis in zebrafish and enhances blood flow and alleviates vascular occlusion. To sum up, HGG or Safflower may protect against ischemia/reperfusion injury and ameliorate thrombus formation.

Data availability statement

The original data of this study are included in the article or Supplementary Material. Further inquiries can be directed to the corresponding authors.

Ethics statement

The animal study was reviewed and approved by AnimalCare and Use Committee of Inner Mongolia University (Ethic approval number: [2020]022).

Author contributions

L-WW: Conception and design, data curation, manuscript writing-revision, and finalization. J-FH: Data collection, visualization. H-YX: Methodology. P-FZ: Revision. JZ: Data curation and analysis. C-CZ: Software, formal analysis. J-NM: Writing-review and editing. C-MM: Conception and design, manuscript writing-review, finalization, project administration. Y-BL: Conception and design, supervision, funding acquisition.

Funding

This work was supported by the National Natural Science Foundation of China (No. 81660711, 81860688) the National Key Research and Development Program of China, National foreign experts' projects (G2022005001), and Inner Mongolia Autonomous Region science and technology plan project (2021GG0030).

Conflict of interest

The authors declare that the research was conducted in the absence of any commercial or financial relationships that could be construed as a potential conflict of interest.

Publisher's note

All claims expressed in this article are solely those of the authors and do not necessarily represent those of their affiliated organizations, or those of the publisher, the editors and the reviewers. Any product that may be evaluated in this article, or claim that may be made by its manufacturer, is not guaranteed or endorsed by the publisher.

Supplementary material

The Supplementary Material for this article can be found online at: https://www.frontiersin.org/articles/10.3389/fphar.2022.974216/full#supplementary-material

References

Bournele, D., and Beis, D. (2016). Zebrafish models of cardiovascular disease. *Heart fail. Rev.* 21 (6), 803–813. doi:10.1007/s10741-016-9579-y

Cao, S., Chen, S., Qiao, X., Guo, Y., Liu, F., Ding, Z., et al. (2022). Protocatechualdehyde rescues oxygen-glucose deprivation/reoxygenation-induced endothelial cells injury by inducing autophagy and inhibiting apoptosis via regulation of SIRT1. *Front. Pharmacol.* 13, 846513. doi:10.3389/fphar.2022.846513

Cao, X., Li, B., Han, X., Zhang, X., Dang, M., Wang, H., et al. (2020). Soluble receptor for advanced glycation end-products promotes angiogenesis through activation of STAT3 in myocardial ischemia/reperfusion injury. *Apoptosis* 25 (5-6), 341–353. doi:10.1007/s10495-020-01602-8

Chen, M., Luo, Y., Xu, J., Chang, M. X., and Liu, J. X. (2019). Copper regulates the susceptibility of zebrafish larvae to inflammatory stimuli by controlling neutrophil/macrophage survival. *Front. Immunol.* 10, 2599. doi:10.3389/fimmu.2019.02599

Chinese Pharmacopoeia Committee (2020). *The Pharmacopoeia of the people's Republic of China*. Beijing: China Medical Science Press.

Collaborators, G. D. A. I., Allen, C., Arora, M., Barber, R. M., Bhutta, Z. A., Brown, A., et al. (2016). Global, regional, and national incidence, prevalence, and years lived with disability for 310 diseases and injuries, 1990-2015: A systematic analysis for the global burden of disease study 2015. *Lancet* 388 (10053), 1545–1602. doi:10.1016/S0140-6736(16)31678-6

Cortellini, G., Caruso, C., and Romano, A. (2017). Aspirin challenge and desensitization: How, when and why. *Curr. Opin. Allergy Clin. Immunol.* 17 (4), 247–254. doi:10.1097/ACI.0000000000000374

Gulati, R., Behfar, A., Narula, J., Kanwar, A., Lerman, A., Cooper, L., et al. (2020). Acute myocardial infarction in young individuals. *Mayo Clin. Proc.* 95 (1), 136–156. doi:10.1016/j.mayocp.2019.05.001

He, D., Zhang, X., Zhu, X., Huang, F., Wang, Z., and Tu, J. (2021). Network Pharmacology and RNA-sequencing reveal the molecular mechanism of xuebijing injection on COVID-19-induced cardiac dysfunction. *Comput. Biol. Med.* 131, 104293. doi:10.1016/j.compbiomed.2021.104293

He, J. B., Yang, X., Luo, Z. Y., Yuan, P. G., Song, D., Xiang, B. Q., et al. (2016). Effects of xuebijing injection on cardiac function and structure in rats with myocardial hypoxia/reoxygenation injury. *Zhongguo Ying Yong Sheng Li Xue Za Zhi* 32 (2), 173–176. doi:10.13459/j.cnki.cjap.2016.02.021

Heusch, G. (2019). Coronary microvascular obstruction: The new frontier in cardioprotection. *Basic Res. Cardiol.* 114 (6), 45. doi:10.1007/s00395-019-0756-8

Ji, D. B., Zhang, L. Y., Li, C. L., Ye, J., and Zhu, H. B. (2009). Effect of hydroxysafflor yellow A on human umbilical vein endothelial cells under hypoxia. *Vasc. Pharmacol.* 50 (3-4), 137–145. doi:10.1016/j.vph.2008.11.009

Kumar, A., and Cannon, C. P. (2009). Acute coronary syndromes: Diagnosis and management, Part I. *Mayo Clin. Proc.* 84 (10), 917–938. doi:10.1016/S0025-6196(11)60509-0

Libby, P. (2013). Mechanisms of acute coronary syndromes and their implications for therapy. *N. Engl. J. Med.* 368 (21), 2004–2013. doi:10.1056/NEJMra1216063

Liu, T., Zhang, L., Joo, D., and Sun, S. C. (2017). NF-κB signaling in inflammation. *Signal Transduct. Target. Ther.* 2, e17023. doi:10.1038/sigtrans.2017.23

Lv, X., Li, Q., Mao, S., Qin, L., and Dong, P. (2020). The protective effects of memantine against inflammation and impairment of endothelial tube formation induced by oxygen-glucose deprivation/reperfusion. *Aging (Albany NY)* 12 (21), 21469–21480. doi:10.18632/aging.103914

Mathiesen, A., Hamilton, T., Carter, N., Brown, M., McPheat, W., and Dobrian, A. (2021). Endothelial extracellular vesicles: From keepers of health to messengers of disease. *Int. J. Mol. Sci.* 22, 4640. doi:10.3390/ijms22094640

Matsui, N., Kasajima, K., Hada, M., Nagata, T., Senga, N., Yasui, Y., et al. (2005). Inhibiton of NF-kappaB activation during ischemia reduces hepatic ischemia/reperfusion injury in rats. *J. Toxicol. Sci.* 30 (2), 103–110. doi:10.2131/jts.30.103

Montrief, T., Davis, W. T., Koyfman, A., and Long, B. (2019). Mechanical, inflammatory, and embolic complications of myocardial infarction: An emergency medicine review. *Am. J. Emerg. Med.* 37 (6), 1175–1183. doi:10.1016/j.ajem.2019.04.003

Neri, M., Riezzo, I., Pascale, N., Pomara, C., and Turillazzi, E. (2017). Ischemia/reperfusion injury following acute myocardial infarction: A critical issue for clinicians and forensic pathologists. *Mediat. Inflamm.* 2017, 7018393. doi:10.1155/2017/7018393

Ong, S. B., Hernandez-Resendiz, S., Crespo-Avilan, G. E., Mukhametshina, R. T., Kwek, X. Y., Cabrera-Fuentes, H. A., et al. (2018). Inflammation following acute myocardial infarction: Multiple players, dynamic roles, and novel therapeutic opportunities. *Pharmacol. Ther.* 186, 73–87. doi:10.1016/j.pharmthera.2018.01.001

Qi, H., Yang, S., and Zhang, L. (2017). Neutrophil extracellular traps and endothelial dysfunction in atherosclerosis and thrombosis. *Front. Immunol.* 8, 928. doi:10.3389/fimmu.2017.00928

Reed, G. W., Rossi, J. E., and Cannon, C. P. (2017). Acute myocardial infarction. *Lancet* 389 (10065), 197–210. doi:10.1016/S0140-6736(16)30677-8

Sattler, S. M., Skibsbye, L., Linz, D., Lubberding, A. F., Tfelt-Hansen, J., and Jespersen, T. (2019). Ventricular arrhythmias in first acute myocardial infarction: Epidemiology, mechanisms, and interventions in large animal models. *Front. Cardiovasc. Med.* 6, 158. doi:10.3389/fcvm.2019.00158

Semenza, G. L. (2007). Hypoxia-inducible factor 1 (HIF-1) pathway. *Sci. STKE* 2007 (407), m8. doi:10.1126/stke.4072007cm8

Somani, Y. B., Pawelczyk, J. A., De Souza, M. J., Kris-Etherton, P. M., and Proctor, D. N. (2019). Aging women and their endothelium: Probing the relative role of estrogen on vasodilator function. *Am. J. Physiol. Heart Circ. Physiol.* 317 (2), H395 H404–H404. doi:10.1152/ajpheart.00430.2018

van Hout, G. P., Arslan, F., Pasterkamp, G., and Hoefer, I. E. (2016). Targeting danger-associated molecular patterns after myocardial infarction. *Expert Opin. Ther. Targets* 20 (2), 223–239. doi:10.1517/14728222.2016.1088005

Wang, L. W., Cui, X. Y., He, J. F., Duan, S., Liu, C. R., Shan, C. B., et al. (2021). Hydroxysafflor yellows alleviate thrombosis and acetaminophen-induced toxicity *in vivo* by enhancing blood circulation and poison excretion. *Phytomedicine.* 87, 153579. doi:10.1016/j.phymed.2021.153579

Wang, X. Y., Zhang, F., Zhang, C., Zheng, L. R., and Yang, J. (2020). The biomarkers for acute myocardial infarction and heart failure. *Biomed. Res. Int.* 2020, 2018035. doi:10.1155/2020/2018035

Wei, A., Xiao, H., Xu, G., Yu, X., Guo, J., Jing, Z., et al. (2020). Hyperoside protects human umbilical vein endothelial cells against anticardiolipin antibody-induced injury by activating autophagy. *Front. Pharmacol.* 11, 762. doi:10.3389/fphar.2020.00762

Wu, H., Wang, X., Gao, S., Dai, L., Tong, H., Gao, H., et al. (2019). Yiqi-huoxue granule (YQHX) downregulates prothrombotic factors by modulating KLF2 and NF-κB in HUVECs following LPS stimulation. *Oxid. Med. Cell. Longev.*, 9425183. doi:10.1155/2019/9425183

Wu, M. Y., Yiang, G. T., Liao, W. T., Tsai, A. P., Cheng, Y. L., Cheng, P. W., et al. (2018). Current mechanistic concepts in ischemia and reperfusion injury. *Cell. Physiol. biochem.* 46 (4), 1650–1667. doi:10.1159/000489241

Wu, Y., Yao, J., and Feng, K. (2020). miR-124-5p/NOX2 Axis modulates the ros production and the inflammatory microenvironment to protect against the cerebral I/R injury. *Neurochem. Res.* 45 (2), 404–417. doi:10.1007/s11064-019-02931-0

Yellon, D. M., and Hausenloy, D. J. (2007). Myocardial reperfusion injury. *N. Engl. J. Med.* 357 (11), 1121–1135. doi:10.1056/NEJMra071667

Yu, H., Zhang, H., Zhao, W., Guo, L., Li, X., Li, Y., et al. (2016). Gypenoside protects against myocardial ischemia-reperfusion injury by inhibiting cardiomyocytes apoptosis via inhibition of chop pathway and activation of Pi3K/akt pathway *in vivo* and *in vitro*. *Cell. Physiol. biochem.* 39 (1), 123–136. doi:10.1159/000445611

Yu, J., Zhang, L., and Zhang, H. (2020). Atorvastatin combined with routine therapy on HIF-1, VEGF concentration and cardiac function in rats with acute myocardial infarction. *Exp. Ther. Med.* 19 (3), 2053–2058. doi:10.3892/etm.2020.8438

Zhang, L. L., Tian, K., Tang, Z. H., Chen, X. J., Bian, Z. X., Wang, Y. T., et al. (2016). Phytochemistry and Pharmacology of Carthamus tinctorius L. *Am. J. Chin. Med.* 44 (2), 197–226. doi:10.1142/S0192415X16500130

Zhao, Z. Q., Nakamura, M., Wang, N. P., Wilcox, J. N., Shearer, S., Ronson, R. S., et al. (2000). Reperfusion induces myocardial apoptotic cell death. *Cardiovasc. Res.* 45 (3), 651–660. doi:10.1016/s0008-6363(99)00354-5

frontiers | Frontiers in Pharmacology

TYPE Original Research
PUBLISHED 04 October 2022
DOI 10.3389/fphar.2022.1009023

OPEN ACCESS

EDITED BY
Xiaoyong Tong,
Chongqing University, China

REVIEWED BY
Ademola Adetokunbo Oyagbemi,
University of Ibadan, Nigeria
Mohamed Fizur Nagoor Meeran,
United Arab Emirates University, United Arab Emirates

*CORRESPONDENCE
R. Elancheran,
srielancheran@gmail.com
Rajlakshmi Devi,
rajlakshmi@iasst.gov.in

SPECIALTY SECTION
This article was submitted to Cardiovascular and Smooth Muscle Pharmacology, a section of the journal Frontiers in Pharmacology

RECEIVED 01 August 2022
ACCEPTED 12 September 2022
PUBLISHED 04 October 2022

CITATION
Bhattacharjee S, Elancheran R, Dutta K, Deb PK and Devi R (2022), Cardioprotective potential of the antioxidant-rich bioactive fraction of Garcinia pedunculata Roxb. ex Buch.-Ham. against isoproterenol-induced myocardial infarction in Wistar rats. *Front. Pharmacol.* 13:1009023. doi: 10.3389/fphar.2022.1009023

Cardioprotective potential of the antioxidant-rich bioactive fraction of *Garcinia pedunculata* Roxb. ex Buch.-Ham. against isoproterenol-induced myocardial infarction in Wistar rats

Swarnali Bhattacharjee[1,2], R. Elancheran[3]*, Kasturi Dutta[1], Prashanta Kumar Deb[4] and Rajlakshmi Devi[1]*

[1]Life Sciences Division, Institute of Advanced Study in Science and Technology, Guwahati, Assam, India, [2]Department of Zoology, Gauhati University, Guwahati, Assam, India, [3]Department of Chemistry, Annamalai University, Chidambaram, TamilNadu, India, [4]Department of Pharmaceutical Chemistry, School of Pharmaceutical Sciences, Shoolini University, Solan, Himachal Pradesh, India

This Study aimed to characterise the phenolic compounds in *Garcinia pedunculata* extract and assess their potential antioxidant activity as well as its cardioprotective potential in isoproterenol-induced cardiac hypertrophy in an experimental animal model. *In vitro* antioxidant properties were determined using DPPH, ABTS, FRAP, PMD assays. *In vitro* lipid peroxidation experiment was also performed with heart tissues. Cardioprotective and cardiotoxicity effects were determined using the cell line studies. The cardioprotective effect of GP was assessed in a rat model of isoproterenol-(ISO-) induced cardiac hypertrophy by subcutaneous administration. Heart weight/tail length ratio and cardiac hypertrophy indicators were reduced after oral administration of GP. Additionally, GP reduced oxidative stress and heart inflammation brought on by ISO. In H9c2 cells, the antihypertrophic and anti-inflammatory effects of the extract of GP were seen in the presence of ISO, which were further supported by the *in vivo* observations. This study makes a compelling case for the possibility that supplementing with dried GP fruit can prevent heart hypertrophy by reducing oxidative stress and inflammation.

KEYWORDS

cardioprotective effect, isoproterenol-induced myocardial infarction, Garcinia pedunculata, phytocompounds, molecular modelling

1 Introduction

The World Health Organisation (WHO) commissioned the Global Burden of Disease (GBD) study in the 1990s, where childhood illness, psychological diseases, and traffic accidents were the leading causes of death worldwide (Mathers, 2020). By the statistics of 2019, the burden shifted to non-communicable diseases (NCDs), claiming about 42 million lives globally, and cardiovascular diseases (CVDs) are among its leading cause independent of the socioeconomic background of the countries (Emadi-Emadi et al., 2021). About 1/3rd of the global deaths happen due to cardiovascular diseases, the most rampant of them being ischemic heart disease (IHD). Myocardial infarction is the most common manifestation of IHD, which might come in the form of coronary artery disease and atherosclerosis (Khan et al., 2020). In the Indian scenario, NCDs were also on the rise from the 1990s to 2016, with CVDs being the principal cause of annual mortality (Mohan et al., 2019). Myocardial infarction (MI), in general terms, heart attack, happens with obstructed circulation leading to localized necrosis in the myocardium with pronounced ischemia. The most common diagnostic criteria include an increase in cardiac troponin I or T and ST-wave elevation or depression in ECG analysis (Saleh & Ambrose, 2018). Initial markers for MI were aspartate transaminase in the mid-1990s, which was then replaced with more specific markers like creatinine kinase (CK), CK-MB, and lactate dehydrogenase (LDH). A widely accepted gold-standard marker for MI was found in elevated troponin T or I levels. The other biomarkers, although not diagnostic, include B-Type natriuretic peptide (BNP), C reactive protein (CRP), IL-6, and TNF-α (Chen et al., 2019a). The patients hospitalised with chest pain are often suspected of MI, and are diagnosed based on advance techniques like electrocardiography (ECG); echocardiography, coronary angiography, cardiac MRI and CT-scan along with the biomarkers (Sandoval & Jaffe, 2019). A multitude of risk factors are associated with MI, of which some prominent modifiable risk factors include smoking, alcohol abuse, diet rich in fats and carbohydrates, lacking fruits and vegetables, sedentary lifestyle, unhealthy weight gain, hypertension, and hyperlipidemia (Ojha and Dhamoon, 2021).

An ideal model to mimic the human MI-related complications is the isoproterenol-induced myocardial injury non-invasive model used to study natural products' cardioprotective or preventive potential. Isoproterenol is a synthetic catecholamine, ß- receptor agonist. A 85 mg/kg of ISO dosage induces myocardial necrosis, degeneration of myofibrils, fibrosis, inflammation, calcium overload, and energy deficit in the rat heart (Wong et al., 2017).

With the impending side effects from the prolonged use of synthetic medicines for cardiac complications, there is an urgent need for safer alternatives. With this in mind, focused research on natural products of herbal origin with negligible side effects to explore their cardioprotective potential came into being (Allawadhi et al., 2018; Shah et al., 2019). Over the years, several plants like *Amaranthus viridis*, *Ginkgo biloba*, *Terminalia arjuna*, *Tinospora cordifolia*, *Curcuma longa*, *Hydrocotyle asiatica*, *Centella asiatica*, *Allium sativum*, *Withania somnifera*, *Garcinia kola, Zingiber officinale,* and many others have been assessed for their cardioprotective potential (Shah et al., 2019; Kumar et al., 2017). Some of the plant-derived bioactive compounds with potent cardioprotective activity include digoxin (arrhythmia treatment), atropine (bradycardia treatment), allicin, kolaviron, caffeic acid, epigallocatechin-3-gallate, resveratrol, carotenoids, with their therapeutic activities like potent antioxidant anti-hypertensive, anti-atherosclerotic, anti-inflammatory, and improving insulin sensitivity properties to name a few (Shah et al., 2019; Sharifi-Rad et al., 2020). One such fruit of interest is *Garcinia pedunculata* Roxb. or GP.

G. pedunculata, an evergreen tree belonging to the Clusiaceae family, bears an acidic, globose fruit with immense therapeutic potential and is a well-known medicinal plant belonging to Northeast India. Although the consumption of raw fruit is traditionally forbidden, the ripened fruit is used to treat gastrointestinal disorders and is lavishly used in cooking various delicacies of Assamese cuisine. Among the prominent medicinal properties reported from the fruit of GP include antioxidant, hypolipidemic, nephroprotective, neuroprotective, and anti-diabetic properties. Also, chemical profiling of GP unraveled multiple compounds like hydroxycitric acid, 2,4,6,3′,5′-pentahydroxybenzophenone, pedunculol, and pedunxanthone A from different parts of the plant (Bhattacharjee and Devi, 2021). Despite the already established therapeutic properties, reports on GP fruit's cardioprotective potential are minimal. Keeping this research gap in mind, this study has been designed to assess the cardioprotective potential of the polyphenol-rich fraction of GP fruit using isoproterenol-induced MI in Wistar rats along with its chemical profiling.

2 Materials and methods

2.1 Chemicals

Chloroform, Ethyl acetate, Hexane, Methanol (analytical grade, Merck); Sodium carbonate, Folin Ciocalteu reagent, Gallic acid, 1, 1-Diphenyl-2-picrylhydrazyl (DPPH), 2,2′-Azino-bis(3-ethylbenzthiazoline-6-sulfonic acid (ABTS), Potassium ferricyanide, Disodium hydrogen phosphate, Monosodium phosphate, Trichloroacetic acid, Iron (III) chloride, Iron (II) sulphate, MTT (3-(4,5-Dimethylthiazol-2-yl)-2,5-Diphenyltetrazolium Bromide), 2′,7′-dichlorodihydrofluorescein diacetate (H2DCFDA), Thiobarbituric acid, Glacial acetic acid, Trolox, Sodium

dodecyl phosphate, Pyrogallol, Ellman's reagent, hydrogen peroxide were purchased from Sigma-Aldrich, United States and Merck, Germany.

2.2 Plant materials

GP fruit was collected from the Kamrup district (25°43′ - 26°19′ North latitude and 90°39′- 91°47′ East latitude), Guwahati, Assam and was taxonomically verified from the Department of Botany, Gauhati University under voucher number Ref. No. *Herb./GUBH/2022/002* and have been submitted to Gauhati University, Herbarium section, under accession number GUBH19815.

2.3 Plant material processing, extraction, and fractionation

The fruits were thoroughly cleaned, and their pulp and rinds were thinly sliced and dried in the Sun without the seeds. Maceration was used to prepare the crude extract (GPC) of the fruit in methanol, and the dried crude extract was then fractionated using column fractionation (Silica, 60–120 mesh) with the appropriate solvents: hexane (GH), chloroform (GC), ethyl acetate (GE), and methanol (GM). A rotary evaporator (Buchi R210, Switzerland) was used to remove the solvents from the extracts, and the material was subsequently lyophilized (FreeZone Freeze Dryer, Labconco). The yield percentage for each extract was calculated, and until usage, it was kept in sealed containers at 4°C–8°C.

2.4 Total phenolic content

The phenolic content was estimated using the methodology of Sarma et al., 2016 with slight modification by adding 1,000 µL of 2% Sodium carbonate (freshly prepared), 100 µL of Folin-Ciocalteu reagent to 100 µL of different extracts and fractions at a concentration of 10 mg/ml, which were mixed well and left in the dark for 30 min of incubation. The absorbance of the resultant mixture was measured spectrophotometrically in a microplate reader (Multiskan GO, Thermo, Germany) at 750 nm. The standard curve was prepared with Gallic acid ($y = 0.006x + 0.322$, $R^2 = 0.988$), and the data were expressed as mg GAE/g (Gallic acid equivalent).

2.5 UHPLC-ESI orbitrap MS/MS analysis

An ultra-high pressure liquid chromatography (UHPLC) system from Dionex Inc. In Sunnyvale, California, was used to perform the chromatographic separation. This system includes a binary pump, a degasser, an autosampler, a thermostated column compartment, and a control module. Chromatographic separation was performed using a UHPLC system connected to an Electron Spray Ionization (ESI) Orbitrap mass spectrometer, and Hypersil Gold C18 column operating at 25 °C. Using the earlier technique, gradient chromatographic separation was carried out for each extract of the samples (Kumari et al., 2017). Using the mass spectrum and its unique fragmentation spectra, the phenolic compounds in the *Garcinia* extract were screened and identified. The key method for potential identification of the phenolic compounds was the comparison of the obtained MS/MS spectra with those published in the literature and mass bank database.

2.6 *In- vitro* screening of antioxidant potential

2.6.1 1, 1-diphenyl-2-picrylhydrazyl radical scavenging assay

To 100 µL of freshly prepared 0.2 mM DPPH solution, 100 µL of extracts and fractions (prepared in methanol) were added in different concentrations, and the absorbance was recorded at 517 nm after an incubation of 30 min in the dark at room temperature. The resulting IC_{50} for each extract was evaluated to compare the radical scavenging activity. If lower the IC_{50}, better the scavenging activity (Iloki-Assanga et al., 2015).

2.6.2 2,2′-Azinobis (3-ethylbenzthiazoline -6-sulphonic acid (ABTS) radical scavenging assay

The antioxidant activity of the extracts was assessed by the increased $ABTS^+$ radical cation scavenging ability with slight modification (Re et al., 1999; Sarma et al., 2016), by adding a 7 mM solution of ABTS in a 1:1 ratio with various quantities of extracts, incubating in the dark for half an hour at room temperature, and measuring absorbance at 734 nm. Following the DPPH experiment, the antioxidant activity was compared.

2.6.3 Ferric reducing assay power

Add 250 µL of 0.2 M phosphate buffer (pH 6.6) and 250 µL of potassium ferricyanide (1%) to 100 µL of extracts and fractions, each taken in a different concentration. After that, this mixture is allowed to stand at 50 °C for 30 min 250 µL of 10% trichloroacetic acid was added to the mixture after incubation. In addition, 250 µL of the resulting mixture was diluted 1:1 with distilled water before being added to a freshly made 0.1 percent ferric chloride solution, which was used to measure the absorbance at 700 nm. Increased antioxidant activity was related to the increase in absorption (Vijayalakshmi & Ruckmani, 2016).

2.6.4 Phosphomolybdenum assay

The 28 mM sodium phosphate and 4 mM ammonium molybdate solution were mixed with 0.6 M sulfuric acid to

form the phosphomolybdate reagent, which was then freshly prepared. The fractions and varying concentrations of the extract are mixed with 150 ml of this reagent and incubated for 90 min at 95 °C. The reducing activity is indicated by the increase in absorbance, which was measured at 695 nm (Khan et al., 2012).

2.6.5 *In- vitro* lipid peroxidation assay

Heart tissue homogenate was tested in an *in vitro* lipid peroxidation experiment, where the Fe^{2+} Ascorbate system was used to induce lipid peroxidation. This assay was carried out with some small alterations to (Sarma et al., 2016). 50 mM phosphate buffer (pH 7.4) was used to prepare 10 percent (w/v) tissue homogenate, which was then employed in the test without centrifugation. The following mixtures are added to 250 µL of tissue extract, 100 µL of 150 mM Tris HCL buffer (pH 7.2), 50 µL of 0.1 mM Ascorbic acid, 50 µL of 4 mM $FeSO_4$, 50 µL of the extract and fractions in different concentrations, 50 µL of H_2O, and 50 µL of Trolox as standard. Following that, this mixture is incubated for 1 hour at 37 °C. The following step is Thiobarbituric Acid Reactive Substance Measurement (TBARS), which involves mixing 50 µL of the abovementioned mixture with 150 µL each of 0.8 percent (w/v) thiobarbituric acid, 20 µL of 8.1 percent SDS, and 30 µL of deionized water. This mixture is incubated at 95°C for an hour, cooled under tap water, and then 500 µL of butanol: pyridine (15:1, v/v) and 100 µL of distilled water are added. The upper layer is then carefully removed to measure the absorbance at 532 nm after the mixture has been vortexed and centrifuged at 4,000 rpm for 10 min. The extract with a lower IC_{50} was more effective at inhibiting lipid peroxidation.

2.7 *In- vitro* screening of cardioprotective effect in cardiomyocytes

The H9c2 cell line (Rat cardiomyoblast) was procured from NCCS in Pune for use in cell culture experiments. They were subcultured at around 80% confluency in a humidified 5 percent CO_2 incubator with DMEM (4.5 g/L glucose, Gibco) containing 10% FBS, 1% antibiotic solution, and 37°C. For all the experiments were performed using 2 to 10 passages.

2.7.1 Establishment of isoproterenol induced *in vitro* cardiotoxicity model

H9c2 cells were plated in the required concentrations in 10 percent FBS-containing DMEM for the ISO-treated cardiotoxicity model, and the medium was changed to 1 percent FBS-containing media after 24 h. The cells were treated with various doses of ISO or ISO + extracts after being serum-deprived for 48 h to promote cellular differentiation (Branco et al., 2011; Sivasangari et al., 2019; Raut et al., 2020).

2.7.1 Cell-culture treatment

Different GC concentrations were applied to the cells for the cell culture experiments 2 hours before the 25 µM ISO treatment. Every day, the used media were replaced. The experimental dilutions were prepared in DMEM with the DMSO concentration kept below 0.01 percent, and 0.01 percent was utilised as the vehicle control, while ISO was prepared in PBS. The stock for GC was prepared in DMSO and maintained at -20 °C (pH 7.4, Gibco).

2.7.1.1 Cell viability assay

For the cardiotoxicity model, the cells were seeded at a concentration of 1×10^4 cells/well in 96 well cell culture plate (Tarsons) and treated with different concentrations of isoproterenol, GC, and ISO+GC. Before adding ISO, cells were pretreated with GC extract for 2 hours. The MTT (3-(4,5-dimethylthiazol-2-yl)-2,5-diphenyl tetrazolium bromide) assay was used to determine the viability of the cells, and the absorbance was measured at 570 nm. The viability is determined by comparing the proportion of living cells in treated concentrations to untreated control cells (Sivasangari et al., 2019).

2.7.1.2 Study of cell morphology with ISO treatment

This assay was performed as per the protocol of Sivasangari et al., 2019, and the unstained cells were photographed using a phase-contrast inverted microscope Leica DMI 3000 B, with a scale of 200 µm.

2.7.1.3 LDH release assay

The LDH release assay was used to assess the extent of cellular damage caused by ISO treatment in H9c2 cells, as well as the role of GC in conferring cardioprotection against ISO. The LDH Test Kit (Himedia, CAT: CCK058-500) was used to perform the assay, and the manufacturer's protocols were followed. The cells were seeded at the same concentration as in the MTT.

2.7.1.4 Intracellular ROS detection

After treatment for 12 h, the spent media was discarded, and the cells were washed with 1X PBS (cell culture grade, pH 7.4, Gibco) twice and then incubated with 10 µM of H_2DCF-DA in phenol red-free DMEM for 45 min at 37 °C. After incubation, the remaining H_2DCF-DA were removed and cells were again washed properly with 1X PBS then their fluorescence intensity was measured at 485 nm (excitation) and 525 nm (emission) using a VarioskanFlash microplate reader (software- SkanIt Software 2.4.5 RE for Varioskan Flash). The ROS is represented as percentage of control (100%) (Hašková et al., 2011; Park et al., 2014; Ozbek et al., 2015).

2.8 *In- vivo* assessment of cardioprotective activity

All of the studies were carried out by following international standards for the use and care of experimental animals. Thirty

Wistar albino rats (male), 10–12 weeks old, were bought from M/S Chakraborty Enterprise in Kolkata. The Institutional Animal Ethics Committee granted the study approval (IAEC no. IASST/2018/07). All of the animals were kept in tidy, empty plastic cages. The room was kept at a constant temperature of 24 ± 3 °C, with a relative humidity of 45 ± 5% and a cycle of light and dark, lasting 12 h. They were fed on standard rat chow and had unrestricted access to food and water *ad libitum*.

2.8.1 Acute toxicity study

Six Wistar albino rats (both male and female) were chosen at random for the acute toxicity research, and their weights were noted. Following a single dosage of the GC extract at a dose of 2000 mg/kg body weight (BW) after an overnight fast in which they had only access to water, the animals were monitored continuously for the following 4 hours and kept in polypropylene cages under the same circumstances as the experimental animals, who had unlimited access to food and water. The animals were monitored for any behavioural abnormalities, toxicity, or mortality for the following 14 days in accordance with OECD (Organisation for Economic Co-operation and Development) 423 recommendations. The dose is deemed harmful if death is 2/3 or greater; if mortality is 1/3 or less, the experiment was to be repeated. If the mortality continued, lowering the dose was to be considered (Sarma et al., 2016).

2.8.2 Development of ISO-induced MI experimental model

For the development of MI in experimental animals, isoproterenol is dissolved in normal saline and a dose of 85 mg/kg BW is injected into the animals subcutaneously on the 28th and 29th days of the experiment, at an interval of 24 h (Rajadurai and Prince, 2006; Ojha et al., 2012; Hassan et al., 2017).

2.8.3 Experimental layout

After 7 days of acclimatization, the thirty rats (160–180 g) were distributed randomly into five groups with six animals each. They were pretreated with GC extract (prepared into a suspension in 0.3% carboxy methyl cellulose) at a dose of 100 and 200 mg/kg BW, every alternate day for 30 days. The experimental layout is as under-

A. Group I/IG1 - Normal control- Without ISO injection or GC.
B. Group II/IG2 - Disease control or ISO injected on the 28th and 29th days.
C. Group III/IG3 - Treated with standard drug (Atenolol) ISO + Atenolol - 5 mg/kg BW, every alternate day, for 30 days in 0.3% CMC.
D. Group IV/IG4 - Treated with 100 mg/kg BW GC- ISO + GC100.
E. Group V/IG5 - Treated with 200 mg/kg BW GC- ISO + GC200.

The ECG of all the animals were recorded after 2nd injection of ISO and after recording ECG all the animals were euthanized on the same day after 24 h of 2nd ISO injection with a combination of ketamine (87 mg/kg BW) and xylazine (13 mg/kg BW) injected intraperitoneally (Van Pelt, 1977) after fasting with just water for 12 h. Blood was collected for both serum and plasma, while heart tissues were collected after being washed with ice-cold physiological saline and stored at -80 °C for further biochemical and histopathological evaluation. Also, at the time of sacrifice, heart weight, body weight, and tail lengths of respective animals were recorded (Anosike & Cajetan, 2015; Shaikh et al., 2019).

2.8.4 Cardiac hypertrophy parameters

The heart weight (mg), heart weight index [heart weight/body weight, (mg/g)] and heart tail index [heart weight/tail length (mg/cm)] were considered the preliminary indicators for hypertrophy in cardiac tissues. After thoroughly cleaning the heart in ice-cold saline and drying it on blotting paper, the heart's weight was recorded at the time of dissection (Syed et al, 2016, Saleem et al., 2018).

2.8.5 Analysis of electrocardiogram

At the time of recording ECG, the rats were anaesthetized using ketamine hydrochloride (100 mg/kg BW) *via* intraperitoneal injection (Kannan & Quine, 2011). Using three 12 mm long needle 29 gauge electrodes, Animal Bio Amp and PowerLab 8/35 (AD Instruments, Australia) ECG was done and the results were analysed using LabChart Pro software (N = 4). The changes in heart rate (bpm), RR- interval, P- duration, QRS interval, QT interval (ms), and ST height (mV) were recorded.

2.8.6 Cardiac injury marker estimation

The following enzymes, viz. CK- MB (Creatinine kinase–MB isozyme), CK- NAC (Creatinine kinase-N-acetyl-L-cysteine), LDH (Lactate dehydrogenase), SGOT (serum glutamic oxaloacetic transaminase/AST), SGPT (serum glutamic pyruvic transaminase/ALT) and ALP (alkaline phosphatase) which are important diagnostic markers of cardiac injury were estimated from the serum using commercially available kits from Coral Clinical Systems (Tulip Diagnostics) (Panda et al., 2017). CK-MB levels were also measured from cardiac tissue extracts with the help of an ELISA kit (CAT IT7209, G- Biosciences) and cardiac troponin-I from serum (ELISA, CAT IT6638, G-Biosciences).

2.8.7 Estimation of a lipid profile

The estimation of total cholesterol, triglyceride, LDL-C, and HDL-C have been estimated using a biochemistry analyzer

(Selectra Junior, Vital Scientific) while VLDL- C was calculated using Friedwald's formula-

$$VLDL - C = \frac{Triglycerides}{5}$$

(Friedwald et al., 1972; Panda et al., 2017). Further the HMG CoA (β-Hydroxyl ß-methylglutaryl- CoA) reductase activity was determined from the liver tissue homogenate by determining the HMG CoA/Mevalonate ratio following the protocol of Rao & Ramakrishnan, 1975.

2.8.8 Myocardial oxidative stress parameters

For these assays, 10% (w/v) heart tissue extract in 0.05 M ice-cold phosphate buffer (pH 7.4). The estimation of lipid peroxidation levels was done using the TBARS estimation method described by Ohkawa et al., 1979 using the tissue extract directly without centrifugation. For SOD, GSH and catalase estimation, the tissue extract was centrifuged at 15,000 rpm for half an hour at 4 °C and was done using the methods described by Marklund and Marklund, 1974, Goth, 1991 respectively.

2.8.9 Serum NO and myocardial iNOS/NOS2 levels

The serum NO was determined following the protocol as described by (Green et al., 1982). The iNOS/NOS2 levels were detected using an ELISA kit from G-Biosciences (CAT. IT6627).

2.8.10 Inflammatory cytokines

The estimation of inflammatory cytokines TNF-α, IL- 1β, IL-6 and IL-10 were measured from serum and cardiac tissue extracts using ELISA kits following the manufacturer's protocol (CAT: IT7716, IT7444, IT17833, IT18454 respectively, G- Biosciences).

2.8.11 Histopathological analysis

After dissection, heart tissues were preserved in 10% neutral buffered formalin and were processed for histopathological analysis by embedding in paraffin. All tissues were sectioned with 5 µm thickness and stained with Haematoxylin- Eosin for general architecture and Masson's Trichome for collagen deposition (blue colored) and observed for histoarchitectural changes. The images have been taken using a Zeiss Primo Star Phase contrast microscope installed with Zeiss Zen 3.3 blue edition software, scale 10 µm, magnification ×400.

2.9 Molecular docking

Human iNOS Reductase and Calmodulin Complex (PDB: 3HR4) and human TNF-alpha in complex with 2-[5-(3-chloro-4-{[(1R)-1-(2-fluorophenyl)ethyl]amino} quinolin-6-yl)pyrimidin-2-yl]propan-2-ol (PDB: 7JRA) were obtained from RCSB protein data bank and refined structural corrections carried out. The molecules were optimized and protein-ligand molecular docking was performed in extra precision mode. The molecular docking studies were carried out by following the standard procedures recommended by Schrodinger (Elancheran et al., 2019; Maruthanila et al., 2022).

2.10 Statistical analysis

The statistical analysis was done using Graphpad Prism Version five software. All data are expressed as mean ± standard deviation. The statistical significance is calculated *via* one-way ANOVA, with Tukey's post hoc test for the biochemical data, and Dunnet's multiple comparison tests for cell culture and animal experiment data. The results have been expressed in $p < 0.05$, 0.01, and 0.001 for statistical significance.

3 Results

3.1 Phytochemical investigation

After fractionating the crude extract (GPC), the obtained percentage yield for hexane and chloroform fractions was 1% and 8.2%, respectively. The ethyl acetate fraction amounted to about 64%, while the methanol fraction was about 20%. The total phenolic content assay revealed that GC (257.833 ± 7.507 mg GAE/g) had the highest phenolic content, followed by GH, GPC, GE, and GM in descending order among the crude and fractions (Supplementary Table S1). In comparison with crude extract, the phenolic content of GC and GH were significantly higher, followed by GE and GM. In between GC and GH, GC have substantially higher phenolic content (significantly higher at $p < 0.05$).

3.2 UHPLC-ESI orbitrap MS/MS analysis

UHPLC-ESI-MS/MS was used for the screening and identification of crude extract (GPC) and the fractions. It shows that intense peaks were observed between 0 and 10 min. By comparing the GP extract mass, retention time, and λ max to those of the reference compounds and preceding literature publications, peak identification was carried out. hydroxycitric acid, hydroxycitric acid lactone, and parvifoliquinone were identified from GP extract with the respective mass $[M-H]^+$, i.e. 189.00397, 207.01472 and 221.03061 respectively (Figure 1). Also, Hydroxycitric acid, GB-1a, Garcinone A, 9-Hydroxycalabaxanthone, Chlorogenic acid, and Garcinol were previously reported in our study.

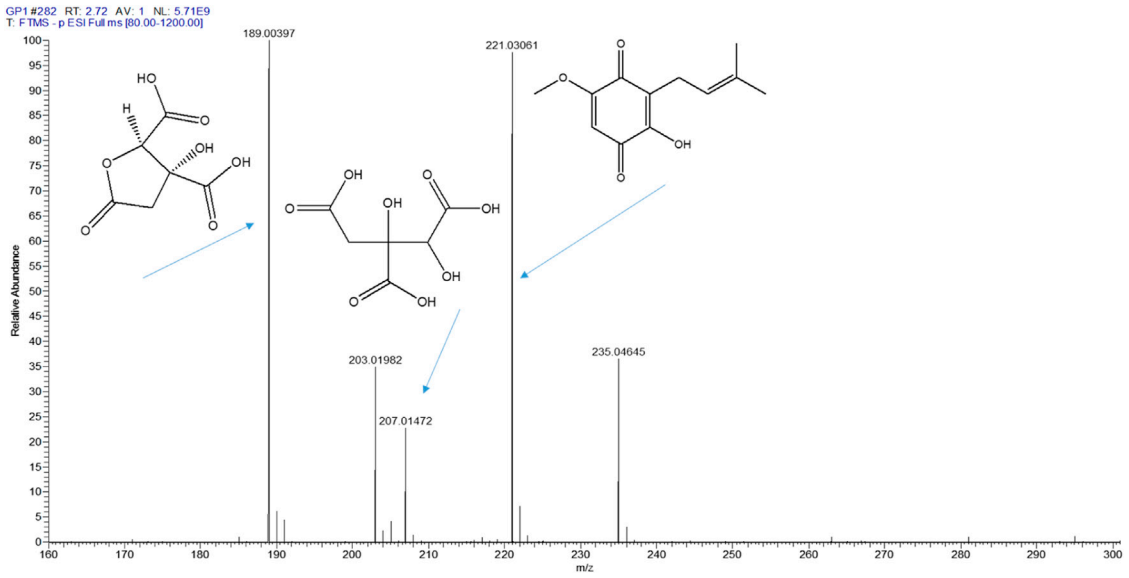

FIGURE 1
Identification of compounds from GP extract.

3.3. *In- vitro* screening of antioxidant potential

Polyphenols are the most abundant secondary metabolites derived from plants which have a common structural skeleton with one or more aromatic rings with single or multiple hydroxyl substitutions. These compounds, have immense antioxidant and therapeutic potential (Swallah et al., 2020). Multiple studies reported the antioxidant properties of various plant extracts rich in polyphenolic compounds in amelioration of diseases like diabetes, cardiovascular, Alzheimer's, and intestinal diseases (Stagos, 2019). The following assays take into account the free radical scavenging activity and metal-reducing power assays as a measure to assess the *in vitro* antioxidant potential of the extracts and fractions of this study.

3.3.1 DPPH and ABTS radical scavenging assay

The results obtained from these two assays demonstrated the radical quenching capacity of the extracts, and GC showed significantly higher scavenging activity when compared to GPC and other extracts. The IC_{50} for the DPPH assay with GC is 31.81 ± 1.4253 μg/ml, which is also significantly lower ($p < 0.05$), exhibiting enhanced radical scavenging activity when compared to GH (62.98 ± 1.8344 μg/ml), followed by GPC, GE, and GM. When compared to GPC (318.66 ± 2.1195 μg/ml), GC and GH had significantly lower IC_{50}, thereby having better activity in comparison. In contrast, GE and GM with significantly higher IC_{50} showed much less scavenging activity. In the ABTS assay, a similar pattern was established with GC exhibiting excellent radical scavenging activity with the lowest IC_{50} (36.31 ± 4.7099 μg/ml), which was significantly lower ($p < 0.05$) than that of GH (51.53 ± 2.4623 μg/ml) and the other extracts as well. Similarly, when compared to GPC (373.78 ± 8.3045 μg/ml), GC and GH showed better radical scavenging activity, whereas GM and GE had significantly inferior activity in comparison. The results are in detail in Supplementary Table S2.

3.3.2 FRAP and PMD assay

Both of these assays comprise a similar chemical reaction involving the reduction of metal ions [Fe^{3+} to Fe^{2+} and Mo (VI) to Mo (V)], also taken as a parameter of antioxidant activity. In FRAP as well as in PMD assay, the EC_{50} of GC (FRAP: 216.14 ± 13.8743 μg/ml; PMD: 269.61 ± 10.9951 μg/ml) was significantly lower when compared to all crude as well as other fractions, which is an indication of its excellent reducing power and in turn the fraction's antioxidant potential. Next, in comparison GPC, GE, and GM, GH exhibited better activity with significantly lower EC_{50} (FRAP: 414.24 ± 5.9386 μg/ml; PMD: 385.31 ± 3.9779 μg/ml). In between GC and GH, GC was more active than GH (Supplementary Table S3).

3.3.3 *In- vitro* lipid peroxidation assay

In this assay, the iron-ascorbate system induces lipid peroxidation *in vitro* conditions *via* hydroxyl radical generation. The extent of inhibition of this reaction is considered a measure of the antioxidative potential. Upon

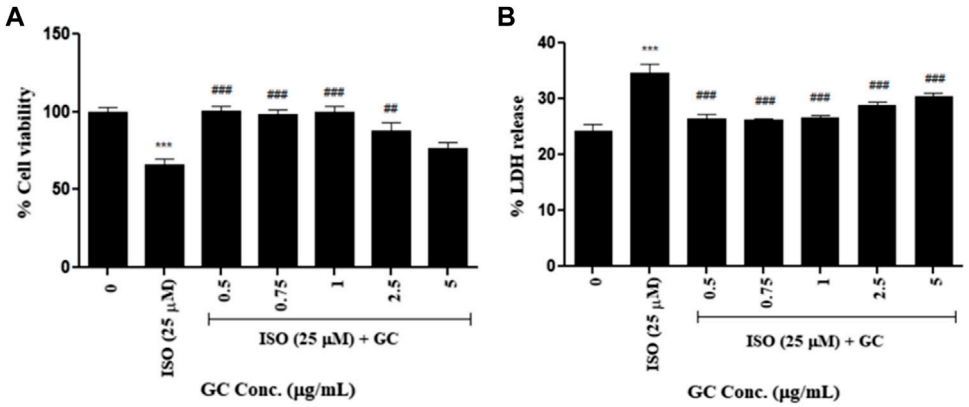

FIGURE 2
Cell viability assay- **(A)** MTT and **(B)** LDH release assay in ISO (25 μM) induced cardiotoxicity model in H9c2 cell line with GC pretreatment at different concentrations (μg/ml). Data expressed as mean ± SD for groups of three observations. Statistically significant *** $p < 0.001$ compared to control group and ### $p < 0.001$ compared to ISO group as calculated by one-way ANOVA followed by Dunnet's multiple comparison tests).

screening all the extracts, GC exhibited better lipid peroxidation inhibitory activity with a significantly lower IC_{50} (310.76 ± 11.6898 μg/ml), as compared to GH (614.92 ± 7.3873 μg/ml). Also, the IC_{50} of GPC, GE, and GM was significantly higher than that of GC, as mentioned in Supplementary Table S4. Following the same pattern as the assays mentioned earlier, GC also exhibits good antioxidant capacity as it actively inhibits the *in vitro* lipid peroxidation in the heart tissue samples.

3.4 *In vitro* assessment of cardioprotective activity in cardiomyocytes

3.4.1 Microscopic observation

After careful microscopic observations, the ISO-treated cells lost their standard elongated shape, and most of them were rounded off and lost their adherent properties. In contrast, the GC-treated cells retained their normal morphology and attachment properties, resembling the untreated control cells (Supplementary Figure S1).

3.4.2 Cell viability assay

On treating H9c2 with just different concentrations of ISO, there was a significant gradual dose-dependent decrease in cell viability from 10 to 100 μM concentration compared to the untreated control. With about 30% cell death, 25 μM dose of ISO was used for the rest of the cell-based assays. After treatment with just GC in H9c2 cells for 24 h, no significant ($p < 0.001$) changes were found up to 100 μg/ml compared to normal control cells. There was a decline in cell viability at a concentration of 200 μg/ml, which was significantly lower ($p < 0.001$) than the control. Therefore, safe doses lower than 10 μg/ml are selected for further studies (Supplementary Figure S2).

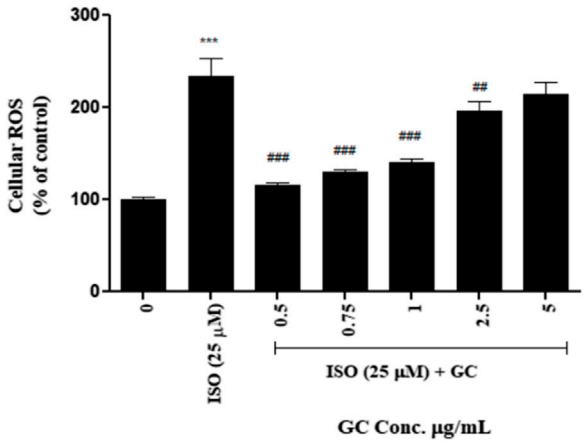

FIGURE 3
Intracellular ROS detection assay in ISO (25 μM) induced cardiotoxicity model in H9c2 cell line with GC pretreatment at different concentrations (μg/ml). Data expressed as mean ± SD for groups of three observations. Statistically significant *** $p < 0.001$ compared to control group and ### $p < 0.001$ compared to ISO group as calculated by one-way ANOVA followed by Dunnet's multiple comparison tests).

In the ISO-induced cardiotoxicity model, for just ISO treated group cell viability decreased significantly ($p < 0.001$) when compared to untreated control and it was seen that pretreatment with GC at concentrations 0.5, 0.75, 1, 2.5 μg/ml significantly ($p < 0.001$) increased the cell viability against ISO treatment which were not significantly different when compared to control cells, thereby indicating the cardioprotective effect of GC against the cardiotoxic effects of ISO (Figure 2). Although, interestingly the lower doses were found to have better protective

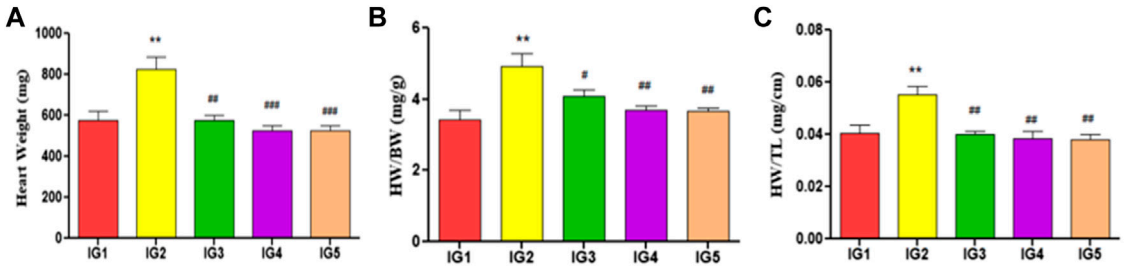

FIGURE 4
Effect of ISO and GC pre-treatment on cardiac hypertrophy parameters-**(A)** Heart weight (mg), **(B)** Heart weight index (mg/g) and **(C)** Heart tail index (g/cm). Results are expressed as mean ± SD for groups of three observations. Statistically significant at *** $p < 0.001$, ** $p < 0.01$, * $p < 0.05$ as compared to IG1 and $^{###}$ $p < 0.001$, $^{##}$ $p < 0.01$, $^{#}$ $p < 0.05$ when compared to IG2 as calculated by one-way ANOVA followed by Dunnet's multiple comparison tests.

activity than the higher doses. The data is represented in Figure 2A.

3.4.3 LDH release assay

This assay showed that LDH release was significantly higher ($p < 0.001$) in the ISO treated group than in the untreated control. A significant reduction in the same ($p < 0.001$) was recorded with GC pretreatment at multiple concentrations of 0.5–5 μg/ml when compared to ISO treated group. The levels of LDH with 0.5, 0.75, and 1 μg/ml of GC treatment were not significantly different from that of the normal cells ($p < 0.001$) (Figure 2B).

3.4.4 Intracellular ROS detection

After measuring the fluorescence intensity from H_2DCF-DA in the treated cells vs. untreated control, it was observed that ROS was significantly increased ($p < 0.001$) in ISO-treated cells after 12 h of treatment. With GC pretreatment at 0.5, 0.75, 1, and 2.5 μg/ml, it was seen that there was a steep significant reduction in ROS ($p < 0.001$) when compared to the ISO group. The 5 μg/mL GC treatment showed some reduction in ROS but was not significantly different from ISO group. Also, among the GC-treated groups, 0.5, 0.75, and 1 μg/ml showed a better reduction in ROS than in 2.5 and 5 μg/ml (Figure 3).

3.5 *In- vivo* assessment of cardioprotective activity

3.5.1 Acute toxicity studies

In the first 4 hours after administration of the drug (GC, 2000 mg/kg BW) orally, none of the animals died or demonstrated any abnormal behaviour on their part. There was no mortality even in the following 2 weeks interval where all the rats survived without any evident clinically abnormal fluctuations in their behaviour. With this, the drug safety was confirmed for 2000 mg/kg BW. Two subsequent doses, 2/10th and 1/10th of this dose, were decided on for further studies.

3.5.2 Cardiac hypertrophy parameters

The body weight gain did not vary significantly between the groups over the experimental period (Supplementary Table S5). However, a significant rise in heart weight ($p < 0.01$) in IG2 was observed as compared to the normal control group, while in Atenolol treated group, a significant decrease ($p < 0.01$) was noted when compared to IG2. There was a significant decrease in both the GC pretreatment groups ($p < 0.001$) compared to the ISO group in terms of heart weight. As a measure of hypertrophy of the heart, the heart weight index (mg/g) and heart tail index (mg/cm) were significantly increased ($p < 0.01$) in IG2 when compared to IG1. With the GC pretreated group, a significant decrease in both ratios was recorded at $p < 0.01$ compared to IG2, with no significant difference when compared to IG1 (Figure 4).

3.5.3 Analysis of parameters of electrocardiogram

From the data obtained (Table 1), a sharp and significant increase in heart rate ($p < 0.01$), ST height or elevation ($p < 0.001$), QRS and QT interval ($p < 0.01$) in the ISO treated disease group was observed along with a significant decrease in R-R interval (ms) and P- duration (ms) on comparison with the normal control group (Figure 5). The ST elevation is often treated as a marker of myocardial infarction pathologically, while the other parameters are an indication of myocardial injury caused due to ISO injection (Jain et al., 2018). Upon treatment with Atenolol, there was a significant ($p < 0.01$) decrease in the heart rate and P duration (0.001). There was also a visible increase in the R-R interval, although not statistically significant.

Also, in IG3, there was a significant decrease ($p < 0.001$) in QRS interval and ST elevation compared to IG2. The interesting finding from this assessment is that GC pretreatment at both concentrations could protect the heart against ISO-induced damage. It was evident from the significantly lowered heart rate and ST elevation ($p < 0.001$), QRS ($p < 0.001$) and QT interval ($p < 0.01$), and also from the significant increase in the R-R interval ($p < 0.001$), P- duration (0.01) when compared to

TABLE 1 Electrocardiographic findings of experimental groups depicting the effect of ISO and GC pretreatment. Results are expressed as mean ± SD for groups of three observations, Statistically significant at *** $p < 0.001$, ** $p < 0.01$, * $p < 0.05$ as compared to IG1 and $^{###}$ $p < 0.001$, $^{##}$ $p < 0.01$, $^{#}$ $p < 0.05$ when compared to IG2 as calculated by one-way ANOVA followed by Dunnet's multiple comparison tests.

Groups	HR (bpm)	R-R interval (ms)	P duration (ms)	QRS interval (ms)	QT interval (ms)	ST height (mV)
IG1	415.8 ± 3.84	144.37 ± 1.37	25.60 ± 2.84	15.76 ± 1.41	51.91 ± 4.07	0.0262 ± 0.005
IG2	535.7 ± 29.47 **	114.56 ± 2.87 *	10.66 ± 1.26 *	39.18 ± 8.28 **	90.54 ± 10.71 **	0.1785 ± 0.015 ***
IG3	434.4 ± 14.16 $^{##}$	138.5 ± 4.92	27.63 ± 1.26 $^{###}$	15.91 ± 2.72 $^{###}$	77.92 ± 2.87	0.0371 ± 0.0106 $^{###}$
IG4	346.07 ± 27.76 $^{###}$	174.5 ± 14.01 *$^{,###}$	23.89 ± 3.34 $^{##}$	13.48 ± 1.50 $^{###}$	61.27 ± 3.22 $^{##}$	0.0254 ± 0.007 $^{###}$
IG5	356.73 ± 30.05 $^{###}$	169.5 ± 14.73 $^{###}$	22.81 ± 2.61 $^{##}$	13.56 ± 2.84 $^{###}$	64.86 ± 4.44 $^{##}$	0.0274 ± 0.007 $^{###}$

FIGURE 5
Representative electrocardiograph recordings of all the experimental groups, with evident ST elevation found in ISO treated disease group.

IG2. These results were comparable to the ECG recording of the normal control group (Table 6). Hence, it will be suitable to infer that GC pretreatment significantly reverses the adverse effects of ISO.

3.5.4 Cardiac injury marker estimation

In this study, the following cardiac injury marker enzymes with diagnostic importance have been estimated from serum, *viz.* CK- MB, CK- NAC, LDH, SGOT, SGPT, and ALP (Figure 6). In the results obtained, it was evident that all the cardiotoxicity marker enzymes were significantly elevated ($p < 0.001$ and $p < 0.01$) with just ISO treated disease group when compared to normal control. With atenolol treatment, these parameters were found to be significantly ($p < 0.001$) reduced to near-normal levels in all except ALP. GC pretreatment could also substantially lower all these marker enzymes ($p < 0.001$ and $p < 0.001$) in both concentrations compared to IG2. These levels were much in the range of the normal control group (Figure 8). In addition to

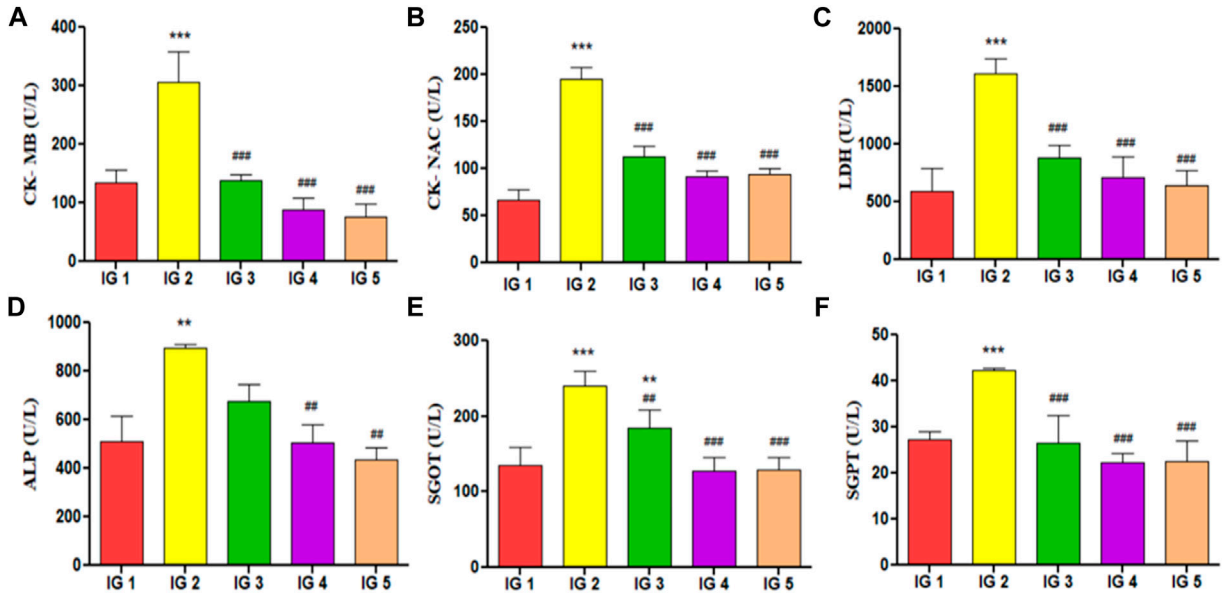

FIGURE 6
The effect of ISO and GC pretreatment on cardiac injury biomarker enzymes in serum of the experimental groups. Results are expressed as mean ± SD for groups of three observations, statistically significant at *** $p < 0.001$, ** $p < 0.01$, * $p < 0.05$ as compared to IG1 and ### $p < 0.001$, ## $p < 0.01$, # $p < 0.05$ when compared to IG2 as calculated by one-way ANOVA followed by Dunnet's multiple comparison tests. **(A)** CK-MB, **(B)** CK-NAC, **(C)** LDH, **(D)** ALP, **(E)** SGOT, **(F)** SGPT.

TABLE 2 Effect of ISO and GC pre- treatment on CK- MB (ng/ml) levels in the heart tissue homogenates and cardiac troponin I (cTnI) in serum.

Groups	IG1	IG2	IG3	IG4	IG5
CK- MB (ng/mg protein)	0.27 ± 0.1381	1.09 ± 0.3099**	0.29 ± 0.1843##	0.32 ± 0.1878##	0.21 ± 0.1469##
Cardiac Troponin I (cTnI, pg/mL)	51.78 ± 2.9788	107.08 ± 9.0561 ***	79.34 ± 5.8476 ###	60.51 ± 4.0515 ###	70.23 ± 3.4798 ###

(Results are expressed as mean ± SD for groups of three observations, statistically significant at *** $p < 0.001$, ** $p < 0.01$, * $p < 0.05$ as compared to IG1 and ### $p < 0.001$, ## $p < 0.01$, # $p < 0.05$ when compared to IG2 as calculated by one-way ANOVA followed by Dunnet's multiple comparison tests.)

these, CK- MB levels were estimated from heart tissue homogenates *via* ELISA to understand its tissue-specific expression levels in all the experimental groups. The results showed a 3-fold significant elevation in the level ($p < 0.01$) of CK- MB in IG2 compared to IG1. In contrast, with atenolol treatment, the expression was significantly suppressed ($p < 0.01$) compared to IG2. A similar trend was observed in GC pretreated groups, where the CK- MB expression levels were significantly reduced ($p < 0.01$) and in the range of the normal untreated control group when compared to IG2 (Table 2). These results strongly indicate that GC pretreatment successfully protected the myocardial tissues against ISO-induced cardiotoxic injury.

Moreover, the cardiac troponin I levels estimated from serum using ELISA revealed a significant ($p < 0.001$) 2.1-fold increase in the ISO treated disease group (IG2) compared to normal untreated control (IG1). With atenolol treatment, the situation improved significantly ($p < 0.001$) bringing the troponin I levels to near normal in IG3. With GC pretreatment, it was observed that IG4 with 100 mg/kg BW showed a better and significant ($p < 0.001$) decrease compared to IG5, which also recorded significant reduction in serum troponin I compared to the disease group. In both the groups, GC pretreatment significantly prohibited the ISO-induced increase in cardiac troponin I levels, thereby protecting the heart successfully.

3.5.5 Estimation of lipid profile

The lipid profile of the ISO-treated group had significantly elevated levels of LDL-C ($p < 0.05$), triglycerides ($p < 0.001$), cholesterol ($p < 0.01$) as well as VLDL-C ($p < 0.001$) when compared to normal control. Also, IG 2 group had significantly depleted ($p < 0.05$) levels of HDL-C as well. In the Atenolol treated group, HDL-C level was only marginally increased, LDL-C and cholesterol were marginally decreased but were not statistically significant. In contrast, the triglycerides and VLDL-C levels were significantly reduced compared to IG2. With GC pretreatment, a significant increase in HDL-C was

10.3389/fphar.2022.1009023

TABLE 3 Effect of ISO and GC pretreatment on the lipid profile.

Groups	HDL-C (mg/dl)	LDL-C (mg/dl)	Triglycerides (mg/dl)	Cholesterol (mg/dl)	VLDL-C (mg/dl)	HMG CoA/Mavalonate
IG1	29.00 ± 6.633	14.75 ± 3.178	61.25 ± 6.449	38.70 ± 2.947	12.25 ± 1.290	1.32 ± 0.0744
IG2	18.50 ± 2.741*	21.98 ± 2.494 *	136.8 ± 13.82 ***	51.80 ± 2.947 **	27.35 ± 2.763 ***	1.12 ± 0.0306 **
IG3	20.75 ± 3.557 #	20.70 ± 4.826 *	93.50 ± 4.359 ###	43.15 ± 1.196	18.70 ± 0.8718 ###	1.21 ± 0.1277
IG4	31.13 ± 3.983 ##	14.35 ± 1.816 #	47.50 ± 7.594 ###	24.40 ± 3.667 ###	9.5 ± 1.519 ###	1.36 ± 0.0569 ##
IG5	29.85 ± 5.176 #	13.03 ± 1.960 ##	51.00 ± 6.481 ###	28.28 ± 6.002 ###	10.20 ± 1.296 ###	1.33 ± 0.0849 ##

(Results are expressed as mean ± SD for groups of three observations, statistically significant at *** $P < 0.001$, ** $P < 0.01$, * $P < 0.05$ as compared to IG1 and ### $P < 0.001$, ## $P < 0.01$, # $P < 0.05$ when compared to IG2 as calculated by one-way ANOVA followed by Dunnet's multiple comparison tests.)

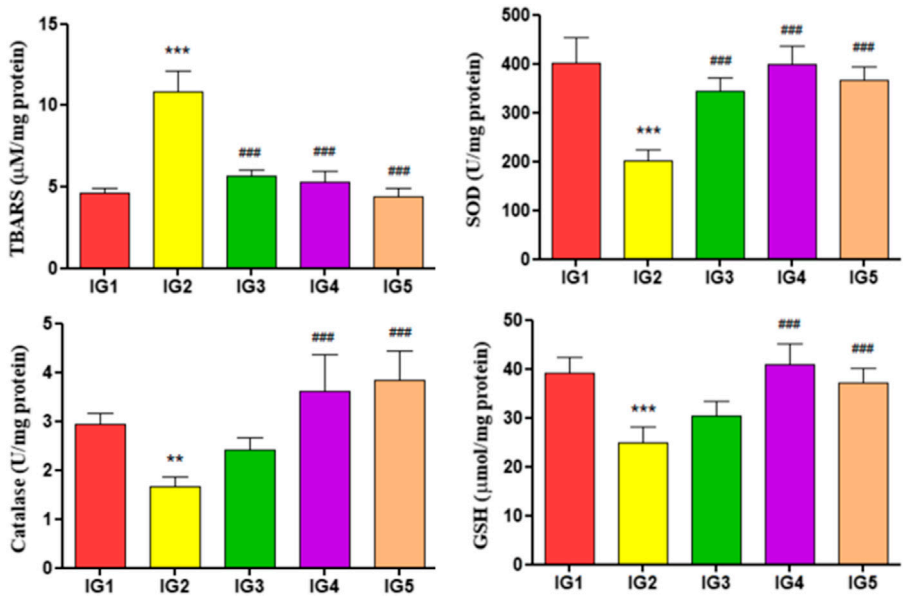

FIGURE 7
The effect of ISO and GC pretreatment on the myocardial endogenous antioxidants and lipid peroxidation levels in the experimental groups. Results are expressed as mean ± SD for groups of three observations, statistically significant at *** $p < 0.001$, ** $p < 0.01$, * $p < 0.05$ as compared to IG1 and ### $p < 0.001$, ## $p < 0.01$, # $p < 0.05$ when compared to IG2 as calculated by one-way ANOVA followed by Dunnet's multiple comparison tests.

seen in both IG4 ($p < 0.01$) and IG5 ($p < 0.05$) when compared to IG2. In the triglycerides, cholesterol and VLDL-C levels, a sharp and significant decline ($p < 0.001$) was seen in both GC pretreated groups again compared to IG2 (Table 3). A significant decrease was also noted in LDL-C (IG4- $p < 0.05$ and IG5- $p < 0.001$) levels upon comparison with ISO treated group. The estimation of HMG CoA reductase activity *via* indirect method revealed that the ISO induced disease group, IG2 showed a significant ($p < 0.01$) 1.2-fold decrease in the HMG CoA/Mavalonate ratio, an indication of increased cholesterol synthesis compared to the normal IG1 group. In the GC pretreated groups, a significant ($p < 0.01$) increase in the HMG CoA/Mavalonate ratio was noted, indicating that GC could reduce overall activity of HMG CoA reductase activity.

3.5.6 Myocardial oxidative stress parameters

The endogenous antioxidants, *i.e.,* SOD, catalase, and GSH levels, were assessed in the heart tissue extracts for all the experimental groups and their lipid peroxidation status (Figure 7). The lipid peroxidation levels were detected by estimating TBARS in respective samples, and in the ISO-treated group, it was significantly elevated ($p < 0.001$) by 2.3-fold compared to IG1. In both the GC pretreated groups, however, the levels of TBARS were significantly reduced ($p < 0.001$) compared to IG2. It was also found that with ISO treatment in the IG2 group, the levels of SOD ($p < 0.001$), GSH ($p < 0.001$), and catalase ($p < 0.01$) were significantly reduced by 1.9-fold, 1.5-fold, and 1.7-fold respectively when compared to IG1. But with GC pretreatment, the levels of

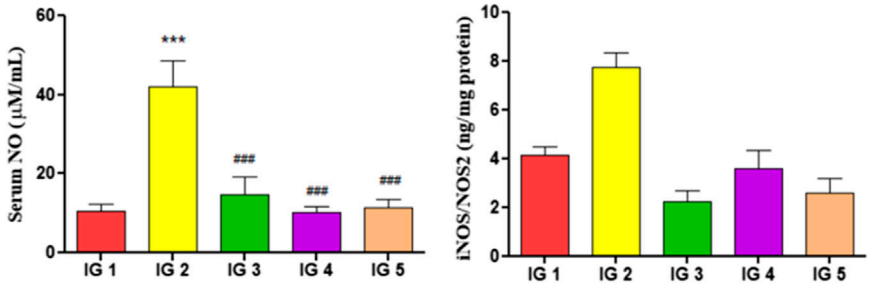

FIGURE 8
The effect of ISO and GC pretreatment on the serum NO and the iNOS/NOS2 levels in the myocardial tissue extracts of the experimental groups. Results are expressed as mean ± SD for groups of three observations, statistically significant at *** $p < 0.001$, ** $p < 0.01$, * $p < 0.05$ as compared to IG1 and ### $p < 0.001$, ## $p < 0.01$, # $p < 0.05$ when compared to IG2 as calculated by one-way ANOVA followed by Dunnet's multiple comparison tests.

these endogenous antioxidants were returned to near-normal levels. They were found to be significantly reduced (SOD and GSH—$p < 0.001$ and catalase—$p < 0.01$ and $p < 0.001$) in both IG4 and IG5 when compared to ISO treated disease group.

3.5.7 Serum NO and myocardial iNOS/NOS2

In ISO treated group IG2, the serum NO and iNOS/NOS2 (Figure 8) in the heart tissue extract were significantly elevated ($p < 0.001$ and $p < 0.01$) by 3.9-fold and 1.8-fold respectively, compared to the normal untreated control group. However, with GC pretreatment, these levels were significantly reduced ($p < 0.001$) in both groups compared to IG2.

3.5.8 Inflammatory cytokines

The inflammatory cytokines like IL-6, IL- 10, TNF- α, and IL-1β were quantified using ELISA from myocardial tissue extracts and serum. When compared to the untreated control group, the levels of pro-inflammatory cytokines IL-6 (2.9-fold), TNF-α (3.4-fold), and IL- 1β (2.4-fold) were significantly elevated ($p < 0.001$), whereas the anti-inflammatory cytokine IL-10 was significantly ($p < 0.01$) reduced by 1.9-fold in the heart tissue extracts of the ISO treated group. In IG4, IL-6, TNF- α, IL- 6 ($p < 0.001$) was significantly reduced, and in IG5 as well, there was a significant decrease in all the pro-inflammatory cytokine levels ($p < 0.01$ and $p < 0.001$) compared to IG2. IL- 10 was significantly increased in both IG4 ($p < 0.01$) and IG5 ($p < 0.05$) when compared to IG2. A similar trend was observed for the inflammatory cytokines in the serum samples, but the results were more pronounced in the tissue samples. It was noted that the pro-inflammatory cytokines TNF-α, IL-6, and IL-1β, increased significantly ($p < 0.001$) in the IG2 group, while the anti-inflammatory IL-10 decreased significantly ($p < 0.01$) in IG2. With GC pretreatment (in IG4 and IG5) this situation was successfully corrected as all the cytokines were revived to the near normal state resembling IG1. It can be concluded from here that the anti-inflammatory action of GC aided in its cardioprotective effect. The detailed results are presented in Figure 9.

3.5.9 Histopathological study

From the histopathological analysis with H& E staining (Figure 10) of heart tissues, it was evident that there was extensive damage to the muscle membrane, with an overall distorted myocardial architecture in the ISO treated group. It was also seen that there were visible gaps between the myofibrils, marked as 'inf' as they depict the infracts with the presence of wavy myofibrils (WMf) surrounding these infract regions, along with a few necrotic regions (N) in the disease group. All these changes marked the ISO induced extensive damage to the myocardial architecture. The normal heart tissues had well-aligned myofibrils arranged in a very compact packing without gaps and well-maintained myocardial membrane integrity without any distortions. The pretreatment with GC could restrict the histo- architectural damages to the heart tissues even after ISO treatment as was seen from the retained near normal packing of the myocardial fibers with intact membrane structure, the absence of necrotic lesions infracts in the tissue sections of IG4 and IG5. With Masson trichome staining (Figure 11), myocardial tissues appear red in colour while collagen stains blue, and were used to study the extent of collagen deposition (blue colored) in the heart tissues. It was seen that ISO treatment greatly increased the collagen deposition among the myocardial fibers, which is an indication of interstitial fibrosis, which was nearly non-existent in the normal untreated control group. These changes were greatly reduced with GC and atenolol treatment as a visible reduction in collagen deposition is seen in the respective groups. These results indicate that with the pre- treatment using GC fraction, the hearts of the rats were well protected against the damages inflicted after ISO injection. These results further emphasize the cardioprotective potential of GC.

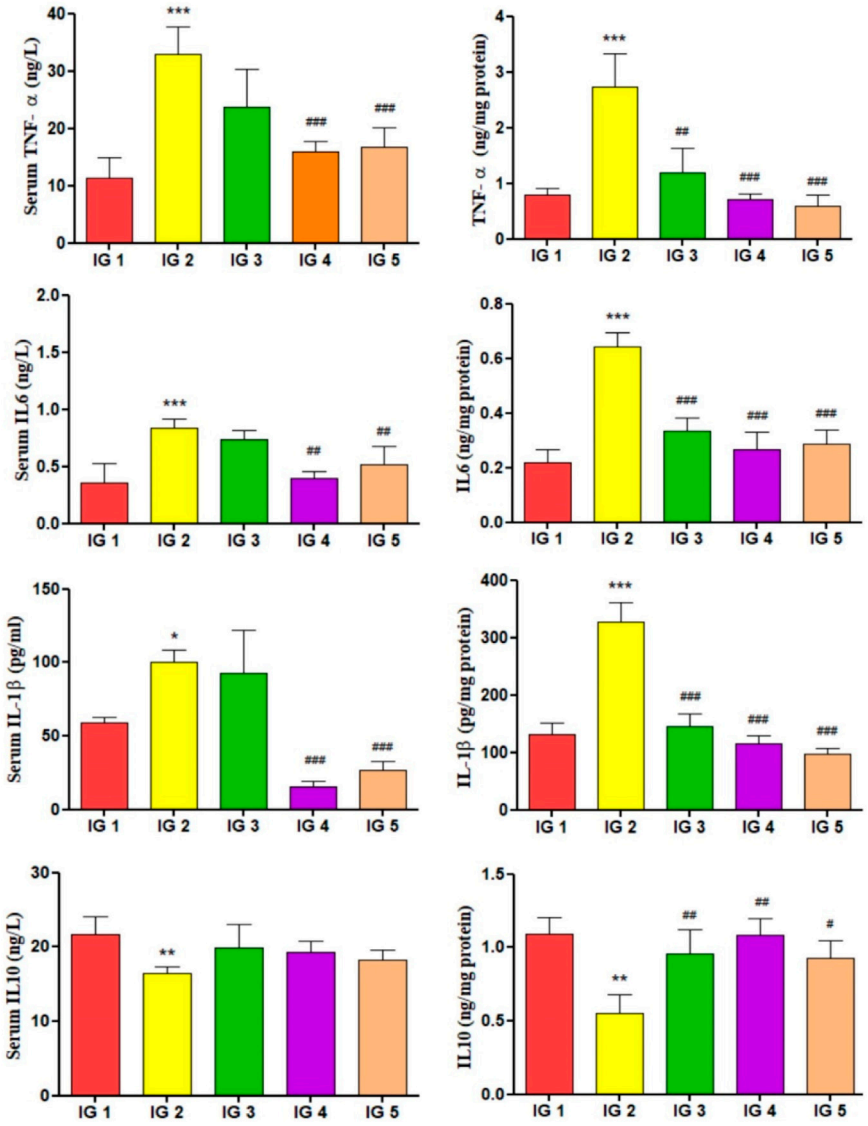

FIGURE 9
The effect of ISO and GC pretreatment on the inflammatory cytokines IL-6, TNF- α, IL- 1β, and IL- 10 levels in the myocardial tissue extracts of the experimental groups. Results are expressed as mean ± SD for groups of three observations, statistically significant at *** $p < 0.001$, ** $p < 0.01$, * $p < 0.05$ as compared to IG1 and ### $p < 0.001$, ## $p < 0.01$, # $p < 0.05$ when compared to IG2 as calculated by one-way ANOVA followed by Dunnet's multiple comparison tests.

3.6 Molecular docking

Molecular docking was performed on the compounds found from UHPLC-MS/MS and the binding interactions and binding energies were calculated. X-ray crystal structures Human iNOS Reductase and Calmodulin Complex and Human TNF-Alpha in complex with 2-[5-(3-chloro-4-{[(1R)-1-(2-fluorophenyl)ethyl]amino} quinolin-6-yl) pyrimidin-2-yl]propan-2-ol were used from the PDB database. The docking studies were performed using the Schrödinger Glide software (Maestro 12.7) with the extra precision (XP) mode [30,31]. The best pose and binding interactions of these compounds were shown in Supplementary Figure S3. The compounds show the lowest binding energies vary from -5.0 to -8.0 shown in Supplementary Table S6. Absorption, Distribution, Metabolism and Elimination (ADME) properties of the compounds were obtained from the pharmacokinetics and pharmacodynamics parameters and assess the drug-likeness. The QikProp (Schrodinger®) is the prediction tool used for the evaluation of some important ADME parameters and their permissible ranges shown in Supplementary Table S7, 8.

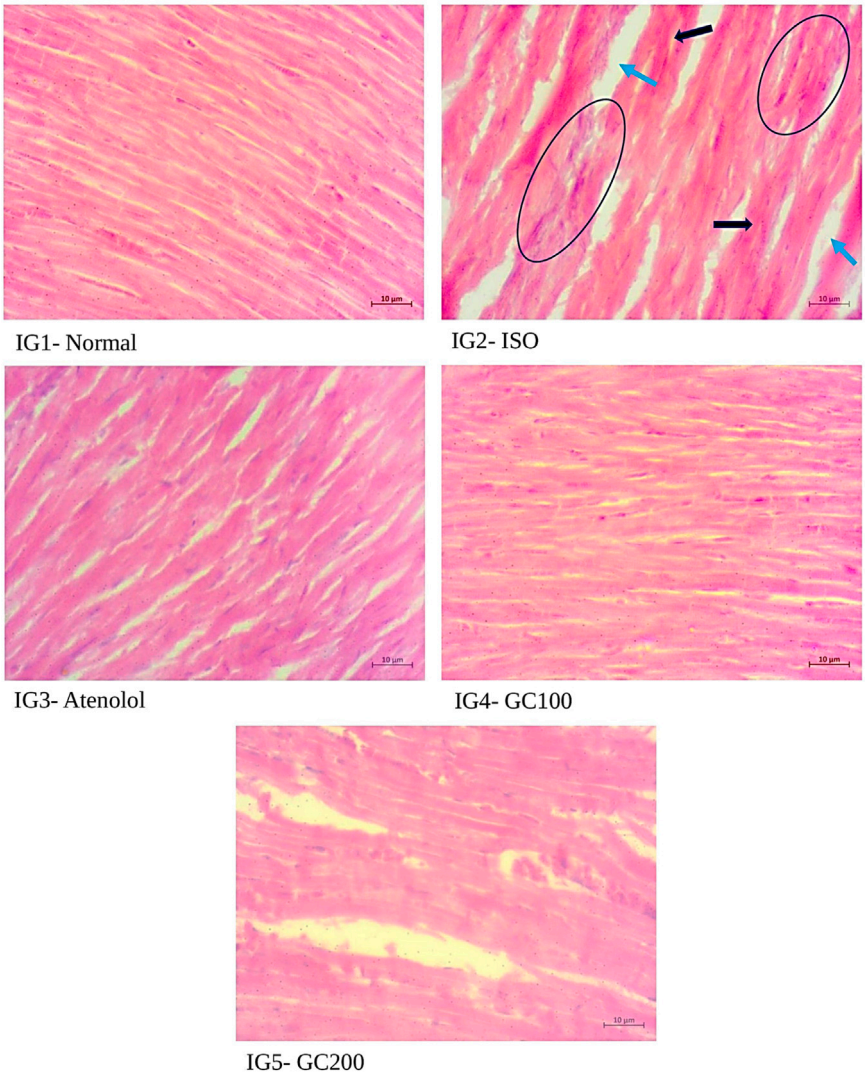

FIGURE 10
Histopathological analysis of H& E staining- a comparison with the normal, ISO treated and GC- pre- treatment experimental groups. Scale bar- 10 μm, Magnification ×400. (Blue arrow- infracts, black arrow- wavy myofibrils, circles—Necrotic region).

4 Discussion

The main objective of this study is to screen the cardioprotective effect of GP in *in-vitro* conditions using H9c2 cells and in the animal model against ISO-induced cardiotoxicity. For the assessment of bioactivity, the antioxidant assays and *in vitro* lipid peroxidation assays were mainly considered keeping in mind the mode of action of ISO in the model. For further ascertaining if GC has any cytotoxic effects and is capable of mitigating oxidative stress, the cell- culture assays of cell viability, LDH release and intracellular ROS detection assays were performed. Taking the results obtained from these assays only, GC was then taken to animal study for further evaluation.

GP is used as a medicinal fruit, especially to treat stomach-related disorders, and is also used for culinary purposes. However, its therapeutic potential is still under-explored. Hence, this study attempted to ascertain the cardioprotective potential of GP fruit in isoproterenol-induced myocardial infarction in Wistar rats. The crude extract of GP was obtained in methanol and then fractionated. All the fractions were compared with the crude extract for comparing bioactivities in terms of antioxidant potential using radical scavenging activity (DPPH and ABTS), metal chelating assays (FRAP and PMD), and *in-vitro* lipid peroxidation inhibition potential. From the assessments, it was clear that GC exhibited the best results in antioxidant potential. Under the ferric-ascorbate-induced *in vitro* conditions in the heart tissue extracts, GC may reduce

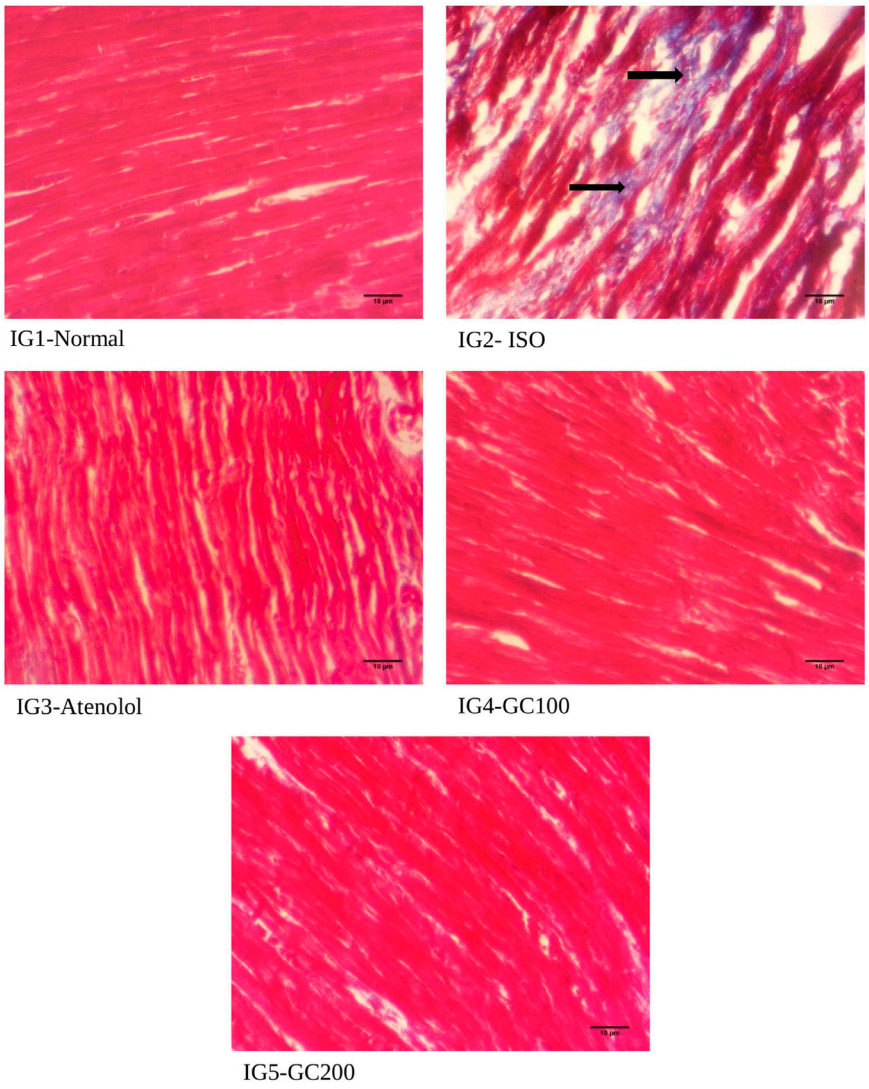

FIGURE 11
Histopathological analysis of Masson trichome staining- a comparison with the normal, ISO treated and GC- pre- treatment experimental groups. Scale bar- 10 μm, Magnification ×400. (Blue stained areas marked with black arrows show collagen deposition, an indication of interstitial fibrosis).

lipid peroxidation. For each of the samples taken, these activities increased dose-dependently. Also, the phenolic content was GC was found to be the highest amongst the crude and fractions of GP. These results tally with the earlier studies on multiple vegetables, spices, and medicinal herbs, where a strong positive correlation was observed between the plants' total phenolic contents and their antioxidant potential (Aryal et al., 2019; Ulewicz-Magulska & Wesolowski, 2019; Rodríguez Madrera et al., 2021). The antioxidant capacities vary depending on the type of compounds as well; the hydrophilic antioxidants give better results in FRAP assay, and the organic ones present better results in DPPH scavenging (Ulewicz-Magulska & Wesolowski, 2019). This correlation may be attributed to the structural similarity of the phenolic compounds found in the fractions. With structural attributes like having one or more aromatic rings, hydroxyl group substitutions, and glycosylations, they are allowed to act as either electron or hydrogen donors participating in redox reactions involving free radicals, forming stable intermediates, thereby supporting their radical scavenging and metal chelating activities (Kasote et al., 2015; Singh et al., 2017). As the lipids are exposed to oxidative stress, they undergo peroxidative damage resulting in degenerative changes in the membrane fluidity and production of hydroperoxides and aldehydes like toxic by-products, which may even contribute to the pathophysiology of inflammation, liver, or cardiac complications. Moreover, it is

observed that treatment with phenolic-rich plant extracts with immense antioxidant potential prevents this lipid peroxidation, as seen with the extracts of *Caralluma tuberculate* and *Annona crassiflora* (Justino et al., 2019; Poodineh & Nakhaee, 2019). Thus, the results of GC in all these assays suggest that this phenol-rich fraction has immense antioxidant potential and is carried forward for cell culture and experimental animal study to assess its cardioprotective potential.

As both MTT and LDH release assays are considered markers of cellular damage and cytotoxicity, as the former is dependent on the mitochondrial reduction of MTT into purple formazan by the live cells, while the latter is more of an indication of cellular membrane damage in apoptotic or necrotic conditions where LDH release form the damaged cells increase steeply (Aslantürk, 2018). In this study with the model of ISO-induced cellular cardiotoxicity, ISO significantly reduced cell viability by 1.5-fold while increasing the cell's LDH release by 1.4-fold. In contrast, the pretreatment with GC for 2 h before ISO treatment successfully restricted its cardiotoxic effects, as demonstrated in significantly increased cell viability and reduced LDH release in the treated groups. Moreover, the microscopic evaluation of the morphological changes shows that GC treatment could easily protect against the cardiotoxic effects of ISO. These results align with previous publications from Cinar et al., 2021; Sivasangari et al., 2019 where the antioxidant potential of gossypin and arbutin was responsible for their cardioprotective effects. In the intracellular ROS detection assay, it was found that GC pretreatment of the cells significantly reduced ISO treatment-induced ROS generation, thereby successfully protecting the cardiac cells from oxidative stress. These results are similar to the previous reports by (Thangaiyan et al., 2018; Chen et al., 2019b; Balkrishna et al., 2021) with bioactive compounds modulating oxidative stress. From this, it can be concluded that the antioxidant potential of GC is responsible for its cardioprotective effect demonstrated in the cellular model of cardiotoxicity.

An interesting consideration here is that GC is more potent and showed better results at lower concentrations than at higher concentrations which puts forth an exciting observation that GC might act as a pro-oxidant at higher concentrations. This behavior is similar to the pro-oxidant action of vitamin C, α-tocopherol at higher concentrations (Sotler et al., 2019). In general, the antioxidant activity of the phenolic compounds is often dependent on their concentration, the pH, the presence of metal ions, and their redox potential, and changes in these may tip them off to act as pro-oxidants (Castañeda-Arriaga et al., 2018; Bayliak et al., 2016).

Isoproterenol, is a sympathomimetic *ß*- adrenoreceptor agonist which is used to induce myocardial infarction, ischemia and cardiac fibrosis like conditions in experimental models and is used in studies pertaining to cardioprtection. Wistar albino rats, injected with two consecutive dosages of 85–100 mg/kg BW of ISO, are an ideal model for studying acute myocardial infarction (Allawadhi et al., 2018). In this model, the injection of ISO is often associated with the increase in the weight of the heart, heart tail index, and heart weight index measured as a parameter for the hypertrophy of the heart (Othman et al., 2017; Hu et al., 2019). Also, the fundamental parameters used in diagnostic procedures for the detection of MI include ECG, along with pathological markers like CK- MB, CK- NAC, LDH, SGOT, SGPT, and ALP. It has been deduced that ISO-inflicted damage to the heart tissues often results in a marked increase in heart rate and a distinct ST-elevation in the ECG. It also shows a noticeable increase in all the pathological markers mentioned above. These changes indicate the presence of myocardial necrosis, damaged membrane integrity, and ischemic injury (Panda et al., 2017; Bhatt et al., 2020). With GC pretreatment, successful reduction of these hypertrophic and pathological markers down to their normal levels was recorded in this study. These results positively indicate that GC could preserve the typical membrane architecture of the myocardium, acting against the induction of cardiac hypertrophy and cardiotoxicity. These GC results align with the earlier reports of (Hu et al., 2019; Bhatt et al., 2020; Feriani et al., 2020; Soumya et al., 2021).

Moreover, apart from CK-MB and CK, cardiac troponin I (cTnI) is the most sensitive diagnostic biomarker for MI. With GC pretreatment, the reduced cardiac troponin I level indicated that the hearts were well protected against ISO-induced MI and its related damage. These findings are in agreement with the studies on the cardioprotective effect of *Fumaria indica*, bergapten, and *Curcuma longa* (Nahar and Akhter, 2018; Sajid et al., 2022; Yang et al., 2022). The increase in heart rate, prolonged QRS and QT interval, pronounced ST elevation, and shortened R-R interval and P- duration in the ECG of the ISO group reflected the presence of infraction, improper conduction of electrical impulses throughout cardiac tissues, AV node, and an overall cumulative cardiotoxic effect of isoproterenol (Boarescu et al., 2019; Bocsan et al., 2021). GC pretreated groups showed marked improvement in their ECG parameters, further providing evidence favoring its protective effect, and these detailed changes in ECG are in agreement with the earlier reports of (Jain et al., 2018; Boarescu et al., 2019; Bocsan et al., 2021; Sajid et al., 2022).

After ISO injection, the assessment of the serum lipid profile showed significant dysregulation with a notable increase in triglycerides, cholesterol, LDL-C, and VLDL-C and a steep decline in HDL-C levels. These results indicate a hyperlipidemic effect that may have occurred due to altered lipid metabolism in the presence of ISO indicating a direct correlation with myocardial infarction (Panda et al., 2017; Lekshmi & Kurup, 2019). An evident decline in triglycerides, total cholesterol, LDL-C, and VLDL-C have been observed after pretreatment with GC in this study, with a substantial increase in the HDL-C levels, revealing the hypolipidemic potency of this fraction. These results are in agreement with the studies of Panda et al., 2017; Lekshmi & Kurup, 2019; Shaik et al., 2020; Soumya et al., 2021. Moreover, from the HMG CoA reductase assay done by the indirect method where the ratio of HMG CoA/Mevalonate is calculated, and this

ratio is inversely proportional to the HMG CoA reductase activity. The more the ratio, the lesser the mevalonate formed, indicating a reduction in HMG CoA reductase activity and consequently reduced cholesterol synthesis (Lekshmi & Kurup, 2019; Pramod et al., 2020). The hypolipidemic activity of GC might result from its HMG CoA reductase activity reduction, which controls cholesterol synthesis. This result is similar to the hypolipidemic and HMG CoA reductase activity reducing capability of sulphated polysaccharides from *Padina tetrastromatica* (Lekshmi & Kurup, 2019).

Excessive free radicals' production with ISO often leads to peroxidation of membrane lipids, which might even lead to necrosis in myocardial tissues. This damage to phospholipids increases the malondialdehyde levels in the tissues, which is detected using the TBARS assay. This resembles the extensive damage to the myocardium in humans during MI. Moreover, with the increased oxidative damage and overaccumulation of peroxide and superoxide anions, compromises the functionality of the endogenous antioxidant system (SOD, GSH, and catalse), further enhancing the ROS-induced damage (Panda et al., 2017; Ahsan et al., 2022). In cardioprotective studies with sericin, bergapten, phenolic compounds rich extracts of *Zygophyllum album*, *Kedrostis foetidissima*, it was seen that their successful treatment reduced the lipid peroxidation and revamped the endogenous antioxidant system, thereby protecting the cardiac muscles against the oxidative damage. This study's results agree with these reports from Pavithra et al., 2020; Feriani et al., 2020; Yang et al., 2022; and Ahsan et al., 2022. The role of GC pretreatment in successfully reducing TBARS in cardiac tissues and increasing the levels of SOD, GSH, and catalase proved its potent antioxidant potential which is responsible for its successful cardioprotective action.

The enhanced expression of pro-inflammatory cytokines (e.g., TNF-α, IL-6, IL-1β) and the decline in anti-inflammatory cytokine (e.g., IL- 10) establish the ISO aggravated assault on the inflammatory state in the heart tissue (Bocsan et al., 2021; Gao et al., 2021). Moreover, GC pretreated groups also showed potent anti-inflammatory activity. It reduced the pro-inflammatory cytokines TNF-α, IL-6, and IL- 1β while increasing the anti-inflammatory cytokine IL10. These results align with Adedapo et al., 2019; Kumari et al., 2020; Gao et al., 2021; Bocsan et al., 2021. NO has an intricate role in the normal smooth functioning of the cardiovascular system and is synthesized by the action of NO synthases of three isoforms, viz. endothelial or eNOS, neuronal or nNOS, and the inducible or iNOS in mammals. eNOS is responsible for NO production in normal endothelium (Ibrahim et al., 2018). A dramatic increase in serum NO and iNOS/NOS2 is evident in the ISO-treated groups, indicating the cytotoxic effects in the form of nitrosative stress, endothelial dysfunction, and increased inflammation (Hassanien, 2020). This experiment shows that GC pretreatment could neutralize the abnormal induction of iNOS, thereby reducing serum NO and tissue iNOS/NOS 2 levels, respectively. These findings are much similar to the earlier reports of Ibrahim et al., 2018; Hassanien, 2020; Khalaf et al., 2020; Sultan et al., 2022.

Even in histopathological analysis with both H&E and Masson trichome staining, the cardioprotective potency of GC was evident from how well the tissue histoarchitecture was protected in the GC—treated groups compared to ISO. These observations are similar to the earlier reports of Shang et al., 2019; Mohammed et al., 2020; Khalaf et al., 2020; Viswanadha et al., 2020.

5 Conclusions and future prospects

In conclusion, the findings demonstrated that GP is one of the promising dietary choices and has superior antioxidant characteristics that can be exploited to prevent cardiac hypertrophy by reducing oxidative stress and inflammation in the hypertrophic heart. The findings of the current study also suggest that GP fruit includes several phenolic antioxidants that may be responsible for the fruit's beneficial impacts on cardiac health, including hydroxycitric acid, hydroxycitric acid lactone, parvifoliquinone, GB-1a, Garcinone A, 9-Hydroxycalabaxanthone, Chlorogenic acid, and Garcinol. However, further investigation can be done to look into GP's potential for developing potent drugs.

Data availability statement

The original contributions presented in the study are included in the article/Supplementary Materials, further inquiries can be directed to the corresponding authors.

Ethics statement

The animal study was reviewed and approved by Institutional Animal Ethics Committee granted the study approval (IAEC no. IASST/2018/07).

Author contributions

SB, RE, and PD conceived and designed the experiment. SB, KD performed the experiment. SB analyzed the data. RE performed the phytochemical investigation and molecular docking experiments. SB and RE wrote the manuscript. RD has done a critical revision of the manuscript for important intellectual content. RD and RE are the corresponding authors and KD and PD contributed equally as third authors. All authors have contributed to the final version and approved the final manuscript.

Acknowledgments

We would like to thank The Director, Institute of Advanced Study in Science and Technology (IASST), Guwahati, India, for providing the necessary facilities to conduct the experiments. RE thanks DST–PURSE Phase II, Annamalai University for Research Associateship.

Conflict of interest

The authors declare that the research was conducted in the absence of any commercial or financial relationships that could be construed as a potential conflict of interest.

Publisher's note

All claims expressed in this article are solely those of the authors and do not necessarily represent those of their affiliated organizations, or those of the publisher, the editors and the reviewers. Any product that may be evaluated in this article, or claim that may be made by its manufacturer, is not guaranteed or endorsed by the publisher.

Supplementary material

The Supplementary Material for this article can be found online at: https://www.frontiersin.org/articles/10.3389/fphar.2022.1009023/full#supplementary-material

References

Adedapo, A. D., Adedapo, A. A., Ayodele, A. E., Adeoye, B. O., Ajibade, T. O., Oyagbemi, A. A., et al. (2019). Cardioprotective effects and antioxidant status of Andrographis paniculata in isoproterenol-induced myocardial infarction in rats. *J. Med. Plants Econ. Dev.* 3 (1), 1–12. doi:10.4102/jomped.v3i1.49

Ahsan, F., Mahmood, T., Wani, T. A., Zargar, S., Siddiqui, M. H., Usmani, S., et al. (2022). Effectual endeavors of silk protein sericin against isoproterenol induced cardiac toxicity and hypertrophy in wistar rats. *Life* 12 (7), 1063. doi:10.3390/life12071063

Allawadhi, P., Khurana, A., Sayed, N., Kumari, P., and Godugu, C. (2018). Isoproterenol-induced cardiac ischemia and fibrosis: Plant-based approaches for intervention. *Phytother. Res.* 32 (10), 1908–1932. doi:10.1002/ptr.6152

Anosike, C. A., and Cajetan, I. C. (2015). Effect of Theobroma cacao polyphenol on isoproterenol-induced myocardial infarction in Wistar rats. *J. Appl. Pharm. Sci.* 5 (7), 076–083. doi:10.7324/JAPS.2015.50713

Aryal, S., Baniya, M. K., Danekhu, K., Kunwar, P., Gurung, R., and Koirala, N. (2019). Total phenolic content, flavonoid content and antioxidant potential of wild vegetables from Western Nepal. *Plants* 8 (4), 96. doi:10.3390/plants8040096

Aslantürk, Ö. S. (2018). *Vitro* cytotoxicity and cell viability assays: principles, advantages, and disadvantages. *Genotoxicity-A Predict. risk our actual world* 2, 64–80. doi:10.5722/intechopen.71923

Balkrishna, A., Rustagi, Y., Tomar, M., Pokhrel, S., Bhattacharya, K., and Varshney, A. (2021). Divya-Arjuna-Kwath (*Terminalia arjuna*) and Divya-HridyAmrit-Vati ameliorate isoproterenol-induced hypertrophy in murine cardiomyocytes through modulation of oxidative stress. *Phytomedicine Plus* 1 (4), 100074. doi:10.1016/j.phyplu.2021.100074

Bayliak, M. M., Burdyliuk, N. I., and Lushchak, V. I. (2016). Effects of pH on antioxidant and prooxidant properties of common medicinal herbs. *Open Life Sci.* 11 (1), 298–307. doi:10.1515/biol-2016-0040

Bhatt, L., Amrutia, J., Chakraborty, M., and Kamath, J. (2020). Evaluation of cardioprotection and bio-efficacy enhancement of stevioside and diltiazem in rats. *Futur. J. Pharm. Sci.* 6 (1), 34–13. doi:10.1186/s43094-020-00054-w

Bhattacharjee, S., and Devi, R. (2021). A comprehensive review of *Garcinia pedunculata* roxb. And its therapeutic potential. *Mini Rev. Med. Chem.* 21 (20), 3113–3143. doi:10.2174/1389557521666210217094152

Boarescu, P. M., Boarescu, I., Bocșan, I. C., Pop, R. M., Gheban, D., Bulboacă, A. E., et al. (2019). Curcumin nanoparticles protect against isoproterenol induced myocardial infarction by alleviating myocardial tissue oxidative stress, electrocardiogram, and biological changes. *Molecules* 24 (15), 2802. doi:10.3390/molecules24152802

Bocsan, I. C., Pop, R. M., Sabin, O., Sarkandy, E., Boarescu, P. M., Roșian, Ș. H., et al. (2021). Comparative protective effect of nigella sativa oil and Vitis vinifera seed oil in an experimental model of isoproterenol-induced acute myocardial ischemia in rats. *Molecules* 26 (11), 3221. doi:10.3390/molecules26113221

Branco, A. F., Pereira, S. L., Moreira, A. C., Holy, J., Sardão, V. A., and Oliveira, P. J. (2011). Isoproterenol cytotoxicity is dependent on the differentiation state of the cardiomyoblast H9c2 cell line. *Cardiovasc. Toxicol.* 11 (3), 191–203. doi:10.1007/s12012-011-9111-5

Castañeda-Arriaga, R., Pérez-González, A., Reina, M., Alvarez-Idaboy, J. R., and Galano, A. (2018). Comprehensive investigation of the antioxidant and pro-oxidant effects of phenolic compounds: A double-edged sword in the context of oxidative stress? *J. Phys. Chem. B* 122 (23), 6198–6214. doi:10.1021/acs.jpcb.8b03500

Chen, Y., Beng, H., Su, H., Han, F., Fan, Z., Lv, N., et al. (2019). Isosteviol prevents the development of isoprenaline induced myocardial hypertrophy. *Int. J. Mol. Med.* 44 (5), 1932–1942. doi:10.3892/ijmm.2019.4342

Chen, Y., Tao, Y., Zhang, L., Xu, W., and Zhou, X. (2019). Diagnostic and prognostic value of biomarkers in acute myocardial infarction. *Postgrad. Med. J.* 95 (1122), 210–216. doi:10.1136/postgradmedj-2019-136409

Cinar, I., Yayla, M., Tavaci, T., Toktay, E., Ugan, R. A., Bayram, P., et al. (2021). *In vivo* and *in vitro* cardioprotective effect of gossypin against isoproterenol-induced myocardial infarction injury. *Cardiovasc. Toxicol.* 22 (1), 52–62. doi:10.1007/s12012-021-09698-3

Elancheran, R., Kabilan, S., Kotoky, J., Ramanathan, M., and Bhattacharjee, A. (2019). *In silico* molecular docking, synthesis of 4-(4-benzoylaminophenoxy) phenol derivatives as androgen receptor antagonists. *Comb. Chem. High. Throughput Screen.* 22 (5), 307–316. doi:10.2174/1386207322666190701124752

Emadi-Emadi, M., Delavari, S., and Bayati, M. (2021). Global socioeconomic inequality in the burden of communicable and non-communicable diseases and injuries: An analysis on global burden of disease study 2019. *BMC public health* 21 (1), 1771–1813. doi:10.1186/s12889-021-11793-7

Feriani, A., Tir, M., Gómez-Caravaca, A. M., del Mar Contreras, M., Talhaoui, N., Taamalli, A., et al. (2020). HPLC-DAD-ESI-QTOF-MS/MS profiling of Zygophyllum album roots extract and assessment of its cardioprotective effect against deltamethrin-induced myocardial injuries in rat, by suppression of oxidative stress-related inflammation and apoptosis via NF-κB signaling pathway. *J. Ethnopharmacol.* 247, 112266. doi:10.1016/j.jep.2019.112266

Friedwald, W. T., Levi, R. I., and Fredrickson, D. S. (1972). Estimation of the concentration of low-density lipoprotein cholesterol in plasma, without use of the preparative ultracentrifuge. *Clin. Chem.* 18 (6), 499–502. doi:10.1093/clinchem/18.6.499

Gao, Y., Liang, X., Tian, Z., Ma, Y., and Sun, C. (2021). Betalain exerts cardioprotective and anti-inflammatory effects against the experimental model of heart failure. *Hum. Exp. Toxicol.* 40 (12), S16–S28. doi:10.1177/09603271211027933

Goth, L. (1991). A simple method for determination of serum catalase activity and revision of reference range. *Clin. Chim. Acta.* 196, 143–151. doi:10.1016/0009-8981(91)90067-M

Green, L. C., Wagner, D. A., Glogowski, J., Skipper, P. L., Wishnok, J. S., and Tannenbaum, S. R. (1982). Analysis of nitrate, nitrite, and [15N] nitrate in biological fluids. *Anal. Biochem.* 126, 131–138. doi:10.1016/0003-2697(82)90118-X

Hašková, P., Koubková, L., Vávrová, A., Macková, E., Hrušková, K., Kovaříková, P., et al. (2011). Comparison of various iron chelators used in clinical practice as protecting agents against catecholamine-induced oxidative injury and cardiotoxicity. *Toxicology* 289 (2-3), 122–131. doi:10.1016/j.tox.2011.08.006

Hassan, M. Q., Akhtar, M., Ahmed, S., Ahmad, A., and Najmi, A. K. (2017). Nigella sativa protects against isoproterenol-induced myocardial infarction by

alleviating oxidative stress, biochemical alterations and histological damage. *Asian pac. J. Trop. Biomed.* 7 (4), 294–299. doi:10.1016/j.apjtb.2016.12.020

Hassanien, M. A. (2020). Ameliorating effects of ginger on isoproterenol-induced acute myocardial infarction in rats and its impact on cardiac nitric oxide. *J. Microsc. Ultrastruct.* 8 (3), 96–103. doi:10.4103/JMAU.JMAU_70_19

Hu, X., Ou-Yang, Q., Wang, L., Li, T., Xie, X., and Liu, J. (2019). AdipoRon prevents l-thyroxine or isoproterenol-induced cardiac hypertrophy through regulating the AMPK-related pathway. *Acta Biochim. Biophys. Sin.* 51 (1), 20–30. doi:10.1093/abbs/gmy152

Ibrahim, M. A., Geddawy, A., and Abdel-Wahab, S. (2018). Sitagliptin prevents isoproterenol-induced myocardial infarction in rats by modulating nitric oxide synthase enzymes. *Eur. J. Pharmacol.* 829, 63–69. doi:10.1016/j.ejphar.2018.04.005

Iloki-Assanga, S. B., Lewis-Luján, L. M., Lara-Espinoza, C. L., Gil-Salido, A. A., Fernandez-Angulo, D., Rubio-Pino, J. L., et al. (2015). Solvent effects on phytochemical constituent profiles and antioxidant activities, using four different extraction formulations for analysis of *Bucida buceras* L. and *Phoradendron californicum*. *BMC Res. Notes* 8 (1), 396–414. doi:10.1186/s13104-015-1388-1

Jain, P. G., Mahajan, U. B., Shinde, S. D., and Surana, S. J. (2018). Cardioprotective role of FA against isoproterenol induced cardiac toxicity. *Mol. Biol. Rep.* 45 (5), 1357–1365. doi:10.1007/s11033-018-4297-2

Justino, A. B., Franco, R. R., Silva, H. C., Saraiva, A. L., Sousa, R. M., and Espindola, F. S. (2019). B procyanidins of *Annona crassiflora* fruit peel inhibited glycation, lipid peroxidation and protein-bound carbonyls, with protective effects on glycated catalase. *Sci. Rep.* 9 (1), 19183–19215. doi:10.1038/s41598-019-55779-3

Kasote, D. M., Katyare, S. S., Hegde, M. V., and Bae, H. (2015). Significance of antioxidant potential of plants and its relevance to therapeutic applications. *Int. J. Biol. Sci.* 11 (8), 982–991. doi:10.7150/ijbs.12096

Khalaf, H. M., Abdalla, A. M., Ahmed, A. F., and Abdel-Aziz, A. M. (2020). Role of nitric oxide in mediating the cardioprotective effect of agomelatine against isoproterenol-induced myocardial injury in rats. *Naunyn. Schmiedeb. Arch. Pharmacol.* 393 (10), 1809–1823. doi:10.1007/s00210-020-01860-y

Khan, M. A., Hashim, M. J., Mustafa, H., Baniyas, M. Y., Al Suwaidi, S. K. B. M., AlKatheeri, R., et al. (2020). Global epidemiology of ischemic heart disease: Results from the global burden of disease study. *Cureus* 12 (7), e9349. doi:10.7759/cureus.9349

Khan, R. A., Khan, M. R., Sahreen, S., and Ahmed, M. (2012). Assessment of flavonoids contents and *in vitro* antioxidant activity of *Launaea procumbens*. *Chem. Cent. J.* 6 (1), 43–11. doi:10.1186/1752-153X-6-43

Kumar, A., Krishna, G., Hullatti, P., and T, T. (2017). Indian plants with cardioprotective activity-A review. *Syst. Rev. Pharm.* 8 (1), 08–12. doi:10.5530/srp.2017.1.3

Kumari, S., Katare, P. B., Elancheran, R., Nizami, H. L., Paramesha, B., Arava, S., et al. (2020). *Musa balbisiana* fruit rich in polyphenols attenuates isoproterenol-induced cardiac hypertrophy in rats via inhibition of inflammation and oxidative stress. *Oxid. Med. Cell. Longev.* 2020, 7147498. doi:10.1155/2020/7147498

Lekshmi, V. S., and Kurup, G. M. (2019). Sulfated polysaccharides from the edible marine algae *Padina tetrastromatica* protects heart by ameliorating hyperlipidemia, endothelial dysfunction and inflammation in isoproterenol induced experimental myocardial infarction. *J. Funct. Foods* 54, 22–31. doi:10.1016/j.jff.2019.01.004

Marklund, S., and Marklund, G. (1974). Involvement of the superoxide anion radical in the autoxidation of pyrogallol and a convenient assay for superoxide dismutase. *Eur. J. Biochem.* 47, 469–474. doi:10.1111/j.1432-1033.1974.tb03714.x

Maruthanila, V. L., Elancheran, R., and Mirunalini, S. (2022). *In silico* approach and molecular docking studies of potent bioactive compounds of *Carica papaya* as anti-breast cancer agents. *Curr. Comput. Aided. Drug Des.* 18, 196–212. doi:10.2174/1573409918666220519112027

Mathers, C. D. (2020). History of global burden of disease assessment at the World Health Organization. *Archives Public Health* 78 (1), 77–13. doi:10.1186/s13690-020-00458-3

Mohammed, S. A., Paramesha, B., Kumar, Y., Tariq, U., Arava, S. K., and Banerjee, S. K. (2020). Allylmethylsulfide, a sulfur compound derived from garlic, attenuates isoproterenol-induced cardiac hypertrophy in rats. *Oxid. Med. Cell. Longev.* 2020, 7856318. doi:10.1155/2020/7856318

Mohan, P., Mohan, S. B., and Dutta, M. (2019). Communicable or noncommunicable diseases? Building strong primary health care systems to address double burden of disease in India. *J. Fam. Med. Prim. Care* 8 (2), 326–329. doi:10.4103/jfmpc.jfmpc_67_19

Nahar, S., and Akhter, Q. S. (2018). Effect of Curcuma longa (Turmeric) on serum creatine kinase-MB and troponin I in isoproterenol induced myocardial infarction in wistar albino rats. *J. Bangladesh Soc. Physiol.* 13 (2), 47–53. doi:10.3329/jbsp.v13i2.39477

Ohkawa, H., Ohishi, N., and Yagi, K. (1979). Assay for lipid peroxides in animal tissues by thiobarbituric acid reaction. *Anal. Biochem.* 95, 351–358. doi:10.1016/0003-2697(79)90738-3

Ojha, S., Goyal, S., Kumari, S., and Arya, D. S. (2012). Pyruvate attenuates cardiac dysfunction and oxidative stress in isoproterenol-induced cardiotoxicity. *Exp. Toxicol. Pathol.* 64 (4), 393–399. doi:10.1016/j.etp.2010.10.004

Ojha, N., and Dhamoon, A. S. (2021). *Myocardial infarction*. Treasure Island, FL: StatPearls Publishing.

Othman, A. I., Elkomy, M. M., El-Missiry, M. A., and Dardor, M. (2017). Epigallocatechin-3-gallate prevents cardiac apoptosis by modulating the intrinsic apoptotic pathway in isoproterenol-induced myocardial infarction. *Eur. J. Pharmacol.* 794, 27–36. doi:10.1016/j.ejphar.2016.11.014

Ozbek, N., Bali, E. B., and Karasu, C. (2015). Quercetin and hydroxytyrosol attenuates xanthine/xanthine oxidase-induced toxicity in H9c2 cardiomyocytes by regulation of oxidative stress and stress-sensitive signaling pathways. *Gen. Physiol. Biophys.* 34 (4), 407–414. doi:10.4149/gpb_2015021

Panda, S., Kar, A., and Biswas, S. (2017). Preventive effect of agnucastoside C against isoproterenol-induced myocardial injury. *Sci. Rep.* 7 (1), 16146–16214. doi:10.1038/s41598-017-16075-0

Park, E. S., Kang, J. C., Jang, Y. C., Park, J. S., Jang, S. Y., Kim, D. E., et al. (2014). Cardioprotective effects of rhamnetin in H9c2 cardiomyoblast cells under H_2O_2-induced apoptosis. *J. Ethnopharmacol.* 153 (3), 552–560. doi:10.1016/j.jep.2014.02.019

Pavithra, K., Sathibabu Uddandrao, V. V., Chandrasekaran, P., Brahmanaidu, P., Sengottuvelu, S., Vadivukkarasi, S., et al. (2020). Phenolic fraction extracted from *Kedrostis foetidissima* leaves ameliorated isoproterenol-induced cardiotoxicity in rats through restoration of cardiac antioxidant status. *J. Food Biochem.* 44 (11), e13450. doi:10.1111/jfbc.13450

Poodineh, J., and Nakhaee, A. (2019). *In vitro* antioxidant and anti-lipid peroxidation activities of hydroalcoholic extracts of Caralluma tuberculata, root and aerial parts. *Jundishapur J. Nat. Pharm. Prod.* 14 (4), e69685. doi:10.5812/jjnpp.69685

Pramod, C., Ratheesh, M., Jose, S. P., and Jose, S. (2020). Evaluation of hypolipidemic activity of ethanolic extract of *Trema orientalis* L. Blume leaves. *J. Pharmacogn. Phytochemistry* 9 (4), 904–911.

Rajadurai, M., and Prince, P. S. M. (2006). Preventive effect of naringin on lipid peroxides and antioxidants in isoproterenol-induced cardiotoxicity in wistar rats: Biochemical and histopathological evidences. *Toxicology* 228 (2-3), 259–268. doi:10.1016/j.tox.2006.09.005

Rao, A. V., and Ramakrishnan, S. (1975). Indirect assessment of hydroxymethylglutaryl-CoA reductase (NADPH) activity in liver tissue. *Clin. Chem.* 21 (10), 1523–1525. doi:10.1093/clinchem/21.10.1523

Raut, G. K., Manchineela, S., Chakrabarti, M., Bhukya, C. K., Naini, R., Venkateshwari, A., et al. (2020). Imine stilbene analog ameliorate isoproterenol-induced cardiac hypertrophy and hydrogen peroxide-induced apoptosis. *Free Radic. Biol. Med.* 153, 80–88. doi:10.1016/j.freeradbiomed.2020.04.014

Re, R., Pellegrini, N., Proteggente, A., Pannala, A., Yang, M., and Rice- Evans, C. (1999). Antioxidant activity applying an improved ABTS radical cation decolorization assay. *Free Radic. Biol. Med.* 26, 1231–1237. doi:10.1016/S0891-5849(98)00315-3

Rodríguez Madrera, R., Campa Negrillo, A., Suárez Valles, B., and Ferreira Fernández, J. J. (2021). Phenolic content and antioxidant activity in seeds of common bean (Phaseolus vulgaris L.). *Foods* 10 (4), 864. doi:10.3390/foods10040864

Sajid, A., Ahmad, T., Ikram, M., Khan, T., Shah, A. J., Mahnashi, M. H., et al. (2022). Cardioprotective potential of aqueous extract of *Fumaria indica* on isoproterenol-induced myocardial infarction in SD rats. *Oxid. Med. Cell. Longev.* 2022, 2112956. doi:10.1155/2022/2112956

Saleem, N., Prasad, A., and Goswami, S. K. (2018). Apocynin prevents isoproterenol-induced cardiac hypertrophy in rat. *Mol. Cell. Biochem.* 445 (1), 79–88. doi:10.1007/s11010-017-3253-0

Saleh, M., and Ambrose, J. A. (2018). Understanding myocardial infarction. *F1000Res.* 7, 1378. doi:10.12688/f1000research.15096.1

Sandoval, Y., and Jaffe, A. S. (2019). Type 2 myocardial infarction: JACC review topic of the week. *J. Am. Coll. Cardiol.* 73 (14), 1846–1860. doi:10.1016/j.jacc.2019.02.018

Sarma, R., Kumari, S., Elancheran, R., Deori, M., and Devi, R. (2016). Polyphenol rich extract of *Garcinia pedunculata* fruit attenuates the hyperlipidemia induced by high fat diet. *Front. Pharmacol.* 7, 294. doi:10.3389/fphar.2016.00294

Shah, S. M. A., Akram, M., Riaz, M., Munir, N., and Rasool, G. (2019). Cardioprotective potential of plant-derived molecules: A scientific and medicinal

approach. *Dose. Response.* 17 (2), 1559325819852243. doi:10.1177/1559325819852243

Shaik, A. H., Al Omar, S. Y., Mohammad, A., and Kodidhela, L. D. (2020). Combined cardio-protective ability of syringic acid and resveratrol against isoproterenol induced cardio-toxicity in rats via attenuating NF-kB and TNF-α pathways. *Sci. Rep.* 10 (1), 3426–3513. doi:10.1038/s41598-020-59925-0

Shaikh, S., Bhatt, L. K., and Barve, K. (2019). Attenuation of isoproterenol-induced cardiotoxicity in rats by Narirutin rich fraction from grape fruit. *Phytomedicine* 55, 222–228. doi:10.1016/j.phymed.2018.06.037

Shang, L., Pin, L., Zhu, S., Zhong, X., Zhang, Y., Shun, M., et al. (2019). Plantamajoside attenuates isoproterenol-induced cardiac hypertrophy associated with the HDAC2 and AKT/GSK-3β signaling pathway. *Chem. Biol. Interact.* 307, 21–28. doi:10.1016/j.cbi.2019.04.024

Sharifi-Rad, J., Rodrigues, C. F., Sharopov, F., Docea, A. O., Can Karaca, A., Sharifi-Rad, M., et al. (2020). Diet, lifestyle and cardiovascular diseases: Linking pathophysiology to cardioprotective effects of natural bioactive compounds. *Int. J. Environ. Res. Public Health* 17 (7), 2326. doi:10.3390/ijerph17072326

Singh, B., Singh, J. P., Kaur, A., and Singh, N. (2017). Phenolic composition and antioxidant potential of grain legume seeds: A review. *Food Res. Int.* 101, 1–16. doi:10.1016/j.foodres.2017.09.026

Sivasangari, S., Asaikumar, L., Vennila, L., and Vijayakumar, N. (2019). Preventive effect of arbutin on isoproterenol-induced oxidative stress, mitochondrial damage and apoptosis in H9c2 cells. *Int. J. Nutr. Pharmacol. Neurol. Dis.* 9 (3), 97. doi:10.4103/ijnpnd.ijnpnd_24_19

Sotler, R., Poljšak, B., Dahmane, R., Jukić, T., Jukić, D. P., Rotim, C., et al. (2019). Prooxidant activities of antioxidants and their impact on health. *Acta Clin. Croat.* 58 (4), 726–736. doi:10.20471/acc.2019.58.04.20

Soumya, R. S., Raj, K. B., and Abraham, A. (2021). Passiflora edulis (var. Flavicarpa) juice supplementation mitigates isoproterenol-induced myocardial infarction in rats. *Plant Foods Hum. Nutr.* 76 (2), 189–195. doi:10.1007/s11130-021-00891-x

Stagos, D. (2019). Antioxidant activity of polyphenolic plant extracts. *Antioxidants* 9 (1), 19. doi:10.3390/antiox9010019

Sultan, F., Kaur, R., Tarfain, N. U., Mir, A. H., Dumka, V. K., Sharma, S. K., et al. (2022). Protective effect of rosuvastatin pretreatment against acute myocardial injury by regulating Nrf2, Bcl-2/Bax, iNOS, and TNF-α expressions affecting oxidative/nitrosative stress and inflammation. *Hum. Exp. Toxicol.* 41, 09603271211066065. doi:10.1177/09603271211066065

Swallah, M. S., Sun, H., Affoh, R., Fu, H., and Yu, H. (2020). Antioxidant potential overviews of secondary metabolites (polyphenols) in fruits. *Int. J. Food Sci.* 2020, 9081686. doi:10.1155/2020/9081686

Syed, A. A., Lahiri, S., Mohan, D., Valicherla, G. R., Gupta, A. P., Kumar, S., Maurya, R., Bora, H.K., Hanif, K., and Gayen, J. R. (2016). Cardioprotective effect of Ulmus wallichiana Planchon in β-adrenergic agonist induced cardiac hypertrophy. Frontiers in Pharmacology, 7, 510. doi:10.3389/fphar.2016.00510

Thangaiyan, R., Robert, B. M., Arjunan, S., Govindasamy, K., and Nagarajan, R. P. (2018). Preventive effect of apigenin against isoproterenol-induced apoptosis in cardiomyoblasts. *J. Biochem. Mol. Toxicol.* 32 (11), e22213. doi:10.1002/jbt.22213

Ulewicz-Magulska, B., and Wesolowski, M. (2019). Total phenolic contents and antioxidant potential of herbs used for medical and culinary purposes. *Plant Foods Hum. Nutr.* 74 (1), 61–67. doi:10.1007/s11130-018-0699-5

Van Pelt, L. F. (1977). Ketamine and xylazine for surgical anesthesia in rats. *J. Am. Vet. Med. Assoc.* 171 (9), 842–844.

Vijayalakshmi, M., and Ruckmani, K. (2016). Ferric reducing antioxidant power assay in plant extract. *Bangladesh J. Pharmacol.* 11 (3), 570–572. doi:10.3329/bjp.v11i3.27663

Viswanadha, V. P., Dhivya, V., Beeraka, N. M., Huang, C. Y., Gavryushova, L. V., Minyaeva, N. N., et al. (2020). The protective effect of piperine against isoproterenol-induced inflammation in experimental models of myocardial toxicity. *Eur. J. Pharmacol.* 885, 173524. doi:10.1016/j.ejphar.2020.173524

Wong, Z. W., Thanikachalam, P. V., and Ramamurthy, S. (2017). Molecular understanding of the protective role of natural products on isoproterenol-induced myocardial infarction: A review. *Biomed. Pharmacother.* 94, 1145–1166. doi:10.1016/j.biopha.2017.08.009

Yang, Y., Han, J., Lilly, R. G., Yang, Q., and Guo, Y. (2022). Bergapten mediated inflammatory and apoptosis through AMPK/eNOS/AKT signaling pathway of isoproterenol-induced myocardial infarction in Wistar rats. *J. Biochem. Mol. Toxicol.* 36, e23143. doi:10.1002/jbt.23143

frontiers | Frontiers in Pharmacology

TYPE Original Research
PUBLISHED 23 November 2022
DOI 10.3389/fphar.2022.942061

OPEN ACCESS

EDITED BY
Guixue Wang,
Chongqing University, China

REVIEWED BY
Kai Qiu,
Chinese Academy of Agricultural Sciences (CAAS), China
Munerah Hamed,
Umm al-Qura University, Saudi Arabia

*CORRESPONDENCE
Shenglong Zhu,
shenglongzhu@jiangnan.edu.cn

SPECIALTY SECTION
This article was submitted to Cardiovascular and Smooth Muscle Pharmacology, a section of the journal Frontiers in Pharmacology

RECEIVED 12 May 2022
ACCEPTED 10 November 2022
PUBLISHED 23 November 2022

CITATION
Jiang X, Ji S, Cui S, Wang R, Wang W, Chen Y and Zhu S (2022), *Apol9a* regulates myogenic differentiation *via* the ERK1/2 pathway in C2C12 cells. *Front. Pharmacol.* 13:942061. doi: 10.3389/fphar.2022.942061

Apol9a regulates myogenic differentiation *via* the ERK1/2 pathway in C2C12 cells

Xuan Jiang[1,2], Siyu Ji[1], Siyuan Cui[3], Rong Wang[1,2], Wei Wang[1], Yongquan Chen[1,4,2] and Shenglong Zhu[1,4]*

[1]Wuxi School of Medicine, Jiangnan University, Wuxi, China, [2]School of Food Science and Technology, Jiangnan University, Wuxi, China, [3]The Wuxi No. 2 People's Hospital, Wuxi, China, [4]Wuxi Translational Medicine Research Center and School of Translational Medicine, Jiangnan University, Wuxi, China

Background: The rising prevalence of obesity and its complications is a big challenge for the global public health. Obesity is accompanied by biological dysfunction of skeletal muscle and the development of muscle atrophy. The deep knowledge of key molecular mechanisms underlying myogenic differentiation is crucial for discovering novel targets for the treatment of obesity and obesity-related muscle atrophy. However, no effective target is currently known for obesity-induced skeletal muscle atrophy.

Methods: Transcriptomic analyses were performed to identify genes associated with the regulation of myogenic differentiation and their potential mechanisms of action. C2C12 cells were used to assess the myogenic effect of *Apol9a* through immunocytochemistry, western blotting, quantitative polymerase chain reaction, RNA interference or overexpression, and lipidomics.

Results: RNA-seq of differentiated and undifferentiated C2C12 cells revealed that *Apol9a* expression significantly increased following myogenic differentiation and decreased during obesity-induced muscle atrophy. *Apol9a* silencing in these C2C12 cells suppressed the expression of myogenesis-related genes and reduced the accumulation of intracellular triglycerides. Furthermore, RNA-seq and western blot results suggest that *Apol9a* regulates myogenic differentiation through the activation of extracellular signal-regulated kinase 1/2 (ERK1/2). This assumption was subsequently confirmed by intervention with PD98059.

Conclusion: In this study, we found that *Apol9a* regulates myogenic differentiation *via* the ERK1/2 pathway. These results broaden the putative function of *Apol9a* during myogenic differentiation and provide a promising therapeutic target for intervention in obesity and obesity-induced muscle atrophy.

Abbreviations: Apol9a, apolipoprotein L 9a; MyHC, myosin heavy chain; MyoD, myoblast determination protein; MyoG, myogenin; HFD, high-fat diet; qPCR, Real-time quantitative polymerase chain reaction; TG, triacylglycerol; PCA, principal component analysis; FAME, fatty acid methyl ester; OPLS-DA, orthogonal partial least squares-discriminant analysis; PE, phosphatidylethanolamine; PC, phosphatidylcholine; VIP, Variable Importance in Projection.

KEYWORDS
obesity, myogenesis, Apol9a, ERK1/2, C2C12

Introduction

Obesity is widely reported to be a potential risk factor for type 2 diabetes mellitus (T2DM), a metabolic disorder typified by chronic hyperinsulinemia, hyperglycemia, and insulin resistance (Astrup and Finer, 2000; Lingvay et al., 2021). Diabetes is reportedly stimulated during obesity because of a failure in appropriate glucose utilization by skeletal muscle, which is the primary target site of insulin-stimulated glucose uptake (DeFronzo and Tripathy, 2009; Lingvay et al., 2021; Mengeste et al., 2021). Obesity-related ectopic fat deposition induces biological dysfunction in skeletal muscle, such as insulin resistance (IR), mitochondrial dysfunction, and inflammation (Wu and Ballantyne, 2017). These processes further exacerbate skeletal muscle loss and physical dysfunction. Maintaining skeletal muscle health is fundamental for general health.

Myogenesis, which includes satellite cell activation, myoblast differentiation, and myotube formation, is responsible for the maintenance of skeletal muscle mass and integrity in general (Schiaffino et al., 2013; Sousa-Victor et al., 2022). Myogenesis dysregulation causes muscle wasting diseases such as sarcopenia and cachexia, increasing the risk of frailty, morbidity, and lethality (Nishikawa et al., 2021a; Wiedmer et al., 2021). Numerous studies have discovered that muscle wasting is caused by various factors that inhibit myogenesis, such as oxidative stress, mitochondrial malfunction, and aging (Bonaldo and Sandri, 2013; McCarthy and Berg, 2021). Obesity has been shown to aggravate the negative effects of muscle loss, leading to sarcopenic obesity (Roh and Choi, 2020; Nishikawa et al., 2021b). Additionally, obesity reduces the capacity of skeletal muscle differentiation and may impact muscle plasticity and function (Brown et al., 2015). Furthermore, another study showed that the low level of inflammation induced by obesity downregulates myogenesis (Du et al., 2010). A deep understanding of myogenesis is crucial for comprehending the mechanisms regulating skeletal muscle mass under pathological disorders. The myogenic differentiation process comprises multiple pathways, and numerous potential targets in myogenesis regulation remain unknown.

To discover the potential targets in the process of myogenic differentiation, we applied RNA sequencing to identify unknown genes that regulate myogenesis in a classical mouse cell model. As a result, we identified *apolipoprotein L9a (Apol9a)* as a key moderator regulating myogenic differentiation. *Apol9a* is a member of the murine apolipoprotein L gene family, and interferon-inducible mouse Apol9a is secreted by macrophages to promote epithelial cell proliferation (Kreit et al., 2015; Sun et al., 2015). However, the biological function of Apol9a in skeletal muscles remains unclear. Experiments have indicated that *Apol9a* knockdown impairs skeletal muscle differentiation, principally by activating the ERK1/2 pathway. Activated ERK1/2 signaling promotes skeletal muscle cell proliferation but negatively regulates myogenic differentiation (Jones et al., 2001) and modulates nuclear factor of activated T cells c1 (NFATc1) (Chen et al., 2017). Studies have indicated that ERK1/2 activation is elevated in atrophic and damaged skeletal muscles (Penna et al., 2010). Our results highlight the potential importance of *Apol9a* in myogenic differentiation, suggesting that modulation of *Apol9a*-ERK activity may help reduce the risk of obesity-related muscle atrophy.

Materials and methods

Animals

Six-week-old male C57BL/6 mice were purchased from Jicui Yaokang Biological Technology Co., (Nanjing, China). All mice were maintained under standard conditions of 22°C ± 2°C, 50%–60% relative humidity, and alternate dark/light cycles. Mice were fed a high-fat diet (HFD) (60 kcal%, D12492, Research Diets) for 10 weeks to induce obesity. Control mice were fed a basal diet (10 kcal%, D12450B, Research Diets). Both groups of mice were sacrificed at 16 weeks of age, and their gastrocnemius muscles were dissected for experimental analyses. Skeletal muscle triglyceride (TG) contents were measured using a Triglyceride Quantification Kit (Nanjing Jiancheng, China). All experiments in this study were authorized by the Ethics Committee of Jiangnan University [NO: JN. No20211030c0700625 (426)].

Cell culture and treatment

C2C12 mouse myoblast cells were purchased from the ATCC (CRL-1772, United States). The C2C12 cell line was cultured in growth medium (GM) supplemented with basic DMEM (11995–065, Gibco, United States), 10% FBS (1009–141, Gibco, United States), and 1% penicillin plus 1% streptomycin (SV30010, Hyclone, United States) at 37°C and 5% CO_2. GM was replaced with differentiation medium (DM) containing DMEM with 2% horse serum (HS, 16050–130, Gibco, United States) and incubated for 4 days in order to induce C2C12 cell differentiation when C2C12 cells reached 90% confluency.

To explore the effect of *Apol9a* on C2C12 cells, small interfering RNA (siRNA, GenePharma, Shanghai, China) was used to knockdown intracellular *Apol9a*, and the overexpression plasmid (GENEWIZ) was used to overexpress *Apol9a*. C2C12 cells were seeded into 6-well plates and cultured for 8 h (equivalent to a cell density of 30%–40%). Next, siRNA and

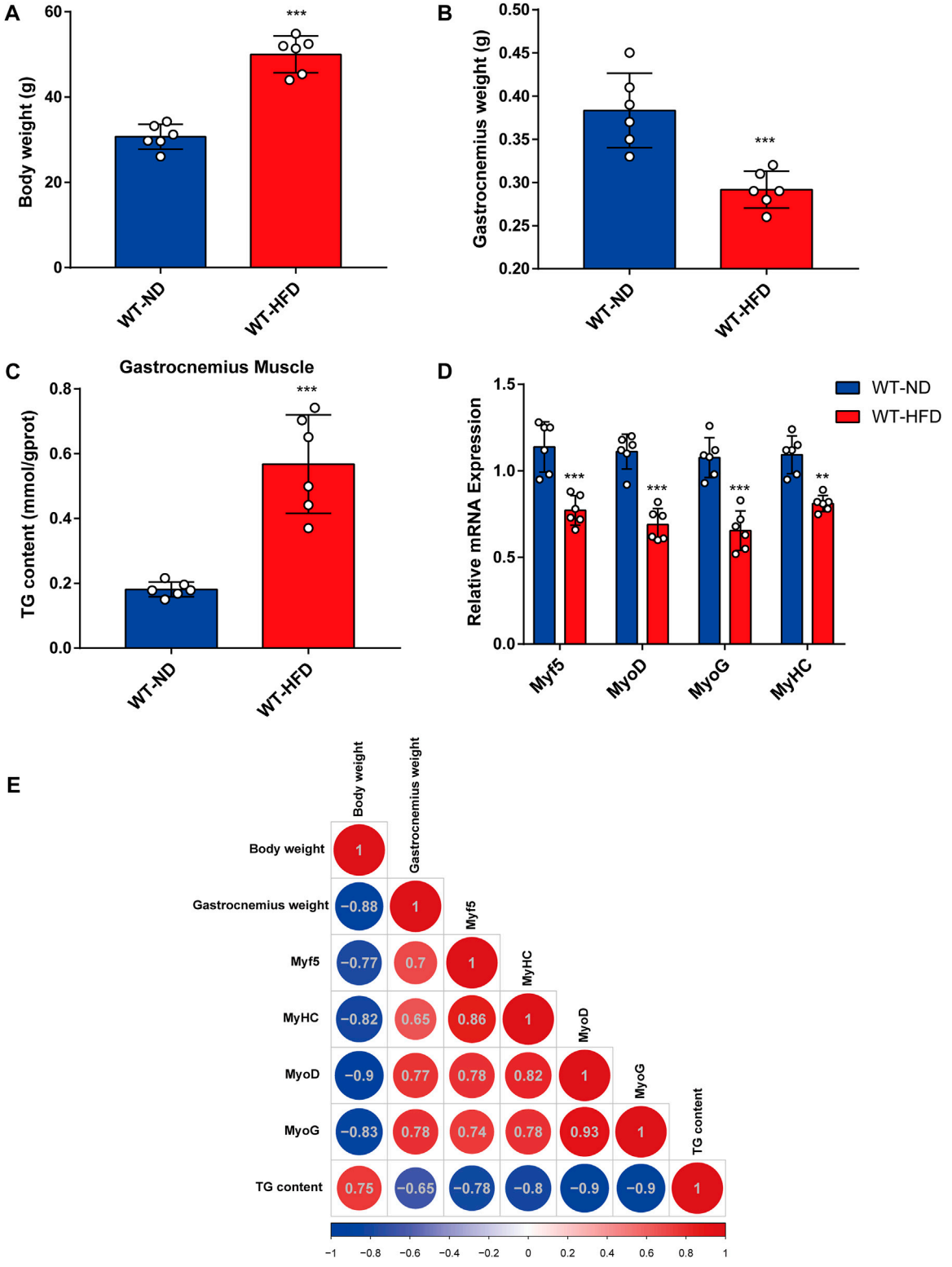

FIGURE 1
Correlation between obesity and myogenic differentiation. Six-week-old male mice were divided into two groups, each fed with normal chow and high-fat diet for 8 weeks. **(A)** Body weight comparison. **(B)** Gastrocnemius muscle weight (GW) comparison. **(C)** Comparison of triglyceride (TG) levels in gastrocnemius muscles from the ND-fed and HFD-fed mice as assessed using the Triglyceride Quantification Kit. **(D)** The mRNA expression levels of myogenesis-related genes (*Myf5*, *MyoD*, *MyoG*, and *MyHC*) in the ND-fed and HFD-fed mice as measured through quantitative real-time PCR (qPCR). **(E)** Correlation heatmap (Pearson correlation) of body weight, TG level, GW, and mRNA levels of myogenesis-related genes. Positive and negative correlations are shown by red and blue colors, respectively. Date are shown as mean ± SEM (n = 6 for each group). *p < 0.05, **p < 0.01, and ***p < 0.001 vs. WT-ND.

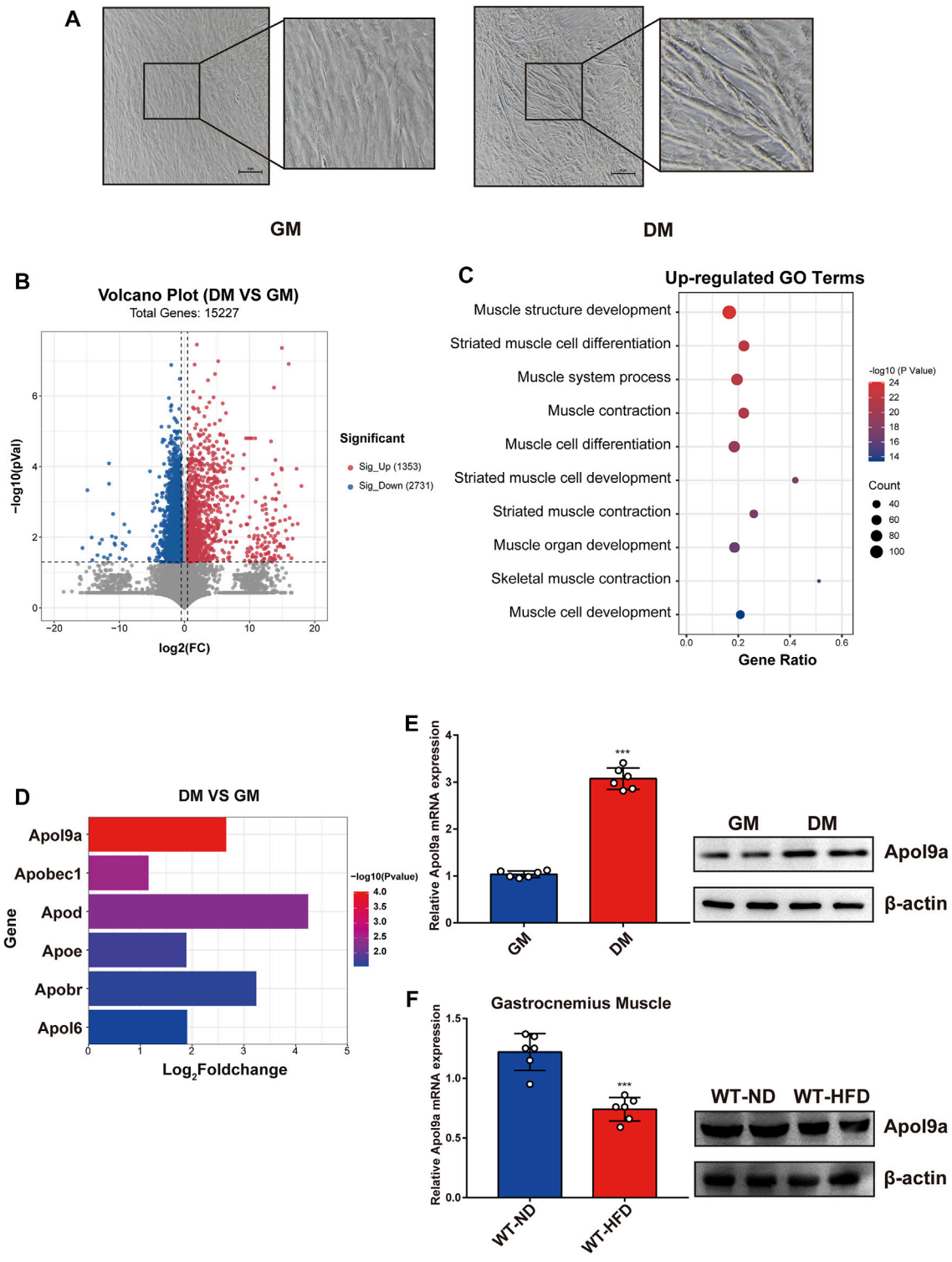

FIGURE 2
Apol9a is increased in myogenic differentiation and decreased in obese mice. RNA sequencing (RNA-seq) data of C2C12 cells with or without myogenic induction were collected. **(A)** Representative images from C2C12 cells in growth medium (GM) and differentiation medium (DM). Scale bar, 100 μm. **(B)** Volcano plot showing differentially expressed genes (DEGs) in differentiated or undifferentiated C2C12 cells. **(C)** Ten most upregulated GO terms during C2C12 differentiation according to the RNA-seq data. **(D)** Expression profiles of apolipoprotein family genes during C2C12 differentiation. **(E)** The relative mRNA expression (left) and protein levels (right) of *Apol9a* during C2C12 differentiation were measured using qPCR and western blotting. **(F)** The relative mRNA expression (left) and protein levels (right) of *Apol9a* in obese skeletal muscle were measured through qPCR and western blotting. The data are presented as mean ± SEM from at least three separate experiments. $^{*}p < 0.05$, $^{**}p < 0.01$, $^{***}p < 0.001$.

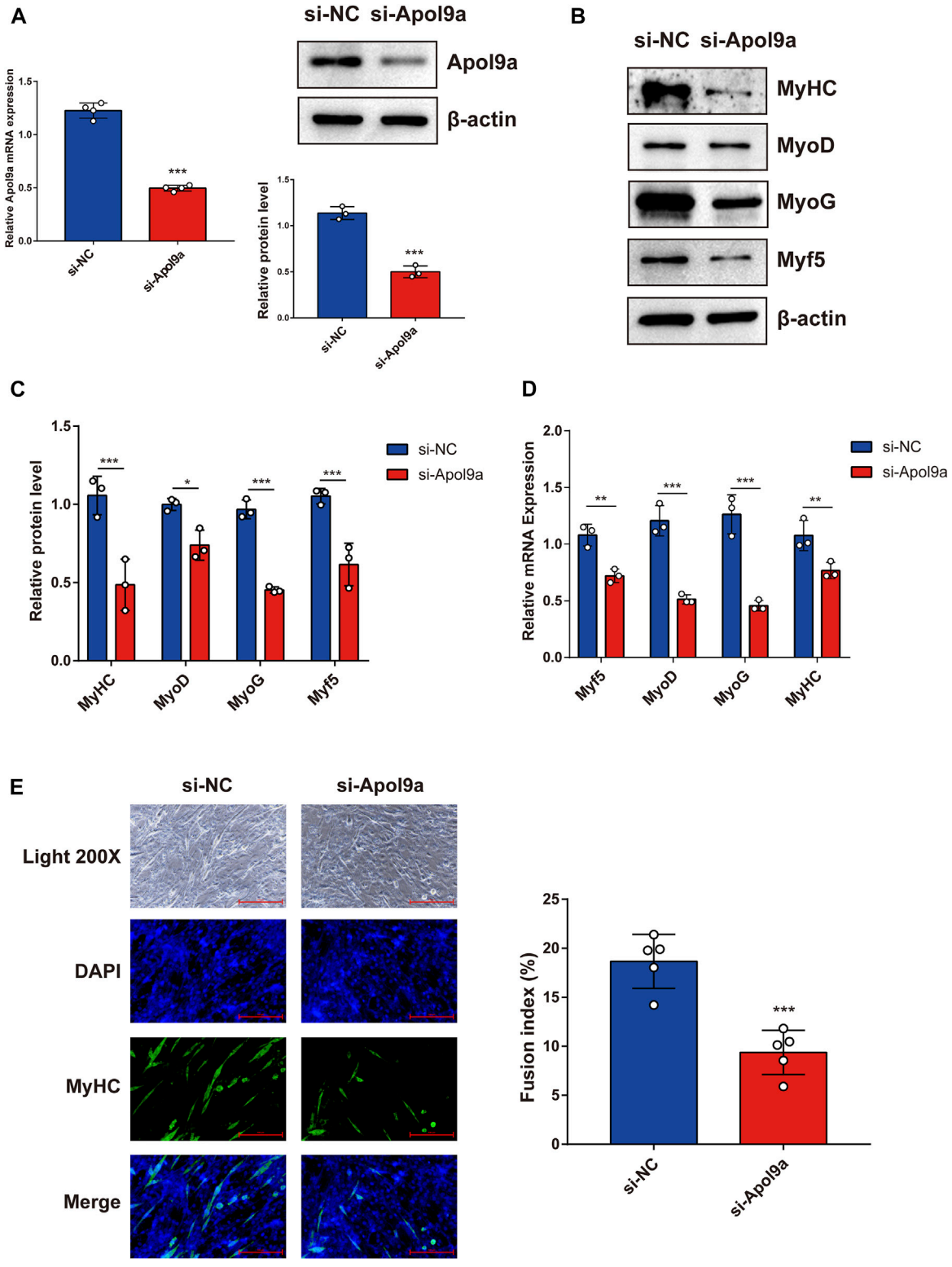

FIGURE 3
Apol9a knockdown inhibits C2C12 myogenesis. C2C12 cells were induced to differentiate after si-NC or si-*Apol9a* transfection for 4 days. **(A)** qPCR and western blot validation of the efficiency of *Apol9a* knockdown in C2C12 cells. **(B)** Protein expression levels of MyHC, MyoD, Myf5, and MyoG were estimated through western blot analysis after si-NC and si-*Apol9a* transfection. **(C)** Gray scale analysis of western blot results of **(B)** determined using ImageJ software. **(D)** qPCR was performed to assess the mRNA expression levels of several myogenic differentiation genes (*Myf5*, *MyoD*, *MyoG*, and *MyHC*). **(E)** Myotube formation can be observed in fluorescence images of DAPI (blue) and MyHC antibody-stained (green) myotubes of C2C12 cells transfected si-NC or si-*Apol9a*. Scale bar, 100 μm. The fusion index (%) was quantified and is shown on the right. The data are expressed as mean ± SEM of at least three independent experiments. $^{*}p < 0.05$, $^{**}p < 0.01$, $^{***}p < 0.001$ vs. si-NC control.

the overexpression plasmid were transfected into cells at a concentration of 50 nM. The jetPRIME® transfection reagent (114–15, Polyplus transfection) was used to transfer siRNAs, the overexpression plasmid, and the empty control plasmid. At 12 h after transfection, the transfection medium was replaced with DM to induce differentiation for 4 days. Specific knockdown of *Apol9a* was validated using two different siRNAs. The two siRNA sequences for mouse *Apol9a* was 5′-UUGUAUCCAAGGCCAAGUUGUTT-3′and 5′-AGCCCU UGAGCAGCACAUGAATT-3′. A random siRNA sequence (A06001, GenePharma, shanghai, China) was applied as control. To inhibit the ERK1/2 signaling pathway, C2C12 myoblasts were treated with 50 μm PD98059 (HY-12028, Med Chem Express) in DM for 4 d (after 8 h transfection). Dimethyl sulfoxide (DMSO, D8418, Sigma-Aldrich) was used as a solvent control.

Myotube diameter measurements were obtained using ImageJ software. The diameter was measured at the widest region of each myotube, and the mean diameter size was compared between conditions.

qPCR

Total RNA was isolated from both C2C12 myoblasts and skeletal muscle tissue by using the RNA extraction kit (K101, JN. BIOTOOLS, Wuxi, China). cDNA was synthesized using the BTS I 1st Strand cDNA Synthesis Kit (K102, JN. BIOTOOLS, Wuxi, China), and 1 μg of total RNA to be used for quantitative real-time PCR (qPCR) was reverse transcribed. qPCR was performed using the Power SYBR Green Master Mix kit (4367659, Invitrogen, United States) in a CFX 96™RealTime PCR Detection System (Bio-Rad, United States). The amplification conditions for qPCR were as follows: 94°C for 5 min, followed by 45 cycles of 94°C for 15 s and 45 s at 59°C. The fold change of gene expression was analyzed according to the $2^{-\Delta\Delta CT}$ method. *β-actin* was utilized as the internal control for normalization. The sequences of all primers used in this research are presented in Supplementary Table S1.

Western blotting

Total proteins were extracted from the cell lysate and determined using the Quick BCA Protein Assay Kit (SYW3-1, Solarbio, China). The lysate proteins were resolved through SDS-PAGE with a 10% gel, transferred to PVDF membranes (IPVH00005, Merck Millipore), blocked, and incubated with primary antibodies against Apol9a (AC-15–1076, Ango Biotechnology, 1:1000); myosin heavy chain (MyHC) (MF-20, 1:1000, Developmental Studies Hybridoma Bank); myogenin (MyoG) (ab 1835, Abcam, 1:2000); myoblast determination protein (MyoD) (18943-1-AP, 1:1000, Proteintech); Myf5 (BD-PT2930, 1:1000, Biodragon); phospho-Erk1/2 (4370, 1:1000, CST); Erk1/2 (4695, 1:1000, CST); phospho-JNK (4668, 1:1000, CST); JNK (9252, 1:1000, CST); phospho-p38 (4511, 1:1000, CST); p38 (9212, 1:1000, CST); and β-actin (ab8227, 1:2000, Abcam). After all membranes were washed, they were treated with specific secondary antibodies (AS014, AS003, Abclonal, China). Specific protein bands were detected using an ECL kit (WBKLS0100, Merck Millipore). The images were observed using the Bio-Rad ChemiDoc MP Imaging System, and then, image bands were quantified through densitometry by using ImageJ plus software. The expression level of each target protein was normalized to that of β-actin, which was used as an internal control.

Immunocytochemistry

C2C12 myoblasts were fixed with paraformaldehyde (4%) for 20 min and treated with 1% Triton X-100 for 5 min. The fixed cell samples were incubated with blocking buffer (A8010, Solarbio, China) in phosphate-buffered saline (PBS) and then incubated with anti-MyHC (MF20, 1:50, DSHB) antibody at 4°C overnight. After washing the samples with PBS, the cell samples were treated with a 1:100 dilution of secondary antibody, which was derived from goat anti-mouse IgG (AS001, Abclonal) and conjugated with FITC, for 2 h. Cell nuclei were counterstained with DAPI staining solution (C1002, Beyotime, China). Finally, the stained cells were viewed using a fluorescence microscope (Leica DM2500, Leica Microsystems), and the images were captured. The fusion index was calculated as the percentage of nuclei in fused myotubes out of the total nuclei. The number of nuclei in each image was evaluated using the ImageJ plus software.

Fatty acid methyl ester analysis

Fatty acid extraction and methyl-esterification were performed as previously described (Zhu et al., 2022a). Briefly, the recovered fatty acid methyl esters were examined through GC-MS (QP2010 ultra mass spectrometer, GC 2010 plus, Thermo Scientific). The electron energy was fixed at 70 eV, and the temperature programming profile was as follows: kept for 5 min at 60°C, up to 120°C in increments of 10°C/min, maintained for 5 min at 120°C, up to 190°C in increments of 5°C/min, kept for 7 min at 190°C, up to 230°C in increments of 2°C/min, and kept for 10 min at 230°C. A 5-MS column (Restek, United States) was used to resolve all samples. The detector and ion source were run at 240°C and 230°C, respectively. The peaks obtained were identified by comparing their retention times with those of known standards (Sigma). Pentadecanoic acid (C15:0) was used as the internal standard, and each sample was normalized to total cellular protein concentration, as measured using the Quick BCA protein assay kit (SYW3-1, Solarbio, China).

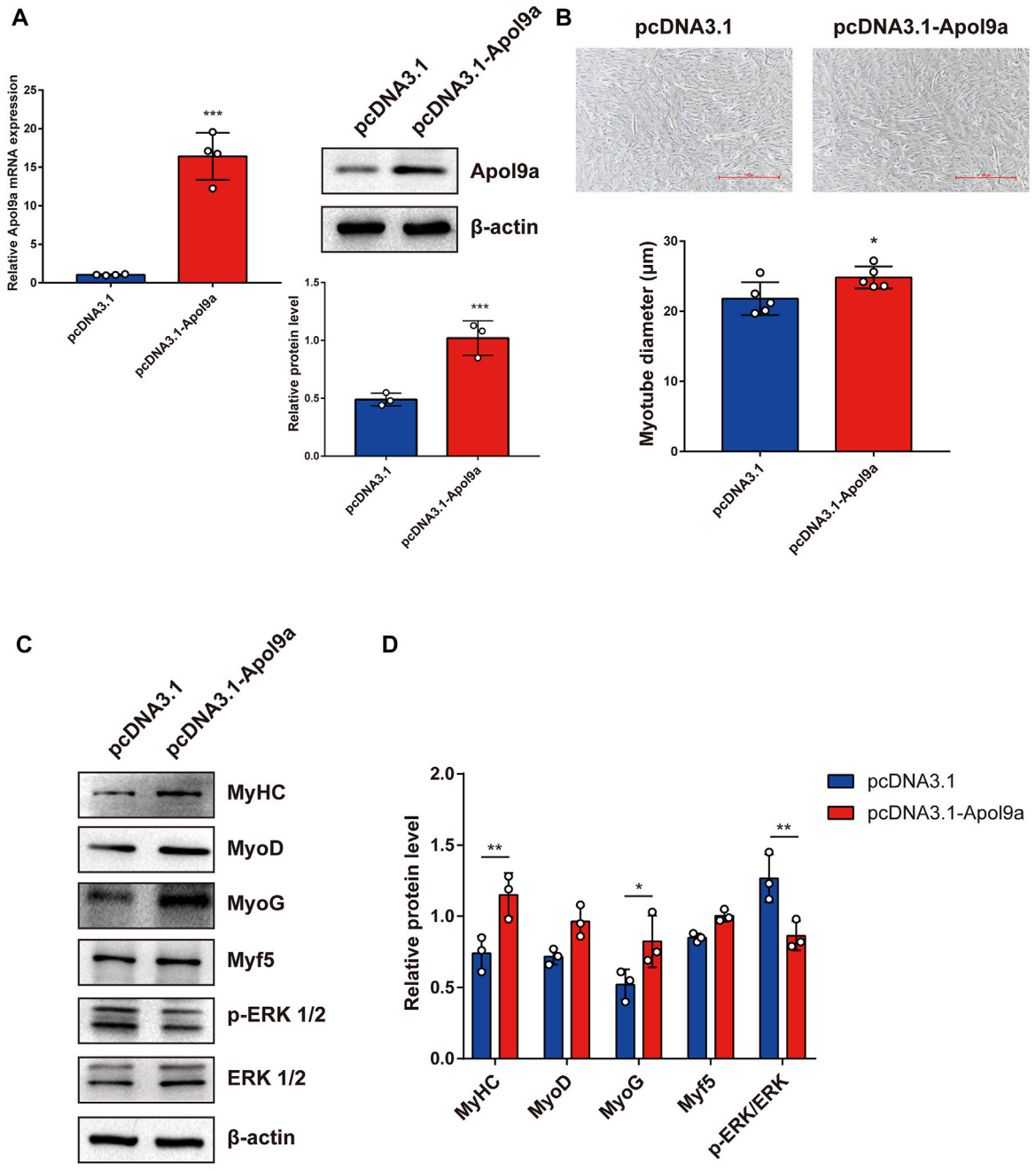

FIGURE 4
Apol9a overexpression promotes myogenic differentiation. C2C12 cells were induced to differentiate after pcDNA3.1 or pcDNA3.1-*Apol9a* transfection for 4 days. **(A)** qPCR and western blot validation of the efficiency of *Apol9a* overexpression in C2C12 cells. **(B)** Morphology of C2C12 cells treated with pcDNA3.1 or pcDNA3.1-*Apol9a*. The results of quantification of average myotube diameter are shown in the right. **(C)** Protein expression levels of MyHC, MyoD, Myf5, MyoG, p-ERK 1/2, ERK 1/2, and β-actin were estimated through western blot analysis after transfection. **(D)** Gray scale analysis of western blot results of **(C)** determined using ImageJ software. The data are expressed as mean ± SEM from at least three independent experiments. *$p < 0.05$, **$p < 0.01$, ***$p < 0.001$ vs. pcDNA3.1 group.

Lipidomic analysis

Cell samples were produced in the manner previously described (Zhu et al., 2022b). Lipidomic analysis was conducted using LC-MS (QExactive Plus Orbitrap mass spectrometer, Thermo Scientific). Acetonitrile:MilliQ water (6: 4 v/v) and isopropanol:acetonitrile (9:1 v/v) were used as solvents A and B, respectively; both solvents contained 10 mm

ammonium acetate. Column chromatography was performed using the Waters ACQUITY UPLC CSHTM C18 column. The gradient profile was as follows: 32%–100% solvent B over 24 min, back to 32% solvent B and 6 min before the next injection, and equilibrate the column. LipidSearch program v4.1.16 (Thermo Scientific) was used to identify the type of lipids. A pool of all lipid extracts was prepared and used for quality control. SIMCA-P (Sweden) was used to import the raw MS data, and an orthogonal projection was performed for latent structures-discriminant analysis (OPLS-DA). The resulting heatmap plots were drawn using R software.

RNA sequencing

RNA sequencing (RNA-seq) was conducted as previously described (Zhang et al., 2021; Zhu et al., 2022c). Briefly, total RNA of C2C12 myoblasts transfected with si-NC or si-*Apol9a* was isolated using the RNA extraction kit (K101, JN. BIOTOOLS, China). Library construction and paired-end sequencing were performed by GENEWIZ Biotech (Suzhou, China). Raw data files were matched to the mouse reference genome by using STAR software (http://www.code.google.com/p/rna-star/). For each sample, fold change was estimated using the fragments per kilobase per million reads values, and differential expression analysis was performed using the DESeq2 package. The standard of fold change ≥1.5 and $p < 0.05$ were defined to screen differentially expressed genes (DEGs). Gene ontology (GO) analysis was conducted to perform the functional enrichment analysis of specific DEGs using Metascape (metascape.org). All RNA-seq data files have been deposited in the SRA database (Accession: PRJNA845924).

Statistical analysis

Statistical analysis was performed using SPSS software version 22.0 and GraphPad Prism 8.0. The results are shown as mean ± SEM from at least three independent experiments. Differences between groups were evaluated using an unpaired Student's t-test (between two groups) or one-way ANOVA (between multiple groups). $^{*}p < 0.05$, $^{**}p < 0.01$, and $^{***}p < 0.001$ were considered statistically significant.

Results

Skeletal muscle mass and differentiation ability decrease in obese mice

To evaluate the effects of obesity on skeletal muscle differentiation, we used the HFD-induced obesity mouse model (Feraco et al., 2021). Body weight and TG content in skeletal muscle tissue were considerably higher in HFD mice than in normal diet (ND) mice (Figures 1A,C). Meanwhile, the HFD mice exhibited a lower gastrocnemius muscle mass (Figure 1B) than the ND mice. Furthermore, a significant decrease in the mRNA expression levels of myogenesis-related genes (including *Myf5*, *MyoD*, *MyoG*, and *MyHC*) was observed in the gastrocnemius muscle from HFD mice (Figure 1D). Based on Pearson's correlation analysis, we investigated the correlations between body weight, gastrocnemius muscle mass, expression levels of myogenesis-related genes, and TG levels in HFD mice (Figure 1E). A notable negative correlation was observed between TG content and gastrocnemius muscle mass. Together, these results demonstrate that muscle mass and myogenesis capacity were decreased in obese mice.

Apol9a levels increase during myogenic differentiation and decrease in obese mice

To determine the critical genes involved in myogenic differentiation, we compared the transcriptome of differentiated C2C12 cells (an established myoblast cell model) with that of undifferentiated C2C12 cells (Yaffe and Saxel, 1977). After myogenic differentiation, C2C12 cells became fused and the myotube diameter increased (Figure 2A). As demonstrated in the volcano plot (Figure 2B), 1353 genes were upregulated following myogenic differentiation and 2731 genes were downregulated (fold change ≥1.5). The upregulated genes were subjected to GO analysis, and the top 10 enriched GO terms were all related to muscle differentiation (Figure 2C). Among the upregulated gene sets, we observed that many apolipoprotein family genes were significantly upregulated following myogenic differentiation (Figure 2D). The most significant change involved *Apol9a*, an understudied cytoplasmic, interferon-inducible gene with antiviral activity (Kreit et al., 2015). To our knowledge, a role for *Apol9a* in myogenic differentiation has not been previously reported. Using qPCR, we confirmed that *Apol9a* mRNA expression levels increased following myogenesis (Figure 2E). However, *Apol9a* mRNA expression levels decreased in obese mice (Figure 2F). Together, these results indicate that *Apol9a* may play a role in myogenic differentiation.

Silencing *Apol9a* inhibits myogenic differentiation and *Apol9a* overexpression promotes myogenic differentiation

To further investigate the function of *Apol9a* in the progress of myogenesis, siRNA was used to interfere with *Apol9a* expression. C2C12 cells were transfected with *Apol9a* siRNA or NC siRNA, and then, the GM was replaced with DM for 4 days. *Apol9a* mRNA expression levels were reduced approximately 60% in *Apol9a* siRNA-transfected cells compared with the si-NC control group (Figure 3A).

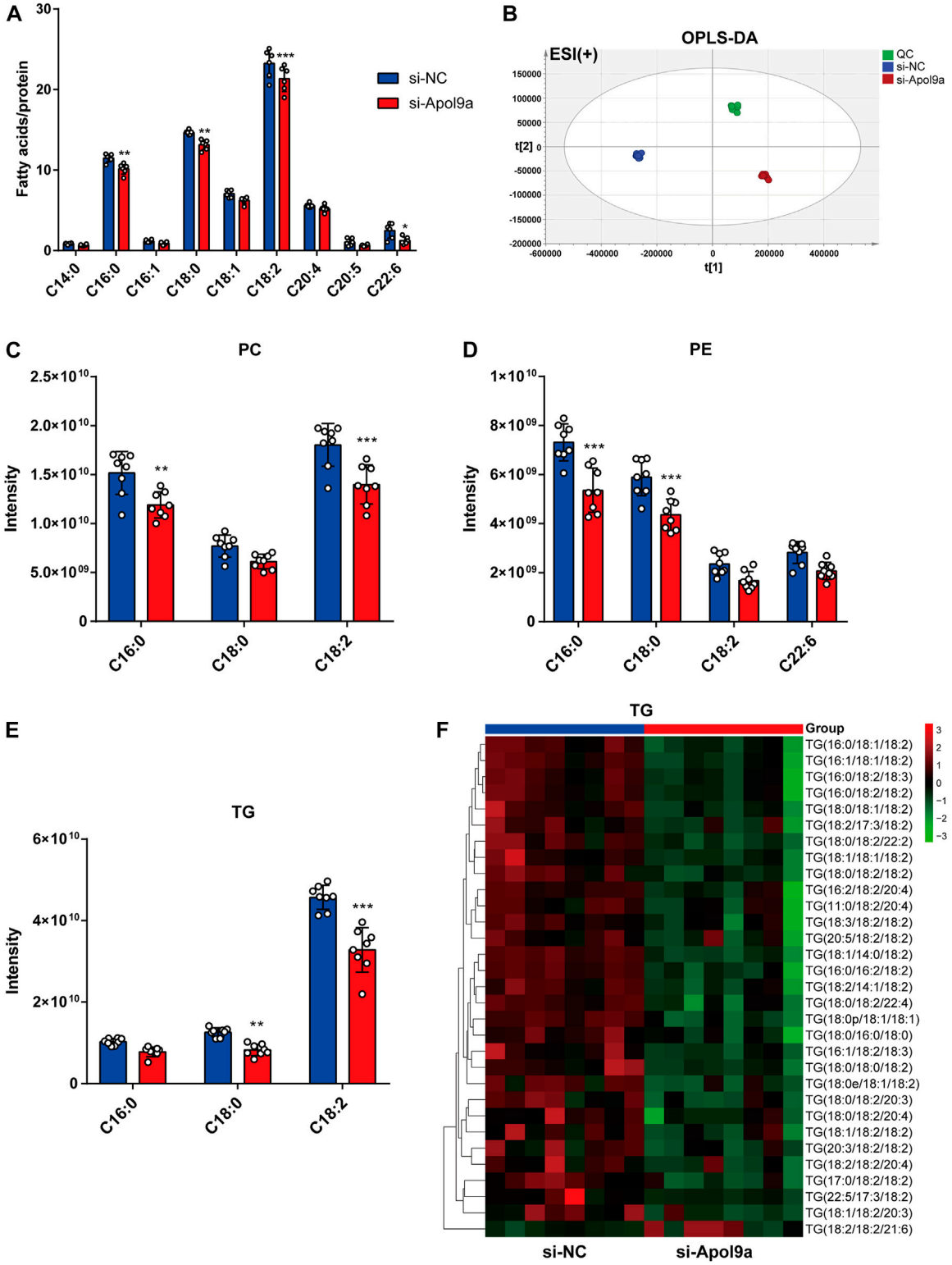

FIGURE 5
Fatty acid methyl ester analysis and lipidomic analysis. After myogenic differentiation for 4 days, C2C12 cells transfected with si-NC or si-*Apol9a* were collected, and cellular fatty acid and lipidomic analyses were performed. **(A)** Cellular fatty acid profiles were detected through GC-MS following C2C12 differentiation. **(B)** orthogonal partial least squares discriminant analysis (OPLS-DA) of lipid profiles in positive ion modes from C2C12 cells with or without *Apol9a* knockdown. **(C)** The composition of phosphatidylcholine (PC) (C16:0, C18:0, C18:2) among all lipids. **(D)** The composition of phosphatidylethanolamine (PE) (C16:0, C18:0, C18:2, C22:6) among all lipids. **(E)** The composition of triacylglycerol (TG) (C16:0, C18:0, C18:2) among all lipids. **(F)** Heatmap showing the differential lipid composition of TGs (C18:0, C18:2). The data are presented as mean ± SEM (n = 8, each group). $^{*}p < 0.05$, $^{**}p < 0.01$, $^{***}p < 0.001$ vs. si-NC group.

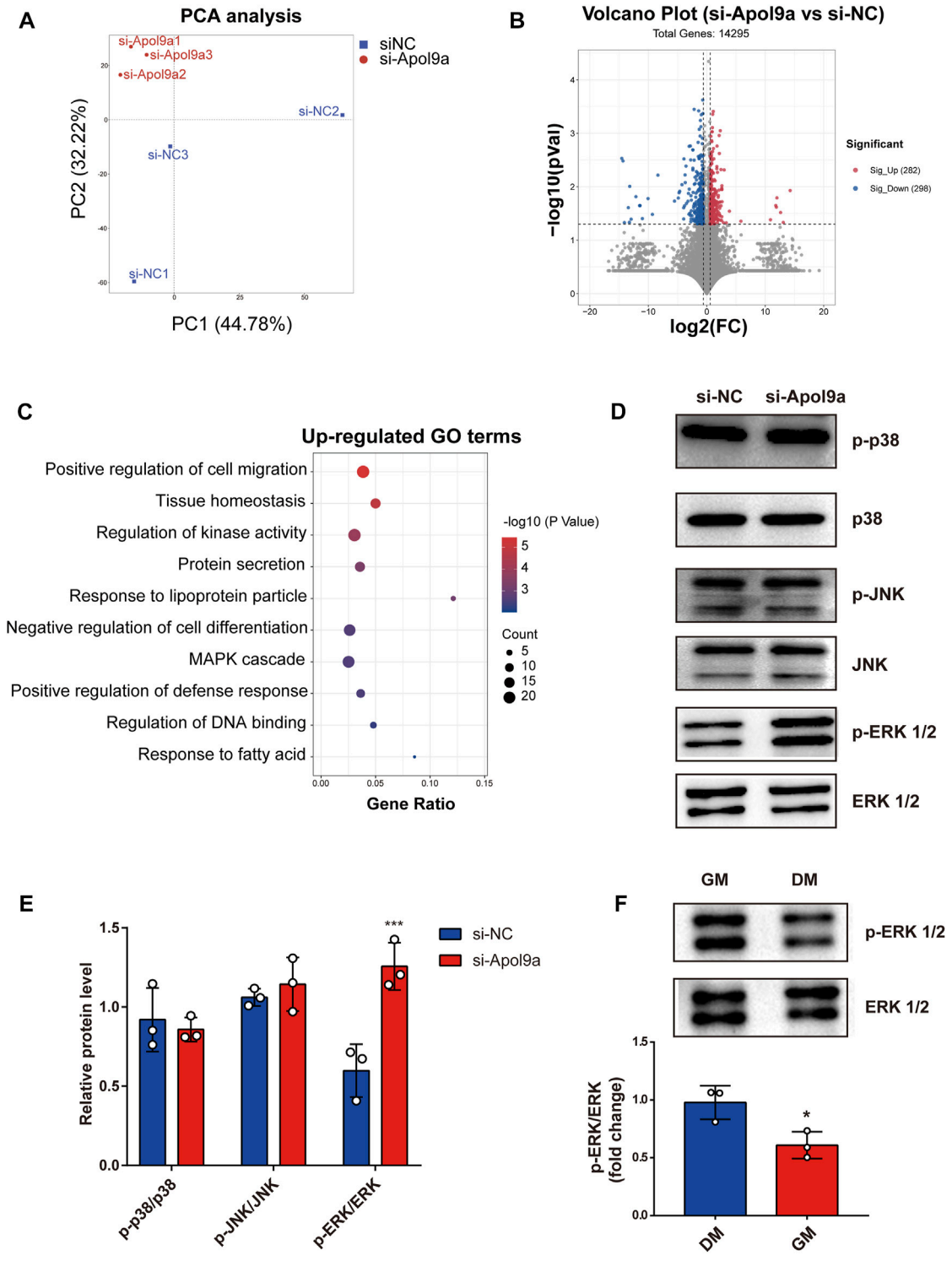

FIGURE 6
Transcriptomic data. C2C12 cells with or without si-*Apol9a* treatment was harvested after myogenic differentiation, and then transcriptomic analysis was performed. **(A)** Principal component analysis of RNA-seq data from C2C12 cells with (si-*Apol9a*) or without (si-NC) *Apol9a* knockdown after myogenic differentiation (n = 3 per group). **(B)** Volcano plot showing the DEGs in C2C12 cells with (si-*Apol9a*) or without (si-NC) *Apol9a* knockdown after myogenic differentiation. **(C)** Gene ontology analysis of upregulated DEGs. **(D)** Western blot analysis showed the protein levels of p-P38, P38, p-JNK, JNK, p-ERK1/2, and ERK1/2. **(E)** Gray scale analysis of western blot results determined using ImageJ software. **(F)** Western blot analysis for p-ERK1/2 and ERK1/2. C2C12 cells were cultured in GM or DM for 4 days. The data are expressed as mean ± SEM. $^{*}p < 0.05$, $^{**}p < 0.01$, $^{***}p < 0.001$ vs. si-NC group.

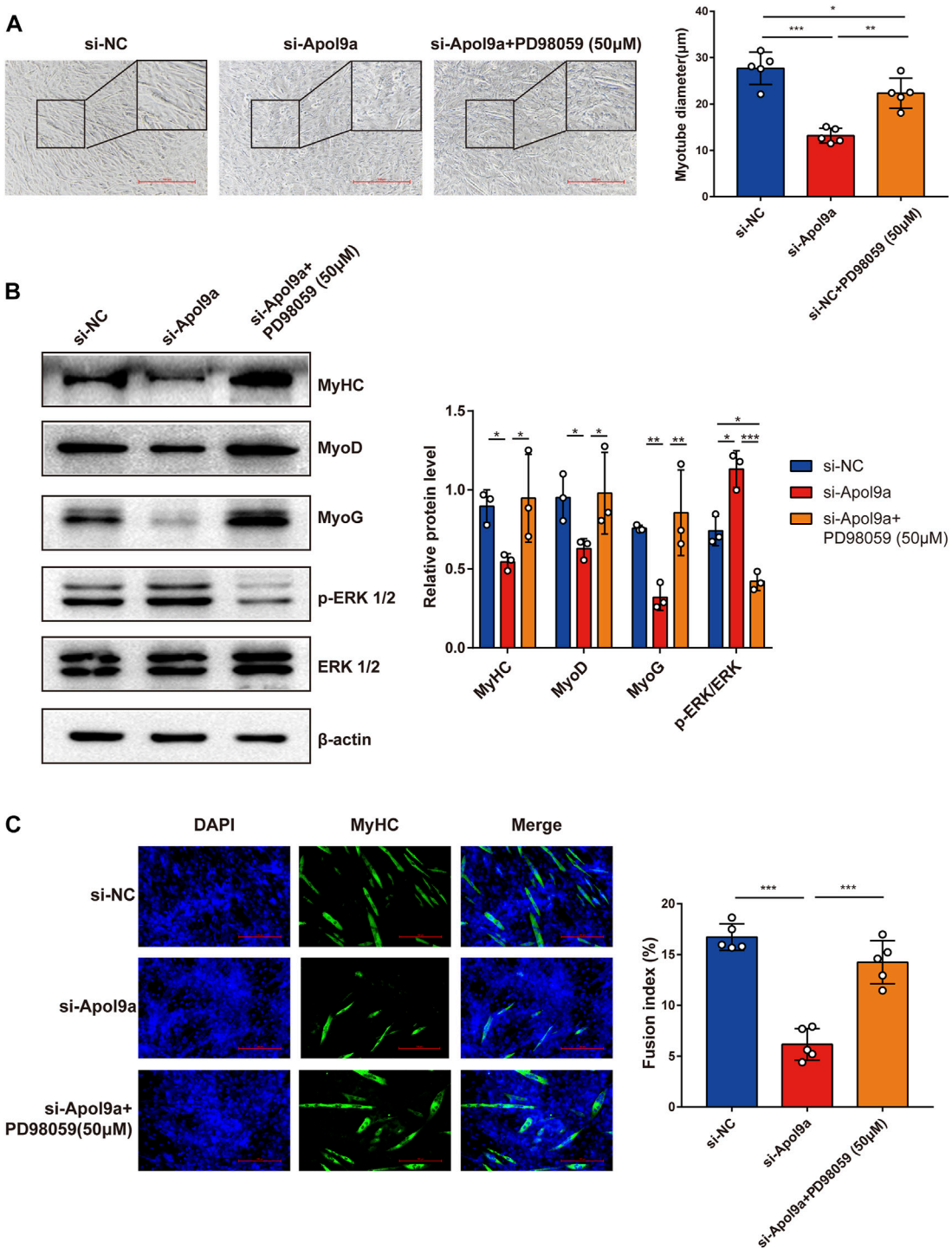

FIGURE 7
ERK inhibitor reverses *Apol9a* knockdown-induced inhibition of myogenesis. C2C12 cells were transfected with NC or *Apol9a* siRNA. After 12 h, the GM was replaced with the DM to induce differentiation or DM containing PD98059 (50 μm). **(A)** Morphology of C2C12 cells treated with si-NC, si-*Apol9a*, and si-*Apol9a* plus PD98059 (50 μm). The results of quantification of average myotube diameter are shown in the right. **(B)** Protein expression levels of MyHC, MyoD, MyoG, p-ERK1/2, and ERK1/2 as detected through western blot analysis. Gray intensity analysis is shown on the right. **(C)** Representative images of immunofluorescence for MyHC (green) are shown. The fusion index (%) was quantified and is shown on the right. Scale bar, 100 μm. Each experiment in this study was repeated at least three independent times. *$p < 0.05$, **$p < 0.01$, ***$p < 0.001$.

Myogenic differentiation is known to start with the induction of a specific set of transcription genes known as myogenic regulatory factors (MRFs), which include *Myf5*, *MyoD*, and *MyoG* (Chargé and Rudnicki, 2004; Ciciliot and Schiaffino, 2010). Comparison with the si-NC control group, the protein and mRNA expression levels of several myogenic differentiation markers, including Myf5, MyoD, MyoG, and MyHC, were remarkably decreased in differentiated C2C12 cells after si-*Apol9a* transfection (Figures 3B–D). To validate the effect of *Apol9a* deficiency on myotube formation, we evaluated the expression of MyHC protein through immunofluorescence in differentiated C2C12 cells and a quantitative analysis of the fusion index. As shown in Figure 3E, *Apol9a* knockdown cells displayed a different morphology and appeared to have shorter myofibers compared with the control group. Moreover, the fusion index was significantly decreased after *Apol9a* silencing (Figure 3E). Furthermore, we explored the effect of *Apol9a* overexpression on myogenic differentiation. Compared with the empty vector group, the Apol9a mRNA expression level was markedly increased in pcDNA3.1-*Apol9a*-transfected cells. Compared with the empty vector group, the Apol9a mRNA expression level was significantly increased in pcDNA3.1-*Apol9a*-transfected cells (Figure 4A), and the myotube diameter was significantly longer after *Apol9a* overexpression (Figure 4B). Western blot analysis showed that *Apol9a* overexpression significantly upregulated MyoG and MyHC protein levels (Figures 4C,D). Together, these results demonstrate that *Apol9a* knockdown inhibited myogenesis and *Apol9a* overexpression promoted myogenic differentiation.

Apol9a silencing decreases the content of cellular fatty acids

Apol9a is an apolipoprotein family member, and previous research has suggested that *Apol9a* has a role in lipid transport (Arvind and Rangarajan, 2016). To identify changes in the types of fatty acids and changes in lipid composition induced by *Apol9a* knockdown after cell differentiation, the types and contents of fatty acid in C2C12 cells with or without *Apol9a* knockdown after myogenic differentiation were determined through GC-MS and LC-MS, respectively. After *Apol9a* knockdown, the levels of various fatty acids (C16:0, C18:0, C18:2, and C22:6) significantly decreased (in comparison with the si-NC transfected cells) (Figure 5A). To further analyze changes in lipid composition, we applied LC-MS-based lipidomics to identify the specific types of lipids whose levels decreased in *Apol9a* knockdown cells. Moreover, orthogonal partial least squares-discriminant analysis (OPLS-DA) indicated different clustering of lipids from NC and *Apol9a*-silenced groups (Figure 5B). While the intensity levels of C16:0 fatty acid were mainly decreased in phosphatidylcholine (PC) and phosphatidylethanolamine (PE), those of C18:0 fatty acid were reduced in TG and PE (Figure 5D). In addition, a significant decrease was observed in the intensity levels of C18:2 fatty acid, especially in PC and TG (Figures 5C,E). Elevated skeletal muscle TG is reported to be related to insulin resistance in obesity and impaired skeletal muscle differentiation (Wu and Ballantyne, 2017), (Eum et al., 2020). Furthermore, our heatmap analysis revealed that many TG species (including C18:0 and C18:2 fatty acids) demonstrate a remarkable decrease (VIP >1 and $p < 0.05$) in C2C12 cells after *Apol9a* knockdown and myogenic differentiation (Figure 5F). Together, these results provide evidence that inhibition of myogenesis following *Apol9a* knockdown may be related to changes in lipid composition, especially changes in TG species.

RNA-seq analysis reveals the ERK1/2 pathway as a downstream target of *Apol9a*

To elucidate the underlying molecular mechanisms of *Apol9a* regulation of myogenesis, RNA sequencing was used to evaluate gene expression differences in C2C12 cells with or without *Apol9a* knockdown. Principal component analysis (PCA) was then performed to discriminate changes in expression between experimental groups. The PCA results revealed that the two groups could be completely separated based on their transcriptomes (Figure 6A). Based on the criteria of fold change ≥1.5 and $p < 0.05$, 580 differentially expressed genes (DEGs) between the two groups were identified, including 282 downregulated genes and 298 upregulated genes (Figure 6B). Then, GO analysis was applied to find the potential functions of the upregulated and downregulated genes. As shown in Figure 6C, significantly enriched functional terms, including “tissue homeostasis,” “response to lipoprotein particle,” “negative regulation of cell differentiation,” and “MAPK cascade,” were identified using the upregulated gene set. However, no specifically enriched biological processes were identified using the downregulated gene set (data not shown). The MAPK cascade pathway is essential for the regulation of myogenic differentiation (Jones et al., 2001; Keren et al., 2006; Xie et al., 2018; Boyer et al., 2019). We hypothesized that the ERK1/2 signaling pathway may play a role in the inhibition of myogenic differentiation induced by *Apol9a* knockdown. This hypothesis was subsequently confirmed by western blotting analyses of the ERK1/2 phosphorylation status and protein levels in C2C12 cells. Thus, while *Apol9a* knockdown markedly increased ERK1/2 phosphorylation during myogenesis, other MAPKs (JNK and p38) remained unchanged (Figure 6D). Moreover, phosphorylated ERK1/2 protein levels were significantly reduced after C2C12 differentiation (Figure 6E). In summary, our data demonstrate that *Apol9a* knockdown

activates the ERK1/2 signaling pathway during myogenic differentiation.

Inhibition of myogenic differentiation by Apol9a knockdown is reversed by an ERK inhibitor

To test the hypothesis that *Apol9a* regulates myogenic differentiation *via* the ERK1/2 signaling-dependent pathway, we applied PD98059, a specific inhibitor of ERK1/2, to the C2C12 cells. In agreement with our hypothesis, *Apol9a* knockdown-induced inhibition of myogenesis was almost completely reversed by PD98059 (Figure 7A). Furthermore, western blot analysis and immunofluorescence experiments demonstrated that ERK inhibition blocked the downregulation of myogenic genes (*MyHC*, *MyoD*, and *MyoG*) otherwise observed during *Apol9a* knockdown (Figures 7B,C). Together, these results provide evidence that *Apol9a* regulates myogenic differentiation *via* the ERK pathway.

Discussion

Skeletal muscle health is very crucial for human life at all stages. Moreover, skeletal muscle mass and myogenesis capacity are impaired in many pathological conditions, including obesity (Fu et al., 2016; Geiger et al., 2020). We confirmed that skeletal muscle mass and myogenesis capacity are decreased in obesity condition through the HFD-induced obesity mouse model. Although considerable attention has been paid to the investigation of therapeutic pharmacological supplements for improving muscle mass and function, progress is limited. Skeletal muscle plasticity is compromised due to impaired myogenesis (Suetta, 2017). By furthering our understanding of the molecular events regulating myogenesis, we may be able to develop an effective strategy for maintaining skeletal muscle integrity and plasticity.

In this study, *Apol9a* was identified as a new target gene critically involved in myogenesis. To our knowledge, this is the first study to report the underlying mechanisms and importance of *Apol9a* in skeletal muscle function. *Apol9a* belongs to the murine apolipoprotein L family and was previously reported to be an interferon-stimulated protein (Smith and Malik, 2009; Kreit et al., 2014). However, not much more is known about the function of *Apol9a*. In general, apolipoproteins play a role in lipid transportation (Su and Peng, 2020). For example, mouse apolipoprotein L9 is reported to be a PE-binding protein (Thekkinghat et al., 2019). In agreement with its proposed role in lipid transportation, our lipidomic data indicates that *Apol9a* knockdown decreased the PE level. Moreover, the TG and PC contents were reduced after *Apol9a* knockdown. Obesity leads to ectopic lipid deposition and abnormal lipid metabolism in skeletal muscle (Girousse et al., 2019). Our study confirmed that *Apol9a* is involved in multiple lipid transport activities, and its related functions should be further studied.

To explore the molecular mechanisms of *Apol9a* regulation of myogenic differentiation, RNA-seq was used to reconstruct *de novo* transcriptomes of *Apol9a* silenced cells. The results provide evidence that ERK signaling plays a crucial role in myogenesis. ERK1/2 signaling pathways are known to regulate numerous cellular processes, including cell proliferation, differentiation, and apoptosis (Cagnol and Chambard, 2010). While activated, ERK1/2 signaling plays a positive role in skeletal muscle cell proliferation, it negatively regulates myogenic differentiation (Jones et al., 2001). Moreover, studies have reported that ERK1/2 activation is elevated in atrophied and damaged skeletal muscles (Weston et al., 2003; Barreto et al., 2016; Oishi et al., 2019). Skeletal muscle differentiation is known to be mediated by several muscle regulatory factors, including MyoD, MyoG, and MyHC (Chal and Pourquié, 2017; Xu et al., 2017; Engquist and Zammit, 2021). *Apol9a* silencing significantly increased ERK1/2 phosphorylation and markedly suppressed the expression of muscle regulatory marker genes, such as *Myf5*, *MyoD*, *MyoG*, and *MyHC*. The experiments of *Apol9a* overexpression proved that *Apol9a* had a promoting effect on myogenic differentiation and significantly inhibited the ERK 1/2 pathway. In addition, MyoG and MyHC are the most significantly altered proteins corresponding to *Apo9a* overexpression. Application of an ERK inhibitor (PD98059) significantly reversed the aforementioned effects, indicating that *Apol9a*-ERK may be an upstream regulator of myogenic differentiation. Together, our results provide evidence that *Apol9a*-ERK may be a key therapeutic target for the management of skeletal muscle integrity and plasticity.

Conclusion

In summary, we indicate that *Apol9a* is a novel regulator of myogenic differentiation. *Apol9a* mRNA expression levels were significantly increased during myogenesis and decreased during obesity-induced muscle atrophy. *Apol9a* knockdown inhibited myogenic differentiation, possibly *via* the ERK1/2 signaling pathway. This study broadens our knowledge of the myogenic differentiation process and identifies a promising therapeutic target for intervention in obesity-related muscle atrophy.

Data availability statement

The datasets presented in this study can be found in online repositories. The names of the repository/repositories and

accession number(s) can be found below: https://www.ncbi.nlm.nih.gov/bioproject/PRJNA845924.

Ethics statement

The animal study was reviewed and approved by the Ethics Committee of Jiangnan University.

Author contributions

SZ and XJ designed the concept and study. XJ, RW, SC, and SZ performed the experiments. XJ and SJ conducted the bioinformatics analysis. SZ, XJ, and WW collected the data. SZ, XJ, and YC prepared, wrote and edited the manuscript. All authors reviewed and gave their approval of the final manuscript to be published.

Funding

This work was supported by the National Natural Science Foundation of China (Grant Nos. 82000808, 82000685), the Major Special Fund for Translational Medicine (Grant Nos. 2020ZHZD03), the Fundamental Research Funds for the Central Universities (Grant Nos. JUSRP12048) and the Innovation and Application Project of Medical and Public Health Technology of Wuxi Science and Technology (Grant Nos. N20202005). This current study was mainly sponsored by the Fund of Wuxi Healthcare Commission and the National Natural Science Foundation of China.

Acknowledgments

We would like to thank Jingwei Zhang for cell culture and technical assistance, Haiyong Zhao for RNA-seq analysis support, Yizhou Zhou for GC-MS and LC-MS analysis, Zhe Jing for qPCR, University of Jiangnan Department of Experimental Medicine animal care takers, and Lengyun Wei for discussions. We are particularly grateful to YC for his valuable suggestions and all members in his lab.

Conflict of interest

The authors declare that the research was conducted in the absence of any commercial or financial relationships that could be construed as a potential conflict of interest.

Publisher's note

Supplementary material

The Supplementary Material for this article can be found online at: https://www.frontiersin.org/articles/10.3389/fphar.2022.942061/full#supplementary-material

References

Arvind, T. A., and Rangarajan, P. N. (2016). Mouse Apolipoprotein L9 is a phosphatidylethanolamine-binding protein. *Biochem. Biophys. Res. Commun.* 479 (4), 636–642. doi:10.1016/j.bbrc.2016.09.161

Astrup, A., and Finer, N. (2000). Redefining type 2 diabetes: 'diabesity' or 'obesity dependent diabetes mellitus. *Obes. Rev.* 1 (2), 57–59. doi:10.1046/j.1467-789x.2000.00013.x

Barreto, R., Waning, D. L., Gao, H., Liu, Y., Zimmers, T. A., and Bonetto, A. (2016). Chemotherapy-related cachexia is associated with mitochondrial depletion and the activation of ERK1/2 and p38 MAPKs. *Oncotarget* 7 (28), 43442–43460. doi:10.18632/oncotarget.9779

Bonaldo, P., and Sandri, M. (2013). Cellular and molecular mechanisms of muscle atrophy. *Dis. Model. Mech.* 6 (1), 25–39. doi:10.1242/dmm.010389

Boyer, J. G., Prasad, V., Song, T., Lee, D., Fu, X., Grimes, K. M., et al. (2019). ERK1/2 signaling induces skeletal muscle slow fiber-type switching and reduces muscular dystrophy disease severity. *JCI Insight* 5 (10), 127356. doi:10.1172/jci.insight.127356

Brown, L. A., Lee, D. E., Patton, J. F., Perry, R. A., Jr., Brown, J. L., Baum, J. I., et al. (2015). Diet-induced obesity alters anabolic signalling in mice at the onset of skeletal muscle regeneration. *Acta Physiol. (Oxf).* 215 (1), 46–57. doi:10.1111/apha.12537

Cagnol, S., and Chambard, J. C. (2010). ERK and cell death: Mechanisms of ERK-induced cell death--apoptosis, autophagy and senescence. *Febs J.* 277 (1), 2–21. doi:10.1111/j.1742-4658.2009.07366.x

Chal, J., and Pourquié, O. (2017). Making muscle: Skeletal myogenesis *in vivo* and *in vitro*. *Development* 144 (12), 2104–2122. doi:10.1242/dev.151035

Chargé, S. B., and Rudnicki, M. A. (2004). Cellular and molecular regulation of muscle regeneration. *Physiol. Rev.* 84 (1), 209–238. doi:10.1152/physrev.00019.2003

Chen, X., Luo, Y., Huang, Z., Jia, G., Liu, G., and Zhao, H. (2017). Akirin2 regulates proliferation and differentiation of porcine skeletal muscle satellite cells via ERK1/2 and NFATc1 signaling pathways. *Sci. Rep.* 7, 45156. doi:10.1038/srep45156

Ciciliot, S., and Schiaffino, S. (2010). Regeneration of mammalian skeletal muscle. Basic mechanisms and clinical implications. *Curr. Pharm. Des.* 16 (8), 906–914. doi:10.2174/138161210790883453

DeFronzo, R. A., and Tripathy, D. (2009). Skeletal muscle insulin resistance is the primary defect in type 2 diabetes. *Diabetes Care* 32, S157–S163. doi:10.2337/dc09-S302

Du, M., Yan, X., Tong, J. F., Zhao, J., and Zhu, M. J. (2010). Maternal obesity, inflammation, and fetal skeletal muscle development. *Biol. Reprod.* 82 (1), 4–12. doi:10.1095/biolreprod.109.077099

Engquist, E. N., and Zammit, P. S. (2021). The satellite cell at 60: The foundation years. *J. Neuromuscul. Dis.* 8 (2), S183–s203. doi:10.3233/JND-210705

Eum, J. Y., Lee, G. B., Yi, S. S., Kim, I. Y., Seong, J. K., and Moon, M. H. (2020). Lipid alterations in the skeletal muscle tissues of mice after weight regain by feeding a high-fat diet using nanoflow ultrahigh performance liquid chromatography-

tandem mass spectrometry. *J. Chromatogr. B Anal. Technol. Biomed. Life Sci.* 1141, 122022. doi:10.1016/j.jchromb.2020.122022

Feraco, A., Gorini, S., Armani, A., Camajani, E., Rizzo, M., and Caprio, M. (2021). Exploring the role of skeletal muscle in insulin resistance: Lessons from cultured cells to animal models. *Int. J. Mol. Sci.* 22 (17), 9327. doi:10.3390/ijms22179327

Fu, X., Zhu, M., Zhang, S., Foretz, M., Viollet, B., and Du, M. (2016). Obesity impairs skeletal muscle regeneration through inhibition of AMPK. *Diabetes* 65 (1), 188–200. doi:10.2337/db15-0647

Geiger, A. E., Daughtry, M. R., Yen, C. N., Kirkpatrick, L. T., Shi, H., and Gerrard, D. E. (2020). Dual effects of obesity on satellite cells and muscle regeneration. *Physiol. Rep.* 8 (15), e14511. doi:10.14814/phy2.14511

Girousse, A., Gil-Ortega, M., Bourlier, V., Bergeaud, C., Sastourné-Arrey, Q., Moro, C., et al. (2019). The release of adipose stromal cells from subcutaneous adipose tissue regulates ectopic intramuscular adipocyte deposition. *Cell Rep.* 27 (2), 323–333. doi:10.1016/j.celrep.2019.03.038

Jones, N. C., Fedorov, Y. V., Rosenthal, R. S., and Olwin, B. B. (2001). ERK1/2 is required for myoblast proliferation but is dispensable for muscle gene expression and cell fusion. *J. Cell. Physiol.* 186 (1), 104–115. doi:10.1002/1097-4652(200101)186:1<104::AID-JCP1015>3.0.CO;2-0

Keren, A., Tamir, Y., and Bengal, E. (2006). The p38 MAPK signaling pathway: A major regulator of skeletal muscle development. *Mol. Cell. Endocrinol.* 252 (1-2), 224–230. doi:10.1016/j.mce.2006.03.017

Kreit, M., Paul, S., Knoops, L., De Cock, A., Sorgeloos, F., and Michiels, T. (2014). Inefficient type I interferon-mediated antiviral protection of primary mouse neurons is associated with the lack of apolipoprotein l9 expression. *J. Virol.* 88 (7), 3874–3884. doi:10.1128/JVI.03018-13

Kreit, M., Vertommen, D., Gillet, L., and Michiels, T. (2015). The interferon-inducible mouse apolipoprotein L9 and prohibitins cooperate to restrict theiler's virus replication. *PLoS One* 10 (7), e0133190. doi:10.1371/journal.pone.0133190

Lingvay, I., Sumithran, P., Cohen, R. V., and le Roux, C. W. (2021). Obesity management as a primary treatment goal for type 2 diabetes: Time to reframe the conversation. *Lancet* 399, 394–405. doi:10.1016/S0140-6736(21)01919-X

McCarthy, D., and Berg, A. (2021). Weight loss strategies and the risk of skeletal muscle mass loss. *Nutrients* 13 (7), 2473. doi:10.3390/nu13072473

Mengeste, A. M., Rustan, A. C., and Lund, J. (2021). Skeletal muscle energy metabolism in obesity. *Obesity* 29 (10), 1582–1595. doi:10.1002/oby.23227

Nishikawa, H., Asai, A., Fukunishi, S., Nishiguchi, S., and Higuchi, K. (2021). Metabolic syndrome and sarcopenia. *Nutrients* 13 (10), 3519. doi:10.3390/nu13103519

Nishikawa, H., Goto, M., Fukunishi, S., Asai, A., Nishiguchi, S., and Higuchi, K. (2021). Cancer cachexia: Its mechanism and clinical significance. *Int. J. Mol. Sci.* 22 (16), 8491. doi:10.3390/ijms22168491

Oishi, Y., Ogata, T., Ohira, Y., and Roy, R. R. (2019). Phosphorylated ERK1/2 protein levels are closely associated with the fast fiber phenotypes in rat hindlimb skeletal muscles. *Pflugers Arch.* 471 (7), 971–982. doi:10.1007/s00424-019-02278-z

Penna, F., Costamagna, D., Fanzani, A., Bonelli, G., Baccino, F. M., and Costelli, P. (2010). Muscle wasting and impaired myogenesis in tumor bearing mice are prevented by ERK inhibition. *PLoS One* 5 (10), e13604. doi:10.1371/journal.pone.0013604

Roh, E., and Choi, K. M. (2020). Health consequences of sarcopenic obesity: A narrative review. *Front. Endocrinol.* 11, 332. doi:10.3389/fendo.2020.00332

Schiaffino, S., Dyar, K. A., Ciciliot, S., Blaauw, B., and Sandri, M. (2013). Mechanisms regulating skeletal muscle growth and atrophy. *Febs J.* 280 (17), 4294–4314. doi:10.1111/febs.12253

Smith, E. E., and Malik, H. S. (2009). The apolipoprotein L family of programmed cell death and immunity genes rapidly evolved in primates at discrete sites of host-pathogen interactions. *Genome Res.* 19 (5), 850–858. doi:10.1101/gr.085647.108

Sousa-Victor, P., García-Prat, L., and Muñoz-Cánoves, P. (2022). Control of satellite cell function in muscle regeneration and its disruption in ageing. *Nat. Rev. Mol. Cell Biol.* 23 (3), 204–226. doi:10.1038/s41580-021-00421-2

Su, X., and Peng, D. (2020). The exchangeable apolipoproteins in lipid metabolism and obesity. *Clin. Chim. Acta.* 503, 128–135. doi:10.1016/j.cca.2020.01.015

Suetta, C. (2017). Plasticity and function of human skeletal muscle in relation to disuse and rehabilitation: Influence of ageing and surgery. *Dan. Med. J.* 64 (8), B5377.

Sun, L., Miyoshi, H., Origanti, S., Nice, T. J., Barger, A. C., Manieri, N. A., et al. (2015). Type I interferons link viral infection to enhanced epithelial turnover and repair. *Cell Host Microbe* 17 (1), 85–97. doi:10.1016/j.chom.2014.11.004

Thekkinghat, A. A., Yadav, K. K., and Rangarajan, P. N. (2019). Apolipoprotein L9 interacts with LC3/GABARAP and is a microtubule-associated protein with a widespread subcellular distribution. *Biol. Open* 8 (9), bio045930. doi:10.1242/bio.045930

Weston, A. D., Sampaio, A. V., Ridgeway, A. G., and Underhill, T. M. (2003). Inhibition of p38 MAPK signaling promotes late stages of myogenesis. *J. Cell Sci.* 116 (14), 2885–2893. doi:10.1242/jcs.00525

Wiedmer, P., Jung, T., Castro, J. P., Pomatto, L. C. D., Sun, P. Y., Davies, K. J. A., et al. (2021). Sarcopenia - molecular mechanisms and open questions. *Ageing Res. Rev.* 65, 101200. doi:10.1016/j.arr.2020.101200

Wu, H., and Ballantyne, C. M. (2017). Skeletal muscle inflammation and insulin resistance in obesity. *J. Clin. Invest.* 127 (1), 43–54. doi:10.1172/JCI88880

Xie, S. J., Li, J. H., Chen, H. F., Tan, Y. Y., Liu, S. R., Zhang, Y., et al. (2018). Inhibition of the JNK/MAPK signaling pathway by myogenesis-associated miRNAs is required for skeletal muscle development. *Cell Death Differ.* 25 (9), 1581–1597. doi:10.1038/s41418-018-0063-1

Xu, X., Ji, S., Li, W., Yi, B., Li, H., Zhang, H., et al. (2017). LncRNA H19 promotes the differentiation of bovine skeletal muscle satellite cells by suppressing Sirt1/FoxO1. *Cell. Mol. Biol. Lett.* 22, 10. doi:10.1186/s11658-017-0040-6

Yaffe, D., and Saxel, O. (1977). Serial passaging and differentiation of myogenic cells isolated from dystrophic mouse muscle. *Nature* 270 (5639), 725–727. doi:10.1038/270725a0

Zhang, J., Wang, W., Feng, N., Jiang, X., Zhu, S., and Chen, Y. Q. (2021). Ndufa6 regulates adipogenic differentiation via Scd1. *Adipocyte* 10 (1), 646–657. doi:10.1080/21623945.2021.2007590

Zhu, S., Wang, W., Zhang, J., Ji, S., Jing, Z., and Chen, Y. Q. (2022). Slc25a5 regulates adipogenesis by modulating ERK signaling in OP9 cells. *Cell. Mol. Biol. Lett.* 27 (1), 11. doi:10.1186/s11658-022-00314-y

Zhu, S., Zhang, J., Jiang, X., Wang, W., and Chen, Y. Q. (2022). Free fatty acid receptor 4 deletion attenuates colitis by modulating Treg Cells via ZBED6-IL33 pathway. *EBioMedicine* 80, 104060. doi:10.1016/j.ebiom.2022.104060

Zhu, S., Zhang, J., Wang, W., Jiang, X., and Chen, Y. Q. (2022). Blockage of NDUFB9-SCD1 pathway inhibits adipogenesis : Blockage of NDUFB9-SCD1 pathway inhibits adipogenesis. *J. Physiol. Biochem.* 78, 377–388. doi:10.1007/s13105-022-00876-7

Frontiers in Pharmacology

Explores the interactions between chemicals and living beings

The most cited journal in its field, which advances access to pharmacological discoveries to prevent and treat human disease.

Discover the latest Research Topics

See more →

Frontiers

Avenue du Tribunal-Fédéral 34
1005 Lausanne, Switzerland
frontiersin.org

Contact us

+41 (0)21 510 17 00
frontiersin.org/about/contact